Supported Tungsten Imido and Iridium Pincer Catalysts Towards Tandem Hydrocarbon Upgrading

by

Christopher M. R. Wright



This thesis is submitted in partial fulfilment of the requirement for the degree of Doctor of Philosophy at the University of Oxford

Wadham College

March 2017

The work described in this thesis was carried out in the Chemistry Research Laboratory, Mansfield Road, Oxford between October 2013 and March 2017 under the supervision of Professor Dermot O'Hare. All the work is my own unless stated to the contrary, and has not been previously submitted for any degree at this or any other university.



Christopher Michael Robert Wright
Wadham College
March 2017

Abstract

Supported Tungsten Imido and Iridium Pincer Catalysts Towards Tandem Hydrocarbon Upgrading

Christopher M. W. Wright **D.Phil Thesis**
Wadham College **Hilary Term 2017**

The principle aims of this thesis have been to develop well-defined heterogeneous catalysts for potential applications in tandem hydrocarbon upgrading. Catalysts for olefin oligomerisation and metathesis of α-olefins and transfer hydrogenation of alkanes based on tungsten mono-imido and PCP pincer iridium complexes have been synthesised and immobilised on solid supports. The reactivity of the immobilised catalysts has been tested and compared with the precursor complexes. Co-immobilisation of the two complexes on the same support has been undertaken.

Chapter One provides a background to the olefin metathesis reaction and the development of highly active tungsten mono-imido and ruthenium alkylidene complexes. A summary of the implementation of the olefin oligomerisation reaction by industry and the development of highly active systems based on group 6 metals is discussed, along with a mechanistic discussion. The SOMC grafting procedure is considered and the immobilisation of catalysts for alkane and olefin metathesis and oligomerisation discussed; with focus on support materials: silica, sMAO and AMO-LDHs. Finally, tandem catalysis and its use in hydrocarbon upgrading and copolymerisation are presented.

Chapter Two details the synthesis of $W(NR)Cl_4(THF)$ complexes and their conversion to $W(NR)Me_3Cl$ complexes employing TMA. The products are characterised by single crystal X-ray diffraction, NMR and FTIR spectroscopy. $W(NR)Me_3Cl$ complexes are shown to be active for the selective dimerisation of ethylene to 1-butene. Attempted formation of possible intermediates in the reaction is presented, and efforts to form mimics for silica supported species are also discussed.

Chapter Three describes the preparation of AMO-LDHs for use as catalyst supports. The effect on the surface hydroxyl content and structural properties of these materials by thermally treating them under vacuum is analysed. Their capability to act as supports for ethylene polymerisation after impregnation with MAO and $(^{n}BuCp)_2ZrCl_2$ is described.

Chapter Four investigates the immobilisation and characterisation of synthesised tungsten mono-imido complexes on sMAO, AMO-LDHs and silica, utilising SSNMR, FTIR and X-ray absorption spectroscopy. The reactivity of the grafted complexes towards ethylene oligomerisation is discussed. For the immobilised species effects of varying the imido ligand, temperature and solvent medium are reported. Attempts to immobilise ruthenium carbene complexes on AMO-LDHs and sMAO is detailed.

Chapter Five gives an account of the immobilisation of $Ir(^{tBu}PCP)HCl$ on sMAO which is characterised by SSNMR and FTIR spectroscopy. Molecular analogues of the supported species are synthesised and reactivity for the hydrogenation of ethylene compared. Transfer hydrogenation reaction with sMAO-$Ir(^{tBu}PCP)HCl$ and COA or ethane with TBE as a sacrificial H_2 acceptor are discussed. Finally, co-immobilisation of $W\{N(2,6\text{-}F\text{-}C_6H_3)\}Cl_4(THF)$ and $Ir(^{tBu}PCP)HCl$ on sMAO was carried out and the solid characterised by SSNMR spectroscopy.

Chapter Six provides experimental details and characterising data for the preceding chapters. An **Appendices** with crystallographic data, and characterising spectra for each chapter is provided, while the **Electronic Appendix** contains a combined CIF and checkcif for all the molecular structures presented.

Acknowledgements

Firstly I would like to thank Professor Dermot O'Hare for allowing me to begin my research career in his group as a Part II student all those years ago, and stay on to conduct this DPhil project. I am grateful for his help and advice, and for supporting multiple grant applications (EPSRC studentship, SCG Innovation Fund, RSC travel grant, ICOMC bursary), which have not only permitted me to undertake this project, but also facilitate travel to present at international conferences in Austria and Australia.

Secondly, huge thanks are reserved for JC and Zoë, who have helped me enormously, both with this project but also in developing my skills as a scientific researcher. To JC, who has taught me the rights, wrongs and 'shortcuts' of organometallic chemistry, who has kept a watchful eye over my project from the off and provided excellent discussion over a beer at the Uni Club. To Zoë, who's been a great fumehood neighbour, has ventured down many times to crystallography either with me or on my behalf, and has dedicated many hours to solving my disordered structures. Most importantly thanks for keeping the HCl/water topped up!

I must thank Dr. Nick Rees for running lots of SSNMR samples for me; Sandy for BET adventures and introduction to the wonders of SolidG; Kate for running all my TGA samples; Yue for guidance on capillary XRD; Zoë and Duncan for DFT; Golf for SEM images; Emma Gibson and Peter Wells at Diamond, who tried to teach me how to conduct EXAFS analysis on some very weak data; Team solid-state (Kate, Chunping, Dana) for helpful discussions about my adventures into the dark-side. I am also grateful to SCG Chemicals Ltd (Thailand) and Norner AS (Norway) for testing my catalysts on a larger scale, and for GPC data for the polymer samples.

I must also thank all those who have found the time to proof-read this thesis (JC, Sandy, Tom R, Zoë, Dana, Duncan and Tom W), your critiques have made this a much more coherent piece of work, for which I am hugely indebted.

Tom Arnold for looking after me as a Part II (I hope I wasn't too much of a pain), for the thrashings every time we played squash (I definitely got better), and your ridiculous wine drinking lifestyle which kept us all entertained.

Sandy for dragging me to circuits (or at least trying) most weeks, for testing my fire safety knowledge and for being Kaji's heir to the sMAO throne, we bow to your wisdom.

To O'Hare group members past and present who have made this such an enjoyable place to work. Hannah for G&T's at the club; Mark for enforced gin rums and asking Sue if she be wanting some grog; safety Sam for amazing cakes and a great time in Sydney; Coops for the after work beers; Dave for being the most fashion conscious chemist ever; Yue for cinema and foodie trips; good Golf and bad Phoom who has followed the Part II and DPhil adventure with me; Duncan for a great time in Sydney, and for redefining a 'weekend trip'; Kate for being incredibly generous and for providing me with food when I was in the CRL late writing; Tom R for amazing pork pies; Tom W and Josh for being good Part II students. To the thousands who have been on the Friday football mailing list but more to the few who have actually played each week, it's about all that has kept me sane. Special mention to the rise and subsequent demise of Organometallica FC, arguably the best Departmental five aside team in Oxford.

To all my friends who have given me escape from the Oxford bubble, especially to Dom and Max who put up with living with me, even if I've had to endure endless lacrosse chat. Here's to epic dinner parties, espresso martinis and virtual rounds of golf.

Finally I cannot thank my family and Al enough for all their help and support. To Dave, who has always faced huge adversity, but carries on with a joke and a smile, you are an inspiration. To mum and dad who have been so loving and supportive of me, and to Al whose encouragement and love I could not have done this without - thank you, I love you all so much.

Abbreviations list

°C	degrees Celcius
Å	Ångström, 10^{-10} m
acac	acetylacetonate, $CH_3COCHCOCH_3$
AMO-LDH	aqueous miscible organic solvent treated layered double hydroxide
AMOST	aqueous miscible organic solvent treatment
α_{OH}	hydroxyl number
Ar^F	3,5-bis(trifluoromethyl)phenyl, 3,5-CF_3-C_6H_3
atm	atmosphere, 101,325 Pa
BET	Brunauer-Emmett-Teller
Biphen	3,3′-di-tertbutyl-5,5′,6,6′-tetramethyl-1,1′-biphenyl-2,2′-diolate
BJH	Barrett-Joyner-Halenda
^{n}Bu	*n*-butyl, $CH_2CH_2CH_2CH_3$
^{t}Bu	*tert*-butyl, CMe_3
cent	centroid
COA	cyclooctane, C_8H_{16}
COE	cyclooctene, C_8H_{14}
Cp	cyclopentadienyl, C_5H_5
Cp*	pentamethylcyclopentadienyl, C_5Me_5
CPMAS	cross polarisation magic angle spinning
CCDC	Cambridge crystallographic data centre
Cy	cyclohexyl, C_6H_{11}
δ	chemical shift
δ_{OH}	hydroxyl density
d	doublet
DBMP	2,6-bis(diphenylmethyl)-4-methylphenyl, 2,6-$CHPh_2$-4-Me-C_6H_2
DCM	dichloromethane, CH_2Cl_2
DEAC	diethylaluminium chloride, $AlEt_2Cl$
DFT	density functional theory
ΔHm	temperature of melting
ΔHc	temperature of crystallisation
ΔHm°	temperature of melting for 100% crystalline polymer
Dipp	diisopropylphenyl, 2,6-^{i}Pr-C_6H_3

DMAC	dimethylaluminium chloride, $AlMe_2Cl$
DME	dimethyl ether, CH_3OCH_3
DNP-SENS	dynamic nuclear polarisation surface enhancement NMR spectroscopy
DPMAS	direct polarisation magic angle spinning
DPPE	1,3-bis(diphenylphosphino)ethane, $Ph_2PCH_2CH_2PPh_2$
DSC	differential scanning calorimetry
DTG	derivative thermogravimetric
η	hapticity
EBI	ethylenebis(indenyl), $C_9H_6(CH_2CH_2)C_9H_6$
EBI*	ethylenebis(hexamethylindenyl), $C_9Me_6(CH_2CH_2)C_9Me_6$
EPR	electron paramagnetic resonance
ESD	estimated standard deviation
Et	ethyl, CH_2CH_3
Et_2O	diethyl ether, $CH_3CH_2OCH_2CH_3$
EXAFS	extended X-ray absorption fine structure
FTIR	Fourier transform infrared
FWHM	full width half maximum
$G_{2.28}$(L)	*G*-parameter calculated at 2.28 Å from ligand L
GCMS	gas chromatography mass spectrometry
GPC	gel permeation chromatography
h	hour
HDPE	high density polyethylene
HOMO	highest occupied molecular orbital
HPDEC	high powered decoupling
Hz	Hertz
ICP	inductively coupled plasma
K	Kelvin
LAO	linear α-olefin
LDH	layered double hydroxide
LDH-MAO	methylaluminoxane impregnated layered double hydroxide
LDO	layered double oxide
LUMO	lowest unoccupied molecular orbital
μ	bridging
m	multiplet

M	mol dm^{-3}; metal
MAS	magic angle spinning
MAO	methylaluminoxane
Me	methyl, CH_3
Mes	mesityl, 2,4,6-Me-C_6H_2
M_n	number-average molecular weight
MO	molecular orbital
M_w	weight-average molecular weight
NHC	N-heterocyclic carbene
NMR	nuclear magnetic resonance
Np	neopentyl, $CH_2{}^tBu$
Ω	solid angle
P	pressure
Pa	Pascal
PDI	polydispersity index
PE	polyethylene
Ph	phenyl, C_6H_5
ppm	parts per million
^{i}Pr	isopropyl, $CHMe_2$
Py	pyridine
PXRD	powder X-ray diffraction
q	quartet
ROMP	ring opening metathesis polymerisation
rpm	revolutions per minute
s	singlet
SEM	scanning electron microscopy
≡SiO	silanol ligand on the surface of silica
sMAO	solid polymethylaluminoxane
SOMC	surface organometallic chemistry
SP	square pyramidal
SSMAO	silica supported methylaluminoxane
SSNMR	solid-state nuclear magnetic resonance
T	temperature
T_m	melting temperature

t	triplet; time
TBA	*tert*-butyl ethane, $CH_3CH_2CMe_3$
TBE	*tert*-butyl ethylene, CH_2CHCMe_3
TBP	trigonal bipyramidal
TEA	triethylaluminium, $AlEt_3$
TGA	thermogravimetric analysis
THF	tetrahydrofuran, C_4H_8O
TIBA	triisobutylaluminium, Al^iBu_3
TMA	trimethylaluminium, $AlMe_3$
TMS	trimethylsilyl, $SiMe_3$
TOF	turnover frequency
TON	turnover number
UHMWPE	ultra-high molecular weight polyethylene
UV/Vis	ultraviolet/visible
XAS	X-ray absorption spectroscopy
XANES	X-ray absorption near edge structure

Key to compound identification

Chapter Two

1.1 W{N(C_6H_5)}Cl_4(THF)

1.2 W{N(2,6-Me-C_6H_3)}Cl_4(THF)

1.3 W{N(3,5-Me-C_6H_3)}Cl_4(THF)

1.4 W{N(2,4,6-Me-C_6H_2)}Cl_4(THF)

1.5 W{N(2,6-^{i}Pr-C_6H_3)}Cl_4(THF)

1.6 W{N(4-OMe-C_6H_4)}Cl_4(THF)

1.7 W{N(2,6-F-C_6H_3)}Cl_4(THF)

1.8 W{N(3,5-CF_3-C_6H_3)}Cl_4(THF)

2.1 W{N(C_6H_5)}Me_3Cl

2.2 W{N(2,6-Me-C_6H_3)}Me_3Cl

2.3 W{N(3,5-Me-C_6H_3)}Me_3Cl

2.4 W{N(2,4,6-Me-C_6H_2)}Me_3Cl

2.5 W{N(2,6-^{i}Pr-C_6H_3)}Me_3Cl

2.6 W{N(4-OMe-C_6H_4)}Me_3Cl

2.7 W{N(2,6-F-C_6H_3)}Me_3Cl

2.8 W{N(3,5-CF_3-C_6H_3)}Me_3Cl

3.6 W{N(4-OMe-C_6H_4)}Me_3Cp

Chapter Four

sMAO- solid polymethylaluminoxane supported

$LDH(X)_y$ Mg_3Al-X (X = CO_3^{2-}, SO_4^{2-} or NO_3^-) AMO-LDH thermally treated under vacuum at y °C for 6 hours

$LDH(X)_y$- AMO-LDH supported

$SiO_{2-(y)}$ silica thermally treated under vacuum at y °C for 6 hours

$SiO_{2-(y)}$- silica supported

G2 Grubbs 2nd generation catalyst, Ru(NHC)(PCy_3)(CHPh)Cl_2

HG2 Hoveyda-Grubbs 2nd generation catalyst, Ru(NHC){CH(2-O^{i}Pr-C_6H_4)}Cl_2

NHC = 1,3-bis(2,4,6-trimethylphenyl)imidazolin-2-ylidene

Chapter Five

$^{t\text{Bu}}$PCP 2,6-($CH_2P^tBu_2$)-C_6H_3

Table of Contents

Chapter One – Introduction 1

1.1. Alkene oligomerisation 2

1.1.1. Industrial applications and catalysts 2

1.1.2. Group 6 selective ethylene oligomerisation catalysts 3

1.1.3. Tungsten imido complexes 4

1.1.4. Oligomerisation mechanisms 7

1.2. Well-defined heterogeneous catalysis 11

1.2.1. Benefits of complex immobilisation 11

1.2.2. Immobilisation of well-defined molecular pre-catalysts 11

1.2.3. Support preparation 13

1.2.4. Influence of the support 15

1.2.5. Supported metathesis catalysts 16

1.2.6. Supported catalysts for alkane metathesis 18

1.2.7. Supported olefin oligomerisation catalysts 18

1.3. Layered double hydroxides (LDHs) 19

1.4. Solid polymethylaluminoxane (sMAO) 21

1.5. Tandem catalysis 22

1.5.1. Underlying principle 22

1.5.2. Hydrocarbon upgrading 22

1.5.3. Copolymerisation 23

1.6. Scope of this thesis 24

1.7. References 25

Chapter Two - Tungsten mono-imido oligomerisation catalysts 30

2.1. Introduction 31

2.2. Synthesis and characterisation of W(NR)Cl_4(THF) complexes 32

2.3. Reactivity towards alkyl aluminium reagents 39

2.3.1. Synthesis and characterisation of W(NR)Me_3Cl complexes 39

2.3.2. Attempted synthesis of W{N(2,6-^{i}Pr-C_6H_3)}Me_2Cl_2 45

2.3.3. Synthesis of W(O)Me_3Cl 46

2.3.4. Attempted synthesis of W{N(2,6-^{i}Pr-C_6H_3)}Np_3Cl utilising $AlNp_3$ 47

2.4. Reactivity of W(NR)Me_3Cl complexes towards α-olefins 48

2.4.1. Oligomerisation of ethylene utilising W{N(2,6-^{i}Pr-C_6H_3)}Me_3Cl (2.5) 48

2.4.2. Reactivity of W(NR)Me_3Cl complexes towards heavier α-olefins 55

2.5. Formation of reactive intermediates 56

2.5.1. Formation of cationic complexes 56

2.5.1.1. Reactions with $NaBAr^{F}_4$ 56

2.5.1.2. Reactions with $AgPF_6$ 58

2.5.2. Attempted metal hydride formation 59

2.5.3. Attempted metallacycle formation 60

2.6. Further reactivity of W(NR)Me_3Cl complexes 60

2.6.1. Synthesis of W{N(4-OMe-C_6H_4)}Me_3Cp (3.6) 60

2.6.2. Attempted alkylidene formation 63

2.6.3. Silica mimic reactions with (^{t}BuO)$_3$SiOH and (^{t}BuO)$_3$SiOLi 64

2.7. Conclusions 66

2.8. References 67

Chapter Three - Preparation of layered double hydroxides for use as single-site catalyst supports 70

3.1. Introduction 71

3.2. LDH synthesis and thermal treatment under vacuum 72

3.2.1. Thermal vacuum treatment of Mg_3Al-SO_4 and Mg_3Al-CO_3 AMO-LDHs 72

3.3. Structure of dehydroxylated Mg_3Al-SO_4 AMO-LDH 73

3.4. Surface hydroxyl concentration 80

3.5. Effect of dehydroxylation temperature on catalytic activity 85

3.5.1. Introduction to supported metallocene catalysts 85

3.5.2. Complex immobilisation on Mg_3Al-SO_4 AMO-LDH-MAO 86

3.5.3. Slurry-phase ethylene polymerisation 86

3.5.4. Polymer characterisation 88

3.6. Conclusions 89

3.7. References 90

Chapter Four - Characterisation and reactivity of solid catalysts 92

4.1. Introduction 93

4.2. Solid polymethylaluminoxane (sMAO) immobilised complexes 94

4.2.1. Immobilisation and characterisation 94

4.2.2. Heterogeneous olefin oligomerisation studies 103

4.2.2.1. Effect of methylating the precursor complex 103

4.2.2.2. Variation of the imido group 105

4.2.2.3. Temperature study 108

4.2.2.4. Solvent Effects 109

4.2.2.5. Loading study 111

4.2.3. Gas phase reaction 111

4.2.4. Scale-up reactions 112

4.2.5. sMAO-W{N(4-OMe-C_6H_4)}Me_3Cp (sMAO-3.6) 114

4.2.6. sMAO-W(O)Cl_4 114

4.3. Layered double hydroxide (LDH) supported complexes 115

4.3.1. Effect of the interlayer anion 115

4.3.1.1. Complex immobilisation 115

4.3.1.2. Characterisation of the supported species 117

4.3.1.3. Decomposition study 118

4.3.1.4. Reactivity towards ethylene 118

4.3.2. Immobilisation procedure and alkyl aluminium co-catalyst effects 120

4.3.3. Dehydroxylation of the support 122

4.3.3.1. Catalyst loading 122

4.3.3.2. Reactivity towards α-olefins 125

4.4. X-ray absorption spectroscopy (XAS) of supported complexes 125

4.5. Silica supported 1.5 ($SiO_{2-(150)}$-1.5) 128

4.6. Supported ruthenium carbene complexes 130

4.7. Conclusions 131

4.8. References 132

Chapter Five - Supported iridium pincer transfer hydrogenation catalysts towards tandem hydrocarbon upgrading 139

5.1. Introduction 136

5.1.1. Transfer hydrogenation 136
5.1.2. Supported pincer iridium complexes 139

5.2. Synthesis of Ir($^{t\text{Bu}}$PCP)H$_4$ 141

5.3. Immobilisation of Ir($^{t\text{Bu}}$PCP)HCl on sMAO 141

5.4. Synthesis of molecular analogues of the supported species 144

5.5. Alkene hydrogenation reactions 149

5.6. Transfer hydrogenation reactions 151

5.7. Co-immobilisation of W{N(2,6-F-C$_6$H$_3$)}Cl$_4$(THF) (1.7) and Ir($^{t\text{Bu}}$PCP)HCl on sMAO 152

5.7.1. Immobilisation and characterisation 152
5.7.2. Reactivity towards ethane 154

5.8. Conclusions 154

5.9. Future work 155

5.10. References 156

Chapter Six - Experimental details 158

6.1. General details 159

6.1.1. Commercially supplied reagents 159
6.1.2. Synthesis of literature compounds 160
6.1.3. Solution-state nuclear magnetic resonance (NMR) spectroscopy 160
6.1.4. Solid-state NMR (SSNMR) spectroscopy 160
6.1.5. Fourier transform infrared (FTIR) spectroscopy 160
6.1.6. Single crystal X-ray diffraction 160
6.1.7. DFT calculations 161
6.1.8. Gas chromatography mass spectrometry (GCMS) analysis 161
6.1.9. Elemental analysis 161
6.1.10. General oligomerisation procedure 162
6.1.11. General ethylene polymerisation procedure 162

6.2. Experimental details for Chapter Two 162

6.2.1. Synthesis of W(NR)Cl$_4$(THF) complexes 162
6.2.2. Reaction of 1.5 and triethylaluminium (TEA) 166
6.2.3. Synthesis of W(NR)Me$_3$Cl complexes 166
6.2.4. Attempted synthesis of W{N(2,6-^{i}Pr-C$_6$H$_3$)}Me$_2$Cl$_2$ 169

6.2.5. Reaction of $W(O)Cl_4$ and TMA 170
6.2.6. Reaction of $1.5(Et_2O)$ and $AlNp_3$ 170
6.2.7. Homogeneous oligomerisations 170
6.2.8. Reaction of 2.5 with $AlCl_3$ 171
6.2.9. Reactions of 2.5 with propylene 172
6.2.10. Reaction of 2.7 with 1-hexene and 1-octene 172
6.2.11. Reaction of 2.5 with MeLi 172
6.2.12. Reaction of 2.5 with AgF 172
6.2.13. Reactions with $NaBAr^F_4$ 173
6.2.14. Reactions with $AgPF_6$ 173
6.2.15. Hydride formation and reduction reactions 174
6.2.16. Reaction of $W\{N(2,6\text{-}^{i}Pr\text{-}C_6H_3)\}Cl_4$ with $BrMgC_4H_8MgBr$ 174
6.2.17. Reactions with lithium or sodium cyclopentadienide (LiCp or NaCp) 174
6.2.18. Synthesis of $W\{N(4\text{-}OMe\text{-}C_6H_4)\}Me_3Cp$ (3.6) 175
6.2.19. Reaction of 3.6 with trityl BAr^F_4 175
6.2.20. Reactions with $(^{t}BuO)_3SiOLi$ 175
6.2.21. Reaction of 2.5 with $(^{t}BuO)_3SiOH$ 177
6.2.22. Reaction with neopentyl lithium 177

6.3. Experimental details for Chapter Three 178

6.3.1. Thermal vacuum treatment of AMO-LDHs 178
6.3.2. Thermogravimetric analysis (TGA) 178
6.3.3. Specific surface area analysis 179
6.3.4. Powder X-ray diffraction (XRD) analysis in capillary mode 179
6.3.5. Scanning electron microscopy (SEM) imaging 179
6.3.6. Surface hydroxyl titrations with $Mg(CH_2Ph)_2(THF)_2$ 179
6.3.7. Modelling the LDH surface structure 179
6.3.8. Synthesis of $Mg_3Al\text{-}SO_4$ AMO-LDH-MAO 180
6.3.9. Immobilisation of $(^{n}BuCp)_2ZrCl_2$ onto $Mg_3Al\text{-}SO_4$ AMO-LDH-MAO 180
6.3.10. Gel permeation chromatography (GPC) 180

6.4. Experimental details for Chapter Four 180

6.4.1. General procedure for the immobilisation of complexes on sMAO 180
6.4.2. General procedure for testing the ethylene oligomerisation activity of the solid catalysts 183

6.4.3. Scale-up oligomerisations 183
6.4.4. Differential scanning calorimetry (DSC) 183
6.4.5. Reactivity towards 1-hexene and 1-octene 183
6.4.6. Immobilisation of 1.5 on $LDH(X)_{150}$ ($X = SO_4^{2-}$, CO_3^{2-} or NO_3^-) 183
6.4.7. Loading study of 1.5 on $LDH(CO_3)_{150}$ 184
6.4.8. Decomposition study of 1.5 with HCl 185
6.4.9. Impregnation of alkyl aluminium reagents on $LDH(SO_4)_{150}$ and subsequent reaction with 1.5 185
6.4.10. Immobilisation by incipient wetness 185
6.4.11. Immobilisation of 2.5 on $LDH(SO_4)_{150}$ 186
6.4.12. Loading study of 2.7 on $LDH(SO_4)_{300/450}$ 186
6.4.13. Immobilisation of $W\{N(2,6\text{-}^{i}Pr\text{-}C_6H_3)\}(CH^{t}Bu)(CH_2{}^{t}Bu)_2$ on $LDH(CO_3)_{150}$. 186
6.4.14. Immobilisation of $W(O)Cl_4$ on $LDH(CO_3)_{150}$ 187
6.4.15. X-ray absorption spectroscopy (XAS) 187
6.4.16. Immobilisation of 1.5 on $SiO_{2\text{-}(150)}$ 187
6.4.17. Reaction of Grubbs 2nd generation (G2) and Hoveyda-Grubbs 2nd generation (HG2) catalysts with $LDH(SO_4)_{250/350/450}$ 187
6.4.18. Immobilisation of G2 or HG2 on sMAO and their subsequent reactivity towards olefins 188

6.5. Experimental details for Chapter Five 188

6.5.1. Synthesis of Ir($^{t\text{Bu}}$PCP)HCl and Ir($^{t\text{Bu}}$PCP)H_4 188
6.5.2. Synthesis of sMAO-Ir($^{t\text{Bu}}$PCP)HCl 189
6.5.3. Reaction of Ir($^{t\text{Bu}}$PCP)HCl with TMA (Al/Ir = 1) 189
6.5.4. Reaction of Ir($^{t\text{Bu}}$PCP)HCl with MAO (Al/Ir = 150) 190
6.5.5. Synthesis of [Ir($^{t\text{Bu}}$PCP)H(N_2)][$BAr^F{}_4$] 190
6.5.6. General procedure for hydrogenation reactions 191
6.5.7. General procedure for transfer hydrogenation reactions 191
6.5.8. Co-immobilisation of 1.7 and Ir($^{t\text{Bu}}$PCP)HCl on sMAO 192
6.5.9. Reaction of sMAO(1.7/Ir($^{t\text{Bu}}$PCP)HCl) with ethane 192

6.6. References 193

Appendices A1

Appendix for Chapter Two A2

2.1. $W(NR)Cl_4(THF)$ complexes (1.1-1.8) A2

2.1.1. Single crystal X-ray diffraction data tables A2

2.1.2. NMR spectra A6

2.1.3. FTIR spectra A15

2.1.4. Solid angle calculations and spacefilled models A19

2.2. $W(NR)Me_3Cl$ complexes (2.1-2.8) A21

2.2.1. Single crystal X-ray diffraction data tables A21

2.2.2. NMR spectra A24

2.2.3. FTIR spectra A33

2.2.4. Solid angle calculations and spacefilled models A35

2.3. Synthesis of $W(O)Me_3Cl$ A37

2.4. Oligomerisation reactions with 2.5 ..... A37

2.5. Reaction of 2.5 with $AlCl_3$ A41

2.6. Temperature study A41

2.7. Reaction of 2.5 with propylene A42

2.8. Reaction of 2.7 with 1-hexene and 1-octene A43

2.9. Reactions with $NaBAr^F{}_4$ A44

2.10. Reactions with $AgPF_6$ A45

2.11. Synthesis of $W\{N(4\text{-}OMe\text{-}C_6H_4)\}Me_3Cp$ (3.6) A47

2.11.1. Single crystal X-ray diffraction data table A47

2.11.2. NMR spectra A48

Appendix for Chapter Three A49

3.1. Thermogravimetric Analysis A49

3.2. PXRD data A55

3.3. BET isotherms and BJH pore volume distributions A56

3.4. SEM imaging A68

3.5. Surface hydroxyl titrations A69

Appendix for Chapter Four A70

4.1. Characterisation of sMAO immobilised complexes A70

4.1.1. Solid-state NMR (SSNMR) spectroscopy A70

4.1.2. FTIR spectroscopy A74

4.2. Oligomerisation studies with sMAO supported complexes A79

4.2.1. Activity correlations with structural and spectroscopic parameters of $W(NR)Cl_4(THF)$ complexes (1.1–1.8) A79
4.2.2. Reactivity towards 1-hexene and 1-octene A80
4.2.3. Temperature study of ethylene oligomerisation utilising sMAO-1.5 ..... A81
4.2.4. Solvent study A81
4.2.5. Loading study A82
4.2.6. Scale-up polymer analysis A82

4.3. Layered double hydroxide (LDH) supported complexes A83

4.3.1. Variation of the interlayer anion A83
4.3.1.1. SSNMR spectroscopy A83
4.3.1.2. FTIR spectroscopy A84
4.3.2. Impregnation with MAO A87
4.3.2.1. $LDH(SO_4)_{150}$-MAO-1.5 ..... A87
4.3.2.2. Immobilisation of a mixture of 1.5 and MAO on $LDH(SO_4)_{150}$ by incipient wetness A89
4.3.3. $LDH(SO_4)_{150}$-2.5 ..... A90
4.3.4. Effect of dehydroxylating the AMO-LDH support A91
4.3.4.1. SSNMR spectroscopy A91
4.3.4.2. FTIR spectroscopy A92
4.3.5. XAS analysis A92

Appendix for Chapter Five A93

5.1. sMAO-Ir($^{t\text{Bu}}$PCP)HCl A93

5.2. Reaction of Ir($^{t\text{Bu}}$PCP)HCl with MAO (Al/Ir = 150) A94

5.3. Reaction of Ir($^{t\text{Bu}}$PCP)HCl with TMA A95

5.4. Reaction of Ir($^{t\text{Bu}}$PCP)HCl with $NaBAr^F_4$ A97

5.4.1. NMR spectroscopy A97
5.4.2. Single crystal X-ray diffraction data table A99

5.5. Hydrogenation reactions A100

5.5.1. Reaction between Ir($^{t\text{Bu}}$PCP)H_4 and ethylene A100
5.5.2. Hydrogenation of ethylene with Ir($^{t\text{Bu}}$PCP)HCl and TMA (Al/W = 1) A100
5.5.3. Reaction of Ir($^{t\text{Bu}}$PCP)HCl and MAO (Al/W = 150) with ethylene A101
5.5.4. Hydrogenation of ethylene with Ir($^{t\text{Bu}}$PCP)HCl and MAO (Al/W = 150) A102

Chapter One – Introduction

"Time is the best appraiser of scientific work, and I am aware that an industrial discovery rarely produces all its fruit in the hands of its first inventor." **Louis Pasteur**

1.1. Alkene oligomerisation

1.1.1. Industrial applications and catalysts

Due to their ubiquitous use in the manufacture of everyday goods such as plastics, lubricants and detergents, there is increasing demand for linear α-olefins (LAOs). Recently, shale gas exploration has resulted in large feedstocks of ethane which can be cracked (thermally or catalytically) on a huge scale to produce ethylene.[1] Ethylene oligomerisation catalysts can convert this monomer selectively into 1-butene, 1-hexene and 1-octene (commonly employed as co-monomers in polyethylene production).[2] However, many of the catalysts used in industry show poor selectivity, producing a statistical (Schulz-Flory) distribution of even numbered α-olefins of varying chain length. For example, the Shell Higher Olefin Process (SHOP)[3] exploits a nickel-phosphine catalyst to oligomerise ethylene, resulting in a mixture of even α-olefins from C_4 to C_{40}, of which only the C_8–C_{16} (detergent) fraction is desired. Double bond isomerisation over a solid potassium catalyst followed by an olefin metathesis reaction utilising an alumina supported molybdate catalyst, converts the undesired fractions into the idealised range.[4] Some processes, like Axens Alphaselect, produce a more selective range of oligomers (C_4–C_{10}) where the distribution can be changed by variation of the metal to co-catalyst ratio, in this case Zr:Al.[5] Axens have also developed Dimersol-E, Dimersol-X and Dimersol-G processes which dimerise ethylene, propylene and butenes feeds to butenes, hexenes and octenes respectively. The Dimersol-G process comprises of a mixture of a nickel (II) salt and ethylaluminium chloride derivative, forming the active catalyst *in situ*. Thirty five Dimersol units have been licensed with a total processing capacity exceeding 4.5 million tons of feed per year.[5]

In 1967, workers at Union Carbide filed a patent which described the selective trimerisation of ethylene to 1-hexene by chromium (III) 2-ethylhexanoate using poly-isobutylaluminium oxide as a co-catalyst with subsequent copolymerisation yielding a butyl branched polymer.[6] In the 1990s, Phillips Petroleum utilised this chromium complex with a 2,5-dimethylpyrrole ligand and Et_2AlCl or $AlEt_3$ as co-catalysts, to produce 1-hexene in high yields (93 wt%) at 115 °C and 100 bar ethylene in cyclohexane. This system produces *ca*. 47,000 tons of 1-hexene per annum.[7] Workers at Sasol have recently reported an ethylene tetramerisation system by combining the PNP pincer ligand $Ph_2PN(^iPr)PPh_2$ with $Cr(acac)_3$ and 300 equivalents of methylaluminoxane (MAO) at 45 °C and 45 bar of ethylene to produce octenes (68 wt%) of which 98.8 wt% is 1-octene.[8]

One of the most selective industrial systems is the Axens AlphaButol process which utilises a titanium based catalyst ($Ti(OBu)_4/AlEt_3$) and is high yielding (~93% conversion in 15 minutes at 2 MPa ethylene pressure) and shows high selectivity towards C_4 olefins (>99%).[9] The AlphaButol process produces 500,000 tons per annum, accounting for almost 25% of the world's 1-butene supply.[5]

1.1.2. Group 6 selective ethylene oligomerisation catalysts

The last decade has seen the development of further selective ethylene oligomerisation catalysts of which dimerisation and trimerisation are most prevalent.[7] However, it should be noted that a high level of selectivity is still difficult to achieve or predict. Transition metal systems have been developed utilising Ti,[10] V,[11] Zr,[12] Ta,[13] Ru[14] and even U[15] for selective ethylene trimerisation and Fe, Co, Ni, Zr, Rh, Ta and Pd amongst others for selective dimerisation.[16,17] Some of the most selective and productive ethylene oligomerisation systems are based on chromium.[18] After the Union Carbide discovery, the real advancement in this field came from the use of tridentate ligands.[19] In 2002, Wass and co-workers at BP utilised a catalyst system comprised of a bis(diarylphosphino)amine PNP ligand, $Ar_2PN(Me)PAr_2$ (Ar = 2-methoxyphenyl), and $CrCl_3(THF)$ activated with MAO which produced 89.9 wt% 1-hexene overall with an activity of over 2,600 $kg_{1\text{-hexene}}mol_{Cr}^{-1}h^{-1}bar^{-1}$.[20,21] Huge variation in this tridentate ligand architecture for ethylene oligomerisation has since been demonstrated utilising P, N, O and S donors. Such modification has resulted in unprecedentedly high activities and selective tuning for oligomer chain lengths.[7,8,18–20]

Moving down group 6, there are far fewer reports of molybdenum and tungsten as selective ethylene oligomerisation catalysts when compared with chromium. Downing *et al*. have explored the use of SNS ligated molybdenum complexes with aluminium co-catalysts for ethylene oligomerisation.[22] Unlike their chromium analogues which are highly active and selective for 1-hexene, the molybdenum systems showed very low activities with trace amounts of butenes and high quantities of polymer formation observed. This was attributed to the softer nature of molybdenum which would render the ligand more tightly bound than in the analogous chromium complexes. In 2012, Wright *et al*. reported that molybdenum bis-imido complexes are active for the selective dimerisation of ethylene to 1-butene. The most active catalyst reported comprised of $Mo(NDipp)_2Cl_2(DME)$ activated with $AlEtCl_2$ (63,820 $mol_{C_2H_4}mol_{Mo}^{-1}h^{-1}$) in chlorobenzene at 60 °C and 40 bar ethylene, displaying a selectivity towards butenes of 90%, of which 64% was 1-butene.[23]

Many of the earliest reported tungsten based olefin metathesis catalysts required aluminium co-catalysts for turnover.[24] In fact, one of the simplest metathesis catalysts was a combination of WCl_6 and $AlEt_3$ which Natta and co-workers had shown was active for ring opening metathesis polymerisation (ROMP) of cyclopentene.[25] In 1975, Menapace *et al*., whilst working for Goodyear, reported that the selectivity of a metathesis catalyst comprised of WCl_6, $PhNH_2$ and $Et_3Al_2Cl_3$ could be changed in favour of alkene dimerisation by increasing the amount of aluminium co-catalyst in the system.[26] In 2010, Hanton *et al*. reported an improvement on this system, whereby inclusion of an amine base neutralised HCl generated in the reaction leading to higher activities for olefin dimerisation (209 *vs* 51 $mol_{C_5H_{10}}mol_W^{-1}h^{-1}$ with addition of one equivalent of Et_3N).[27] The system was active towards a range of α-olefins with selectivities as high as >99% for the dimerisation of 1-hexene. It was proposed that the active species in these ill-defined systems was a tungsten imido complex formed *in situ*.

1.1.3. Tungsten imido complexes

Imido groups have been widely employed as ancillary ligands in Schrock type alkylidene complexes for olefin metathesis. Initially, tungsten oxo alkylidene complexes were shown to be active for olefin metathesis, however, they were difficult to prepare and often underwent bimolecular decomposition to yield inactive species.[28,29] One overriding factor in tungsten alkylidene formation to that point had been the presence of strong π-bonding ligands; focus moved towards imido fragments which are stronger π-donors than oxo groups with a formal triple bond between the nitrogen and metal centre and the ability to add a sterically demanding R group for protection. To achieve this Bradley and co-workers reacted $W(O)Cl_4$ with phenylisocyanate furnishing $W(NPh)Cl_4$. Further reaction with $MgMe_2$ in the presence of PMe_3 yielded the trimeric oxo-bridged complex $[W(NPh)(\mu\text{-}O)Me_2(PMe_3)]_3$ (Figure 1.1).[30] The bridging oxo groups have one short (1.7768(4)–1.8038(4) Å) and one long (2.1035(5)–2.1147(5) Å) bond, the latter being *trans* to the imido group, with a wide W–O–W angle of 153°. The linear imido fragment exerts a large *trans* influence on the oxo substituent which preferentially π-bonds to the tungsten atom where it is *trans* to the π-acceptor phosphorous ligand.

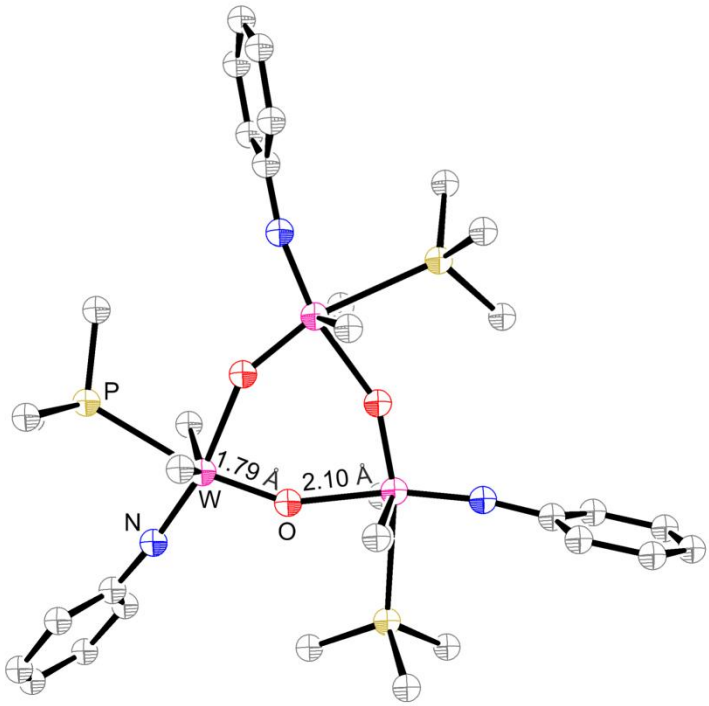


Figure 1.1. Molecular structure of $[W(NPh)(\mu\text{-}O)Me_2(PMe_3)]_3$.[30] Bridging oxo groups have one short bond *trans* to PMe_3, and one long bond *trans* to the imido group. Ellipsoids shown at isotropic spheres, hydrogens omitted for clarity.

In 1982, Pedersen *et al*. reported the first stable, isolable, monomeric tungsten imido alkylidene complex $W(NPh)(CH^tBu)(PMe_3)_2Cl_2$ by reaction of $W(NPh)(OC^tBu)_4$ with $Ta(CH^tBu)(PMe_3)_2Cl_3$.[31] The bonding in such alkylidene complexes is viewed as coupling of a triplet state metal with a triplet carbene (Figure 1.2).

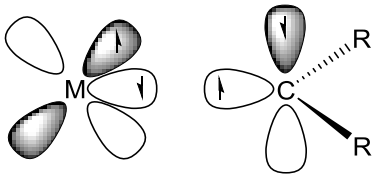


Figure 1.2. Dewar-Chatt-Duncanson model[32,33] for the bonding in a Schrock carbene from a molecular orbital perspective.

Variation in the steric and electronic properties of the imido group has also been shown to have a large effect on activity. More electron deficient and sterically less demanding imido moieties in $W(NAr)(CH^tBu)(ODBMP)_2$ (DBMP = 2,6-$CHPh_2$-4-Me-C_6H_2) complexes were found to be more active for the polymerisation of 2,3-dicarbomethoxynorbornadiene.[34]

Along with molybdenum analogues, a whole family of Schrock imido alkylidene complexes have now been developed and many are commercially available (Figure 1.3). They are capable of a variety of metathesis reactions such as ring opening metathesis

polymerisation (ROMP), ring closing metathesis (RCM) cross metathesis (CM), as well as enantioselective olefin metathesis.[35–37]

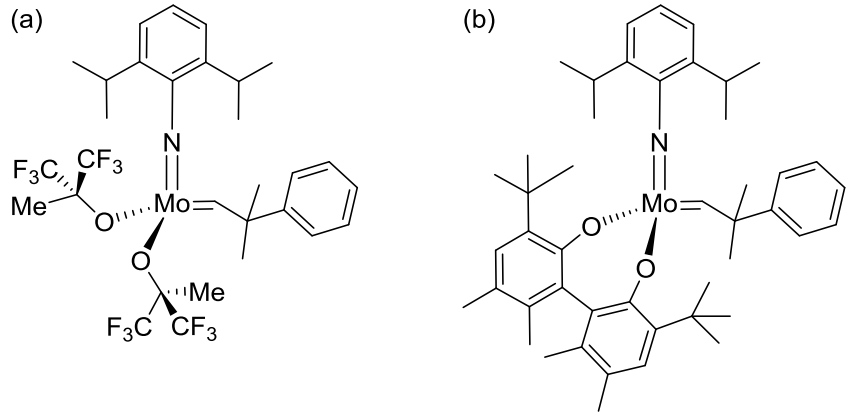
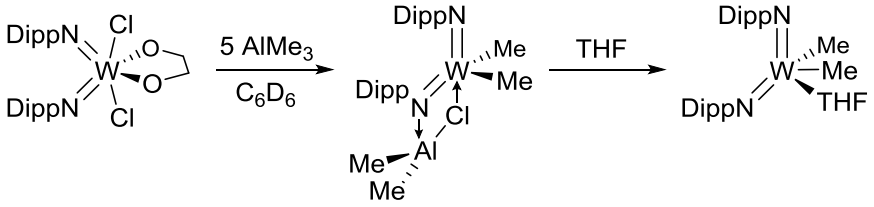


Figure 1.3. Commercialised molybdenum imido Schrock-Hoveyda alkylidene catalyst for ROMP, RCM, CM (a)[35] and enantioselective olefin metathesis (b).[36]

Activation of well-defined tungsten mono-imido complexes with aluminium co-catalysts has yielded catalysts active for the dimerisation of α-olefins.[38] Olivier *et al*. demonstrated that W{N(2,6-Me-C_6H_3)}Cl_4 and $AlEt_2Cl$ (Al/W = 40) were capable of oligomerising ethylene (6 MPa) at 40 °C in chlorobenzene to predominantly butenes (83%) and hexenes (16%) with a turnover number (TON) of 22,300 $mol_{C_2H_4}mol_W^{-1}$ and 1-butene comprising 99% of the C_4 fraction. Variation in the aryl group in both the aniline in the Goodyear $WCl_6/ArNH_2/AlEtCl_2$ catalyst and imido group for the $W(NAr)Cl_4/AlEtCl_2$ system indicated that electron withdrawing substituents led to the highest activity for propene dimerisation, with the most active being Ar = 4-F-C_6H_4. However, no characterisation of the active species was performed.

Recently, Dyer and co-workers have disclosed the reaction of the tungsten bis-imido complex $W(NDipp)_2Cl_2(DME)$ with 5 equivalents of trimethylaluminium (TMA) (Scheme 1.1).[39] This resulted in methylation of the two chloride positions and coordination of $AlMe_2Cl$ to the imido group affording $W(NDipp)\{(NDipp)AlMe_2(\mu\text{-}Cl)\}Me_2$ (Figure 1.4). Addition of excess THF led to simultaneous dissociation of the coordinated aluminium species and THF adduct formation at tungsten. Reaction of the resulting $W(NDipp)_2Me_2(THF)$ with 5 equivalents of ethylene at room temperature in chlorobenzene yields 1-butene and methane (4:1) with concomitant dissociation of the THF observed.



Scheme 1.1. Formation of $W(NDipp)_2Me_2(THF)$ from $W(NDipp)_2Cl_2(DME)$ *via* a coordinated aluminium species.[39]

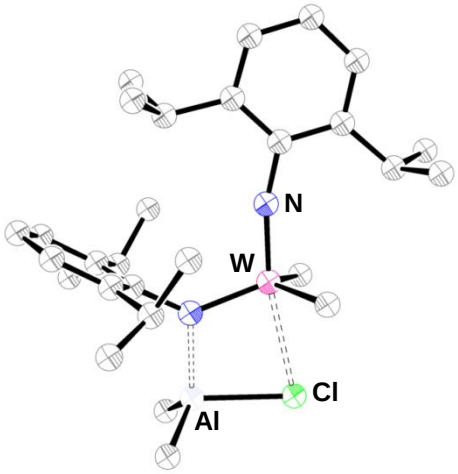


Figure 1.4. Molecular structure of $W(NDipp)\{(NDipp)AlMe_2(\mu\text{-}Cl)\}Me_2$.[39] Ellipsoids shown as isotropic spheres. Hydrogens omitted for clarity.

1.1.4. Oligomerisation mechanisms

There are two generally accepted mechanisms for the oligomerisation of ethylene, the Cossee-Arlman mechanism and the metallacycle mechanism. The Cossee-Arlman mechanism involves successive ethylene coordination and insertion steps leading to chain growth (Figure 1.5).[40–42] For oligomerisation to occur the rate of β-hydride elimination must be similar to the rate of chain growth, otherwise high molecular weight polymer will be the resulting product. Such a relationship is what leads to the Schulz-Flory distribution (Equation 1.1)[43,44] of even numbered oligomers observed in many oligomerisation processes.

Equation 1.1. Schulz-Flory distribution:[43,44]

$W_m = \alpha^{m-1}(1-\alpha)^2$

$W_m =$ weight fraction of m oligomer of oligoethylene

$\alpha =$ rate of propagation/(rate of propagation + rate of chain transfer) $k_1/(k_1 + k_2)$

In such a distribution, dimerisation is favoured when the rate of chain termination (k_2) is very high *i.e.* α is close to zero. Such a mechanism involves formation of a discrete hydride species upon β-hydride elimination.

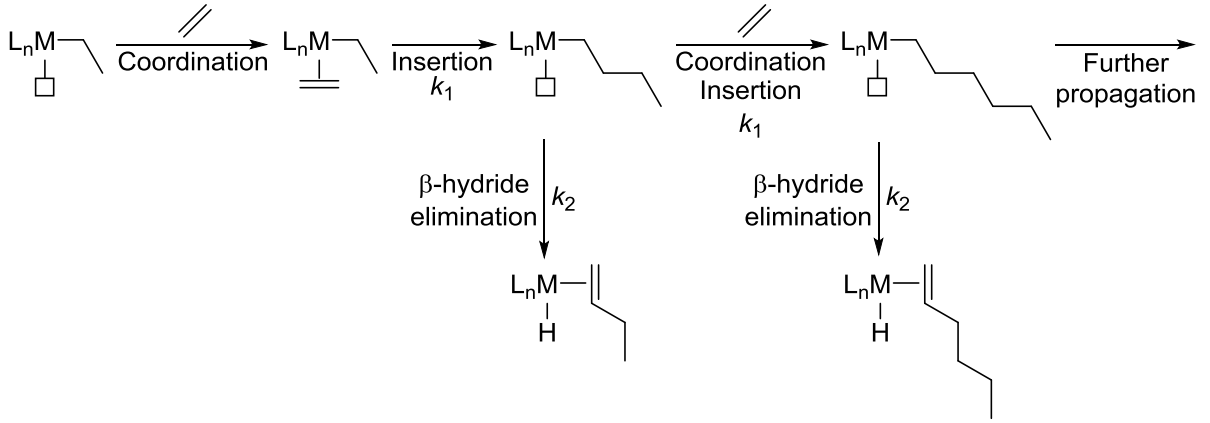


Figure 1.5. Cossee-Arlman mechanism[40–42] for the oligomerisation of ethylene involving subsequent coordination insertion steps, with β-hydride elimination yielding a distribution of oligomers.

The Cossee-Arlman mechanism is, however, unable to explain examples of selective trimer- and tetramerisation described previously. Workers at Union Carbide suggested that chromium metallacycloheptane formation would explain the high selectivity they observed towards 1-hexene (Figure 1.6).[15] This mechanism involves oxidative coupling of two ethylene monomers producing a metallacyclopentane moiety. Subsequent insertion of a further ethylene unit leads to a metallacycloheptane from which 1-hexene can be eliminated either by β-hydride elimination or a migratory 3,7-hydride-shift.[45] Such a mechanism was further supported by decomposition studies of Pt metallacycles by Whitesides and co-workers who observed release of α-olefins but also increased thermal stability of metallacyclopentanes over metallacycloheptanes.[46] This preference for metallacycloheptane formation over elimination from metallacyclopentane has been attributed to the increased ring strain in the metallacyclopentane unit, which disfavours β-hydride elimination.[47] This was further demonstrated by Emrich *et al*. who reacted $\{Cp^*(C_2H_2)NMe_2\}CrCl_2$ with $C_4H_8Li_2$ and $ClMg(CH_2)_3MgCl$, isolating the molecular structures of the metallacyclopentane and metallacycloheptane complexes respectively. The greater stability of the metallacyclopentane complex was noted and the metallacycloheptane complex was demonstrated to decompose releasing 1-hexene.[48]

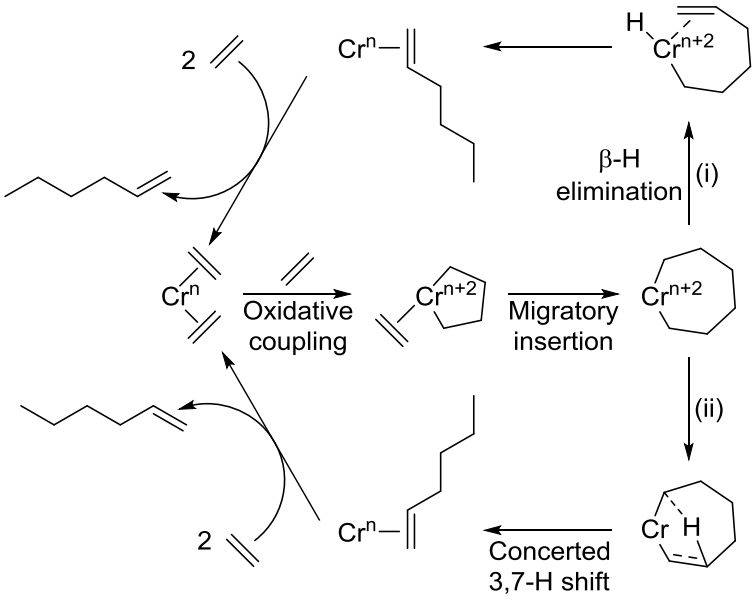
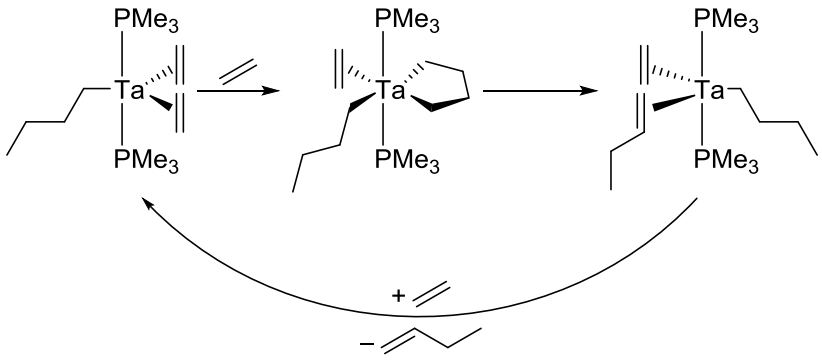


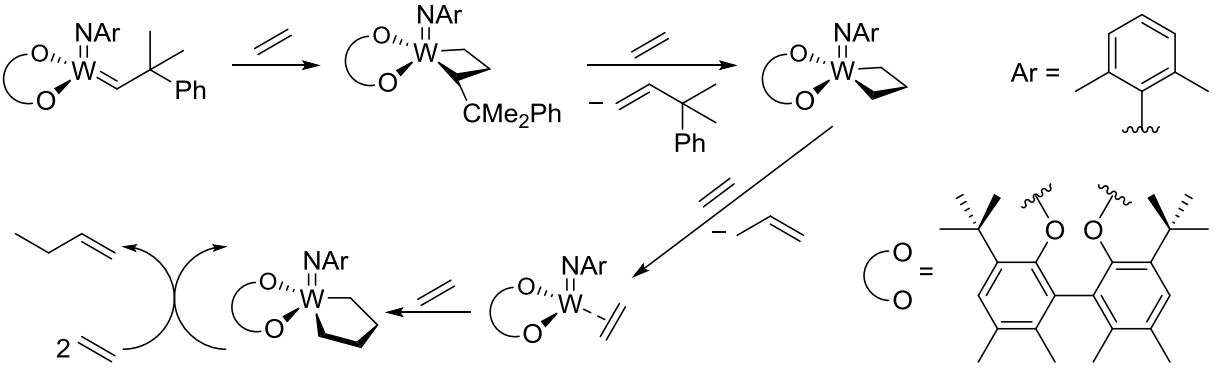
Figure 1.6. Metallacycle mechanism for selective ethylene trimerisation with chromium complexes. Elimination of 1-hexene can occur *via* either β-hydride elimination (i) or a concerted 3,7-H shift (ii).[45]

Despite the large energy barrier to elimination from a metallacycloheptane, there are examples of selective ethylene dimerisation which operate by a metallacycle mechanism. Schrock and co-workers have shown that tantalum complexes catalyse the dimerisation of olefins *via* metallacyclic species.[49,50] Reaction of $TaCp^*(C_2H_4)Cl_2$ with ethylene at 50 °C in toluene yielded solely 1-butene. Fellmann *et al*. showed that reaction of $Ta(CH_2{}^tBu)(CH{}^tBu)_2(PMe_3)_2$ with ethylene (30 psi) in pentane at 0 °C, resulted in rapid dimerisation to form 1-butene (~0.5 $mol_{C_2H_4}mol_{Ta}{}^{-1}min^{-1}$) with loss of *tert*-butyl ethylene observed. The major active component is proposed to be $Ta(C_2H_4)_2(C_4H_9)(PMe_3)_2$ with metallacyclopentane formation resulting in highly selective oligomerisation (no internal butenes observed) (Scheme 1.2).[51]



Scheme 1.2. Proposed mechanism for the selective dimerisation of ethylene to 1-butene by $Ta(C_2H_4)_2(C_4H_9)(PMe_3)_2$.[51]

With respect to tungsten based catalysts, high selectivity towards dimer formation in both the Goodyear and imido systems has led to suggestions that a metallacycle mechanism may be in operation. Tobisch performed a DFT study on the feasibility of such a mechanism on $W(NR)R_2Cl_2$, the proposed pre-catalyst formed from $WCl_6/PhNH_2$ complexes activated by alkyl aluminium reagents.[52] The results indicated that the aluminium co-catalyst plays an important role in activating the complexes. The 'bare' mono-imido metallacyclopentane complex displayed a very high barrier for reductive elimination of 42.4 $kcalmol^{-1}$, and actually showed a propensity towards further chain growth. However, by factoring in interactions of the aluminium co-catalyst, the barrier to β-H abstraction is reduced to 31.0 $kcalmol^{-1}$ and the alternative path for metallacycle growth is closed owing to the kinetically more unfavourable olefin insertion. In 1997, Boncella and co-workers provided evidence for such a mechanism by isolating the metallacyclopentane complex $W(NPh)(C_4H_8)\{o\text{-}(Me_3SiN)_2C_6H_4\}$ from the reaction of $W(NPh)\{o\text{-}(Me_3SiN)_2C_6H_4\}(CH_2{}^tBu)_2$ and ethylene.[53] The same complex could be formed by reacting the starting bis-chloride complex, $W(NPh)\{o\text{-}(Me_3SiN)_2C_6H_4\}Cl_2$, with $BrMg(C_4H_8)MgBr$. It was demonstrated that the metallacyclopentane complex was unreactive to further equivalents of ethylene even at elevated temperatures. However, despite heating the complex to its decomposition temperature (150 °C) no 1-butene was observed, suggesting the steric constraints of the complex do not facilitate β-hydride elimination. Tsang *et al*. also showed tungstacyclopentane formation when $W\{N(2,6\text{-}Me\text{-}C_6H_3)\}(CHCMe_2Ph)$(Biphen) (Biphen = 3,3′-di-*tert*-butyl-5,5′,6,6′-tetramethyl-1,1′-biphenyl-2,2′-diolate) was reacted with excess ethylene (Scheme 1.3). Addition of further equivalents of ethylene resulted in slow 1-butene formation in a catalytic cycle.[54]



Scheme 1.3. Formation of the tungstacyclopentane complex $W\{N(2,6\text{-}Me\text{-}C_6H_3)\}(C_4H_8)$(Biphen) and its catalytic conversion of ethylene to 1-butene.[54]

Despite these results, C_2H_4/C_2D_4 labelling studies of both the Goodyear system and Dyer and co-workers bis-imido catalyst indicate that in fact a Cossee-Arlman mechanism may be in operation.[27,39] For a metallacycle mechanism, reaction of a mixed 50:50 C_2H_4/C_2D_4 feed should lead to the selective formation of 3 products in a 1:2:1 ratio (C_4H_8, $C_4H_4D_4$ and C_4D_8), however, in both cases complete scrambling of the dimeric products was observed, consistent with the formation of a discrete hydride species.

1.2. Well-defined heterogeneous catalysis

1.2.1. Benefits of complex immobilisation

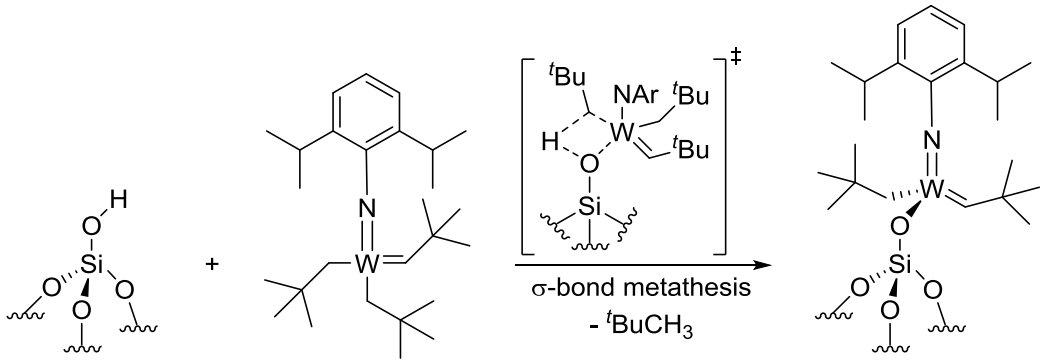
Heterogeneous catalysts are involved in several important industrial applications, such as the Fisher-Tropsch process (Co/SiO_2) producing alkanes from syn gas (CO and H_2)[55] and Ziegler-Natta olefin polymerisation catalysis ($TiCl_4/MgCl_2/AlEt_2Cl$) producing polyolefins which are used worldwide in the production of plastics.[56] However, many of these industrial catalysts are ill-defined requiring harsh conditions (high temperatures and pressures) to generate the active species. Heterogeneous catalysts are favoured industrially due their recyclability, improved product separation and compatibility with continuous flow processes.[57] With the development of highly active, single-site, molecular catalysts, focus has now turned to immobilising such species to form well-defined heterogeneous catalysts. This has the benefits of greater activities and selectivities by tuning the ligand architecture, as all catalyst sites should be uniform and active during catalysis, as well as reducing bimolecular decomposition.[58] One problem associated with this approach is the higher cost related to formation of the molecular precursors; to be industrially viable, supported species need to show increased activity, selectivity and stability compared to their ill-defined counterparts, and ideally require as few preparative steps as possible.[59]

1.2.2. Immobilisation of well-defined molecular pre-catalysts

To form a well-defined heterogeneous catalyst, molecular pre-catalysts must be appended to a relatively inert support material *e.g.* silica, alumina, zeolites. This can be achieved by covalent bonding *via* tethering,[60] electrostatic interactions or adsorption by weak Van der Waals interactions with the surface of the support.[61] To maintain defined active species, complexes that are to be immobilised should be comprised of ligands that are relatively inert to substitution *e.g.* cyclopentadienyl (Cp) or polydentate ligands. Covalent bonding to the surface is most often achieved by functionalisation of either the surface groups of the support material or one of the ligands on the molecular complex or in some cases both. For example,

Grubbs 1st and 2nd generation and Hoveyda-Grubbs 2nd generation catalysts have all been immobilised by functionalisation of the phosphine, NHC and benzylidene fragments respectively.[60,61] One issue with such an approach is that it can be synthetically challenging to introduce compatible groups, and large structural changes can influence the catalytic activity. Sels and co-workers were able to avoid this problem by demonstrating that the 2nd generation Hoveyda-Grubbs catalyst could be adhered to mesoporous silica by physisorption, most likely due to hydrogen bonding interactions.[62] It was concluded that a high density of surface silanols, especially geminal silanols, was required for strong adhesion to the surface, with siloxanes shown to decompose the complex. The immobilised catalyst was active for the metathesis of a wide variety of carbon-carbon double bonds,[62,63] and the best system (TUD-1 silica, 0.2 wt% Ru) displayed a turnover number (TON) of 18,000 for the metathesis of *cis*-cyclooctene after 9 hours at room temperature in hexane, comparable to the homogeneous catalyst.

One recent approach to complex immobilisation is termed surface organometallic chemistry (SOMC), and utilises the surface hydroxyl groups of the support as ligands that can covalently bond to the metal centre.[64] In such a case a labile ligand *e.g.* an alkyl group, is protonated and displaced by a surface hydroxyl in a σ-bond metathesis reaction (Scheme 1.4).[65]



Scheme 1.4. Immobilisation of W(NDipp)(CH^{t}Bu)(CH$_2$^{t}Bu)$_2$ on silica to form (≡SiO)W(NDipp)(CH^{t}Bu)(CH$_2$^{t}Bu), utilising the SOMC methodology.[65]

Research in this area has grown significantly over the last 20 years, pioneered by the groups of Copéret and Basset amongst others.[57,60,65–67] Spectroscopic techniques such as solid-state NMR (SSNMR), Fourier transform infrared (FTIR), extended X-ray absorption fine structure (EXAFS) and diffuse reflective UV/Vis can be employed to identify and characterise the surface species, which due to low complex loadings can be very challenging, allowing for comparison with molecular models of the immobilised systems.[57] Recently,

Copéret and co-workers have reported a novel SSNMR technique for the study of molecular species known as dynamic nuclear polarisation surface enhancement NMR spectroscopy (DNP-SENS).[68,69] By combining an organic radical, with the surface species in a solution frozen at 100 K and irradiating at the EPR transition of the radical, polarisation transfer from the radical to the solvent can occur. Cross-polarisation from the solvent to the surface nuclei results in large signal enhancements (*ca*. 100 times), decreasing collection times by several orders of magnitude (250,000). This allows for the detection of nuclei with low abundance, but also can remove the need for isotopic enrichment of the immobilised species.

1.2.3. Support preparation

For the SOMC grafting approach to be successful, careful control of the support surface structure is required. One of the most commonly employed support materials in heterogeneous catalysts is calcined silica. This is due to its relatively inert nature and uniform surface functionality which can be controlled by thermal vacuum treatment.[57] Many studies have been undertaken on the hydroxyl concentration and type of silanol sites remaining after thermal vacuum treatment at a range of temperatures.[70–72] The resulting species are often referred to as $SiO_{2-(x)}$ where x is the temperature of thermal treatment. Techniques have been developed in order to measure the type and number of surface hydroxyl groups on metal oxides (*e.g.* silica, alumina and zeolites), such as FTIR,[70,73] thermogravimetric analysis (TGA),[74] SSNMR[75] and mass spectrometry after deuterium exchange.[73] One of the simplest methods is titration of the surface hydroxyl groups using organometallic reagents.[76,77] For example, reaction of surface hydroxyl groups with $Mg(CH_2Ph)_2(THF)_2$[78] liberates toluene that can be integrated against an internal standard using ^{1}H NMR spectroscopy.

There are four distinct types of surface silica environment present on a silica particle (isolated, geminal and vicinal silanols and siloxanes) and the ratio can be altered by changing the temperature of thermal treatment under vacuum (Figure 1.7 and Table 1.1).

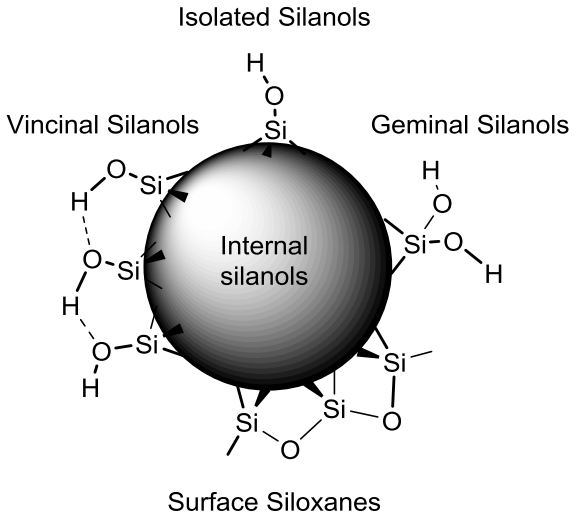
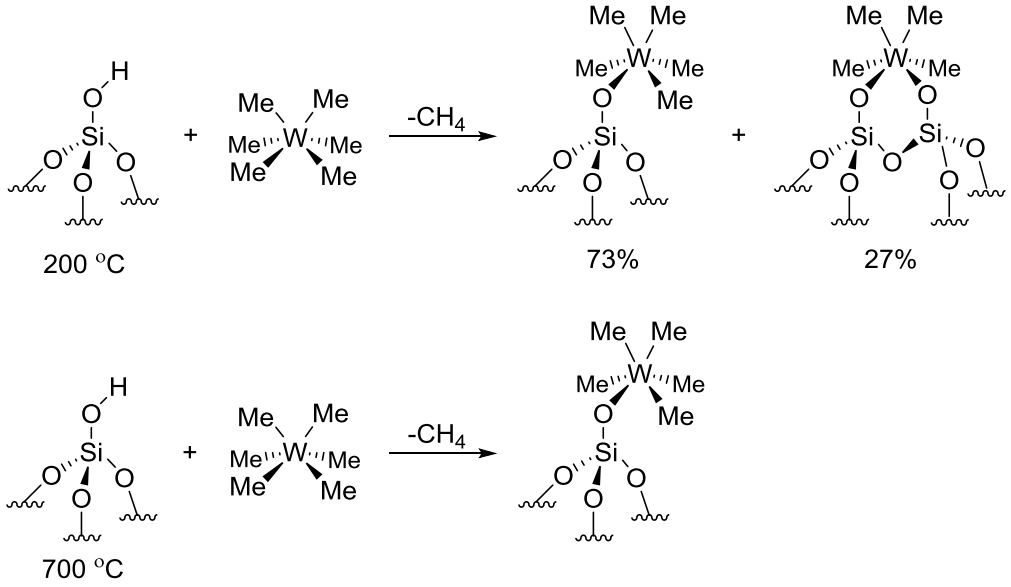


Figure 1.7. Silica environments present on the surface of amorphous silica.[70]

Table 1.1. Percentage of surface silanol groups on dehydroxylated silica at various dehydroxylation temperatures.[70]

Dehydroxylation temperature (°C)	Hydroxyl number, αOH (OH nm^{-2})	Isolated silanols (%)	Geminal silanols (%)	Vicinal silanols (%)
200	4.60	26	13	61
500	1.80	86	14	0
700	1.15	78	22	0
900	0.40	100	0	0

In order to maintain a defined complex in the immobilised species, it is preferable to bind to a single surface silanol during SOMC grafting. To achieve this, a high percentage of isolated silanols is desirable, as proximal hydroxyl groups can result in formation of multipodal species. The most commonly used temperatures of treatment are 500 and 700 °C as these show a good balance between a high percentage of isolated silanols (86 and 78%) whilst maintaining reasonable hydroxyl numbers (α_{OH} = 1.15 and 1.80 OH nm^{-2}) (Table 1.1). Work by Basset and co-workers demonstrated that when WMe_6 was supported on dehydroxylated silica treated at 200 °C, both monopodal (≡SiO)WMe_5 and bipodal $(≡SiO)_2WMe_4$ formed due to the presence of vicinal silanols, whereas only the monopodal species was observed when silica treated at 700 °C was used (Scheme 1.5).[79]



Scheme 1.5. Immobilisation of WMe_6 on SiO_2 thermally treated at 200 and 700 °C resulting in monopodal $(\equiv SiO)WMe_5$ in both cases but also bipodal $(\equiv SiO)_2WMe_4$ for $SiO_{2\text{-}(200)}$.[79]

Taoufik *et al.* investigated the effect the dehydroxylation temperature of silica had on the activity of $(^{n}BuCp)_2ZrCl_2$ supported on methylaluminoxane (MAO) coated silica. Their findings demonstrated that there was an increase in the number of active sites with increasing dehydroxylation temperature but that the nature of these sites did not change.[80]

1.2.4. Influence of the support

Heterogeneous catalyst supports are often chosen due to their inertness towards the chemicals used in catalysis. However, covalent bonding to the metal centre when grafted by the SOMC procedure alters the sterics and electronics of the homogeneous pre-catalyst. In most cases this leads to reduced activity compared to the molecular analogues but in a few cases enhancement has been demonstrated. There can also be a large difference depending on the support used *e.g.* silica *vs* alumina.[81] Copéret and co-workers reported that the well-defined silica-supported rhenium alkylidene complex $(\equiv SiO)Re(C^{t}Bu)(CH^{t}Bu)(CH_2{}^{t}Bu)$ is active for propylene metathesis, whereas its molecular precursor $Re(C^{t}Bu)(CH^{t}Bu)(CH_2{}^{t}Bu)_2$ is inactive. The suggested reason behind this is that the siloxy substituent increases the electrophilicity of the metal centre.[82] Work from the same group on the rhenium oxo alkylidene complex $Re(O)(CHCHCPh_2)(OCMe(CF_3)_2)_3(THF)$ showed it to be completely inactive towards alkene metathesis when grafted on silica. However, it displayed very good activity when immobilised on an aluminosilicate, $Al\{OSi(O^{t}Bu)_3\}_3$,

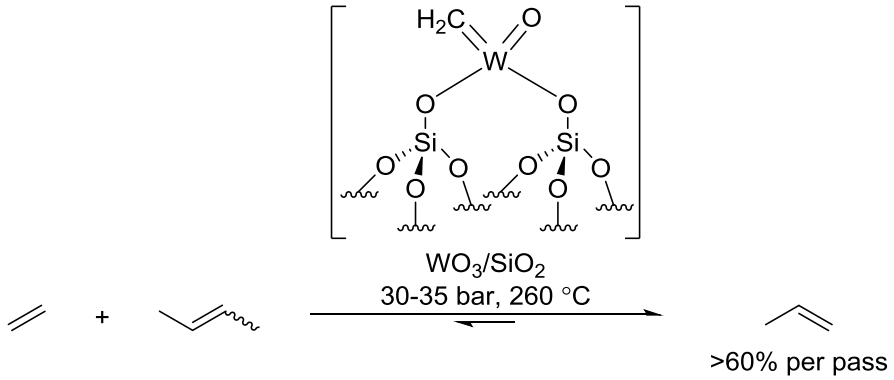
thought to be due to the interaction of the Lewis acidic aluminium sites with the oxide group.[83]

1.2.5. Supported metathesis catalysts

The vast majority of reports utilising the SOMC procedure have focused on immobilising metathesis catalysts, mainly Schrock type alkylidene complexes;[84–88] one example being the immobilisation of W(NDipp)(CH^{t}Bu)(CH$_2{}^t$Bu)$_2$ on $SiO_{2-(700)}$ to form (≡SiO)W(NDipp)(CH^{t}Bu)(CH$_2{}^t$Bu) (Scheme 1.4).[84] Grafting of the complex was confirmed by an EXAFS study showing preservation of the imido, neopentylidene and one neopentyl group and formation of a new Si–O–W bond. The supported complex was shown to be active for the cross metathesis of propylene (TOF = 8.4 $mol_{C_3H_6}mol_W^{-1}min^{-1}$ after 6 minutes) and was also shown to be active under flow conditions.

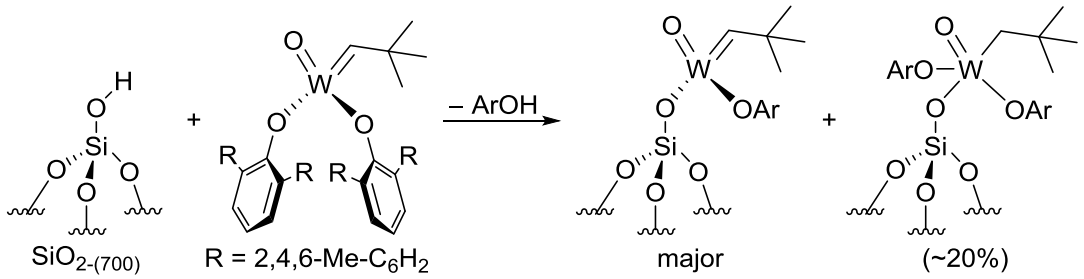
Recently, Mougel *et al*. were able to identify the formation of metallacyclobutane intermediates formed during the self-metathesis of *cis*-4-nonene by (≡SiO)W(NAr)(CH^{t}Bu)(OR) (OR = O^{t}BuF$_9$, O^{t}BuF$_6$, O^{t}BuF$_3$, O^{t}Bu and OSi(O^{t}Bu)$_3$) by using solid state ^{13}C-{^{1}H} CPMAS NMR spectroscopy.[89] The ratio between trigonal bypyramidal (TBP) and square pyramidal (SP) tungstacyclobutane intermediates were determined and fell in the order O^{t}Bu < O^{t}BuF$_3$ < OSi(O^{t}Bu)$_3$ < O^{t}BuF$_6$ < O^{t}BuF$_9$. This ratio is important as it is the TBP intermediate that is reactive towards olefin metathesis, whereas the SP intermediate is a resting state that can even lead to catalyst deactivation.[90] This matched exactly with the order of reactivity of the complexes indicating that weaker σ-donors result in more active catalysts with a TOF after 3 minutes for the most active catalyst of 115 *vs* 93 $mol_{products}mol_W^{-1}min^{-1}$ for the unsupported analogue.

Focus in this area has turned to mimicking the industrial Phillips triolefin process by immobilising defined oxo alkylidene species,[85,91–95] known to be the active species formed *in situ* in this process,[96] onto a support. The industrial system utilises a WO_3/SiO_2 catalyst, converting a mixture of 2-butenes and ethylene at 30–35 bar and 260 °C to propylene at 60% and above per pass, with a selectivity of 90% (Scheme 1.6).[97] The proposed active species is a tungsten methylidene formed *in situ* during the reaction.[98] This process is used to produce over 9 million tons of propylene worldwide,[99] and is of growing importance as global consumption is projected to rise from 80 to 130 million tons by 2025.[4,100]



Scheme 1.6. Olefin conversion technology to produce propylene from ethylene and 2-butenes utilising WO_3/SiO_2.[97]

Conley *et al.* have demonstrated that the immobilisation of $W(O)(ArO)_2(CH^tBu)$ (ArO = 2,6-mesitylphenoxide) on $SiO_{2\text{-}(700)}$ afforded the defined alkylidene complex $(\equiv SiO)W(O)(ArO)(CH^tBu)$ as well as a small amount of $(\equiv SiO)W(O)(OAr)_2(CH_2{}^tBu)$ (Ar = 2,6-dimesitylphenyl) (Scheme 1.7).[85] This catalyst is extremely active for the self-metathesis of *cis*-4-nonene at 30 °C (at 0.1 mol% catalyst equilibrium is achieved after only 3 minutes, TOF = 170 $mol_{products}mol_W^{-1}min^{-1}$), outperforming the corresponding imido complex, $(\equiv SiO)W(NDipp)(CH^tBu)(2,5\text{-Me-Py})$ (TOF = 4 $mol_{products}mol_W^{-1}min^{-1}$) and the best supported molybdenum catalyst, $(\equiv SiO)Mo(NDipp)(CH^tBu)(OCMe(CF_3)_2)$ (TOF = 46 $mol_{products}mol_W^{-1}min^{-1}$). Unlike the industrial WO_3/SiO_2 catalyst this supported complex can even tolerate ester functionality (methyl oleate metathesis).



Scheme 1.7. Formation of a well-defined silica supported oxo alkylidene catalyst *via* the SOMC grafting procedure.[85]

Another method involves immobilisation of the precursor complex $W(O)Cl_4$ onto silica to yield $(\equiv SiO)W(O)Cl_3$. A surface alkylation strategy can then be employed with $ZnMe_2$ or $SnMe_4$ to generate $(\equiv SiO)W(O)Me_3$ which is active for both the metathesis of isobutene to 2,3-dimethylbutene,[91] and conversion of ethylene to propylene most likely *via* a dimerisation (ethylene to 1-butene), isomerisation (1-butene to 2-butenes) and cross metathesis (2-butenes and ethylene to propylene) pathway.[95]

1.2.6. Supported catalysts for alkane metathesis

In 1997, Basset and co-workers reported the conversion of ethane (1 atm) to propane (44%) and methane (53%) (150 °C, 50–80 h) by a silica supported tantalum monohydride species $(\equiv SiO)_2TaH$ formed by reacting $(\equiv SiO)Ta(CH^tBu)(CH_2{}^tBu)$ with hydrogen at 150 °C overnight.[101] This reaction, termed alkane metathesis, involves the conversion of linear alkanes to their next higher and lower homologues *via* a metallacyclobutane intermediate.[102,103] Following this discovery, it was shown that analogously synthesised tungsten hydrides immobilised on silica, alumina and silica-alumina were also active for alkane metathesis, displaying higher activities than their tantalum hydride analogues.[104,105] Utilising the SOMC approach, Basset and co-workers have also been able to stabilise the highly reactive WMe_6 by grafting it on silica to yield $(\equiv SiO)WMe_5$ which is stable at moderate temperatures, whereas the precursor decomposes at −20 °C.[79] Heating the immobilised complex above 70 °C results in formation of tungsten methylidene species. All the characterised complexes were shown to be more active for alkane metathesis than the tantalum hydride species with $(\equiv SiO)WMe_5$ displaying the highest TON (127 $mol_{C_3H_8}mol_W^{-1}$ at 150 °C). Since this discovery, *in situ* alkylation has been employed as it circumvents the need to handle the highly reactive tungsten hexamethyl complex. To do this, either WCl_6 or $W(O)Cl_4$ can be immobilised on silica prior to treatment with an alkylating agent *e.g.* $ZnMe_2$. The resulting tungsten methyl species are active for cyclooctane metathesis yielding ring-expansion and contraction products.[95,106] Finally, Callens *et al*. have shown that the immobilised Schrock neopentylidyne complex $(\equiv SiO)W(C^tBu)(CH_2{}^tBu)$ is active towards the metathesis of *n*-decane producing a statistical distribution linear alkane products at 200 °C over 3 days.[107]

1.2.7. Supported olefin oligomerisation catalysts

As described previously, the majority of oligomerisation catalysts require a co-catalyst, usually in the form of an aluminium alkyl species, and often in large excess. To account for this during immobilisation, the support material can be coated in a layer of co-catalyst to yield for example SiO_2-MAO. Reaction with a defined complex then leads not only to immobilisation but also activation of the complex on the surface. One issue with this approach is that reaction of silica with aluminium alkyls often results in alkyl transfer to siloxane bridges, which are then incapable of activating metal complexes.[108–110] In 2014, Kermagoret *et al*. reported the grafting of $NiCl_2(PBu_3)_2$ on $AlEt_2Cl$ activated silicas. The most

active catalyst towards ethylene dimerisation displayed a TOF of 498,000 $mol_{C_2H_4}mol_{Ni}^{-1}h^{-1}$ after 5 minutes with a 95 wt% selectivity towards butenes, of which only 5% corresponded to 1-butene (30 °C, 5 bar ethylene in toluene solvent).[111] Wass and co-workers have also described immobilisation of a PNP chromium complex formed from $CrCl_3(THF)$ and $\{C_6H_4(OMe)\}_2PN(Me)P\{C_6H_4(OMe)\}_2$, which is active for ethylene trimerisation, on MAO-modified silica with no apparent loss of activity or selectivity.[21]

In 2001, Sen *et al*. described the activation of $TaCl_5$ by alkylating agents *e.g.* $AlMe_3$, to form both $TaMe_3Cl_2$ and $TaMe_2Cl_3$ species, the latter shown to be active towards ethylene trimerisation to 1-hexene.[13] Following this report, Basset and co-workers showed that $TaMe_3Cl_2$ could be grafted onto $SiO_{2-(700)}$ liberating methane to afford $(\equiv SiO)TaMe_2Cl_2$. This system selectively catalyses the oligomerisation of ethylene without the need for a co-catalyst to form predominantly 1-hexene (~80 wt%) with an activity of 375 $mol_{C_2H_4}mol_{Ta}^{-1}h^{-1}$ in toluene at 100 °C and 50 bar ethylene pressure *via* a proposed metallacycle mechanism.[112]

1.3. Layered double hydroxides (LDHs)

Layered Double Hydroxides (LDHs) are a class of anionic clays, consisting of positively charged Brucite-like layers with weakly bound intercalated anions (Figure 1.8).[113] They can be represented by the formula $[M^{z+}_{1-x}M^{3+}_x(OH)_2]^{q+}(X^{n-})_{q/n}\cdot yH_2O$ where most commonly z = 2. Examples of M^{2+} include Mg^{2+} and Ca^{2+}, M^{3+} is usually Al^{3+} and X^{n-} may be a variety of anions such as Cl^-, NO_3^-, CO_3^{2-} and SO_4^{2-}. LDHs are commonly referred to in the format $M^{2+}M^{3+}X^{n-}$, *e.g.* $MgAlCO_3$.

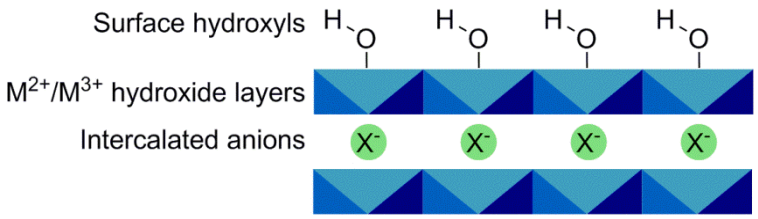


Figure 1.8. Basic structure of a layered double hydroxide.

In 2013, O'Hare and co-workers reported the synthesis of a new family of dispersible, hydrophobic LDHs using the aqueous miscible organic solvent treatment (AMOST) method.[114] These so called AMO-LDHs disperse in non-polar hydrocarbons, retaining the crystalline structure of LDHs but remarkably exhibit surface areas in excess of 400 m^2/g and pore volumes greater than 2.15 cc/g, nearly two orders of magnitude higher than conventional LDHs.[115,116]

LDHs have been widely used for catalysis[117,118] as their properties tailor them well to this role; variations in both surface area and composition are possible depending on the synthetic method and starting materials employed,[119] many compositions display low toxicity,[120] they have been shown to act as efficient ion scavengers[121,122] and their surfaces contain both acidic and basic sites which are altered by thermal treatment.[123] Their main use in heterogeneous catalysis has been to support simple metallic species (*e.g.* palladium nanoparticles for coupling reactions or Ziegler catalysts for ethylene polymerisation).[118,124,125] One relatively underexplored area is their ability to act as effective catalyst supports for well-defined molecular complexes. Recent work in the O'Hare group has focused on supporting olefin polymerisation complexes on LDHs in the presence of an activator.[126–129] For example, Buffet *et al*. reported that reaction of AMO-LDHs with MAO led to coating of the support by the aluminoxane species to yield AMO-LDH-MAO. This material could then be used to support metallocene catalysts (e.g. *rac*-ethylenebis(1-indenyl) zirconium dichloride, (EBI)$ZrCl_2$) which were active for the polymerisation of ethylene (activities as high as 5,613 $kg_{PE}mol_{Zr}^{-1}h^{-1}$) forming high molecular weight polymer (M_w = 270,964 $gmol^{-1}$).[127] It was also shown, that variation of either the mixed metal cations or interlayer anions, had a marked effect upon the activity of the supported complex (Table 1.2), with MgAl-SO_4 the most active support, although the reasons behind this are still unexplained.

Table 1.2. Ethylene polymerisation activities, molecular weights (M_w) and polydispersities (M_w/M_n) of AMO-LDH-MAO-EBI$ZrCl_2$ catalysts.[127]

LDH	**Activity ($kg_{PE}mol_{Zr}^{-1}h^{-1}$)**	**M_w ($gmol^{-1}$)**	**M_w/M_n**
CaAl-NO_3	1,983	195,404	3.08
MgAl-CO_3	936	221,647	3.29
MgAl-Cl	2,545	244,467	3.08
MgAl-SO_4	5,613	270,964	3.14
MgAl-CO_3	3,405	286,980	3.47
MgAl-Borate	898	240,361	3.47
MgGa-CO_3	3,256	275,826	3.39

In terms of immobilisation of well-defined complexes *via* the SOMC methodology, LDHs are completely unexplored, and there have been no reports on the effect the thermal treatment temperature (under vacuum) has on the support properties or the surface hydroxyl concentration.

1.4. Solid polymethylaluminoxane (sMAO)

A large amount of focus has been placed on immobilising single-site catalysts on supports coated with an activator.[130] The development of new activators is also crucial as currently the large excess of MAO required to activate metallocene polymerisation catalysts is anticipated to make up between a third and half of the total cost.[131] In 2010, Kaji *et al*. reported the synthesis of a new type of MAO that was insoluble in most common solvents, and thus showed promise as a single-site catalyst support.[132] This so called solid polymethylaluminoxane (sMAO) is formed from the reaction of trimethylaluminium (TMA) with benzoic acid (2.4 eq., 15 °C, 0.5 h) followed by a two-step heat treatment (80 °C for 28 h, 100 °C for 14 h), as a white solid.[133] Much like conventional MAO,[134] the material has pockets of 'free' TMA present, and adopts similar cage-like structures. This multifunctional material is capable of acting as a support, scavenger and activator in slurry phase ethylene polymerisation reactions.[133,135,136] Activities observed are much higher than for other supports; sMAO-*rac*-ethylenebis(1-permethylindenyl) zirconium dichloride (sMAO-*rac*-(EBI*)$ZrCl_2$) is more than 3 times as active than its silica supported MAO counterpart (5,365 *vs* 1,649 $kg_{PE}mol_{Zr}^{-1}h^{-1}bar^{-1}$). It should be noted that this activity is much lower than the unsupported analogue (61,800 $kg_{PE}mol_{Zr}^{-1}h^{-1}bar^{-1}$).[137] One of the benefits of using supported catalysts is that they can influence the polymer morphology. This occurs *via* a templating effect in which the polymer grows around the support mimicking its morphology (Figure 1.9).[138]

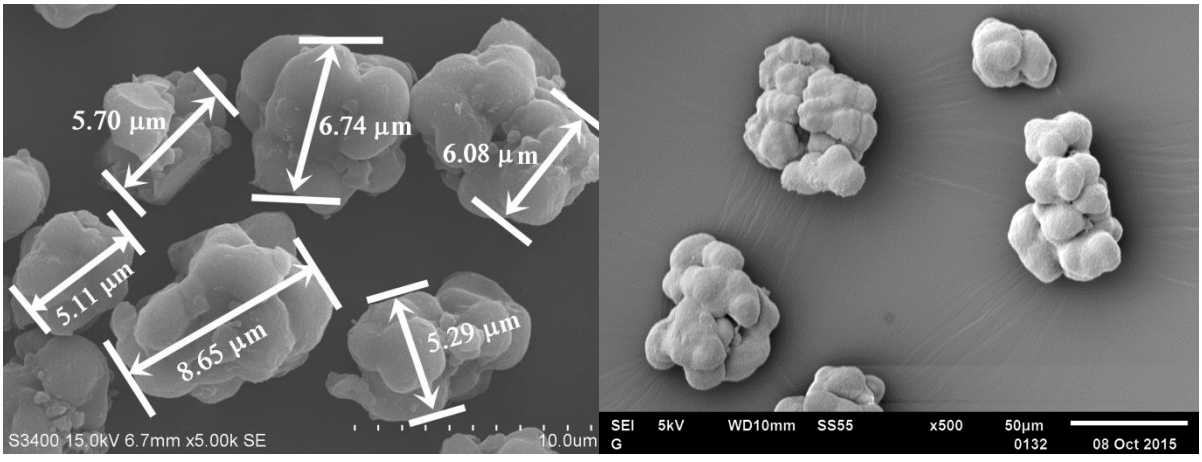


Figure 1.9. SEM images of sMAO (left) and polyethylene produced by sMAO-EBI$ZrCl_2$.[133]

1.5. Tandem catalysis

1.5.1. Underlying principle

A large volume of work has focused on developing discrete catalyst systems that perform a single transformation. However, it is beneficial to combine reactions in a 'one pot' style, as this can result in higher yields by removing product separation and purification steps.[139] Such procedures have been known for a long time in organic synthesis, often termed domino or cascade reactions.[140] It is only recently that such an approach has been applied to metal based catalysts. This has focused mainly on orthogonal catalysts *i.e.* ones that do not interact and catalyse different processes during the cycle.[141] In such a system, catalyst 1 can convert molecule A to B and then catalyst 2 can convert molecule B to the final product C (Figure 1.10).

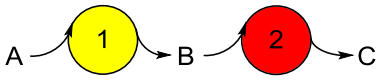


Figure 1.10. Orthogonal tandem catalysis involving conversion by catalyst 1 of reagent A to intermediate B and then to C by catalyst 2.[141]

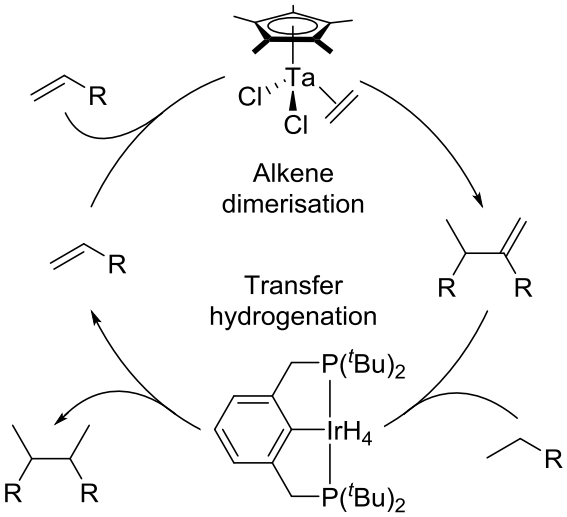
1.5.2. Hydrocarbon upgrading

As the crude oil market becomes more volatile, both economically and politically, interest is growing in alternative fuel sources such as coal, natural gas and biomass.[142] Production of optimal fuel-range hydrocarbons (C_8–C_{22}) from such sources usually exploit the Fischer-Tropsch process[143] or catalytic cracking,[144] which display poor selectivity and produce lighter alkanes in abundance. Ethane and methane are also released during Shale gas extraction, a process which has seen a large increase in the U.S..[1] These low molecular weight hydrocarbons ($C_{<6}$) are volatile and have low volumetric energy densities meaning that they have little value as fuels and are often burnt in flare stacks. Finding a way to upgrade these feedstocks to their higher molecular weight homologues is therefore of great value.

One such method, known as alkane metathesis, combines alkane dehydrogenation and alkene metathesis, converting two C_n alkanes to a C_{2n-2} alkane and ethane in the ideal case. For example, Brookhart and co-workers have employed both an iridium transfer hydrogenation catalyst and a molybdenum olefin metathesis catalyst for the metathesis of *n*-hexane.[145] Whilst this system did yield the desired *n*-decane, it was formed as part of a statistical distribution of alkanes. An improvement on this system was made by screening over 40 molybdenum and tungsten olefin metathesis catalysts along with different pincer ligated

iridium complexes for the metathesis on *n*-octane, which showed that tungsten complexes performed the best.[146] The most active system involved W(NDipp)(CHCMe$_2$Ph)(OSiPh$_3$)$_2$ (16 mM) and [C$_6$H$_3${OP(^{t}Bu)$_2$}$_2$]Ir(C$_2$H$_4$) (10 mM) producing 3,380 mM products with a distribution between C$_2$–C$_{15}$ which peaked at C$_7$ at 125 °C after 4 days. An immobilised system has also been developed by modifying the *para* position of the pincer ligand bound to iridium, to introduce basic groups such as phosphinite, which can adsorb onto the surface of γ-alumina. In combination with Re$_2$O$_7$/Al$_2$O$_3$ a long-lived catalyst (14 days at 175 °C) was formed with a TON of 2,440 $mol_{C_{10}H_{22}} mol_{Ir}^{-1}$, but again resulted in a large distribution of olefins.[147,148]

In 2014, Bercaw *et al*. described a different approach to tandem alkane upgrading. A transfer hydrogenation catalyst, IrH$_4${2,6-(CH$_2$P^{t}Bu$_2$)-C$_6$H$_3$}, and an olefin dimerisation catalyst, Cp*TaCl$_2$(C$_2$H$_4$), were employed in tandem, to try to upgrade a mixed feed of 1-hexene and *n*-heptane (Scheme 1.8).[149–151] They were able to couple the two monomers in solution cooperatively to some degree. Unfortunately, problems with competing isomerisation and the difficulty in finding conditions that suited both catalysts meant a range of products were formed.



Scheme 1.8. Idealised upgrading scheme *via* tandem transfer hydrogenation and alkene dimerisation to upgrade an alkane and an alkene.[149]

1.5.3. Copolymerisation

The main uses of the even α-olefins C$_4$–C$_8$ are as additives in polyethylene production. Another focus of tandem catalytic systems has been to combine ethylene oligomerisation catalysts with ethylene polymerisation catalysts, as such a system should be able to form a copolymer from a single feed of ethylene.[152–155] Combination of an ethylene trimerisation

catalyst $(CpCMe_2Ph)TiCl_3$ and the constrained geometry polymerisation catalyst $\{Cp^*SiMe_2(N^tBu)\}TiCl_2$ with a modified MAO co-catalyst, resulted in a system active for tandem copolymerisation of ethylene to yield an ethylene/hexene copolymer. The percentage of 1-hexene incorporation could be adjusted be changing the reaction conditions (0.3–14.2%), and over 98% of the total branches were butyl branches.[153]

Recently, focus has turned to immobilising these systems, which can help prevent reactor fouling.[156–158] In one example, Duchateau and co-workers have reported the immobilisation of the Mitsui phenoxyimine titanium ethylene trimerisation catalyst and the olefin polymerisation catalyst $(^nBuCp)_2ZrCl_2$ on silica coated with Al^iBu_3.[156] The results showed that co-immobilisation on the same support resulted in deactivation of the complexes, presumably by bimolecular interaction. Independent immobilisation followed by mixing of the two supported complexes, however, did yield an active system with a 1-hexene content of between 2.7 and 7.6% in the resulting copolymer (1 h, 58 °C, 10 bar ethylene).

1.6. Scope of this thesis

The aim of the thesis is to take new and known catalysts for ethylene dimerisation and alkane dehydrogenation, to independently immobilise these complexes on solid inorganic supports (sMAO, AMO-LDHs and silica) and to test their individual catalytic competence with a view towards potential applications in tandem ethane upgrading.

Development of well-defined tungsten mono-imido complexes for the selective dimerisation of ethylene is discussed in Chapter Two. Variations in the imido group and additional ligand sphere of such complexes and their impact on activity are discussed, along with the attempted formation of reactive intermediates and mimics for immobilised complexes. Chapter Three describes the preparation of AMO-LDHs for use as catalyst supports by thermal treatment under vacuum. Structural changes are examined by a range of spectroscopic techniques and the surface hydroxyl content determined by titration with an organometallic reagent. The capability of these materials to activate $(^nBuCp)_2ZrCl_2$ after prior impregnation with MAO is also disclosed. Grafting of the well-defined tungsten imido complexes discussed in Chapter Two onto the surface of inorganic solids (sMAO, AMO-LDHs and silica) is detailed in Chapter Four. Spectroscopic characterisation of the supported complexes by a combination of SSNMR, FTIR and X-ray absorption spectroscopy (XAS) along with reactivity studies with α-olefins are presented, and the effects of varying the imido ligand, temperature, loading and solvent in the ethylene dimerisation reaction

discussed. Chapter Five describes the immobilisation of the iridium pincer complex Ir($^{t\text{Bu}}$PCP)HCl on the surface of sMAO. Comparison of the structure and subsequent reactivity towards hydrogenation and transfer hydrogenation of olefins and alkanes respectively with molecular mimics is made. Finally, co-immobilisation of both tungsten mono-imido and iridium pincer pre-catalysts on the surface of sMAO is reported, and a preliminary investigation into the capability of this system to upgrade ethane is discussed.

1.7. References

1. R. Trager, *Chem. World*, 2015, **12**, 18–19.
2. G. Lappin, *Alpha olefins applications handbook*, CRC Press, 1989.
3. W. Keim, *Angew. Chem. Int. Ed.*, 2013, **52**, 12492–12496.
4. J. Mol, *J. Mol. Catal. A Chem.*, 2004, **213**, 39–45.
5. A. Forestière, H. Olivier-Bourbigou, and L. Saussine, *Rev. IFP*, 2009, **64**, 649–667.
6. R. M. Manyik, W. E. Walker, and T. P. Wilson, *Continuous processes for the production of ethylene polymers and catalysts suitable therefor*, 1967, US3300458.
7. D. S. McGuinness, *Chem. Rev.*, 2011, **111**, 2321–2341.
8. A. Bollmann, K. Blann, J. T. Dixon, F. M. Hess, E. Killian, H. Maumela, D. S. McGuinness, D. H. Morgan, A. Neveling, S. Otto, M. Overett, A. M. Z. Slawin, P. Wasserscheid, and S. Kuhlmann, *J. Am. Chem. Soc.*, 2004, **126**, 14712–14713.
9. F. Grasset and L. Magna, *Method for dimerization of ethylene into butene-1 using a catalyst composition containing a titanium complex and an alkoxy ligand functionalized by a heteroatom*, 2011, EP2388069 (A1).
10. P. J. W. Deckers, B. Hessen, and J. H. Teuben, *Organometallics*, 2002, **21**, 5122–5135.
11. R. Santi, A. M. Romano, M. Grande, A. Sommazzi, F. Masi, and A. Proto, *Process for the preparation of 1-hexene*, 2001, WO0168572 (A1).
12. M. Wang, R. Li, M. Qian, X. Yu, and R. He, *J. Mol. Catal. A Chem.*, 2000, **160**, 337–341.
13. C. Andes, S. B. Harkins, S. Murtuza, K. Oyler, and A. Sen, *J. Am. Chem. Soc.*, 2001, **123**, 7423–7424.
14. T. Kondo, K. Yamamoto, D. Takagi, L. Shen, Y. Yoshida, Y. Kimura, A. Toshimitsu, M. Kuramoto, and Y. Shiraki, *ChemCatChem*, 2010, **2**, 1565–1568.
15. R. Manyik, *J. Catal.*, 1977, **47**, 197–209.
16. A. M. Al-Jarallah, J. A. Anabtawi, M. A. B. Siddiqui, A. M. Aitani, and A. W. Al-Sa'doun, *Catal. Today*, 1992, **14**, 1–124.
17. S. M. Pillai, M. Ravindranathan, and S. Sivaram, *Chem. Rev.*, 1986, **86**, 353–399.
18. T. Agapie, *Coord. Chem. Rev.*, 2011, **255**, 861–880.
19. J. T. Dixon, M. J. Green, F. M. Hess, and D. H. Morgan, *J. Organomet. Chem.*, 2004, **689**, 3641–3668.
20. D. F. Wass, *Dalton Trans.*, 2007, **8**, 816–819.
21. A. Carter, S. A. Cohen, N. A. Cooley, A. Murphy, J. Scutt, and D. F. Wass, *Chem. Commun.*, 2002, **3**, 858–859.
22. S. P. Downing, M. J. Hanton, A. M. Z. Slawin, and R. P. Tooze, *Organometallics*, 2009, **28**, 2417–2422.
23. W. R. H. Wright, A. S. Batsanov, A. M. Messinis, J. A. K. Howard, R. P. Tooze, M. J. Hanton, and P. W. Dyer, *Dalton Trans.*, 2012, **41**, 5502–5511.
24. J. H. Wengrovius, R. R. Schrock, M. R. Churchill, J. R. Missert, and W. J. Youngs, *J. Am. Chem. Soc.*, 1980, **102**, 4515–4516.
25. G. Natta, G. Dall'Asta, and G. Mazzanti, *Angew. Chemie Int. Ed.*, 1964, **3**, 723–729.
26. H. R. Menapace, N. A. Maly, J. L. Wang, and L. G. Wideman, *J. Org. Chem.*, 1975, **40**, 2983–2985.

27. M. J. Hanton, L. Daubney, T. Lebl, S. Polas, D. M. Smith, and A. Willemse, *Dalton Trans.*, 2010, **39**, 7025–7037.
28. R. R. Schrock, *Nobel Lecture: Multiple Metal-Carbon Bonds for Catalytic Metathesis Reactions*, 2005.
29. D. V. Peryshkov, R. R. Schrock, M. K. Takase, P. Müller, and A. H. Hoveyda, *J. Am. Chem. Soc.*, 2011, **133**, 20754–20757.
30. D. C. Bradley, M. B. Hursthouse, K. M. A. Malik, and A. J. Nielson, *J. Chem. Soc., Chem. Commun.*, 1981, 103–104.
31. S. F. Pedersen and R. R. Schrock, *J. Am. Chem. Soc.*, 1982, **104**, 7483–7491.
32. M. J. S. Dewar, *Bull. Soc. Chim. Fr.*, 1951, **18**, C71–C79.
33. J. Chatt and L. A. Duncanson, *J. Chem. Soc.*, 1953, 2939–2947.
34. J. C. Axtell, R. R. Schrock, P. Müller, S. J. Smith, and A. H. Hoveyda, *Organometallics*, 2014, **33**, 5342–5348.
35. A. Fürstner, *Angew. Chem. Int. Ed.*, 2000, **39**, 3012–3043.
36. R. R. Schrock and A. H. Hoveyda, *Angew. Chem. Int. Ed.*, 2003, **42**, 4592–4633.
37. R. R. Schrock, *Chem. Rev.*, 2002, **102**, 145–180.
38. H. Olivier and P. Laurent-Gérot, *J. Mol. Catal. A Chem.*, 1999, **148**, 43–48.
39. W. R. H. Wright, A. S. Batsanov, J. A. K. Howard, R. P. Tooze, M. J. Hanton, and P. W. Dyer, *Dalton Trans.*, 2010, **39**, 7038–7045.
40. P. Cossee, *J. Catal.*, 1964, **3**, 80–88.
41. E. Arlman, *J. Catal.*, 1964, **3**, 89–98.
42. E. Arlman, *J. Catal.*, 1964, **3**, 99–104.
43. G. V. Schulz, *Z. Phys. Chem.*, 1935, **30**, 379–398.
44. P. J. Flory, *J. Am. Chem. Soc.*, 1936, **58**, 1877–1885.
45. D. Takeuchi and K. Osakada, *Organometallic Reactions and Polymerization*, Springer Berlin Heidelberg, Berlin, Heidelberg, 2014, vol. 85.
46. J. X. McDermott, J. F. White, and G. M. Whitesides, *J. Am. Chem. Soc.*, 1976, **98**, 6521–6528.
47. F. Zheng, A. Sivaramakrishna, and J. R. Moss, *Coord. Chem. Rev.*, 2007, **251**, 2056–2071.
48. R. Emrich, O. Heinemann, P. W. Jolly, C. Krüger, and G. P. J. Verhovnik, *Organometallics*, 1997, **16**, 1511–1513.
49. S. J. McLain and R. R. Schrock, *J. Am. Chem. Soc.*, 1978, **100**, 1315–1317.
50. R. Schrock, S. McLain, and J. Sancho, *Pure Appl. Chem.*, 1980, **52**, 729–732.
51. J. D. Fellmann, G. A. Rupprecht, and R. R. Schrock, *J. Am. Chem. Soc.*, 1979, **101**, 5099–5101.
52. S. Tobisch, *Organometallics*, 2007, **26**, 6529–6532.
53. S.-Y. S. Wang, D. D. VanderLende, K. A. Abboud, and J. M. Boncella, *Organometallics*, 1998, **17**, 2628–2635.
54. W. C. P. Tsang, K. C. Hultzsch, J. B. Alexander, P. J. Bonitatebus, R. R. Schrock, and A. H. Hoveyda, *J. Am. Chem. Soc.*, 2003, **125**, 2652–2666.
55. H. Jahangiri, J. Bennett, P. Mahjoubi, K. Wilson, and S. Gu, *Catal. Sci. Technol.*, 2014, **4**, 2210–2229.
56. A. Shamiri, M. Chakrabarti, S. Jahan, M. Hussain, W. Kaminsky, P. Aravind, and W. Yehye, *Materials*, 2014, **7**, 5069–5108.
57. C. Copéret, A. Comas-Vives, M. P. Conley, D. P. Estes, A. Fedorov, V. Mougel, H. Nagae, F. Núñez-Zarur, and P. A. Zhizhko, *Chem. Rev.*, 2016, **116**, 323–421.
58. J. M. Thomas and R. Raja, *Top. Catal.*, 2006, **40**, 3–17.
59. S. Hübner, J. G. de Vries, and V. Farina, *Adv. Synth. Catal.*, 2016, **358**, 3–25.
60. C. Copéret and J.-M. Basset, *Adv. Synth. Catal.*, 2007, **349**, 78–92.
61. A. Dewaele, F. Verpoort, and B. Sels, *ChemCatChem*, 2016, **8**, 3010–3030.
62. A. Dewaele, B. Van Berlo, J. Dijkmans, P. a. Jacobs, and B. F. Sels, *Catal. Sci. Technol.*, 2016, **6**, 2580–2597.
63. B. Van Berlo, K. Houthoofd, B. F. Sels, and P. A. Jacobs, *Adv. Synth. Catal.*, 2008, **350**, 1949–1953.
64. J.-M. Basset, R. Psaro, D. Roberto, and R. Ugo, Eds., *Modern Surface Organometallic*

Chemistry, Wiley-VCH Verlag GmbH & Co. KGaA, Weinheim, Germany, 2009.
65. C. Copéret, *Chem. Rev.*, 2010, **110**, 656–680.
66. C. Copéret, M. Chabanas, R. Petroff Saint-Arroman, and J.-M. Basset, *Angew. Chem. Int. Ed.*, 2003, **42**, 156–181.
67. J. D. A. Pelletier and J.-M. Basset, *Acc. Chem. Res.*, 2016, **49**, 664–677.
68. A. J. Rossini, A. Zagdoun, M. Lelli, A. Lesage, C. Copéret, and L. Emsley, *Acc. Chem. Res.*, 2013, **46**, 1942–1951.
69. O. B. Lapina, *Catal. Today*, 2016, 1–15.
70. L. T. Zhuravlev, *Colloids Surf., A* , 2000, **173**, 1–38.
71. L. T. Zhuravlev and V. V. Potapov, *Russ. J. Phys. Chem.*, 2006, **80**, 1119–1128.
72. L. T. Zhuravlev, *Langmuir*, 1987, **3**, 316–318.
73. V. Y. Davydov, A. V. Kiselev, and L. T. Zhuravlev, *Trans. Faraday Soc.*, 1964, **60**, 2254–2264.
74. R. Mueller, H. K. Kammler, K. Wegner, and S. E. Pratsinis, *Langmuir*, 2003, **19**, 160–165.
75. M. Lelli, D. Gajan, A. Lesage, M. A. Caporini, V. Vitzthum, P. Miéville, F. Héroguel, F. Rascón, A. Roussey, C. Thieuleux, M. Boualleg, L. Veyre, G. Bodenhausen, C. Copéret, and L. Emsley, *J. Am. Chem. Soc.*, 2011, **133**, 2104–2107.
76. K. L. Fujdala and T. D. Tilley, *J. Am. Chem. Soc.*, 2001, **123**, 10133–10134.
77. J. J. Fripiat and J. Uytterhoeven, *J. Phys. Chem.*, 1962, **66**, 800–805.
78. P. J. Bailey, R. A. Coxall, C. M. Dick, S. Fabre, L. C. Henderson, C. Herber, S. T. Liddle, D. Loroño-González, A. Parkin, and S. Parsons, *Chem. Eur. J.*, 2003, **9**, 4820–4828.
79. M. K. Samantaray, E. Callens, E. Abou-Hamad, A. J. Rossini, C. M. Widdifield, R. Dey, L. Emsley, and J.-M. Basset, *J. Am. Chem. Soc.*, 2014, **136**, 1054–1061.
80. M. A. Bashir, T. Vancompernolle, R. M. Gauvin, L. Delevoye, N. Merle, V. Monteil, M. Taoufik, T. F. L. McKenna, and C. Boisson, *Catal. Sci. Technol.*, 2016, **6**, 2962–2974.
81. F. Rascón, R. Wischert, and C. Copéret, *Chem. Sci.*, 2011, **2**, 1449–1456.
82. C. Copéret, *New J. Chem.*, 2004, **28**, 1–10.
83. M. Valla, D. Stadler, V. Mougel, and C. Copéret, *Angew. Chem. Int. Ed.*, 2016, **55**, 1124–1127.
84. B. Rhers, A. Salameh, A. Baudouin, E. A. Quadrelli, M. Taoufik, C. Copéret, F. Lefebvre, J.-M. Basset, X. Solans-Monfort, O. Eisenstein, W. W. Lukens, L. P. H. Lopez, A. Sinha, and R. R. Schrock, *Organometallics*, 2006, **25**, 3554–3557.
85. M. P. Conley, V. Mougel, D. V Peryshkov, W. P. Forrest, D. Gajan, A. Lesage, L. Emsley, C. Copéret, and R. R. Schrock, *J. Am. Chem. Soc.*, 2013, **135**, 19068–19070.
86. W. A. Herrmann, A. W. Stumpf, T. Priermeier, S. Bogdanović, V. Dufaud, and J.-M. Basset, *Angew. Chem. Int. Ed.*, 1996, **35**, 2803–2805.
87. F. Blanc, A. Salameh, J. Thivolle-Cazat, J.-M. Basset, C. Copéret, A. Sinha, and R. R. Schrock, *Comptes Rendus Chim.*, 2008, **11**, 137–146.
88. F. Blanc, M. Chabanas, C. Copéret, B. Fenet, and E. Herdweck, *J. Organomet. Chem.*, 2005, **690**, 5014–5026.
89. V. Mougel and C. Copéret, *Chem. Sci.*, 2014, **5**, 2475–2481.
90. X. Solans-Monfort, C. Copéret, and O. Eisenstein, *Organometallics*, 2015, **34**, 1668–1680.
91. Y. Bouhoute, A. Garron, D. Grekov, N. Merle, K. C. Szeto, A. De Mallmann, I. Del Rosal, L. Maron, G. Girard, R. M. Gauvin, L. Delevoye, and M. Taoufik, *ACS Catal.*, 2014, **4**, 4232–4241.
92. D. Grekov, Y. Bouhoute, K. C. Szeto, N. Merle, A. De Mallmann, F. Lefebvre, C. Lucas, I. Del Rosal, L. Maron, R. M. Gauvin, L. Delevoye, and M. Taoufik, *Organometallics*, 2016, **35**, 2188–2196.
93. M. Pucino, V. Mougel, R. Schowner, A. Fedorov, M. R. Buchmeiser, and C. Copéret, *Angew. Chem. Int. Ed.*, 2016, **55**, 4300–4302.
94. E. Mazoyer, N. Merle, A. de Mallmann, J.-M. Basset, E. Berrier, L. Delevoye, J.-F. Paul, C. P. Nicholas, R. M. Gauvin, and M. Taoufik, *Chem. Commun.*, 2010, **46**, 8944–8946.
95. A. Hamieh, Y. Chen, S. Abdel-Azeim, E. Abou-hamad, S. Goh, M. Samantaray, R. Dey, L. Cavallo, and J. M. Basset, *ACS Catal.*, 2015, **5**, 2164–2171.
96. J. G. Howell, Y.-P. Li, and A. T. Bell, *ACS Catal.*, 2016, 7728–7738.

97. S. I. Kantorowicz, in *2nd Asian Petrochemicals Technology Conference*, 2002.
98. N. Popoff, E. Mazoyer, J. Pelletier, R. M. Gauvin, and M. Taoufik, *Chem. Soc. Rev.*, 2013, **42**, 9035–9054.
99. CB&I, *http://www.cbi.com/What-We-Do/Technology/Petrochemicals/Olefins/Ethylene-Production/Complementary-Technologies-(Ethylene-Production)/Olefins-Conversion-(OCT)*.
100. Nexant, *CHEMSYSTEMS prospectus, Evolving Popylene Sources - Solution to Supply Shortages?*, 2012, 1–115.
101. V. Vidal, *Science*, 1997, **276**, 99–102.
102. J. M. Basset, C. Copéret, D. Soulivong, M. Taoufik, and J. Thivolle Cazat, *Acc. Chem. Res.*, 2010, **43**, 323–334.
103. J. M. Basset, C. Copéret, L. Lefort, B. M. Maunders, O. Maury, E. Le Roux, G. Saggio, S. Soignier, D. Soulivong, G. J. Sunley, M. Taoufik, and J. Thivolle-Cazat, *J. Am. Chem. Soc.*, 2005, **127**, 8604–8605.
104. E. Le Roux, M. Taoufik, A. Baudouin, C. Copéret, J. Thivolle-Cazat, J. M. Basset, B. M. Maunders, and G. J. Sunley, *Adv. Synth. Catal.*, 2007, **349**, 231–237.
105. E. Le Roux, M. Taoufik, C. Copéret, A. de Mallmann, J. Thivolle-Cazat, J.-M. Basset, B. M. Maunders, and G. J. Sunley, *Angew. Chem. Int. Ed.*, 2005, **44**, 6755–6758.
106. A. Hamieh, R. Dey, M. K. Samantaray, S. Abdel-Azeim, E. Abou-Hamad, Y. Chen, J. D. A. Pelletier, L. Cavallo, and J.-M. Basset, *Organometallics*, 2016, **35**, 2524–2531.
107. E. Callens, N. Riache, K. Talbi, and J.-M. Basset, *Chem. Commun.*, 2015, **51**, 15300–15303.
108. J. Li, J. A. DiVerdi, and G. E. Maciel, *J. Am. Chem. Soc.*, 2006, **128**, 17093–17101.
109. R. N. Kerber, A. Kermagoret, E. Callens, P. Florian, D. Massiot, A. Lesage, C. Copéret, F. Delbecq, X. Rozanska, and P. Sautet, *J. Am. Chem. Soc.*, 2012, **134**, 6767–6775.
110. A. Kermagoret, R. N. Kerber, M. P. Conley, E. Callens, P. Florian, D. Massiot, C. Copéret, F. Delbecq, X. Rozanska, and P. Sautet, *Dalton Trans.*, 2013, **42**, 12681–12687.
111. A. Kermagoret, R. N. Kerber, M. P. Conley, E. Callens, P. Florian, D. Massiot, F. Delbecq, X. Rozanska, C. Copéret, and P. Sautet, *J. Catal.*, 2014, **313**, 46–54.
112. Y. Chen, E. Callens, E. Abou-Hamad, N. Merle, A. J. P. White, M. Taoufik, C. Copéret, E. Le Roux, and J.-M. Basset, *Angew. Chem. Int. Ed.*, 2012, **51**, 11886–11889.
113. J. Zhang, F. Zhang, L. Ren, D. G. Evans, and X. Duan, *Mater. Chem. Phys.*, 2004, **85**, 207–214.
114. D. O'Hare and Q. Wang, *Modification of Layered Double Hydroxides*, 2014, WO2014051530 (A2).
115. Q. Wang, and D. O'Hare, *Chem. Comm.*, 2013, **49**, 6301–6303.
116. C. Chen, M. Yang, Q. Wang, J.-C. Buffet, and D. O'Hare, *J. Mater. Chem. A*, 2014, **2**, 15102–15110.
117. G. Fan, F. Li, D. G. Evans, and X. Duan, *Chem. Soc. Rev.*, 2014, **43**, 7040–7066.
118. Z. P. Xu, J. Zhang, M. O. Adebajo, H. Zhang, and C. Zhou, *Appl. Clay Sci.*, 2011, **53**, 139–150.
119. T. Tamaki, N. Nakanishi, H. Ohashi, and T. Yamaguchi, *Electrochem. Commun.*, 2012, **25**, 50–53.
120. M. L. Parello, R. Rojas, and C. E. Giacomelli, *J. Colloid Interface Sci.*, 2010, **351**, 134–139.
121. L. Yang, Z. Shahrivari, P. K. T. Liu, M. Sahimi, and T. T. Tsotsis, *Ind. Eng. Chem. Res.*, 2005, **44**, 6804–6815.
122. K.-H. Goh, T.-T. Lim, and Z. Dong, *Water Res.*, 2008, **42**, 1343–1368.
123. W. Kagunya, Z. Hassan, and W. Jones, *Inorg. Chem.*, 1996, **35**, 5970–5974.
124. H. Frielingsdorf, H. Mueller-Tamm, G. Schweier, and L. Reuter, *Inorganic Carriers for Ziegler catalysts and the use thereof in the manufacture of olefin polymers*, 1975, GB1380949.
125. B. M. Choudary, S. Madhi, N. S. Chowdari, M. L. Kantam, and B. Sreedhar, *J. Am. Chem. Soc.*, 2002, **124**, 14127–14136.
126. D. O'Hare, *Catalyst systems for polymerization of olefins comprising layered double hydroxide catalyst support*, 2014, WO2014051529 A2.
127. J.-C. Buffet, N. Wanna, T. A. Q. Arnold, E. K. Gibson, P. P. Wells, Q. Wang, J. Tantirungrotechai, and D. O'Hare, *Chem. Mater.*, 2015, **27**, 1495–1501.

128. J.-C. Buffet, Z. R. Turner, R. T. Cooper, and D. O'Hare, *Polym. Chem.*, 2015, **6**, 2493–2503.
129. J.-C. Buffet, C. F. H. Byles, R. Felton, C. Chen, and D. O'Hare, *Chem. Commun.*, 2016, **52**, 4076–4079.
130. G. G. Hlatky, *Chem. Rev.*, 2000, **100**, 1347–1376.
131. A. H. Tullo, *Chem. Eng. News*, 2001, **79**, 38–39.
132. E. Kaji and E. Yoshioka, *Solid polymethylaluminoxane composition and process for manufacturing same*, 2010, WO2010055652.
133. A. F. R. Kilpatrick, J.-C. Buffet, P. Nørby, N. H. Rees, N. P. Funnell, S. Sripothongnak, and D. O'Hare, *Chem. Mater.*, 2016, **28**, 7444–7450.
134. F. Ghiotto, C. Pateraki, J. Tanskanen, J. R. Severn, N. Luehmann, A. Kusmin, J. Stellbrink, M. Linnolahti, and M. Bochmann, *Organometallics*, 2013, **32**, 3354–3362.
135. D. A. X. Fraser, Z. R. Turner, J.-C. Buffet, and D. O'Hare, *Organometallics*, 2016, **35**, 2664–2674.
136. T. A. Q. Arnold, Z. R. Turner, J.-C. Buffet, and D. O'Hare, *J. Organomet. Chem.*, 2016, **822**, 85–90.
137. P. Ransom, A. E. Ashley, N. D. Brown, A. L. Thompson, and D. O'Hare, *Organometallics*, 2011, **30**, 800–814.
138. F. Junges, R. F. de Souza, J. H. Z. dos Santos, and O. L. Casagrande, *Macromol. Mater. Eng.*, 2005, **290**, 72–77.
139. D. E. Fogg and E. N. dos Santos, *Coord. Chem. Rev.*, 2004, **248**, 2365–2379.
140. L. F. Tietze, *Chem. Rev.*, 1996, **96**, 115–136.
141. T. L. Lohr and T. J. Marks, *Nat. Chem.*, 2015, **7**, 477–482.
142. M. P. Hekkert, F. H. J. F. Hendriks, A. P. C. Faaij, and M. L. Neelis, *Energy Policy*, 2005, **33**, 579–594.
143. M. E. Dry, *Catal. Today*, 2002, **71**, 227–241.
144. J. E. Otterstedt, S. B. Gevert, S. G. Jääs, and P. G. Menon, *Appl. Catal.*, 1986, **22**, 159–179.
145. A. S. Goldman, A. H. Roy, Z. Huang, R. Ahuja, W. Schinski, and M. Brookhart, *Science*, 2006, **312**, 257–261.
146. B. C. Bailey, R. R. Schrock, S. Kundu, A. S. Goldman, Z. Huang, and M. Brookhart, *Organometallics*, 2009, **28**, 355–360.
147. Z. Huang, E. Rolfe, E. C. Carson, M. Brookhart, A. S. Goldman, S. H. El-Khalafy, and A. H. Roy MacArthur, *Adv. Synth. Catal.*, 2010, **352**, 125–135.
148. M. C. Haibach, S. Kundu, M. Brookhart, and A. S. Goldman, *Acc. Chem. Res.*, 2012, **45**, 947–958.
149. D. C. Leitch, J. A. Labinger, and J. E. Bercaw, *Organometallics*, 2014, **33**, 3353–3365.
150. J. A. Labinger, D. C. Leitch, J. E. Bercaw, M. A. Deimund, and M. E. Davis, *Top. Catal.*, 2015, **58**, 494–501.
151. D. C. Leitch, Y. C. Lam, J. A. Labinger, and J. E. Bercaw, *J. Am. Chem. Soc.*, 2013, **135**, 10302–10305.
152. J. Zhang, B.-G. Li, H. Fan, and S. Zhu, *J. Polym. Sci. Part A Polym. Chem.*, 2007, **45**, 3562–3569.
153. F. Alobaidi, Z. Ye, and S. Zhu, *J. Polym. Sci. Part A Polym. Chem.*, 2004, **42**, 4327–4336.
154. O. Sperber and W. Kaminsky, *Macromolecules*, 2003, **36**, 9014–9019.
155. S. Guo, H. Fan, Z. Bu, B. Li, and S. Zhu, *Macromol. Chem. Phys.*, 2014, **215**, 1661–1667.
156. F. F. Karbach, T. Macko, and R. Duchateau, *Macromolecules*, 2016, **49**, 1229–1241.
157. J. Zhang, H. Fan, B.-G. Li, and S. Zhu, *Ind. Eng. Chem. Res.*, 2008, **47**, 5369–5375.
158. D. C. Aluthge, A. Sattler, M. A. Al-Harthi, J. A. Labinger, and J. E. Bercaw, *ACS Catal.*, 2016, **6**, 6581–6584.

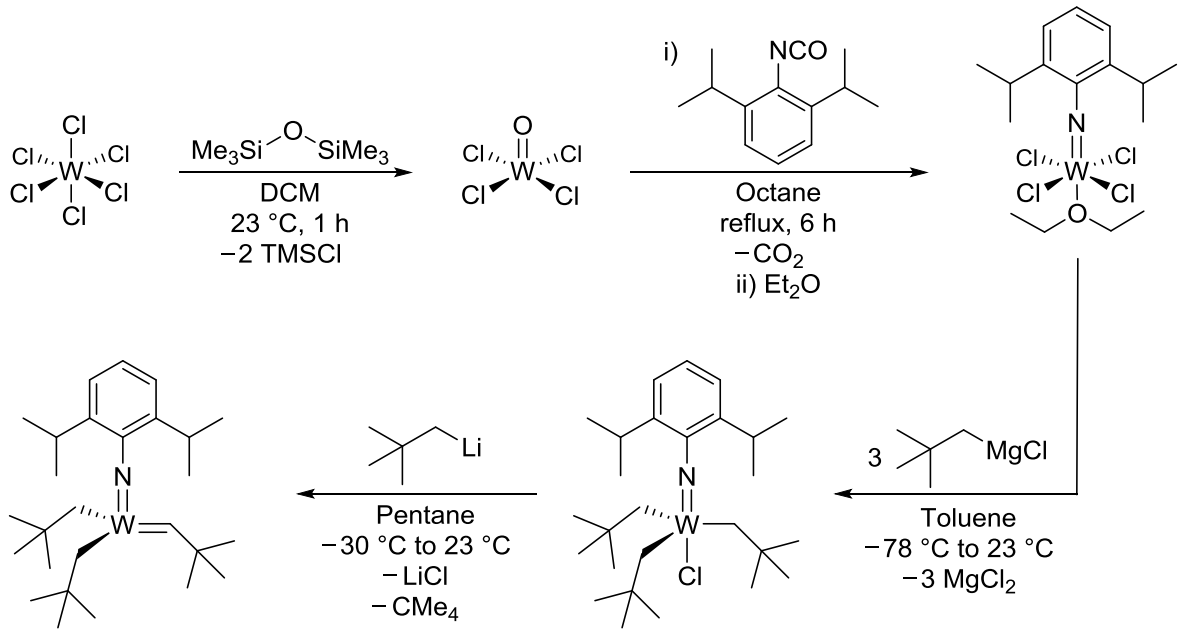
Chapter Two – Tungsten mono-imido oligomerisation catalysts

"A catalyst is a substance which alters the velocity of a chemical reaction without appearing in the final products." **Carl Wilhelm Wolfgang Ostwald**

2.1. Introduction

In 1981, Bradley and co-workers described the simple synthesis of the tungsten mono-imido complex $W(NPh)Cl_4$ from $W(O)Cl_4$ and PhNCO.[1] $W(O)Cl_4$ can be readily produced from the reaction of WCl_6 with hexamethyldisiloxane (HMDSO) in DCM.[2] Addition of THF to $W(NPh)Cl_4$ resulted in adduct formation and a six coordinate tungsten centre, although no structural characterisation was reported.[3] The base free tetrachloroimido compounds, shown to be dimers in the solid-state,[4] react with phosphines resulting in reduction to W^V d^1 complexes of the type $W(NR)Cl_3L_2$ (R = Ph or Et, L = PMe_3 or PMe_2Ph).[3] The first structurally characterised tetrachloroimido THF complex, $W\{N(4\text{-}Me\text{-}C_6H_4)\}Cl_4(THF)$, confirmed the octahedral arrangement about tungsten with the THF *trans* to the axial imido ligand and the chloride ligands occupying the equatorial plane.[5] The imido group acts as a 4 electron donor resulting in a near linear W–N–C_{ipso} angle of 177.4(4)°. In 1990, Schrock and co-workers reported the analogous tungsten imido complex $W\{N(2,6\text{-}^i Pr\text{-}C_6H_3)\}Cl_4(L)$ (L = Et_2O or THF).[6] Reaction of $W\{N(2,6\text{-}^i Pr\text{-}C_6H_3)\}Cl_4(Et_2O)$ with 3 equivalents of NpMgCl (Np = $CH_2{}^tBu$; neopentyl) yielded $W\{N(2,6\text{-}^i Pr\text{-}C_6H_3)\}Np_3Cl$, which adopts a trigonal bipyramidal arrangement about tungsten. Further reaction with one equivalent of NpLi, results in α-hydride abstraction and σ-bond metathesis, liberating neopentane and furnishing $W\{N(2,6\text{-}^i Pr\text{-}C_6H_3)\}(CH_2{}^tBu)_2(CH^tBu)$, in an analogous synthetic route to that of $Ta(CH_2{}^tBu)_3(CH^tBu)$ (Scheme 2.1).[7] The resulting tungsten neopentylidene complex was shown to be active towards propene metathesis.

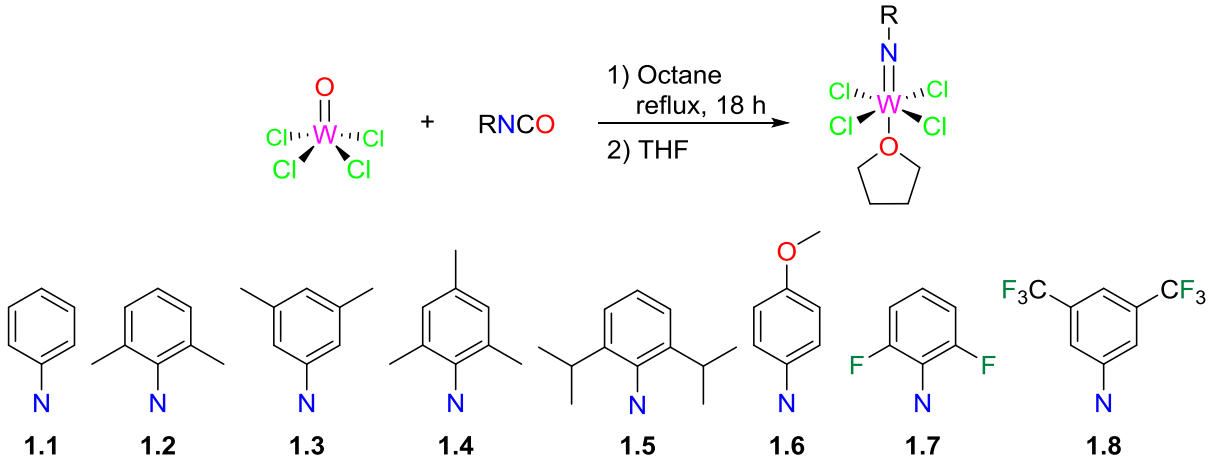
As described in Chapter One, oligomerisation systems based on tungsten complexes with alkyl aluminium co-catalysts have shown promise in the area of selective α-olefin dimerisation.[8–10] The proposed active species in these examples contain imido ligands, though, no definitive characterisation has been reported. This Chapter focuses on the elucidation of well-defined pre-catalysts formed by reaction of tungsten mono-imido precursors with alkyl aluminium reagents, and their propensity to oligomerise ethylene. Variations in both the imido fragment and ancillary ligand set have been attempted, and the effect on the structure and activity analysed. The attempted synthesis of proposed intermediates in the catalytic cycle is also discussed.



Scheme 2.1. Synthesis of W{N(2,6-^{i}Pr-C_6H_3)}($CH_2{}^{t}Bu$)$_2$($CH^{t}Bu$) from WCl_6.[6]

2.2. Synthesis and characterisation of W(NR)Cl$_4$(THF) complexes

The facile synthesis of mono-imido tetrachloride complexes utilising isocyanate reagents described by Bradley and co-workers, allows access to a variety of arylimido functionality. Despite being highly toxic, many isocyanates are commercially available. In order to probe the steric and electronic effects of the imido group in catalysis, aryl isocyanates with variable alkyl substitution (C_6H_5, 2,6-Me-C_6H_3, 3,5-Me-C_6H_3, 2,4,6-Me-C_6H_2, 2,6-^{i}Pr-C_6H_3) or electron donating/withdrawing groups (4-OMe-C_6H_4, 2,6-F-C_6H_3, 3,5-CF_3-C_6H_3) on the phenyl ring were explored. Refluxing the aryl isocyanate in octane (140 °C) with W(O)Cl$_4$ yields the corresponding tetrachloroimido complexes W(NR)Cl$_4$ (R = C_6H_5 (**1.1**),[3] 2,6-Me-C_6H_3 (**1.2**),[11] 3,5-Me-C_6H_3 (**1.3**), 2,4,6-Me-C_6H_2 (**1.4**), 2,6-^{i}Pr-C_6H_3 (**1.5**), 4-OMe-C_6H_4 (**1.6**),[12,13] 2,6-F-C_6H_3 (**1.7**), 3,5-CF_3-C_6H_3 (**1.8**)[13]), which can be crystallised from coordinating solvents such as THF or Et_2O (Scheme 2.2) in 60–80% yield. Bulk purity of **1.1**–**1.8** was confirmed by elemental analysis. Recrystallisation of the tetrachloroimido THF complexes from hexane yielded crystals suitable for structural determination by single crystal X-ray diffraction (Figure 2.1). A comparison of selected structural parameters and spectroscopic data for **1.1**–**1.8** and comparable literature examples: [W{N(4-Me-C_6H_4)}Cl_3]$_2$(μ-Cl)$_2$ (**A**),[4] W{N(4-Me-C_6H_4)}Cl$_4$(THF) (**B**),[5] W{N(4-I-C_6H_4)}Cl$_4$(NCMe) (**C**),[14] Mo{N(4-Me-C_6H_4)}Cl$_4$(THF) (**D**)[15] and Mo{N(3,5-CF_3-C_6H_3)}Cl$_4$(THF) (**E**)[16] is provided in Table 2.1. Full crystallographic data are given in the Appendix.



Scheme 2.2. Synthesis of $W(NR)Cl_4(THF)$ from $W(O)Cl_4$ and the corresponding aryl isocyanate. Atom colours correspond to those in the molecular structures shown below.

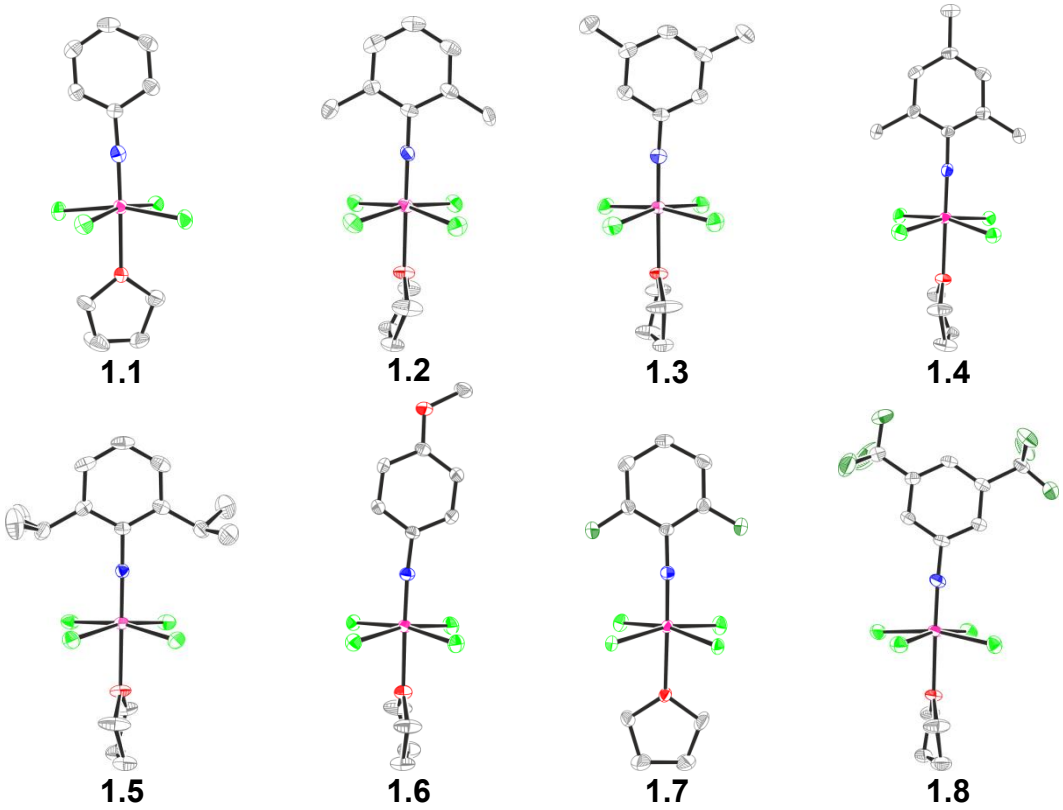


Figure 2.1. Molecular structures of the $W(NR)Cl_4(THF)$ complexes. Hydrogen atoms omitted for clarity, ellipsoids shown at 50% probability. $W\{N(C_6H_5)\}Cl_4(THF)$ (**1.1**), $W\{N(2,6\text{-}Me\text{-}C_6H_3)\}Cl_4(THF)$ (**1.2**), $W\{N(3,5\text{-}Me\text{-}C_6H_3)\}Cl_4(THF)$ (**1.3**), $W\{N(2,4,6\text{-}Me\text{-}C_6H_2)\}Cl_4(THF)$ (**1.4**), $W\{N(2,6\text{-}^{i}Pr\text{-}C_6H_3)\}Cl_4(THF)$ (**1.5**), $W\{N(4\text{-}OMe\text{-}C_6H_4)\}Cl_4(THF)$ (**1.6**),[13] $W\{N(2,6\text{-}F\text{-}C_6H_3)\}Cl_4(THF)$ (**1.7**), $W\{N(3,5\text{-}CF_3\text{-}C_6H_3)\}Cl_4(THF)$ (**1.8**).[13]

Table 2.1. Comparison of selected bond lengths (Å), angles (°), $^{13}C\{^1H\}$ C_{ipso} and, where applicable, $^{19}F\{^1H\}$ NMR spectroscopic chemical shifts (ppm), $G_{2.28}$(imido) (%)[17] and pKa values for the parent anilines[18] for W(NR)Cl_4(THF) unless specified otherwise. Estimated standard deviations (ESDs) are given in parentheses.

Complex	R	W–N	W–N–C_{ipso}	δ C_{ipso} [b]	δ ^{19}F	$G_{2.28}$(imido)[17]	pKa (RNH_3^+)[18]
A[4]	[W{N(4-Me-C_6H_4)}Cl_3]$_2$(μ-Cl)$_2$	1.712(18)	177.3(15)	-	-	12.74	4.99
B[5]	4-Me-C_6H_4	1.711(7)	178.38(1)	-	-	12.82	4.99
C[14,a]	4-I-C_6H_4	1.723(9)	174.4(9)	-	-	12.74	3.86
D[15]	Mo{N(4-Me-C_6H_4)}Cl_4(THF)	1.717(3)	174.6(3)	-	-	12.74	4.99
E[16]	Mo{N(3,5-CF_3-C_6H_3)}Cl_4(THF)	1.711(3)	171.4(3)	152.8	−62.7	12.88	2.35
1.1	C_6H_5	1.717(4)	177.1(3)	149.6	-	12.76	4.64
1.2	2,6-Me-C_6H_3	1.722(5)	179.5(5)	148.1	-	15.98	4.31
1.3	3,5-Me-C_6H_3	1.722(3)	176.0(3)	149.6	-	12.77	5.07
1.4	2,4,6-Me-C_6H_2	1.732(3)	177.4(3)	146.4	-	16.05	4.65
1.5	2,6-^{i}Pr-C_6H_3	1.723(3)	178.4(3)	156.1	-	18.62	4.00
1.6[13]	4-OMe-C_6H_4	1.733(3)	171.9(3)	144.0	-	12.83	5.11
1.7	2,6-F-C_6H_3	1.722(2)	176.22(18)	164.5	−111.0	13.99	0.69
1.8[13]	3,5-CF_3-C_6H_3	1.727(3)	172.9(3)	150.0	−63.1	12.88	2.35

[a] Coordinating solvent NCMe. [b] $^{13}C\{^1H\}$ NMR spectroscopy in d_6-benzene.

The ^{1}H, $^{13}C\{^{1}H\}$ and $^{19}F\{^{1}H\}$ NMR spectra of **1.7** are shown in Figure 2.2 as a representative example, NMR spectra for the other complexes are provided in the Appendix (Figures A1–A18). For **1.1**–**1.8**, resonances in the ^{1}H NMR spectrum corresponding to the aromatic imido protons between 7.43 and 5.62 ppm are observed, along with bound THF resonances at 4.55–4.39 and 1.30–1.24 ppm. For **1.7** and **1.8** a single fluorine resonance is observed at −111.0 and −63.1 ppm respectively. In all cases, single sharp resonances for equivalent groups on the imido fragment are observed, indicative of free rotation about the C–N bond in solution.

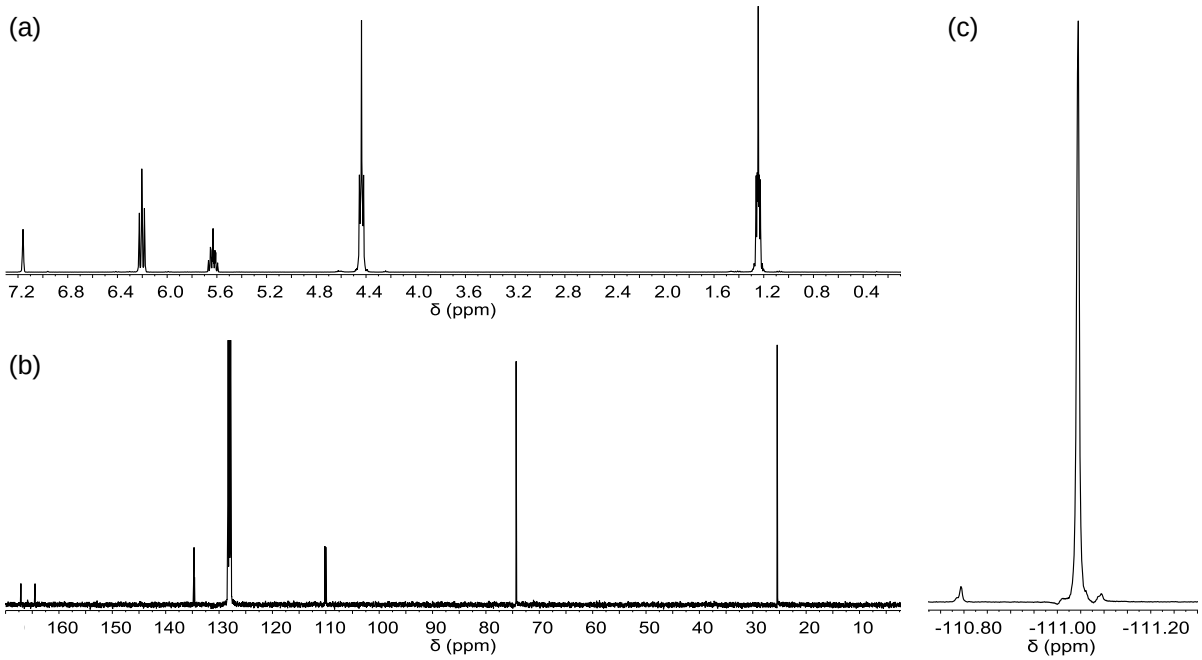


Figure 2.2. (a) ^{1}H (b) $^{13}C\{^{1}H\}$ and (c) $^{19}F\{^{1}H\}$ NMR spectra (400 MHz, 23 °C) of **1.7** in d_6-benzene.

The FTIR spectra for the compounds (Figures A19–A26) all display peaks around 3,000 cm^{-1} corresponding to aromatic C–H stretches, 1,500–1,400 cm^{-1} for aromatic C–C stretches, 1,335–1,250 cm^{-1} for the aromatic C–N stretch and 900–675 cm^{-1} for the C–H out-of-plane ('oop') bending mode. W–N imido stretches are known to be weak in nature and overlapped with stretches from other ligands, making their assignment very difficult,[19] and so they could not be unequivocally assigned for **1.1**–**1.8**. DFT calculations at the BP86[20–22] level of theory suggest that a significant contribution to bands in the region 1,000–900 cm^{-1}, arise from a coupling of the W–N stretch to a ring breathing mode.

From the molecular structures it can be seen that both the W–N bond lengths (1.717(4)–1.7330(1) Å) and W–N–C_{ipso} angles (171.9(3)–179.5(5)°) are consistent with previously reported complexes **A**–**E** (1.711(7)–1.723(9) Å and 171.4(3)–178.38(1)°). The

linearity of the W–N–C_{ipso} bond is indicative of triple bond character corresponding to donation of 4 electrons from the imido group in all cases. In all the complexes the chloride groups are bent slightly out of the equatorial plane away from the bulky imido groups (average N–W–Cl = ~96°) as has been observed in complexes **A**–**E**. The W–O bond length for the THF molecules bound *trans* to the imido group ranges from 2.230(3)–2.258(3) Å. This bond length correlates well with the W–N–C_{ipso} angle, as imido groups that approach linearity have better orbital overlap and donate more electron density to the metal centre and exert a stronger *trans* influence. The W–O bond (2.289(9) Å) for coordinated THF in the *trans* oxo complex $[(THF)_2(\mu\text{-}H)][\{W(O)Cl_3(THF)\}_2(\mu\text{-}O)]$[23] is longer than for any of the imido groups, consistent with the fact that oxo groups exhibit a larger *trans* influence.[24] The structure of the imido complexes when compared with the molybdenum analogues (**D** and **E**) are very similar. Due to the lanthanide contraction, the ionic radii of the two metals are almost identical (59 and 60 pm for Mo(VI) and W(VI) respectively),[25,26] which has been related to comparable structural and reactivity profiles in their complexes.[27]

In order to understand the subtle effects that varying the substituents on the imido group has on the bonding, comparison of different steric and electronic parameters was undertaken (Table 2.1). To identify differences in electronic donation by the imido group, both the ^{13}C chemical shift of the C_{ipso} resonance for **1.1**–**1.8** and the pKa values for the protonated parent anilines (RNH_3^+) were compared.[18,28,29] There is a large variation in the electronic properties by changing from electron donating to electron withdrawing substituents; pKa values lying in the order 4-OMe>3,5-Me>4-Me>2,4,6-Me>C_6H_5>2,6-Me>2,6-^{i}Pr>4-I>>3,5-CF_3>>2,6-F closely mirroring the ^{13}C δ values for the C_{ipso} resonances of the complexes: 4-OMe<2,4,6-Me<2,6-Me<C_6H_5≈3,5-Me<3,5-CF_3<2,6-^{i}Pr<<2,6-F. To probe the steric effects of the imido ligands, solid angle calculations were performed.[17] These can be visualised by projecting a sphere of radius *r* from the metal centre, which itself is viewed as a light source (Figure 2.3(a)). The shadow cast by a given ligand on this sphere of area *A*, can then be related to the solid angle Ω by the following equation:

Equation 2.1. Solid angle calculation:

$$\Omega = \frac{A}{r^2}$$

The benefit of this approach is that, unlike Tolman cone angles,[30] the area *A* is not necessarily spherical. The solid angle (Ω) can be described in terms of the unitless Steradian (sr) with a

maximum value of 4π, resulting from complete coverage. The percentage coverage of the sphere, or *G*-parameter (%), can therefore be calculated by the following equation:

Equation 2.2. Calculation of the *G*-parameter:

$$G = 100\frac{A}{4\pi r^2}$$

This *G*-parameter is entropic in nature and measures the probability of an incoming reagent accessing the metal centre. The *G*-parameter values are calculated based upon atomic coordinates available from experimental single crystal X-ray diffraction analysis. The *G*-parameter is independent of the ligand size, shape, symmetry and hapticity and can be calculated either for an individual ligand or for an entire metal complex even accounting for ligand overlap. Normalising the *G*-parameter by setting M–L to 2.28 Å ($G_{2.28}$), means comparison of the same ligand set in different complexes can be achieved. Figure 2.3(b) shows the visual projection of $G_{2.28}$ for the ligands in W{N(2,6-^{i}Pr-C_6H_3)}Cl_4(THF). The bulky 2,6-^{i}Pr group casts the largest shadow of any of the imido groups ($G_{2.28}$ = 18.62%). Substitution in the 2- and 6-positions results in the largest percentage coverage of the metal centre with $G_{2.28}$(imido) lying in the order 2,6-^{i}Pr>2,4,6-Me≈2,6-Me>2,6-F>3,5-CF_3≈4-OMe≈3,5-Me≈C_6H_5. Visualisations for the other imido complexes are shown in the Appendix (Figures A27–A34).

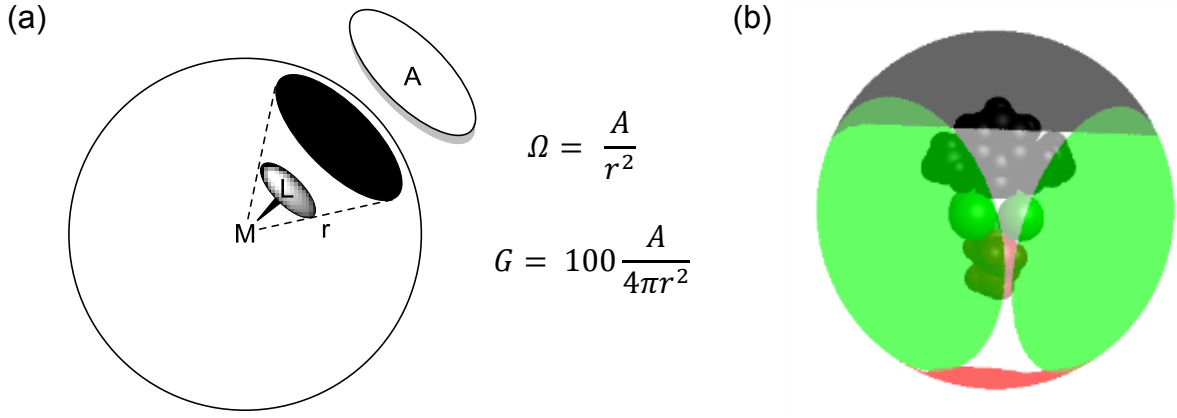


Figure 2.3. (a) Geometrical solid angle, *Ω*. The *G*-parameter for a ligand describes the fraction of a circumscribing sphere in the shadow of a ligand. (b) $G_{2.28}$ calculated for W{N(2,6-^{i}Pr-C_6H_3)}Cl_4(THF).

Comparison of these factors with both the W–N bond length and W–N–C_{ipso} bond angle data for **1.1**–**1.8** does not show a clear trend. However, comparing only the phenyl and methyl substituted imido groups shows that increasing the number of substituents around the ring

leads to a general increase in both the W–N bond length and $G_{2.28}$(imido) **1.4**>**1.2**≈**1.3**>**1.1**≈**B** with all the W–N–C_{ipso} angles closer to linearity (176.0(3)–179.5(5)°) than the imido groups with more electron withdrawing (**C** (174.4(9)°) or **1.8** (172.9(3)°)) or donating (**1.6** (171.9(3)°)) substituents. The sterically demanding 2,6-^{i}Pr group of **1.5** is the most electron deficient alkyl substituted imido reflected in both its pKa and δ C_{ipso} values, making it more withdrawing than the unsubstituted **1.1** (4.00 and 156.1 ppm *vs* 4.64 and 149.6 ppm respectively). Substitution of hydrogen by fluorine (**1.1** *vs* **1.7** and **1.3** *vs* **1.8**) leads to an increase in the W–N bond length and further deviation away from linearity of the W–N–C_{ipso} bond, which may be a result of poorer overlap of the nitrogen lone pair with the metal d orbitals.

Density functional theory (DFT) calculations at the BP86[20–22] level of theory were carried out on W{N(2,6-^{i}Pr-C_6H_3)}Cl_4(THF) (**1.5**) with the calculated structural parameters matching well with those observed experimentally (Figure 2.4 and Table 2.2). The HOMO shows a π-bonding interaction between the W d_{yz} and the imido N p_y orbitals. The LUMO is mainly centred on the W d_{xy} orbitals as would be expected form the molecular orbital description of the bonding from simple MO treatment (Figure 2.5).[12]

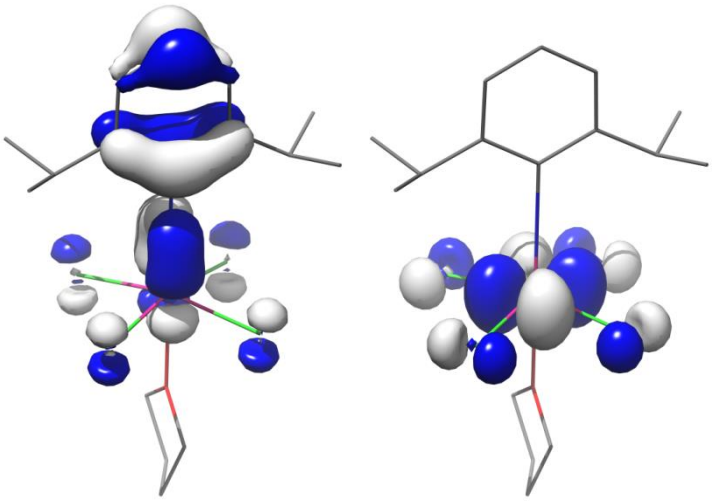


Figure 2.4. DFT-computed (BP86) HOMO (left) and LUMO (right) W{N(2,6-^{i}Pr-C_6H_3)}Cl_4(THF).

Table 2.2. Comparison of selected calculated and experimental bond lengths (Å) and angles (°) for W{N(2,6-^{i}Pr-C_6H_3)}Cl_4(THF). Estimated standard deviations (ESDs) are given in parentheses.

Parameter	Experimental	Calculated – BP86
W–Cl av.	2.3348	2.3525
W–N	1.7226(1)	1.749
W–O	2.2549(1)	2.334
W–N–C_{ipso}	178.38(1)	179.76
O–W–N	179.27(1)	179.92
Cl–W–Cl	167.22(1)	165.60

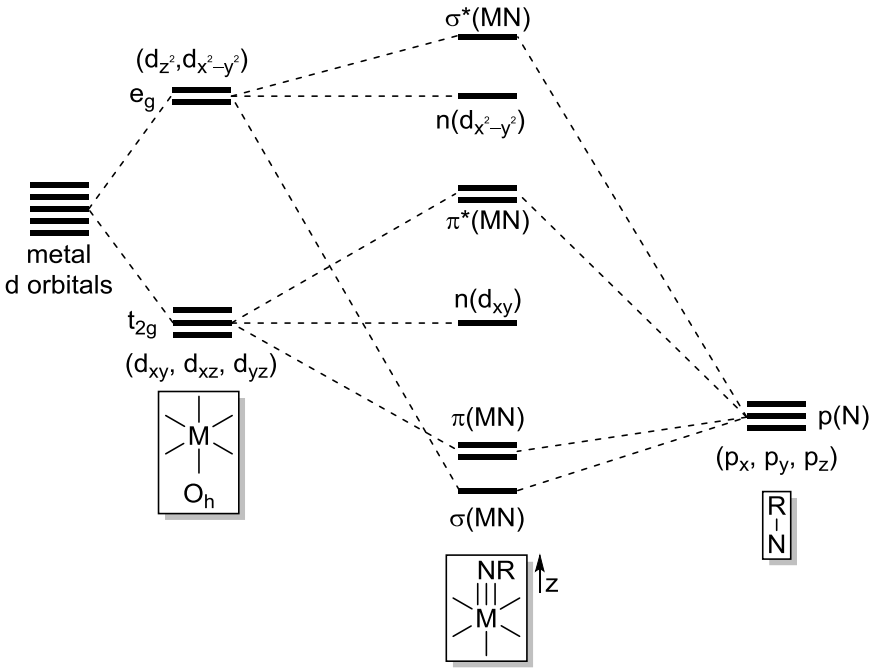


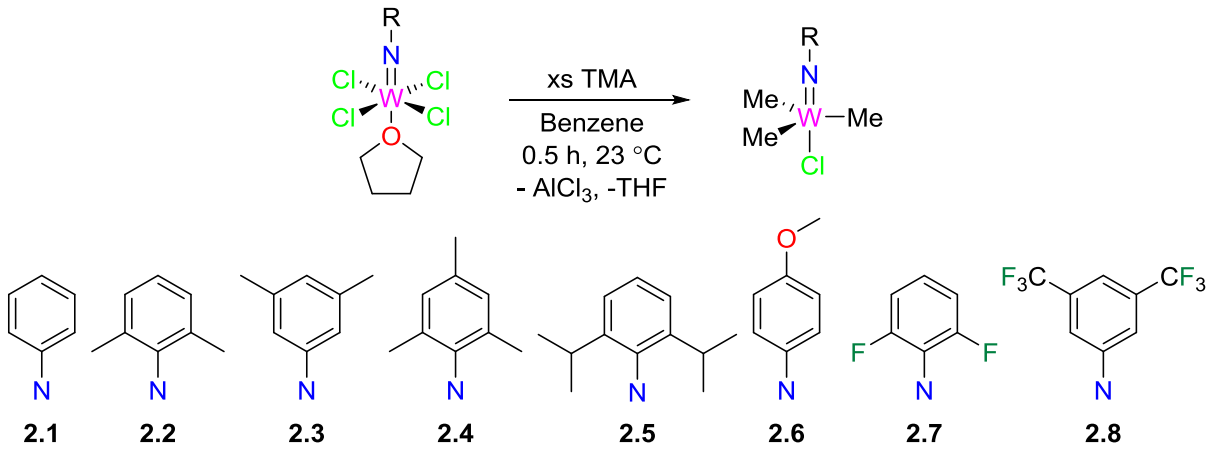
Figure 2.5. Orbital energy diagram for a linear imido complex with octahedral geometry.[12]

2.3. Reactivity towards alkyl aluminium reagents

2.3.1. Synthesis and characterisation of W(NR)Me$_3$Cl complexes

Alkyl aluminium activators are commonly employed as co-catalysts for ethylene oligomerisation with tungsten initiators.[8–10,31] To try and identify the active species formed from tungsten imido pre-catalysts and ethylaluminium reagents described by Olivier *et al.*,[9] a d_6-benzene solution of W{N(2,6-^{i}Pr-C_6H_3)}Cl_4(THF) (**1.5**) was reacted with one equivalent of triethylaluminium (TEA). The reaction was accompanied by an immediate colour change from green to dark brown. The ^{1}H NMR spectrum exhibited a large quantity of ethane, but no identifiable tungsten products. It is proposed that initial formation of a tungsten ethyl complex occurs but that the propensity for such a species to β-hydride eliminate results in rapid evolution of ethane, with formation of multiple ill-defined tungsten products following

tungsten hydride formation. To avoid this possible decomposition pathway, methylated aluminium reagents were chosen as they do not contain β-hydrogens. **1.1**–**1.8** were reacted with trimethylaluminium (TMA) in benzene. Following work-up and recrystallisation at −33 °C, W(NR)Me_3Cl complexes **2.1**–**2.8** were isolated in 20–80% yield (Scheme 2.3). This reactivity is analogous to the reaction of W{N(C_6H_5)}Cl_4 with an excess of $ZnMe_2$ described by Schrock and co-workers; the chemical equivalence of the methyl groups was ascribed to a trigonal bipyramidal structure, but no solid-state structural characterisation was reported.[32] Analogous reactivity was observed when employing excess methylaluminoxane (MAO) or dimethylaluminium chloride (DMAC). At room temperature, no additional alkylation was observed with excess TMA or DMAC. An isolated sample of **2.5** was shown to be stable up to 100 °C for 18 hours in a d_6-benzene solution, with no significant changes in the ^{1}H NMR spectroscopic resonances over the temperature range observed.



Scheme 2.3. Synthesis of W(NR)Me_3Cl complexes. Atom colours correspond to the molecular structures.

Recrystallisation from hexanes allowed for elucidation of the solid-state molecular structures of six of these complexes (**2.1**–**2.3** and **2.5**–**2.7**), which display a trigonal bipyramidal structure about tungsten, with the three methyl groups in the equatorial plane (Figure 2.6). Unlike the molecular structure of the bis-imido complex, W(NDipp){(NDipp)$AlMe_2$(μ-Cl)}Me_2 (Dipp = 2,6-^{i}Pr-C_6H_3) reported by Dyer and co-workers,[33] no aluminium coordination is observed. Bulk purity of the crystallised complexes was confirmed by elemental analysis. Comparison of key structural parameters and spectroscopic data for the isolated complexes are given in Table 2.2. Full crystallographic data are given in the Appendix.

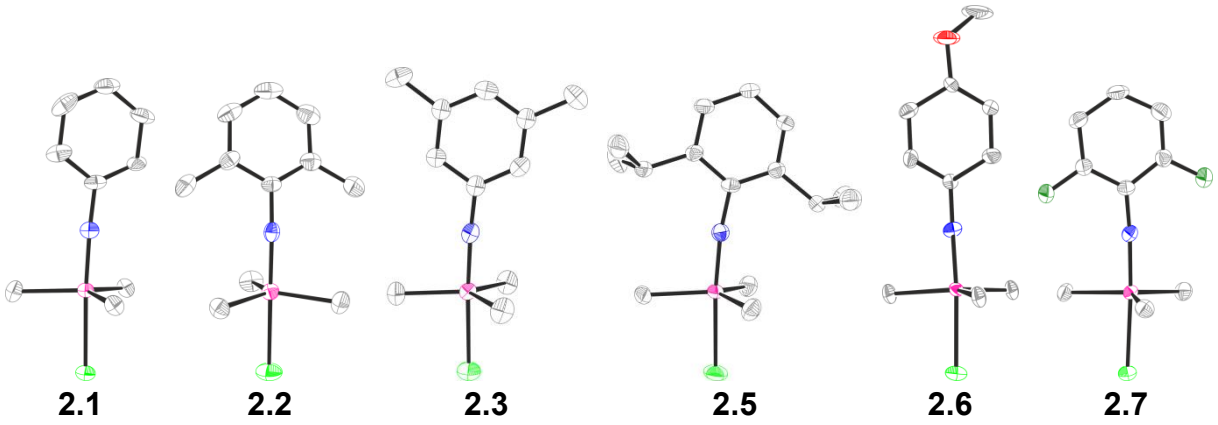


Figure 2.6. Molecular structures of the $W(NR)Me_3Cl$ complexes. Hydrogen atoms omitted for clarity, ellipsoids shown at 50% probability. $W\{N(C_6H_5)\}Me_3Cl$ (**2.1**), $W\{N(2,6\text{-Me-}C_6H_3)\}Me_3Cl$ (**2.2**), $W\{N(3,5\text{-Me-}C_6H_3)\}Me_3Cl$ (**2.3**), $W\{N(2,6\text{-}^{i}\text{Pr-}C_6H_3)\}Me_3Cl$ (**2.5**), $W\{N(4\text{-OMe-}C_6H_4)\}Me_3Cl$ (**2.6**)[13] and $W\{N(2,6\text{-F-}C_6H_3)\}Me_3Cl$ (**2.7**).

For this set of complexes, the change in the W–N bond length reflects the change in the electronics of the imido group, following the order of the pKa values for the parent anilines, with the most electron deficient groups exhibiting the longest bonds. An increase in the W–N–C_{ipso} angle is noted as the size of the substituents in the 2- and 6- positions are increased, and is attributed to the steric clash between these substituents and one of the methyl groups. The W–Cl bonds are much longer than in the precursor complexes (*e.g.* 2.412(2) *vs* 2.3348 Å for **2.5** and **1.5** respectively) due to the *trans* influence of the imido group, which may labilise the bond towards further reactivity. The structural parameters for both the imido and methyl groups are consistent with the previously reported tungsten and molybdenum bis-imido complexes **H** and **J**.[33,34] The elongated chloride bond *trans* to the imido group is observed in complexes **F** and **G**,[16,35] which also adopt trigonal bipyramidal arrangements.

Analysis of the ^{1}H and $^{19}F\{^{1}H\}$ (where applicable) NMR spectra (Figures A35–A52) show a shift to lower frequency in the imido resonances compared to the $W(NR)Cl_4(THF)$ complexes, which again show magnetic equivalence due to free rotation in solution. A new singlet in the ^{1}H NMR spectra accompanied by tungsten satellites is observed between 1.24–1.41 ppm, consistent with the formation of three equivalent W–Me bonds and hence a more electron rich complex; a corresponding resonance is also observed in the $^{13}C\{^{1}H\}$ NMR spectra. For example, the ^{1}H NMR spectrum of **2.5** exhibits a singlet at 1.41 ppm accompanied by tungsten satellites ($^{2}J_{W-H}$ = 7.0 Hz and a resonance at 56.5 ppm ($^{1}J_{W-C}$ = 156 Hz) in the $^{13}C\{^{1}H\}$ spectrum (Figure 2.7). The W–Me groups in **2.8** are much more shielded than expected for an electron withdrawing imido group; the ^{1}H NMR spectroscopic resonance for the methyl groups appears at 1.24 ppm, the lowest of all the complexes.

Table 2.3. Comparison of selected bond lengths (Å), angles (°), $^{13}C\{^{1}H\}$ C_{ipso}, ^{1}H W–CH_3 and, where applicable, $^{19}F\{^{1}H\}$ NMR spectroscopic chemical shifts (ppm) and $G_{2.28}$(imido) (%)[17] for the synthesised W(NR)Me_3Cl complexes and relevant literature compounds. Estimated standard deviations (ESDs) are given in parentheses.

Complex	R	W–N	W–X (X=Cl, Br)	W–C_α (av.)	W–N–C_{ipso}	δ C_{ipso} [a]	δ W–CH_3	δ ^{19}F	$G_{2.28}$(imido)[17]
F[35,36]	W($OAlBr_3$)Np_3Br	1.77(1)	2.428(3)	2.11(1)	172(1)	-	-	-	-
G[16]	Mo{N(3,5-CF_3-C_6H_3)}Np_3Cl	1.7471(17)	2.3944(5)	2.142(16)	174.94(15)	-	-	−62.5	-
H[33]	W$(NDipp)_2Me_2$(THF)	1.764(4) [b]	-	2.158(5)	176.9(4) [b]	152.8	1.25	-	-
I[1]	[W(NPh)$(PMe_3)Me_2$(μ-O)]$_3$	1.7513(4) [c]	-	2.2139(5)[c]	169.49(2)[c]	-	-	-	-
J[34]	Mo$(NDipp)_2Me_2$	1.749(4) [b]	-	2.109(5)	159.6(3) [b]	153.1	1.39	-	-
2.1	C_6H_5	1.740(8)	2.415(2)	2.109(9)	174.9(6)	152.1	1.29	-	12.79
2.2	2,6-Me-C_6H_3	1.746(4)	2.4324(14)	2.098(5)	171.7(3)	150.4	1.34	-	15.99
2.3	3,5-Me-C_6H_3	1.731(8)	2.404(3)	2.100(8)	176.3(7)	152.3	1.34	-	12.77
2.4	2,4,6-Me-C_6H_2	-	-	-	-	149.0	1.41	-	-
2.5	2,6-^{i}Pr-C_6H_3	1.743(9) [d]	2.414(3) [d]	2.108(12)[d]	172.0(6)[d]	150.4	1.41	-	18.47
2.6[13]	4-OMe-C_6H_4	1.737(10)	2.416(2)	2.106(8)	178.0(3)	159.7	1.30	-	12.76
2.7	2,6-F-C_6H_3	1.753(4)	2.4239(13)	2.103(5)	174.8(4)	163.9	1.45	−117.6	13.96
2.8	3,5-CF_3-C_6H_3	-	-	-	-	153.2	1.24	−62.9	-

[a] $^{13}C\{^{1}H\}$ NMR in d_6-benzene. [b] Calculated for the linear imido fragment. [c] Average of the three tungsten centres. [d] Average of the two molecules in the asymmetric unit. Np = neopentyl. Dipp = 2,6-^{i}Pr-C_6H_3.

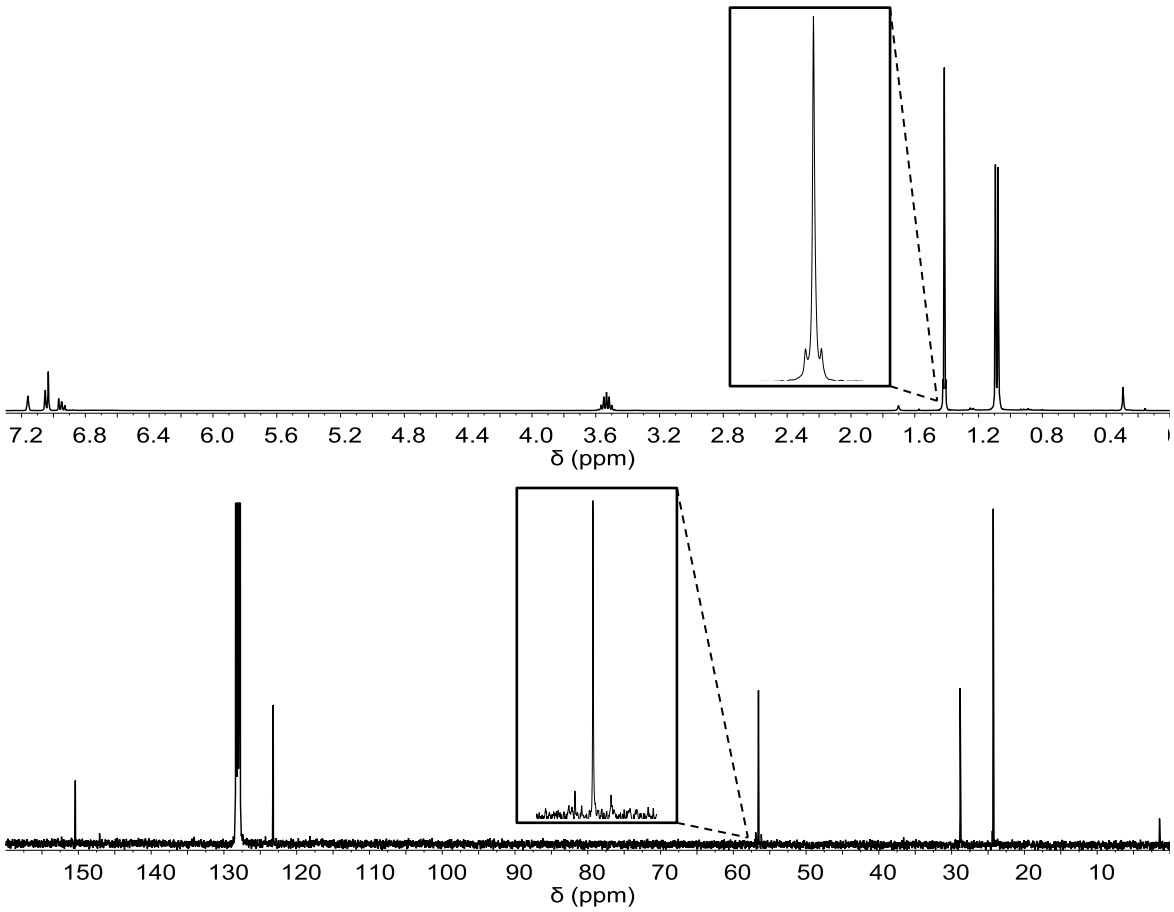


Figure 2.7. ^{1}H and $^{13}C\{^{1}H\}$ NMR spectra (400 MHz, 23 °C) of **2.5** in d_6-benzene. W–Me resonances at 1.41 and 56.6 ppm respectively showing tungsten satellites are highlighted.

DFT calculations on **2.5** show that the HOMO displays a bonding interaction between the W d_{yz} and N p_y orbitals (Figure 2.8), as was seen for **1.5**. The LUMO differs from the precursor in that it is now an antibonding interaction between these orbitals rather than a non-bonding d_{xy} orbital. As can be seen from the molecular orbital description of the bonding, this non-bonding orbital now sits above the π* orbitals in energy due to the change in geometry from octahedral to trigonal bipyramidal (Figure 2.9).[37]

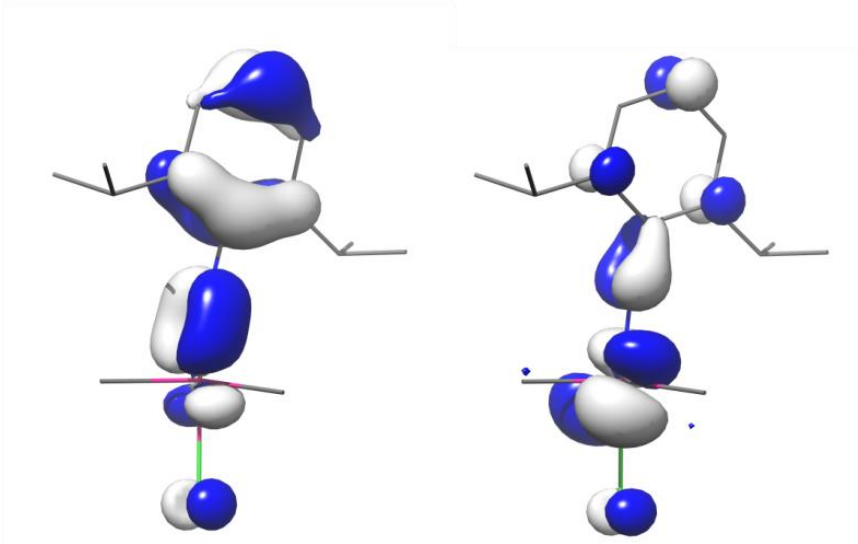


Figure 2.8. DFT-computed (BP86) HOMO (left) and LUMO (right) W{N(2,6-^{i}Pr-C_6H_3)}Me_3Cl.

Table 2.4. Comparison of selected calculated and experimental bond lengths (Å) and angles (°) for W{N(2,6-^{i}Pr-C_6H_3)}Me_3Cl. Estimated standard deviations (ESDs) are given in parentheses.

Parameter	Experimental	Calculated – BP86
W–Me av.	2.1081	2.214
W–N	1.7370(1)	1.775
W–Cl	2.4156(1)	2.400
W–N–C_{ipso}	172.51	172.06
Cl–W–N	174.95	174.02
Me–W–Me	122.76	122.54

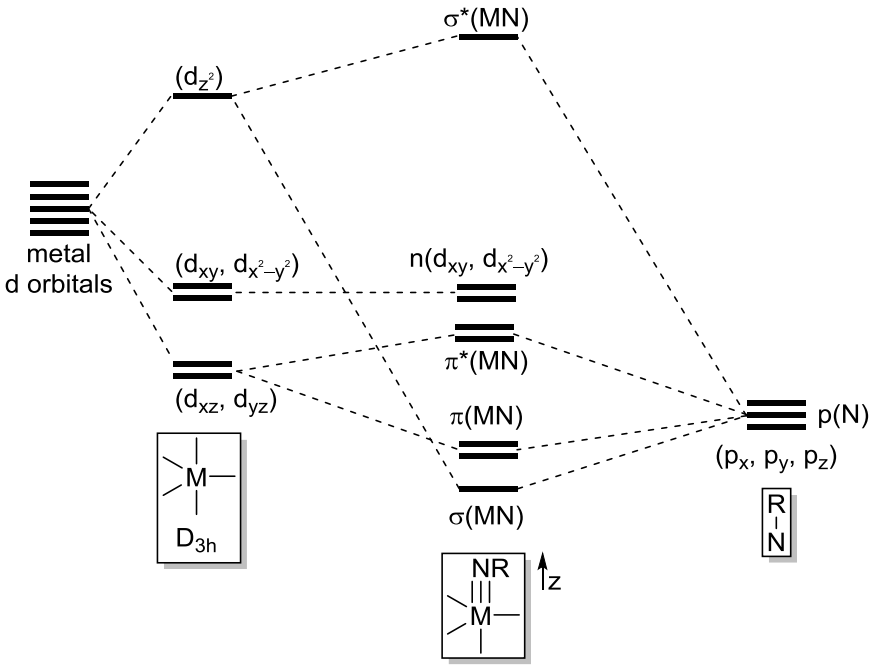


Figure 2.9. Orbital energy diagram for linear imido complex in a trigonal bipyramidal geometry.[37]

Solid angle calculations on **2.5** show that this trigonal bipyramidal arrangement affords less steric protection to the metal centre than for **1.5** (G_{total}(complex) = 82.55% *vs* 92.31%) (Figure 2.10). Visualisations for the other W(NR)Me_3Cl complexes are given in the Appendix (Figures A58–A63).

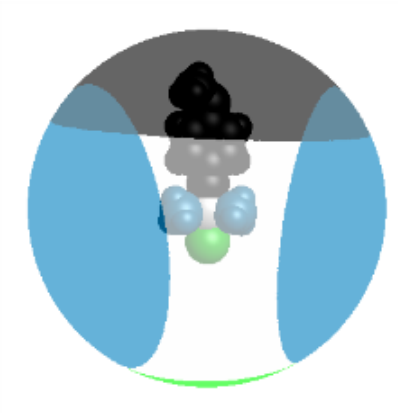
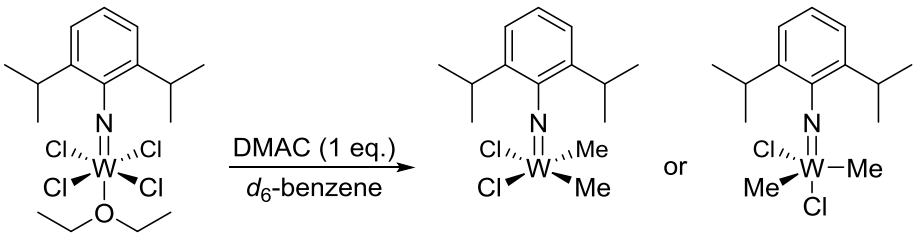


Figure 2.10. Visualisation of solid angle calculation for W{N(2,6-^{i}Pr-C_6H_3)}Me_3Cl (**2.5**).

2.3.2. Attempted synthesis of W{N(2,6-^{i}Pr-C_6H_3)}Me_2Cl_2

As reaction of TMA with W(NR)Cl_4(THF) led to trimethylation, dimethylation using one equivalent of DMAC was attempted. Formation of a complex of the type W(NR)Me_2Cl_2 was of interest to determine its structural preference, either for the trigonal bipyramidal geometry adopted by the W(NR)Me_3Cl complexes, or a square pyramidal structure (Scheme 2.4).



Scheme 2.4. Postulated products that may form from reaction of **1.5**(Et_2O) with DMAC.

Addition of DMAC (1 eq.) to a green solution of W{N(2,6-^{i}Pr-C_6H_3)}Cl_4(Et_2O) (**1.5**(Et_2O)) in d_6-benzene yielded an orange solution. ^{1}H NMR spectroscopy indicated that a small amount of the desired W{N(2,6-^{i}Pr-C_6H_3)}Me_2Cl_2 complex had formed by observation of a singlet at 1.70 ppm with apparent tungsten satellites; and corresponding resonances for the imido substituent. Due to the presence of starting material, more DMAC was added; however, preferential formation of W{N(2,6-^{i}Pr-C_6H_3)}Me_3Cl was observed. An analogous reaction was carried out on a larger scale (0.35 mmol). Following work-up and recrystallisation from hexane, a mixture of the di- and trimethylated complexes were

identified by ^{1}H NMR spectroscopy in a 10:90 ratio with diethyl ether remaining coordinated (Figure 2.11). Recrystallisation attempts yielded only the trimethyl species **2.5**.

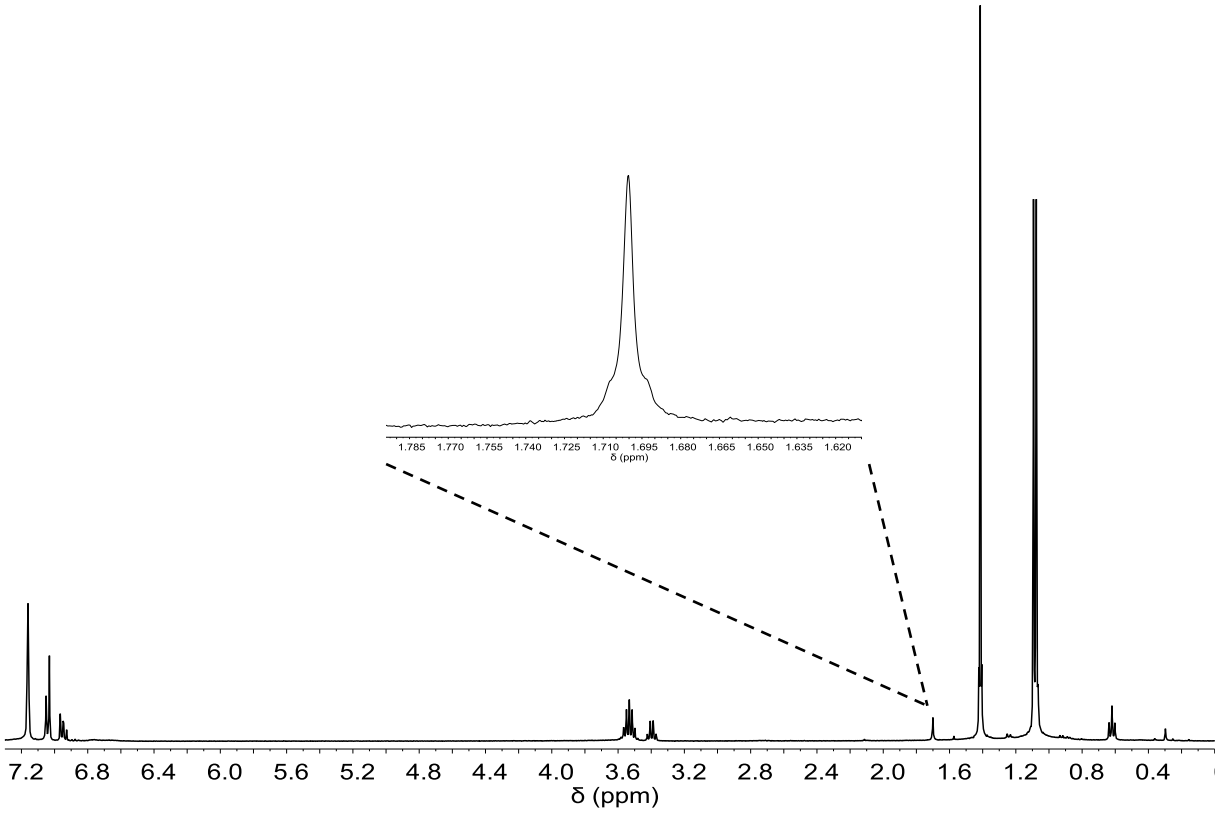
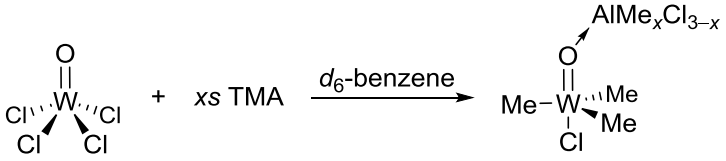


Figure 2.11. ^{1}H NMR spectrum (400 MHz, 23 °C) in d_6-benzene (7.16 ppm) of the products from the reaction between **1.5**(Et_2O) and DMAC.

2.3.3. Synthesis of W(O)Me_3Cl

Alkylation of silica supported tungsten oxo complexes have been demonstrated to yield active catalysts for metathesis and ethylene to propylene conversion reactions.[38,39] Synthesis of a homogeneous tungsten oxo methyl complex was targeted in order to compare the reactivity with ethylene to the W(NR)Me_3Cl imido complex. Reaction of W(O)Cl_4 with TMA (1.1 eq.) in d_6-benzene resulted in a darkening of the solution to dark brown with formation of a black precipitate. ^{1}H NMR spectroscopy indicated that trimethylation had occured in an analogous manner to W(NR)Me_3Cl, by observation of one singlet for the new W–Me groups at 1.83 ppm ($^{2}J_{W–H}$ = 8.8 Hz) (Figure A64). It is proposed that the Lewis acidic aluminium datively bonds to the lone pair of W(O)Me_3Cl (Scheme 2.5) in an analogous manner to that observed for W(O)Np_3Cl.[35,36]

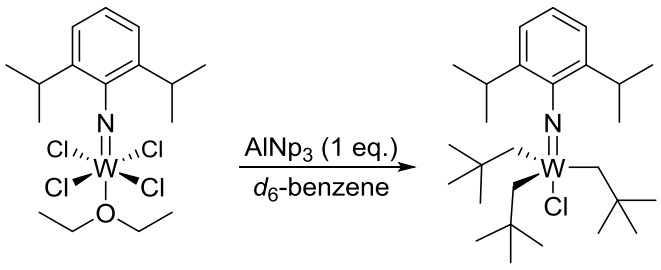


Scheme 2.5. Reaction of $W(O)Cl_4$ with TMA to yield $W(O)Me_3Cl$.

Work-up of the reaction utilising either hexane or a mixture of hexane and THF led to precipitation of a flocculent solid, however, no proton environments could be observed by ^1H NMR spectroscopy, indicating decomposition had occurred. When toluene was employed no such decomposition was observed. Cooling of the solution to −33 °C, afforded small brown crystals. Unfortunately, further analysis by X-ray diffraction was thwarted by their high instability in the absence of solvent, with immediate decomposition to a blue solution occurring upon removal from the Schlenk flask. Osborn and co-workers reported that addition of $AlBr_3$ to $W(O)Np_3Br$, leads to precipitation of the adduct which can be recrystallised from toluene.[36] Such complexes were observed to release neopentane photochemically in sunlight. It is proposed that the lack of steric protection from the methyl groups in $W(O)Me_3Cl$ compared to neopentyl ligands, may facilitate bimolecular decomposition pathways.

2.3.4. Attempted synthesis of W{N(2,6-^{i}Pr-C_6H_3)}Np_3Cl utilising $AlNp_3$

Schrock and co-workers reported the preparation of W{N(2,6-^{i}Pr-C_6H_3)}Np_3Cl by reaction of **1.5**(Et_2O) with 3 equivalents of NpMgCl (Scheme 2.1).[6] However, the reaction is relatively low yielding (35%) and limits preparation of the defined alkylidene complex W{N(2,6-^{i}Pr-C_6H_3)}($CH_2{}^t$Bu)$_2$(CH^tBu), on a useful scale. Having observed selective trimethylation of **1.5** with TMA, it was proposed that reaction with $AlNp_3$[40] may yield the desired trigonal bipyramidal trisneopentyl complex in better yields (Scheme 2.6).



Scheme 2.6. Postulated formation of W{N(2,6-^{i}Pr-C_6H_3)}Np_3Cl from **1.5**(Et_2O) and $AlNp_3$.

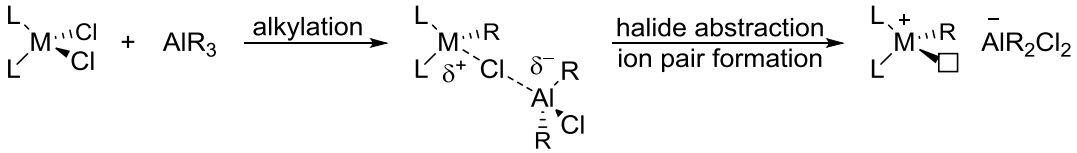
Mixing $AlNp_3$ and **1.5**(Et_2O) in d_6-benzene resulted in a colour change from green to orange. Analysis of the ^1H NMR spectrum indicated that a symmetrical W–Np environment had been formed (singlet at 2.79 ppm with accompanying ^{183}W satellites) although the

resonance was shifted downfield from that expected for W{N(2,6-^{i}Pr-C_6H_3)}($CH_2{}^{t}$Bu)$_3$Cl (2.48 ppm). The major product formed (~80%) was the alkylidene complex W{N(2,6-^{i}Pr-C_6H_3)}(CH^{t}Bu)$_3$($CH_2{}^{t}$Bu)$_2$,[6] with neopentane and diethyl ether also observed. Attempts to scale the reaction up in benzene, yielded a yellow solid after cooling of a hexane solution to −33 °C, however, this was shown to be an intractable mixture of products.

2.4. Reactivity of W(NR)Me$_3$Cl complexes towards α-olefins

2.4.1. Oligomerisation of ethylene utilising W{N(2,6-^{i}Pr-C_6H_3)}Me$_3$Cl (2.5)

Aluminium based co-catalysts are often employed, in order to activate olefin oligomerisation and polymerisation catalysts.[9,41,42] The role of such compounds is well understood, especially in the activation of metallocene catalysts for ethylene polymerisation.[41] This proceeds *via* alkylation of a metal-halide bond followed by abstraction of the remaining halogen by the Lewis acidic aluminium centre to form an ion pair. This provides a vacant coordination site where ethylene can bind, prior to insertion into the metal-alkyl bond (Scheme 2.7).

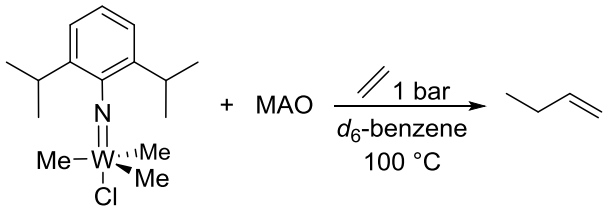


Scheme 2.7. Activation of metal complexes by alkyl aluminium cocatalysts.[41]

In 1981, Kaminsky and co-workers reported the synthesis of a new aluminium activator, formed by addition of 1 equivalent of water to TMA. This species, labelled methylaluminoxane (MAO), was capable of activating metallocene pre-catalysts for ethylene polymerisation, leading to activities up to 10,000 times greater than those observed with the simple aluminium alkyl species used extensively in Ziegler systems.[43] While the exact structure of MAO is still unknown, extensive analysis of this material indicates that it contains oligomeric chains of [$Al_4O_3Me_6$] units which cluster together forming cage and tubular structures.[41,44,45] For metallocene catalysts, MAO is often required in large excess to achieve high activities. One possible mechanism of alkylation is believed to occur from residual TMA present in the oligomeric structure. Even if alkylation of both halide groups occurs, MAO is capable of abstracting a methyl group to yield the catalytically competent cationic species. The is due to the presence of electron withdrawing oxygen atoms in MAO, which increase its Lewis acidity compared to simple alkyl aluminium species. Performing the

same role as for polymerisation pre-catalysts, MAO has been widely employed as an activator for olefin oligomerisation pre-catalysts.[42,46]

W{N(2,6-^{i}Pr-C_6H_3)}Me_3Cl (**2.5**) was tested for its reactivity towards ethylene utilising MAO as a cocatalyst. Contacting **2.5** with ethylene in d_6-benzene containing pyridine (9.93 μmol) as an internal standard under mild conditions (1 bar, 100 °C) in a J. Young valve NMR spectroscopy tube in the presence of MAO (W:Al = 1:2, 1:5, 1:10 and 1:20) resulted in selective dimerisation to yield 1-butene in the soluble fraction with trace polymer formation observed (Scheme 2.8).



Scheme 2.8. Selective dimerisation of ethylene to 1-butene by **2.5** and MAO.

The W:Al ratio had a large impact upon the activity and selectivity of the reaction. Higher concentrations of MAO resulted in decomposition of the trimethyl complex to an intractable mixture of products, with W:Al = 1:40 completely inactive towards ethylene. This observation is in contradiction to the W{N(2,6-Me-C_6H_4)}Cl_4/$AlEt_2Cl$ system, where a ratio of 1:40 gave an active catalyst but 1:11 was totally inactive.[9] Similarly, chromium systems often require very high MAO ratios to yield active oligomerisation systems (up to 500 equivalents).[47] Decomposition was observed visually by a darkening of the solution in the NMR tube, and ^{1}H NMR spectroscopy showed a decrease in intensity of the W–Me resonance (1.41 ppm) and the appearance of broad resonances in the alkyl region (Figure 2.12).

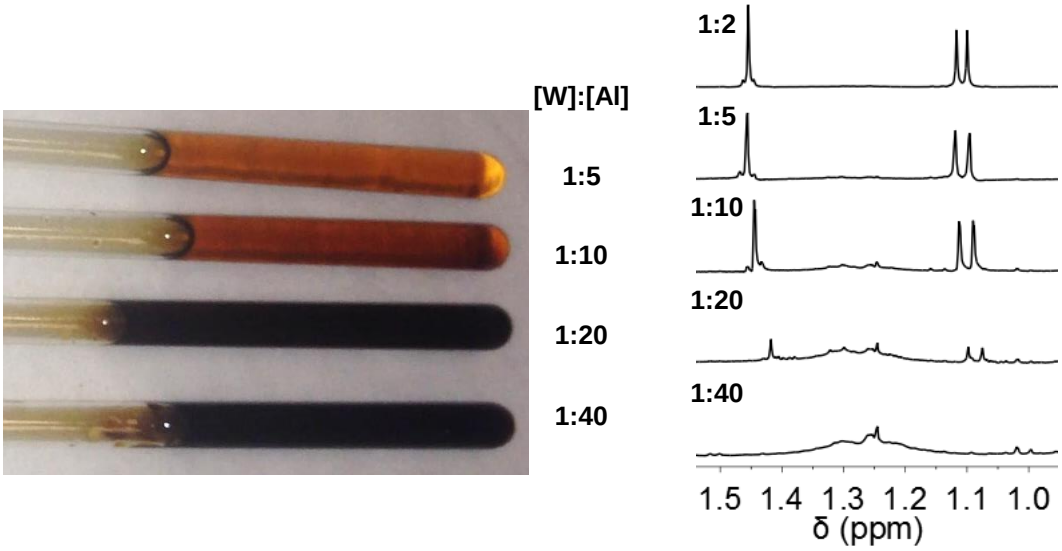


Figure 2.12. Decomposition of **2.5** at higher MAO ratios observed visually by darkening of the solution in the NMR spectroscopy tube (left), and spectroscopically by a decrease in the intensity of the W–Me and ^{i}Pr resonances in the ^{1}H NMR spectra (1.41 and 1.11 ppm, d_6-benzene, 400 MHz, 23 °C).

Lower co-catalyst ratios yielded more active catalysts, with a W:Al of 1:2 found to be the most active (turnover number (TON) of 24 $mol_{C_2H_4}mol_W^{-1}$, activity of 0.7 $mol_{C_2H_4}mol_W^{-1}h^{-1}bar^{-1}$, after 36 hours) (Figure 2.13). This is significantly lower than the TONs previously reported for other group 6 ethylene dimerisation systems, although ethylene pressures are much lower (1 bar) and no stirring is employed (Table 2.5).

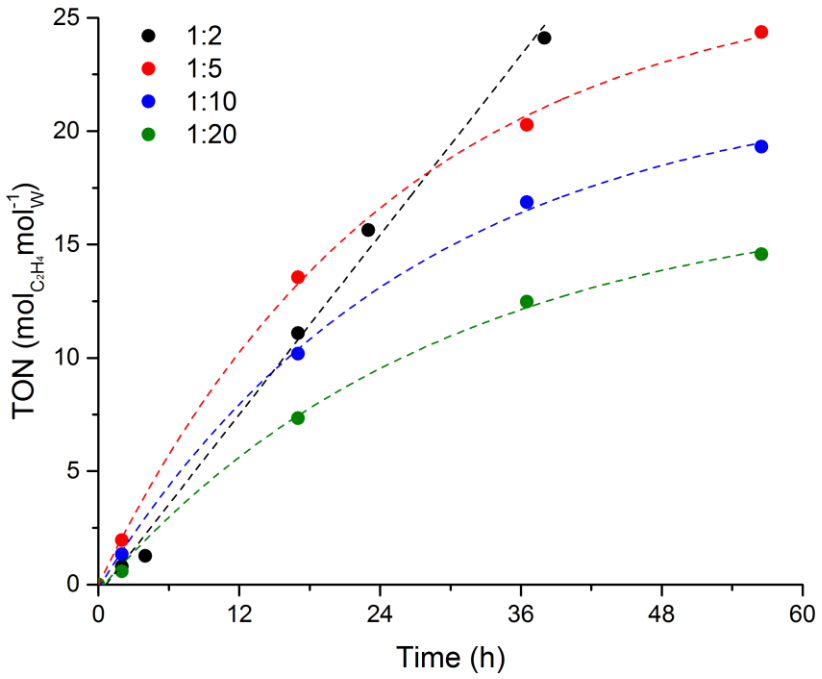


Figure 2.13. Turnover numbers (TONs) of ethylene for reaction of **2.5** and ethylene (1 bar) with MAO co-catalyst (W:Al = 1:2, 1:5, 1:10 and 1:20). 100 °C, d_6-benzene, [**2.5**]$_0$ = 4.55 μmol.

Table 2.5. Selected group 6 ethylene dimerisation systems.

Complex	Co-catalyst	Al/M	Solvent	T (°C)	$P_{C_2H_4}$ (bar)	Activity	1-C_4 (%)
$MoCl_2(NDipp)_2(DME)$[48]	$AlEtCl_2$	15	chlorobenzene	60	40	1,596[a]	57
$W\{N(2,6\text{-}Me\text{-}C_6H_3)\}Cl_4$[9]	$AlEt_2Cl$	40	chlorobenzene	40	60	81[a]	82
WCl_6/2,6-Me-$C_6H_3NH_2$ (1:2)[8]	$AlEt_2Cl$	80	benzene	40	34	5,341[a]	98
$CrCl_3(4\text{-}EtPy)_3$[49]	$AlEtCl_2$	50	chlorobenzene	50	34	1,220[b]	43
2.5	MAO	2	d_6-benzene	100	1	0.7[a]	>99

[a] $mol_{C_2H_4}mol_M^{-1}h^{-1}bar^{-1}$. [b] $mol_{C_4H_8}mol_M^{-1}h^{-1}bar^{-1}$. Dipp = 2,6-^{i}Pr-$C_6H_3$. Py = pyridine.

Contacting **2.5** with ethylene without a co-catalyst present at 100 °C, resulted in low reactivity (1-butene resonances appear only after 24 h of heating). Therefore, halide or methyl abstraction must be a key step in formation of the active species. Reaction of **2.5** with $AlCl_3$ (1 eq.) afforded two products in a 1:1 mixture by ^{1}H NMR spectroscopy, proposed to arise from coordination of the Lewis acid to the halide ligand, and chloride abstraction and ion pair formation (Figure A68). This reactivity with $AlCl_3$ is analogous to that reported by Osborn and co-workers for $W(NR)(CH_2{}^tBu)_3X$ (R = Me, ^{i}Pr, ^{t}Bu or 2,6-^{i}Pr-C_6H_3, X = F, Cl or Br).[50] It is therefore postulated that the initial step to form the active species is chloride abstraction by MAO. Lower MAO ratios yielded much higher selectivity towards 1-butene, which was largely isomerised to 2-butenes at higher loadings (Figure 2.14).

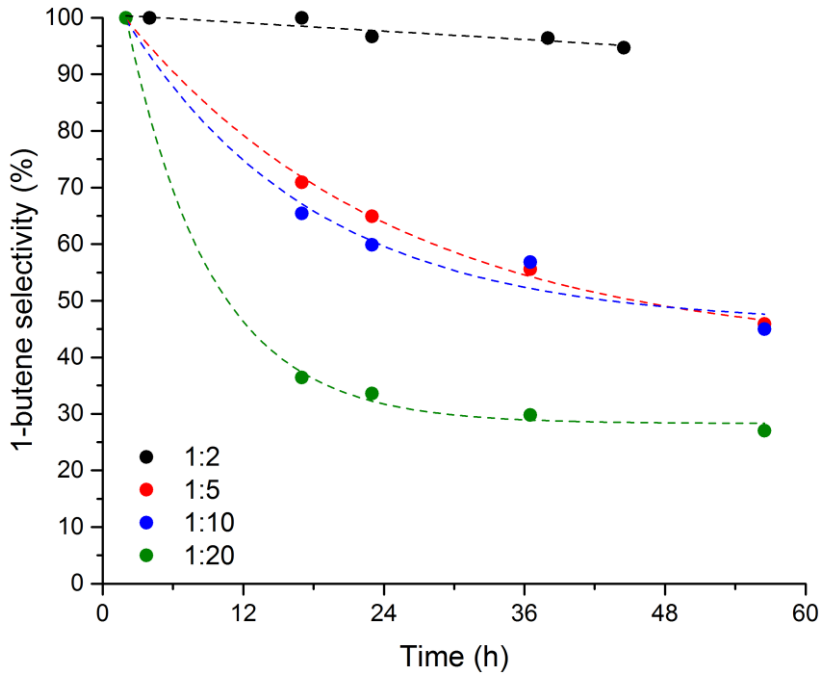


Figure 2.14. Selectivity for 1-butene (%) for the oligomerisation reactions with **2.5** and MAO (W:Al = 1:2, 1:5, 1:10 and 1:20). 100 °C, d_6-benzene, 1 bar ethylene, $[\mathbf{2.5}]_0$ = 4.55 μmol.

The observed degradation of the defined complex structure at higher ratios, combined with the loss of selectivity, indicates that the decomposition product may be a tungsten hydride species, which would infer that a Cossee-Arlman type coordination-insertion mechanism may be in operation. This is further supported by the observation of ethane, propane and butane in the ^{1}H NMR spectra, confirmed by GCMS (Table A4), which are more prevalent at higher MAO ratios. It is proposed that higher MAO loadings may yield more of these tungsten hydrides and hence isomerisation and hydrogenation is observed to a greater degree. The large reduction in isomerisation for the lowest MAO loading is complementary with either a metallocycle, or a Cossee-Arlman mechanism in which the tungsten hydride formed is very short lived (rate of ethylene insertion>>1-butene).

For the reaction of **2.5** and ethylene with 5 equivalents of MAO, isomerisation to yield 2-butenes and the presence of ethylene, leads to formation of propylene *via* cross metathesis (Figure 2.15).

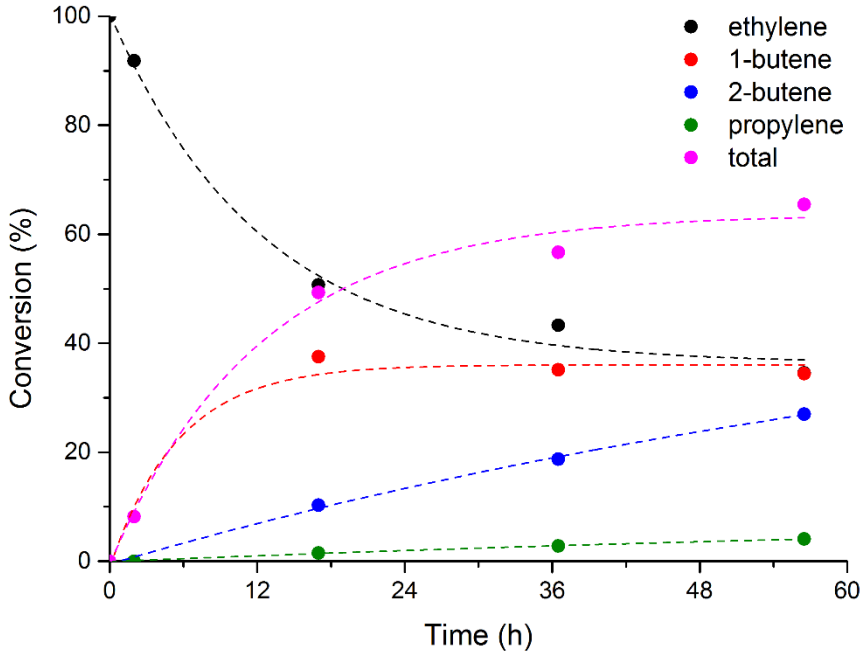


Figure 2.15. Product distribution for the reaction of **2.5** and ethylene (1 bar) with MAO (W:Al = 1:5) at 100 °C in d_6-benzene. $[\mathbf{2.5}]_0$ = 4.55 μmol.

To probe the effect of the aluminium co-catalyst on the reaction, TMA and DMAC were employed as alternative co-catalysts, under analogous conditions to those with MAO, utilising a W:Al ratio of 1:2. Reaction with 2 equivalents of DMAC did yield an active catalyst, however, TONs were half of those observed when MAO was employed (8 *vs* 16 $mol_{C_2H_4}mol_W^{-1}$ after 24 h) (Figure 2.16). Kulangara *et al*. observed that switching the

co-catalyst for ethylene oligomerisation from MAO to $AlMeCl_2$ with $[\{Ph_2C(C_4H_3N)(C_5H_6N)\}Cr(THF)(\mu\text{-}Cl)]_2$, switched the selectivity of the catalyst from a statistical distribution of olefins to a selective trimerisation system although oligomer yields were much lower (3.5 *vs* 15.5 g for Al/Cr of 100 *vs* 700).[51]

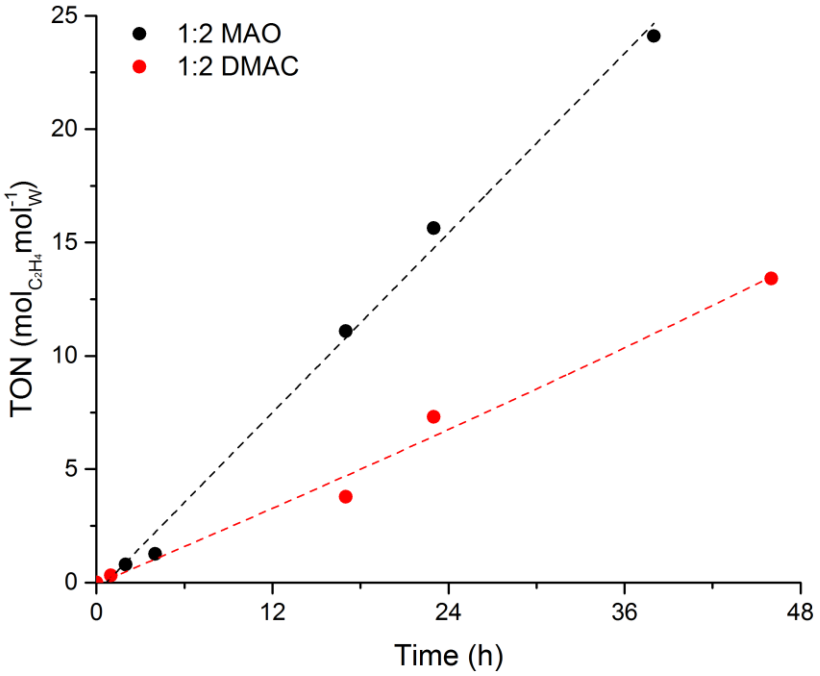


Figure 2.16. TONs for reaction of **2.5** and ethylene (1 bar) with either MAO or DMAC as the co-catalyst (W:Al = 1:2). 100 °C, d_6-benzene, $[\mathbf{2.5}]_0$ = 4.55 μmol.

When TMA was employed as the co-catalyst at 100 °C, no reactivity was observed. Analysis of the ^{1}H NMR spectrum of the reaction of **2.5** and TMA (W:Al = 1:2) at 100 °C, showed the emergence of multiple new alkyl resonances containing tungsten satellites (−0.5–0.2 ppm) (Figure 2.17). This infers that further methylation of **2.5** and subsequent decomposition can occur at higher temperatures when the more electron rich TMA, a better alkyl transfer agent, is employed; no decomposition was observed with DMAC. Attempts to isolate the products from the reaction by extraction with aliphatic solvents were, however, unsuccessful.

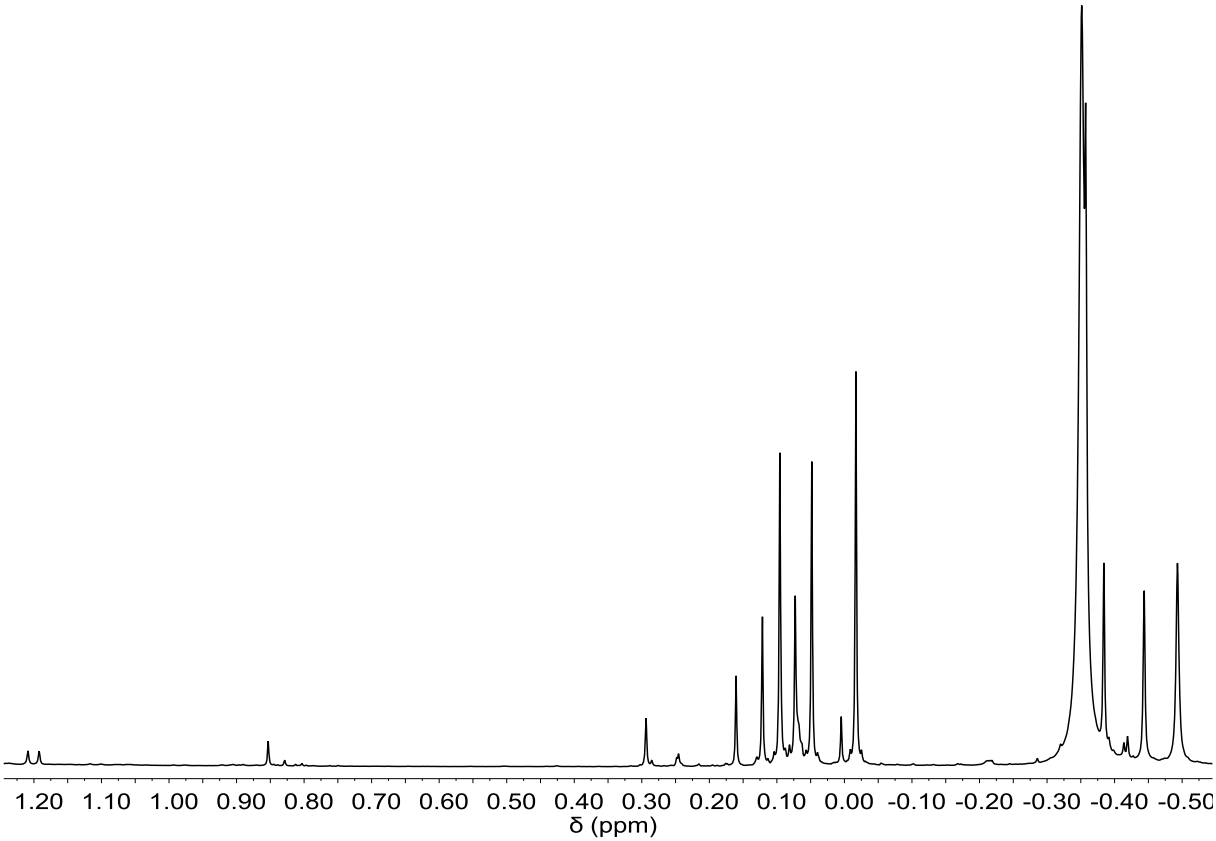
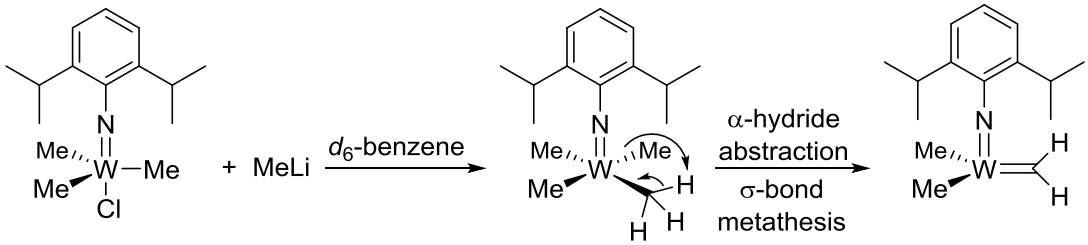


Figure 2.17. ^{1}H NMR spectrum (400 MHz, 23 °C) in d_6-benzene of the reaction between **2.5** and TMA (W:Al = 1:2) at 100 °C focussed between 1.4 and −0.6 ppm showing multiple methyl type resonances with coupling to tungsten.

Having observed further methylation by TMA with heating, reaction of **2.5** with MeLi was attempted to see if methylidene formation by α-hydride abstraction was possible (Scheme 2.9). Contacting **2.5** and MeLi (1 eq.) in d_6-benzene resulted in a colour change from orange to yellow followed by rapid decomposition to a dark orange/brown solution with no observable resonances in the ^{1}H NMR spectrum, as described previously for W{N(C_6H_5)}Me_3Cl.[32] It is proposed that an unstable tetramethyl species is formed which decomposes, most likely *via* a transient methylidene, formed from α-hydride extraction and σ-bond metathesis, as seen in the synthesis of W{N(2,6-^{i}Pr-C_6H_3)}($CH_2{}^{t}$Bu)$_2$(CH^{t}Bu).[6]



Scheme 2.9. Proposed formation of W{N(2,6-^{i}Pr-C_6H_3)}Me_4 from **2.5** and MeLi in d_6-benzene, postulated to decompose *via* W{N(2,6-^{i}Pr-C_6H_3)}(CH_2)Me_2 at 23 °C.

A study into the temperature dependence of the ethylene oligomerisation reaction utilising W{N(4-OMe-C_6H_4)}Me_3Cl (**2.6**) and MAO has been performed previously (50, 75 and 100 °C, W:Al = 1:2, d_6-benzene containing mesitylene as an internal standard (20 μmol) and 1 bar ethylene) (Figure A69).[13] The highest rates of oligomerisation were noted at lower temperatures (50 and 75 °C), whereas at 100 °C polymer formation was observed. A reduction in the intensity of resonances corresponding to **2.6** in the ^{1}H NMR spectrum suggests decomposition may also occur at this temperature (80% decrease at 100 °C *vs* 15% at 50 °C after 24 hours). This may also explain the loss of selectivity towards 1-butene which after 24 hours was 28, 49 and 86% at 100, 75 and 50 °C respectively. Comparison of the oligomerisation reaction utilising **2.5** and **2.6** at 100 °C, shows similar reactivity profiles for both complexes (TONs of 16 and 21 $mol_{C_2H_4}mol_W^{-1}$ after 24 hours). **2.6** appears to demonstrate a much faster initial rate and a much lower selectivity (28 *vs* 97% after 24 hours) indicating that **2.5** has a higher thermal stability.

Variation of the halide ligand was also attempted to investigate the impact on complex activation by the co-catalyst. A simple halogen exchange 'halex' type reaction,[52] employing AgF in d_2-DCM with **2.5,** was attempted. However, despite sonication and heating of the sample, no shift in the complex resonances was observed by ^{1}H NMR spectroscopy.

2.4.2. Reactivity of W(NR)Me_3Cl complexes towards heavier α-olefins

To test the scope of monomers that could be employed in the oligomerisation reaction, **2.5**, MAO (Al:W = 1:2) and propylene (1 bar) were reacted at 100 °C in d_6-benzene. However, **2.5** was observed to be inactive towards propylene oligomerisation. This is attributed to unfavourable steric crowding from chain lengths >C_2 and hence no further chain growth than C_4 is observed with ethylene, and propylene insertion to yield a C_6 chain is inhibited. Complex **2.5** did react with propylene without a co-catalyst under similar conditions, affording ethylene and 2-butenes as the self-metathesis products (Figure A70). Whilst the resonances for the complex appear unchanged during the reaction, the activity is attributed to formation of an alkylidene species, most likely a methylidene, which then undergoes cycloaddition and reversion steps. Similarly, **2.7** reacts with either 1-hexene or 1-octene yielding ethylene and internal *trans*-5-undecene or *trans*-6-tridecene respectively (Figures A71 and A72).

2.5. Formation of reactive intermediates

As discussed in Chapter One there are two generally accepted mechanisms for olefin oligomerisation; Cossee-Arlman and metallacycle. One way to identify which mechanism is in operation is to synthesise proposed intermediates in each cycle *e.g.* cationic, metal hydride and metallacycle complexes and investigate their competency as catalysts.

2.5.1. Formation of cationic complexes

2.5.1.1. Reactions with $NaBAr^F_4$

Having observed coordination of and halide abstraction by $AlCl_3$, it was proposed that the active species in olefin oligomerisation is a cationic complex formed from halide extraction by the aluminium co-catalyst (Scheme 2.7).[41] The *in situ* UV-vis, NMR and EPR spectral studies of the selective ethylene trimerisation system $Cr(PNP)Cl_3$ (PNP = bis(diarylphosphino)alkylamine) and MAO, indicate that after alkylation of the halide positions, alkyl abstraction occurs to yield a cationic complex, with further reduction to lower valent chromium species observed.[53] Despite accounting for the majority of species formed, none of these were shown to be active towards ethylene. Buchmeiser and co-workers have also shown that cationic tungsten and molybdenum alkylidene complexes, are highly active towards olefin metathesis with TONs as high as 210,000 $mol_{C_8H_{16}}mol_M^{-1}$ for the self-metathesis of 1-octene.[54,55] These could be prepared by reacting the alkylidene precursors bearing a halide group, with the silver borate reagent $[Ag(CH_3CN)_2][BAr^F_4]$ (Ar^F = 3,5-CF_3-C_6H_3).

Reaction of **2.2** with $NaBAr^F_4$ in d_2-DCM, afforded a colour change from yellow to purple and then red over the course of 3 days. The ^{1}H NMR spectrum showed a shift to higher frequency in the complex resonances with splitting of the W–Me resonances into an apparent doublet and the presence of 0.5 eq. $[BAr^F_4]^-$ by integration (Figure 2.18). The $^{11}B\{^1H\}$ spectrum showed a single resonance at −6.6 ppm indicative of a tetra-coordinated boron (Figure A74). The $^{19}F\{^1H\}$ NMR spectrum displays a major peak at −62.8 ppm attributed to the borane paired with the complex, and a weaker resonance at −63.5 ppm which could not be assigned (Figure A75). This indicates that a mono-chloride bridged dimer had formed; however, the symmetry must be distorted, rendering the two sets of methyl environments inequivalent. Despite further sonication and heating, formation of the mono cation was not observed. Filtration away from sodium chloride, and drying yielded an impure green solid.

Attempts to recrystallise from DCM or DCM layered with pentane lead to decomposition and an intractable mixture of products.

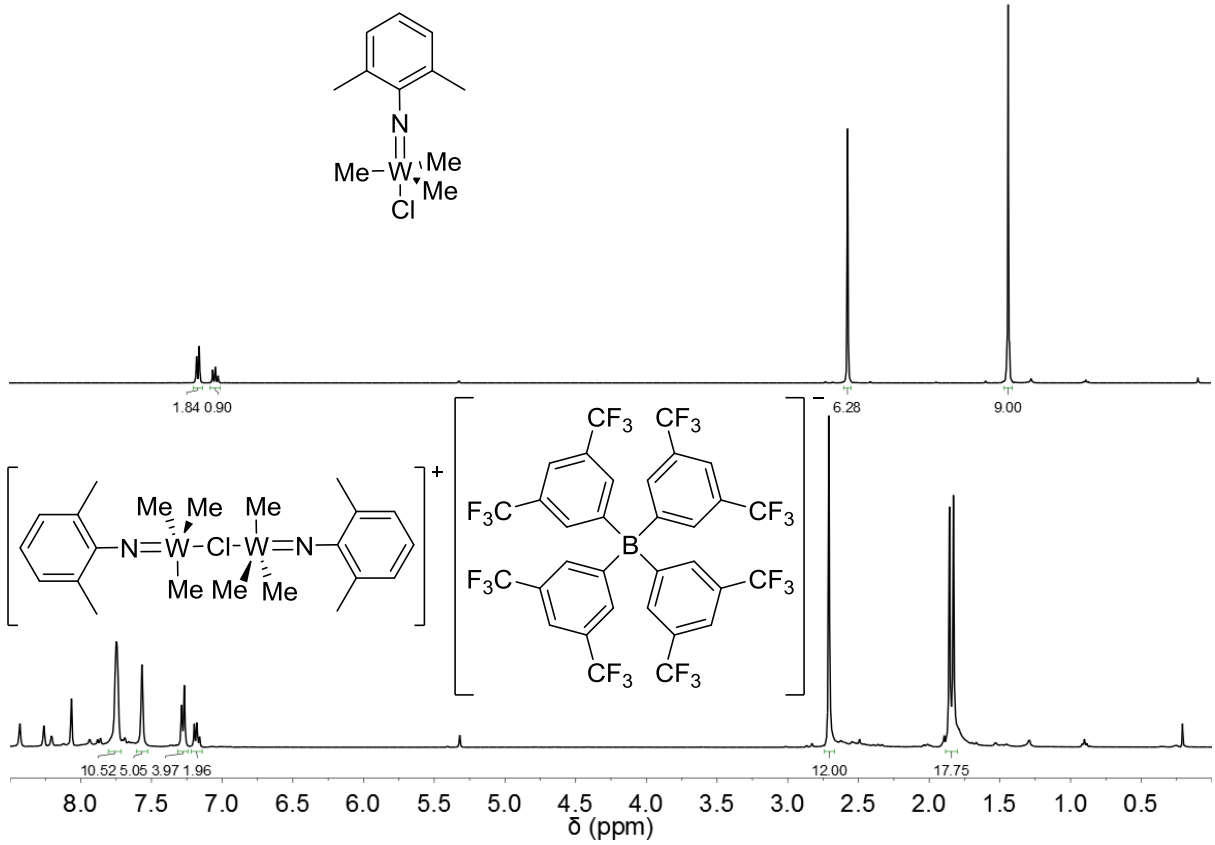


Figure 2.18. ^{1}H NMR spectrum (400 MHz, 23 °C) in d_2-DCM (5.32 ppm) of the reaction between **2.2** and NaBAr$^{F}_{4}$ after 3 days at room temperature.

A scale-up reaction with **2.5** in DCM, exhibited the same reaction profile over 3 days (Figure 2.19), however, an aliquot of the final red solution indicated that decomposition had occurred, and no discernible products could be isolated. It should be noted that no reactivity between **2.5** and NaBAr$^{F}_{4}$ was observed in d_8-THF.

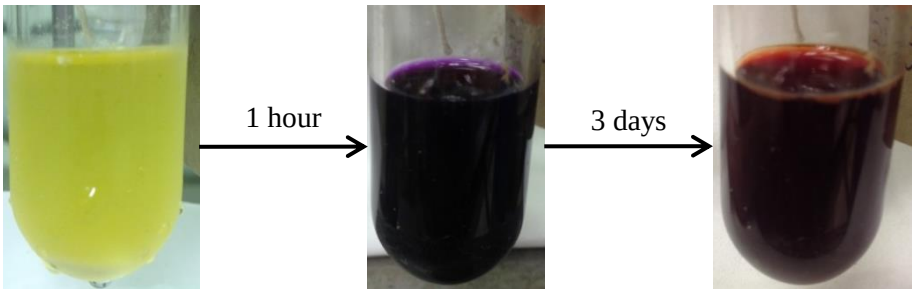


Figure 2.19. Reaction of **2.5** with NaBAr$^{F}_{4}$ in DCM.

2.5.1.2. Reactions with $AgPF_6$

To try and form a mono cationic mono metallic complex, **2.2** was contacted with $AgPF_6$ in d_2-DCM. The ^{1}H NMR spectrum displayed a downfield shift in the NMR spectroscopic resonances, indicative of a more electron poor tungsten centre, with maintenance of the singlet resonance for the methyl groups, unlike that observed from reaction with $NaBAr^F{}_4$ (Figure 2.20).

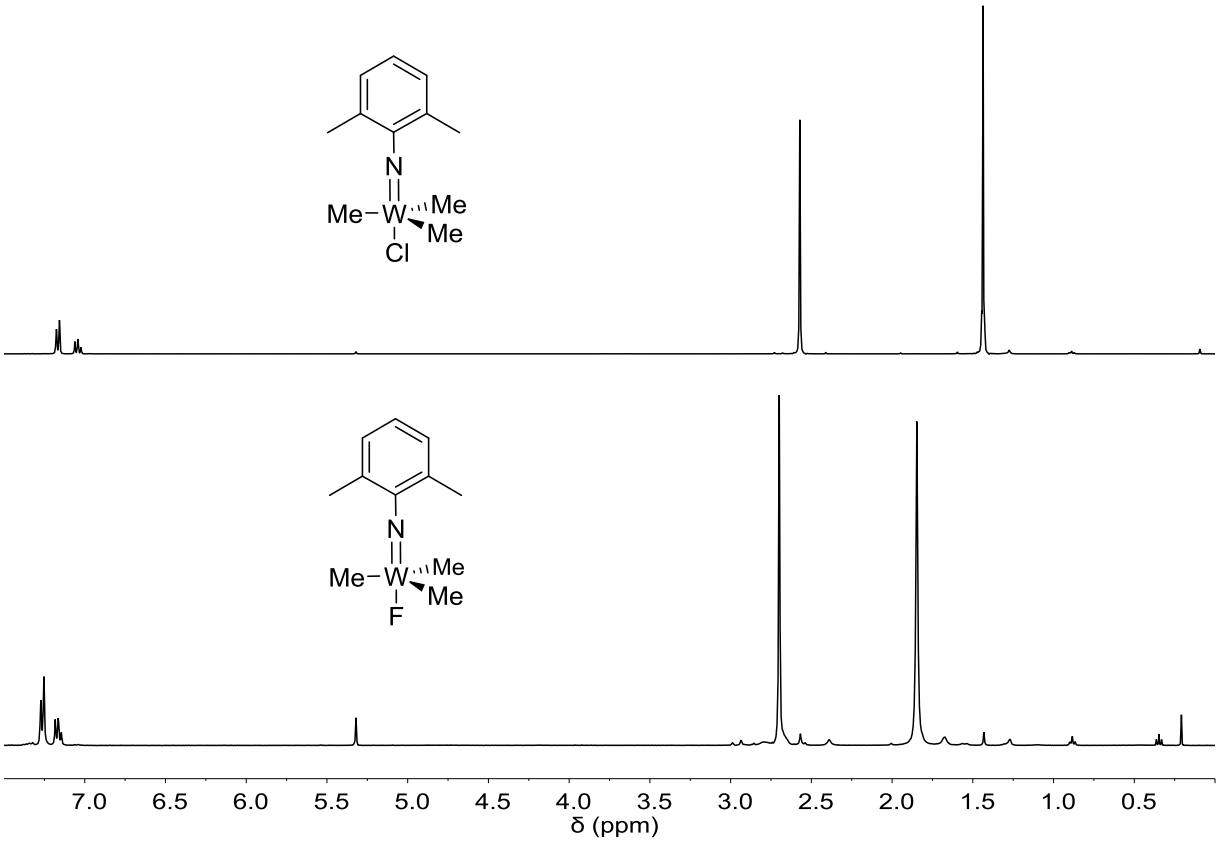


Figure 2.20. ^{1}H NMR spectra (400 MHz, 23 °C) in d_2-DCM (5.32 ppm) comparing **2.2** (top) and the product from the reaction with $AgPF_6$ (bottom).

The $^{31}P\{^1H\}$ NMR spectrum, however, showed an apparent quartet centred at −34.9 ppm ($^1J_{P–F}$ = 2143 Hz) (Figure A77), whereas the PF_6^- anion is expected to display a septet resonance around −143 ppm, suggesting that cation formation may not have occurred. This $^{31}P\{^1H\}$ resonance corresponds to that observed for $P(O)F_3$,[57] which is formed readily from PF_5 in glass apparatus.[58] From this it can be inferred that abstraction of fluoride from PF_6^- has occurred to yield $W\{N(2,6\text{-}Me\text{-}C_6H_3)\}Me_3F$, and thus the electronegative fluoride shifts the resonances downfield. Wengrovius *et al*. have previously observed that reaction of $W(O)(CH^tBu)Cl_2(PEt_3)_2$ with $AgPF_6$ resulted in formation of the monofluoride complex, postulated to occur *via* abstraction of fluoride from the anion by an incipient cation.[56] Hersh

and co-workers have demonstrated that addition of [NO][PF_6] to W(PMe_3)($CO)_5$ yielded a complex in which the PF_6^- anion was coordinated to tungsten *via* a bridging fluoride. However, in such an arrangement the ^{31}P NMR spectrum displayed a sharp sextet of doublets at −142.7 ppm. Inspection of the $^{19}F\{^1H\}$ NMR spectrum shows a doublet centred at −88.6 ppm ($^1J_{F-P}$ = 2143 Hz) (Figure A78). However, for W(O)(CH^{t}Bu)(Cl)(F)($PEt_3)_2$ and $P(O)F_3$, $^{19}F\{^1H\}$ NMR spectroscopic resonances occur at 226 and 49.4 ppm respectively, which fall outside the spectral window that was employed. Decomposition of the compound was observed overnight. Scale-up reactions utilising **2.2** or **2.3** in DCM, also yield the halide exchange product, but this could not be readily isolated.

2.5.2. Attempted metal hydride formation

If a coordination-insertion mechanism is operating, β-hydride elimination would yield a metal hydride species which could then insert an ethylene monomer. To test this, attempts to form a discrete tungsten hydride were pursued. Previously, Boncella and co-workers have demonstrated that tungsten (VI) mono-imido hydride species can be formed by reaction of alkyl imido complex W{N(C_6H_5)}($CH_2{}^t$Bu)$_2$(1,2-NSiMe_3-C_6H_4) with molecular hydrogen in the presence of trialkylphosphines (PMe_3 or PMe_2Ph), resulting in formation of a seven coordinate dihydride complex.[59] Exposure of this complex to ethylene (1 atm) at room temperature afforded one equivalent of ethane and formation of an ethylene complex. Interestingly, reaction of the dihydride complex with ligated DPPE ($Ph_2PC_2H_4PPh_2$) and excess ethylene furnishes ethane and the metallacyclopentane complex W{N(C_6H_5)}(1,2-NSiMe_3-C_6H_4)(C_5H_8).

A mixture of **2.5** and KH in d_8-THF showed no change even with prolonged heating at 70 °C. In d_5-pyridine, a slow reaction occurred with the solution turning black. ^{1}H NMR spectroscopy revealed decomposition with multiple resonances forming a broad feature between 0.5 and 2.5 ppm. Attempts were also made utilising **2.2** and $LiAlH_4$. Reaction in d_8-THF resulted in an immediate colour change from yellow to dark brown. The ^{1}H NMR spectrum showed complete disappearance of the complex resonances and formation of broad features (0.5–3 and 6–7 ppm) which may indicate reduction to yield a paramagnetic species. Attempted recrystallisation from a hexane solution was unsuccessful precluding further identification of this compound. No reactivity between $LiAlH_4$ and **2.2** was observed in d_6-benzene. Olivier and co-workers have previously reported the synthesis of the reduced

tungsten imido complexes W{N(C_6H_5)}Cl_3(PMe_3)$_2$ and W{N(C_6H_5)}Cl_2(PMe_3)$_3$, which are active dimerisation catalysts in the presence of $AlCl_3$ or $AlEt_2Cl$.[9]

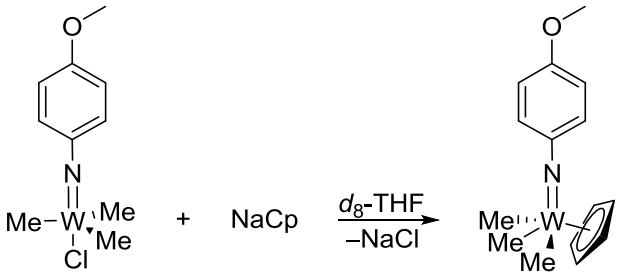
2.5.3. Attempted metallacycle formation

To probe the possibility of a metallacycle mechanism, W{N(2,6-^{i}Pr-C_6H_3)}Cl_4 was reacted with $BrMgC_4H_8MgBr$ (0.14 M in THF) in d_6-benzene. Darkening of the solution was observed and complete decomposition was indicated by no observable resonances for the imido fragment in the ^{1}H NMR spectrum. It is proposed that the lack of steric protection around the tungsten makes the intermediate species unstable. Wang *et al.* reported tungstacyclopentane formation by such a method using a bulky N,N′-bis-(trimethylsilyl)-*o*-phenylenediamide ligand.[60]

2.6. Further reactivity of W(NR)Me_3Cl complexes

2.6.1. Synthesis of W{N(4-OMe-C_6H_4)}Me_3Cp (3.6)

The lability of the axial chloride ligand and its importance in catalytic activity was studied by salt metathesis reactions. NMR spectroscopic scale reactions of **2.3**, **2.5** or **2.6** with either cyclopentadienyl (Cp) lithium or sodium in d_8-THF or d_6-benzene furnished the corresponding Cp complexes and metal chloride salt in all cases (Scheme 2.10).



Scheme 2.10. Reaction of **2.6** and NaCp in d_8-THF to afford W{N(4-OMe-C_6H_4)}Me_3Cp (**3.6**).

Analysis of the ^{1}H NMR spectrum showed a singlet for the Cp ligand at 5.12 ppm, indicative of free rotation and η^5-coordination, but splitting of the resonances for the methyl groups into two singlets at 1.31 and 0.96 ppm, integrated as 6 and 3 protons respectively (Figure 2.21). This is also reflected in the ^{13}C{^{1}H} NMR spectrum, where two resonances at 23.5 and 17.9 ppm are observed (Figure A80). This suggests that unlike the chloride in the precursor, the Cp ligand does not occupy the axial site *trans* to the imido group, as the methyl groups are inequivalent. The W–Me proton and carbon resonances are shifted upfield when compared to **2.6** (δ_H = 1.30 ppm and δ_C = 53.5 ppm), indicative of a more electron rich metal centre.

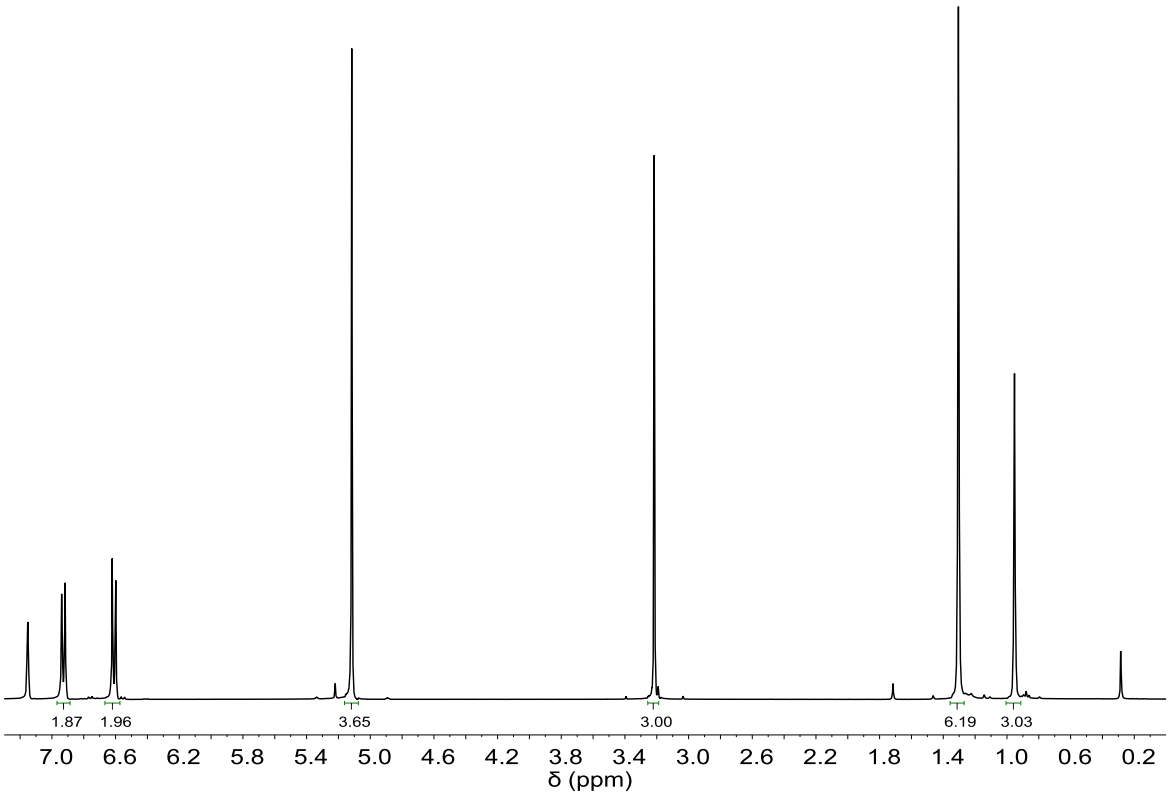


Figure 2.21. ^{1}H NMR spectrum (400 MHz, 23 °C) of the reaction between **2.6** and NaCp in d_6-benzene (7.16 ppm) to yield W{N(4-OMe-C_6H_4)}Me_3Cp (**3.6**).

A scale-up reaction of **2.6** and NaCp in THF at 0 °C, with subsequent warming to room temperature, resulted in a slight colour change from yellow/orange to orange. Extraction of the product in hexane and cooling to −33 °C, afforded orange crystals shown to be W{N(4-OMe-C_6H_4)}Me_3Cp (**3.6**) by a single crystal X-ray diffraction study (Figure 2.22 and Table 2.6). Analysis of the molecular structure shows that there is a distortion away from the trigonal bipyramidal geometry of the precursor (**2.6**) to a tetragonal pyramidal geometry. Viewing the structure 'side on' with respect to the aryl group, shows a vertical mirror plane through the molecule which renders two of the methyl groups (C8 and C10) inequivalent to the third (C9) which sits on the mirror plane. The W–Me bond W–C9 is also elongated compared to W–C8 and W–C10 (2.234(4) *vs* 2.211(4) and 2.212(3) Å) respectively. The W–N bond length is increased compared to **2.6**, most likely due to the introduction of the π-donating Cp ligand which donates into the same metal d-orbitals as the imido group. The Cp ligand is shown to bind to tungsten in an η^5-arrangement with an M–Cp_{cent} distance of 2.0584(16) Å. Such a distance is comparable with the bis-imido complexes W{N(2,4,6-Me-C_6H_2)}$_2$(η^1-C_5H_5)(η^5-C_5H_5) (W–Cp_{cent} = 2.123(3) Å)[61] and W{N(2,6-^{i}Pr-C_6H_3)}$_2$Cp*Cl (W–Cp*$_{cent}$ = 2.1015(2) Å).[62]

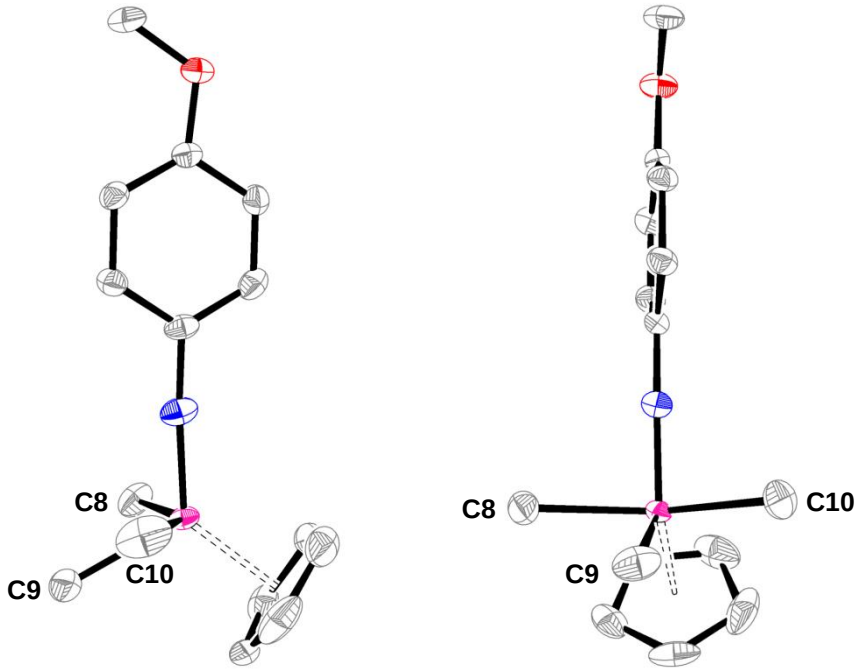


Figure 2.22. Molecular structure of W{N(4-OMe-C_6H_4)}Me_3Cp (**3.6**) 'face on' to the imido group (left) and side on (right) showing the inequivalence of the methyl groups (C8, C9 and C10). Ellipsoids shown at 50% probability. Hydrogens omitted for clarity.

Table 2.6. Selected bond lengths (Å) and angles (°) for W{N(4-OMe-C_6H_4)}Me_3Cp (**3.6**).

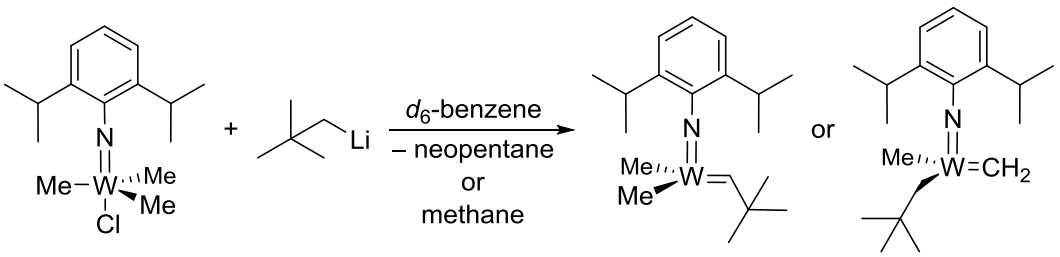
Parameter	Bond lengths (Å)/Angles (°)
W–N	1.756(3)
W–Cp_{cent}	2.0584(16)
W–C8	2.211(4)
W–C9	2.234(4)
W–C10	2.212(3)
W–N–C_{ipso}	175.6(2)
W–N–Cp_{cent}	129.78(11)

The reactivity of **3.6** towards ethylene was assessed utilising MAO (W:Al = 1:2) as a co-catalyst at 75 °C in d_6-benzene with mesitylene (20 μmol) as an internal standard. Slow formation of 1-butene was observed (TON = 7 $mol_{C_2H_4}mol_W^{-1}$ after 12 hours), with polyethylene formation (~3 mg) observed. This activity is much lower than for **2.6** under analogous conditions (TON = 36 $mol_{C_2H_4}mol_W^{-1}$), indicating that either the chloride ligand or the trigonal bipyramidal arrangement of the pre-catalyst is an important factor. After 12 hours, a weak resonance at 1.67 ppm accompanied by tungsten satellites had grown into the 1H NMR spectrum. This is hypothesised to be the complex resulting from methyl abstraction by MAO from **3.6**, as weak resonances for the remaining ligands could also be observed. No reactivity towards ethylene is observed without the MAO co-catalyst present.

MAO activation of **3.6** was modelled by reaction with $[CPh_3][BAr^F{}_4]$[63] in d_5-chlorobenzene. This reagent has been successfully utilised to abstract a methyl group from $W\{N(C_6H_5)\}(N_2N_{py})Me_2$ (N_2N_{py} = $MeC(2\text{-}C_5H_4N)(CH_2NSiMe_3)_2$) giving quantitative conversion to the cation.[64] An immediate darkening of the orange solution of **3.6** was observed on contact, yielding a brown solution. The ^1H NMR spectrum showed that the resonances for the precursor complex had shifted. Integration of these resonances indicated that methyl abstraction had occurred with formation of Ph_3CMe observed (7.14–7.05 and 2.03 ppm).[65] Broadening of the resonance corresponding to the two remaining methyl groups was also observed (1.22 ppm). The $^{11}B\{^1H\}$ and $^{19}F\{^1H\}$ NMR spectra both displayed a single resonance at −6.0 ppm and −61.9 ppm respectively, consistent with the $[BAr^F{}_4]^-$ counterion. Attempted recrystallisation was unfortunately not successful.

2.6.2. Attempted alkylidene formation

As reactivity towards olefin metathesis with the synthesised mono-imido complexes had been observed, attempts to form a defined alkylidene complex were pursued. A well-known route to alkylidene formation involves α-hydride extraction from a neighbouring alkyl group following peralkylation.[6] Having observed that $W\{N(2,6\text{-}^i Pr\text{-}C_6H_3)\}Me_4$ rapidly decomposed rather than form a stable methylidene species, reaction of **2.5** with NpLi (1 eq.) was attempted, as it was postulated that the bulkier group may stabilise a resulting methylidene or neopentylidene species (Scheme 2.11).



Scheme 2.11. Postulated alkylidene complexes that could be formed by reaction of **2.5** with NpLi after α-hydride extraction and σ-bond metathesis.

A yellow d_6-benzene solution of **2.5** became orange on addition of NpLi, with some gas evolution observed. The ^1H NMR spectrum indicated that there were two discrete tungsten species in a 60:40 ratio. The major set of resonances coincides with the previously reported neopentylidene complex, $W\{N(2,6\text{-}^i Pr\text{-}C_6H_3)\}(CH_2{}^tBu)_2(CH{}^tBu)$,[6] indicating that a ligand redistribution must have occurred. The other set of resonances are tentatively assigned to the neopentylidene complex, $W\{N(2,6\text{-}^i Pr\text{-}C_6H_3)\}(CH{}^tBu)(CH_2{}^tBu)Me$; there is a multiplet at

3.85 ppm corresponding to the isopropyl methine group, a singlet at 1.14 ppm representing the isopropyl methyl groups and a singlet at 6.67 ppm integrated as a single proton with tungsten satellites ($^2J_{W–H}$ = 15.0 Hz) which is indicative of alkylidene formation

Attempted scale-up lead to the formation of an apparent methylidene complex W{N(2,6-^{i}Pr-C_6H_3)}(CH_2)($CH_2{}^t$Bu)Me as the major product, along with W{N(2,6-^{i}Pr-C_6H_3)}(CH^tBu)($CH_2{}^t$Bu)$_2$ and W{N(2,6-^{i}Pr-C_6H_3)}(CH^tBu)($CH_2{}^t$Bu)Me. Over time this was seen to decompose yielding a 50:50 mixture of W{N(2,6-^{i}Pr-C_6H_3)}(CH^tBu)($CH_2{}^t$Bu)$_2$ and W{N(2,6-^{i}Pr-C_6H_3)}(CH^tBu)($CH_2{}^t$Bu)Me by ^{1}H NMR spectroscopy. Attempted isolation of individual complexes by fractional crystallisation was unsuccessful.

2.6.3. Silica mimic reactions with (^{t}BuO)$_3$SiOH and (^{t}BuO)$_3$SiOLi

Having shown that homogeneous W(NR)Me_3Cl complexes were active oligomerisation catalysts, interest turned to studying their behaviour when immobilised on solid supports (Chapter Four). In an attempt to bridge the gap between the homogeneous and supported complexes, reactions were performed with selected W(NR)Me_3Cl complexes and the silica mimics, (^{t}BuO)$_3$SiOH and (^{t}BuO)$_3$SiOLi, which are commonly employed for this purpose.[66,67] ^{1}H NMR spectroscopy indicates that reaction of **2.5** with an excess of (^{t}BuO)$_3$SiOLi in d_6-benzene yields W{N(2,6-^{i}Pr-C_6H_3)}Me_3OSi(O^{t}Bu)$_3$, with an instantaneous colour change from orange to yellow (Figure 2.23). The singlet at 1.36 ppm observed for the methyl protons around the tungsten implies that the trigonal bipyramidal structure is maintained. Scale-up proved unsuccessful, yielding an orange gel, which formed a glassy solid upon drying and precluded any further characterisation. Analogous reactivity was also observed between (^{t}BuO)$_3$SiOLi and **2.1**, **2.2**, **2.3** or **2.6**. An isolated sample of W{N(3,5-Me-C_6H_3)}Me_3OSi(O^{t}Bu)$_3$ was reacted with ethylene in the presence of two equivalents of MAO at 75 °C in d_6-benzene. 1-Butene was formed with high selectivity but once again the activity was much lower (TON = 3 $mol_{C_2H_4}mol_W^{-1}$ after 17 h) than for the W(NR)Me_3Cl complexes.

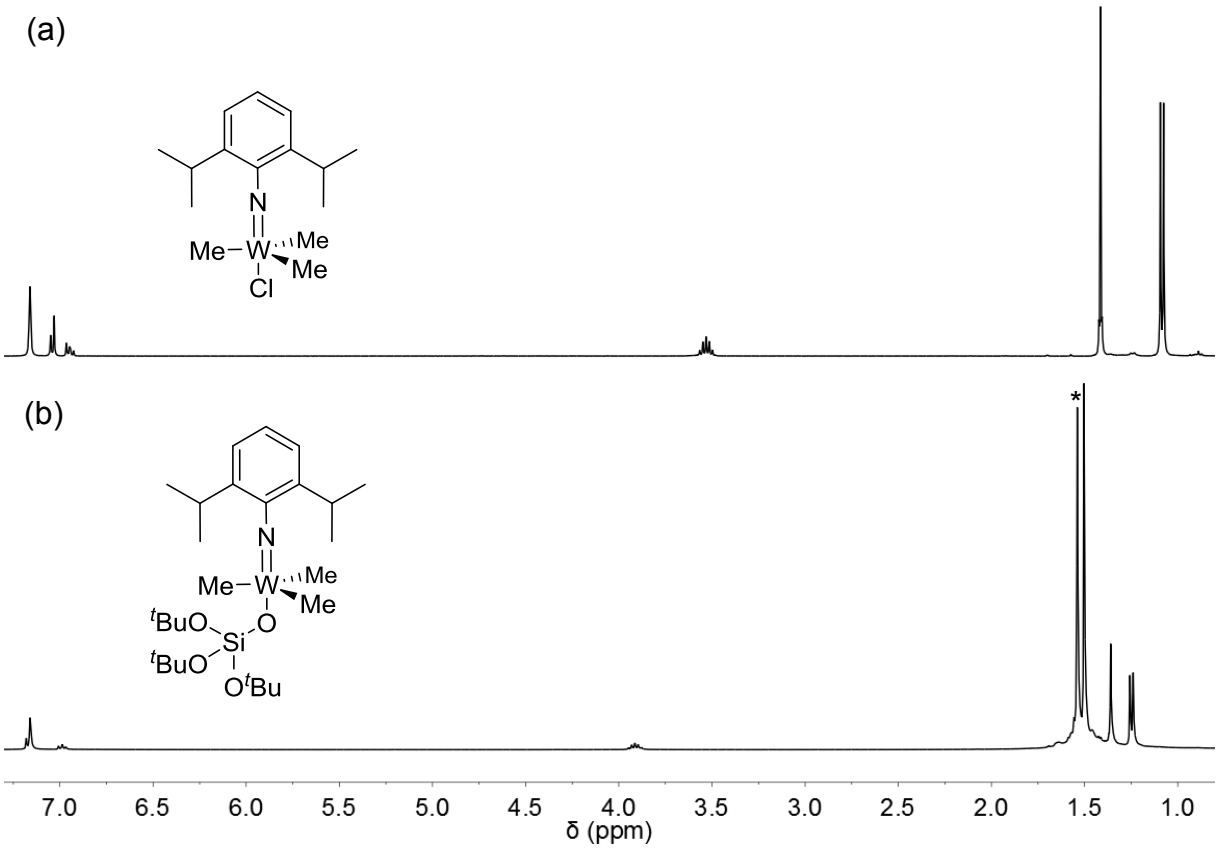


Figure 2.23. ^{1}H NMR spectra (400 MHz, 23 °C) in d_6-benzene (7.16 ppm) of (a) **2.5** and (b) W{N(2,6-^{i}Pr-C_6H_3)}$Me_3OSi(^{t}BuO)_3$ formed from **2.5** and $(^{t}BuO)_3SiOLi$. * = unreacted $(^{t}BuO)_3SiOLi$.

Reaction of $(^{t}BuO)_3SiOH$ with **2.5** proceeds slowly even with heating at 100 °C, forming four apparent species each with distinct resonances for the methine proton on the isopropyl groups (Figure 2.24). Formation of W{N(2,6-^{i}Pr-C_6H_3)}$Me_3OSi(O^{t}Bu)_3$ was observed, but other more prominent methine resonances were also detected. These are attributed to reaction of the silanol at the methyl positions, yielding methane (0.16 ppm). Taoufik and co-workers have reported that reaction of $W(O)Np_3Cl$ with $(^{t}BuO)_3SiOH$ at 60 °C results in exclusive substitution at the halide with no neopentane evolution observed. Yields of ~85% could be achieved by bubbling argon through the mixture to remove HCl which catalyses the reverse reaction.[68]

The multiple isopropyl methine proton resonances (3.4–4.6 ppm) are postulated to be the various isomers that can form which cannot be superimposed and a shift in geometry from trigonal bipyramidal as observed for $W(NAr)Me_3Cl$ to a square or tetragonal pyramidal structure. Alternatively, these resonances may be due to further addition of $(^{t}BuO)_3SiO$ groups to the same complex. Gauvin *et al*. described how 1:1 reaction of $Ca\{N(SiMe_3)_2\}_2(THF)_2$ with $(^{t}BuO)_3SiOH$ led to formation of half an equivalent of the homoleptic complex

$Ca(OSi(O^tBu)_3)_2$ and half an equivalent of starting material.[69] This is due to the Schlenk equilibrium in such complexes falling on the side of the homoleptic complexes.

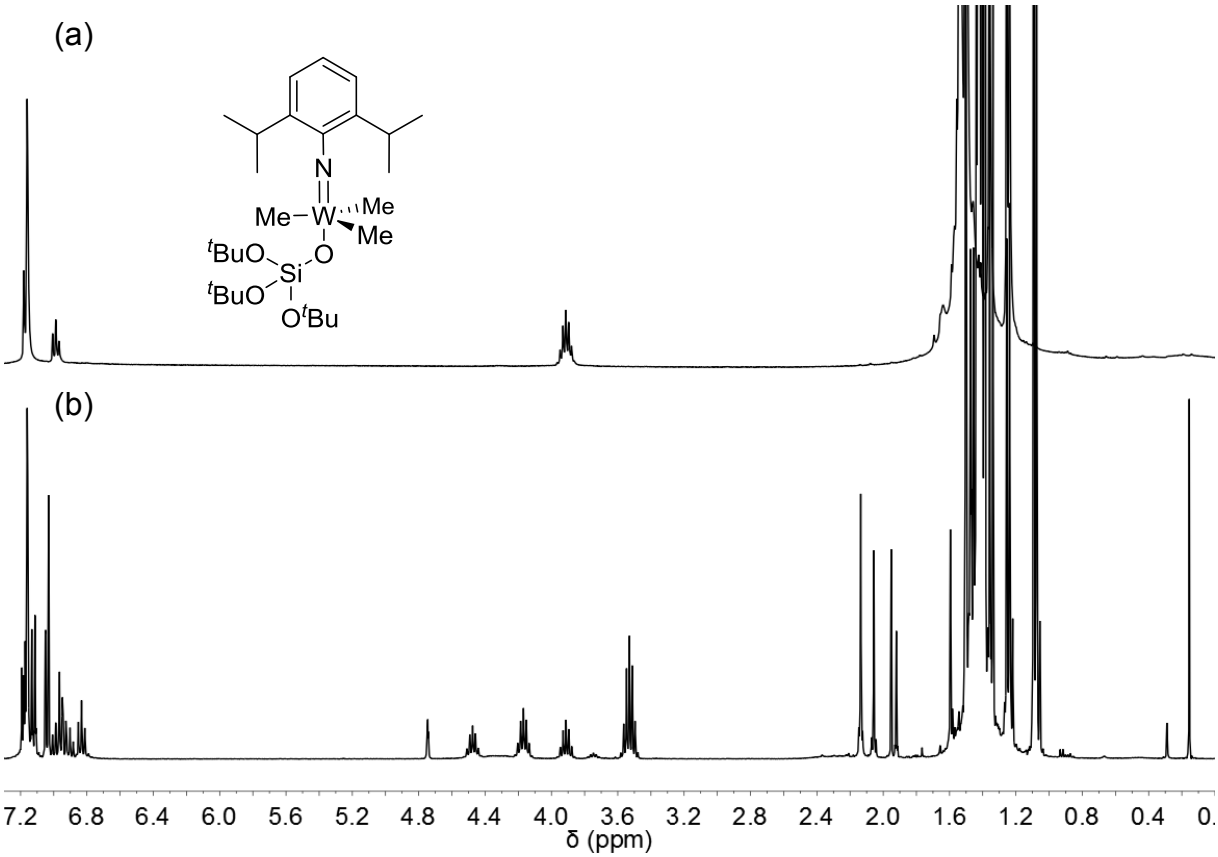


Figure 2.24. ^{1}H NMR spectra (400 MHz, 23 °C) in d_6-benzene (7.16 ppm) comparing (a) W{N(2,6-^{i}Pr-C_6H_3)}$Me_3OSi(O^tBu)_3$ and (b) the products from **2.5** and $(^tBuO)_3SiOH$.

2.7. Conclusions

A series of tungsten mono-arylimido complexes of the type $W(NR)Cl_4(THF)$ (R = C_6H_5 (**1.1**), 2,6-Me-C_6H_3 (**1.2**), 3,5-Me-C_6H_3 (**1.3**), 2,4,6-Me-C_6H_2 (**1.4**), 2,6-^{i}Pr-C_6H_3 (**1.5**), 4-OMe-C_6H_4 (**1.6**), 2,6-F-C_6H_3 (**1.7**) and 3,5-CF_3-C_6H_3 (**1.8**)) bearing different substituents on the phenyl ring have been synthesised. Subtle changes in the octahedral structures are observed based on the electronic properties and steric effects which are most notable in the 2,6-position. Reaction of these tetrachloro complexes with TMA led to methylation of three of the chloride positions to afford $W(NR)Me_3Cl$ (**2.1**–**2.8**). Changes in the W–N bond length match the electronic properties of the imido fragments determined indirectly from the pKas of their parent anilines. Analogous reactivity is also observed reacting $W(O)Cl_4$ and TMA, however the resulting complex was very unstable.

Reaction of **2.5** and ethylene in the presence of MAO led to the selective formation of 1-butene under mild conditions (1 bar ethylene). Although turnover numbers were low, high

selectivity for 1-butene over isomerisation could be achieved by using low W:Al ratios (1:2). A temperature study of catalysis using **2.6** showed greater activity at lower temperatures (75 and 50 °C) and indicated that this complex may be less thermally robust than the bulkier **2.5**.

To gain further insight into the mechanism attempts to form cationic complexes were successful on an NMR spectroscopic scale, however, scale-up reactions and isolation of products proved to be a challenge. Similarly, efforts to form a discrete hydride or metallacycle complexes resulted in decomposition of the defined species, highlighting the highly reactive nature of such species and precluding any further comments on the mechanism of oligomerisation.

The chloride ligand *trans* to the imido group in the $W(NR)Me_3Cl$ complexes could be substituted by salt metathesis reactions; reaction of **2.6** with NaCp yielded $W\{N(2,6\text{-}Me\text{-}C_6H_3)\}Me_3Cp$ (**3.6**). Reaction with ethylene in the presence of MAO did yield 1-butene slowly. However, polymer formation was observed to a much larger degree.

Attempts to form a defined alkylidene complex by reaction of **2.5** with MeLi resulted in immediate decomposition. More success was had utilising NpLi but multiple neopentylidene and methylidene complexes were formed, including $W\{N(2,6\text{-}^{i}Pr\text{-}C_6H_3)\}(CH_2{}^{t}Bu)_2(CH{}^{t}Bu)$, which could not be separated.

Finally, formation of homogeneous silica supported mimics $W(NR)Me_3OSi(O{}^{t}Bu)_3$ was achieved utilising $({}^{t}BuO)_3SiOLi$ and $({}^{t}BuO)_3SiOH$ in order to compare with heterogeneous catalysts discussed in Chapter Four. Reaction of $W\{N(3,5\text{-}Me\text{-}C_6H_3)\}Me_3OSi(O{}^{t}Bu)_3$ with ethylene again selectively yields 1-butene, but with a much lower activity than the precursor compound, indicating that halide extraction may be an important step in complex activation.

2.8. References

1. D. C. Bradley, M. B. Hursthouse, K. M. A. Malik, and A. J. Nielson, *J. Chem. Soc., Chem. Commun.*, 1981, 103–104.
2. V. C. Gibson, T. P. Kee, and A. Shaw, *Polyhedron*, 1988, **7**, 579–580.
3. D. C. Bradley, M. B. Hursthouse, K. M. A. Malik, A. J. Nielson, and R. L. Short, *J. Chem. Soc. Dalton Trans.*, 1983, 2651–2656.
4. W. Clegg and R. J. Errington, *Acta Crystallogr. Sect. C Cryst. Struct. Commun.*, 1987, **43**, 2223–2224.
5. D. C. Bradley, R. J. Errington, M. B. Hursthouse, R. L. Short, B. R. Ashcroft, G. R. Clark, A. J. Nielson, and C. E. F. Rickard, *J. Chem. Soc. Dalton Trans.*, 1987, 2067–2075.
6. R. R. Schrock, R. T. DePue, J. Feldman, K. B. Yap, D. C. Yang, W. M. Davis, L. Park, M. DiMare, M. Schofield, J. Anhaus, E. Walborsky, E. Evitt, C. Krüger, and P. Betz, *Organometallics*, 1990, **9**, 2262–2275.
7. R. R. Schrock and J. D. Fellmann, *J. Am. Chem. Soc.*, 1978, **100**, 3359–3370.
8. L. Wideman, *Preparation of 1-butene*, 1974, US3813453 (A).
9. H. Olivier and P. Laurent-Gérot, *J. Mol. Catal. A Chem.*, 1999, **148**, 43–48.

10. M. J. Hanton, L. Daubney, T. Lebl, S. Polas, D. M. Smith, and A. Willemse, *Dalton Trans.*, 2010, **39**, 7025–7037.
11. L. K. Johnson, R. H. Grubbs, and J. W. Ziller, *J. Am. Chem. Soc.*, 1993, **115**, 8130–8145.
12. D. C. Bradley, S. R. Hodge, J. D. Runnacles, M. Hughes, J. Mason, and R. L. Richards, *J. Chem. Soc. Dalton Trans.*, 1992, 1663–1668.
13. T. J. Williams, *Part II Thesis, University of Oxford*, 2016.
14. J. C. Duhacek, T. A. Siddiquee, D. W. Bennett, and D. C. Duncan, *J. Chem. Crystallogr.*, 2008, **38**, 431–435.
15. C. Y. Chou, J. C. Huffman, and E. A. Maatta, *J. Chem. Soc. Chem. Commun.*, 1984, **2**, 1184–1185.
16. T. S. Pilyugina, R. R. Schrock, A. S. Hock, and P. Müller, *Organometallics*, 2005, **24**, 1929–1937.
17. I. A. Guzei and M. Wendt, *Dalton Trans.*, 2006, 3991–3999.
18. ChemAxon, http://www.chemicalize.org/.
19. W. P. Griffith, A. J. Nielson, and M. J. Taylor, *J. Chem. Soc. Dalton Trans.*, 1988, 647–649.
20. A. D. Becke, *J. Chem. Phys.*, 1986, **84**, 4524–4529.
21. J. P. Perdew and W. Yue, *Phys. Rev. B*, 1986, **33**, 8800–8802.
22. J. P. Perdew, *Phys. Rev. B*, 1986, **33**, 8822–8824.
23. S. Bianchi, M. Bortoluzzi, V. Castelvetro, F. Marchetti, G. Pampaloni, C. Pinzino, and S. Zacchini, *Polyhedron*, 2016, **117**, 769–776.
24. X. Solans-Monfort, C. Copéret, and O. Eisenstein, *Organometallics*, 2012, **31**, 6812–6822.
25. R. D. Shannon and C. T. Prewitt, *Acta Crystallogr.*, 1969, **25**, 925–946.
26. R. D. Shannon, *Acta Crystallogr. Sect. A*, 1976, **32**, 751–767.
27. E. Wiberg and N. Wiberg, *Inorganic Chemistry*, Academic Press, 2001.
28. F. G. Bordwell, X. M. Zhang, and J. P. Cheng, *J. Org. Chem.*, 1993, **58**, 6410–6416.
29. F. G. Bordwell and D. J. Algrim, *J. Am. Chem. Soc.*, 1988, **110**, 2964–2968.
30. C. a Tolman, *Chem. Rev.*, 1977, **77**, 313–348.
31. H. R. Menapace, N. A. Maly, J. L. Wang, and L. G. Wideman, *J. Org. Chem.*, 1975, **40**, 2983–2985.
32. S. F. Pedersen and R. R. Schrock, *J. Am. Chem. Soc.*, 1982, **104**, 7483–7491.
33. W. R. H. Wright, A. S. Batsanov, J. A. K. Howard, R. P. Tooze, M. J. Hanton, and P. W. Dyer, *Dalton Trans.*, 2010, **39**, 7038–7045.
34. V. C. Gibson, C. Redshaw, G. L. P. Walker, J. A. K. Howard, V. J. Hoy, J. M. Cole, L. G. Kuzmina, and D. S. De Silva, *J. Chem. Soc. Dalton Trans.*, 1999, 161–166.
35. J. Fischer, J. Kress, J. A. Osborn, L. Ricard, and M. Wesolek, *Polyhedron*, 1987, **6**, 1839–1842.
36. J. Kress, M. Wesolek, J.-P. Le Ny, and J. A. Osborn, *J. Chem. Soc. Chem. Commun.*, 1981, 1039–1040.
37. A. R. Rossi and R. Hoffmann, *Inorg. Chem.*, 1975, **14**, 365–374.
38. Y. Bouhoute, A. Garron, D. Grekov, N. Merle, K. C. Szeto, A. De Mallmann, I. Del Rosal, L. Maron, G. Girard, R. M. Gauvin, L. Delevoye, and M. Taoufik, *ACS Catal.*, 2014, **4**, 4232–4241.
39. A. Hamieh, Y. Chen, S. Abdel-Azeim, E. Abou-hamad, S. Goh, M. Samantaray, R. Dey, L. Cavallo, and J. M. Basset, *ACS Catal.*, 2015, **5**, 2164–2171.
40. E. P. Schram and N. Sudha, *Inorg. Chim. Acta*, 1991, **183**, 213–216.
41. E. Y.-X. Chen and T. J. Marks, *Chem. Rev.*, 2000, **100**, 1391–1434.
42. D. S. McGuinness, *Chem. Rev.*, 2011, **111**, 2321–2341.
43. W. Kaminsky, *Macromolecules*, 2012, **45**, 3289–3297.
44. F. Ghiotto, C. Pateraki, J. Tanskanen, J. R. Severn, N. Luehmann, A. Kusmin, J. Stellbrink, M. Linnolahti, and M. Bochmann, *Organometallics*, 2013, **32**, 3354–3362.
45. H. S. Zijlstra and S. Harder, *Eur. J. Inorg. Chem.*, 2015, **2015**, 19–43.
46. T. Agapie, *Coord. Chem. Rev.*, 2011, **255**, 861–880.
47. A. C. Pinheiro, T. Roisnel, E. Kirillov, J.-F. Carpentier, and O. L. Casagrande, *Dalton Trans.*, 2015, **44**, 16073–16080.

48. W. R. H. Wright, A. S. Batsanov, A. M. Messinis, J. A. K. Howard, R. P. Tooze, M. J. Hanton, and P. W. Dyer, *Dalton Trans.*, 2012, **41**, 5502–5511.
49. E. A. Zuech, *J. Polym. Sci. Part A Polym. Chem.*, 1972, **10**, 3665–3672.
50. J. P. Le Ny and J. A. Osborn, *Organometallics*, 1991, **10**, 1546–1550.
51. S. Vadake Kulangara, D. Haveman, B. Vidjayacoumar, I. Korobkov, S. Gambarotta, and R. Duchateau, *Organometallics*, 2015, **34**, 1203–1210.
52. A. Vigalok, *Organometallics*, 2011, **30**, 4802–4810.
53. L. H. Do, J. A. Labinger, and J. E. Bercaw, *ACS Catal.*, 2013, **3**, 2582–2585.
54. R. Schowner, W. Frey, and M. R. Buchmeiser, *J. Am. Chem. Soc.*, 2015, **137**, 6188–6191.
55. S. Sen, R. Schowner, D. a. Imbrich, W. Frey, M. Hunger, and M. R. Buchmeiser, *Chem. Eur. J.*, 2015, **21**, 13778–13787.
56. J. H. Wengrovius and R. R. Schrock, *Organometallics*, 1982, **1**, 148–155.
57. C. L. Campion, W. Li, and B. L. Lucht, *J. Electrochem. Soc.*, 2005, **152**, A2327–A2334.
58. L. Maier and R. Schmutzler, *J. Chem. Soc. D Chem. Commun.*, 1969, **1**, 961–962.
59. J. M. Boncella, S. S. Wang, and D. D. VanderLende, *J. Organomet. Chem.*, 1999, **591**, 8–13.
60. S.-Y. S. Wang, D. D. VanderLende, K. A. Abboud, and J. M. Boncella, *Organometallics*, 1998, **17**, 2628–2635.
61. U. Radius, J. Sundermeyer, K. Peters, and H.-G. von Schnering, *Eur. J. Inorg. Chem.*, 2001, **2001**, 1617–1623.
62. S. R. Huber, T. C. Baldwin, and D. E. Wigley, *Organometallics*, 1993, **12**, 91–97.
63. S. R. Bahr and P. Boudjouk, *J. Org. Chem.*, 1992, **57**, 5545–5547.
64. B. D. Ward, G. Orde, E. Clot, A. R. Cowley, L. H. Gade, and P. Mountford, *Organometallics*, 2004, **23**, 4444–4461.
65. E. J. Stoebenau and R. F. Jordan, *J. Am. Chem. Soc.*, 2006, **128**, 8638–8650.
66. F. Blanc, C. Copéret, J. Thivolle-Cazat, J. M. Basset, A. Lesage, L. Emsley, A. Sinha, and R. R. Schrock, *Angew. Chem. Int. Ed.*, 2006, **45**, 1216–1220.
67. C. Copéret, M. Chabanas, R. Petroff Saint-Arroman, and J.-M. Basset, *Angew. Chem. Int. Ed.*, 2003, **42**, 156–181.
68. N. Merle, G. Girard, N. Popoff, A. De Mallmann, Y. Bouhoute, J. Trébosc, E. Berrier, J. F. Paul, C. P. Nicholas, I. Del Rosal, L. Maron, R. M. Gauvin, L. Delevoye, and M. Taoufik, *Inorg. Chem.*, 2013, **52**, 10119–10130.
69. R. M. Gauvin, F. Buch, L. Delevoye, and S. Harder, *Chem. Eur. J.*, 2009, **15**, 4382–4393.

Chapter Three – Preparation of layered double hydroxides for use as single-site catalyst supports

"I would like to start by emphasizing the importance of surfaces. It is at a surface where many of our most interesting and useful phenomena occur. We live for example on the surface of a planet. It is at a surface where the catalysis of chemical reactions occur. It is essentially at a surface of a plant that sunlight is converted to a sugar. In electronics, most if not all active circuit elements involve non-equilibrium phenomena occurring at surfaces. Much of biology is concerned with reactions at a surface." **Walter Brattain**

3.1. Introduction

As described in Chapter One, layered double hydroxides (LDHs) are a class of inorganic anionic clays comprised of positively charged, mixed metal hydroxide, Brucite-like layers bearing surface hydroxyl functionality, with weakly bound anions intercalated between them (Figure 3.1).[1] Recently, O'Hare and co-workers have reported the synthesis of a new class of LDH materials by employing an Aqueous Miscible Organic Solvent Treatment (AMOST) method.[2–4] These so called AMO-LDHs, have much higher surface areas than their conventionally synthesised counterparts and are easily dispersed in most organic solvents. AMO-LDHs can be represented by the general formula $[M^{2+}_{1-x}M^{3+}_{x}(OH)_2]^{q+}(X^{n-})_{q/n}\cdot yH_2O\cdot w$(AMO-solvent) and are commonly referred to in the form $M^{2+}_{1-x}M^{3+}_{x}$-X *e.g.* Mg_3Al-SO_4.

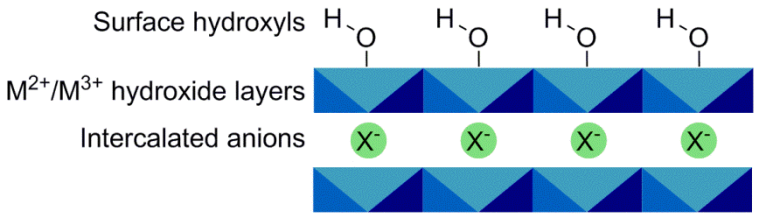


Figure 3.1. Schematic representation of the basic structure of a layered double hydroxide (LDH).

These high surface area materials have shown promise in the area of single-site heterogeneous catalysis as the surface is capable of anchoring methylaluminoxane (MAO), allowing activation and immobilisation of metallocene pre-catalysts,[5–9] in an analogous fashion to silica supported MAO (ssMAO).[10] In some cases, AMO-LDH-MAO supported catalysts (AMO-LDH thermally pre-treated under vacuum at 150 °C) have been shown to outperform their ssMAO counterparts,[7,8] with variation of the LDH composition also impacting on the activity of the immobilised species; Mg_3Al-SO_4 was shown to be the most active composition.[6] A study of ethylene-bis(1-indenyl)zirconium dichloride, (EBI)$ZrCl_2$, supported on Mg_3Al-CO_3 AMO-LDH-MAO, where the AMO-LDH had been dehydroxylated under vacuum at incremental temperature steps between 23 and 190 °C, demonstrated that treatment at 125 or 150 °C led to the highest activities (1,263 and 1,276 $kg_{PE}mol_{Zr}^{-1}h^{-1}bar^{-1}$ respectively).[5] The dip in reactivity above 150 °C was reasoned to be a result of the decreased hydroxyl functionality leading to possible complex aggregation. However, no study on the properties of these materials after thermal vacuum treatment has of yet been performed, leading to difficulties in rationalising these reactivity differences based on the properties of the starting AMO-LDH materials alone.

Due to their surface hydroxyl functionality, there is also interest in employing LDHs as defined supports for other types of catalysts, utilising the surface organometallic chemistry (SOMC) methodology to graft the complexes onto a surface hydroxyl site.[11] For such an approach to be successful, careful control of the degree and uniformity of surface hydroxyl sites is required. As described in Chapter One, for silica this is achieved by thermally treating the material under vacuum.[12] This dehydroxylates the surface, decreasing the number of vicinal and germinal sites, yielding mainly isolated silanols.

This Chapter focusses on the preparation, thermal vacuum treatment and characterisation of $[Mg_{0.75}Al_{0.25}(OH)_2](SO_4)_{0.125}\cdot 0.71H_2O\cdot 0.17$(acetone) or $Mg_3Al\text{-}SO_4$ AMO-LDH, with a view to employing this material as a catalyst support using the SOMC methodology. A variety of spectroscopic techniques have been utilised to analyse changes in the LDH structure, as well as the degree of surface hydroxyl functionality after such treatment. Finally, a preliminary study on the effect the treatment temperature has on the reactivity of $(^n BuCp)_2ZrCl_2$ immobilised on the MAO coated material has been performed.

3.2. LDH synthesis and thermal treatment under vacuum

3.2.1. Thermal vacuum treatment of $Mg_3Al\text{-}SO_4$ and $Mg_3Al\text{-}CO_3$ AMO-LDHs

Due to the scale required in order to employ multiple characterisation techniques and subsequent immobilisations and reactivity studies, $Mg_3Al\text{-}SO_4$ was supplied by SCG Chemicals Co. Ltd (Thailand) as a uniform bulk sample (20 g). Both the $Mg_3Al\text{-}SO_4$ and $Mg_3Al\text{-}CO_3$ AMO-LDHs were synthesised by co-precipitation according to a literature procedure.[3] $Mg_3Al\text{-}SO_4$ was dehydroxylated under vacuum for 6 hours over a range of temperatures (23, 100, 150, 200, 250, 275, 300, 350, 400 and 450 °C), $Mg_3Al\text{-}CO_3$ was dehydroxylated at 200 °C for 6 hours for comparison. The LDH precursor (~1 g) was loaded into a crucible and place inside a quartz tube that was sealed at on end. This was then connected to a vacuum/nitrogen manifold at the other and placed under dynamic vacuum (10^{-3} mbar). By utilising a tube furnace the sample could be heated to a desired temperature at a controlled ramp rate of 5 °C min^{-1} at which it was held for six hours. After cooling, the tube was transferred to a nitrogen filled glovebox under static vacuum, where the dehydroxylated samples were stored in sealed vials. After calcination, inspection of the liquid nitrogen cooled solvent trap showed the presence of water, and the mass of the powdered samples was seen to have decreased. The resulting LDH powders appeared greyer and darker in colour with increasing dehydroxylation temperature.

3.3. Structure of dehydroxylated Mg_3Al-SO_4 AMO-LDH

To probe the structure of the AMO-LDH material after thermal vacuum treatment, capillary powder X-ray diffraction (PXRD) spectroscopy, Fourier transform infrared (FTIR) spectroscopy, thermogravimetric analysis (TGA), Brunauer-Emmett-Teller (BET) surface area measurements and scanning electron microscopy (SEM) imagery were utilised and compared with the starting AMO-LDH material.

Calcination of conventional layered double hydroxide materials in air, or under a flow of gas (*e.g.* N_2) leads to changes in the structural composition.[13] Thermogravimetric analysis (TGA) over a temperature range of 23–600 °C allows identification of the key steps in this process, which are loss of co-ordinated surface and interlayer water and solvent molecules (50–200 °C, minima in the 1st derivative labelled T_1), dehydroxylation of the surface hydroxyl groups leading to a layered double oxide (LDO) structure (200–400 °C, minima labelled T_2), and further decomposition to mixed metal oxides.[13,14] Peng and co-workers have utilised solid-state ^1H and ^{27}Al MAS NMR and FTIR spectroscopy to investigate the dehydroxylation process for a series of MgAl-X LDHs (X = NO_3^-, CO_3^{2-}, Cl^- and ClO_4^-) with varying Mg:Al ratios.[15] Results indicated that in all cases after dehydration (up to 150 °C), dehydroxylation of 'Mg_2AlOH' groups along with formation of four coordinate aluminium ions occurs at lower temperatures than dehydroxylation of 'Mg_3OH' groups, leading to a non-uniform distribution of hydroxyls sites.

TGA of AMO-LDHs show they exhibit lower maxima for these decomposition events than their conventionally synthesised analogues.[3] For example, AMO treated Mg_3Al-CO_3 LDH exhibits a maxima for T_2 at 340 °C, whereas, for the conventionally synthesised, water washed sample, the maxima occurs at 424 °C. This difference has been attributed to the better dispersion of the AMO-LDH particles. The TGA data for the untreated Mg_3Al-SO_4 AMO-LDH is shown in Figure 3.2. In this sample, the minima in the DTG for T_1 and T_2 occur at 142 and 394 °C respectively (Figure A81 and Table A7), compared to 240 and 455 °C for conventionally synthesised Mg_3Al-SO_4 LDH.[16]

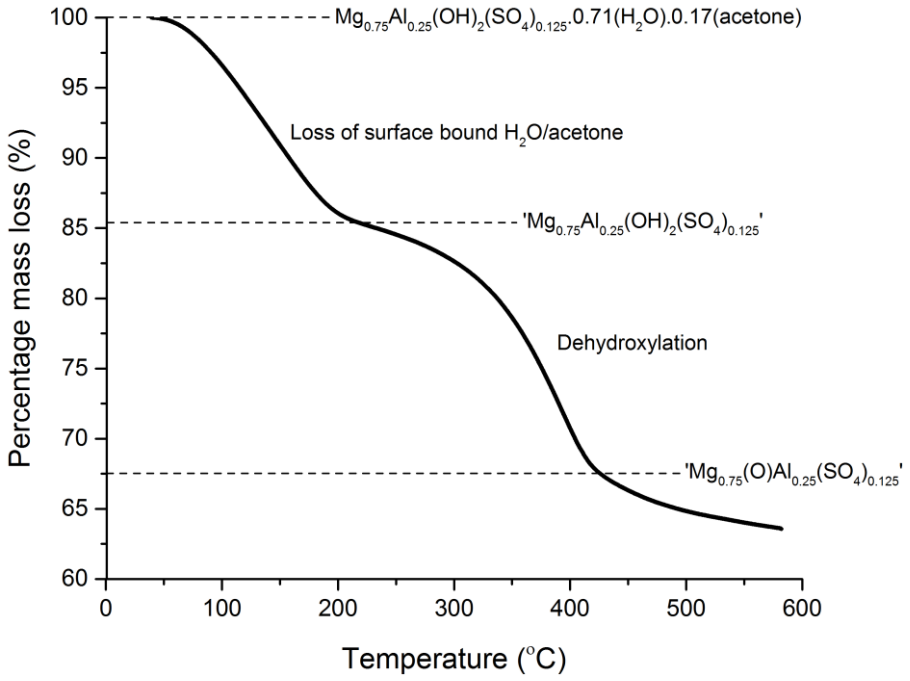


Figure 3.2. TGA of the $Mg_3Al\text{-}SO_4$ AMO-LDH starting material. Approximated molecular formulae are given at each step in the mass loss.

Comparison with the TGA data reported by Constantino *et al*. further emphasises the difference between conventionally synthesised and AMO-LDH materials. At 150 °C a percentage mass loss of ~9% is observed for the $Mg_3Al\text{-}SO_4$ AMO-LDH compared to 3.4% for conventional $Mg_{2.32}Al\text{-}SO_4$, ascribed to the low boiling point and thus ease of removal of the AMO solvent.[13] Theoretically, complete removal of surface and interlayer water and acetone from $[Mg_{0.75}Al_{0.25}(OH)_2](SO_4)_{0.125}\cdot 0.71H_2O\cdot 0.17(\text{acetone})$ would result in a percentage mass loss of ~24% and formation of $[Mg_{0.75}Al_{0.25}(OH)_2](SO_4)_{0.125}$, with further dehydration yielding $[Mg_{0.75}(O)Al_{0.25}](SO_4)_{0.125}$, with a total percentage mass loss of 43%. As can be seen from the TGA, the two observed steps correspond to percentage mass losses of 15 and 32%, hence it is postulated that some hydroxyl groups persist even at temperatures >400 °C.

In this study, TGA analysis was performed on all of the $Mg_3Al\text{-}SO_4$ AMO-LDH compounds thermally treated under vacuum, which were compared with the starting AMO-LDH (Figure 3.3). TGA was performed under a flow of N_2 to ensure that rehydration of the LDH structure did not occur. It has been shown that LDHs exhibit a 'memory effect' having been calcined up to 450–600 °C, whereby, exposure to air leads to complete rehydration and restructuring of the LDH material.[17] Individual TGA plots with DTG analysis are shown in the Appendix (Figures A81–A93).

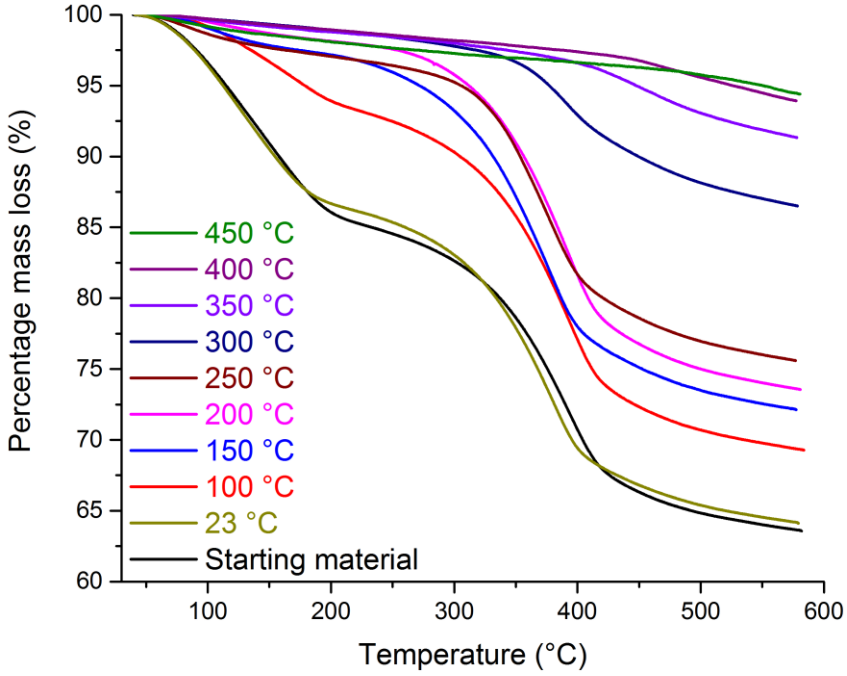


Figure 3.3. TGA analysis of the dehydroxylated samples compared to $Mg_3Al\text{-}SO_4$ AMO-LDH.

Analysis of the TGA curves for the dehydroxylated samples (Figure 3.3) shows that as the temperature is increased the associated percentage weight loss only begins to change at the temperature the material was treated at, as expected. For samples treated above 300 °C, only a small decrease in the mass is observed, suggesting almost complete dehydroxylation has occurred. Comparison of the sample evacuated at room temperature with the starting material shows that the end point for the first weight loss event is at a lower temperature, indicating that some of the surface bound water/solvent is removed by such a process.

Powder X-ray diffraction (PXRD) was utilised to identify the structure of the material after thermal vacuum treatment. In order to prevent rehydration, the samples were packed into capillaries and sealed in the glovebox. Experiments were run in capillary mode on the spectrometer by mounting on a goniometer which was spun during collection. Comparison of the PXRD patterns for the dehydroxylated samples with the starting AMO-LDH is depicted in Figure 3.4. A shift in the *003* Bragg reflection up to 200 °C was observed, signifying a decrease in the interlayer spacing with the peak widths (FWHM) remaining constant (Table 3.1). Constantino *et al.* have attributed the reduction in the interlayer spacing seen for $Mg_{2.32}Al\text{-}SO_4$ calcined in air to sulfate grafting occurring between the layers.[13]

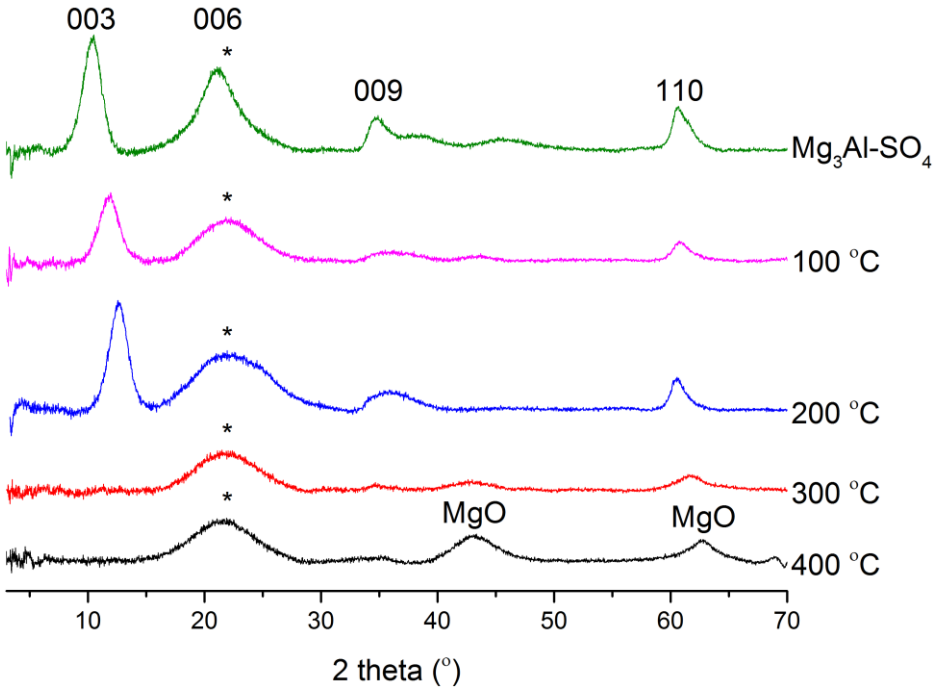


Figure 3.4. Powder XRD patterns of the starting $Mg_3Al\text{-}SO_4$ AMO-LDH and samples dehydroxylated at 100, 200, 300 and 400 °C. * The broad feature at 21° is an artefact due to the capillary spinner.

Table 3.1. Comparison of the *003* peak position, full width half maximum (FWHM) value and interlayer spacing (*c*) for $Mg_3Al\text{-}SO_4$ and samples thermally treated under vacuum at 100 and 200 °C.

Sample	*003* position, 2θ (°)	FWHM (°)	Interlayer spacing, *c* (Å)
$Mg_3Al\text{-}SO_4$	10.4	1.8	8.5
100 °C	11.9	1.9	7.4
200 °C	12.7	1.8	7.0

Above 300 °C, the *003* Bragg reflection is no longer present, indicating decomposition of the layered structure may have occurred, consistent with observations from the TGA data. This broad almost featureless pattern is analogous to that observed when $Mg_3Al\text{-}SO_4$ LDH is calcined at 450 °C under a flow of nitrogen,[13] again highlighting the increased rate of decomposition observed with vacuum. At 400 °C, formation of small amounts of MgO (2θ = 43 and 63°) is observed. The presence of aluminium to yield Mg(Al)O in calcined LDH structures has also been shown, due to the *a* parameter being smaller than pure MgO, resulting from incorporation of smaller Al^{3+} ions.[18] A neutron diffraction study on the thermal decomposition of $Mg_{0.71}Al_{0.29}(OH)_2(CO_3)_{0.145}{\cdot}mH_2O$ by Gazzano *et al*. also demonstrated a reduction in the *c* parameter, with complete disappearance of the *003* peak observed above 600 K.[19] Above 600 K, an Mg–Al oxide structure similar to MgO was identified. An increase

in the *a* parameter with temperature was also observed, which may indicate the removal of Al^{3+} ions from the oxide lattice.[20] From the data obtained for Mg_3Al-SO_4 AMO-LDH, a small increase in the *110* peak and thus *a* parameter is also observed between 200 and 300 °C (2θ = 60.6 *vs* 61.4°) (Table A8).

FTIR spectroscopy of the samples shows a clear decrease in both the width and intensity of the OH stretches, which are associated with bound water molecules as well as surface and interlayer hydroxyl groups (Figure 3.5). A small amount of intercalated carbonate is also observed by the ν_3 CO_3 stretch.

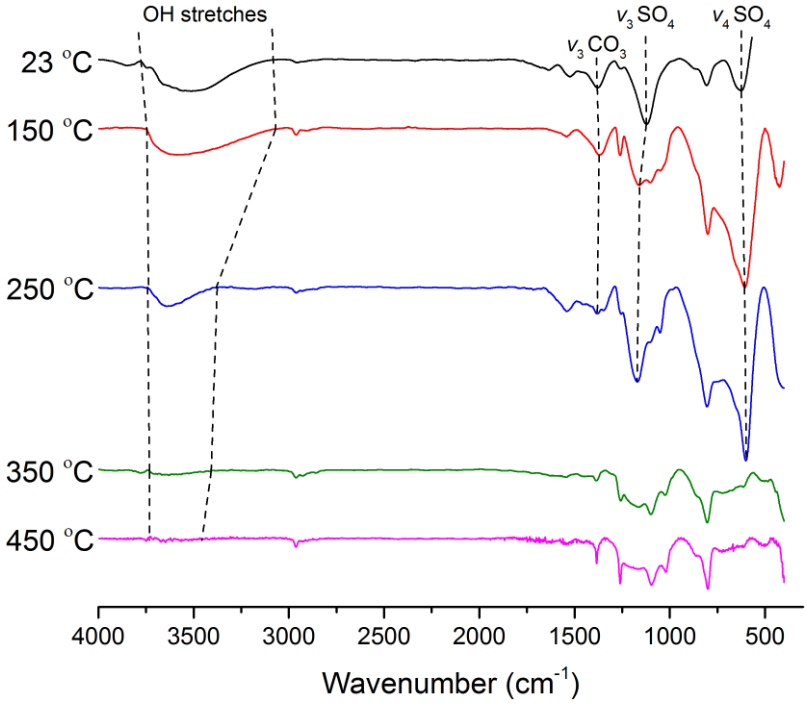


Figure 3.5. Comparison of the FTIR spectra for Mg_3Al-SO_4 LDH calcined at 23, 150, 250, 350 and 450 °C under vacuum.

There is a marked difference in the bands associated with the interlayer sulfate ions over the temperature range. The sulfate molecules are proposed to have restricted rotation within the gallery, with the symmetrical υ_3 band for tetrahedral sulfate, observed at 1,121 cm^{-1} for the 23 °C sample, split at higher temperatures due to a lowering of T_d symmetry in the intercalate.[13] The band at 1,100 cm^{-1} appears to shift to slightly higher wavenumbers over the temperature range 23–250 °C (Table 3.2); the splitting of this band is indicative of sulfate grafting to the internal LDH surface,[13] supporting the observed decrease in the *c* dimension from the PXRD. Above this temperature, the relative intensity of these bands is markedly reduced, suggesting loss of interlayer sulfate ions due to formation of metal oxide salts.

Table 3.2. Shift in the frequency of the maxima of the IR peaks corresponding to OH stretches and SO_4^{2-} ν_3 and ν_4 stretches.

Dehydroxylation temperature (°C)	**OH stretching (cm^{-1})**	**SO_4^{2-} ν_3 (cm^{-1})**	**SO_4^{2-} ν_4 (cm^{-1})**
23	3,512	1,121	627
100	3,581	1,160	605
150	3,585	1,169	610
200	3,616	1,178	601
250	3,629	1,174	601
275	3,649	1,170[a]	599[a]
300	3,649	-	-
350	3,647[a]	-	-
400	3,652[a]	-	-
450	-	-	-

[a] Weak intensity, broad absorptions.

The specific surface area of the AMO-LDH samples were determined by N_2 gas physisorption using Brunauer-Emmett-Teller (BET) theory, which revealed that the surface area of the samples increases with increasing dehydroxylation temperature (Figure 3.6). There appear to be two almost linear regimes, one below 275 °C and one above 300 °C, with a large jump between them (95 to 158 m^2g^{-1} respectively), further demonstrating the structural change occurring in this material. Complete erosion of the layered structure would yield single layer mixed metal oxide sheets, thus increasing the surface area. Bellotto *et al*. have also previously observed a large increase in the surface area of calcined $[Mg_{0.64}Al_{0.36}(OH)_2](CO_3)_{0.18}\cdot 0.46H_2O$ after loss of the layered structure is observed.[21]

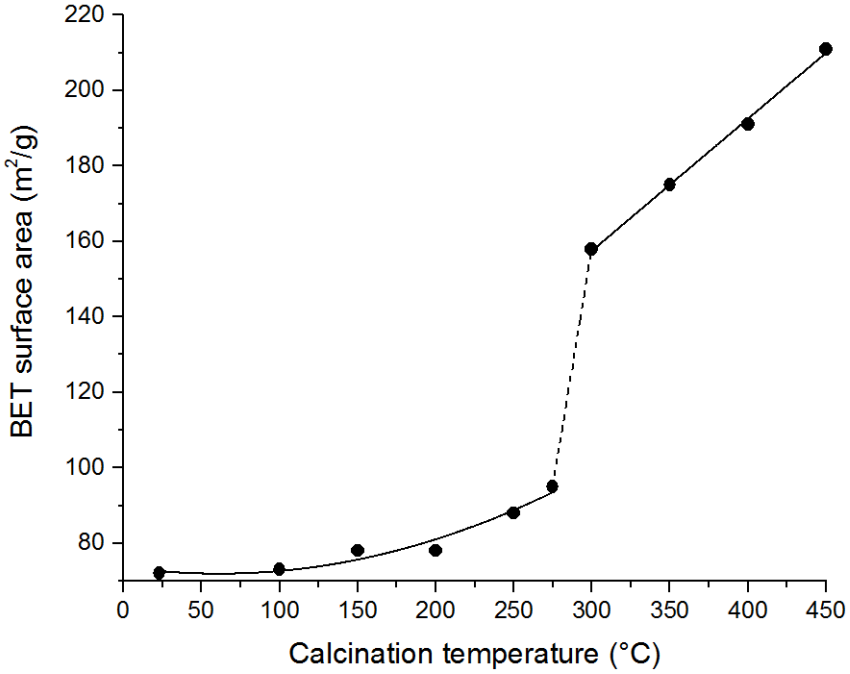


Figure 3.6. BET surface area measurements for $Mg_3Al\text{-}SO_4$ AMO-LDH samples treated between 23 and 450 °C. Trend lines are a guide for the eye.

BET and pore volume data (Table A9) along with individual BET isotherms and pore volume distributions (Figures A94–A115) are provided in the Appendix. The isotherms follow classical type II and type IV shapes indicating that the material is mesoporous.[22] At higher temperatures, the total pore volume increases (calculated by the Barrett-Joyner-Halenda (BJH) method), with a greater H3 hysteresis loop (Figure 3.7) indicating that there are additional cylindrical pores occurring between aggregated LDH platelet shaped particles.[22,23] From the pore volume distributions, an increase in mesopores of size ranging between 30–50 Å is observed (4.4% of total pores in the starting material *vs* 27% at 450 °C). The most notable increase in pores of this size occurs between 275 and 300 °C, where it doubles from 8 to 16% of the total. This is also the temperature range where loss of the layered structure and increase in the surface area are observed.

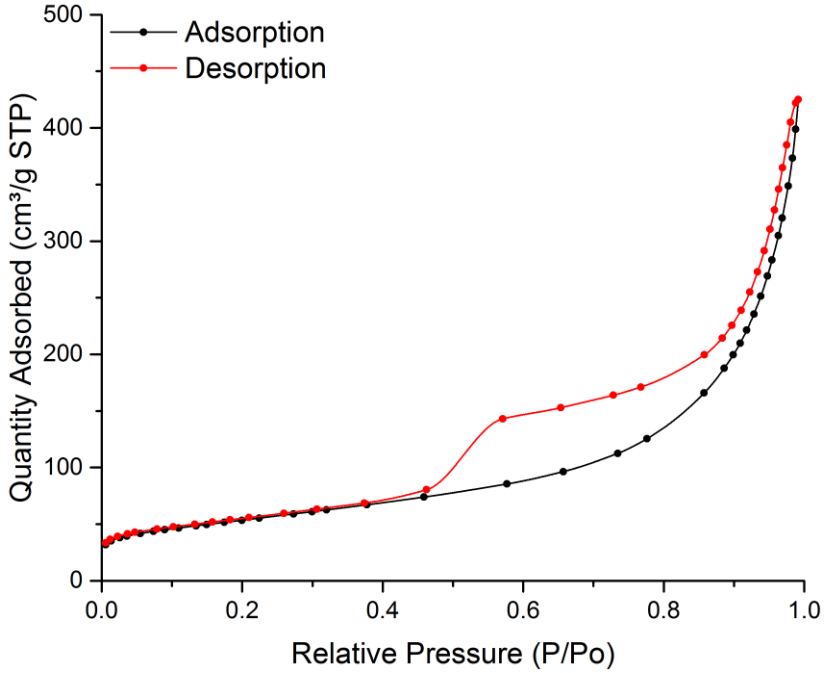
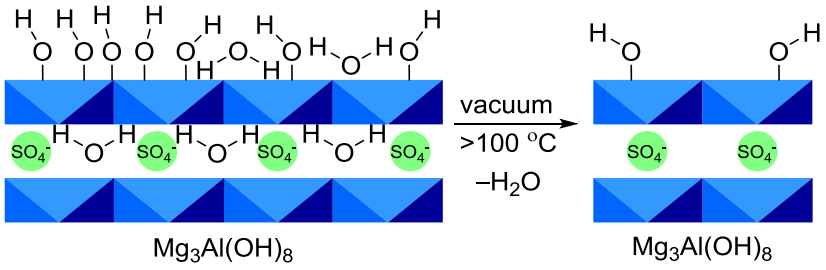


Figure 3.7. BET adsorption and desorption isotherms for Mg_3Al-SO_4 AMO-LDH treated at 400 °C under vacuum displaying a H3 type hysteresis.

Despite the apparent changes to the structural composition over the temperature range, SEM imagery shows very little difference in the macroscopic structure of the particles (Figure A116). In all cases, similar aggregation of the particles is observed, with no clear evidence this is greater at higher temperatures as the BET data may suggest.

3.4. Surface hydroxyl concentration

Heating the AMO-LDH samples under vacuum leads to removal of surface bound water molecules and dehydroxylation (Scheme 3.1), as observed by the mass loss in the TGA (Figure 3.2).



Scheme 3.1. Schematic dehydroxylation of Mg_3Al-SO_4 AMO-LDH heated under vacuum.

By focussing on the hydroxyl region (3,000–4,000 cm^{-1}) of the FTIR spectra for the calcined samples (Figure 3.8), a reduction in both the width and intensity of the bands is clearly observed with increasing temperature. Three groups of similar width and intensity are

observed (23–150, 200–300 and 350–450 °C) matching the mass loss events in the TGA. There is a clear shift in the minima between 23 and 300 °C towards higher wavenumbers (3,512 *vs* 3,649 cm^{-1}). Between 200 and 300 °C, the loss of surface water and concomitant dehydroxylation yields bands with approximately half the area of the samples treated at lower temperatures. Above 300 °C near complete dehydroxylation is seen to occur with only very weak stretches between 3,400–3,700 cm^{-1} present. The observed hydroxyl bands are not as narrow as those observed for dehydroxylated silica samples[24] due to the presence of internal hydroxyl groups within the layers broadening the observed bands.

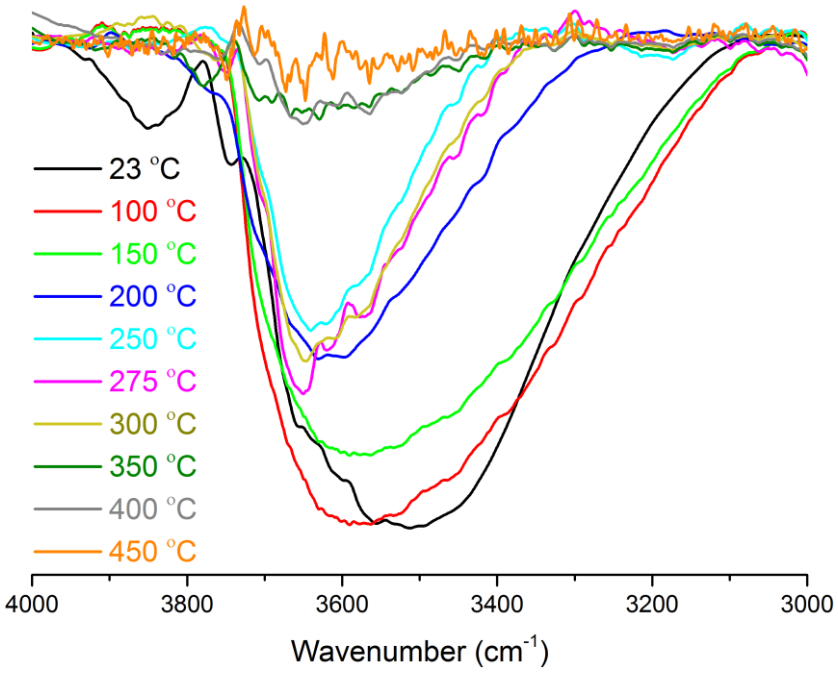
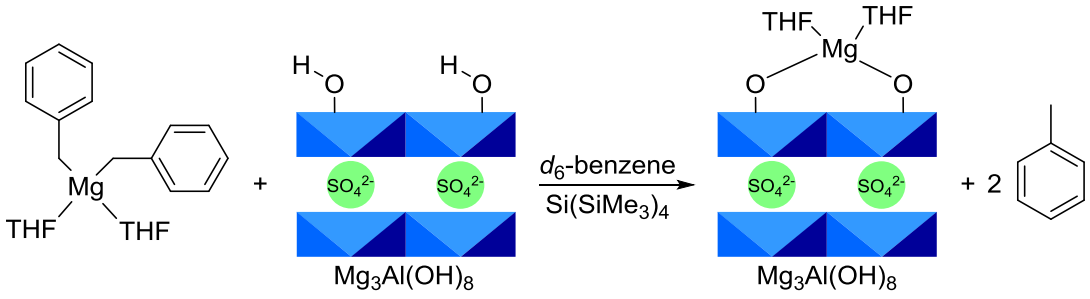


Figure 3.8. Comparison of the OH region of the FTIR spectrum (3,000–3,800 cm^{-1}) for Mg_3Al-SO_4 AMO-LDH thermally treated between 23–450 °C under vacuum.

In order to quantify the surface hydroxyl concentration, titrations were performed in J. Young valve NMR spectroscopy tubes utilising $Mg(CH_2Ph)_2(THF)_2$,[25] liberating toluene that can be integrated against an internal standard (Scheme 3.2 and Figure A117).



Scheme 3.2. Titration of Mg_3Al-SO_4 AMO-LDH with $Mg(CH_2Ph)_2(THF)_2$.

From the titration and BET data obtained the hydroxyl number (α_{OH}, the number of hydroxyl groups per square nanometre) can be calculated for each sample (Figure 3.9 and Table 3.3).

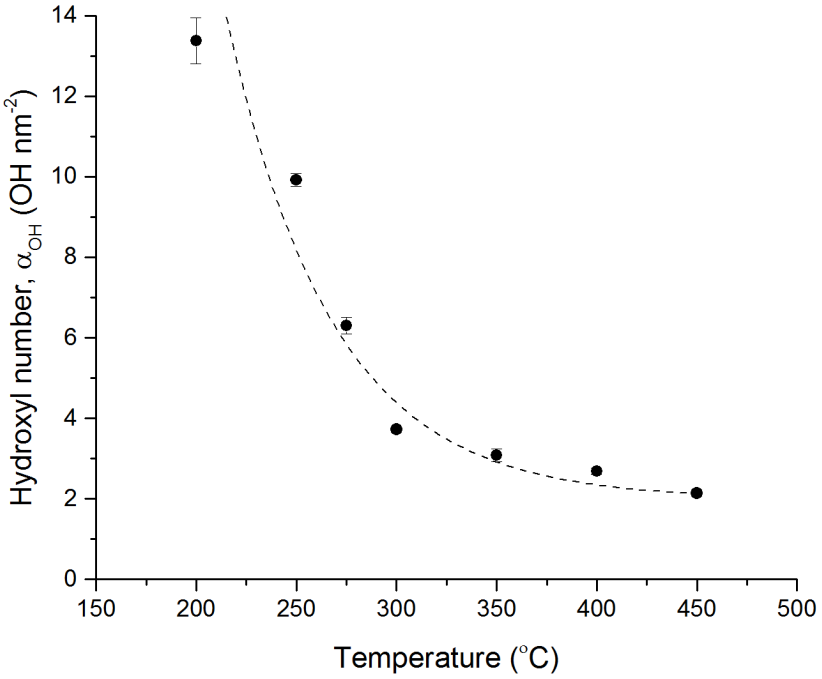


Figure 3.9. Hydroxyl number of Mg_3Al-SO_4 AMO-LDH, α_{OH}, as a function of dehydroxylation temperature.

Table 3.3. Measures of surface hydroxylation calculated from titration and BET data for thermally treated Mg_3Al-SO_4 and Mg_3Al-CO_3 AMO-LDHs, compared with $SiO_{2\text{-}(500)}$.[12]

Temperature (°C)	**μMol_{OH}**	**$mMol_{OH}\ g^{-1}$**	**BET surface area (m^2g^{-1})**	**OH density, δ_{OH} ($mol_{OH}\ nm^{-2}$ x10^{-23})**	**Hydroxyl number, α_{OH} (OH nm^{-2})**
200	8.55	1.71	76.7	2.23	13.4
250	7.25	1.45	87.6	1.65	9.9
275	4.88	0.98	95.3	1.02	6.2
300	4.93	0.99	158.4	0.62	3.7
350	4.51	0.90	175.3	0.52	3.1
400	4.28	0.86	191.2	0.45	2.7
450	3.76	0.75	210.5	0.36	2.1
Mg_3Al-CO_3 200	36.5	7.29	312.9	2.33	14.0
$SiO_{2\text{-}(500)}$[12]	-	-	11–905	0.30	1.8

As the temperature is increased from 200 to 450 °C, the degree of hydroxylation (α_{OH}) falls from 13.4 to 2.1 OH nm^{-2}, following an exponential decay type pattern. It should be noted that the silica used as a single-site support, is usually treated at 700 °C and is known to

have a hydroxyl number of 1.15.[12] At the rate of dehydroxylation observed, this would be achieved at around 550 °C if the same trend were to continue.

The results for the Mg_3Al-SO_4 AMO-LDH samples were also compared with the analogous Mg_3Al-CO_3 AMO-LDH thermally treated under vacuum at 200 °C. Firstly, comparison of the TGA data for the starting carbonate and sulfate samples demonstrates the lower thermal stability of the carbonate AMO-LDH (Figure 3.10). From the DTG, T_1 and T_2 events occur at 140 and 336 °C respectively (Mg_3Al-SO_4 T_1 = 142 and T_2 = 396 °C) (Figure A90). The total percentage mass lost after 600 °C is also much larger for Mg_3Al-CO_3 AMO-LDH (42 *vs* 35% at 500 °C). The Mg_3Al-CO_3 AMO-LDH thermally treated at 200 °C under vacuum has a much larger BET surface area than its sulfate analogue (313 *vs* 77 m^2g^{-1}), which results in a larger number of accessible surface groups and hence easier removal. Also, thermally treating carbonate LDHs results in decarboxylation thus loss of the interlayer anion,[26] which does not occur for the sulfate analogue.

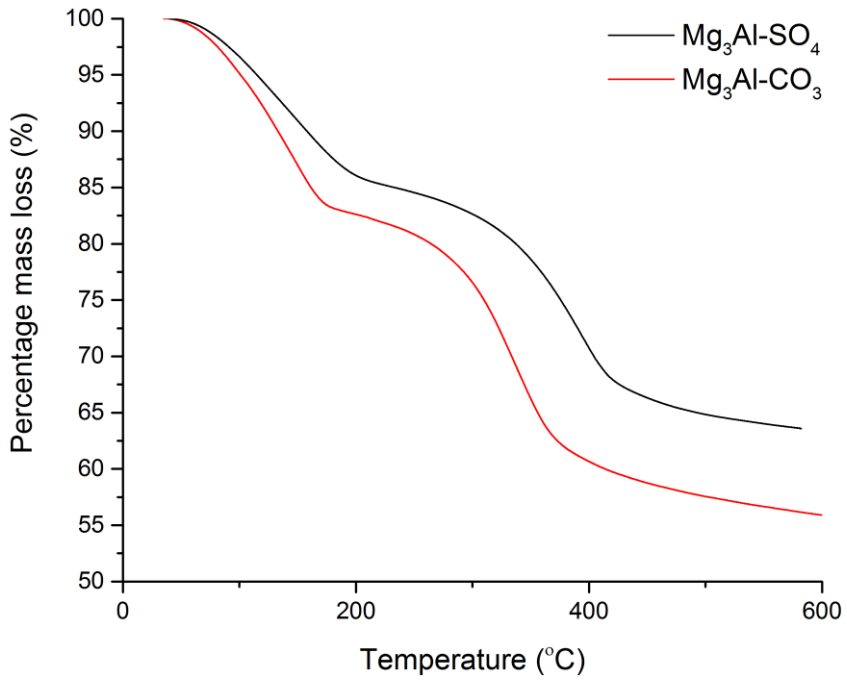


Figure 3.10. TGA curves for Mg_3Al-SO_4 and Mg_3Al-CO_3 AMO-LDHs.

The hydroxyl number (α_{OH}) for Mg_3Al-CO_3 AMO-LDH thermally treated at 200 °C under vacuum, is calculated as 14.0 OH nm^{-2}, which is close to that of the analogously treated sulfate sample (13.4 OH nm^{-2}). From this result it can be inferred that both variation in the interlayer anion, or surface area of the AMO-LDH have little effect on the degree of dehydroxylation of the surface. Zhuravlev and co-workers have previously shown that the α_{OH}

of amorphous silicas are independent of the specific surface area, as the hydroxyl number, δ_{OH} ($mol_{OH}\ g^{-1}$), increases linearly with surface area.[12]

O'Hare and co-workers have previously reported a structural determination from powder neutron diffraction data of the layered double hydroxide $LiAl_2(OD)_6Cl$, which was treated under vacuum at 90 °C (Figure 3.11).[27]

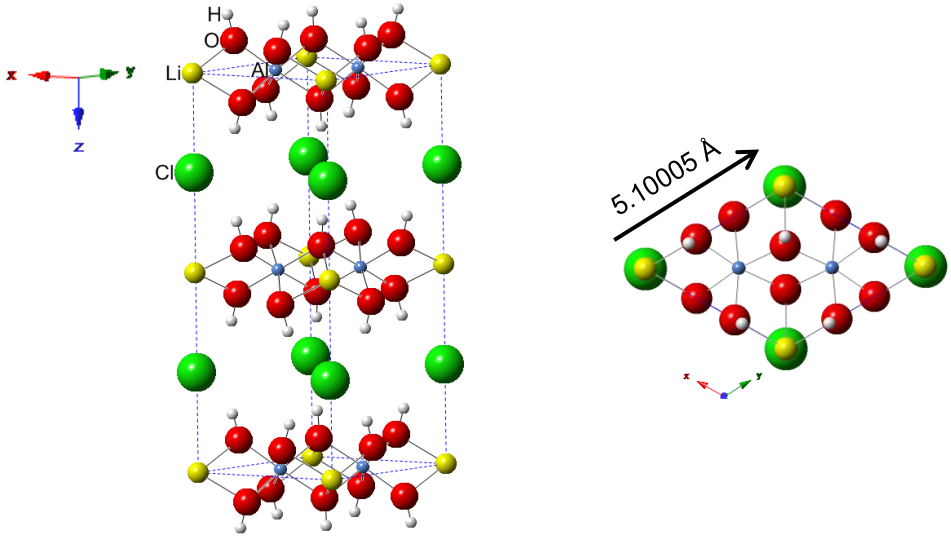


Figure 3.11. Unit cell of $LiAl_2(OD)_6Cl$ determined from neutron diffraction data (left), and top view of structure showing surface OD groups in the unit cell (right).[27]

Using this data as a basis, the density of surface hydroxyl groups per mm^{-2} for this archetypical LDH can be determined. The unit cell surface area was measured and a hydroxyl number for the material determined (Equation 3.1).

Equation 3.1. Calculation of hydroxyl number (α_{OH}) from unit cell.

$$Area = 2 \times \frac{\sqrt{3}}{4} a^2$$

$$a = 0.510005 \text{ nm}$$

$$Area = 0.225 \text{ nm}^2$$

$$\alpha_{OH} = \frac{3}{0.225} = 13.32 \text{ OHnm}^{-2}$$

The unit cell is found to contain a total of 3 OD groups (1 full, 4 x 1/2 shared) (Figure 3.11). The unit cell dimensions are $a = b = 5.10005$ Å, thus the surface area of the unit cell is 0.0225 nm^2. The hydroxyl number (α_{OH}) is therefore calculated as being as 13.32 OH nm^{-2}

within error of the value obtained experimentally for $Mg_3Al\text{-}SO_4$ dehydroxylated at 200 °C (13.38 OH nm^{-2}).

Reconstruction of the model using the hydroxyl numbers determined by NMR spectroscopy titrations allows for a rough measurement of the mean OH proximity (Figure 3.12 and Table 3.4).

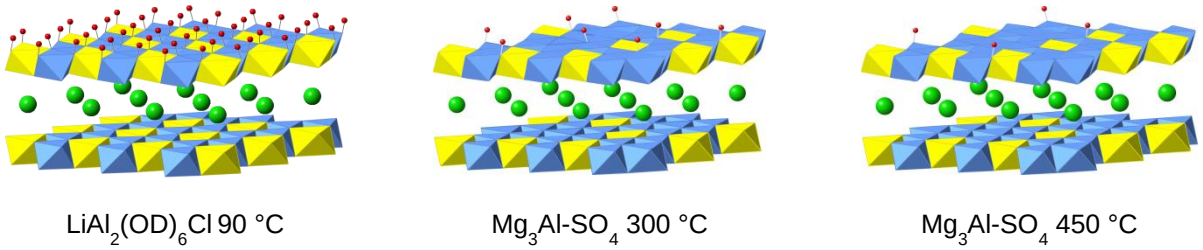


Figure 3.12. Surface hydroxyl concentration on $LiAl_2(OD)_6Cl$ (neutron diffraction) after treatment at 90 °C,[27] a schematic representation of $[Mg_{0.75}Al_{0.25}(OH)_2](SO_4)_{0.125}$ dehydroxylated at 300 and 450 °C based on the calculated hydroxyl concentration (α_{OH}).

Table 3.4. Surface hydroxyl proximity for the dehydroxylated samples.

LDH sample / dehydroxylation temperature	α_{OH} (OH nm^{-2})	OH proximity (Å)
$LiAl_2(OH)_6Cl$ / 90 °C[27]	13.32*	3
$Mg_3Al\text{-}SO_4$ / 300 °C	3.73	5–6
$Mg_3Al\text{-}SO_4$ /450 °C	2.14	8–10

* Determined from the calculated models.

As the temperature is increased, the hydroxyl groups become more dispersed reaching a distance of around 9 Å for samples treated at 450 °C. It should be noted that the pictorial representations of $Mg_3Al\text{-}SO_4$ especially at 450 °C are inaccurate as it has been shown that a layered structure no longer exists, hence a single mixed metal sheet would better describe the structure. The hydroxyl concentrations and proximities are at a level where these materials are viable candidates for use as supports for SOMC reactions.

3.5. Effect of dehydroxylation temperature on catalytic activity

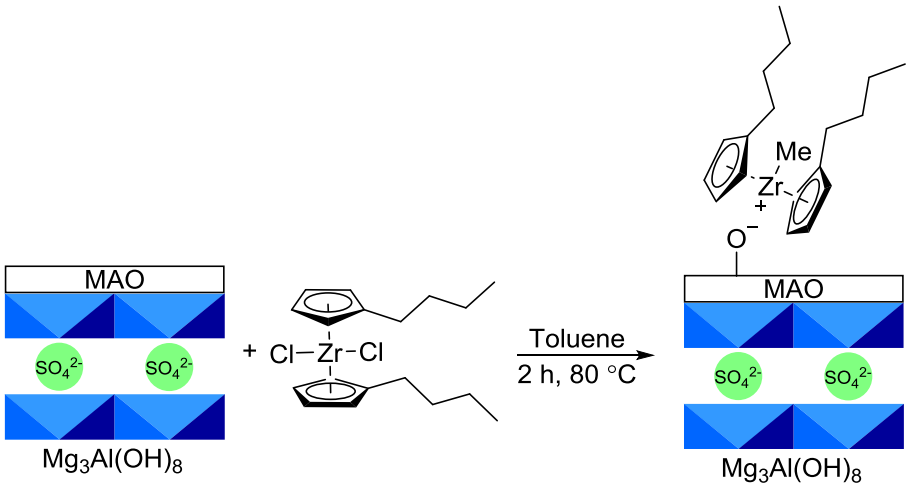
3.5.1. Introduction to supported metallocene catalysts

As described previously, layered double hydroxides have been utilised as supports for aluminium activators and olefin polymerisation catalysts.[5–9,28–30] Solid oxide supports are commonly impregnated with aluminium co-catalysts *e.g.* MAO, which bind to the surface hydroxyl groups, prior to grafting of a metallocene pre-catalyst.[10,31] Immobilisation of metallocene pre-catalysts is desirable as they are capable of producing polymers with narrow molecular weight distributions and uniform and tuneable microstructures.[10,32,33] By

controlling particle growth and morphology, reactor fouling can be avoided and high bulk densities can be achieved.[10]

3.5.2. Complex immobilisation on Mg_3Al-SO_4 AMO-LDH-MAO

In order to both activate and affix the metallocene pre-catalyst, the dehydroxylated AMO-LDH samples were first coated in MAO. Reaction in a 2:1 LDH:MAO ratio, based on the initial LDH structure, in toluene at 80 °C for 2 hours, yielded, after filtration and drying, an off-white solid in all cases. The isolated AMO-LDH-MAO compounds were reacted with $(^n\text{BuCp})_2ZrCl_2$ (Al/Zr = 200) in toluene at 80 °C for 2 hours (Scheme 3.3). Addition of the solvent to the Schlenk flask yielded an orange coloured solution. Swirling with heating led to a gradual paling of the solution which ultimately became clear and colourless, indicative of complete immobilisation of the metallocene precursor. The resulting powders after drying were pale yellow. The proposed active species grafted on the surface is a cationic $[(^n\text{BuCp})_2ZrMe]^+$ fragment, formed by methylation and halide abstraction of the precursor complex, which then forms an ionic interaction with the aluminoxane surface. Such a bonding scheme has previously been proposed for $(EBI)ZrCl_2$ immobilised on Mg_3Al-SO_4 AMO-LDH-MAO, and was corroborated by *in situ* EXAFS analysis.[6]



Scheme 3.3. Immobilisation of $(^n\text{BuCp})_2ZrCl_2$ on Mg_3Al-SO_4 AMO-LDH coated with MAO.

3.5.3. Slurry-phase ethylene polymerisation

Polymerisations were conducted in duplicate in hexane at 70 °C utilising triisobutylaluminium (TIBA) as a scavenger. The activities of polymerisation range between 983 and 1,660 $kg_{PE}mol_{Zr}^{-1}h^{-1}bar^{-1}$ (Figure 3.13). Similar activities are observed for the LDHs dehydroxylated at 150 and 350 °C with a decrease in activity observed at 250 and 450 °C. The

jump in activity between 250 and 350 °C is in the same range that loss of the layered LDH structure is seen to occur, along with a large increase in the surface area of the material. Increase in surface area means the active sites are better dispersed and can lead to higher activity.[34] Grieken *et al*. have reported the effect the calcination temperature of silica, silica-alumina and aluminophosphate, has on the activity of the supported (^{n}BuCp)$_2$ZrCl$_2$/MAO system, which was immobilised onto the calcined support using the incipient wetness method in toluene.[35] Results show a large decrease in activity with increasing calcination temperature for the silica-alumina system, especially when compared to the uncalcined material, attributed to the presence of Al^{3+} Lewis acidic sites. The silica system showed very little change in the activity over the temperature range, with a slight increase observed at 400 and 600 °C. Taoufik and co-workers employed a different approach by first immobilising MAO onto silica dehydroxylated over a range of temperatures (200, 450 and 600 °C) and characterising the different SiO_2/MAO materials. The resulting polymerisation activity after immobilisation of (^{n}BuCp)$_2$ZrCl$_2$ indicated that more active sites are produced at higher dehydroxylation temperatures, as higher activities were obtained.

Activities for the Mg_3Al-SO_4 AMO-LDH-MAO immobilised complex (1,660 $kg_{PE}mol_{Zr}^{-1}h^{-1}bar^{-1}$) are much higher than both those reported for dehydroxylated silica systems formed from either the incipient wetness method (300–400 $kg_{PE}mol_{Zr}^{-1}h^{-1}bar^{-1}$; [Zr] = 0.0015 mmol, heptane (200 mL), 1.2 bar ethylene, 70 °C, 30 minutes, TIBA scavenger Al/Zr = 800),[35] or immobilisation onto silica supported MAO (ssMAO) dehydroxylated at 600 °C (51 $kg_{PE}mol_{Zr}^{-1}h^{-1}bar^{-1}$; 30–40 mg cat., heptane (500 mL), 8 bar ethylene, 80 °C, 1 h, TIBA (1 mL, 1 M solution)).[36] This increased activity is attributed to the presence of Lewis acidic aluminium sites on the surface of the LDH.[37] Work by Basset and co-workers on supported zirconocene complexes, utilising silica, silica-alumina and alumina surfaces, have shown the importance of Lewis acids in activating supported metallocene catalysts towards ethylene polymerisation.[32] Silica supported systems showed no activity, whereas, for the oxides containing Lewis acidic sites, polymerisation activity was observed. This could be further enhanced by addition of co-catalysts, although the activities were still much lower than the homogeneous MAO activated systems. Addition of Lewis acidic $AlCl_3$ to homogeneous MAO activated (EBI)ZrCl$_2$ has also been observed to lead to an increase in the activity compared to the pure MAO activated system.[38]

Comparison of the activity with solid polymethylaluminoxane (sMAO) supported (^{n}BuCp)ZrCl$_2$ (Al/Zr = 200) under equivalent polymerisation conditions, emphasises the

activity enhancement of the sMAO bifunctional support and activator (1,660 *vs* 7,584 $kg_{PE}mol_{Zr}^{-1}h^{-1}bar^{-1}$),[39] however, there is a much larger cost associated with this support. (^{n}BuCp)$ZrCl_2$ has also been supported on Mg_3Al-CO_3 AMO-LDH-MAO which had been calcined at 150 °C.[5] Polymerisation at 60 and 80 °C showed marked activity differences (2,141 and 540 $kg_{PE}mol_{Zr}^{-1}h^{-1}bar^{-1}$ respectively), the polymerisations on Mg_3Al-SO_4 AMO-LDH-MAO at 70 °C fall within this window.

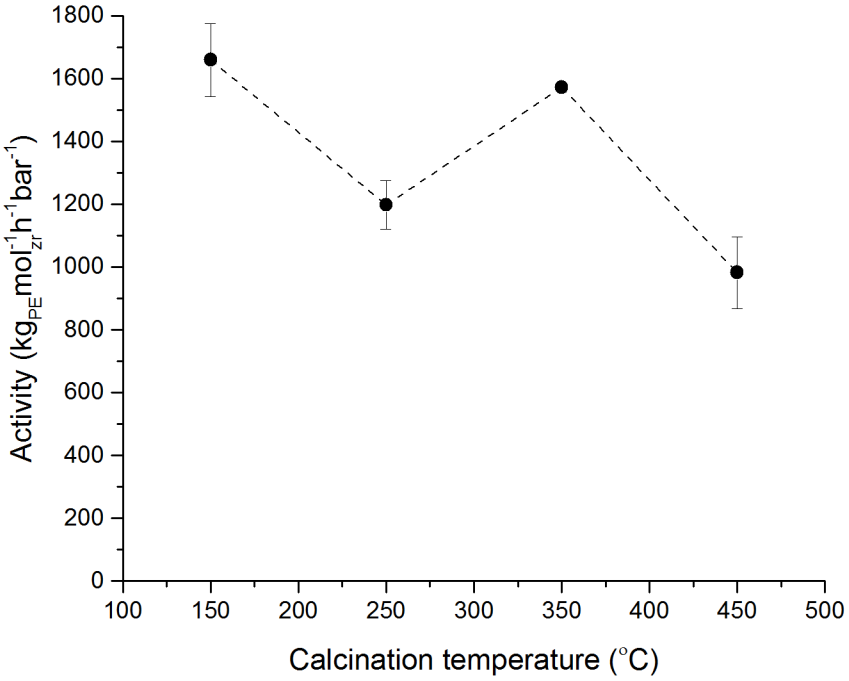


Figure 3.13. Ethylene polymerisation activity of the Mg_3Al-SO_4 AMO-LDH-MAO-(^{n}BuCp)$_2ZrCl_2$ catalysts where the AMO-LDH had been thermally treated at 150, 250, 350 and 450 °C under vacuum.

3.5.4. Polymer characterisation

Gel permeation chromatography showed formation of high density polyethylene (HDPE) in all cases (M_w = 341,400–419,000 $gmol^{-1}$) (Figure 3.14 and Table 3.5). The molecular weight distributions are very similar for all dehydroxylation temperatures, with uniform polydispersities (2.6) close to 2, the theoretical value for a single-site catalyst. The molecular weights are higher than the analogous SiO_2/MAO systems (122,100–207,783 $gmol^{-1}$), with much narrower PDI values than the incipient wetness silica system (3.27–3.89).[35,36] For the Mg_3Al-CO_3 AMO-LDH-MAO supported system, the temperature of the polymerisation was seen to have a large effect on the molecular weight and PDI of the resulting polymer (M_w = 744,533 and 128,531 $gmol^{-1}$, PDI = 3.40 and 2.85 at 60 and 80 °C respectively).[5] Such a decrease in molecular weight with increasing temperature is due to increased chain transfer rates at higher temperatures.[40] For polymerisations conducted at 70 °C with Mg_3Al-SO_4

AMO-LDH thermally treated under vacuum, the molecular weight of the polymer falls in the middle of this range, however, the dispersity of the polymer is much more uniform.

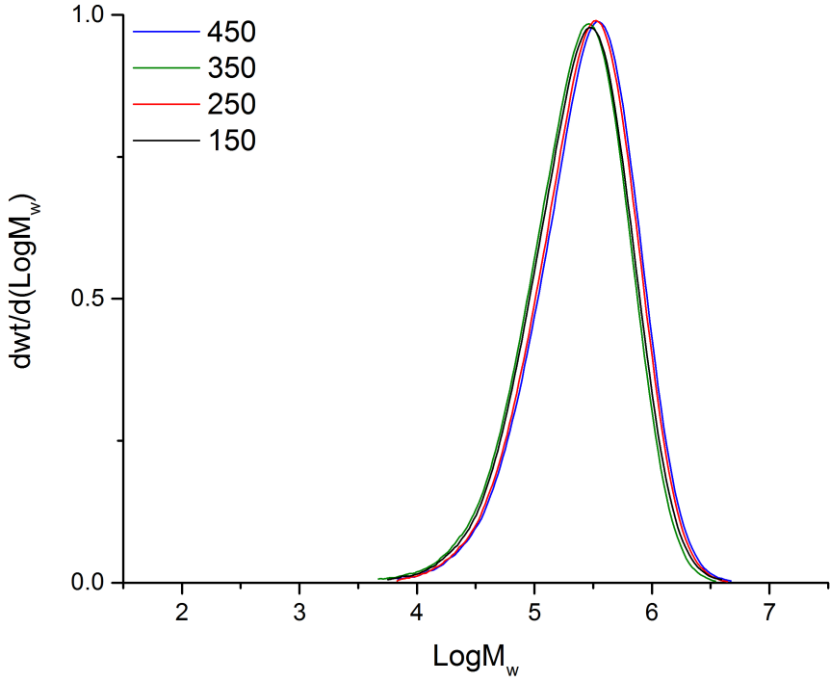


Figure 3.14. GPC data for polyethylene formed by Mg_3Al-SO_4 AMO-LDH-MAO-(^{n}BuCp)$_2$ZrCl$_2$ catalysts where the AMO-LDH had been thermally treated at 150, 250, 350 and 450 °C under vacuum.

Table 3.5. GPC data for polyethylene formed by Mg_3Al-SO_4 AMO-LDH-MAO-(^{n}BuCp)$_2$ZrCl$_2$ catalysts where the AMO-LDH had been thermally treated at 150, 250, 350 and 450 °C under vacuum, showing the weight-average molecular weight (M_w), number-average molecular weight (M_n) and polydispersity (M_w/M_n).

Dehydroxylation temperature (°C)	M_w **(gmol^{-1})**	M_n **(gmol^{-1})**	M_w **/** M_n
150	359,850	141,250	2.6
250	402,000	159,550	2.6
350	342,100	132,850	2.6
450	416,450	165,100	2.6

3.6. Conclusions

Mg_3Al-SO_4 AMO-LDH has been thermally treated under vacuum at a range of temperatures (150, 200, 250, 275, 300, 350, 400 and 450 °C). The thermal decomposition of this material mirrors analogous conventional $Mg_{2.32}Al$-SO_4 calcined in air, although significant decomposition events appear to occur at lower temperatures due to the application of vacuum. PXRD shows a complete disappearance of the layered structure at 300 °C, accompanied by a large increase in the surface area determined by BET. A large decrease in

the surface hydroxyl concentration was observed with increasing temperature, by a combination of NMR spectroscopic titrations and FTIR spectroscopy. Modelling the hydroxyl numbers for these materials based on the reported neutron structure for $LiAl_2(OD)_6Cl$, indicates the hydroxyl functionality is well dispersed (8–10 Å at 450 °C). The hydroxyl numbers are in the range where these materials can now be tested as supports utilising the SOMC methodology.

A preliminary investigation into the effect these dehydroxylated AMO-LDH materials have on the polymerisation activity of immobilised $(^{n}BuCp)_2ZrCl_2$ when coated with MAO was undertaken. Results showed an overall decrease in activity over the range 150–450 °C, although the increased surface area at 350 °C appeared influential. The resulting polymer was shown to be HDPE with the molecular weight not impacted by the dehydroxylation temperature. Polydispersities were reasonably low inferring the metallocene had maintained its single-site nature on the surface. The activities were seen to be higher than analogous SiO_2/MAO systems, warranting further study of this system.

3.7. References

1. J. Zhang, F. Zhang, L. Ren, D. G. Evans, and X. Duan, *Mater. Chem. Phys.*, 2004, **85**, 207–214.
2. Q. Wang, and D. O'Hare, *Chem. Comm.*, 2013, **49**, 6301–6303.
3. C. Chen, M. Yang, Q. Wang, J.-C. Buffet, and D. O'Hare, *J. Mater. Chem. A*, 2014, **2**, 15102–15110.
4. C. Chen, A. Wangriya, J.-C. Buffet, and D. O'Hare, *Dalton Trans.*, 2015, **44**, 16392–16398.
5. J.-C. Buffet, Z. R. Turner, R. T. Cooper, and D. O'Hare, *Polym. Chem.*, 2015, **6**, 2493–2503.
6. J.-C. Buffet, N. Wanna, T. A. Q. Arnold, E. K. Gibson, P. P. Wells, Q. Wang, J. Tantirungrotechai, and D. O'Hare, *Chem. Mater.*, 2015, **27**, 1495–1501.
7. J.-C. Buffet, T. A. Q. Arnold, Z. R. Turner, P. Angpanitcharoen, and D. O'Hare, *RSC Adv.*, 2015, **5**, 87456–87464.
8. D. A. X. Fraser, Z. R. Turner, J.-C. Buffet, and D. O'Hare, *Organometallics*, 2016, **35**, 2664–2674.
9. J.-C. Buffet, C. F. H. Byles, R. Felton, C. Chen, and D. O'Hare, *Chem. Commun.*, 2016, **52**, 4076–4079.
10. J. R. Severn, J. C. Chadwick, R. Duchateau, and N. Friederichs, *Chem. Rev.*, 2005, **105**, 4073–4147.
11. C. Copéret, A. Comas-Vives, M. P. Conley, D. P. Estes, A. Fedorov, V. Mougel, H. Nagae, F. Núñez-Zarur, and P. A. Zhizhko, *Chem. Rev.*, 2016, **116**, 323–421.
12. L. T. Zhuravlev, *Colloids Surf., A* , 2000, **173**, 1–38.
13. V. R. L. Constantino and T. J. Pinnavaia, *Inorg. Chem.*, 1995, **34**, 883–892.
14. M. J. Hudson, S. Carlino, and D. C. Apperley, *J. Mater. Chem.*, 1995, **5**, 323–329.
15. G. Yu, Y. Zhou, R. Yang, M. Wang, L. Shen, Y. Li, N. Xue, X. Guo, W. Ding, and L. Peng, *J. Phys. Chem. C*, 2015, **119**, 12325–12334.
16. S. Miyata, *Clays Clay Miner.*, 1977, **25**, 14–18.
17. F. Cavani, F. Trifirò, and A. Vaccari, *Catal. Today*, 1991, **11**, 173–301.
18. J. S. Valente, G. Rodriguez-Gattorno, M. Valle-Orta, and E. Torres-Garcia, *Mater. Chem. Phys.*, 2012, **133**, 621–629.

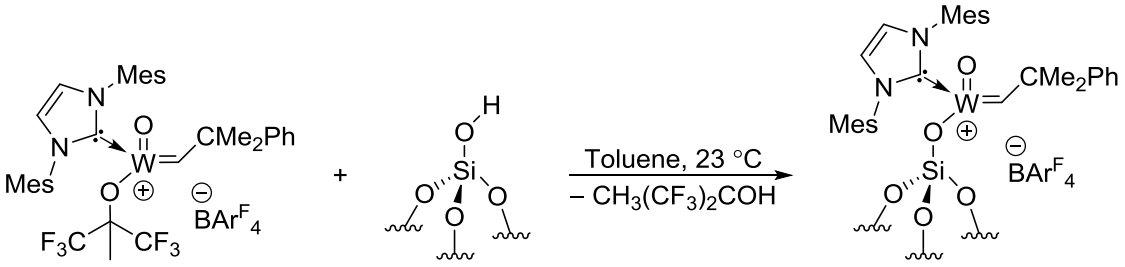
19. M. Gazzano, W. Kagunya, D. Matteuzzi, and A. Vaccari, *J. Phys. Chem. B*, 1997, **101**, 4514–4519.
20. N. N. Leont'eva, S. V. Cherepanova, and V. A. Drozdov, *J. Struct. Chem.*, 2014, **55**, 1326–1341.
21. M. Bellotto, B. Rebours, O. Clause, J. Lynch, D. Bazin, and E. Elkaïm, *J. Phys. Chem.*, 1996, **100**, 8535–8542.
22. M. Thommes, K. Kaneko, A. V Neimark, J. P. Olivier, F. Rodriguez-reinoso, J. Rouquerol, and K. S. W. Sing, *Pure Appl. Chem.*, 2015, **87**, 1051–1069.
23. Q. Wang, Y. Gao, J. Luo, Z. Zhong, A. Borgna, Z. Guo, and D. O'Hare, *RSC Adv.*, 2013, **3**, 3414–3420.
24. F. Rascón, R. Wischert, and C. Copéret, *Chem. Sci.*, 2011, **2**, 1449–1456.
25. P. J. Bailey, R. A. Coxall, C. M. Dick, S. Fabre, L. C. Henderson, C. Herber, S. T. Liddle, D. Loroño-González, A. Parkin, and S. Parsons, *Chem. Eur. J.*, 2003, **9**, 4820–4828.
26. W. Yang, Y. Kim, P. K. T. Liu, M. Sahimi, and T. T. Tsotsis, *Chem. Eng. Sci.*, 2002, **57**, 2945–2953.
27. A. V Besserguenev, A. M. Fogg, R. J. Francis, S. J. Price, D. O'Hare, V. P. Isupov, and B. P. Tolochko, *Chem. Mater.*, 1997, **9**, 241–247.
28. H. Frielingsdorf, H. Mueller-Tamm, G. Schweier, and L. Reuter, *Inorganic Carriers for Ziegler catalysts and the use thereof in the manufacture of olefin polymers*, 1975, GB1380949.
29. D. O'Hare, *Catalyst systems for polymerization of olefins comprising layered double hydroxide catalyst support*, 2014, WO2014051529 A2.
30. F.-A. He and L.-M. Zhang, *J. Colloid Interface Sci.*, 2007, **315**, 439–444.
31. G. G. Hlatky, *Chem. Rev.*, 2000, **100**, 1347–1376.
32. M. Jezequel, V. Dufaud, M. J. Ruiz-Garcia, F. Carrillo-Hermosilla, U. Neugebauer, G. P. Niccolai, F. Lefebvre, F. Bayard, J. Corker, S. Fiddy, J. Evans, J.-P. Broyer, J. Malinge, and J.-M. Basset, *J. Am. Chem. Soc.*, 2001, **123**, 3520–3540.
33. D. Harrison, I. M. Coulter, S. Wang, S. Nistala, B. A. Kuntz, M. Pigeon, J. Tian, and S. Collins, *J. Mol. Catal. A Chem.*, 1998, **128**, 65–77.
34. K. T. Li, C. L. Dai, and C. W. Kuo, *Catal. Commun.*, 2007, **8**, 1209–1213.
35. R. Van Grieken, A. Carrero, I. Suarez, and B. Paredes, *Eur. Polym. J.*, 2007, **43**, 1267–1277.
36. M. A. Bashir, T. Vancompernolle, R. M. Gauvin, L. Delevoye, N. Merle, V. Monteil, M. Taoufik, T. F. L. McKenna, and C. Boisson, *Catal. Sci. Technol.*, 2016, **6**, 2962–2974.
37. L. Wang, F. Wang, and L. Xu, *Indian J. Chem. A*, 2015, **54A**, 607–612.
38. P. G. Belelli, M. L. Ferreira, and D. E. Damiani, *Macromol. Chem. Phys.*, 2000, **201**, 1458–1465.
39. A. F. R. Kilpatrick, J.-C. Buffet, P. Nørby, N. H. Rees, N. P. Funnell, S. Sripothongnak, and D. O'Hare, *Chem. Mater.*, 2016, **28**, 7444–7450.
40. M. Eskelinen and J. V. Seppälä, *Eur. Polym. J.*, 1996, **32**, 331–335.

Chapter Four – Characterisation and reactivity of solid catalysts

"God made the bulk; surfaces were invented by the devil." **Wolfgang Pauli**

4.1. Introduction

Having synthesised and characterised defined tungsten mono-imido catalysts active for the selective dimerisation of ethylene in Chapter Two, focus turned to the immobilisation of these species on solid supports. Such an approach would allow for slurry-phase or flow conditions to be employed, which are preferred industrially as product separation is simplified. By employing the surface organometallic chemistry (SOMC) procedure[1,2] described in Chapter One, a direct comparison of the activity for the discrete complex with the supported species can be made, as the active site is preserved. For example, Buchmeiser and co-workers have developed highly active and functional group tolerant homogeneous cationic tungsten oxo alkylidene N-heterocyclic carbene olefin metathesis catalysts.[3] Immobilisation of these complexes on the isolated surface silanols of $SiO_{2-(700)}$ (Scheme 4.1), yielded complexes that displayed extremely high turnover numbers (TONs) of over 1 million for the self-metathesis of propylene.[4] The dissymmetry of the supported species is the proposed reason for the higher activities observed for these supported metathesis catalysts compared to their homogeneous counterparts, with site isolation leading to high stability. Such increased activity, functional group tolerance and stability over current ill-defined industrial catalysts, means these immobilised species are becoming attractive for use in scale-up processes, despite their higher associated cost (£/g).



Scheme 4.1. SOMC grafting of a cationic tungsten oxo alkylidene N-heterocyclic carbene complex on the isolated silanols of $SiO_{2-(700)}$, with retention of the active alkylidene fragment after immobilisation.[4]

Beneficially, supports that activate complexes *in situ* upon their surface can also be utilised *e.g.* MAO impregnated silicas for metallocene ethylene polymerisation catalysis.[5,6] Such procedures decrease the number of synthetic steps and facilitate a reduction in the equivalents of co-catalyst required, thus reducing the cost of the final system. Despite this, there are only a few examples of defined ethylene oligomerisation catalysts immobilised on solid supports (Chapter One).

This chapter focuses on immobilising the well-defined complexes synthesised in Chapter Two onto solid polymethylaluminoxane (sMAO), layered double hydroxides (LDHs) and silica. Grafting will be attempted utilising the principles of SOMC, and characterisation of the immobilised complexes performed (SSNMR, FTIR, XAS). The solid catalysts are tested for their reactivity towards linear alpha olefins and compared to the molecular precursors. For the sMAO supported complexes, the effect of varying the imido substituent, temperature, solvent medium and loading will be investigated. For AMO-LDHs, particular attention will be paid to the effect of varying the interlayer anion and the effect of dehydroxylating the surface utilising the treated Mg_3Al-SO_4 AMO-LDH materials described in Chapter Three.

4.2. Solid polymethylaluminoxane (sMAO) immobilised complexes

4.2.1. Immobilisation and characterisation

In Chapter Two methylaluminoxane (MAO) was shown to methylate and activate $W(NR)Cl_4(THF)$ complexes (**1.1**–**1.8**) in solution to yield $W(NR)Me_3Cl$ complexes that could dimerise ethylene. It was proposed that immobilising $W(NR)Cl_4(THF)$ complexes on solid polymethylaluminoxane (sMAO)[7,8] would lead to similar *in situ* activation during immobilisation on the solid surface, as has been suggested for sMAO supported metallocenes.[9] Crystalline samples of **1.1**–**1.8** were supported on sMAO (Al/W = 150), utilising the concept of surface organometallic chemistry (SOMC).[1,2] This was achieved by intermittent swirling of a slurry of the complex and sMAO in toluene at room temperature for 1 hour. Immobilisation was observed by decolouring of the solution and colouring of the support. A final clear and colourless solution was indicative of complete immobilisation of the complex. Filtration followed by drying *in vacuo*, in all cases, yielded pale coloured powders in quantitative yield (example shown in Figure 4.1).

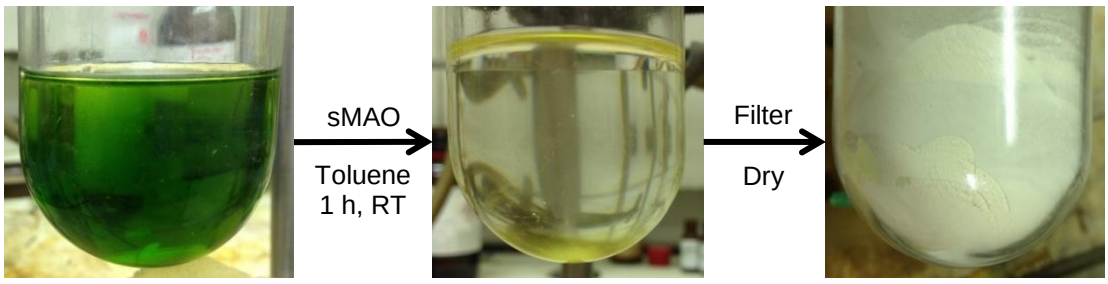


Figure 4.1. Immobilisation of **1.5** on sMAO to yield sMAO-**1.5** as a pale yellow solid.

Reaction between $W\{N(3,5\text{-}Me\text{-}C_6H_3)\}Cl_4(THF)$ (**1.3**) and sMAO (10 mg, Al/W = 150) in d_6-benzene resulted in complete decolourisation of the yellow solution and colouring of the

white powder, yielding a yellow solid. Analysis of the solution by ^{1}H NMR spectroscopy showed the complete disappearance of any resonances attributed to the imido complex, with a small amount of methane observed (0.16 ppm). The partial solubility of sMAO in d_8-THF, has allowed for its residual TMA content to be determined.[8] A ^{1}H NMR spectrum of sMAO-W{N(2,6-^{i}Pr-C_6H_3)}Cl_4(THF) (sMAO-**1.5**) in d_8-THF was measured, to see if the immobilised species could also be observed (Figure 4.2).

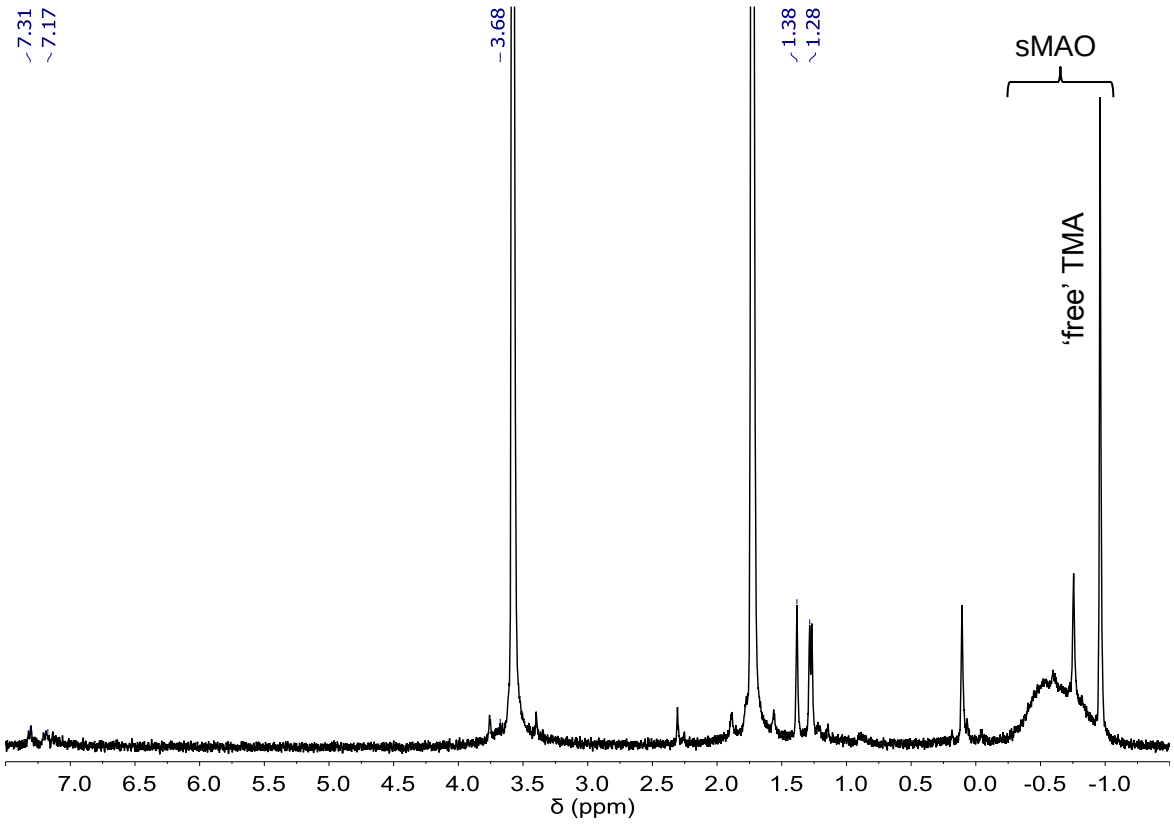
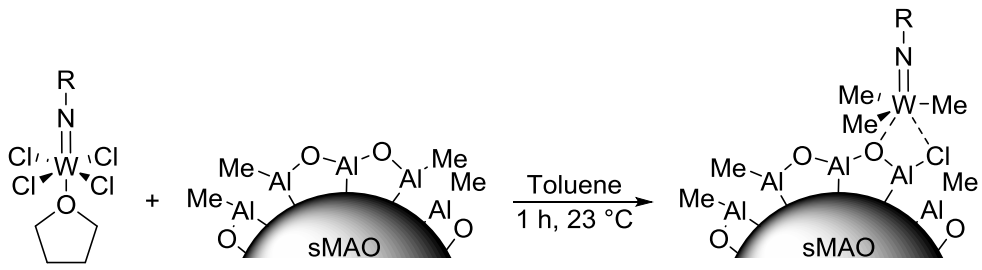


Figure 4.2. ^{1}H NMR spectrum (400 MHz, 23 °C) in d_8-THF (3.58 and 1.72 ppm) of solid polymethylaluminoxane (sMAO) supported W{N(2,6-^{i}Pr-C_6H_3)}Cl_4(THF) (sMAO-**1.5**) indicating leaching of the complex W{N(2,6-^{i}Pr-C_6H_3)}Me_3Cl (**2.5**) which is proposed to form *in situ* on the surface.

The methyl region of the spectrum showed the appearance of resonances corresponding to the W–Me and ^{i}Pr protons for the free methylated complex W{N(2,6-^{i}Pr-C_6H_3)}Me_3Cl (**2.5**), indicating that some leaching had occurred. This provides evidence that sMAO does methylate the starting complex *in situ*. No such leaching is observed in non-coordinating solvents, suggesting that the polar THF solvent may disrupt the proposed ionic interaction between the complex and the aluminoxane surface. Ghiotto *et al*. have also reported that addition of THF to MAO solutions leads to dissociation of $[AlMe_2(THF)_2]^{+}$ cations, observed by ^{1}H NMR spectroscopy.[10] The resonance for such species is seen to shift between −0.3 and

−0.7 ppm dependent on the concentration of THF. The resonance at −0.76 ppm for sMAO-**1.5** is proposed to result from similar cation formation, as this resonance has shifted from −0.60 ppm for the 'bound' TMA in the initial sMAO structure.[8] It is therefore concluded that during immobilisation, methylation occurs on the surface, exchanging proximal aluminium-methyl groups for chloride, and rendering a $[W(NR)Me_3]^+$ fragment bound to the surface (Scheme 4.2).



Scheme 4.2. SOMC[2] grafting procedure for arlyimido complexes on sMAO.

To further probe the structure of the supported complexes, solid-state NMR (SSNMR) and FTIR spectroscopy were utilised. The ^{13}C-{^1H} CPMAS NMR spectrum of sMAO-**1.5** displays a major resonance centred at 0 ppm, corresponding to the bulk aluminium-methyl groups present in sMAO (Figure 4.3). Weaker resonances around 130 and 170 ppm result from benzoate groups which are incorporated in the structure of sMAO (synthesised by reaction of TMA with benzoic acid).[8] These resonances are present in all of the ^{13}C-{^1H} CPMAS SSNMR spectra of the sMAO immobilised complexes characterised by SSNMR and thus are inferred for all spectra. Two weak resonances in the alkyl region (15–25 ppm) appear to show the preservation of the isopropyl groups from the diisopropylphenyl moiety on the surface. Two resonances observed at 18 and 68 ppm are proposed to be coordinated THF molecules originating from the starting complex. A broad resonance at 46 ppm is postulated to derive from the tungsten methyl groups that have formed *in situ* on the surface. By comparison, the solution-state $^{13}C\{^1H\}$ NMR W–Me resonance for **2.5** in d_6-benzene occurs at 56.5 ppm. For sMAO-**1.5**, the aromatic benzoate resonances from the support, and weak signal to noise, prevent identification of the resonances corresponding to the aromatic carbons of the imido group.

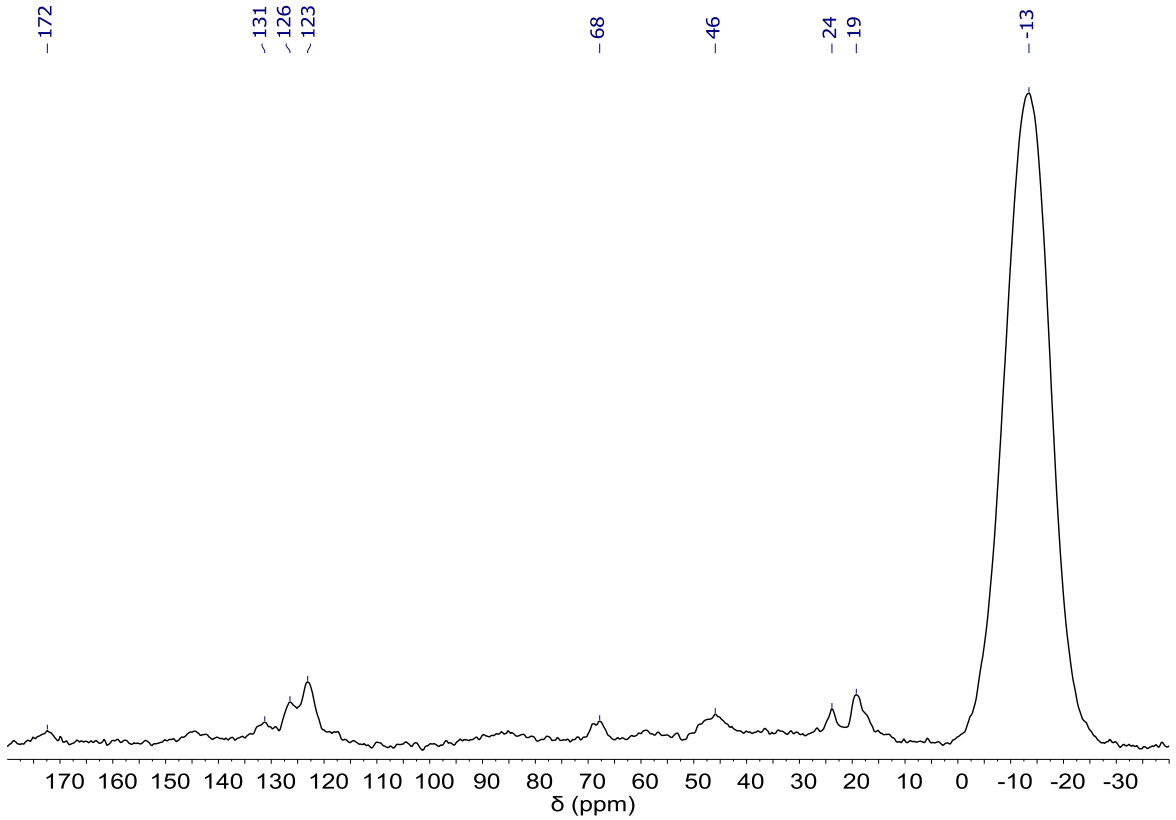


Figure 4.3. ^{13}C-{^{1}H} CPMAS SSNMR spectrum (10 kHz, 400 MHz, 23 °C) of solid polymethylaluminoxane supported W{N(2,6-^{i}Pr-C_6H_3)}Cl_4(THF) (sMAO-**1.5**).

Much more diagnostic are the ^{19}F{^{1}H} HPDEC SSNMR spectra for sMAO-W{N(2,6-F-C_6H_3)}Cl_4(THF) (sMAO-**1.7**) and sMAO-W{N(3,5-CF_3-C_6H_3)}Cl_4(THF) (sMAO-**1.8**), as the observed signals can only arise from fluorine atoms present in the precursor complexes. The solid-state ^{19}F{^{1}H} HPDEC NMR spectrum (Figure 4.4) of sMAO-**1.7** indicates homogeneity in the surface supported species with only one resonance observed (−123 ppm). This is shifted to lower frequency with respect to both W{N(2,6-F-C_6H_3)}Cl_4(THF) (**1.7**) and W{N(2,6-F-C_6H_3)}Me_3Cl (**2.7**) (−111.0 and −117.6 ppm respectively) but closer to that of the methylated complex resonance, further supporting surface methylation of the compound. Again, two resonances are observed in the ^{13}C-{^{1}H} CPMAS {^{19}F} decoupled SSNMR spectrum at 67 and 18 ppm and are attributed to bound THF (Figure A121). The solution-state ^{13}C{^{1}H} NMR W–Me resonance for **2.7** is observed at 54.4 ppm in solution, however, no clear resonance could be observed in this region from the ^{13}C-{^{1}H} CPMAS {^{19}F} decoupled SSNMR spectrum of sMAO-**1.7**.

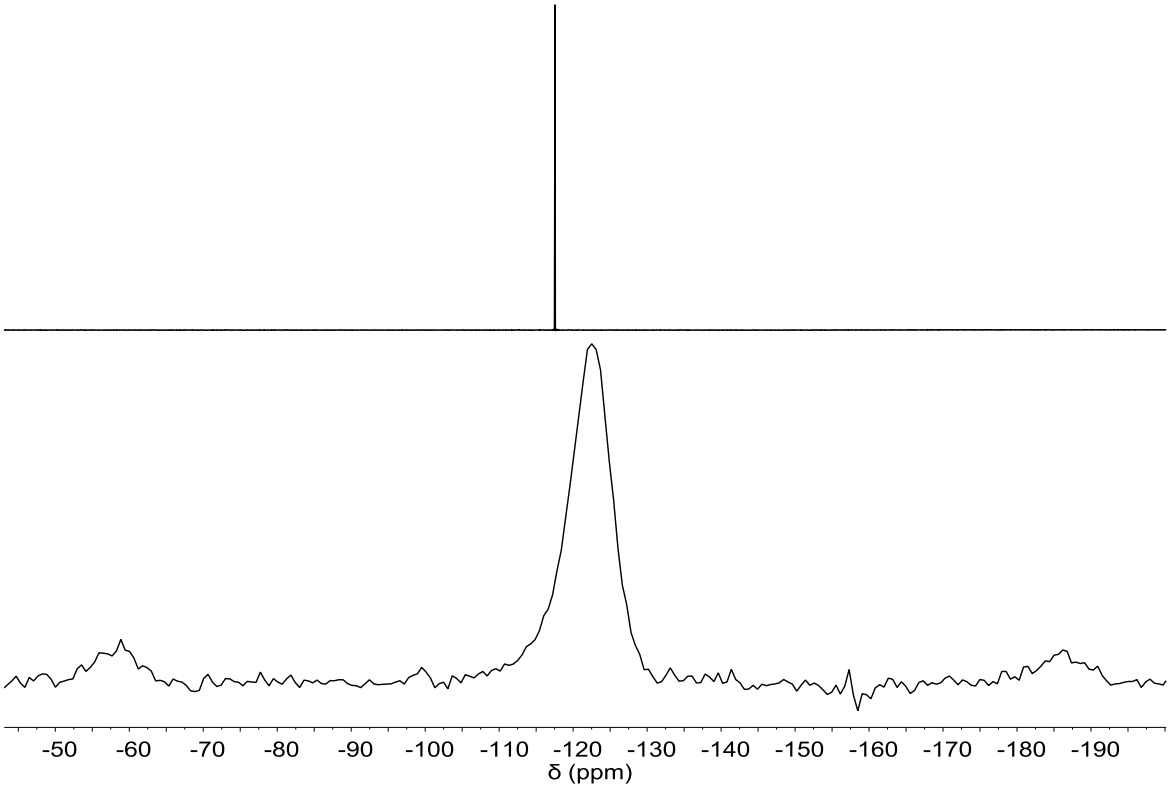


Figure 4.4. Solution-state $^{19}F\{^{1}H\}$ NMR spectrum (400 MHz, 23 °C) of **2.7** (top) and $^{19}F\{^{1}H\}$ HPDEC SSNMR spectrum (24 kHz, 400 MHz, 23 °C) of sMAO-**1.7** (bottom).

The molecular complex **2.7** was also studied by SSNMR spectroscopy. The $^{19}F\{^{1}H\}$ HPDEC SSNMR spectrum showed a resonance centred at −116 ppm accompanied by spinning side bands (Figure A123). The ^{13}C-$\{^{1}H\}$ CPMAS $\{^{19}F\}$ decoupled SSNMR spectrum displays 4 resonances for the imido carbons at 162, 161, 129 and 110 ppm (Figure 4.5). Analysis of the ^{13}C-$\{^{19}F\}$ CPMAS $\{^{1}H\}$ decoupled spectrum shows an enhancement in all of the signals, from the polarisation transfer (Figure A124). A slightly larger increase in the resonance at 162 ppm compared to the resonance at 161 ppm leads to assignment as the $Ar_{ortho}F$ and $Ar_{ipso}N$ carbons respectively, matching observations from the solution NMR data. There are two resonances for the W–Me groups at 59 and 55 ppm in keeping with the molecular structure (Chapter Two), in which one methyl group sits in the symmetry plane of the imido ligand. The fluxional behaviour in solution renders these groups equivalent, hence a singlet is observed.

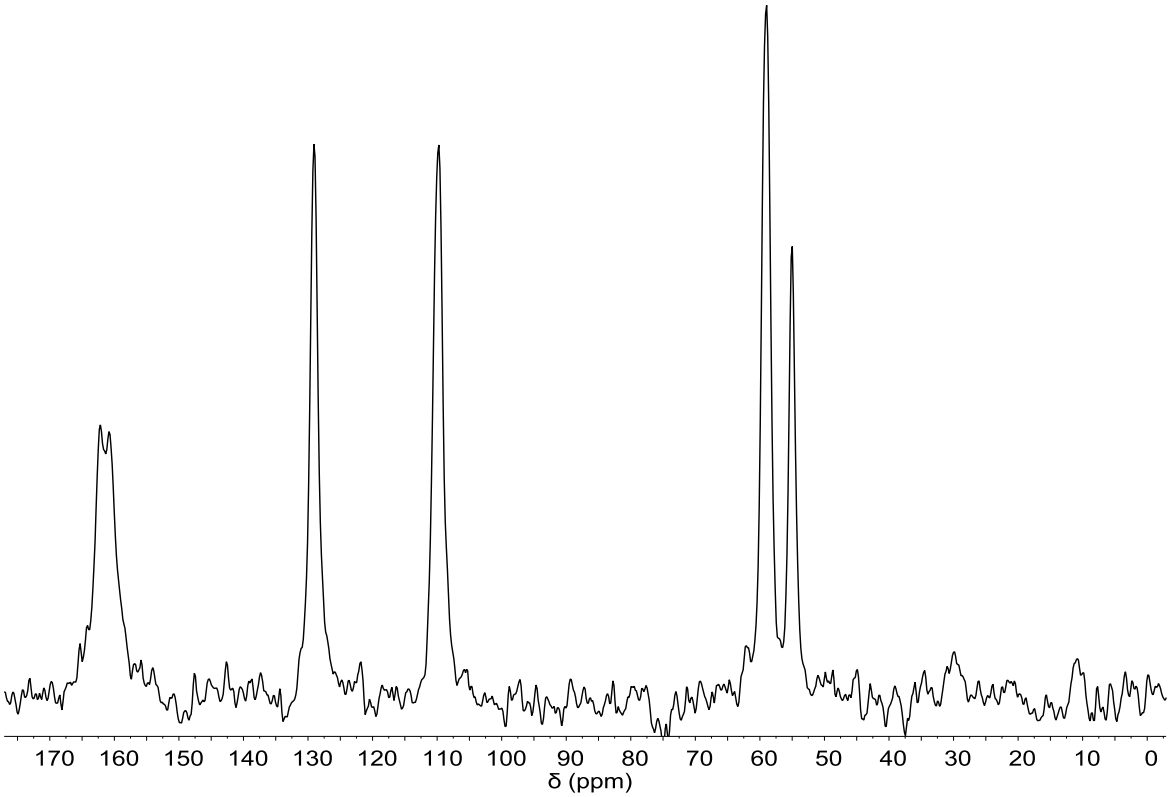


Figure 4.5. ^{13}C-{^{1}H} CPMAS {^{19}F} decoupled SSNMR spectrum (10 kHz, 400 MHz, 23 °C) of **2.7**.

To gain further insight into the nature of the supported species, W{N(2,6-F-C_6H_3)}($^{13}CH_3$)$_3$Cl (**2.7***) was synthesised, utilising ^{13}C-enriched TMA as the methylating reagent. The complex was then reacted with sMAO and the resulting pale yellow solid studied by SSNMR spectroscopy. The ^{13}C-{^{1}H} CPMAS {^{19}F} decoupled SSNMR spectrum, displays two discernible resonances, a weaker resonance at 56 ppm and a more intense resonance at 45 ppm (Figure 4.6), the latter matching almost exactly with **2.7***. It is proposed that these two bands result from two methyl environments in the immobilised complex due to the absence of fluxionality in the solid-state as is observed for **2.7** (Figure 4.5). However, the intensities of these two resonances are reversed when compared to **2.7**, which may be due to interactions with the sMAO support. Neither of these signals is as intense as may have been anticipated for a labelled complex, which may be due to methyl exchange with the surface. The difference in frequency observed between the W–Me resonances for sMAO-**2.7*** and that of sMAO-**1.7**, may be due to the difference in the number of chloride ions that can be exchanged with the surface (1 and 4 respectively). The close proximity of the halide groups, which may interact with the complex on the surface, would render the metal centre more electron deficient and hence deshield the methyl groups.

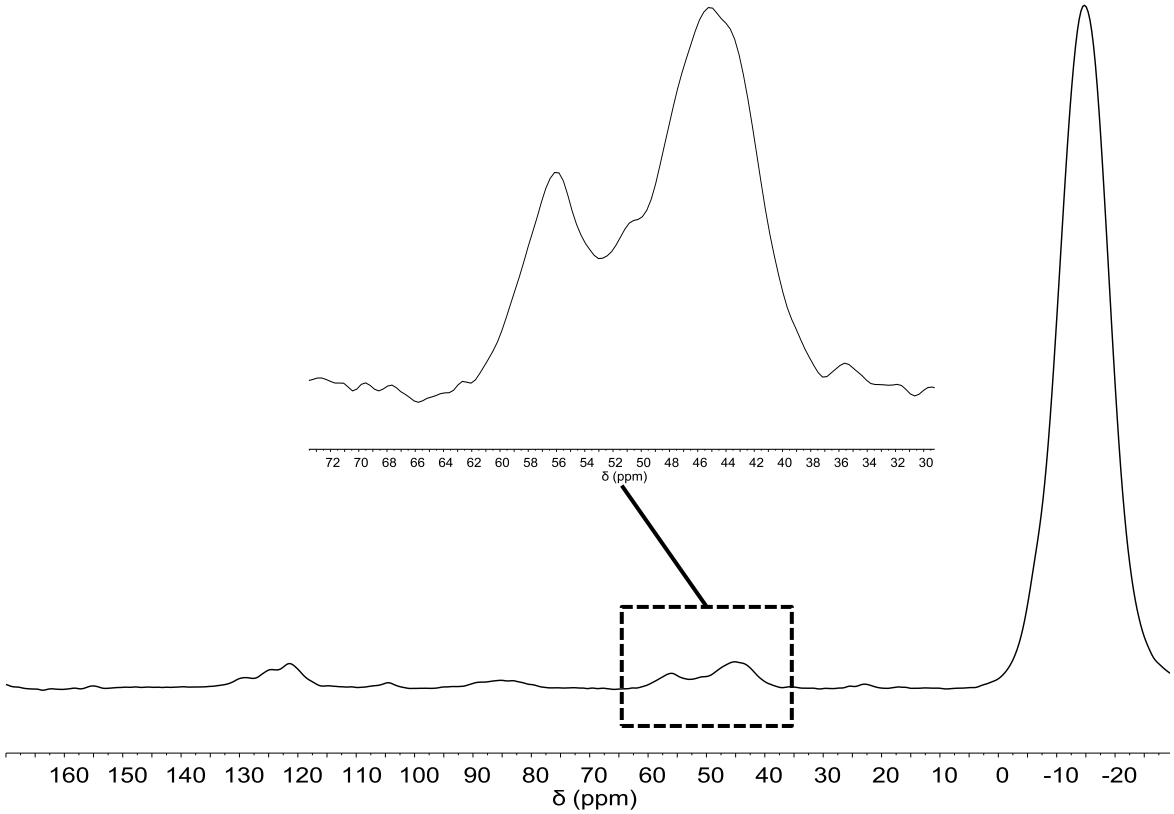


Figure 4.6. ^{13}C-{^{1}H} CPMAS {^{19}F} decoupled SSNMR spectrum (10 kHz, 400 MHz, 23 °C) of sMAO-**2.7***. Resonances between 38 and 62 ppm are attributed to W(^{13}**C**H$_3$) groups of the supported complex.

The ^{19}F{^{1}H} HPDEC solid-state NMR spectrum of sMAO-**2.7*** (Figure 4.7) displays a single fluorine environment centred at −123.4 ppm, which is similar to that observed for sMAO-**1.7** (−122.5 ppm), and shifted upfield from that observed in the SSNMR spectrum of the molecular complex **2.7** (−116.3 ppm).

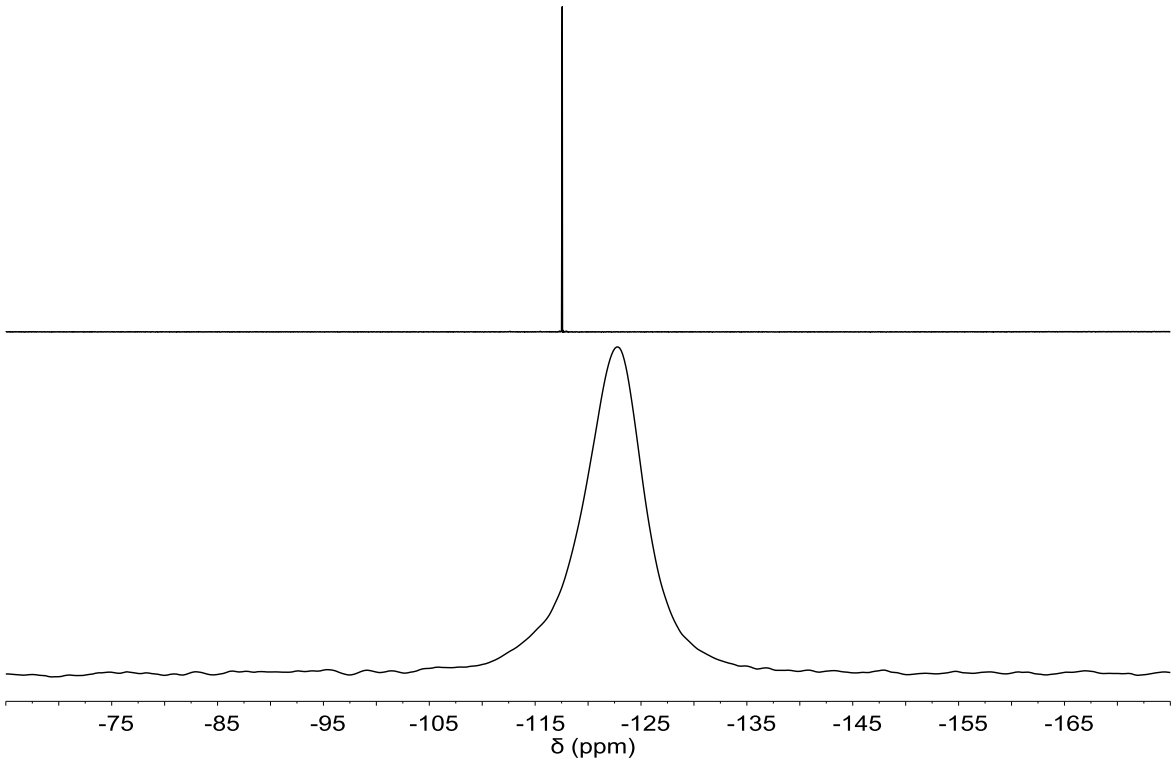
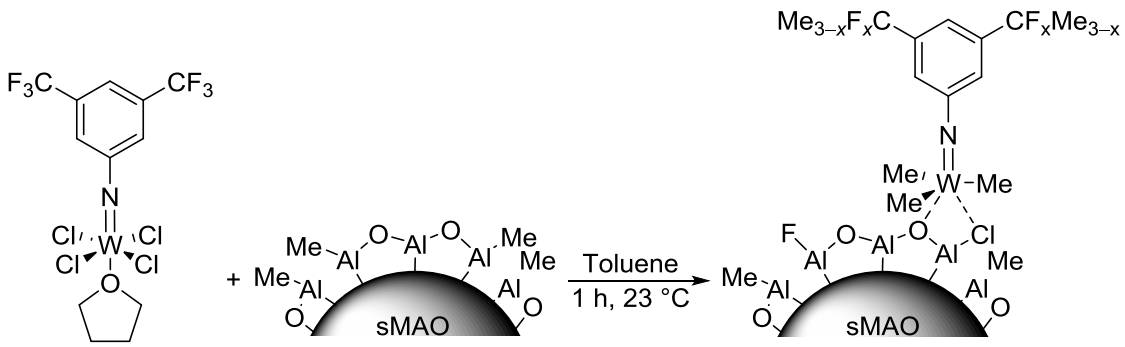


Figure 4.7. Solution-state $^{19}F\{^{1}H\}$ NMR spectrum (400 MHz, 23 °C) of **2.7*** (top) and solid-state $^{19}F\{^{1}H\}$ HPDEC NMR spectrum (24 kHz, 400 MHz, 23 °C) of sMAO-**2.7*** (bottom).

The $^{19}F\{^{1}H\}$ HPDEC NMR spectrum of sMAO-**1.8** (Figure 4.8),[11] shows the presence of two fluorine environments at −69.3 and −141.9 ppm with the former assigned to the surface-supported complex. The high upfield shift of the latter resonance infers that C–F activation may have occurred, with transfer of the fluoride onto the aluminoxane surface (Scheme 4.3).



Scheme 4.3. Proposed species formed from the reaction of **1.8** and sMAO, with exchange of fluorine atoms from the CF_3 groups with surface methyl groups bound to aluminium.

Work by Grey and co-workers, fluorinating the surface of alumina, has demonstrated that the surface Al–F species display ^{19}F MAS NMR resonances between −110 and −165 ppm.[12]

Terao *et al*. described how the C–F bonds of various benzotrifluorides could be converted to C–Me bonds utilising an excess of $AlMe_3$.[13,14] Despite the large excess of sMAO, the fact that the complex is immobilised may be why complete defluorination is not observed.

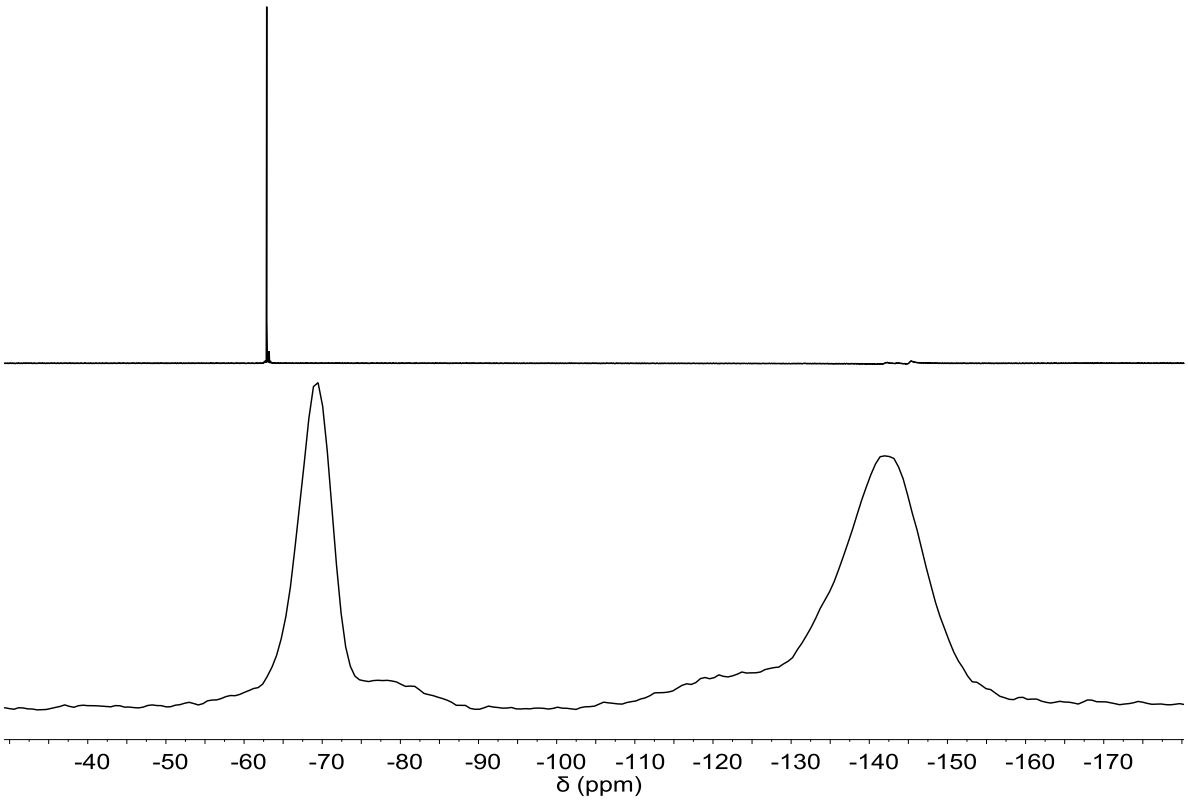


Figure 4.8. Solution-state $^{19}F\{^1H\}$ NMR spectrum (400 MHz, 23 °C) of **1.8** (top) and solid-state $^{19}F\{^1H\}$ HPDEC NMR spectrum (24 kHz, 400 MHz, 23 °C) of sMAO-**1.8** (bottom).

In all of the above cases the ^{27}Al DPMAS or Hahn echo SSNMR spectra (Appendix) displayed a broad set of resonances between 500 and −500 ppm, characteristic of the sMAO support.[8] Such broad resonances due to the quadropolar aluminium nuclei make drawing any firm conclusions about the surface aluminium species very difficult. FTIR spectra of the supported catalysts (Figures A127–A135) were compared with the molecular complexes. Due to the low loading and generally weak absorptions of the complexes, the spectra for the supported species are dominated by absorptions from the sMAO support. For these supported species, an increase in intensity for the broad band between 500 and 900 cm^{-1} compared to the sMAO precursor, was observed in all cases.

4.2.2. Heterogeneous olefin oligomerisation studies

4.2.2.1. Effect of methylating the precursor complex

Having established that treatment of **1.5** with sMAO leads to *in situ* methylation and thus proposed active species on the surface, comparison of the activity of sMAO immobilised **1.5** and **2.5** towards ethylene was pursued. If similar reactivity could be observed by simple activation of the $W(NR)Cl_4(THF)$ complexes on the surface, this would save an extra preparative step, reducing catalyst cost. Complex **2.5** was grafted on sMAO in a similar fashion to **1.5** (Al/W = 150), yielding a pale yellow solid after work-up. An analogous oligomerisation procedure to that described in Chapter Two was carried out, employing pyridine as the internal NMR spectroscopic standard (5 mg cat., 0.4 μmol$_W$, d_6-benzene, 1 bar ethylene, 100 °C). sMAO-**1.5** was found to be significantly more active than the homogeneous complex **2.5** in conjunction with MAO (Al/W = 2) (Chapter 2), exhibiting a greater than seven fold increase in activity (5.2 *vs* 0.7 $mol_{C_2H_4}mol_W^{-1}h^{-1}bar^{-1}$). Such increases in activity for supported compared to homogeneous catalysts are rare, however, activities are still far below those reported for homogeneous group 6 ethylene dimerisation systems (15–1,000 times) (Table 2.5).[15–18] Employing sMAO-**2.5** in the dimerisation reaction, led to an increase in activity (7.2 $mol_{C_2H_4}mol_W^{-1}h^{-1}bar^{-1}$), however, leaching of the complex (**2.5**) into the solution was observed both visually and by ^{1}H NMR spectroscopy. Heating samples of sMAO-**1.5** and sMAO-**2.5** at 100 °C in d_6-benzene containing pyridine (9.93 μmol) again resulted in the latter leaching into solution. This leaching is attributed to the disruption of the ionic bonding to the surface by the polar pyridine, as previously described for d_8-THF. The increased stability of sMAO-**1.5** (no leaching observed), is attributed to the greater number of chloride ions that are exchanged with the surface upon grafting. This is proposed to result in more W–Cl–Al interactions on the surface for **1.5** *vs* **2.5** (Scheme 4.2). As described in Chapter 2, such interactions were observed when **2.5** was reacted with $AlCl_3$. Similar reactivity has also been observed between $AlCl_3$ and $W(NR)(CH_2{}^tBu)_3Cl$ complexes.[19] The importance of such M–Cl–Al interactions has also been demonstrated for related chromium ethylene oligomerisation catalysts.[20–22] For example, Vidyaratne *et al*. reported the formation of the dimeric chromium complex $[\{\eta^5\text{-}2,3,4,5\text{-}Me_4C_4N(AlClMe_2)Cr\}_2(\mu\text{-}Me)_2]$ from tetramethylpyrrole, TMA and $CrCl_3(THF)_3$ in toluene (Figure 4.9).

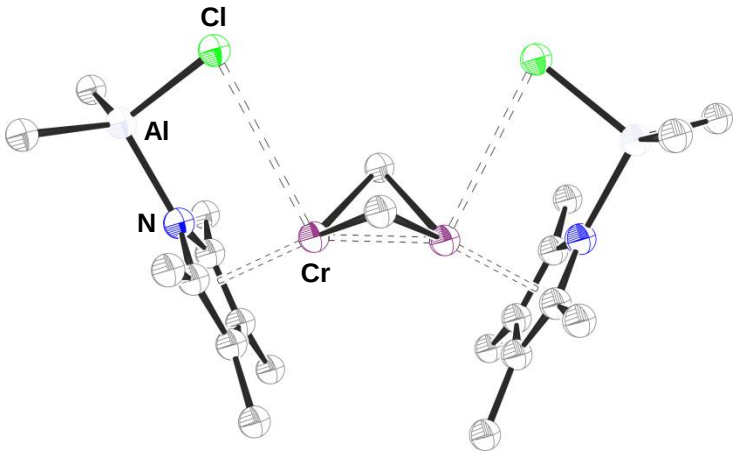


Figure 4.9. Molecular structure of $[\{\eta^5\text{-}2,3,4,5\text{-}Me_4C_4N(AlClMe_2)Cr\}_2(\mu\text{-}Me)_2]$.[22] Hydrogens omitted for clarity, atoms depicted as isotropic ellipsoids.

The complex has an Al–Cl–Cr contact at each chromium centre (3.489(8) and 3.675(8) Å) and is active for the trimerisation of ethylene in methylcyclohexane (667 $mol_{C_2H_4}mol_{Cr}^{-1}h^{-1}bar^{-1}$, 95% selectivity towards 1-hexene). Addition of $AlMe_2Cl$ (4 eq.) results in an almost two-fold increase in activity, whilst TMA was seen to have a poisoning effect.

For the supported $W(NR)Cl_4(THF)$ complexes, variation of the imido fragment also had an effect on the catalyst stability. $W\{N(2,4,6\text{-}Me\text{-}C_6H_2)\}Me_3Cl$ (**2.4**) was observed to leach from sMAO-$W\{N(2,4,6\text{-}Me\text{-}C_6H_2)\}Cl_4(THF)$ (sMAO-**1.4**) into solution under similar oligomerisation conditions (5 mg cat., 0.4 μmol_W, d_6-benzene, 1 bar ethylene, 100 °C). Switching the internal standard from pyridine to the less polar, non-coordinating mesitylene, prevented leaching of both sMAO-**2.5** or sMAO-**1.4**. Activities for sMAO-**1.4** were lower than when pyridine was utilised (3.1 *vs* 5.2 $mol_{C_2H_4}mol_W^{-1}h^{-1}bar^{-1}$) and sMAO-**2.5** was seen to only form polyethylene (~5 mg) after 2 hours. Despite this, mesitylene was chosen as the internal standard for subsequent slurry-phase oligomerisations, as it allowed for comparison of truly heterogeneous catalysts.

As coordinating solvent were seen to affect the activity and stability of the solid catalysts, comparison of the activity of sMAO-**1.5** with the unsolvated analogue sMAO-$W\{N(2,6\text{-}^i Pr\text{-}C_6H_3)\}Cl_4$ was studied to see if THF from the starting complex, which was observed in the SSNMR spectra of the solids, influences the reactivity. Assessment of the activity of the two catalysts after 8 hours under analogous conditions (5 mg cat., Al/W = 150, 100 °C, 1 bar ethylene, d_6-benzene, mesitylene internal standard), showed sMAO-**1.5** to be the more active and selective catalyst (3.3 *vs* 2.2 $mol_{C_2H_4}mol_W^{-1}h^{-1}bar^{-1}$, 79 *vs* 70% for

1-butene). A small amount of polar, coordinating solvent appears to boost activity, potentially by stabilising cationic reactive intermediates. Due to their greater activity and crystallinity (ensuring bulk purity which may be replicated in the active sites), comparison of the reactivity of the varying imido complexes was undertaken, utilising the immobilised THF complexes (**1.1**–**1.8**).

4.2.2.2. Variation of the imido group

To investigate the effect of varying the imido group of the supported catalysts on their respective activities towards ethylene oligomerisation, the solid catalysts (sMAO-(**1.1**–**1.8**)) (W:Al = 1:150) were reacted at 100 °C in d_6-benzene with ethylene (1 bar) utilising mesitylene as the internal standard. A plot of TONs against time for (sMAO-(**1.1**–**1.8**)) is depicted in Figure 4.10.

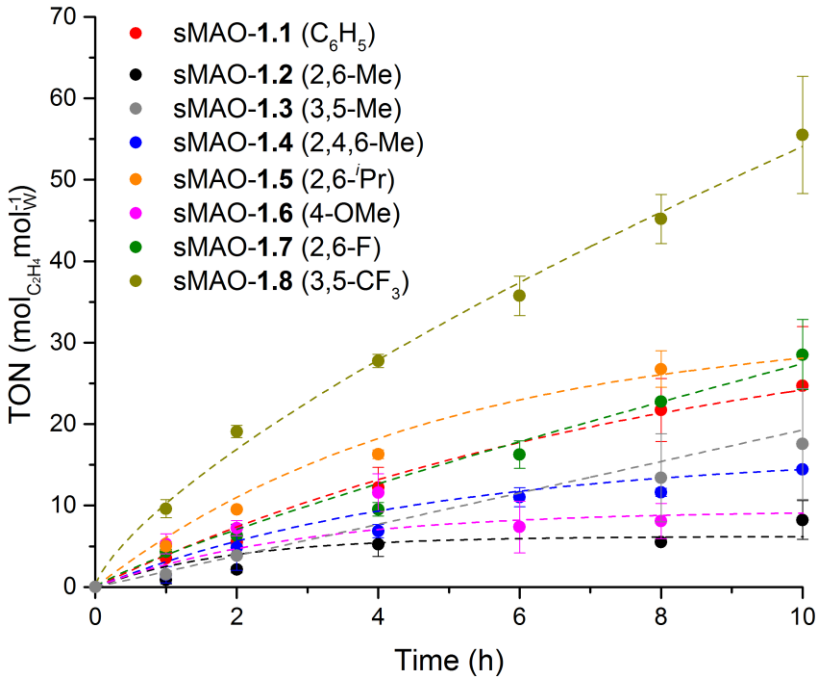


Figure 4.10. Turnover numbers (TONs) of ethylene for the various sMAO supported tungsten arylimido complexes. 5 mg cat. (0.4 μmol$_W$) in d_6-benzene at 100 °C, 1 bar ethylene and Al/W = 150.

Table 4.1. Activities and selectivities towards 1-butene for the various sMAO supported catalysts.

Complex	R	Activity[a] ($mol_{C_2H_4}mol_W^{-1}h^{-1}bar^{-1}$)	Selectivity towards 1-butene[a] (%)
sMAO-**1.1**	C_6H_5	2.72	87
sMAO-**1.2**	2,6-Me-C_6H_3	0.69	69
sMAO-**1.3**	3,5-Me-C_6H_3	1.68	68
sMAO-**1.4**	2,4,6-Me-C_6H_2	1.45	81
sMAO-**1.5**	2,6-^{i}Pr-C_6H_3	3.34	79
sMAO-**1.6**	4-OMe-C_6H_4	1.01	77
sMAO-**1.7**	2,6-F-C_6H_3	2.86	71
sMAO-**1.8**	3,5-CF_3-C_6H_3	5.65	91

[a] Calculated after 8 hours.

Electron deficient imido groups are seen to yield the most active catalysts, with sMAO-**1.8** displaying the highest turnover numbers (63 $mol_{C_2H_4}mol_W^{-1}$ after 12 hours). This has previously been observed in homogeneous propene oligomerisation reactions using $W(NR)Cl_4(THF)$ complexes and diethylaluminium chloride (DEAC) as a co-catalyst, where activity followed the order R = 4-F-C_6H_4>C_6H_5>2,6-Me-C_6H_3>2,6-^{i}Pr-C_6H_3.[16] It should be noted that the activity of the sMAO supported systems presented here is significantly lower than for the homogeneous DEAC activated system (TON = 389 $mol_{C_2H_4}mol_W^{-1}h^{-1}bar^{-1}$ for W{N(4-F-C_6H_4)}Cl_4/$AlEtCl_2$, 60 °C, toluene, Al/W = 11).

In terms of supported dimerisation systems, Kermagoret *et al*. have described an immobilised nickel catalyst which selectively dimerises ethylene, by contacting $NiCl_2(PBu_3)_2$ with silica supported dimethylaluminium chloride. Activities as high as 99,600 $mol_{C_2H_4}mol_{Ni}^{-1}h^{-1}bar^{-1}$ with 95% selectivity for 1-butenes have been reported, utilising MCM-41 silica (5 bar ethylene, 30 °C, Al/Ni = 10).[23] Interestingly, the complex supported on silica impregnated with trialkylaluminium species shows no activity for this reaction.[1] Whilst for both the homogeneous and supported systems described above DEAC may lead to higher activities for this reaction, it was previously observed that use of ethylaluminium compounds resulted in formation of ill-defined species, with ethane evolution observed (Chapter Two).

Whilst a more electron withdrawing imido group will destabilise the proposed cationic transition state formed from halide or methyl abstraction, it will increase its affinity to bind ethylene and stabilise a propagating chain. The observed C–F activation of sMAO-**1.8** (*vide supra*) could also contribute to its enhanced reactivity. Kaminsky and co-workers have

reported that fluorinated half-sandwich titanium complexes show an increase in activity for styrene polymerisation of up to 50 times compared to the chlorinated analogues, using MAO as a co-catalyst.[24] Marks and co-workers have also demonstrated that a bulky (perfluoroaryl)fluoroaluminate counterion, $[(C_{12}F_9)_3AlF]^-$, can stabilise metallocene cations *via* an Al–F–M interaction.[25,26]

Interestingly, the bulky W{N(2,6-^{i}Pr-C_6H_3)}Cl_4(THF) supported complex (sMAO-**1.5**) also displays relatively high turnover numbers of ethylene, similar to those of the supported 2,6-fluorophenyl and phenyl imido complexes (sMAO-**1.7** and sMAO-**1.1** respectively). This is attributed to the increased steric bulk and a more electron deficient imido fragment (discussed in Chapter Two), which may enhance the rate of reductive elimination of 1-butene, inhibiting further chain propagation. A statistical correlation ranking of steric and electronic factors for the molecular complexes (determined from the molecular structures and NMR spectroscopic data, Chapter Two) *vs* the turnover frequency (TOF), calculated after 8 hours, showed the strongest correlation between pKa values for the parent anilines (Pearson's $r = -0.58$), but essentially no correlation between the steric factors indicating that it is the electronics of the imido substituent that are the dominating factor (Table A10). Comparison of the steric and electronic parameters of the phenyl and four alkyl-substituted imido groups with the TOFs shows an even stronger correlation (Pearson's $r = 0.81$) between the C_{ipso} resonance of the W(NR)Cl_4(THF) complexes and the TOFs of the supported catalysts (Table A11). The selectivity of all the catalysts towards 1-butene compared to isomerisation or metathesis to form propylene show no clear correlation with either the steric or electronic properties of the imido complexes. It should be noted that no higher oligomers were observed, but in most cases a small amount of polyethylene formation was observed (1–2 mg). As there was no further oligomerisation with 1-butene, reaction of sMAO-**1.7** (W:Al =1:150) with the longer chain linear alpha olefins 1-hexene and 1-octene was attempted, to ascertain whether the scope of the olefin monomer was limited to ethylene. Reactions were performed at 75 °C in d_6-benzene employing 5 mg cat. and 40 μmol of 1-olefin. In both cases isomerisation reactions occurred, yielding the internal olefins with near complete conversion (>91%) after heating for 4 hours (Figures A136 and A137). This suggests that olefin binding to the complex can occur. However, a second olefin is not able to insert to propagate the chain and hence isomerisation to the more stable internal isomers occurs.

4.2.2.3. Temperature study

A study examining the effect of temperature on the oligomerisation reaction was performed with sMAO-**1.6**[11] and sMAO-**1.5** (Figure 4.11 and A138). Reaction of sMAO-**1.5** with ethylene in d_6-benzene at 25, 75 and 100 °C, indicated that the highest activity was observed at 75 °C, followed by 100 °C. A peak in activity at 75 °C was also observed for sMAO-**1.6**. For this complex oligomerisation reactivity at 100 °C is seen to almost completely shut off after 4 hours, with polymer formation observed. For sMAO-**1.5** selectivity towards 1-butene after 36 hours was high at all temperatures (>97%), whereas for sMAO-**1.6** it was seen to decrease at high temperature (85% *vs* 70% at 75 and 100 °C respectively). The presence of butane, ethane, and methane in the NMR spectra, observed to a much greater extent at high temperatures, suggests that there may be a tungsten hydride species being formed as part of the catalytic cycle which would imply a Cossee type mechanism.[27] The lower selectivity for 1-butene in part due to isomerisation, indicates that ethylene insertion into this hydride is relatively slow and thus competing 1-butene insertion and isomerisation can occur.

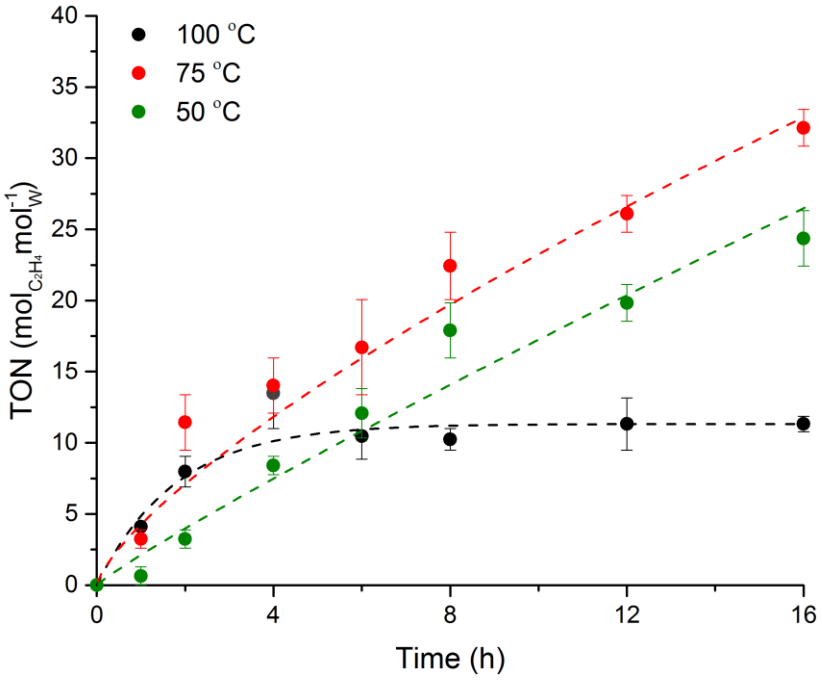


Figure 4.11. Temperature study using sMAO-**1.6** at 50, 75 and 100 °C in d_6-benzene with 1 bar ethylene and W:Al = 1:150.[11]

An alternative mechanism involves metallocycle formation. Such a mechanism has been observed for selective ethylene dimerisation utilising tantalum systems, whereby, formation of the metallacycloheptane is disfavoured, hence sterically more demanding β-hydride

elimination from the tantalacyclopentane selectively yields 1-butene.[28–30] Such a mechanism has previously been suggested for tungsten initiators displaying high selectivity in dimerisation,[16] and a DFT study on mono-imido complexes activated by MAO concluded such a route was feasible.[31] However, oligomerisation reactions with a mixture of C_2H_4/C_2D_4 (1:1) and either the $WCl_6/Et_3N/PhNH_2/AlEt_2Cl$ or $MoCl_2\{N(2,6\text{-}^{i}Pr\text{-}C_6H_3)\}_2(DME)/AlEtCl_2$ systems, have shown complete scrambling of the resulting oligomer, indicative of a Cossee mechanism, corroborating potential hydride formation in the sMAO supported species.[32,33]

4.2.2.4. Solvent Effects

Previous work in the group utilising sMAO-**1.6**, has shown that variation of the solvent in the oligomerisation reaction conducted at 75 °C, can have a large impact on the activity.[11] Variation of the deuterated NMR solvent: d_6-benzene, d_8-toluene, d_8-THF, d_2-DCM and d_{18}-octane, indicated that the more polar, non-coordinating toluene resulted in the highest activity. To support these conclusions, the study was expanded to d_5-chlorobenzene and d_5-bromobenzene (Figure 4.12 and Table 4.2).

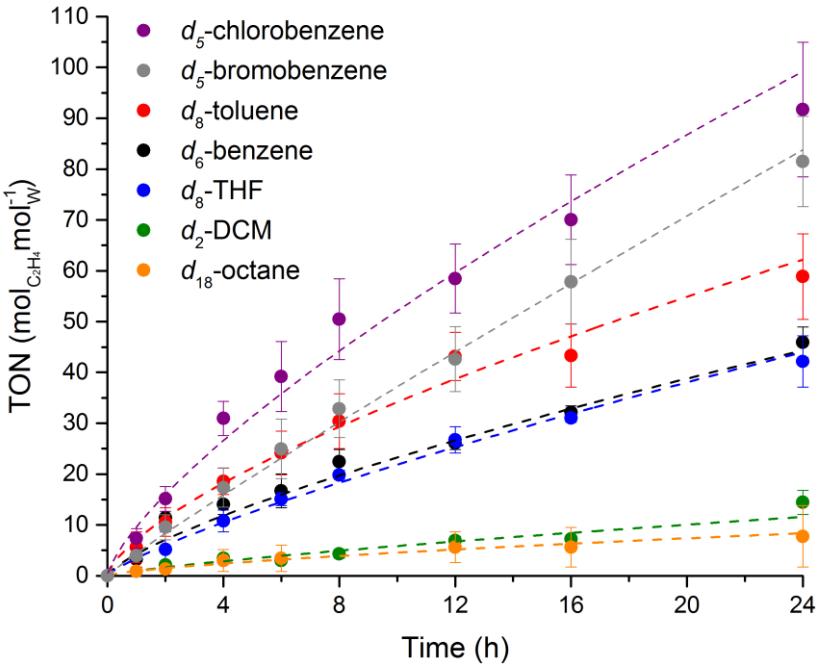


Figure 4.12. Effect of varying the solvent in the oligomerisation reaction using sMAO-**1.6** at 75 °C, 1 bar ethylene and W:Al = 1:150.

Table 4.2. Turnover frequencies (TOFs) and selectivities towards 1-butene for sMAO-**1.6** with variation of the solvent medium.

Solvent	TOF[a] ($mol_{C_2H_4}mol_W^{-1}h^{-1}$)	Selectivity towards 1-butene[a] (%)
d_{18}-octane	0.57	>99
d_6-benzene	2.8	84
d_8-toluene	3.8	91
d_5-chlorobenzene	6.31	90
d_5-bromobenzene	4.11	85
d_8-THF	2.48	>99
d_2-DCM	0.54	>99

[a] Calculated after 8 hours.

The highest rates of oligomerisation are observed with polar aromatic solvents, with d_5-chlorobenzene leading to the highest turnover numbers. This is likely to be due to two main factors. Firstly, the active species formed on the surface after halide abstraction involves a positive charge on the metal centre and proposed ionic interaction with the surface. Polar solvents may destabilise this surface interaction opening up the metal centre for ethylene binding and subsequent oligomerisation. However, coordination of the solvent to the metal would block a coordination site, preventing ethylene binding, thus reducing the rate of oligomerisation. A table of dielectric constants and donor numbers are shown in Table A13.[34,35]

For non-coordinating solvents (those with a low donor number) the trend in the rates of oligomerisation increase with the increase in polarity; d_{18}-octane>d_6-benzene>d_8-toluene> d_5-bromobenzene>d_5-chlorobenzene (TOFs of 0.57, 2.8, 3.8, 4.11 and 6.31 $mol_{C2H4}mol_W^{-1}h^{-1}$ respectively after 8 hours). d_8-THF and d_2-DCM however, can both coordinate to the metal centre through interactions of lone pairs of electrons on the heteroatoms, blocking olefin coordination. For d_8-THF the balance between its higher polarity and stronger donor ability results in a solvent medium similar to that of d_6-benzene. d_2-DCM has been observed to react with the support, with a change in colour and colouring of the solution indicating that decomposition had occurred. A high level of selectivity towards 1-butene is observed for all of the solvents employed in this study (≥84%). Bercaw and co-workers have also observed that more polar non-coordinating solvents lead to increased oligomerisation activity. Variation of the solvent medium from toluene to the more polar chlorobenzene resulted in higher activity, stability and selectivity towards trimer- and tetramerisation, with reduced polymer formation, for bis(diphenylphosphino)amine ligated chromium catalysed ethylene oligomerisation.[36] Variation of the reaction solvent by Hanton *et al*. on the ill-defined $WCl_6/Et_3N/PhNH_2/AlEt_2Cl$ system also yielded similar results, with chlorobenzene the most

active medium for 1-hexene dimerisation and donor solvents (THF, MeCN) inhibiting the reactivity.[32]

4.2.2.5. Loading study

A loading study of **1.6** on sMAO has previously been conducted (W/Al = 100, 150 and 200) with the resulting oligomerisation reactions showing that a W/Al of 150 has the highest activity followed by 200, with 100 almost 10 times less active (TONs of 22.4, 15.5 and 6.5 $mol_{C_2H_4}mol_W^{-1}$ respectively after 8 hours) (Figure A139).[11] Selectivities towards 1-butene over the loading range remain constant (~85%) At high loadings of tungsten (Al/W = 100), blocking of the active sites and bimetallic decomposition pathways may be facilitated due to the close proximity of the immobilised complexes, leading to poorer activity.

4.2.3. Gas phase reaction

One benefit of immobilising single-site catalysts is that it can allow them to be utilised in gas phase reactions. To test the capability of the sMAO supported systems, sMAO-**1.5** was loaded into a J. Young valve NMR spectroscopy tube, and ethylene (1 bar) added in the absence of solvent. Heating the mixture at 100 °C for 4 hours resulted in the formation of 1-butene (~5% ethylene conversion, 66% of C_4 fraction) along with 2-butenes observed by ^{1}H NMR spectroscopy (Figure 4.13). Further heating overnight resulted in a small increase in the dimer fraction (8% ethylene conversion), with a large quantity of ethylene still remaining.

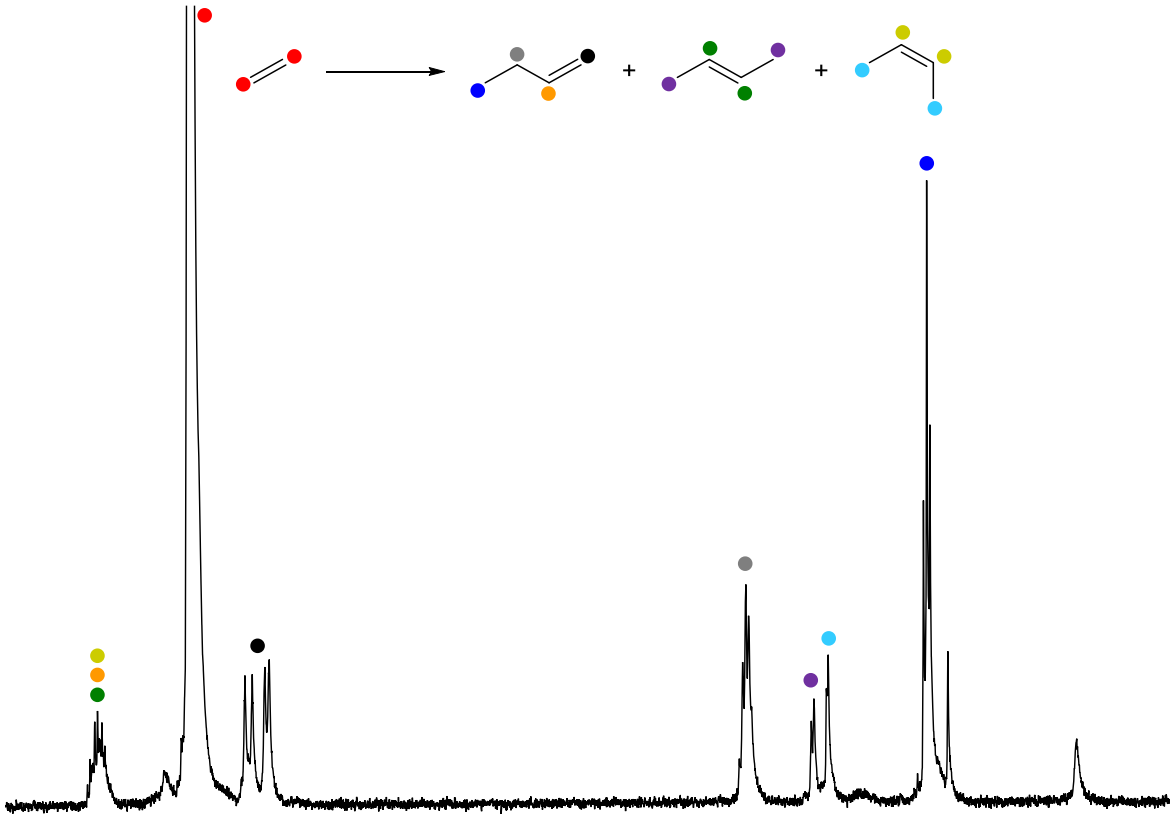


Figure 4.13. ^{1}H NMR spectrum (400 MHz, 23 °C) of the gas phase reaction between sMAO-**1.5** (5 mg) and ethylene (1 bar) at 100 °C. Sample was run unlocked so the ppm scale has been removed as it is unreferenced.

4.2.4. Scale-up reactions

sMAO-**1.5** was sent to Norner, Norway, for slurry phase ethylene oligomerisation tests under continuous ethylene flow, in a 200 mL batch reactor. The temperature for the oligomerisations was set at 75 °C, as the highest activity for sMAO-**1.5** was observed at this temperature (*vide supra*). The solvent utilised was either hexane or toluene, with a stirring speed of 320 rpm and variation of the ethylene partial pressure from 1–19 bar. The results are summarised in Table 4.3 and compared with the homogeneous commercial dimerisation catalyst Ni(^{n}Bu$_3$P)$_2$Cl$_2$ tested under analogous conditions.

Table 4.3. Scale-up reactions of sMAO-**1.5** compared with Ni(^{n}Bu$_3$P)$_2$Cl$_2$.

Catalyst	Amount (mg)	Co-catalyst	T (°C)	Solvent	$P_{C_2H_4}$ (bar)	Activity[a]	Selectivity 1-C_4 (%)
sMAO-**1.5**	30	-	75	Toluene	9	1.56	>99[c]
sMAO-**1.5**	100	-	75	Hexane	9	0.06	>99[d]
sMAO-**1.5**	60	-	75	Toluene	19	0.39	>99
Ni(^{n}Bu$_3$P)$_2$Cl$_2$	8	DEAC[b]	50	Hexane	14.6	3,072	15.1

[a] $mol_{products} mol_{M}^{-1} h^{-1} bar^{-1}$. [b] Al/Ni = 70. [c] Polyethylene formed. [d] Small quantity of polymer formation observed. Reaction times = 24 h. Stirring speed = 320 rpm. $[W]_0$ = 0.09 μmol mg^{-1}. $[Ni]_0$ = 14.7 μmol.

Under all conditions sMAO-**1.5** displays low activities for the dimerisation reaction (0.06–1.56 $mol_{C_4H_8}mol_W^{-1}h^{-1}bar^{-1}$), especially when compared to the nickel system (3,072 $mol_{products}mol_M^{-1}h^{-1}bar^{-1}$). The selectivity of sMAO-**1.5** towards 1-butene was remarkably high (>99%) in all cases, compared to the nickel system (15.1%). From the data recorded for sMAO-**1.5**, increasing the pressure appeared to have a detrimental effect on the activity. Toluene also yielded a more active catalyst than hexane, in keeping with the data for sMAO-**1.6**.

In an attempt to boost the activity, 1 drop of triethylaluminium was added to the catalysts slurry in toluene prior to reaction (100 mg cat., toluene, 75 °C, 19 bar ethylene, 24 hours). Upon opening the reactor, 3.5 g of polyethylene was obtained (activity = 0.83 $kg_{PE}mol_W^{-1}h^{-1}bar^{-1}$). Analysis of the polymer by FTIR showed it to be linear polyethylene. DSC analysis (Figure A140) showed it to have a melting temperature (T_m) of 142.2 °C and a crystallisation temperature (T_c) of 111.7 °C, corresponding to ultra-high molecular weight polyethylene (UHMWPE).[37] By integrating the areas under the peaks for T_m and T_c and dividing by the heating rate, the heats of melting (ΔH_m) and crystallisation (ΔH_c) were determined as 146 and 105 Jg^{-1} respectively. From Equation 4.1, it can be seen that the percentage crystallinity of the sample can be calculated by dividing the difference between the heat of melting and the heat of crystallisation by the reference for 100% crystalline polyethylene ($\Delta H_m° = 293\ Jg^{-1}$).[38]

Equation 4.1. Percentage crystallinity of a polymer:

$$\%\ crystallinity = \frac{(\Delta H_m - \Delta H_c)}{\Delta H_m^\circ} \times 100\%$$

$\Delta H_m =$ heat of melting

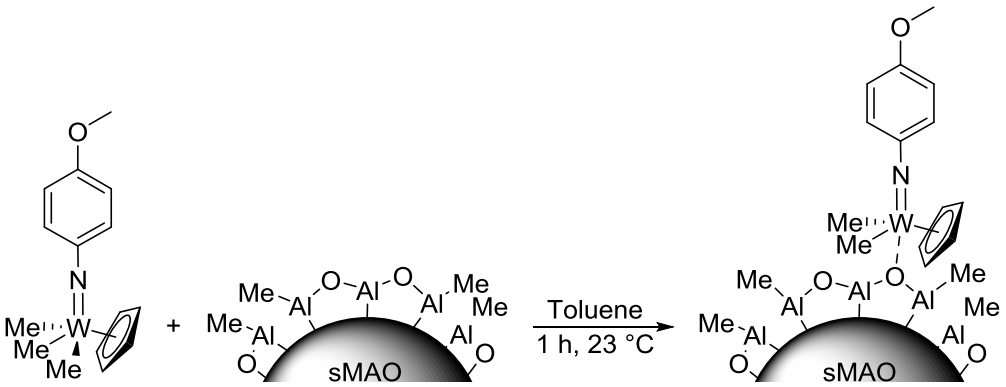
$\Delta H_c =$ heat of crystallisation

$\Delta H_m^\circ =$ heat of melting for 100% crystalline polyethylene $= 293\ Jg^{-1}$

The UHMWPE sample was found to have a crystallinity of 14%, which is relatively low, however, this is unsurprising as it has not been annealed.[39] The chemical inertness, impact and abrasive resistance of UHMWPE make it a desirable industrial polymer. One of its main uses is in orthopaedics, as it is used in the manufacture of implants for joint replacements.[40]

4.2.5. sMAO-W{N(4-OMe-C_6H_4)}Me_3Cp (sMAO-3.6)

The effect of varying the ancillary ligands was also investigated utilising W{N(4-OMe-C_6H_4)}Me_3Cp (**3.6**). Reaction of **3.6** with sMAO in toluene (Al/W = 150), yielded a pale yellow solid after filtering and drying. In the absence of a halide ligand, the complex is still able to bind to the surface, indicating that sMAO is capable of abstracting a methyl group in an analogous manner to MAO (Scheme 4.4).[6]



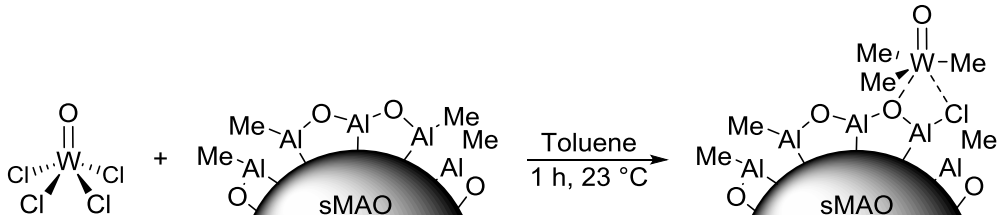
Scheme 4.4. Postulated product from the immobilisation of **3.6** on sMAO (Al/W = 150) *via* methyl abstraction by the support.

Reaction of sMAO-**3.6** with ethylene under standard oligomerisation conditions (1 bar ethylene, 75 °C, d_6-benzene) resulted in solely polymer formation (~5 mg) with no oligomers observed by ^{1}H NMR spectroscopy after 8 hours. To test the full capacity of this supported complex towards ethylene polymerisation, scale-up polymerisations were undertaken initially employing TIBA as a scavenger (10 mg cat., 2 bar ethylene, 150 mg TIBA, hexane, 80 °C, 1 hour). Only a small amount of polymer was obtained from the reaction (5 mg). It was proposed that this may be due to the presence of TIBA, which has previously been seen to shut down the reactivity of sMAO-**1.6**.[11] To avoid this, the scavenger was changed to MAO (20 mg), however, equally low activities were observed (5–10 mg polyethylene). After one of the runs, the hexane solution was cooled and analysed by ^{1}H NMR spectroscopy in d_6-benzene, revealing no oligomers in solution.

4.2.6. sMAO-W(O)Cl_4

To probe the importance of the imido moiety on the catalytic activity of the supported species, W(O)Cl_4 was immobilised on sMAO (Al/W = 150). It was observed that W(O)Cl_4 could be methylated by TMA, however, the resulting species was highly unstable (Chapter Two). It was proposed that *in situ* methylation and grafting may stabilise the

resulting oxo complex and prevent bimolecular decomposition. Swirling $W(O)Cl_4$ and sMAO in toluene resulted in grafting of the molecular complex and yielded a pale orange solid after filtration and drying (Scheme 4.5).



Scheme 4.5. Immobilisation of $W(O)Cl_4$ on sMAO (Al/W = 150), with prosed formation of $[W(O)Me_3]^+$ on the surface.

Reaction of sMAO-$W(O)Cl_4$ with ethylene (1 bar, 100 °C, d_6-benzene, mesitylene internal standard) resulted in dimerisation to yield butenes (selectivity towards 1-butene of 50% after 12 hours), along with the cross-metathesis product, propylene. The activity after 12 hours (0.81 $mol_{C_4H_8}mol_W^{-1}h^{-1}bar^{-1}$) was much lower than all of the imido systems except sMAO-**1.2**, with the selectivity for 1-butene markedly reduced. The bulkier imido groups most likely help to inhibit 1-butene coordination over ethylene, and thus reduce the rate of isomerisation. As cross-metathesis of 2-butenes and ethylene was observed with sMAO-$W(O)Cl_4$, its reactivity towards propylene was pursued. Metathesis to yield ethylene and 2-butenes was observed with an activity of 4.8 $mol_{C_3H_6}mol_W^{-1}h^{-1}bar^{-1}$.

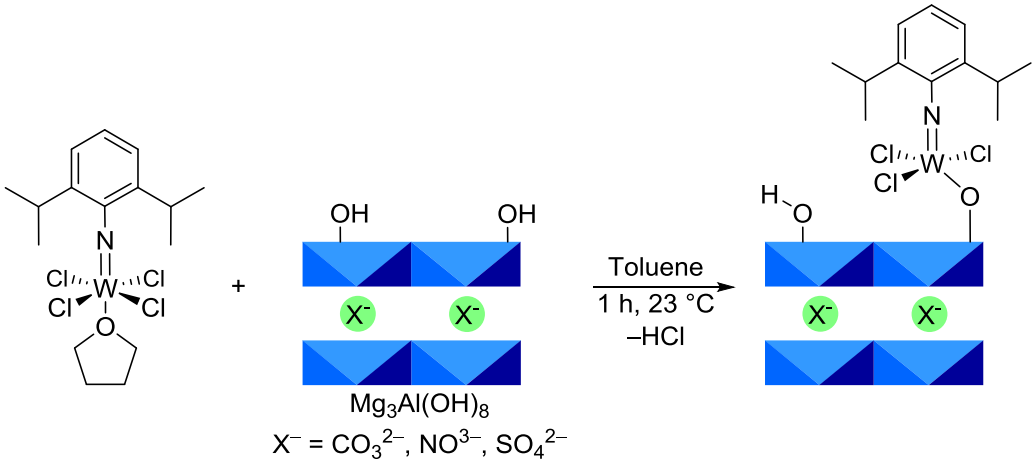
4.3. Layered double hydroxide (LDH) supported complexes

4.3.1. Effect of the interlayer anion

4.3.1.1. Complex immobilisation

AMO-LDHs, as described in Chapter Three, were also employed as catalyst supports. Along with Mg_3Al-SO_4, Mg_3Al-CO_3 and Mg_3Al-NO_3 both synthesised by the same AMOST co-precipitation method,[41–44] were utilised. For initial comparison of the effect of the interlayer anions, these AMO-LDHs were thermally treated under vacuum at 150 °C for 6 hours. From this point onwards these materials will be described as $LDH(X)_y$ where X = SO_4, CO_3 or NO_3 and y is the temperature of thermal vacuum treatment in °C *e.g.* $LDH(SO_4)_{150}$. After treatment, white powders were isolated in all cases and stored under N_2 to prevent rehydration. The propensity of these materials to graft molecular species was analysed using **1.5** (5 wt% with respect to the AMO-LDH) (Scheme 4.6). Swirling the green solution in

toluene at room temperature for 1 hour led to complete decolourisation of the solution, consistent with complete grafting of the tungsten complex.



Scheme 4.6. Supporting of W{N(2,6-^{i}Pr-C_6H_3)}Cl_4(THF) (**1.5**) on LDH(X)$_{150}$ (X = SO_4, NO_3 and CO_3).

Interestingly, the resulting colour of the isolated solids differed depending on the interlayer anion, yielding off white, beige and bright yellow powders for the LDH$(SO_4)_{150}$, LDH$(CO_3)_{150}$ and LDH$(NO_3)_{150}$ grafted species respectively (Figure 4.14). This difference is postulated to result from interaction of the interlayer anions, some of which may be present on the LDH surface, with the immobilised species.



Figure 4.14. Isolated solids from the reaction of **1.5** with LDH$(SO_4)_{150}$ (off white), LDH$(CO_3)_{150}$ (beige) and LDH$(NO_3)_{150}$ (yellow).

A study into the maximum loading of complex onto the AMO-LDH surface was undertaken using LDH$(CO_3)_{150}$ and **1.5**. Loadings of up to 20 wt% of complex were attempted. It was found that for loadings above 10 wt% there was no longer complete decolouration of the solution, even after 2 hours of swirling at 23 °C. Complete impregnation could be achieved at these loadings if the mixture was heated at 60 °C. However, a ^{1}H NMR spectroscopic study of the grafting process at this temperature showed the presence of 2,6-diisopropyl aniline in solution. A possible reason for the observed decomposition may be

that calcining the AMO-LDH at 150 °C leaves a large concentration of OH groups on the surface (Chapter Three). Heating may result in proximal surface hydroxyls reacting with the complex yielding multipodal species and protonating the imido group. Precedence for this has been demonstrated by Basset and co-workers, who have shown that the supported tungsten complex (≡SiO)WMe_5 forms a bi-podal methylidene species when heated at 70 °C on silica dehydroxylated at 700 °C, as a result of reaction with other surface hydroxyl groups.[45]

4.3.1.2. Characterisation of the supported species

^{13}C-{^1H} CPMAS SSNMR spectra of $LDH(SO_4)_{150}$ and $LDH(NO_3)_{150}$ supported complexes have low signal to noise (S:N) ratios, however, resonances in the aromatic and methyl regions, corresponding to the phenyl imido protons and isopropyl groups respectively, can be observed (Figure 4.15 and A141).

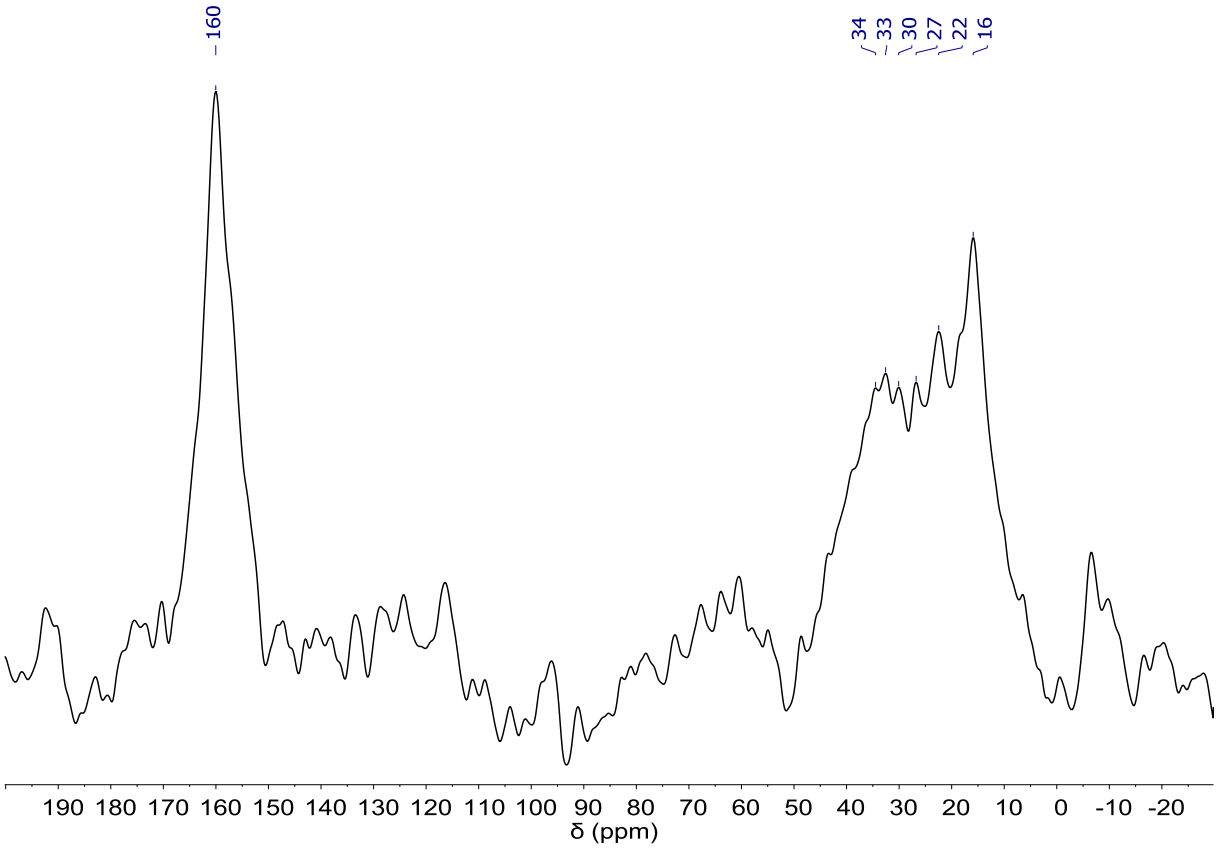


Figure 4.15. ^{13}C-{^1H} CPMAS SSNMR spectrum (10 kHz, 400 MHz, 23 °C) of $LDH(SO_4)_{150}$-**1.5**.

The sharp resonance at 160 ppm is postulated to derive from a combination of imido resonances and residual carbonate in the AMO-LDH material,[46] which can be observed in the FTIR spectra at 1,650 cm^{-1} (Figure A144). The spectra show multiple resonances in the alkyl region, especially for the nitrate containing sample, which may be indicative of

decomposition of the defined complex structure. For reference, the solution $^{13}C\{^{1}H\}$ NMR ^{i}Pr resonances for **1.5** appear at 26.3 and 27.9 ppm in d_6-benzene.

The ^{27}Al DPMAS SSNMR spectra of the LDH-supported species exhibit a relatively low intensity resonance at ~77 ppm attributed to tetrahedral aluminium sites formed from thermally treating the material, whilst the resonance at ~8 ppm represents the bulk octahedral aluminium environment of the LDH (Figures A142 and A143).[47]

FTIR spectra of the immobilised complex compared to the precursor AMO-LDH materials (Figures A144–A149) shows small absorbances at 2,950 and 1,250 cm^{-1} assigned to the C–H stretches for the aromatic imido groups and W–N–C_{ipso} symmetric stretch respectively. The spectra are dominated by absorptions from the LDH materials (OH and interlayer anions), whereas the imido groups are in a low loading and have generally weak IR absorptions.

4.3.1.3. Decomposition study

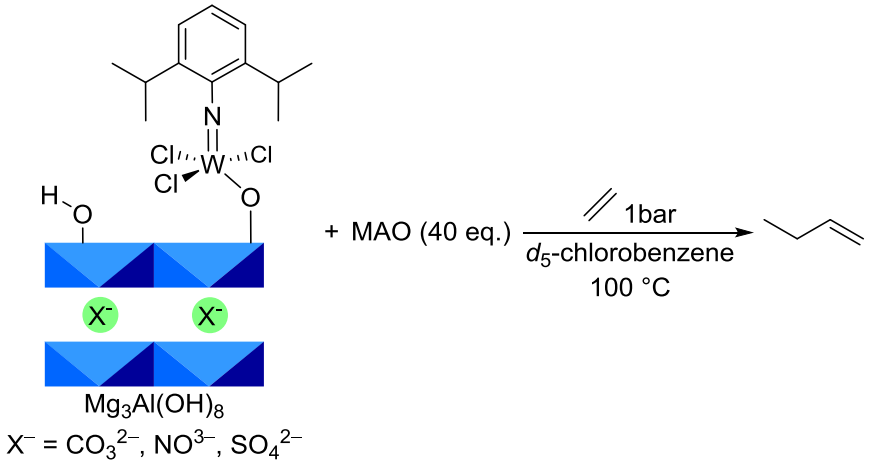
It was proposed that hydrogen chloride is released during immobilisation of **1.5**, which may then react with the complex, either bound, or in solution or with the LDH. Hydrochloric acid is known to dissolve LDHs, hence why they have found use in drug intercalation.[48] However, there was no significant decrease in the yield observed for the supporting reactions. Potentially, the LDH may act as a buffer in solution due to its basic nature and thus may be able to tolerate mild acidic conditions. To test the stability of the free complex towards an acidic environment, excess anhydrous HCl in a solution of diethyl ether was added to **1.5** in a J. Young valve NMR spectroscopy tube. There was no apparent decomposition of the complex after 24 hours at 23 °C. There was also no evident decomposition when the mixture was heated at 60 °C for 18 hours.

4.3.1.4. Reactivity towards ethylene

The propensity of $LDH(CO_3)_{150}$-**1.5** to oligomerise ethylene was tested, with an excess of MAO added as a co-catalyst (1 bar ethylene, d_6-benzene, 100 °C, Al/W = 80). Selective formation of 1-butene was observed after 1 hour. The supported complex showed no sign of deactivation and the concentration of 1-butene increased over the course of 5 days, after which the experiment was stopped with only a small quantity of ethylene remaining. By comparison, a homogeneous sample with MAO (Al/W = 10) was run in tandem, displaying a much lower activity with clear degradation after 18 hours at 100 °C and polymer formation observed (1–2 mg). From an analysis of this polymer by $^{13}C\{^{1}H\}$ NMR spectroscopy in

d_4-*o*-dichlorobenzene at 100 °C, it was inconclusive as to whether any 1-butene had been incorporated.

As polar aromatic solvents, in particular chlorobenzene, have been shown to lead to more active and selective oligomerisation catalysts with chromium and tungsten based species with aluminium co-catalysts (*vide supra*),[32,36,49] comparison of the activity of the different AMO-LDH supported complexes was undertaken using d_5-chlorobenzene as the solvent medium (1 bar ethylene, Al/W = 40, Scheme 4.7).

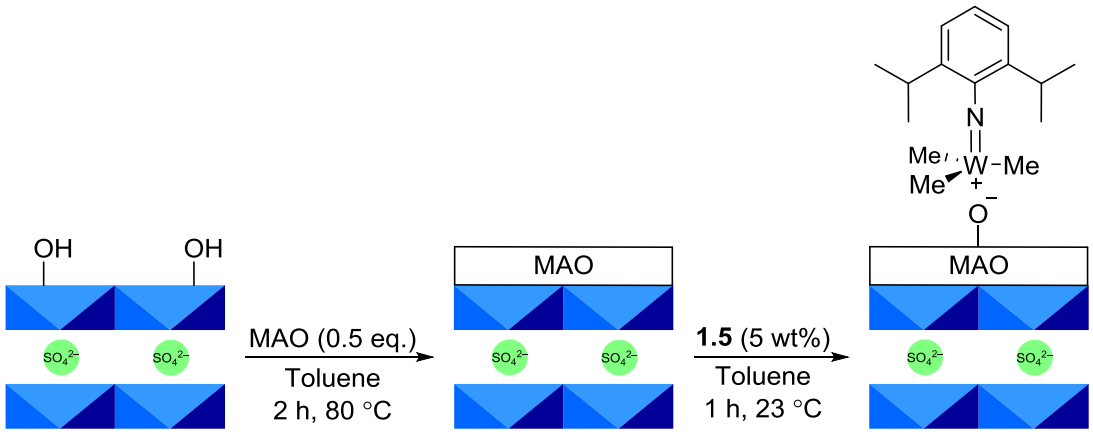


Scheme 4.7. Reaction of LDH$(CO_3)_{150}$-**1.5**, LDH$(SO_4)_{150}$-**1.5** and LDH$(NO_3)_{150}$-**1.5** with ethylene, yielding 1-butene for the sulfate and carbonate supported complex.

LDH$(SO_4)_{150}$-**1.5** was the only solid catalyst observed to yield 1-butene at 23 °C within a few hours of ethylene addition. After 48 hours resonances for 1-butene were seen for LDH$(CO_3)_{150}$-**1.5**, however, no resonances corresponding to 1-butene were observed for LDH$(NO_3)_{150}$-**1.5**, even after a week. The reactions were repeated with a reaction temperature of 100 °C. Again, LDH$(SO_4)_{150}$-**1.5** demonstrated the fastest 1-butene formation (1 hour), with only a small amount observed for LDH$(CO_3)_{150}$-**1.5** after 38 hours heating and no 1-butene formation observed for LDH$(NO_3)_{150}$-**1.5**. All of the reactions suffered from competing polymerisation in the order LDH$(NO_3)_{150}$-**1.5** (~10 mg of polyethylene) > LDH$(CO_3)_{150}$-**1.5** > LDH$(SO_4)_{150}$-**1.5**, which formed around the LDHs and may have blocked active sites. The greater activity observed for the Mg_3Al-SO_4 AMO-LDH over CO_3 or NO_3, corroborates previous work on supported metallocene catalysts for ethylene polymerisation.[50] For this reason, Mg_3Al-SO_4 AMO-LDH was chosen for further study.

4.3.2. Immobilisation procedure and alkyl aluminium co-catalyst effects

Having observed selective dimerisation by addition of MAO as a co-catalyst, two different immobilisation methods were employed along with variation of the methyl aluminium co-catalyst (MAO, TMA and DMAC). Firstly, $LDH(SO_4)_{150}$ was reacted with the methyl aluminium reagent (0.5 eq.) in toluene at 80 °C, yielding colourless solids in all cases, followed by addition of a toluene solution of **1.5** (5 wt%), which was swirled at room temperature for one hour. Addition of **1.5** to either $LDH(SO_4)_{150}$-TMA or $LDH(SO_4)_{150}$-DMAC yielded a yellow solution, but no immobilisation was observed. Analysis of the supernatant by ^{1}H NMR spectroscopy showed formation of **2.5**, but there was no colouration of the solid observed after work-up. Heating the mixtures at 80 °C still did not lead to any grafting. In contrast, contacting **1.5** with $LDH(SO_4)_{150}$-MAO resulted in complete decolourisation of the solution and formation of a pale yellow solid after filtration and drying. The difference is attributed to the presence of oxo groups in MAO, which appear to be important in the grafting process, with proposed formation of **2.5** on the MAO coated surface (Scheme 4.8).



Scheme 4.8. Impregnation of MAO onto $LDH(SO_4)_{150}$ followed by reaction with **1.5**, leading to proposed formation of $[W\{N(2,6\text{-}^{i}Pr\text{-}C_6H_3)\}Me_3]^+$ on the surface.

The ^{13}C-{^{1}H} CPMAS SSNMR spectrum of $LDH(SO_4)_{150}$-MAO-**1.5** (Figure A150), displayed an intense sharp resonance at 160 ppm (interlayer carbonate) with a weaker broad set of resonances between 155–120 ppm attributed to the ring carbon atoms of the aromatic imido group. A broad set of resonances are observed between 85–10 ppm and are attributed to the isopropyl groups on the imido fragment, as well as tungsten and aluminium methyl groups. The fact there are numerous resonances suggests that multiple species may have formed on the surface. The ^{27}Al DPMAS SSNMR spectrum (Figure A152), is analogous to

that observed for $LDH(SO_4)_{150}$-**1.5** (*vide supra*). The FTIR spectrum of $LDH(SO_4)_{150}$-MAO-**1.5** (Figure A151) exhibits absorptions at 3,000 cm^{-1} for the aromatic C–H groups, 1,250 cm^{-1} ascribed to the symmetric W–N–C stretch, and multiple broad peaks between 1,200–500 cm^{-1} for the sulphate ions and, surface aluminoxane species.

Further evidence for the importance of surface oxo groups was obtained by employing the incipient wetness immobilisation technique for complex immobilisation. In this process, **1.5** and the methyl aluminium reagent (MAO, TMA or DMAC, 2 eq.) were mixed in a minimum amount of toluene prior to addition onto $LDH(SO_4)_{150}$. An initial yellow solution was formed in all cases, indicative of formation of **2.5**. Addition of this solution onto $LDH(SO_4)_{150}$ furnished pale yellow solids after filtering and drying in all cases. It is proposed that immobilisation occurs in this case with TMA and DMAC as co-catalysts, as the complex is able to bind to available surface hydroxyl groups on the AMO-LDH support. When the LDH surface has been pre-treated with an alkyl aluminium reagent, these hydroxyls react with and anchor the co-catalyst, thus are unavailable to the complex. ^{13}C-{^{1}H} CPMAS SSNMR spectroscopy was utilised to study the solid catalyst formed from this method with MAO ($LDH(SO_4)_{150}$-(**1.5** + 2MAO), Figure A153). Only a single sharp resonance was observed in the aromatic region at 160 ppm, attributed to a combination of residual carbonate in the LDH support, and aromatic imido resonances. Resonances between 45 and 0 ppm were observed corresponding to the isopropyl groups on the imido moiety and W–Me bonds. The narrower range of resonances observed is indicative of a more defined immobilised species, which may be due to the lower ratio of co-catalyst employed. For $LDH(SO_4)_{150}$-MAO-**1.5** Al/W = 60 whereas for incipient wetness Al/W = 2. It was previously observed that MAO/W ratios above 5 resulted in decomposition of **2.5** forming multiple ill-defined species (Chapter Two).

The reactivity towards ethylene of $LDH(SO_4)_{150}$-MAO-**1.5** and the three supported complexes formed by incipient wetness was studied (1 bar ethylene, 100 °C, d_6-benzene). For the solids formed by the incipient wetness technique, decomposition of the imido complex was observed, by the appearance of resonances attributed to diisopropylaniline in the ^{1}H NMR spectra. $LDH(SO_4)_{150}$-MAO-**1.5** did display reactivity, albeit extremely low (TON = 2.5 $mol_{C_4H_8}mol_W^{-1}$ after 24 hours). This is in good agreement with observations from the solid-state NMR and results obtained in Chapter Two, whereby high Al/W ratios for the homogeneous catalyst **2.5** and MAO, led to a significant reduction in reactivity. For example, Al/W = 40 was completely inactive towards ethylene dimerisation. The MAO on the surface

of $LDH(SO_4)_{150}$-MAO-**1.5** is believed to exert a similar influence, as Al/W = 60 for the immobilised species.

2.5 was also immobilised on $LDH(SO_4)_{150}$ in toluene in the absence of a co-catalyst, with grafting observed to occur at a much slower rate than for **1.5**. Such a result was surprising as it was envisaged that protonation of the methyl group would be facile compared to halide exchange. Analysis of the solid obtained after work-up by ^{13}C-{^{1}H} CPMAS SSNMR spectroscopy (Figure A155), yielded a near identical spectrum to that obtained for $LDH(SO_4)_{150}$-(**1.5** + 2MAO) formed by incipient wetness. Preservation of the imido fragment was observed by resonances at 22 and 16 ppm attributed to the isopropyl groups on the imido ligand. A broad resonance between 47 and 30 ppm is postulated to be due to remaining W–Me bonds for the immobilised species. Subsequent reaction with ethylene (1 bar, 100 °C, d_6-benzene), led to formation of diisopropylaniline. This is thought to occur due to the high concentration of proximal surface OH groups which may lead to decomposition and protonation of the imido group.

Independently, $LDH(SO_4)_{150}$-DEAC was prepared (LDH/Al = 2) by occasional swirling of $LDH(SO_4)_{150}$ and DEAC in toluene at 80 °C. **1.8** was chosen as the complex for immobilisation as it yielded the most active sMAO supported catalyst, but was also among the most active towards propene dimerisation in the analogous homogeneous $W(NR)Cl_4/AlEtCl_2$ system.[16] Grafting of **1.8** onto the surface of $LDH(SO_4)_{150}$-DEAC, resulted in a pale brown solid. However, no oligomerisation of ethylene was observed under conditions imposed previously (5 mg cat., 1 bar ethylene, 100 °C, d_6-benzene).

4.3.3. Dehydroxylation of the support

As decomposition attributed to high surface hydroxyl density had been observed with $LDH(SO_4)_{150}$, study of the effect that dehydroxylation of the support had on the immobilisation and subsequent activity towards oligomerisation was undertaken, employing the $LDH(SO_4)$ materials described in Chapter Three.

4.3.3.1. Catalyst loading

It was previously observed for the $LDH(CO_3)_{150}$ immobilised complexes (**1.5** and **2.5**), that a maximum loading of 10 wt% could be achieved, above which complete decolourisation of the supernatant was no longer observed. Having measured the hydroxyl concentration of $LDH(SO_4)$ after thermal treatment at various temperatures under vacuum, molar titrations of complex *vs* OH groups were attempted. $W\{N(2,6\text{-}F\text{-}C_6H_3)\}Me_3Cl$ (**2.7**) was chosen as any

decomposition of the complex in solution should be observable by a combination of ^{1}H and ^{19}F{^{1}H} NMR spectroscopy. One equivalent of complex based on the hydroxyl content (determined in Chapter Three) was mixed with LDH$(SO_4)_{300}$ and LDH$(SO_4)_{450}$ in J. Young valve NMR spectroscopy tubes at 23 °C in d_6-benzene containing Si$(SiMe_3)_4$ (3 µmol) as an internal standard. For LDH$(SO_4)_{300}$ a loading of 22 mol% was achieved after the standard 1 hour treatment, but a maximum loading of 37 mol% could be achieved after a reaction time of 24 hours. This total loading corresponds to 14.3 wt% complex matching observations for LDH$(CO_3)_{150}$-**2.5** where addition of 15 wt% complex resulted in incomplete immobilisation. No decomposition of the unsupported **2.7** was observed by either ^{1}H or ^{19}F{^{1}H) NMR spectroscopy. For LDH$(SO_4)_{450}$, a loading of 37 mol% for **2.7** was achieved after 1 hour, however, significant decomposition of the remaining complex in solution was observed overnight, yielding a bright yellow solution with multiple resonances between 4.5 and 5.5 ppm, and the presence of the aniline in the ^{1}H NMR spectrum. Multiple resonances were also observed in the ^{19}F{^{1}H} spectrum. At this temperature of thermal vacuum treatment, the defined layered LDH structure was lost and significant dehydroxylation had occurred. This may open up surface metal sites that can interact with the excess complex in solution, facilitating decomposition pathways. To further analyse the immobilised species, scale models of the proposed LDH surface after thermal vacuum treatment, and the molecular structure of **2.5** were constructed (Figure 4.16).

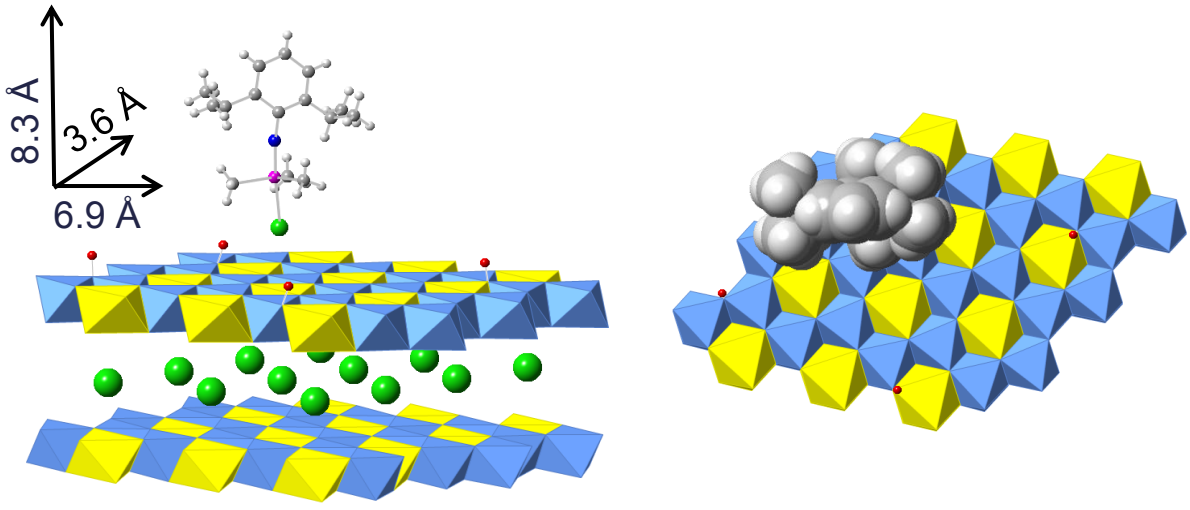


Figure 4.16. Scale models of the LDH$(SO_4)_{450}$ and **2.5** from side on (left) and above, with the space-filled model of **2.5** located directly above a surface hydroxyl (right).

From the top view, with the space-filled model of **2.5**, the bulk of the imido group is clearly observed. Whilst neighbouring OH groups appear to be located far enough away to

avoid interaction with the complex, it is clear that there is not enough space for a second molecule bind. This steric crowding may explain why only 37 mol% coverage can be achieved.

To ensure total complex immobilisation, a sample of **2.7** was grafted onto $LDH(SO_4)_{250/350/450}$ in a 10 mol% ratio based on the hydroxyl content (5.7 wt%). Complete immobilisation was observed after 1 hour swirling at 23 °C, yielding a pale yellow solid after work-up. $^{19}F\{^1H\}$ HPDEC SSNMR spectroscopy of the $LDH(SO_4)_{250}$ supported complex demonstrated a major species with a resonance centred at −134 ppm with a low intensity resonance observed at −83 ppm (Figure 4.17).

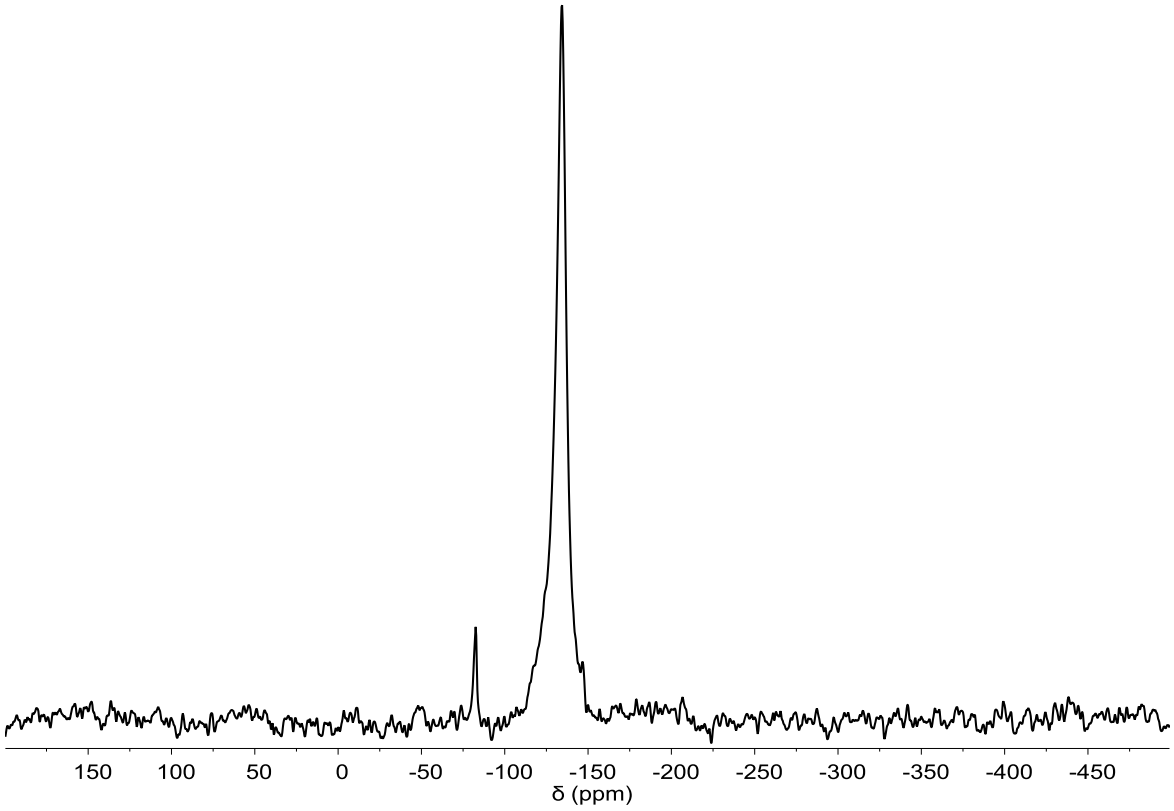


Figure 4.17. $^{19}F\{^1H\}$ HPDEC SSNMR spectrum (24 kHz, 400 MHz, 23 °C) of $LDH(SO_4)_{250}$-**2.7**.

The surface has a large effect on the electronics of the complex, as the resonances for the supported complex are shifted upfield when compared to molecular **2.5** (−117.6 ppm). From the $^{13}C\text{-}\{^1H\}$ CPMAS $\{^{19}F\}$ decoupled SSNMR spectrum only the imido carbons at 164 and 165 ppm could be observed, with no resonances observed for the remaining methyl groups (Figure A157). Attempted enhancement of the C–F carbons by $^{13}C\text{-}\{^{19}F\}$ CPMAS $\{^1H\}$ decoupled SSNMR spectroscopy resulted in no observable carbon resonances. The ^{27}Al DPMAS SSNMR spectrum (Figure A158) displays two resonances, an intense sharper

resonance at 6 ppm and a weaker broad resonance at 69 ppm, due to octahedrally and tetrahedrally coordinated aluminium in the treated LDH material, as was observed previously for LDH$(SO_4)_{150}$-**1.5** (*vide supra*).

FTIR spectra of LDH$(SO_4)_{250/350/450}$-**2.7** (Figure A159) display weak absorptions for the aromatic imido C–H stretches around 3,000 cm^{-1} and a sharp peak at 1,350 cm^{-1} attributed to the imido C–F stretch. The spectra are dominated by absorptions from the AMO-LDH support which match those observed in Chapter Three.

4.3.3.2. Reactivity towards α-olefins

The reactivities of LDH$(SO_4)_{250/350/450}$-**2.7** towards ethylene and 1-octene were tested and compared to the molecular analogue **2.7**. It was proposed that Lewis acidic aluminium sites present on the surface of the LDH, may be able to promote reactivity, thus removing the need for a co-catalyst. In all cases, no reactivity towards either ethylene (1 bar) or 1-octene (3 µL) was observed, even after 8 hours at 80 °C in d_6-benzene. Whilst **2.7** shows extremely low turnovers of ethylene to 1-butene without a co-catalyst, it promotes the metathesis of 1-octene to yield ethylene and 7-tetradecene. This indicates that either the defined trimethyl species has been lost after immobilisation, or that the surface deactivates the supported species, inhibiting alkylidene formation. To further probe this, a defined alkylidene complex would need to be immobilised on the treated LDH surface.

4.4. X-ray absorption spectroscopy (XAS) of supported complexes

In order to further understand the structure of the AMO-LDH supported complexes, five samples were analysed at the B18 beamline at Diamond Light Source for a W L1-edge XAS study. Due to the ordered structure of AMO-LDHs, LDH$(SO_4)_{150}$ impregnated with MAO has been successfully employed in a Zr K-edge EXAFS study of immobilised (EBI)$ZrCl_2$.[50] Furthermore, Rhers *et al*. have previously utilised EXAFS at the W L3-edge to probe the surface structure of W{N(2,6-^{i}Pr-C_6H_3)}(CH^{t}Bu)($CH_2{}^t$Bu)$_2$ grafted on $SiO_{2\text{-}(700)}$, demonstrating retention of the defined alkylidene on the surface.[51] For this reason, LDH$(CO_3)_{150}$ immobilised W(O)Cl_4, **1.5** and W{N(2,6-^{i}Pr-C_6H_3)}(CH^{t}Bu)($CH_2{}^t$Bu)$_2$ were chosen for this study. To aid the analysis, W(O)Cl_4 and **1.5** were run as standards by mixing with boron nitride prior to pelletisation. An FTIR study of LDH$(CO_3)_{150}$-W{N(2,6-^{i}Pr-C_6H_3)}(CH^{t}Bu)($CH_2{}^t$Bu)$_2$ indicated that retention of the defined structure of the LDH had been achieved by preservation of the absorptions from the defined complex in the immobilised spectrum (Figure 4.18).

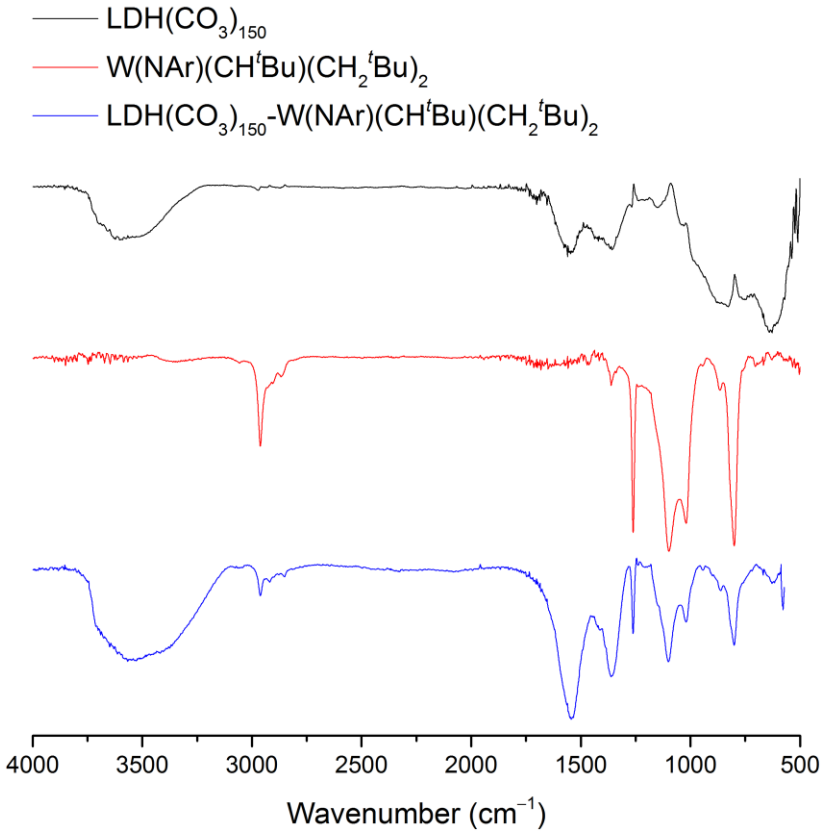


Figure 4.18. Comparison of the FTIR spectra for $LDH(CO_3)_{150}$, $W\{N(2,6\text{-}^{i}Pr\text{-}C_6H_3)\}(CH^{t}Bu)(CH_2{}^{t}Bu)_2$ and $LDH(CO_3)_{150}$-$W\{N(2,6\text{-}^{i}Pr\text{-}C_6H_3)\}(CH^{t}Bu)(CH_2{}^{t}Bu)_2$.

$LDH(CO_3)_{150}$ supported $W(O)Cl_4$, **1.5** and $W\{N(2,6\text{-}^{i}Pr\text{-}C_6H_3)\}(CH^{t}Bu)(CH_2{}^{t}Bu)_2$ were pressed into pellets as pure samples. The samples were then mounted on Kapton tape inside an air sensitive cell and the W L1-edge X-ray absorption spectra measured (Figure 4.19).

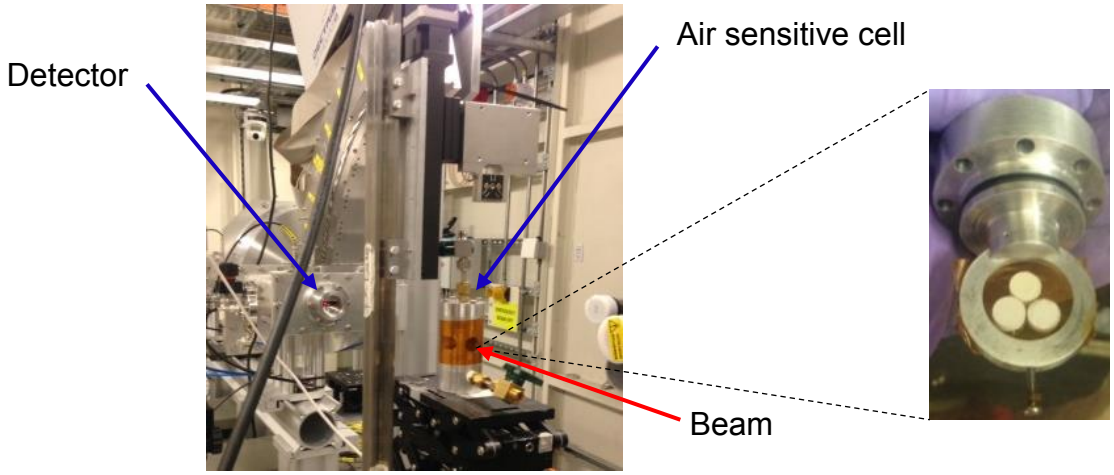


Figure 4.19. B18 beamline at Diamond Light Source. Pellets were supported on Kapton tape and loaded into an air sensitive cell.

The XAS spectra for the samples is shown in Figure 4.20. The main edge arises from the symmetry allowed W 2s→6p transition, and can be measured from the maxima in the first

derivative spectra (Figure A160). The maxima in the XAS spectra, known as the white line energy, arises from ejection of a core 2s electron into the continuum. Interestingly, for the LDH$(CO_3)_{150}$ immobilised species a prominent pre-edge feature can be observed at ~12,103 eV. This stems from a 2s→5d transition, which is symmetry forbidden in octahedral systems. In these compounds a distortion away from O_h symmetry must be occurring, with mixing of the p orbitals of tungsten and the ligand into empty d orbitals.[52] In contrast, no pre-edge feature is observed for **1.5** which adopts an octahedral arrangement about tungsten. This dissymmetry may explain why an absorption attributed to the W–N–C symmetric stretch is apparent at 1,250 cm^{-1} for supported species, but cannot be assigned for the homogeneous complexes.

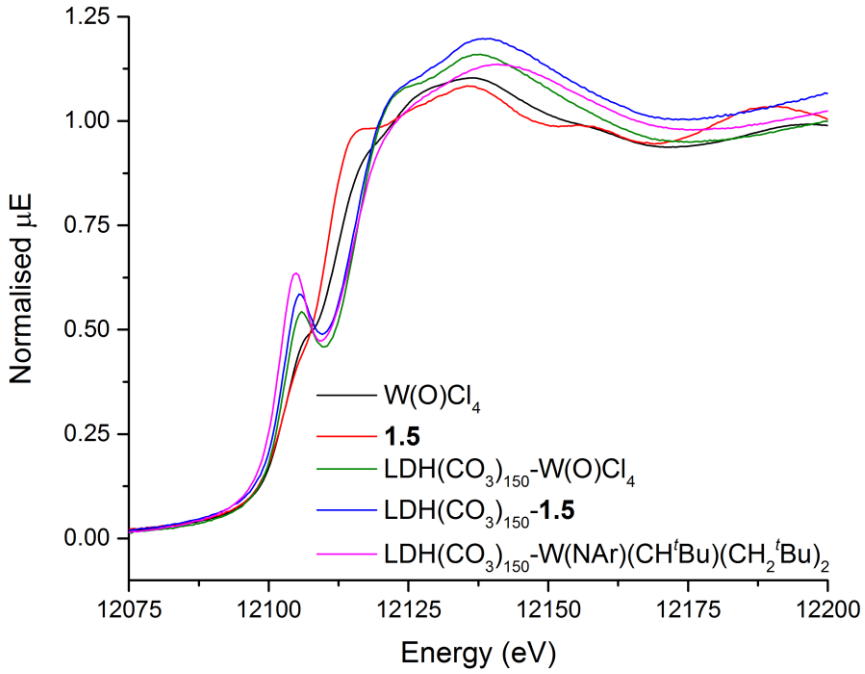


Figure 4.20. XAS spectra for the molecular and Mg_3Al-CO_3 AMO-LDH supported complexes, focussed on the XANES region. Ar = 2,6-^{i}Pr-C_6H_3.

The edge energies (Table 4.4) indicate that both unsupported and supported $W(O)Cl_4$ are more electron poor than their diisopropylphenyl imido analogues, requiring higher energies to promote core electrons. LDH$(CO_3)_{150}$-**1.5** has a slightly higher edge energy than the Schrock alkylidene immobilised species, attributed to the electron withdrawing effects of the chloride ligands compared to alkyl groups. The pre-edge feature for the alkylidene complex is the most intense of all. For the silica immobilised system, the best fit model of the EXAFS data indicated a pseudo-tetrahedral *syn* structure,[51] which would lead to a relaxation of the electronic selection rules. Unfortunately, the EXAFS data obtained for the AMO-LDH

supported complexes were too weak to allow fitting of any structural parameters for the complexes, ascribed to the low loadings on the surface.

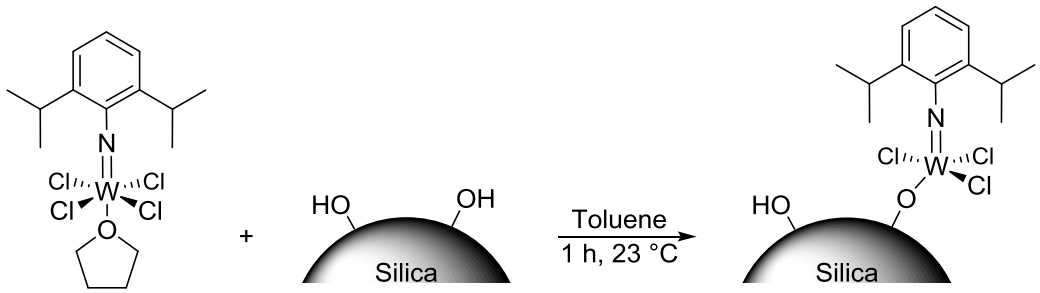
Table 4.4. Selected W L1-edge XANES data for $W(O)Cl_4$, **1.5**, $LDH(CO_3)_{150}$-$W(O)Cl_4$, $LDH(CO_3)_{150}$-**1.5** and $LDH(CO_3)_{150}$-$W\{N(2,6\text{-}^{i}Pr\text{-}C_6H_3)\}(CH^{t}Bu)(CH_2{}^{t}Bu)_2$.

Sample	Pre-edge energy (eV)	Edge energy (eV)	White line energy (eV)
$W(O)Cl_4$	12,103.5[a]	12,111.8	12,133.6
1.5	12,103.1[b]	12,110.5	12,118.8
$LDH(CO_3)_{150}$-$W(O)Cl_4$	12,102.7	12,117.0	12,126.7
$LDH(CO_3)_{150}$-**1.5**	12,103.1	12,116.0	12,124.9
$LDH(CO_3)_{150}$-$W(NAr)(CH^{t}Bu)(CH_2{}^{t}Bu)_2$	12,102.5	12,115.3	12,123.4

Pre-edge and edge energies determined from the 1st derivative. [a] Weak feature. [b] Very weak feature, only observed from the 1st derivative. Ar = $2,6\text{-}^{i}Pr\text{-}C_6H_3$.

4.5. Silica supported 1.5 ($SiO_{2\text{-}(150)}$-1.5)

Immobilisation of **1.5** onto Aerosil 500 fumed silica, thermally treated under vacuum at 150 °C ($SiO_{2\text{-}(150)}$), was conducted in toluene at 23 °C for 1 hour (Scheme 4.9).



Scheme 4.9. Supporting of $W\{N(2,6\text{-}^{i}Pr\text{-}C_6H_3)\}Cl_4(THF)$ (**1.5**) on $SiO_{2\text{-}(150)}$.

The resulting tan solid after work-up was analysed by $^{13}C\text{-}\{^{1}H\}$ CPMAS SSNMR spectroscopy, which appeared to show preservation of the ^{i}Pr groups for the imido fragment on the surface (23 and 17 ppm, Figure 4.21).

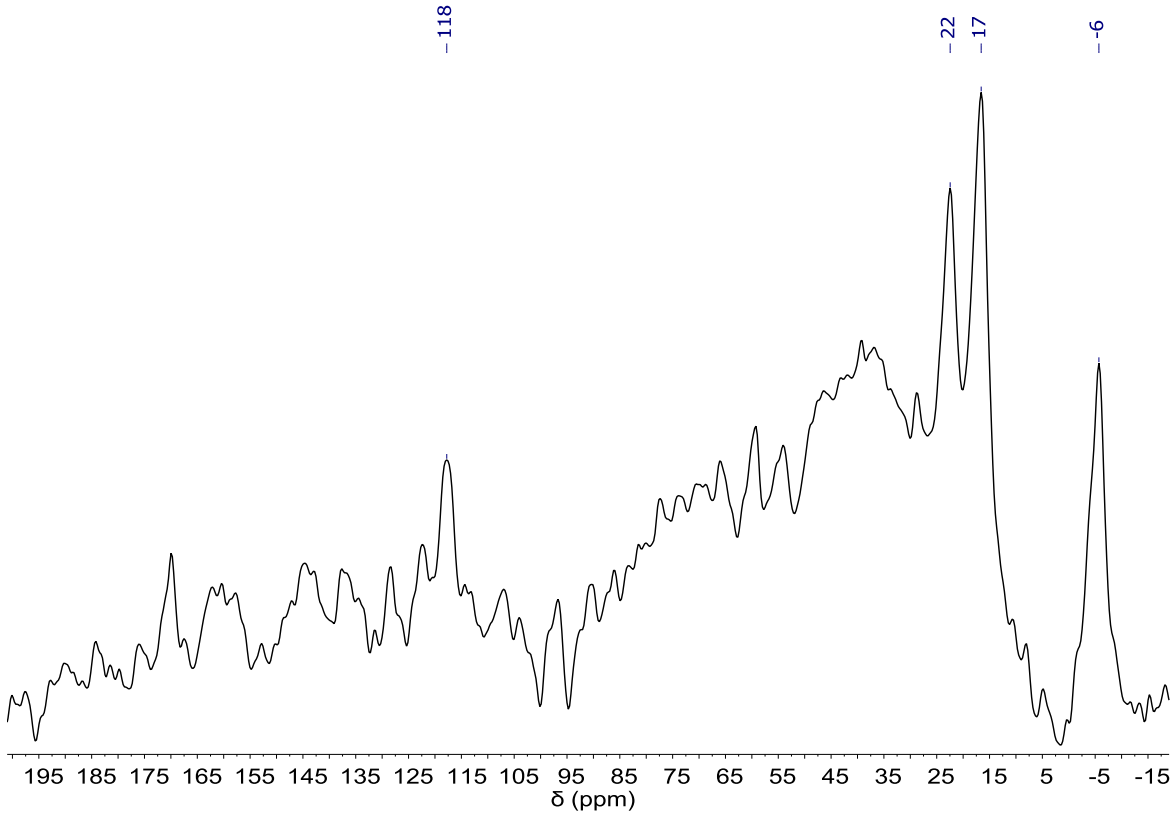


Figure 4.21. ^{13}C-{^{1}H} CPMAS SSNMR spectrum (10 kHz, 400 MHz, 23 °C) of $SiO_{2\text{-}(150)}$-**1.5**.

The immobilised complex was tested for its reactivity towards ethylene in solution with addition of MAO as a co-catalyst, as was previously described for AMO-LDH immobilised complexes (5 mg cat., Al/W = 80, 1 bar ethylene, d_6-benzene). Selective dimerisation to yield solely 1-butene was observed for this system (TON = 9.39 $mol_{C_2H_4}mol_W^{-1}$ after 20 hours).

These results were compared with $LDH(SO_4)_{150}$ and sMAO supported **1.5,** along with the most active **2.5**/MAO (Al/W = 2) system under analogous conditions (1 bar ethylene, 100 °C, d_6-benzene) (Figure 4.22). The AMO-LDH and silica supported species display much lower activities than the homogeneous catalyst (observed activities were 30 and 92% lower for $SiO_{2\text{-}(150)}$-**1.5** and $LDH(SO_4)_{150}$-**1.5** respectively). The difference between them is attributed to the different electronic properties of the supports. The sMAO supported catalyst is by far the most active and selective, displaying almost complete selectivity for 1-butene with an activity almost 7 times that of the homogenous **2.5**/MAO system (Al/W = 2) (4.0 *vs* 0.6 $mol_{C_2H_4}mol_W^{-1}h^{-1}bar^{-1}$ after 38 hours).

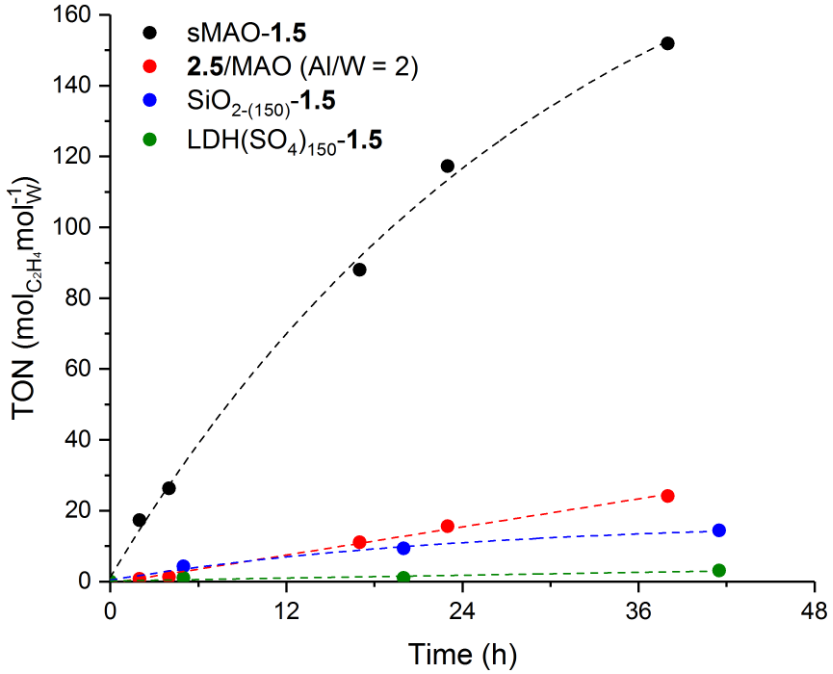


Figure 4.22. Comparison of the turnover numbers (TONs) of sMAO, $SiO_{2-(150)}$ and $LDH(SO_4)_{150}$ supported **1.5** with the homogeneous **2.5**/MAO system (Al/W = 2). 1 bar ethylene, 100 °C, d_6-benzene, pyridine internal standard, for $SiO_{2-(150)}$-**1.5** and $LDH(SO_4)_{150}$-**1.5** MAO (2 mg, Al/W = 40) was added as a co-catalyst.

4.6. Supported ruthenium carbene complexes

In 2008, Sels and co-workers demonstrated that the second generation Hoveyda-Grubbs catalyst (**HG2**), could be grafted on silica powder or pellets by simple mixing in toluene.[53] The resulting green solids were active for a variety of alkene metathesis reactions. Later, it was shown that the interaction between the complex and silica surface was due to physisorption, through hydrogen bonding interactions.[54] The strength of this interaction depended on the surface silanol concentration with the complex displaying particular affinity for germinal silanols. For this reason, low calcination temperatures were preferred. The resulting catalyst was shown to be as active as the homogeneous system for the metathesis of *cis*-cyclooctene, and could be used in a fixed bed reactor. To avoid complex leaching apolar solvents (hexane) were required, indicating the weak nature of the interaction between the complex and surface.

Based on these findings, it was proposed that ruthenium carbene complexes may show some affinity towards the surface hydroxyl groups of layered double hydroxides. To test this, both Grubbs second generation (**G2**) and Hoveyda-Grubbs second generation (**HG2**) complexes were reacted with $LDH(SO_4)_{250/350/450}$. However, in all cases, no immobilisation of

the complex was observed, and the AMO-LDH powders obtained after work-up were shown to be inactive towards 1-octene, which the pure complex readily self-metathesises.

Immobilisation on sMAO was also attempted as the carbene complexes contain a halide ligand that can be activated.[55] Mixing either **G2** or **HG2** with sMAO (Al/Ru = 150) in toluene resulted in almost instantaneous grafting, affording pale yellow and salmon pink solids respectively after work-up.

Reaction of either sMAO-**G2** or sMAO-**HG2** with ethylene (1 bar, d_6-benzene, 23 °C) yielded only a small amount of 1-butene after 1 hour. Heating either reaction at 75 °C, however, led to no further formation, indicative of decomposition of the active sites. The solid catalysts were also reacted with 1-octene (3 µL, d_6-benzene, 23 °C) and yielded a small amount of ethylene and 7-tetradecene. Even with heating at 75 °C, the supported species were markedly less active than the pure carbene complexes, suggesting the aluminoxane support has a poisoning effect.

4.7. Conclusions

Defined molecular complexes of the types $W(NR)Cl_4(THF)$ and $W(NR)Me_3Cl$ have been immobilised on solid polymethylaluminoxane (sMAO), layered double hydroxides and silica, and tested for their reactivity towards linear alpha olefins. The sMAO support was demonstrated to methylate $W(NR)Cl_4(THF)$ complexes *in situ* during grafting, to yield supported species (sMAO-(**1.1–1.8**)) analogous to the $W(NR)Me_3Cl$ complexes described in Chapter Two. For sMAO-**1.**5 and sMAO-**1.7** SSNMR spectroscopy indicated preservation of the defined structures on the surface. This was further supported by comparison with the $^{13}C\{^1H\}$ CPMAS and $^{19}F\{^1H\}$ HPDEC SSNMR spectra of **2.7** and $W\{N(2,6\text{-}F\text{-}C_6H_3)\}(^{13}CH_3)_3Cl$ (**2.7***) immobilised on sMAO (sMAO-**2.7***), which both displayed two methyl environments in the solid-state. For sMAO-**1.8**, C–F activation was observed by $^{19}F\{^1H\}$ HPDEC SSNMR spectroscopy between the complex and the surface, yielding surface Al–F groups. Immobilisisation of $W(NR)Cl_4(THF)$ complexes was observed to yield more stable species than $W(NR)Me_3Cl$ which leached from the surface. This was attributed to interactions between the immobilised complex and proximal halide groups deposited during immobilisation. Testing the reactivity of sMAO-(**1.1**–**1.8**) towards ethylene established that electron withdrawing imido moieties yielded the most active catalysts, with sMAO-**1.8** the most active and selective for ethylene dimerisation (activity of 5.65 $mol_{C2H4}mol_W^{-1}h^{-1}bar^{-1}$ after 8 hours and 91% selectivity towards 1-butene). Of the alkyl

substituted catalysts, the diisopropylphenylimido moiety sMAO-**1.5** yielded the highest activity attributed to the steric demand and more electron deficient nature of this group, potentially increasing rates of reductive elimination. This complexes was also active for dimerisation in the gas phase. Utilising sMAO-**1.6,** solvent, temperature and loading studies led to optimisation of the reaction conditions (d_5-chlorobenzene, 75 °C and W:Al = 1:150). Scale-up reactions at high pressure (up to 19 bar) with sMAO-**1.5**, yielded disappointing results, with very low activities observed. In one case 3.5 g of polyethylene was formed and was shown to be UHMWPE by FTIR and DSC analysis.

For Mg_3Al-X AMO-LDH supported **1.5** (X = SO_4, CO_3 or NO_3), the interlayer anion had a large effect on reactivity and selectivity of the reaction. $LDH(SO_4)_{150}$-**1.5** was the most active for the selective dimerisation reaction followed by $LDH(CO_3)_{150}$-**1.5** with $LDH(NO_3)_{150}$-**1.5** yielding solely polymer. Utilising **2.7**, the dehydroxylated Mg_3Al-SO_4 AMO-LDH samples described in Chapter Three were tested as supports. A loading study with $LDH(SO_4)_{300/450}$ showed that a maximum loading of 37 mol% based on the molar surface hydroxyl concentration could be achieved, matching well with steric models of the immobilised species. Despite demonstrating that the imido fragment remained intact after grafting, $LDH(SO_4)_{250/350/450}$-**2.7** displayed no activity towards ethylene or 1-octene, indicating that either decomposition had occurred or binding of the support deactivates the complex. An XAS study at the W L1-edge of AMO-LDH immobilised complexes, showed a change in structure upon grafting, with the symmetry forbidden 2s→5d transition relaxed, leading to a large pre-edge feature due to p/d mixing.

Finally, the ruthenium carbene complexes **G2** and **HG2** were reacted with AMO-LDHs and sMAO. Unlike silica, these complexes were not able to physisorb onto the surface of the AMO-LDH. Reaction did occur with sMAO, although the support had a poisoning effect on the catalyst activity, which struggled to activate the self-metathesis of 1-octene.

4.8. References

1. C. Copéret, A. Comas-Vives, M. P. Conley, D. P. Estes, A. Fedorov, V. Mougel, H. Nagae, F. Núñez-Zarur, and P. A. Zhizhko, *Chem. Rev.*, 2016, **116**, 323–421.
2. J.-M. Basset, R. Psaro, D. Roberto, and R. Ugo, Eds., *Modern Surface Organometallic Chemistry*, Wiley-VCH Verlag GmbH & Co. KGaA, Weinheim, Germany, 2009.
3. R. Schowner, W. Frey, and M. R. Buchmeiser, *J. Am. Chem. Soc.*, 2015, **137**, 6188–6191.
4. M. Pucino, V. Mougel, R. Schowner, A. Fedorov, M. R. Buchmeiser, and C. Copéret, *Angew. Chem. Int. Ed.*, 2016, **55**, 4300–4302.
5. J. R. Severn, J. C. Chadwick, R. Duchateau, and N. Friederichs, *Chem. Rev.*, 2005, **105**, 4073–4147.
6. E. Y.-X. Chen and T. J. Marks, *Chem. Rev.*, 2000, **100**, 1391–1434.

7. E. Kaji and E. Yoshioka, *Solid polymethylaluminoxane composition and process for manufacturing same*, 2010, WO2010055652.
8. A. F. R. Kilpatrick, J.-C. Buffet, P. Nørby, N. H. Rees, N. P. Funnell, S. Sripothongnak, and D. O'Hare, *Chem. Mater.*, 2016, **28**, 7444–7450.
9. D. A. X. Fraser, Z. R. Turner, J.-C. Buffet, and D. O'Hare, *Organometallics*, 2016, **35**, 2664–2674.
10. F. Ghiotto, C. Pateraki, J. Tanskanen, J. R. Severn, N. Luehmann, A. Kusmin, J. Stellbrink, M. Linnolahti, and M. Bochmann, *Organometallics*, 2013, **32**, 3354–3362.
11. T. J. Williams, *Part II Thesis, University of Oxford*, 2016.
12. P. J. Chupas and C. P. Grey, *J. Catal.*, 2004, **224**, 69–79.
13. J. Terao, S. A. Begum, Y. Shinohara, M. Tomita, Y. Naitoh, and N. Kambe, *Chem. Commun.*, 2007, 855–857.
14. J. Terao, M. Nakamura, and N. Kambe, *Chem. Commun.*, 2009, 6011–6013.
15. W. R. H. Wright, A. S. Batsanov, A. M. Messinis, J. A. K. Howard, R. P. Tooze, M. J. Hanton, and P. W. Dyer, *Dalton Trans.*, 2012, **41**, 5502–5511.
16. H. Olivier and P. Laurent-Gérot, *J. Mol. Catal. A Chem.*, 1999, **148**, 43–48.
17. L. Wideman, *Preparation of 1-butene*, 1974, US3813453 (A).
18. E. A. Zuech, *J. Polym. Sci. Part A Polym. Chem.*, 1972, **10**, 3665–3672.
19. J. P. Le Ny and J. A. Osborn, *Organometallics*, 1991, **10**, 1546–1550.
20. C. Temple, A. Jabri, P. Crewdson, S. Gambarotta, I. Korobkov, and R. Duchateau, *Angew. Chem. Int. Ed.*, 2006, **45**, 7050–7053.
21. A. Jabri, P. Crewdson, S. Gambarotta, I. Korobkov, and R. Duchateau, *Organometallics*, 2006, **25**, 715–718.
22. I. Vidyaratne, G. B. Nikiforov, S. I. Gorelsky, S. Gambarotta, R. Duchateau, and I. Korobkov, *Angew. Chem. Int. Ed.*, 2009, **48**, 6552–6556.
23. A. Kermagoret, R. N. Kerber, M. P. Conley, E. Callens, P. Florian, D. Massiot, F. Delbecq, X. Rozanska, C. Copéret, and P. Sautet, *J. Catal.*, 2014, **313**, 46–54.
24. W. Kaminsky, S. Lenk, V. Scholz, H. W. Roesky, and A. Herzog, *Macromolecules*, 1997, **30**, 7647–7650.
25. Y. Chen, C. L. Stern, and T. J. Marks, *J. Am. Chem. Soc.*, 1997, **119**, 2582–2583.
26. Y. X. Chen, M. V. Metz, L. Li, C. L. Stern, and T. J. Marks, *J. Am. Chem. Soc.*, 1998, **120**, 6287–6305.
27. P. Cossee, *J. Catal.*, 1964, **3**, 80–88.
28. R. Schrock, S. McLain, and J. Sancho, *Pure Appl. Chem.*, 1980, **52**, 729–732.
29. S. J. McLain and R. R. Schrock, *J. Am. Chem. Soc.*, 1978, **100**, 1315–1317.
30. J. D. Fellmann, G. A. Rupprecht, and R. R. Schrock, *J. Am. Chem. Soc.*, 1979, **101**, 5099–5101.
31. S. Tobisch, *Organometallics*, 2007, **26**, 6529–6532.
32. M. J. Hanton, L. Daubney, T. Lebl, S. Polas, D. M. Smith, and A. Willemse, *Dalton Trans.*, 2010, **39**, 7025–7037.
33. W. R. H. Wright, A. S. Batsanov, J. A. K. Howard, R. P. Tooze, M. J. Hanton, and P. W. Dyer, *Dalton Trans.*, 2010, **39**, 7038–7045.
34. C. Reichardt and T. Welton, *Solvents and Solvent Effects in Organic Chemistry*, Wiley-VCH Verlag GmbH & Co. KGaA, Weinheim, Germany, 2010, vol. 16.
35. F. Cataldo, *Eur. Chem. Bull.*, 2015, **4**, 92–97.
36. P. R. Elowe, C. McCann, P. G. Pringle, S. K. Spitzmesser, and J. E. Bercaw, *Organometallics*, 2006, **25**, 5255–5260.
37. Y. Zhu, L. Chang, and S. Yu, *J. Therm. Anal.*, 1995, **45**, 329–333.
38. F. M. Mirabella and A. Bafna, *J. Polym. Sci. Part B Polym. Phys.*, 2002, **40**, 1637–1643.
39. S. C. Moyses and J. Zukermann-Schpector, *Polym. J.*, 2004, **36**, 679–683.
40. F. Cover and S. M. Kurtz, *The UHMWPE Handbook: Ultra-High Molecular Weight Polyethylene in Total Joint Replacement*, Academic Press, 2004.
41. C. Chen, A. Wangriya, J.-C. Buffet, and D. O'Hare, *Dalton Trans.*, 2015, **44**, 16392–16398.
42. C. Chen, M. Yang, Q. Wang, J.-C. Buffet, and D. O'Hare, *J. Mater. Chem. A*, 2014, **2**, 15102–

15110.
43. Q. Wang, and D. O'Hare, *Chem. Comm.*, 2013, **49**, 6301–6303.
44. D. O'Hare and Q. Wang, *Modification of Layered Double Hydroxides*, 2014, WO2014051530 (A2).
45. M. K. Samantaray, E. Callens, E. Abou-Hamad, A. J. Rossini, C. M. Widdifield, R. Dey, L. Emsley, and J.-M. Basset, *J. Am. Chem. Soc.*, 2014, **136**, 1054–1061.
46. A. van der Pol, B. L. Mojet, E. van de Ven, and E. de Boer, *J. Phys. Chem.*, 1994, **98**, 4050–4054.
47. J. Rocha, M. del Arco, V. Rives, and M. A. Ulibarri, *J. Mater. Chem.*, 1999, **9**, 2499–2503.
48. D. O'Hare, *Drug delivery system comprising a drug intercalated between a layered double hydroxide*, 2002, WO2002047729 A2.
49. J. E. Bercaw and P. R. Elowe, *Solvent, additive and co-catalyst effects for ethylene oligomerization catalysis*, 2009, WO 2009046144 A1.
50. J.-C. Buffet, N. Wanna, T. A. Q. Arnold, E. K. Gibson, P. P. Wells, Q. Wang, J. Tantirungrotechai, and D. O'Hare, *Chem. Mater.*, 2015, **27**, 1495–1501.
51. B. Rhers, A. Salameh, A. Baudouin, E. A. Quadrelli, M. Taoufik, C. Copéret, F. Lefebvre, J.-M. Basset, X. Solans-Monfort, O. Eisenstein, W. W. Lukens, L. P. H. Lopez, A. Sinha, and R. R. Schrock, *Organometallics*, 2006, **25**, 3554–3557.
52. S. Yamazoe, Y. Hitomi, T. Shishido, and T. Tanaka, *J. Phys. Chem. C*, 2008, **112**, 6869–6879.
53. B. Van Berlo, K. Houthoofd, B. F. Sels, and P. A. Jacobs, *Adv. Synth. Catal.*, 2008, **350**, 1949–1953.
54. A. Dewaele, B. Van Berlo, J. Dijkmans, P. a. Jacobs, and B. F. Sels, *Catal. Sci. Technol.*, 2016, **6**, 2580–2597.
55. A. Dewaele, F. Verpoort, and B. Sels, *ChemCatChem*, 2016, **8**, 3010–3030.

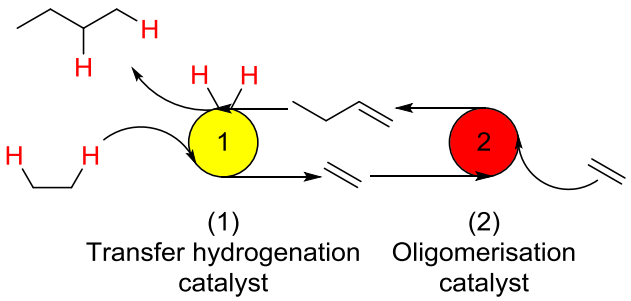
Chapter Five – Supported iridium pincer transfer hydrogenation catalysts towards tandem hydrocarbon upgrading

"Chemistry without catalysis, would be a sword without a handle, a light without brilliance, a bell without sound." **Alwin Mittasch**

5.1. Introduction

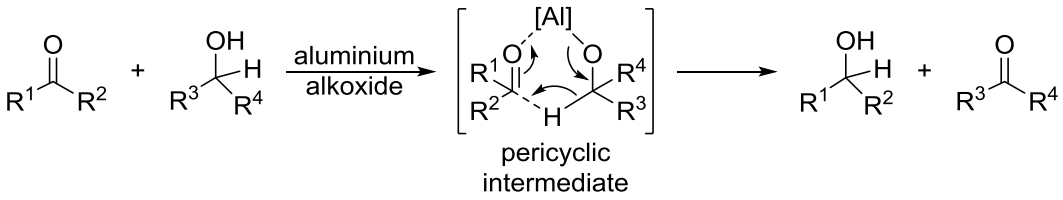
5.1.1. Transfer hydrogenation

In order to upgrade hydrocarbon feedstocks *via* tandem catalysis, alkane subunits must first undergo dehydrogenation to yield an alkene which can then be converted to a higher homologue. Hydrogenation of this new olefin, utilising the hydrogen abstracted from the starting alkane, would yield the desired upgraded alkane product (Scheme 5.1).[1] Such a method of H_2 addition from independent donors and acceptors that are non-hydrogen sources is termed transfer hydrogenation.[2]



Scheme 5.1. Idealised reaction scheme for the upgrading of ethane to butane, utilising transfer hydrogenation and ethylene dimerisation catalysts orthogonally in tandem.[1]

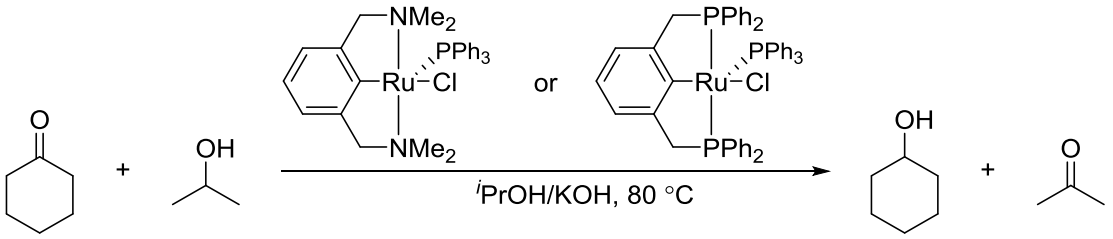
One of the most renowned transfer hydrogenation reactions, the Meerwein-Ponndorf-Verley reaction, was discovered in 1925 and involves hydrogen donation from a primary alcohol to a ketone by employing an aluminium alkoxide promoter (Scheme 5.2).[3–5] The beauty of this approach lies in the high chemoselectivity, whereby aldehydes are reduced before ketones, and alkenes and alkynes remain untouched. This has resulted in its widespread implementation in organic synthesis.[6]



Scheme 5.2. Meerwein-Ponndorf-Verley reaction,[3–5] which proceeds *via* a six-membered pericyclic transition state.[7]

In 1952, Linstead *et al*. demonstrated that palladium black could catalyse the transfer hydrogenation of a series of unsaturated compounds under reflux in saturated solvents.[8] For example, ethylene could be converted to ethane in 100% yield after 43 hours in refluxing in THF. Late transition metals (groups 8–11), have since been demonstrated to be highly

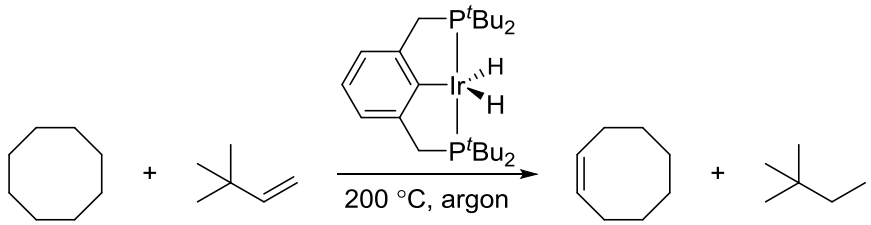
effective for transfer hydrogenation reactions, most notably ruthenium and iridium complexes, with multiple ligand architectures yielding active catalysts.[9] Of these, tridentate pincer ligands have been extensively employed due to their high stability and tuneable steric and electronic properties, yielding highly active catalysts.[10] For example, switching of the pincer backbone from 2,6-(CH_2NMe_2)-C_6H_3 (NCN) to 2,6-(CH_2PPh_2)-C_6H_3 (^{Ph}PCP) in the ruthenium complexes Ru(NCN)PPh_3Cl and Ru(^{Ph}PCP)PPh_3Cl, led to a dramatic increase in the turnover frequency (TOF) for the transfer hydrogenation of cyclohexanone to cyclohexanol with ^{i}PrOH/KOH as the reducing agent (1,100 *vs* 10,000 $moles_{cyclohexanone}moles^{-1}{}_{Ru}h^{-1}$, 98% conversion achieved after 3.3 and 1.8 hours respectively, cyclohexanone (200 mmol), ^{i}PrOH (200 mL), [KOH]/[Ru] = 20, 80 °C) (Scheme 5.3).[11]



Scheme 5.3. Variation in the pincer ligand from Ru(NCN)PPh_3Cl to Ru(^{Ph}PCP)PPh_3Cl increases the TOF for transfer hydrogenation of cyclohexanone and isopropanol from 1,100 to 10,000 $moles_{cyclohexanone}moles^{-1}{}_{Ru}h^{-1}$.[11]

In 1976, Shaw and co-workers reported the synthesis of the bulky diphosphine pro-ligand 2,6-$(CH_2P^tBu_2)$-C_6H_4 (^{tBu}PCP) by reaction of di-*tert*-butyl phosphine with 1,3-bis(bromomethyl)benzene to yield the diphosphonium salt, followed by treatment with sodium acetate to yield the desired product.[12] Bulky tertiary di-*tert*-butyl phosphines are known to bond less strongly to metal centres than sterically less demanding diphosphines (*e.g.* PEt_3). For example, PEt_3 readily reacts with nickel chloride to yield *trans*-{$NiCl_2(PEt_3)_2$}, whereas reaction with P^tBu_2Et does not result in complexation.[12] However, the nickel complex, Ni(^{tBu}PCP)Cl, is afforded almost instantaneously with the bulky PCP ligand from hydrated nickel chloride in ethanol at 20 °C. Metalation occurs at the carbon *ortho* to the two $CH_2P^tBu_2$ groups, yielding a tridentate bonding motif. Complexes of rhodium and iridium could readily be formed with this ligand by refluxing with the hydrated metal trichloride salts in ^{i}PrOH, yielding the hydrido chloride complexes M(^{tBu}PCP)HCl (M = Ir or Rh). The coordinatively unsaturated iridium complex was seen to bind carbon

monoxide, with the hydride and CO ligands in a *trans* arrangement. Errington *et al*. demonstrated that the iridium PCP hydrido chloride complex bearing an alkyl backbone, Ir{(^{t}Bu$_2$P)C$_2$H$_4$CHC$_2$H$_4$(P^{t}Bu$_2$)}HCl, could be converted to the tetra-hydride complex, Ir{(^{t}Bu$_2$P)C$_2$H$_4$CHC$_2$H$_4$(P^{t}Bu$_2$)}H$_4$, by reaction with NaO^{i}Pr/^{i}PrOH in a H_2 atmosphere.[13] McLoughlin *et al*. showed that the corresponding dihydride complex could be generated by heating this tetrahydride complex under dynamic vacuum.[14] Jenson and co-workers utilised this knowledge to synthesise Ir($^{t\text{Bu}}$PCP)H$_2$, which was shown to be stable up to 200 °C, and was catalytically competent towards the transfer hydrogenation of cyclooctane (COA) to cyclooctene (COE), employing *tert*-butyl ethylene (TBE) as a sacrificial hydrogen acceptor (12 turnovers min^{-1}, 200 °C, COA (37 mmol), TBE (1.6 mmol), Ir($^{t\text{Bu}}$PCP)H$_2$ (0.005 mmol)) (Scheme 5.4).[15]



Scheme 5.4. Transfer dehydrogenation of cyclooctane (COA) and *tert*-butyl ethylene (TBE) catalysed by Ir($^{t\text{Bu}}$PCP)H$_2$ to yield cyclooctene (COE) and *tert*-butyl ethane (TBA).[15]

High concentrations of TBE were observed to inhibit reactivity, thus high TONs are achieved by periodic addition of TBE to the reaction. Activity is strongly inhibited by the presence of nitrogen in the system, which competes with the alkane for coordination at the metal centre. Thus, to achieve high activities, all vestiges of nitrogen were removed under vacuum, and reactions were conducted under argon. Lee *et al.* reported that reaction of Ir($^{t\text{Bu}}$PCP)H$_2$ with excess TBE in a cyclohexane solution under 1 atm of N_2 resulted in stoichiometric hydrogenation and the formation of a bridging dinitrogen complex, {Ir($^{t\text{Bu}}$PCP)}$_2$(μ-N$_2$) (Figure 5.1).[16] Formation of this species, in which the two $^{t\text{Bu}}$PCP ligands are mutually perpendicular and encapsulate the bridging nitrogen ligand, is proposed to completely shut down any catalytic activity at the iridium centre.

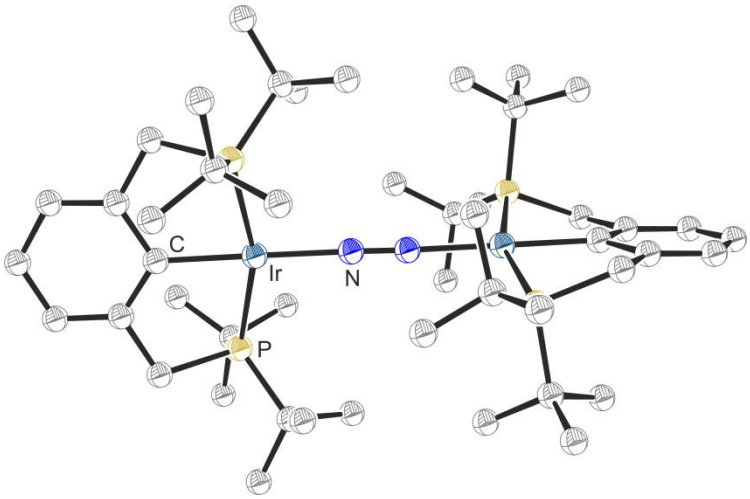


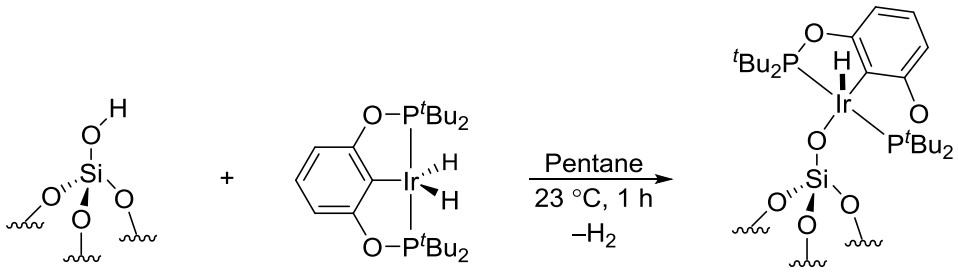
Figure 5.1. Molecular structure of $\{Ir(^{tBu}PCP)\}_2(\mu\text{-}N_2)$.[16] Hydrogen atoms omitted for clarity, ellipsoids shown as isotropic spheres.

One of the big challenges in transfer hydrogenation has been the development of acceptorless dehydrogenation reactions, which removes excess organic waste generated by the use of sacrificial hydrogen acceptors (*e.g.* TBE).[17] In such reactions, hydrogen liberated from the substrate can be released as gaseous H_2 or used to hydrogenate an intermediate in the catalytic cycle, known as 'hydrogen autotransfer'. In 1997, Xu *et al*. demonstrated that $Ir(^{tBu}PCP)H_2$ could promote the acceptorless dehydrogenation of COA to liberate COE and molecular dihydrogen, with 190 turnovers obtained after 120 hours ($[Ir(^{tBu}PCP)H_2]$ = 2 mM, refluxing COA, argon atmosphere).[18] This system was also effective for the acceptorless dehydrogenation of cyclodecane under reflux conditions, to yield *cis*- and *trans*-cyclodecene (360 turnovers after 24 hours, 201 °C, 1 mM cat.). This was despite the fact that cyclodecane has a much larger dehydrogenation enthalpy than cyclooctane (30–33 *vs* 23 $kcalmol^{-1}$).

5.1.2. Supported pincer iridium complexes

Due to their high activity and thermal stability, immobilisation of PCP and POCOP (2,6-(O-PR_2)-$C_6R'_3$) pincer iridium complexes on solid supports to yield heterogeneous systems has been reported.[19–22] One common approach to doing so is to tailor the phenyl backbone in the para position, allowing for adsorption on aluminas or grafting to silica, Merrifield resin or metal organic frameworks *via* a pendant group (*e.g.* alkoxy silane groups for silica grafting).[19,20] Whilst the silica and Merrifield resin immobilised POCOP iridium complexes showed low activity for the transfer hydrogenation with COA and TBE, the complexes adsorbed on alumina demonstrated high activities (TONs of up to 7,000 for the COA/TBE transfer hydrogenation reaction) and were shown to be recyclable (up to 8 times).[19]

In 2013, Rimoldi *et al*. reported the immobilisation of Ir(POCOP)H_2 (POCOP = 2,6-(O-P^{t}Bu$_2$)-C_6H_3) on the surface silanols of mesoporous silica *via* surface organometallic chemistry (SOMC), to yield $SiO_{2\text{-}(400)}$-Ir(POCOP)H (Scheme 5.5). Grafting of the complex was confirmed by ^{1}H and ^{31}P SSNMR and FTIR spectroscopy as well as ICP analysis, which indicated formation of a square pyramidal mono-hydride complex.



Scheme 5.5. Immobilisation of Ir(POCOP)H_2 on $SiO_{2\text{-}(400)}$ to afford $SiO_{2\text{-}(400)}$-Ir(POCOP)H.

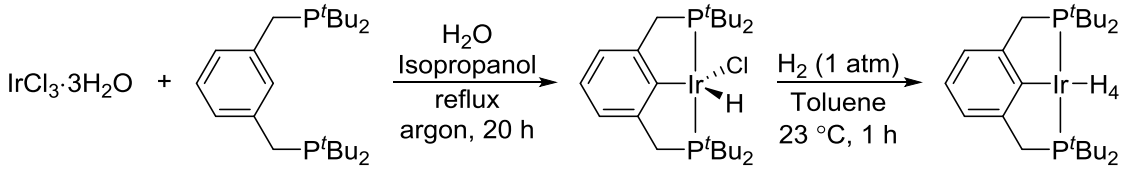
The immobilised species was tested for its capability to hydrogenate ethylene and propylene (2 bar total pressure, 50:50 H_2:alkene, 20 mg cat., 6.1 wt% loading Ir(POCOP)H_2, 23 °C). Complete conversion to the alkane was observed after 9 and 15 hours for ethylene and propylene respectively. Heating the reaction at 70 °C, yielded 79 and 68% conversion after 30 minutes, corresponding to TOFs of 28.7 and 24.7 $mol_{alkene}mol_{Ir}^{-1}h^{-1}$ for ethylene and propylene respectively. The catalyst could be recovered and used three times with negligible loss in activity. Further studies showed that Ir($^{t\text{Bu}}$PCP)H_2 could also be immobilised on surface silanols.[22] Reaction of this supported complex with CO showed formation of the six coordinate species $SiO_{2\text{-}(400)}$-Ir($^{t\text{Bu}}$PCP)H(CO), which remained stable on the silica surface. Under the same conditions, the aforementioned $SiO_{2\text{-}(400)}$-Ir(POCOP)H formed an analogous CO complex. However, this was observed to reductively eliminate the silanol to yield the Ir(I) complex Ir(POCOP)CO. The difference is attributed to the differing electronic properties of the pincer ligands, with greater π-donation from the C_{ipso} of the pincer backbone for POCOP ligands into the filled d_{xy} orbital on iridium, destabilising Ir(III) complexes with respect to square planar Ir(I) complexes.

This chapter focusses on the $^{t\text{Bu}}$PCP pincer iridium complexes Ir($^{t\text{Bu}}$PCP)HCl and Ir($^{t\text{Bu}}$PCP)H_4 and their immobilisation on solid polymethylaluminoxane (sMAO) utilising SOMC. Characterisation of the grafted species by solid-state NMR (SSNMR) and FTIR spectroscopy has been undertaken, and the immobilised complexes tested for their activity towards alkene hydrogenation and transfer dehydrogenation. Reactivity has been compared with the homogeneous complexes, and synthesis of molecular anologues for the immobilised

species has been attempted. Finally, immobilisation of Ir($^{t\text{Bu}}$PCP)HCl and W{N(2,6-F-C_6H_3)}Cl_4(THF) (**1.7**) together on the surface of sMAO has been attempted and the solid analysed by a combination of ^{13}C, ^{31}P, ^{27}Al and ^{19}F SSNMR spectroscopy.

5.2. Synthesis of Ir($^{t\text{Bu}}$PCP)H_4

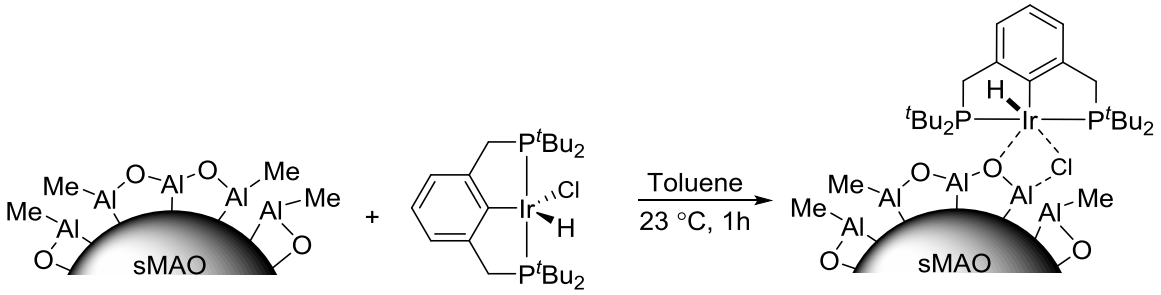
Based on their high thermal stability and reactivity towards alkene hydrogenation and transfer hydrogenation (both using a sacrificial hydrogen acceptor or in an acceptorless fashion), $^{t\text{Bu}}$PCP iridium complexes were chosen for study. As has previously been reported,[22] Ir($^{t\text{Bu}}$PCP)HCl can be synthesised from commercially available $IrCl_3{\cdot}3H_2O$ and 2,6-($CH_2P^tBu_2$)-C_6H_4 by refluxing in a solution of water and ^{i}PrOH at 80 °C for 20 hours. Ir($^{t\text{Bu}}$PCP)HCl can then be converted to Ir($^{t\text{Bu}}$PCP)H_4 by reaction with NaO^{t}Bu under a hydrogen atmosphere (toluene, 23 °C for 1 hour) (Scheme 5.6). Along with Ir($^{t\text{Bu}}$PCP)H_4, traces of Ir($^{t\text{Bu}}$PCP)H_2 could be observed by ^{1}H NMR spectroscopy as described in the reported procedure.



Scheme 5.6. Synthesis of Ir($^{t\text{Bu}}$PCP)H_4 from $IrCl_3{\cdot}3H_2O$ and 2,6-($CH_2P^tBu_2$)-C_6H_4 *via* Ir($^{t\text{Bu}}$PCP)HCl.[22]

5.3. Immobilisation of Ir($^{t\text{Bu}}$PCP)HCl on sMAO

Ir($^{t\text{Bu}}$PCP)HCl was chosen for immobilisation on sMAO, as it was postulated that grafting may occur in a similar fashion to that observed for the W(NR)Cl_4(THF) or W(NR)Me_3Cl complexes described in Chapter Four, and so a halide group would be required. Contacting Ir($^{t\text{Bu}}$PCP)HCl and sMAO (Al/Ir = 150) in toluene yielded a red/orange solution, which was seen to decolourise over the course of 1 hour with regular swirling. Removal of the supernatant by filtration and drying furnished the immobilised species sMAO-Ir($^{t\text{Bu}}$PCP)HCl as a bright yellow powder in quantitative yield. It is proposed that abstraction of the chloride ligand yields a cation, which either bonds ionically with the surface or covalently *via* an Al–O linker (Scheme 5.7), in an analogous manner to that proposed for sMAO supported W(NR)Cl_4(THF) complexes (Chapter Four).



Scheme 5.7. Immobilisation of Ir($^{t\text{Bu}}$PCP)HCl on sMAO, *via* halide abstraction by the surface.

The ^{13}C-{^{1}H} CPMAS SSNMR spectrum of sMAO- Ir($^{t\text{Bu}}$PCP)HCl (Figure 5.2), exhibited resonances corresponding to the sMAO support at 177, 136, 132 and 128 ppm (benzoate) and 7 ppm (Al–Me) as previously observed (Chapter Four).[23] Three resonances in the alkyl region at 37, 29 and 27 ppm are attributed to the $CH_2P(C(CH_3)_3)_2$ carbons, matching well with the molecular complex.[22] Due to relatively low signal to noise ratio, no resonances for the aromatic ring carbons could be observed.

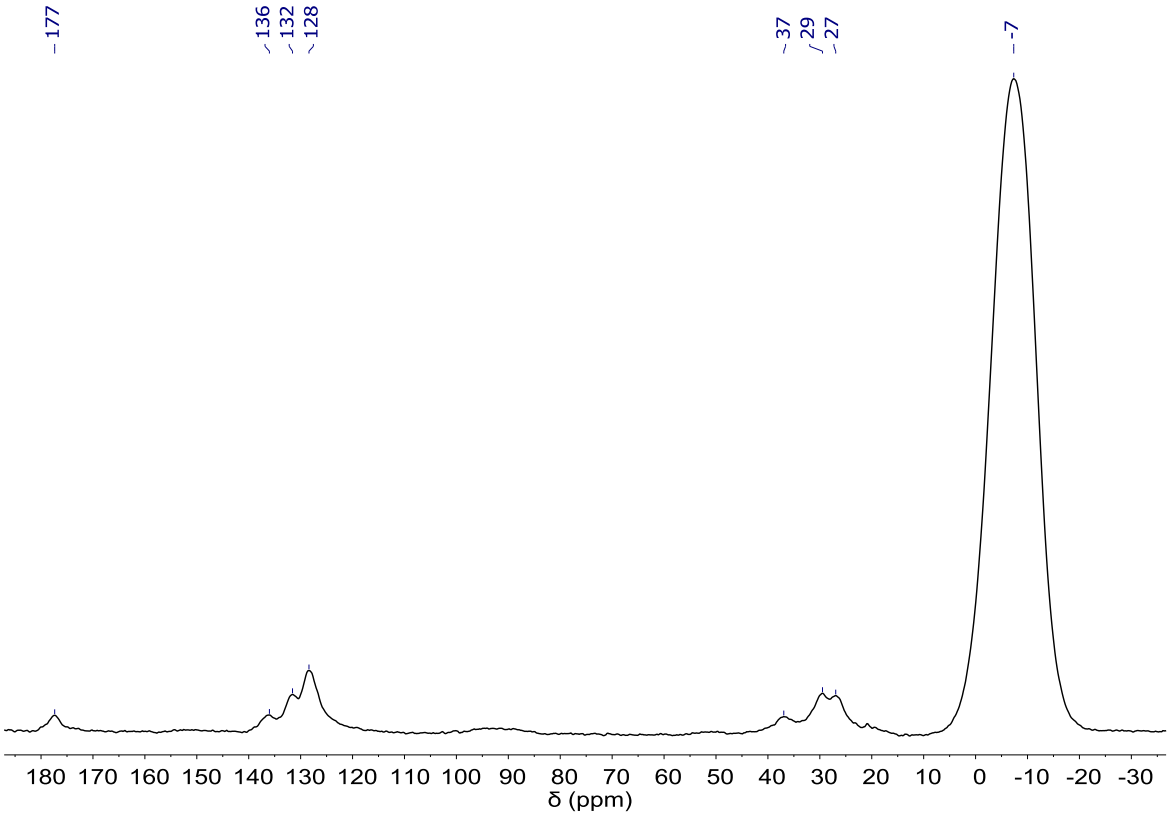


Figure 5.2. ^{13}C-{^{1}H} CPMAS SSNMR spectrum (10 kHz, 400 MHz, 23 °C) of sMAO-Ir($^{t\text{Bu}}$PCP)HCl.

The ^{31}P-{^{1}H} CPMAS spectrum displayed a single resonance centred at 78 ppm (Figure 5.3), which is shifted to higher frequency with respect to Ir($^{t\text{Bu}}$PCP)HCl (67 ppm), Ir($^{t\text{Bu}}$PCP)H_4 (73 ppm) and $SiO_{2\text{-}(400)}$-Ir($^{t\text{Bu}}$PCP)H (67 ppm).[22] Such a downfield shift would be

consistent with formation of a cationic complex on the surface. ^{27}Al DPMAS showed a broad set of resonances between 500 and −500 ppm (Figure A161), as observed for sMAO supported complexes in Chapter Four.

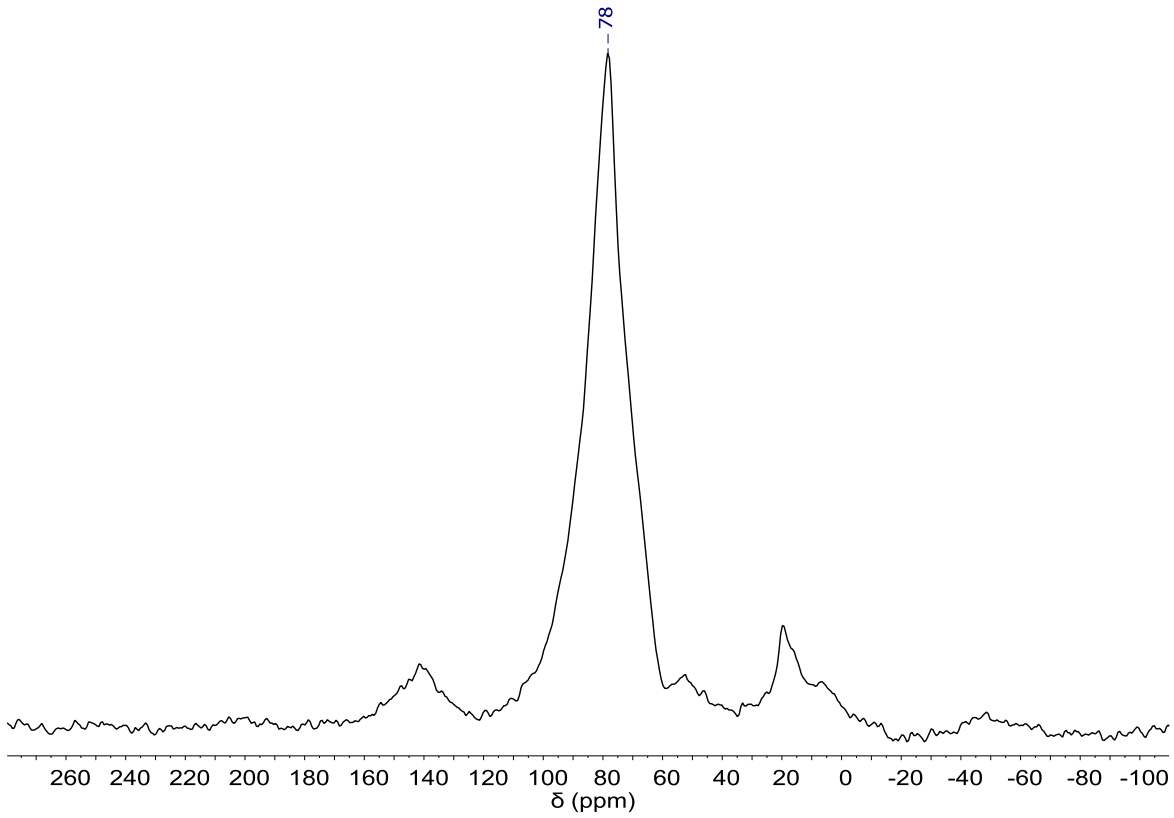


Figure 5.3. ^{31}P-{^{1}H} CPMAS spectrum (10 kHz, 400 MHz, 23 °C) of sMAO-Ir($^{t\text{Bu}}$PCP)HCl.

Comparison of the FTIR spectra of sMAO-Ir($^{t\text{Bu}}$PCP)HCl was made with the precursor complex Ir($^{t\text{Bu}}$PCP)HCl and the tetra-hydride complex Ir($^{t\text{Bu}}$PCP)H_4 to see if similar hydride stretches could be observed (Figure 5.4). The $^{t\text{Bu}}$PCP ligand stretches apparent in both molecular complexes are observed as weak absorptions in the spectrum of the supported complex, though the spectrum is dominated by a strong absorption attributed to the sMAO support (685 cm^{-1}). For Ir($^{t\text{Bu}}$PCP)H_4, stretches associated with the Ir–H bonds at 2,069 and 1,902 cm^{-1} are observed, these are not present in either spectra of Ir($^{t\text{Bu}}$PCP)HCl or sMAO-Ir($^{t\text{Bu}}$PCP)HCl.

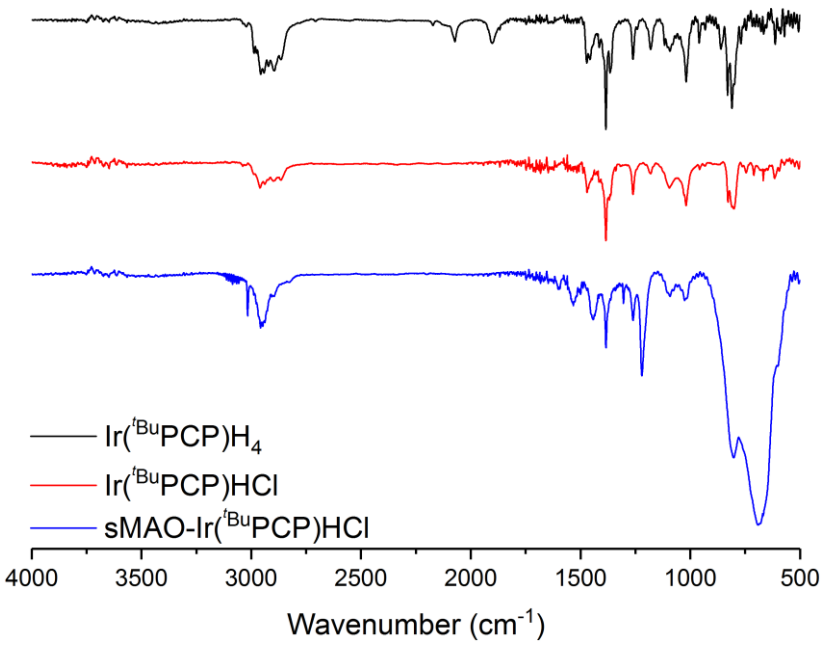


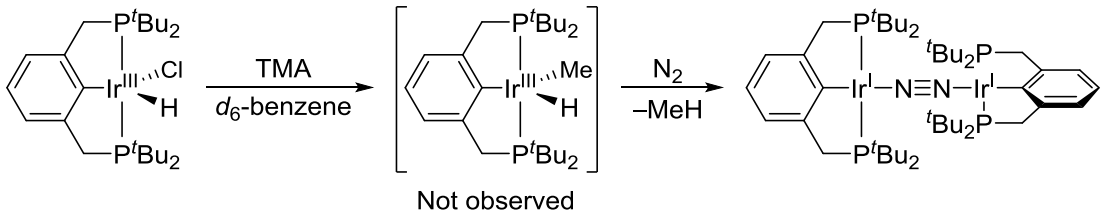
Figure 5.4. Comparison of the FTIR spectra for Ir($^{t\text{Bu}}$PCP)H_4, Ir($^{t\text{Bu}}$PCP)HCl and sMAO-Ir($^{t\text{Bu}}$PCP)HCl.

5.4. Synthesis of molecular analogues of the supported species

To try and further understand the nature of the supported species formed from the reaction of sMAO and Ir($^{t\text{Bu}}$PCP)HCl, attempts to synthesise molecular analogues were undertaken. Ir($^{t\text{Bu}}$PCP)HCl was reacted with MAO (Al/Ir = 150) to mimic the sMAO immobilisation procedure. This resulted in a colour change from orange to yellow, analogous to the colour of the sMAO supported species. Two resonances at 72.5 and 72.1 ppm were observed in the $^{31}P\{^{1}H\}$ NMR spectrum (Figure A162), the latter attributed to Ir($^{t\text{Bu}}$PCP)(N_2) (*vide infra*), compared to a single resonance at 78 ppm for sMAO-Ir($^{t\text{Bu}}$PCP)HCl. However, the ^{1}H NMR spectrum was ill-defined, with a broad set of resonances between 1.8 and 0.8 ppm (Figure A163).

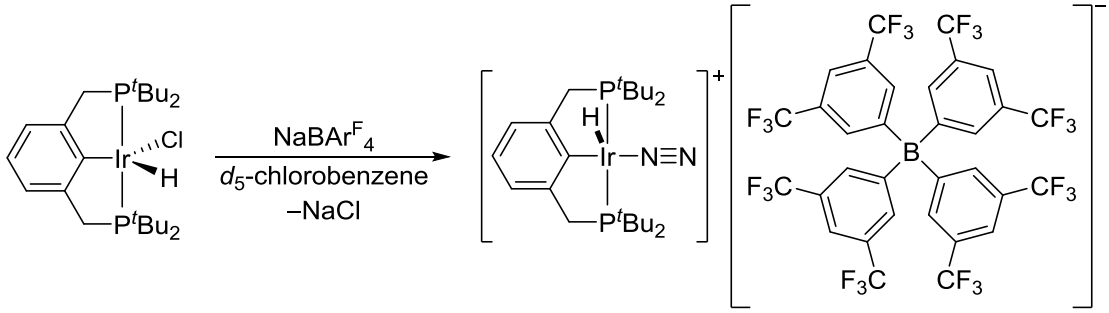
As a broad undefined species was formed with MAO, the reactivity of Ir($^{t\text{Bu}}$PCP)HCl towards trimethylaluminium (TMA) was investigated. TMA is known to be present in the sMAO structure,[23,24] and it was postulated that characterisation of resulting species may be more facile, owing to the simpler structure of TMA compared to MAO. Reaction of Ir($^{t\text{Bu}}$PCP)HCl and TMA (1 eq.) in d_6-benzene yielded an orange solution. $^{31}P\{^{1}H\}$ NMR spectroscopy showed two intense phosphorous environments at 72.2 and 68.1 ppm and a weaker resonance at 68.7 ppm (Figure A164). The ^{1}H NMR spectrum showed the complete disappearance of the hydride signal at −44 ppm and the apparent formation of three $^{t\text{Bu}}$PCP

complexes in a 48:37:15 ratio, with some methane also evolved (Figure A165 and A166). Slow evaporation from a solution of hexane after work-up, yielded orange crystals (15% isolated yield), shown to be the dinitrogen complex $\{Ir(^{tBu}PCP)\}_2(\mu\text{-}N_2)$[16] by a single crystal X-ray diffraction study (Figure 5.1). Goldman and co-workers have previously reported that at high N_2:Ir(^{tBu}PCP) ratios the dimer is in equilibrium with the monomeric nitrogen bound complex, with the equilibrium lying heavily in favour of the monomereric species at 1 atm of N_2 (20:1).[25] Despite this, the dimer has been observed to selectively crystallise at ambient temperatures. The NMR spectroscopic data for the monomeric complex, Ir(^{tBu}PCP)(N_2), reported by Goldman and co-workers, was consistent with the resonances for the second most abundant complex observed in the ^{1}H NMR spectrum and the resonance at 72.2 ppm in the $^{31}P\{^1H\}$ NMR spectrum. Interestingly, there appears to be no evidence in the solution NMR spectrum of the dimeric species $\{Ir(^{tBu}PCP)\}_2(\mu\text{-}N_2)$ ($^{31}P\{^1H\}$ = 73.5 ppm).[25] The two other sets of resonances in the ^{1}H NMR spectrum exhibit splitting of the methylene resonances into two doublets of triplets and the *tert*-butyl resonances into two triplets respectively, for each complex. This may arise from coordination of alkyl aluminium species in solution to the either the phosphine groups of the monomeric or dimeric dinitrogen complexes or *via* a bridging chloride to iridium. Formation of $\{Ir(^{tBu}PCP)\}_2(\mu\text{-}N_2)$ in this case is postulated to occur *via* methylation at the chloride position in the precursor, followed by reductive elimination of methane, yielding the iridium (I) ^{tBu}PCP complex, two molecules of which activate dinitrogen (Scheme 5.8). It is proposed that formation of this nitrogen bridged dimer on the surface of sMAO may be disfavoured as the molecular complex grafts to the surface and may be well separated from other immobilised species, preventing dimer formation.



Scheme 5.8. Proposed formation of $\{Ir(^{tBu}PCP)\}_2(\mu\text{-}N_2)$ from Ir(^{tBu}PCP)HCl and TMA *via* reductive elimination of methane from Ir(^{tBu}PCP)MeH.

It was postulated that the immobilised species may be a zwitterionic in nature as a result of halide extraction by sMAO leading to a cationic iridium species. Therefore, reactions of Ir(^{tBu}PCP)HCl with $NaBAr^F{}_4$ were attempted and found to generate the cationic complex $[Ir(^{tBu}PCP)H(N_2)][BAr^F{}_4]$ (Scheme 5.9).



Scheme 5.9. Reaction of Ir($^{t\text{Bu}}$PCP)HCl with $NaBAr^F_4$ in d_5-chlorobenzene to afford [Ir($^{t\text{Bu}}$PCP)H(N_2)][BAr^F_4].

Reaction in d_5-chlorobenzene resulted in a colour change from orange to red, with broadening of the resonances for the $^{t\text{Bu}}$PCP ligand observed in the ^{1}H NMR spectrum, which suggests fluxionality in the structure. The ^{1}H NMR spectrum was consistent with the cationic species, with resonances corresponding to the $[BAr^F_4]^-$ counterion and aromatic methylene and *tert*-butyl methyl resonances for the $^{t\text{Bu}}$PCP ligand (Figure 5.5). The hydride region exhibited two resonances in an approximate 50:50 ratio, a sharp resonance at −41.3 ppm and a broad resonance at−44.5 ppm.

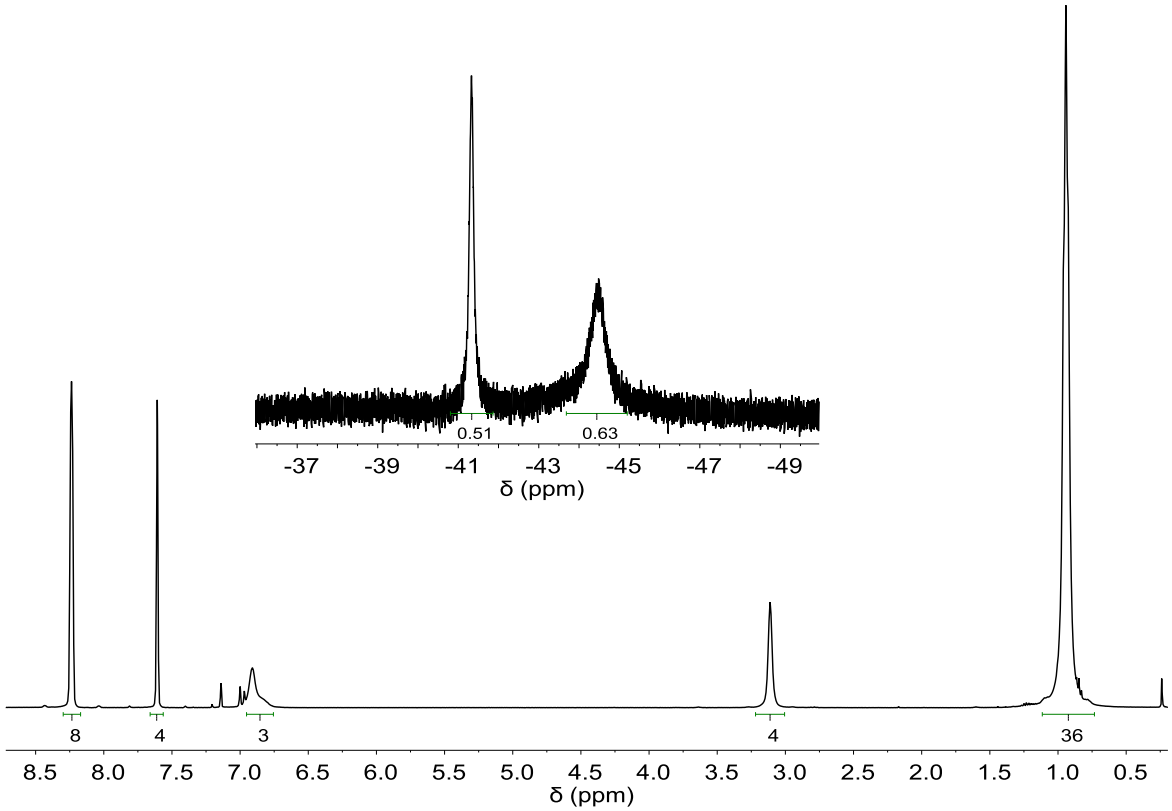
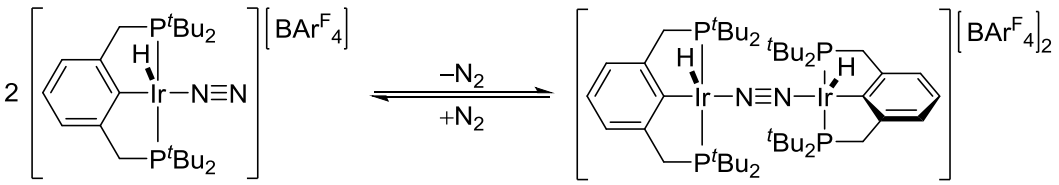


Figure 5.5. ^{1}H NMR spectrum (400 MHz, 23 °C) of the reaction between Ir($^{t\text{Bu}}$PCP)HCl and $NaBAr^F_4$ in d_5-chlorobenzene (7.14, 6.99 and 6.96 ppm) showing formation of [Ir($^{t\text{Bu}}$PCP)H(N_2)][BAr^F_4].

The $^{31}P\{^{1}H\}$ NMR spectra also exhibited two relatively broad signals at 74.4 and 71.0 ppm (Figure A167), which are shifted downfield from those observed for Ir($^{t\text{Bu}}$PCP)HCl (67 ppm), as expected for a cationic metal centre. The $^{11}B\{^{1}H\}$ and $^{19}F\{^{1}H\}$ NMR spectra both exhibited a single resonance at −5.9 and −61.9 ppm respectively (Figures A168 and A169), indicative of a tetra-coordinated $[BAr^{F}_{4}]^{-}$ counterion. The broadness of the NMR spectra and multiple hydride and phosphorus resonances are postulated to arise from a monomer-dimer equilibrium in solution, facilitated by a bridging nitrogen ligand in an analogous fashion to $\{Ir(^{t\text{Bu}}PCP)\}_2(\mu\text{-}N_2)$ (Scheme 5.10). To further probe this fluxionality, variable temperature and exchange NMR spectroscopy experiments are required, however, due to time constraints, such a study is yet to be undertaken.



Scheme 5.10. Proposed monomer-dimer equilibrium of [Ir($^{t\text{Bu}}$PCP)H(N_2)][BAr^{F}_{4}] *via* a bridging nitrogen ligand.

Slow evaporation of the solvent from the d_5-chlorobenzene reaction mixture, furnished orange crystals suitable for a single crystal X-ray diffraction study. This confirmed the solid-state connectivity of [Ir($^{t\text{Bu}}$PCP)H(N_2)][BAr^{F}_{4}] (Figure 5.6 and Table 5.1). Full crystallographic data is provided in the Appendix.

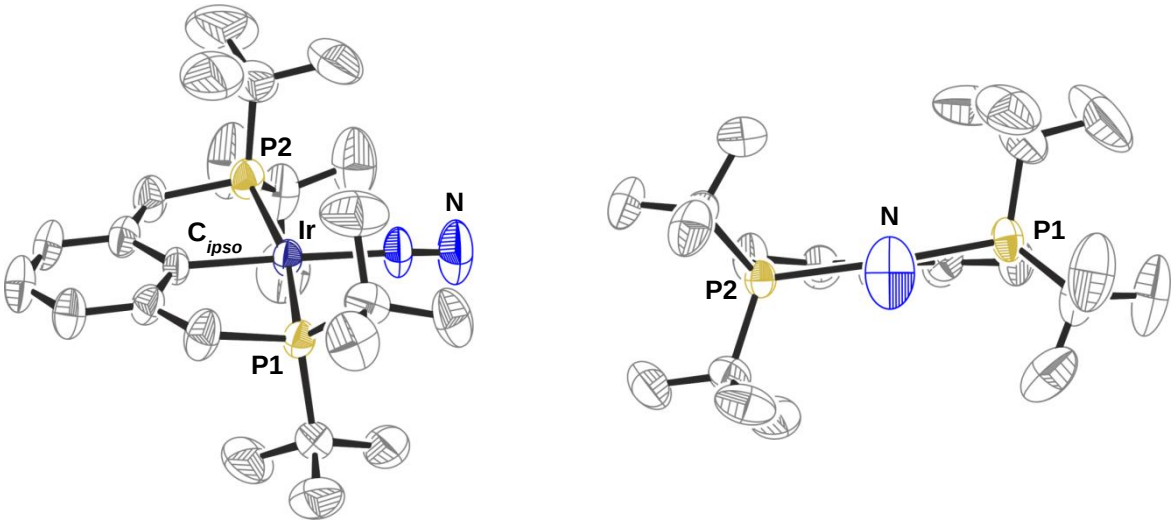


Figure 5.6. Molecular structure of [Ir($^{t\text{Bu}}$PCP)H(N_2)][BAr^{F}_{4}] viewed 'side on' to the nitrogen (left) and down the dinitrogen bond with the $^{t\text{Bu}}$PCP phenyl ring in the horizontal plane (right). Ellipsoids are shown at 50% probability. For clarity, hydrogen atoms and the coordinated $[BAr^{F}_{4}]^{-}$ counter ion have been omitted. The iridium hydride could not be located in the structure.

Table 5.1. Selected bond lengths (Å) and angles (°) for [Ir($^{t\text{Bu}}$PCP)H(N_2)][BAr^F_4] and [Ir($^{t\text{Bu}}$PCP)H(CO)][$NaBAr^F_4$].[26]

Parameter	Bond lengths (Å)/Angles (°)	
	[Ir($^{t\text{Bu}}$PCP)H(N_2)][BAr^F_4]	**[Ir($^{t\text{Bu}}$PCP)H(CO)][$NaBAr^F_4$][26]**
Ir–C_{ipso}	2.035(3)	2.074(2)
Ir–P1, Ir–P2	2.3260(9), 2.3300(8)	2.3321(6), 2.3360(6)
Ir–L (L = N_2 or CO)	2.051(3)	1.924(3)
N–N or C–O	1.092(5)	1.134(3)
Ir–H	-	1.59(6)
C_{ipso}–Ir–L (L = N_2 or CO)	178.20(16)	177.04(10)
P1–Ir–P2	165.93(3)	164.28(2)
Ir–N–N or Ir–C–O	176.5(5)	177.5(3)

The molecular structure adopts the same unit cell parameters as the isostructural and isoelectronic carbonyl complex [Ir($^{t\text{Bu}}$PCP)H(CO)][BAr^F_4] described by Goldman and co-workers, formed from reaction of the iridium (I) complex Ir($^{t\text{Bu}}$PCP)(CO) with Brookhart's oxonium acid [$H(OEt_2)_2$][BAr^F_4].[26] For [Ir($^{t\text{Bu}}$PCP)H(N_2)][BAr^F_4] the iridium hydride could not be located; in [Ir($^{t\text{Bu}}$PCP)H(CO)][BAr^F_4] it is shown to occupy the vacant axial site to yield a square pyramidal structure about iridium, with an Ir–H bond length of 1.59(6) Å. The P–Ir–P angle which would be expected to be linear for a square planar iridium centre, is bent away from linearity (165.93(3)°). This is due to the steric constraint of the pincer ligand and this is observed for all crystallographically characterised Ir($^{t\text{Bu}}$PCP) complexes in the CCDC database (154.978–167.213°).[27] The N–N bond length (1.092(5) Å) is within error of both the N_2 complex Ir($^{t\text{Bu}}$PCP)(N_2)[25] (1.107(2) Å) and molecular dinitrogen (1.0976(2) Å),[28] indicative of triple bond character and weak N_2 activation. However, the N–N bond length may not be the best probe of N_2 activation and IR or Raman spectroscopy may be more useful.[29] From Figure 5.6 it can be seen that the ligating phosphorus groups lie above and below the plane of the phenyl ring. The angle of the P–Ir–P plane to the plane of the aromatic ring is calculated as 15.45°. In solution, the molecular motion of the phosphine groups in and out of the plane is expected to be rapid and, consistent with this, for [Ir($^{t\text{Bu}}$PCP)H(CO)][BAr^F_4] only a single phosphorus and hydride environment is observed (83.0 and −36.8 ppm respectively in d_2-DCM), despite the fact that the molecular structure has the same out of plane bending (16.3°).[26] This may suggest that if dimerisation is occurring in [Ir($^{t\text{Bu}}$PCP)H(N_2)][BAr^F_4], that it may be *via* a bridging dinitrogen ligand. To determine if the fluxionality was due to a solvent effect with d_5-chlorobenzene, Ir($^{t\text{Bu}}$PCP)HCl was reacted

with $NaBAr^F_4$ in d_2-DCM, yielding a similarly broad ^1H NMR spectrum. Once again, two resonances were observed in the $^{31}P\{^1H\}$ NMR spectrum (74.4 and 73.0 ppm).

5.5. Alkene hydrogenation reactions

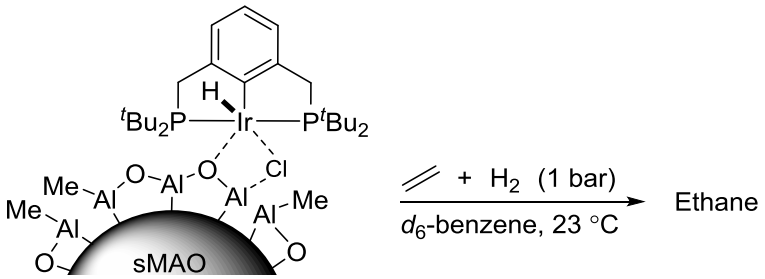
As described previously, $SiO_{2\text{-}(400)}$-Ir(POCOP)H (POCOP = 2,6-(O-P^{t}Bu$_2$)-C_6H_3) was shown to be active for the hydrogenation of alkenes (ethylene and propylene) under a hydrogen atmosphere.[21] Therefore, sMAO-Ir($^{t\text{Bu}}$PCP)HCl was also tested for this reaction, utilising the reported catalyst Ir($^{t\text{Bu}}$PCP)H_4, along with proposed molecular analogues of the supported species, Ir($^{t\text{Bu}}$PCP)HCl/TMA (Al/Ir = 1) and Ir($^{t\text{Bu}}$PCP)HCl/MAO (Al/Ir = 150), for direct comparison (Table 5.2).

Table 5.2. Hydrogenation reactions with ethylene.

Catalyst	μmol$_{Ir}$	Al/Ir	Time (h)	TOF (mol$_{C_2H_4}$mol$_{Ir}^{-1}$h^{-1})
sMAO-Ir($^{t\text{Bu}}$PCP)HCl	0.46[a]	150	<0.5	≥288
Ir($^{t\text{Bu}}$PCP)HCl/TMA	3.21[b]	1	16	0.9
Ir($^{t\text{Bu}}$PCP)HCl/MAO	3.21[b]	150	<1	≥21
Ir($^{t\text{Bu}}$PCP)H_4	3.21[b]	-	16	1.1
$SiO_{2\text{-}(400)}$-Ir(POCOP)H[21,c]	2.06	-	9	120

Conditions: Hydrogen (1 bar), 23 °C, d_6-benzene. [a] 5 mg cat. [b] 2 mg cat. [c] 20 mg cat., 1:1 ethylene:hydrogen, total pressure 2 bar, reactor volume 55 mL.

Initially, the reactivity of sMAO-Ir($^{t\text{Bu}}$PCP)HCl towards ethylene was assessed in the absence of dihydrogen (5 mg cat., 0.46 μmol$_{Ir}$, 75 °C, d_6-benzene). Only a very small amount of ethane along with minor polymer formation around the support was observed after 8 hours. However, conducting the analogous reaction in the presence of H_2 at 23 °C, resulted in rapid reaction and complete conversion to ethane within 30 minutes (TOF ≥288 mol$_{C_2H_4}$mol$_{Ir}^{-1}$h^{-1}, Scheme 5.11).



Scheme 5.11. Catalytic hydrogenation of ethylene by sMAO-Ir($^{t\text{Bu}}$PCP)HCl in the presence of hydrogen.

For $SiO_{2\text{-}(400)}$-Ir(POCOP)H, complete conversion to ethane at 23 °C required 9 hours reaction time at the same complex loading (6.1 wt%), although the scale was much larger (55 mL reactor volume) and the reaction was in the gas phase.[21] By comparison, Ir($^{t\text{Bu}}$PCP)H_4 required long reaction times (16 hours) to reach full conversion (3 μmol_{Ir}, 23 °C, d_6-benzene). For this molecular complex, alkene binding is observed by colour change of the solution from yellow to red. Choi *et al*. have previously observed formation of Ir($^{t\text{Bu}}$PCP)(C_2H_4) by reaction of ethoxybenzene with Ir($^{t\text{Bu}}$PCP)(CHCH^tBu)H in *p*-xylene.[30] Agitating the solution in the presence of H_2 slowly leads to complete reformation of a yellow solution (Figure A170); over time the alkene complex begins to form again, until all the alkene has been hydrogenated. The relative stability of this alkene complex is the proposed reasoning behind the slower reactivity of the molecular complex. It should be noted that no colour change is observed for sMAO-Ir($^{t\text{Bu}}$PCP)HCl upon alkene addition, inferring that a similar stable alkene complex does not form. Pure sMAO was also tested for the hydrogenation reaction and it was shown to be unreactive with no methane evolution, indicating the support is stable under a hydrogen atmosphere.

Comparison of the reactivity of sMAO-Ir($^{t\text{Bu}}$PCP)HCl with ethylene to the proposed molecular analogues was also pursued. For the Ir($^{t\text{Bu}}$PCP)HCl/TMA (Al/Ir = 1) and ethylene reaction, a colour change from red to orange was observed upon addition of H_2. An upfield shift in the $^{31}P\{^1H\}$ resonance attributed to the $^{t\text{Bu}}$PCP ligand was noted, with a singlet observed at 58.7 ppm (Figure A171), with only one $^{t\text{Bu}}$PCP species observable by ^1H NMR spectroscopy (Figure A172). This mixture was seen to hydrogenate ethylene at a rate similar to that of Ir($^{t\text{Bu}}$PCP)H_4 with complete conversion obtained after 16 hours. Reaction of a combination of Ir($^{t\text{Bu}}$PCP)HCl/MAO (Al/Ir = 150) with ethylene yielded two new phosphorus environments in the $^{31}P\{^1H\}$ NMR spectrum at 62.6 and 62.5 ppm (Figure A173). However, the ^1H NMR spectrum remained ill-defined. Addition of hydrogen to the reaction resulted in very fast formation of ethane (70% conversion after 15 minutes (Figure A174) and complete conversion within 1 hour), with no change to the $^{31}P\{^1H\}$ NMR spectrum (Figure A175). Ir($^{t\text{Bu}}$PCP)HCl/MAO (Al/Ir = 150) appears to be the best molecular analogue for sMAO-Ir($^{t\text{Bu}}$PCP)HCl as it displays a similar reactivity profile. The lower activity observed for the homogeneous MAO system, however, may be due to the formation of catalytically inactive species *via* intermolecular decomposition pathways. The well-defined SSNMR spectra of the immobilised complex, sMAO- Ir($^{t\text{Bu}}$PCP)HCl, implies a defined active site, in

analogy to the difference observed between solution and solid MAO for $W(NR)Cl_4(THF)$ complexes (Chapters Two and Four).

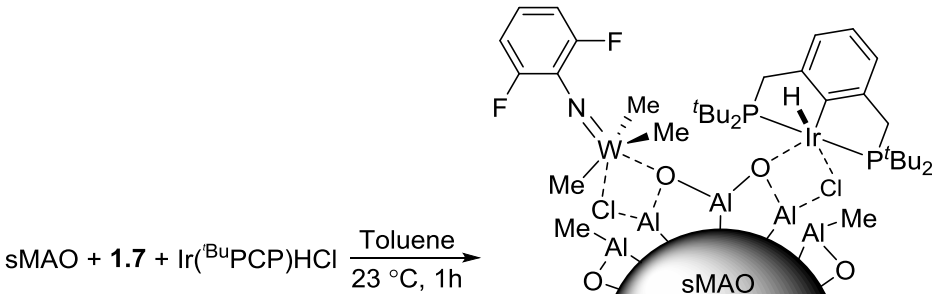
5.6. Transfer hydrogenation reactions

Pincer iridium complexes have been widely utilised in alkane dehydrogenation reactions, with the COA/TBE transfer hydrogenation often employed as the standard reaction to compare reactivity.[31] Hence, the immobilised species were tested for the transfer hydrogenation of ethane (1 bar) or COA, utilising TBE as a sacrificial hydrogen acceptor. Transfer dehydrogenation of ethane was targeted, as formation of ethylene would be required, in order to employ the ethylene dimerisation systems discussed in Chapter Four in tandem catalytic reactions. Reactions were carried out in d_6-benzene at 100 °C (under argon for the COA reaction to avoid N_2 dimer formation) with an Ir:COE:TBA = 1:300:300. Such conditions were chosen, as the supported oligomerisation catalysts discussed in Chapter Four were shown to be active under these conditions, and the intention is to later use an oligomerisation catalyst in tandem on a support surface for alkane upgrading. Also, high concentrations of TBE are known to inhibit reactivity as C–H elimination of *tert*-butyl ethane from $Ir(^{tBu}PCP)H_2(CH_2CH_2{}^tBu)$ is the rate limiting step,[32] whereas active systems have been observed previously for TBE/Ir = 300.[15] Very low reactivity was observed for sMAO-$Ir(^{tBu}PCP)HCl$, with only 0.2% conversion of COA after 5 days of reaction (TON = 0.6 $mol_{COA}mol_{Ir}^{-1}$). By comparison over the same time period, $Ir(^{tBu}PCP)H_4$ achieved 4.7% conversion (TON = 1.86 $mol_{COA}mol_{Ir}^{-1}$). Such TONs are much lower than those for $Ir(^{tBu}PCP)H_2$ (20.5 turnovers per hour at 100 °C).[15] One reason behind this may be that COA is used neat as a solvent in these reactions. The lower activity observed may therefore be a concentration effect, or d_6-benzene may have a retarding effect on the activity. Such a suggestion is supported by a report from Goldman and co-workers, who described how reaction of $Ir(^{tBu}PCP)H_2$ with TBE or norbornene in benzene, results in hydrogenation of the alkene and C–H activation of the arene to yield $Ir(^{tBu}PCP)(Ph)H$.[33] This suggests that competing C–D activation may be the cause of the slower observed rate for transfer dehydrogenation. When ethane was utilised instead of COA, no ethylene evolution could be observed by ^1H NMR spectroscopy after 5 days at 100 °C. This suggests that much harsher conditions may be required to dehydrogenate this short chain alkane. For example, industrial steam cracking of ethane to yield ethylene operates at temperatures up to 1,100 °C.[34] Due to time constraints, no optimisation of the conditions for either reaction was attempted.

5.7. Co-immobilisation of W{N(2,6-F-C_6H_3)}Cl_4(THF) (1.7) and Ir(^{tBu}PCP)HCl on sMAO

5.7.1. Immobilisation and characterisation

The initial aim of this project was to develop a well-defined heterogeneous tandem system that could upgrade hydrocarbon monomers. Therefore, as a proof of concept, a tungsten mono-imido ethylene oligomerisation pre-catalyst (Chapter Two and Four) and a transfer dehydrogenation pre-catalyst were co-immobilised onto sMAO. W{N(2,6-F-C_6H_3)}Cl_4(THF) (**1.7**) was chosen as it allowed identification of the immobilised complex by ^{19}F SSNMR spectroscopy along with Ir(^{tBu}PCP)HCl (*vide supra*) (Al:Ir:W = 300:1:1) (Scheme 5.12).



Scheme 5.12. Proposed surface species formed from co-immobilisation of **1.7** and Ir(^{tBu}PCP)HCl on sMAO.

Swirling a mixture of the three components in toluene for 1 hour at 23 °C, resulted in complete decolouration of the solution, and a yellow solid was obtained after work-up in quantitative yield. Analysis of the solid by ^{13}C-{^{1}H} CPMAS {^{19}F} decoupled SSNMR spectroscopy, showed characteristic resonances for the sMAO support (177, 136, 130, 128 and 8 ppm), as well as weak signals in the alkyl region (37, 34 and 30 ppm) similar to that observed for sMAO-Ir(^{tBu}PCP)HCl (Figure 5.7). Due to the low concentration of the immobilised species no other resonances for the molecular complexes could be unequivocally assigned. Attempted enhancement of signals by ^{13}C-{^{19}F} CPMAS {^{1}H} decoupling resulted in no observable resonances in the SSNMR spectrum.

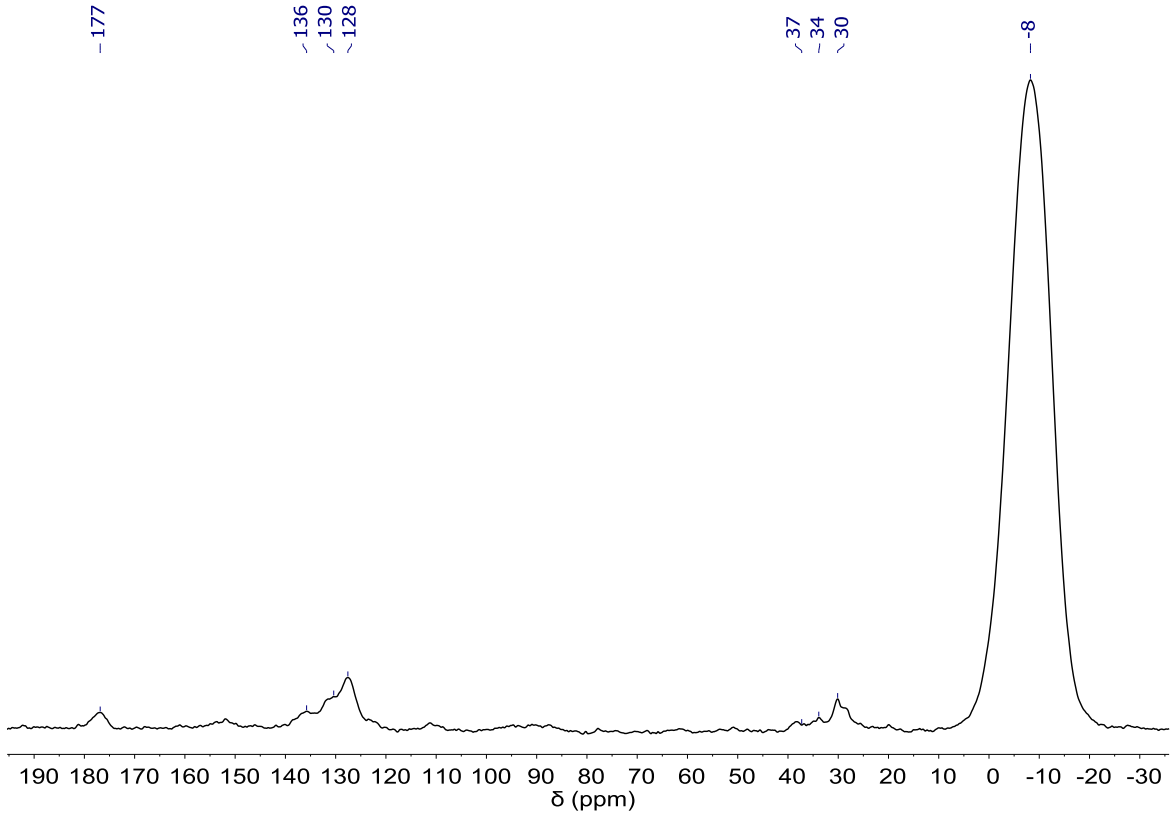


Figure 5.7. ^{13}C-{^{1}H} CPMAS {^{19}F} decoupled SSNMR spectrum (10 kHz, 400 MHz, 23 °C) of sMAO-(**1.7**/Ir($^{t\text{Bu}}$PCP)HCl).

The $^{19}F\{^{1}H\}$ DPMAS SSNMR spectrum displayed a single resonance at −123 ppm (Figure 5.8) exactly matching that observed for sMAO-**1.7** suggesting the same surface species is formed upon grafting.

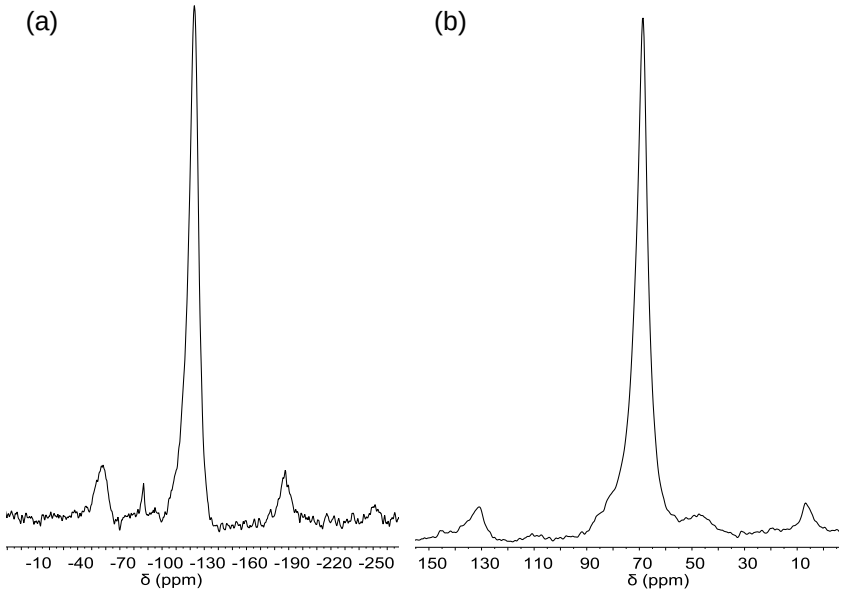


Figure 5.8. (a) $^{19}F\{^{1}H\}$ DPMAS SSNMR spectrum (24 kHz, 400 MHz, 23 °C) and (b) ^{31}P-{^{1}H} CPMAS SSNMR spectrum (10 kHz, 400 MHz, 23 °C) of sMAO-(**1.7**/Ir($^{t\text{Bu}}$PCP)HCl).

The ^{31}P-{^{1}H} CPMAS SSNMR spectrum of the solid exhibited a single phosphorus resonance centred at 69 ppm (Figure 5.8). This is shifted upfield from that observed for sMAO-Ir($^{t\text{Bu}}$PCP)HCl (78 ppm) and is much closer to the precursor complex Ir($^{t\text{Bu}}$PCP)HCl (67 ppm). This suggests a more electron rich metal centre, which may be due to weaker surface interaction as a result of the presence of the co-immobilised tungsten complex. Postulated interaction between tungsten and iridium orthogonal tandem catalysts has previously been reported by Bailey *et al*.. Studies into alkane metathesis reactions utilising the tungsten alkylidene complex W{N(2,6-^{i}Pr-C_6H_3)}(CHCMe$_2$Ph){OC(CF$_3$)$_3$}$_2$ and the transfer hydrogenation catalyst Ir(POCOP)(C_2H_4) (POCOP = 2,6-OP^{t}Bu$_2$-C_6H_3), concluded that high concentrations of the tungsten complex decreased the reactivity of the system towards *n*-octane.[35] However, no spectroscopic evidence for any interaction was reported.

5.7.2. Reactivity towards ethane

To test whether this dual catalytic system could upgrade ethane monomers to higher homologues in tandem, a preliminary test reaction was undertaken employing conditions under which both complexes could potentially operate. sMAO-(**1.7**/Ir($^{t\text{Bu}}$PCP)HCl) was contacted with ethane (1 bar) and TBE (8.9 μL, 69 μmol, TBE/Ir = 300) in d_6-benzene at 100 °C for 3 days. Analysis of the solution by ^{1}H NMR spectroscopy however, indicated that no reaction had occurred, consistent with the observation that sMAO-Ir($^{t\text{Bu}}$PCP)HCl was incapable of dehydrogenating ethane under analogous conditions.

5.8. Conclusions

Ir($^{t\text{Bu}}$PCP)HCl was immobilised on sMAO with SSNMR and FTIR spectroscopy indicating preservation of the $^{t\text{Bu}}$PCP ligand on the surface species. The chemical shift for the phosphorus in sMAO-Ir($^{t\text{Bu}}$PCP)HCl (78 ppm) was shifted downfield from that of Ir($^{t\text{Bu}}$PCP)HCl (67 ppm) and Ir($^{t\text{Bu}}$PCP)H_4 (73 ppm), suggesting the surface may have an electron withdrawing effect.

Synthesis of molecular mimics of the supported species were attempted, by reaction of Ir($^{t\text{Bu}}$PCP)HCl with TMA (1 eq.), MAO (150 eq.) and NaBAr$^{F}_4$. Reaction with TMA in a nitrogen atmosphere, yielded the previously reported complex, {Ir($^{t\text{Bu}}$PCP)}$_2$(N_2), after proposed methylation at the halide position and reductive elimination of methane. Contacting Ir($^{t\text{Bu}}$PCP)HCl with 150 equivalents of MAO in d_6-benzene yielded a yellow solution similar in colour to sMAO-Ir($^{t\text{Bu}}$PCP)HCl, however, the ^{1}H NMR spectrum was broad and ill-defined suggesting multiple species in solution. Finally, extraction of the chloride by NaBAr$^{F}_4$ yielded

[Ir($^{t\text{Bu}}$PCP)H(N_2)][$BAr^F{}_4$]. The molecular structure adopts a square planar geometry with dinitrogen weakly bound *trans* to the *ipso* carbon. The ^{1}H NMR spectrum was broad suggesting there may be fluxionality in the structure, which may arise from dimerisation in solution.

sMAO-Ir($^{t\text{Bu}}$PCP)HCl was shown to be highly active for the hydrogenation of ethylene (TOF ≥ 228 $mol_{C_2H_4}mol_{Ir}^{-1}h^{-1}$), far outperforming the molecular complex Ir($^{t\text{Bu}}$PCP)H_4 (TOF = 16 $mol_{C_2H_4}mol_{Ir}^{-1}h^{-1}$). Comparison with the molecular analogues Ir($^{t\text{Bu}}$PCP)HCl/TMA (Al/Ir = 1) and Ir($^{t\text{Bu}}$PCP)HCl/MAO (Al/Ir = 150) showed the MAO system to be the best model, although activities were still much lower than sMAO-Ir($^{t\text{Bu}}$PCP)HCl (TOFs of 0.9 and ~21 $mol_{C_2H_4}mol_{Ir}^{-1}h^{-1}$ respectively), which may be due to partial decomposition of the active species.

sMAO-Ir($^{t\text{Bu}}$PCP)HCl displayed very low activity for the transfer hydrogenation of cyclooctane (TON = 0.6 $mol_{COA}mol_{Ir}^{-1}$), and no propensity to dehydrogenate ethane, utilising *tert*-butyl ethylene as a sacrificial hydrogen acceptor in d_6-benzene. Ir($^{t\text{Bu}}$PCP)H_4 also displayed lower reactivity profile towards COA dehydrogenation than previously reported, attributed to potential C–D activation of the solvent medium. Further optimisation of conditions is required, especially if this system is to be employed in tandem for ethane upgrading.

Finally, as a proof of concept that iridium and tungsten catalysts could be immobilised on the same support using the SOMC procedure, Ir($^{t\text{Bu}}$PCP)HCl and W{N(2,6-F-C_6H_3)}Cl_4(THF) (**1.7**) were grafted onto sMAO. SSNMR spectroscopy indicated the presence of both the imido and $^{t\text{Bu}}$PCP ligands on the surface species. Whilst the tungsten complex appeared unchanged when compared to sMAO-**1.7**, the chemical shift for the phosphorus nuclei in the tandem system had shifted upfield when compared to sMAO-Ir($^{t\text{Bu}}$PCP)HCl (69 *vs* 78 ppm). This was postulated to be due to close contact between the complexes on the surface. No reactivity of this tandem system towards ethane could be observed.

5.9. Future work

For this tandem system to be viable, optimisation of transfer dehydrogenation reactions with the sMAO supported iridium system is required. Reactions should be conducted in neat conditions in the absence of additional solvent, with the effect of varying the reaction temperature and concentration of sacrificial hydrogen acceptor also explored. Further characterisation of the sMAO supported tandem species by techniques such as FTIR, X-ray

absorption spectroscopy and energy dispersive X-ray spectroscopy with comparison to the individual systems are required to gain additional insight into the nature of the immobilised species. For tandem catalytic studies, comparison between the activity of the co-immobilised system with a mixture of the two independently immobilised catalysts should be made. A two chamber setup in which conditions for the individual sMAO supported catalysts can be optimised should also be attempted.

5.10. References

1. T. L. Lohr and T. J. Marks, *Nat. Chem.*, 2015, **7**, 477–482.
2. E. A. Braude and R. P. Linstead, *J. Chem. Soc.*, 1954, 3544–3547.
3. H. Meerwein and R. Schmidt, *Justus Liebig's Ann. der Chemie*, 1925, **444**, 221–238.
4. W. Ponndorf, *Zeitschrift für Angew. Chem.*, 1926, **39**, 138–143.
5. A. Verley, *Bull. Soc. Chim. Fr.*, 1925, **37**, 537–542.
6. V. Polshettiwar and R. S. Varma, *Green Chem.*, 2009, **11**, 1313–1316.
7. R. Cohen, C. R. Graves, S. T. Nguyen, J. M. L. Martin, and M. A. Ratner, *J. Am. Chem. Soc.*, 2004, **126**, 14796–14803.
8. R. P. Linstead, F. A. Braude, P. W. D. Mitchell, K. R. H. Wooldridge, and L. M. Jackman, *Nature*, 1952, **169**, 100–103.
9. D. Wang and D. Astruc, *Chem. Rev.*, 2015, **115**, 6621–6686.
10. J. Ito and H. Nishiyama, *Tetrahedron Lett.*, 2014, **55**, 3133–3146.
11. P. Dani, T. Karlen, R. A. Gossage, S. Gladiali, and G. van Koten, *Angew. Chem. Int. Ed.*, 2000, **39**, 743–745.
12. C. J. Moulton and B. L. Shaw, *J. Chem. Soc., Dalton Trans.*, 1976, 1020–1024.
13. R. J. Errington and B. L. Shaw, *J. Organomet. Chem.*, 1982, **238**, 319–325.
14. M. A. McLoughlin, R. J. Flesher, W. C. Kaska, and H. A. Mayer, *Organometallics*, 1994, **13**, 3816–3822.
15. M. Gupta, C. Hagen, R. J. Flesher, W. C. Kaska, and C. M. Jensen, *Chem. Commun.*, 1996, **36**, 2083–2084.
16. D. W. Lee, W. C. Kaska, and C. M. Jensen, *Organometallics*, 1998, **17**, 1–3.
17. C. Gunanathan and D. Milstein, *Science*, 2013, **341**, 1229712.
18. W. Xu, G. P. Rosini, K. Krogh-Jespersen, A. S. Goldman, M. Gupta, C. M. Jensen, and W. C. Kaska, *Chem. Commun.*, 1997, 2273–2274.
19. Z. Huang, M. Brookhart, A. S. Goldman, S. Kundu, A. Ray, S. L. Scott, and B. C. Vicente, *Adv. Synth. Catal.*, 2009, **351**, 188–206.
20. M. Rimoldi, A. Nakamura, N. A. Vermeulen, J. J. Henkelis, A. K. Blackburn, J. T. Hupp, J. F. Stoddart, and O. K. Farha, *Chem. Sci.*, 2016, **7**, 4980–4984.
21. M. Rimoldi, D. Fodor, J. a van Bokhoven, and A. Mezzetti, *Chem. Commun.*, 2013, **49**, 11314–11316.
22. M. Rimoldi and A. Mezzetti, *Inorg. Chem.*, 2014, **53**, 11974–11984.
23. A. F. R. Kilpatrick, J.-C. Buffet, P. Nørby, N. H. Rees, N. P. Funnell, S. Sripothongnak, and D. O'Hare, *Chem. Mater.*, 2016, **28**, 7444–7450.
24. E. Kaji and E. Yoshioka, *Solid polymethylaluminoxane composition and process for manufacturing same*, 2010, WO2010055652.
25. R. Ghosh, M. Kanzelberger, T. J. Emge, G. S. Hall, and A. S. Goldman, *Organometallics*, 2006, **25**, 5668–5671.
26. J. D. Hackenberg, S. Kundu, T. J. Emge, K. Krogh-Jespersen, and A. S. Goldman, *J. Am. Chem. Soc.*, 2014, **136**, 8891–8894.
27. C. R. Groom, I. J. Bruno, M. P. Lightfoot, and S. C. Ward, *Acta Crystallogr. Sect. B Struct. Sci. Cryst. Eng. Mater.*, 2016, **72**, 171–179.

28. L. E. Sutton, *Tables of Interatomic Distances and Configuration in Molecules & Ions*, The Chemical Society, London, 1958.
29. S. M. Mansell, N. Kaltsoyannis, and P. L. Arnold, *J. Am. Chem. Soc.*, 2011, **133**, 9036–9051.
30. J. Choi, Y. Choliy, X. Zhang, T. J. Emge, K. Krogh-Jespersen, and A. S. Goldman, *J. Am. Chem. Soc.*, 2009, **131**, 15627–15629.
31. J. Choi, A. H. R. MacArthur, M. Brookhart, and A. S. Goldman, *Chem. Rev.*, 2011, **111**, 1761–1779.
32. K. B. Renkema, Y. V. Kissin, and A. S. Goldman, *J. Am. Chem. Soc.*, 2003, **125**, 7770–7771.
33. M. Kanzelberger, B. Singh, M. Czerw, K. Krogh-Jespersen, and A. S. Goldman, *J. Am. Chem. Soc.*, 2000, **122**, 11017–11018.
34. T. Ren, M. Patel, and K. Blok, *Energy*, 2006, **31**, 425–451.
35. B. C. Bailey, R. R. Schrock, S. Kundu, A. S. Goldman, Z. Huang, and M. Brookhart, *Organometallics*, 2009, **28**, 355–360.

Chapter Six – Experimental details

"Chemistry is necessarily an experimental science: its conclusions are drawn from data, and its principles supported by evidence from facts." **Michael Faraday**

6.1. General details

All reactions were performed under an inert nitrogen or argon atmosphere using standard Schlenk line techniques and, where required, an MBraun UNIlab glovebox. Pentane, hexane, benzene, DCM and toluene were dried and degassed using an MBraun SPS-800 solvent purification system. Octane was dried over dry degassed 4 Å molecular sieves for a minimum of 24 hours. Mesitylene was dried by refluxing under reduced pressure over sodium. THF was distilled from Na/benzophenone and diethylether was distilled from Na/K. All solvents were stored in Rotaflo ampoules either over a potassium mirror (pentane, hexane, octane, toluene and diethyl ether) or dry degassed 4 Å molecular sieves (benzene, DCM, THF and mesitylene) and degassed under partial vacuum before use. d_6-Benzene (Sigma Aldrich), d_8-toluene, d_2-DCM, d_{18}-octane, d_5-chlorobenzene, d_5-bromobenzene, d_4-*o*-dichlorobenzene (Goss Scientific) and d_8-THF (Fluorochem) were dried at reflux under partial vacuum either over K (d_6-benzene, d_8-toluene and d_{18}-octane) or CaH_2 (d_2-DCM, d_5-chlorobenzene, d_5-bromobenzene, d_4-*o*-dichlorobenzene and d_8-THF). They were freeze-pump-thaw degasssed three times and stored under N_2.

6.1.1. Commercially supplied reagents

WCl_6, TMA, TEA, DMAC, MAO, anhydrous $AlCl_3$, HMDSO, MeLi, 1-hexene, 1-octene, KH, $LiAlH_4$, ^{t}BuOK, benzylmagnesium chloride, $^{13}CH_3I$, anhydrous dodecane, anhydrous HCl, $Si(SiMe_3)_4$, mesitylene, 1,4-dibromobutane, AgF, $(^t BuO)_3SiOH$, Grubbs 2nd generation catalyst, Hoveyda-Grubbs 2nd generation catalyst, fumed silica, iridium (II) chloride hydrate, 1,3-bis(di-*tert*-butylphosphinomethyl)benzene, 3,3-dimethyl-1-butene, cyclooctane, phenyl isocyanate, 2,6-dimethylphenyl isocyanate, 4-methoxyphenyl isocyanate, 3,5-dimethylphenyl isocyanate were purchased from Sigma Aldrich; $AgPF_6$, LiCp, 2,4,6-trimethylphenyl isocyanate, 2,6-difluorophenyl isocyanate and 3,5-bis(trifluoromethyl)phenyl isocyanate were purchased from Alfa Aesar. Isocyanates were freeze-pump-thaw degassed three times prior to use. 1-hexene and 1-octene were dried over 4 Å molecular sieves. Propylene, ethane and hydrogen lecture bottles, CONCOA regulators and flashback arrestors were supplied by CK Gas Products Limited. Borosilicate XRD capillary tubes were supplied by Capillary tube supplies LTD. $[Mg_{0.75}Al_{0.25}(OH)_2](SO_4)_{0.125}\cdot 0.71H_2O\cdot 0.17$(acetone) ($Mg_3Al$-$SO_4$ AMO-LDH) was supplied by SCG Chemicals Co. Ltd (Thailand), having been synthesised according to a literature procedure.[1]

6.1.2. Synthesis of literature compounds

The following compounds were synthesised according to literature procedures: $W(O)Cl_4$,[2] $W\{N(2,6\text{-}^{i}Pr\text{-}C_6H_3)\}Cl_4(Et_2O)$,[3] $W\{N(2,6\text{-}^{i}Pr\text{-}C_6H_3)\}(CH^{t}Bu)(CH_2{}^{t}Bu)_2$,[3] $Al(^{13}CH_3)_3$,[4] $AlNp_3$,[5] $(^{t}BuO)_3SiOLi$,[6] $Mg(CH_2Ph)_2(THF)_2$,[7] $^{t}BuCH_2Li$,[8] $Ir(^{tBu}PCP)HCl$,[9] $Ir(^{tBu}PCP)H_4$,[9] $BrMgC_4H_8MgBr$,[10] $^{t}BuCH_2MgCl$.[11] Grignards were titrated according to a literature procedure with menthol and 1,10-phenanthroline as an indicator.[12]

$Mg_3Al\text{-}CO_3$ and $Mg_3Al\text{-}NO_3$ AMO-LDHs were synthesised by Dr. Chunping Chen according to a literature procedure.[1] $NaBAr^{F}{}_4$ and trityl $BAr^{F}{}_4$ were synthesised by Mr. Duncan Fraser according to 'in house' and literature procedures respectively.[13] Solid polymethylaluminoxane (sMAO) was synthesised by Dr. Alexander Kilpatrick according to literature procedures.[14,15]

6.1.3. Solution-state nuclear magnetic resonance (NMR) spectroscopy

Solution samples for NMR spectroscopy were made up in the glovebox, using 5 mm J. Young valve NMR spectroscopy tubes. Spectra were recorded either on a Bruker Avance III HD Nanobay 400 MHz or 500 MHz NMR spectrometers at 298 K and were referenced to the residual protio-solvent peak. $^{13}C\{^{1}H\}$ NMR spectral assignments were confirmed by 2D correlation spectroscopy (HSQC and HMBC experiments).

6.1.4. Solid-state NMR (SSNMR) spectroscopy

Solid-state NMR spectra were recorded by Dr. Nicholas Rees on a Bruker Avance III HD Nanobay 400 MHz NMR spectrometer in 4 mm OD rotors using contact times for CPMAS spectra of 3000 μs. Samples were spun at the magic angle (54.71°) at spin rates of 10 or 24 kHz and referenced to adamantane (^{13}C), teflon (^{19}F), $Al(NO_3)_3$ (^{27}Al) and H_3PO_4 (85%) with ADP as a secondary reference (^{31}P).

6.1.5. Fourier transform infrared (FTIR) spectroscopy

Air sensitive samples were prepared in the glove box as pressed KBr discs, using a specially designed press and cell. Spectra were recorded on a Nicolet iS5 ThermoScientific spectrometer in transmission mode (range 4000-400 cm^{-1}, resolution 1 cm^{-1}).

6.1.6. Single crystal X-ray diffraction

Single crystal X-ray diffraction data were collected and solved either under the supervision of, or solely by Dr. Zoë Turner. Crystals were mounted on MiTeGen

MicroMounts using perfluoropolyether oil and rapidly transferred to a goniometer head on a diffractometer fitted with an Oxford Cryosystems Cryostream open-flow nitrogen cooling device.[16] Data collections were carried out at 150 K either using an Oxford Diffraction Supernova diffractometer using mirror-monochromated Cu Kα radiation (λ = 1.54184 Å) with data processed by CrysalisPro[17] or using an Enraf-Nonius Kappa CCD diffractometer using graphite-monochromated Mo Kα radiation (λ = 0.71073 Å), where raw frame data were reduced using the DENZO-SMN package,[18] and corrected for absorption using SORTAV.[19] The structures were solved using direct methods (SIR-92)[20] or a charge-flipping algorithm (SUPERFLIP)[21] and refined by full-matrix least-squares procedures using the Win-GX software suite.[22,23] Molecular structures were depicted utilising Ortep,[22] with ellipsoids shown at 50% probability. Molecular bond lengths and angles were calculated using Platon.[24,25]

6.1.7. DFT calculations

DFT calculations were performed by either Dr. Zoë Turner or Mr. Duncan Fraser utilising the ORCA program package.[26] The geometry optimisations of the complexes and single-point calculations on the optimised geometries were carried out at the BP86[27–29] level of DFT. Relativistic effects were accounted for by including the zeroth-order regular approximation (ZORA).[30–32] The def2-TZVP(-f) basis set in the scalar relativistic recontraction reported by Neese *et al.* (segmented all-electron relativistic basis sets, SARC) was applied.[33,34] For all elements up to bromine, the SARC basis sets are simply scalar relativistic recontractions of the basis sets developed by the Ahlrichs group,[35,36] while for heavier elements, the primitives and contraction patterns were designed in references 33 and 34. The Coulomb fitting basis set of Weigend[37] was used in uncontracted form in all calculations. The RI[38–40] approximation was used to accelerate the calculations. Orbitals were generated with the program Chimera.[41]

6.1.8. Gas chromatography mass spectrometry (GCMS) analysis

GCMS samples were recorded on an Agilent Technologies 7820A GC system equipped with a PLOT column (27.5 m x 0.32 mm x 5 μm), coupled to an Agilent Technologies 5977E MSD instrument.

6.1.9. Elemental analysis

Elemental analyses (CHN) were performed by Mr. Stephen Boyer at London Metropolitan University, North Campus, Holloway Road, London, N7 8DB.

6.1.10. General oligomerisation procedure

All oligomerisation reactions were performed in oven-dried J. Young valve NMR spectroscopy tubes which were loaded in the glovebox, degassed and ethylene added *via* a vacuum/nitrogen/ethylene manifold. Deuterated solvent (500 μL) containing either mesitylene (20.1 μmol), pyridine (9.93 μmol) or $Si(SiMe_3)_4$ (3.11 μmol) was added *via* microliter syringe to each NMR tube prior addition of ethylene. Runs were periodically analysed by ^1H NMR spectroscopy and once stopped, by GCMS.

6.1.11. General ethylene polymerisation procedure

TIBA (150 mg, 0.76 mmol) was dissolved in hexane (10 mL), added to a 100 mL Rotaflo ampoule and swirled to ensure no contaminants were present. Supported catalyst (10 mg) was added and washed down with hexane (40 mL), after which the ampoule was sealed. Polymerisations were conducted on a specially designed vacuum/nitrogen manifold, with a separate ethylene feed that was dried through a column of activated molecular sieves. Prior to ethylene addition, all the tubing and headspace were cycled between vacuum and N_2 three times, after which the internal atmosphere of the ampoule was evacuated, and the tubing cycled between vacuum and ethylene 3 times. Polymerisations were conducted at 70 °C, 2 bar ethylene with a stirring speed of 1000 rpm for 1 hour. The resulting polyethylene was collected on a frit and washed with pentane (3 x 25 mL), before being dried under vacuum overnight at room temperature.

6.2. Experimental details for Chapter Two

6.2.1. Synthesis of $W(NR)Cl_4(THF)$ complexes

The following syntheses were based on literature procedures.[3,42,43] $W(O)Cl_4$ was introduced into a 500 mL all-in-one RBF condenser. Octane (~250 mL) was added, followed by dropwise addition of 1.1 equivalents of the relevant aryl isocyanate reagent with stirring. The mixture was heated to reflux for 16 hours, after which it was allowed to cool to room temperature. The slurry was transferred to a Schlenk and the solvent removed by filtration. Drying of the resulting solid yielded powders in all cases. The solids were dissolved in THF resulting in a colour change and dried. Crystals suitable for single crystal X-ray diffraction studies were grown from hexane at −33 °C unless otherwise stated.

$W(NPh)Cl_4(THF)$ (1.1). $W(O)Cl_4$ (5.0 g, 14.6 mmol) and phenyl isocyanate (1.9 g, 16.1 mmol) yielded $W(NPh)Cl_4$ (5.6 g) as a dark red solid in 92% yield. Dissolution in THF

led to a dark green solution and a green solid after drying. Recrystallisation yielded green crystals of **1.1** in an isolated yield of 75%.

Anal. Calcd (found) (%) C 24.57 (24.48), H 2.68 (2.61), N 2.87 (2.87).

^{1}H NMR (d_6-benzene) δ (ppm): 7.01 (d, 2H, Ar**H**$_{ortho}$), 6.92 (t, 2H, Ar**H**$_{meta}$), 6.17 (m, 1H, Ar**H**$_{para}$), 4.47 (m, 4H, **THF**), 1.27 (m, 4H, **THF**).

^{13}C{^{1}H} NMR (d_6-benzene) δ (ppm): 149.6 (**Ar**$_{ipso}$N), 133.9 (**Ar**$_{para}$H), 131.7 (**Ar**$_{ortho}$H), 127.2 (**Ar**$_{meta}$H), 73.9 (**THF**), 25.4 (**THF**).

FTIR (KBr mull) (cm^{-1}): 2961 (broad, aromatic C–H), 1578 (weak, aromatic C–C), 1476 (weak, aromatic C–C), 1384 (weak), 1256 (weak), 1097 (weak), 999 (broad), 835 (strong, broad), 759 (strong, C–H oop), 672 (C–H oop).

W{N(2,6-Me-C$_6$H$_3$)}Cl$_4$(THF) (1.2). W(O)Cl$_4$ (5.0 g, 14.6 mmol) and 2,6-dimethylphenyl isocyanate (2.4 g, 16.1 mmol) generated W{N(2,6-Me-C$_6$H$_3$)}Cl$_4$ (4.0 g) as a dark red solid in 62% yield. Recrystallisation afforded orange crystals of **1.2** in an isolated yield of 70%.

Anal. Calcd (found) (%) C 27.88 (28.00), H 3.32 (3.32), N 2.71 (2.80).

^{1}H NMR (d_6-benzene) δ (ppm): 6.78 (d, 2H, Ar**H**$_{meta}$), 5.91 (dd, 1H, Ar**H**$_{para}$), 4.43 (m, 4H, **THF**), 3.35 (s, 6H, Ar$_{ortho}$C**H**$_3$), 1.27 (m, 4H, **THF**).

^{13}C{^{1}H} NMR (d_6-benzene) δ (ppm): 148.1 (**Ar**$_{ipso}$N), 145.6 (**Ar**$_{ortho}$CH$_3$), 133.8 (**Ar**$_{para}$H), 126.2 (**Ar**$_{meta}$H), 73.6 (**THF**), 25.4 (**THF**), 17.7 (Ar$_{ortho}$**C**H$_3$).

FTIR (KBr mull) (cm^{-1}): 2961 (broad, aromatic C–H), 1584 (weak, aromatic C–C), 1465 (weak, aromatic C–C), 1384 (weak), 1256 (weak), 1051 (weak), 1009, 851 (strong, broad), 779 (strong, C–H oop).

W{N(3,5-Me-C$_6$H$_3$)}Cl$_4$(THF) (1.3). W(O)Cl$_4$ (5.0 g, 14.6 mmol) and 3,5-dimethylphenyl isocyanate (2.4 g, 16.1 mmol) generated W{N(3,5-Me-C$_6$H$_3$)}Cl$_4$ (7.0 g) as a dark red solid in 84% yield. Recrystallisation afforded orange crystals of **1.3** in an isolated yield of 73%.

Anal. Calcd (found) (%) C 27.88 (27.86), H 3.32 (3.35), N 2.71 (2.72).

^{1}H NMR (d_6-benzene) δ (ppm): 6.84 (s, 2H, Ar**H**$_{ortho}$), 5.85 (s, 1H, Ar**H**$_{para}$), 4.50 (m, 4H, **THF**), 1.60 (s, 6H, Ar$_{meta}$C**H**$_3$), 1.30 (m, 4H, **THF**).

^{13}C{^{1}H} NMR (d_6-benzene) δ (ppm): 148.6 (**Ar**$_{ipso}$N), 137.1 (**Ar**$_{meta}$CH$_3$), 137.0 (**Ar**$_{para}$H), 129.6 (**Ar**$_{ortho}$H), 73.9 (**THF**), 25.5 (**THF**), 21.1 (Ar$_{meta}$**C**H$_3$).

FTIR (KBr mull) (cm^{-1}): 2963 (broad, aromatic C–H), 1599 (weak, aromatic C–C), 1451 (weak, aromatic C–C), 1378 (weak), 1261, 1083 (broad), 1014 (broad, strong), 851 (strong), 798 (strong, C–H oop), 677 (C–H oop).

W{N(2,4,6-Me-C_6H_2)}Cl_4(THF) (1.4). $W(O)Cl_4$ (10.6 g, 31.0 mmol) and 2,4,6-trimethylphenyl isocyanate (5.0 g, 31.0 mmol) yielded $W\{N(C_6H_2(2,4,6\text{-}Me)\}Cl_4$ (10.2 g) as a dark red solid in 72% yield.

^{1}H NMR (d_6-benzene) δ (ppm): 6.43 (s, 2H, Ar**H**$_{meta}$), 3.06 (s, 6H, $Ar_{ortho}C\mathbf{H}_3$), 2.57 (s, 3H, $Ar_{para}C\mathbf{H}_3$).

Dissolution in THF led to a dark green/brown solution and an orange solid after drying. Recrystallisation afforded orange crystals of **1.4**, isolated yield of 80%.

Anal. Calcd (found) (%) C 29.41 (29.46), H 3.61 (3.78), N 2.64 (2.57).

^{1}H NMR (d_6-benzene) δ (ppm): 6.55 (s, 2H, Ar**H**$_{meta}$), 4.55 (m, 4H, **THF**), 3.39 (s, 6H, $Ar_{ortho}C\mathbf{H}_3$), 2.6 (s, 3H, $Ar_{para}C\mathbf{H}_3$), 1.27 (m, 4H, **THF**).

^{13}C{^{1}H} NMR (d_6-benzene) δ (ppm): 146.4 (**Ar**$_{ipso}$N), 145.8 (**Ar**$_{ortho}CH_3$), 145.3 (**Ar**$_{para}CH_3$), 126.6 (**Ar**$_{meta}$H), 73.5 (**THF**), 25.4 (**THF**), 19.9 ($Ar_{para}\mathbf{C}H_3$), 17.6 ($Ar_{ortho}\mathbf{C}H_3$).

FTIR (KBr mull) (cm^{-1}): 2958 (broad, aromatic C–H), 1604 (aromatic C–C), 1462 (weak, aromatic C–C), 1404 (weak, aromatic C–C), 1304 (weak), 1267, 1103 (broad), 1014 (broad), 846 (strong, C–H oop), 798 (strong, C–H oop).

W{N(2,6-^{i}Pr-C_6H_3)}Cl_4(THF) (1.5). $W(O)Cl_4$ (10.0 g, 29.3 mmol) and 2,6-diisopropylphenyl isocyanate (6.5 g, 32.2 mmol) yielded $W\{N(2,6\text{-}^i\text{Pr-}C_6H_3)\}Cl_4$ (9.2 g) as a dark red solid in 63% yield.

^{1}H NMR (d_6-benzene) δ (ppm): 7.08 (d, 2H, Ar**H**$_{meta}$), 6.20 (m, 1H, Ar**H**$_{para}$), 4.64 (m, 2H, $Ar_{ortho}C\mathbf{H}(CH_3)_2$), 1.21 (d, 12H, $Ar_{ortho}CH(C\mathbf{H}_3)_2$).

Dissolution in THF led to a dark green solution and a green solid after drying. Recrystallisation afforded green crystals of **1.5**, isolated yield of 70%.

^{1}H NMR (d_6-benzene) δ (ppm): 7.21 (d, 2H, Ar**H**$_{meta}$), 6.26 (m, 1H, Ar**H**$_{para}$), 4.98 (m, 2H, $Ar_{ortho}C\mathbf{H}(CH_3)_2$), 4.44 (m, 4H, **THF**), 1.37 (d, 12H, $Ar_{ortho}CH(C\mathbf{H}_3)_2$), 1.25 (m, 4H, **THF**).

^{13}C{^{1}H} NMR (d_6-benzene) δ (ppm): 156.2 (**Ar**$_{ipso}$N), 146.0 (**Ar**$_{meta}$H), 134.3 (**Ar**$_{ortho}CH(CH_3)_2$), 122.2 (**Ar**$_{para}$H), 73.6 (**THF**), 27.9 ($Ar_{ortho}\mathbf{C}H(CH_3)_2$), 26.3 ($Ar_{ortho}CH(\mathbf{C}H_3)_2$), 25.4 (**THF**).

^{1}H NMR (d_2-DCM) δ (ppm): 7.57 (d, 2H, Ar**H**$_{meta}$), 6.69 (m, 1H, Ar**H**$_{para}$), 4.72 (m, 4H, **THF**), 4.54 (m, 2H, Ar$_{ortho}$C**H**(CH$_3$)$_2$), 2.16 (m, 4H, **THF**), 1.37 (d, 12H, Ar$_{ortho}$CH(C**H**$_3$)$_2$).

^{13}C{^{1}H} NMR (d_2-DCM) δ (ppm): 156.4 (**Ar**$_{ipso}$N), 140.0 (**Ar**$_{meta}$H), 134.8 (**Ar**$_{ortho}$CH(CH$_3$)$_2$), 122.3 (**Ar**$_{para}$H), 74.3 (**THF**), 28.0 (Ar$_{ortho}$**C**H(CH$_3$)$_2$), 26.5 (Ar$_{ortho}$CH(**C**H$_3$)$_2$), 26.3 (**THF**).

FT-IR (KBr mull) (cm^{-1}): 2974 (broad, aromatic C–H), 1583 (weak, aromatic C–C), 1457 (weak, aromatic C–C), 1383, 1361, 1261 (weak), 1103 (weak), 1051 (weak), 1003, 935 (weak), 850 (broad, strong), 798 (strong, C–H oop), 745 (C–H oop).

W{N(4-OMe-C$_6$H$_4$)}Cl$_4$(THF) (1.6). W(O)Cl$_4$ (10.0 g, 29.3 mmol) and 4-methoxyphenyl isocyanate (4.8 g, 32.2 mmol) yielded W{N(4-OMe-C$_6$H$_4$)}Cl$_4$ (10.2 g) as a dark blue solid in 88% yield. Dissolution in THF and drying afforded a dark red solid. Recrystallisation from pentane at −33 °C yielded dark red crystals of **1.6** in an isolated yield of 67%.

Anal. Calcd (found) (%) C 27.33 (27.22), H 3.13 (3.02), N 2.90 (2.70).

^{1}H NMR (d_6-benzene) δ (ppm): 6.98 (d, 2H, Ar**H**$_{ortho}$), 6.41 (d, 2H, Ar**H**$_{meta}$), 4.51 (m, 4H, **THF**), 3.10 (Ar$_{para}$OC**H**$_3$), 1.29 (m, 4H, **THF**).

^{13}C{^{1}H} NMR (d_6-benzene) δ (ppm): 164.8 (**Ar**$_{para}$OCH$_3$), 144.0 (**Ar**$_{ipso}$N), 134.3 (**Ar**$_{ortho}$H), 112.5 (**Ar**$_{meta}$H), 73.8 (**THF**), 56.0 (Ar$_{para}$O**C**H$_3$), 25.4 (**THF**).

FT-IR (KBr mull) (cm^{-1}): 2969 (broad, aromatic C–H), 1588 (aromatic C–C), 1503 (weak, aromatic C–C), 1372 (weak), 1304 (weak), 1266 (strong, C–O), 1166, 1103 (weak), 1024 (C–O), 835 (strong, C–H oop), 798 (C–H oop).

W{N(2,6-F-C$_6$H$_3$)}Cl$_4$(THF) (1.7). W(O)Cl$_4$ (5.0 g, 14.6 mmol) and 2,6-difluorophenyl isocyanate (2.5 g, 16.1 mmol) yielded W{N(2,6-F-C$_6$H$_3$)}Cl$_4$ (6.1 g) as a dark red solid (79% yield). Dissolution in THF led to a dark green solution and a dark green solid after drying. Recrystallisation yielded dark green crystals of **1.7** in an isolated yield of 80%.

Anal. Calcd (found) (%) C 22.89 (22.75), H 2.11 (2.12), N 2.67 (2.76).

^{1}H NMR (d_6-benzene) δ (ppm): 6.20 (t, 2H, Ar**H**$_{meta}$), 5.62 (m, 1H, Ar**H**$_{para}$), 4.45 (m, 4H, **THF**), 1.24 (m, 4H, **THF**).

^{13}C{^{1}H} NMR (d_6-benzene) δ (ppm): 167.1 (**Ar**$_{ortho}$F), 164.5 (**Ar**$_{ipso}$N), 134.7 (**Ar**$_{para}$H), 110.0 (**Ar**$_{meta}$H), 74.3 (**THF**), 25.4 (**THF**).

^{19}F{^{1}H} NMR (d_6-benzene) δ (ppm): −111.04.

FT-IR (KBr mull) (cm^{-1}): 2969 (broad, aromatic C–H), 1609 (strong, aromatic C–C), 1473 (strong, aromatic C–C), 1251 (weak), 1020 (broad), 846 (strong, C–H oop), 782 (strong, C–H oop).

W{N(3,5-CF_3-C_6H_3)}Cl_4(THF) (1.8). W(O)Cl_4 (5.0 g, 14.6 mmol) and 3,5-bis(trifluoromethyl)phenyl isocyanate (4.1 g, 16.1 mmol) yielded W{N(3,5-CF_3-C_6H_3)}Cl_4 (5.35 g) as a dark green solid in 65% yield. W{N(3,5-CF_3-C_6H_3)}Cl_4 (100 mg) was dissolved in THF and dried. Dichromic yellow/blue crystals of **1.8** were grown from pentane at −33 °C in a crystalline yield of 25%.

Anal. Calcd (found) (%) C 23.07 (23.21), H 1.77 (1.79), N 2.24 (2.33).

^{1}H NMR (d_6-benzene) δ (ppm): 7.43 (s, 2H, Ar**H**$_{ortho}$), 6.96 (s, 1H, Ar**H**$_{para}$), 4.39 (m, 4H, **THF**), 1.24 (m, 4H, **THF**).

^{13}C{^{1}H} NMR (d_6-benzene) δ (ppm): 150.0 (**Ar**$_{ipso}$N), 130.6 (**Ar**$_{para}$H), 126.0 (**Ar**$_{ortho}$H), 124.4 (**Ar**$_{meta}$$CF_3$), 121.6 (Ar$_{meta}$**C**$F_3$), 74.6 (**THF**), 25.4 (**THF**).

^{19}F{^{1}H} NMR (d_6-benzene) δ (ppm): −63.15.

FT-IR (KBr mull) (cm^{-1}): 3083 (weak, 2969 (broad, aromatic C–H), 1457 (aromatic C–C), 1404 (strong), 1320 (strong), 1278 (strong), 1183 (broad, strong), 1135 (broad, strong), 1062 (strong), 1003, 898 (strong), 845 (broad, strong), 687 (broad).

6.2.2. Reaction of 1.5 and triethylaluminium (TEA)

1.5 (45.2 mg, 0.08 mmol) was added to a J. Young valve NMR spectroscopy tube and dissolved in d_6-benzene. TEA (9 mg, 0.08 mmol) was added and the tube sealed and shaken. Effervescence was observed with a colour change from green to a red/orange solution and a red solid. ^{1}H NMR spectroscopy showed a strong resonance for ethane (0.8 ppm), with multiple broad resonances in the methyl, methine and aromatic regions. Extraction of the product from hexane, gave a similarly broad ill-defined spectrum.

6.2.3. Synthesis of W(NR)Me_3Cl complexes

Individually, complexes **1.1**–**1.8** (0.5-1 g) were charged into a Rotaflo ampoule and dissolved in benzene (20 mL). Excess TMA was added (~1.2 eq.) and the mixture stirred for 1 hour. An immediate colour change was observed upon mixing in all cases. After drying *in vacuo*, the product was extracted from hexane and purified by fractional crystallisation at −33 °C. Crystals of **2.1**-**2.3** and **2.5**-**2.7** suitable for single crystal X-ray diffraction studies were grown from hexane once all the residual aluminium compounds had been removed.

W(NPh)Me$_3$Cl (2.1). Pale yellow crystalline solid in 20% crystalline yield.

Anal. Calcd (found) (%) C 30.41 (30.54), H 3.97 (4.08), N 3.94 (3.97).

^{1}H NMR (d_6-benzene) δ (ppm): 7.01 (m, 2H, Ar**H**$_{meta}$), 6.99 (d, 2H, Ar**H**$_{ortho}$), 6.88 (m, 2H, Ar**H**$_{para}$), 1.29 (s, 9H, W(C**H**$_3$)$_3$, $^2J_{W–H}$ = 6.8 Hz).

^{13}C{^{1}H} NMR (d_6-benzene) δ (ppm): 152.1 (**Ar**$_{ipso}$N), 128.8 (**Ar**$_{meta}$H), 127.9 (**Ar**$_{para}$H), 127.6 (**Ar**$_{ortho}$H), 53.6 (W(**C**H$_3$)$_3$, $^1J_{W–C}$ = 299 Hz).

FT-IR (KBr mull) (cm^{-1}): 2984 (broad, aromatic C–H), 1483 (strong, aromatic C–C), 1362 (strong), 1257 (weak), 1098 (weak), 1072 (weak), 1020, 988 (weak), 803 (broad, weak), 767 (C–H oop), 687 (strong, CH–oop), 530 (broad).

W{N(2,6-Me-C$_6$H$_3$)}Me$_3$Cl (2.2). Orange crystalline solid in 42% crystalline yield.

Anal. Calcd (found) (%) C 34.45 (34.53), H 4.73 (4.82), N 3.65 (3.66).

^{1}H NMR (d_6-benzene) δ (ppm): 6.83 (d, 2H, Ar**H**$_{meta}$), 6.74 (t, 1H, Ar**H**$_{para}$), 2.21 (s, 6H, Ar$_{ortho}$C**H**$_3$), 1.34 (s, 9H, W(C**H**$_3$)$_3$, $^2J_{W–H}$ = 7.2 Hz).

^{13}C{^{1}H} NMR (d_6-benzene) δ (ppm): 150.4 (**Ar**$_{ipso}$N), 139.6 (**Ar**$_{ortho}$CH$_3$), 127.9 (**Ar**$_{meta}$H), 127.4 (**Ar**$_{para}$H), 56.1 (W(**C**H$_3$)$_3$, $^1J_{W–C}$ = 302 Hz), 19.4 (Ar$_{ortho}$**C**H$_3$).

^{1}H NMR (d_2-DCM) δ (ppm): 7.16 (d, 2H, Ar**H**$_{meta}$), 7.04 (t, 1H, Ar**H**$_{para}$), 2.57 (s, 6H, Ar$_{ortho}$C**H**$_3$), 1.43 (s, 9H, W(C**H**$_3$)$_3$, $^2J_{W–H}$ = 7.2 Hz).

^{13}C{^{1}H} NMR (d_2-DCM) δ (ppm): 149.7 (**Ar**$_{ipso}$N), 140.1 (**Ar**$_{ortho}$CH$_3$), 128.4 (**Ar**$_{meta}$H), 128.0 (**Ar**$_{para}$H), 57.0 (W(**C**H$_3$)$_3$, $^1J_{W–C}$ = 307 Hz), 19.8 (Ar$_{ortho}$**C**H$_3$).

^{1}H NMR (d_8-THF) δ (ppm): 7.16 (d, 2H, Ar**H**$_{meta}$), 7.02 (t, 1H, Ar**H**$_{para}$), 2.57 (s, 6H, Ar$_{ortho}$C**H**$_3$), 1.39 (s, 9H, W(C**H**$_3$)$_3$, $^2J_{W–H}$ = 7.2 Hz).

FT-IR (KBr mull) (cm^{-1}): 2966 (broad, aromatic C–H), 1471 (weak, aromatic C–C), 1374 (strong), 1333 (weak), 1256 (weak), 1102 (weak), 1020 (broad), 800, 779 (strong C–H oop), 523.

W{N(3,5-Me-C$_6$H$_3$)}Me$_3$Cl (2.3). Yellow crystalline solid in 61% crystalline yield.

Anal. Calcd (found) (%) C 34.45 (34.38), H 4.73 (4.85), N 3.65 (3.60).

^{1}H NMR (d_6-benzene) δ (ppm): 6.85 (s, 2H, Ar$_{ortho}$**H**), 6.58 (s, 1H, Ar$_{para}$**H**), 1.99 (s, 6H, Ar$_{meta}$C**H**$_3$), 1.34 (s, 9H, W(C**H**$_3$)$_3$, $^2J_{W–H}$ = 7.20 Hz).

^{13}C{^{1}H} NMR (d_6-benzene) δ (ppm): 152.3 (**Ar**$_{ipso}$N), 138.5 (**Ar**$_{meta}$CH$_3$), 130.4 (**Ar**$_{para}$H), 125.3 (**Ar**$_{ortho}$H), 53.6 (W(**C**H$_3$)$_3$, $^1J_{W–C}$ = 276 Hz), 21.1 (Ar$_{meta}$**C**H$_3$).

W{N(2,4,6-Me-C_6H_2)}Me_3Cl (2.4). Yellow solid in 20% isolated yield.

^{1}H NMR (d_6-benzene) δ (ppm): 6.57 (s, 2H, Ar_{meta}**H**), 2.13 (s, 3H, $Ar_{para}C\mathbf{H}_3$), 2.08 (s, 6H, $Ar_{ortho}C\mathbf{H}_3$), 1.41 (s, 9H, $W(C\mathbf{H}_3)_3$, $^2J_{W–H}$ coupling not observed).

^{13}C{^{1}H} NMR (d_6-benzene) δ (ppm): 149.0 (**Ar_{ipso}**N), 140.1 (**Ar_{para}**CH_3), 139.2 (**Ar_{ortho}**CH_3), 129.1 (**Ar_{meta}**H), 64.3 ($W(\mathbf{C}H_3)_3$, $^1J_{W–C}$ = 306 Hz), 21.1 ($Ar_{para}\mathbf{C}H_3$), 19.0 ($Ar_{ortho}\mathbf{C}H_3$).

W{N(2,6-^{i}Pr-C_6H_3)}Me_3Cl (2.5) orange crystalline solid in 79% crystalline yield.

Anal. Calcd (found) (%) C 40.98 (40.92), H 5.96 (5.88), N 3.19 (3.18).

^{1}H NMR (d_6-benzene) δ (ppm): 7.04 (d, 2H, Ar**H$_{meta}$**), 6.97 (dd, 1H, Ar**H$_{para}$**), 3.53 (sept, 2H, $Ar_{ortho}C\mathbf{H}(CH_3)_2$), 1.41 (s, 9H, $W(C\mathbf{H_3})_3$, $^2J_{W–H}$ = 7.0 Hz), 1.08 (d, 12H, $Ar_{ortho}CH(C\mathbf{H}_3)_2$).

^{13}C{^{1}H} NMR (d_6-benzene) δ (ppm): 150.42 (**Ar_{ipso}**N), 128.3 (**Ar_{meta}**H), 128.13 (**Ar_{ortho}**$CH(CH_3)_2$), 123.22 (**Ar_{para}**H), 56.54 ($W(\mathbf{C}H_3)_3$, $^1J_{W–C}$ = 312 Hz), 28.83 ($Ar_{ortho}\mathbf{C}H(CH_3)_2$), 24.28 ($ArCH(\mathbf{C}H_3)_2$).

^{1}H NMR (d_8-THF) δ (ppm): 7.31 (d, 2H, Ar**H$_{meta}$**), 7.19 (m, 1H, Ar**H$_{para}$**), 3.68 (m, 2H, $Ar_{ortho}C\mathbf{H}(CH_3)_2$), 1.38 (s, 9H, $W(C\mathbf{H_3})_3$, $^2J_{W–H}$ = 7.1 Hz), 1.27 (d, 12H, $Ar_{ortho}CH(C\mathbf{H}_3)_2$).

FT-IR (KBr mull) (cm^{-1}): 2963 (broad, aromatic C–H), 1462 (broad, weak, aromatic C–C), 1366 (broad, weak), 1262, 1094 (broad), 1025 (broad), 798 (strong, C–H oop), 750 (C–H oop), 513.

W{N(4-OMe-C_6H_4)}Me_3Cl (2.6). Yellow crystalline solid in 23% crystalline yield.

Anal. Calcd (found) (%) C 31.15 (30.88), H 4.18 (4.29), N 3.63 (3.65).

^{1}H NMR (d_6-benzene) δ (ppm): 6.99 (d, 2H, Ar**H$_{ortho}$**), 6.61 (d, 2H, Ar**H$_{meta}$**), 3.23 (s, 3H, $Ar_{para}OC\mathbf{H}_3$), 1.30 (s, 9H, $W(C\mathbf{H}_3)_3$, $^2J_{W–H}$ = 6.9 Hz).

^{13}C{^{1}H} NMR (d_6-benzene) δ (ppm): 160.0 (**Ar_{para}**OCH_3), 144.0 (**Ar_{ipso}**N), 129.1 (**Ar_{ortho}**H), 114.1 (**Ar_{meta}**H), 55.1 ($Ar_{para}O\mathbf{C}H_3$), 53.5 ($W(\mathbf{C}H_3)_3$, $^1J_{W–C}$ = 301 Hz).

FT-IR (KBr mull) (cm^{-1}): 2952 (broad, aromatic C–H), 1596 (aromatic C–C), 1497 (strong, aromatic C–C), 1377, 1295, 1242 (strong, C–O), 1164, 1098, 1029 (strong, C–O), 827 (strong, C–H oop), 790 (C–H oop), 681 (broad, weak), 530 (broad, weak).

W{N(2,6-F-C_6H_3)}Me_3Cl (2.7). Orange crystalline solid in 35% crystalline yield.

Anal. Calcd (found) (%) C 27.61 (27.49), H 3.09 (2.98), N 3.58 (3.59).

^{1}H NMR (d_6-benzene) δ (ppm): 6.36 (m, 2H, Ar**H$_{meta}$**), 6.30 (m, 1H, Ar**H$_{para}$**), 1.45 (s, 9H, $W(C\mathbf{H}_3)_3$, $^2J_{W–H}$ = 7.4 Hz).

^{13}C{^{1}H} NMR (d_6-benzene) δ (ppm): 163.9 (**Ar**$_{ipso}$N), 161.3 (**Ar**$_{ortho}$F), 127.6 (**Ar**$_{para}$H), 111.5 (**Ar**$_{meta}$H), 54.4 (W(**C**H$_3$)$_3$, $^{1}J_{W–C}$ = 296 Hz).

^{19}F{^{1}H} NMR (d_6-benzene) δ (ppm): −117.6.

^{13}C-{^{1}H} CPMAS {^{19}F} decoupled SSNMR δ (ppm): 162.2 (**Ar**$_{ortho}$F), 160.8 (**Ar**$_{ipso}$N), 129.1 (**Ar**$_{para}$H), 109.8 (**Ar**$_{meta}$H), 59.0 (W(**C**H$_3$)$_2$), 55.0 (W(**C**H$_3$)).

^{19}F{^{1}H} HPDEC SSNMR δ (ppm): −116.3.

FT-IR (KBr mull) (cm^{-1}): 2985 (broad, aromatic C–H), 1614 (weak), 1577 (aromatic C–C), 1473 (strong, aromatic C–C), 1357, 1240, 1009 (strong), 776 (strong, C–H oop), 724 (C–H oop), 523.

W{N(3,5-CF$_3$-C$_6$H$_3$)}Me$_3$Cl (2.8). Red crystalline solid in 60% isolated yield.

^{1}H NMR (d_6-benzene) δ (ppm): 7.51 (s, 1H, Ar**H**$_{para}$), 7.34 (s, 2H, Ar**H**$_{ortho}$), 1.24 (s, 9H, W(C**H**$_3$)$_3$, $^{2}J_{W–H}$ = 6.9 Hz).

^{13}C{^{1}H} NMR (d_6-benzene) δ (ppm): 153.2 (**Ar**$_{ipso}$N), 127.0 (**Ar**$_{ortho}$H), 127.0 (Ar$_{meta}$**C**F$_3$), 121.9 (**Ar**$_{meta}$CF$_3$), 120.7 (**Ar**$_{para}$H), 55.1 (W(**C**H$_3$)$_3$, $^{1}J_{W–C}$ = 291 Hz).

^{19}F{^{1}H} NMR (d_6-benzene) δ (ppm): −62.9.

6.2.4. Attempted synthesis of W{N(2,6-^{i}Pr-C$_6$H$_3$)}Me$_2$Cl$_2$

Dimethylaluminium chloride (DMAC) (1 M in hexanes, 15 mg, 0.02 mmol) was mixed with d_6-benzene and added to a J. Young valve NMR spectroscopy tube containing **1.5**(Et$_2$O) (12.9 mg, 0.02 mmol). Upon mixing, an orange solution was formed. ^{1}H NMR spectroscopy showed mainly resonances attributed to the starting material, and so 1 more drop of DMAC was added. Preferential formation of **2.5** was observed. Scale-up of the reaction was attempted by dropwise addition of DMAC (1 M in hexanes, 30.4 mL, 0.35 mmol) into a stirred solution of **1.5**(Et$_2$O) (200 mg, 0.35 mmol) in benzene (30 mL). The green solution immediately turned orange. Extraction from hexane and drying yielded an orange oil, which was analysed by ^{1}H NMR spectroscopy. The major product observed was **2.5** (90%) along with a W-CH$_3$ resonance attributed to formation of W{N(2,6-^{i}Pr-C$_6$H$_3$)}Me$_2$Cl$_2$ (10%) and excess Et$_2$O. Attempts at fractional crystallisation from hexane or toluene solutions yielded solely **2.5**.

^{1}H NMR (d_6-benzene) δ (ppm): 6.88 (t, 1H, Ar**H**$_{para}$), 1.70 (s, 6H, W(C**H**$_3$)$_2$), 1.07 (d, 12H, Ar$_{ortho}$CH(C**H**$_3$)$_2$, partially obscured by **2.5**), Ar**H**$_{meta}$ and Ar$_{ortho}$C**H**(CH$_3$)$_2$ unobserved due to resonances from **2.5**.

6.2.5. Reaction of $W(O)Cl_4$ and TMA

$W(O)Cl_4$ (28 mg, 0.08 mmol) was charged in a J. Young valve NMR spectroscopy tube and dissolved in d_6-benzene. TMA (one drop, ~5-10 mg, ~1-2 eq.) was added, resulting a colour change from orange to dark brown, and formation of a dark precipitate.

^{1}H NMR (d_6-benzene) δ (ppm): 1.83 ppm (s, W(C**H**$_3$), $^2J_{W–H}$ = 8.8 Hz), proposed to be $W(O)Me_3Cl$ in an analogous structure to the $W(NR)Me_3Cl$ complexes.

TMA (105.5 mg, 1.46 mmol) dissolved in benzene (20 mL) was added dropwise to a benzene solution (20 mL) of $W(O)Cl_4$ (500 mg, 1.46 mmol) yielding a dark purple solution, with a dark precipitate. Extraction from hexane yielded an orange solution, with rapid decomposition to yield a fluffy grey solid observed. Solid shown to be silent by ^{1}H NMR spectroscopy. Cooling the remaining orange solution to −30 °C resulted in similar decomposition. Dissolution in toluene gave a red/brown solution in which the complex appeared stable. Small crystals were grown at −33 °C, however, data collection was thwarted by their high instability, yielding a blue solution as soon as solvent was removed. To try and stabilise the complex the reaction was repeated with THF (5 mL) added to the hexane extraction, which yielded a purple solution from which a blue grey NMR silent solid precipitated.

6.2.6. Reaction of 1.5(Et_2O) and $AlNp_3$

1.5(Et_2O) (26 mg, 0.05 mmol) was dissolved in d_6-benzene in a J. Young valve NMR spectroscopy tube and $AlNp_3$ (11 mg, 0.05 mmol) added. The tube was shaken, and effervescence was observed with a colour change from green to orange.

W{N(2,6-^{i}Pr-C_6H_3)}(CH^{t}Bu)(CH$_2$^{t}Bu)$_2$.[3] **^{1}H NMR** (d_6-benzene) δ (ppm): 7.12 (d, 2H, Ar**H**$_{meta}$), 7.06 (t, 1H, Ar**H**$_{para}$), 6.75 (s, 1H, WC**H**C$(CH_3)_3$)), 3.94 (m, 2H, Ar$_{ortho}$C**H**$(CH_3)_2$), 2.73 (d, 2H, WC**H**$_2$C$(CH_3)_2$), 1.31 (d, 12H, ArCH$_2$(C**H**$_3$)$_2$), 1.19 (s, 18H, WCH$_2$C(C**H**$_3$)$_3$), 1.19 (s, 9H, WCHC(C**H**$_3$)$_3$), 0.43 (d, 2H, WC**H$_2$**C$(CH_3)_2$). Formation of neopentane (0.91 ppm) was observed.

6.2.7. Homogeneous oligomerisations

$W(NR)Me_3Cl$ (2 mg) and MAO (Al/W = 2, 5, 10 and 20) were added to a J. Young valve NMR spectroscopy tube and dissolved in d_6-benzene (500 µL) containing pyridine as an internal standard (9.93 µmol). The solution was freeze-pump-thaw degassed three times. Ethylene (1 bar) was added and the tube heated at 100 °C. Formation of 1-butene was observed by periodic ^{1}H NMR spectroscopic analysis along with some isomerisation to

2-butenes and a small amount of propylene as the metathesis product. It should be noted that a small amount of methane was also observed. Product distributions were also analysed by GCMS. Samples were cooled in ice before transferring and sealing in vials ready for analysis. The same procedure was utilised when varying the co-catalyst to TMA and DMAC with Al/W = 2. For the temperature study with **2.5**, oligomerisations were run at 25, 75 and 100 °C with MAO co-catalyst (Al/W = 2). TONs were calculated by product analysis, as ethylene measuring consumption proved unreliable. Similar procedures were employed with propylene (1 bar), 1-hexene (5 µL, 0.04 µmol) and 1-octene (3 µL, 0.04 µmol) utilising $Si(SiMe_3)_4$ (3.11 µmol) as the internal standard.

1-Butene. ^{1}H NMR (d_6-benzene) δ (ppm): 5.79 (m, 1H, C**H**=$CH_{trans}H_{cis}$), 4.98 (m, 1H, CH=CH_{trans}**H**$_{cis}$), 4.93 (m, 1H, CH=C**H**$_{trans}H_{cis}$), 1.92 (dq, 2H, C**H**$_2$), 0.89 (t, 3H, C**H**$_3$).

^{13}C{^{1}H} NMR (d_6-benzene) δ (ppm): 140.54 (CH_3CH_2CH=**C**H_2), 113.48 (CH_3CH_2**C**H=CH_2), 27.03 (CH_3**C**H_2CH=CH_2), 13.28 (**C**H_3CH_2CH=CH_2). ^{1}H NMR (d_5-chlorobenzene) δ (ppm): 5.78 (m, 1H, C**H**=$CH_{trans}H_{cis}$), 4.97 (m, 1H, CH=CH_{trans}**H**$_{cis}$), 4.91 (m, 1H, CH=C**H**$_{trans}H_{cis}$), 1.95 (dq, 2H, C**H**$_2$), 0.9 (t, 3H, C**H**$_3$).

***cis*-2-Butene. ^{1}H NMR** (d_6-benzene) δ (ppm): 5.47 (m, 2H, CH_3C**H**=C**H**CH_3), 1.5 (d, 6H, C**H**$_3$CH=CHC**H**$_3$).

***trans*-2-Butene. ^{1}H NMR** (d_6-benzene) δ (ppm): 5.47 (m, 2H, CH_3C**H**=C**H**CH_3), 1.57 (d, 6H, C**H**$_3$CH=CHC**H**$_3$).

6.2.8. Reaction of 2.5 with $AlCl_3$

2.5 (10 mg, 0.02 mmol) and $AlCl_3$ (3 mg, 0.02 mmol) were dissolved in d_6-benzene. The ^{1}H NMR spectrum indicated the formation of two products in a 50:50 ratio ascribed to complexes with a bound and dissociated $AlCl_4^-$ moiety.

[W{N(2,6-^{i}Pr-C$_6$H$_3$)}Me$_3$][AlCl$_4$]. ^{1}H NMR (d_6-benzene) δ (ppm): 6.97 (m, 2H, Ar**H**$_{meta}$), 6.77 (broad, 1H, Ar**H**$_{para}$), 3.33 (m, 2H, Ar_{ortho}C**H**$(CH_3)_2$), 1.44 (s, 9H, W(C**H**$_3)_3$), 1.02 (d, 12H, Ar_{ortho}CH(C**H**$_3)_2$).

W{N(2,6-^{i}Pr-C$_6$H$_3$)}Me$_3$(μ-Cl)AlCl$_3$. ^{1}H NMR (d_6-benzene) δ (ppm): 6.93 (m, 2H, Ar**H**$_{meta}$), 6.67 (broad, 1H, Ar**H**$_{para}$), 3.24 (m, 2H, Ar_{ortho}C**H**$(CH_3)_2$), 1.43 (s, 9H, W(C**H**$_3)_3$), 0.99 (d, 12H, Ar_{ortho}CH(C**H**$_3)_2$).

6.2.9. Reactions of 2.5 with propylene

2.5 (2 mg, 5 μmol) was added to two J. Young valve NMR spectroscopy tubes and dissolved in d_6-benzene containing mesitylene (20 μmol) as an internal standard. MAO (0.5 mg. 0.9 μmol, Al/W = 2) was added to one of the tubes. The contents were freeze-pump-thaw degassed three times prior to propylene (1 bar) addition and heated to 100 °C. For the tube containing MAO, no higher oligomers were observed. A small quantity of ethylene and 2-butenes could be observed after heating for 16 hours. Resonances corresponding to *cis*- and *trans*-2-butenes and ethylene could be observed for the MAO free reaction after 1 hour.

6.2.10. Reaction of 2.7 with 1-hexene and 1-octene

2.7 (2 mg, 5 μmol) was dissolved in d_6-benzene containing $Si(SiMe_3)_4$ (3 μmol) as an internal standard. 1-hexene (5 μL, 40 μmol) or 1-octene (3 μL, 40 μmol) were added *via* microlitre syringe and the mixtures heated at 75 °C. Resonances corresponding to ethylene (5.25 ppm) and either *trans*-5-undecene (multiplets at 5.45, 2.02, 1.31 and 0.88 ppm) or *trans*-6-tridecene (multiplets at 5.49, 2.09, 2.04, 1.38, 0.89 ppm) respectively, had begun to appear in the ^1H NMR spectra after heating for 16 hours. No decomposition of **2.5** was observed by either ^1H or $^{19}F\{^1H\}$ NMR spectroscopy.

6.2.11. Reaction of 2.5 with MeLi

2.5 (10 mg, 0.02 mmol) was charged in a J. Young valve NMR spectroscopy tube and dissolved in d_8-THF. MeLi (1.6 M in Et_2O, 14.4 μL, 0.02 mmol) was added *via* syringe and the contents mixed. An immediate colour change from orange to yellow was observed (postulated to be formation of $W\{N(2,6\text{-}^iPr\text{-}C_6H_3)\}Me_4$) before fast decomposition which yielded a dark solid. ^1H NMR spectroscopy displayed no resonances corresponding to a tungsten imido complex.

6.2.12. Reaction of 2.5 with AgF

2.2 (10 mg, 0.03 mmol) and AgF (3.31 mg, 0.03 mmol) were charged in a J. Young valve NMR spectroscopy tube, and d_2-DCM added to yield an orange slurry. No reaction was shown to have occurred by ^1H NMR spectroscopy, even after heating the tube at 80 °C overnight.

6.2.13. Reactions with $NaBAr^F_4$

2.5 (10 mg, 0.02 mmol) and sodium tetrakis-bistrifluoromethylphenyl borate ($NaBAr^F_4$) (20 mg, 0.02 mmol) were mixed in d_2-DCM. The mixture turned from orange to violet and finally red/orange over the course of five days at room temperature with periodic sonication. **[(W{N(2,6-^{i}Pr-C_6H_3)}Me_3)$_2$(μ-Cl)][BAr^F_4]. ^{1}H NMR** (d_2-DCM) δ (ppm): 7.71 (s, 8H, B(Ar**H**$_{ortho}$)$_4$), 7.55 (s, 4H, B(Ar**H**$_{para}$)$_4$), 7.39 (d, 2H, NAr**H**$_{para}$), 7.36 (d, 4H, NAr**H**$_{meta}$), 3.67 (sept, 4H, ^{i}Pr**H**), 1.80 (d, 18H, W(C**H**$_3$)$_3$), 1.36 (d, 24H, ^{i}**Pr**).

^{13}C{^{1}H} NMR (d_2-DCM) δ (ppm): 135.4 (B(**Ar**H$_{ortho}$)$_4$), 124.1 (N**Ar**H$_{para}$), 123.51 (N**Ar**H$_{meta}$), 118.0 (B(**Ar**H$_{para}$)$_4$), 62.6 (W(**C**H$_3$)$_3$), 29.7 (**C**H(CH$_3$)$_2$), 24.6 (CH(**C**H$_3$)$_2$).

2.2 (50 mg, 0.13 mmol) and $NaBAr^F_4$ (116 mg, 0.13 mmol) were charged into a J. Young valve NMR spectroscopy tube and d_2-DCM added. The tube was sonicated changing from yellow to red and finally purple.

[(W{N(2,6-Me-C_6H_3)}Me_3)$_2$(μ-Cl)][BAr^F_4]. ^{1}H NMR (d_2-DCM) δ (ppm): 7.75 (s, 8H, BAr**H**$_{ortho}$), 7.57 (s, 4H, BAr**H**$_{para}$), 7.28 (d, 4H, Ar**H**$_{meta}$), 7.18 (t, 2H, Ar**H**$_{para}$), 2.71 (s, 12H, Ar$_{ortho}$C**H**$_3$), 1.85 (d, 18H, W(C**H**$_3$)$_3$).

^{11}B{^{1}H} NMR (d_2-DCM) δ (ppm): −6.6.

^{19}F{^{1}H} NMR (d_2-DCM) δ (ppm):−62.8.

6.2.14. Reactions with $AgPF_6$

2.2 (10 mg, 0.03 mmol) and $AgPF_6$ (6.6 mg, 0.03 mmol) were charged into a J. Young valve NMR spectroscopy tube and d_2-DCM was added. A slight darkening of the yellow solution was observed with formation of a fluffy beige precipitate proposed to be AgCl. The product is proposed to be W{N(2,6-Me-C_6H_3)}Me_3F, along with P(O)F_3.

^{1}H NMR (d_2-DCM) δ (ppm): 7.26 (d, 2H, Ar**H**$_{meta}$), 7.16 (t, 1H, Ar**H**$_{para}$), 2.70 (Ar$_{ortho}$C**H**$_3$), 1.85 (s, 9H, W(C**H**$_3$)$_3$).

^{31}P{^{1}H} NMR (d_2-DCM) δ (ppm): −34.9 (q, $^1J_{P–F}$ = 2143 Hz).

^{19}F{^{1}H} NMR (d_2-DCM) δ (ppm): −88.6 (d, $^1J_{F–P}$ = 2143 Hz).

2.2 (50 mg, 0.13 mmol) and $AgPF_6$ (33 mg, 0.13 mmol) were charged in a Schlenk and DCM (20 mL) added with stirring. After 1 hour the product was filtered away from AgCl and cooled to −33 °C. A white precipitate was formed but displayed no resonances when analysed by ^{1}H NMR spectroscopy. Analysis of the solution indicated decomposition of the defined

complex. Similar decomposition was observed for **2.3** (100 mg, 0.26 mmol) and $AgPF_6$ (66 mg, 0.26 mmol).

6.2.15. Hydride formation and reduction reactions

2.5 (10 mg, 0.02 mmol) and KH (0.91 mg, 0.02 mmol) were mixed in d_8-THF. ^{1}H NMR spectroscopy indicated no reaction had occurred, even after heating of the sample at 70 °C overnight. Reaction in d_5-pyridine led to a colour change from orange to black. Broad resonances in both the alkyl and aromatic region indicated decomposition of the defined species.

2.2 (10 mg, 0.03 mmol) and $LiAlH_4$ (1 mg, 0.03 mmol) were added to a J. Young valve NMR spectroscopy tube and d_6-benzene added. No colour change for the complex was observed and ^{1}H NMR spectroscopy indicated no reaction had occurred even after heating overnight at 70 °C. Switching the solvent to d_8-THF led to an immediate colour change from red to dark brown, with a dark brown precipitate appearing. The ^{1}H NMR spectrum displayed broad resonances centred at 2 and 6 ppm, with no remaining resonances for **2.2**. The solution was dried and product extracted with d_6-benzene. Slow evaporation yielded a brown oil.

6.2.16. Reaction of W{N(2,6-^{i}Pr-C_6H_3)}Cl_4 with $BrMgC_4H_8MgBr$

W{N(2,6-^{i}Pr-C_6H_3)}Cl_4 (20 mg, 0.04 mmol) and $BrMgC_4H_8MgBr$ (0.17 M in THF, 9 mg, 0.04 mmol) were mixed in d_8-THF. A colour change from orange to dark brown was observed. However, ^{1}H NMR spectroscopy showed no resonances attributed to a tungsten imido complex, indicating decomposition of the defined structure.

6.2.17. Reactions with lithium or sodium cyclopentadienide (LiCp or NaCp)

2.5 (10 mg, 0.02 mmol) and NaCp (2 mg, 0.02 mmol) were mixed in d_8-THF yielding a bright yellow solution of W{N(2,6-^{i}Pr-C_6H_3)}Me_3Cp.

^{1}H NMR (d_8-THF) δ (ppm): 7.02 (s, 3H, Ar**H**$_{meta}$ and Ar**H**$_{para}$), 5.82 (s, 5H, η^5-C_5**H**$_5$), 3.55 (m, 2H, $Ar_{ortho}C$**H**$(CH_3)_2$), 1.20 (d, 12H, $Ar_{ortho}CH(C$**H**$_3)_2$), 0.98 (s, 6H, W(C**H**$_3)_2$), 0.49 (s, 3H, W(C**H**$_3$)).

2.2 (100 mg, 0.26 mmol) and LiCp (18.8 mg, 0.26 mmol) were contacted in d_6-benzene yielding a bright yellow solution of W{N(2,6-Me-C_6H_3)}Me_3Cp. The product was extracted from hexane and dried to yield an impure yellow oil (90% pure by ^{1}H NMR spectroscopy). Attempted recrystallisation from hexane failed.

^{1}H NMR (d_8-THF) δ (ppm): 6.77 (s, 2H, Ar**H**$_{meta}$), 6.56 (s, 1H, Ar**H**$_{para}$), 5.13 (s, 5H, η^5-C_5**H**$_5$), 2.06 (s, 6H, Ar$_{ortho}$C**H**$_3$), 1.34 (s, 6H, W(C**H**$_3$)$_2$, $^2J_{W–H}$ = 5.6 Hz), 0.96 (s, 3H, W(C**H**$_3$), $^2J_{W–H}$ = 6.72 Hz).

6.2.18. Synthesis of W{N(4-OMe-C_6H_4)}Me_3Cp (3.6)

2.6 (100 mg, 0.26 mmol) and NaCp (25 mg, 0.29 mmol) were charged in a Schlenk containing a stirrer bar. THF was added at 0 °C with stirring and the reaction allowed to warm to room temperature and left to stir for 1 hour, resulting in a bright yellow solution. The product was extracted with hexane, reduced to minimum volume and cooled to −33 °C. Pale pink crystals were isolated (40 mg, 37% yield).

Anal. Calcd (found) (%) C 43.39 (45.22), H 5.10 (5.03), N 3.37 (4.8).

^{1}H NMR (d_6-benzene) δ (ppm): 6.94 (dt, 2H, Ar**H**$_{ortho}$), 6.62 (dt, 2H, Ar**H**$_{meta}$), 5.12 (s, 5H, η^5-C_5**H**$_5$), 3.22 (s, 3H, Ar$_{para}$OC**H**$_3$), 1.31 (s, 6H, W(C**H**$_3$)$_2$, $^2J_{W–H}$ = 5.4 Hz), 0.96 (s, 3H, W(C**H**$_3$), $^2J_{W–H}$ = 6.12 Hz).

^{13}C{^{1}H} NMR (d_6-benzene) δ (ppm): 157.3 (**Ar**$_{para}$OCH$_3$), 152.2 (**Ar**$_{ipso}$N), 124.6 (**Ar**$_{ortho}$H), 114.0 (**Ar**$_{meta}$H), 103.9 (η^5-**C**$_5$H$_5$), 55.0 (Ar$_{para}$O**C**H$_3$), 23.5 (W(**C**H$_3$), $^1J_{W–C}$ = 225 Hz), 17.9 (W(**C**H$_3$)$_2$, $^1J_{W–C}$ = 168 Hz).

^{1}H NMR (d_5-chlorobenzene) δ (ppm): 6.90 (m, 2H, Ar**H**$_{ortho}$), 6.62 (m, 2H, Ar**H**$_{meta}$), 5.39 (s, 5H, η^5-C_5**H**$_5$), 3.45 (s, 3H, Ar$_{para}$OC**H**$_3$), 1.18 (s, 6H, W(C**H**$_3$)$_2$), 0.76 (s, 3H, W(C**H**$_3$)).

6.2.19. Reaction of 3.6 with trityl BAr^F_4

3.6 (15 mg, 0.04 mmol) was reacted with [CPh$_3$][BAr$^F_4$] (40 mg, 0.04 mmol) in d_5-chlorobenzene affording a dark brown solution. ^{1}H NMR spectroscopy indicated formation of [W{N(4-OMe-C_6H_4)}Me_2Cp][BAr$^F_4$]. Slow evaporation yielded a brown oil.

^{1}H NMR (d_5-chlorobenzene) δ (ppm): 8.21 (s, 8H, BAr**H**$_{ortho}$), 7.59 (s, 4H, BAr**H**$_{para}$), 7.14-7.05 (m, 15H, (C$_6$**H**$_5$)$_3$C(CH$_3$)), 6.84 (d, 2H, Ar**H**$_{ortho}$), 6.65 (d, 2H, Ar**H**$_{meta}$), 5.49 (s, 5H, η^5-C_5**H**$_5$), 3.47 (s, 3H, Ar$_{para}$OC**H**$_3$), 2.03 (s, 3H, (C$_6$H$_5$)$_3$C(C**H**$_3$)), 1.22 (broad s, 6H, W(C**H**$_3$)$_2$).

^{11}B{^{1}H} NMR (d_5-chlorobenzene) δ (ppm): −6.0.

^{19}F{^{1}H} NMR (d_5-chlorobenzene) δ (ppm): −61.9.

6.2.20. Reactions with (^{t}BuO)$_3$SiOLi

2.5 (10 mg, 0.02 mmol) and (^{t}BuO)$_3$SiOLi (6.2 mg, 0.02 mmol) were mixed in d_6-benzene yielding a bright yellow solution of W{N(2,6-^{i}Pr-C_6H_3)}Me_3OSi(O^{t}Bu)$_3$.

^{1}H NMR (d_6-benzene) δ (ppm): 7.17 (d, 2H, Ar**H**$_{meta}$), 6.99 (t, 1H, Ar**H**$_{para}$), 3.91 (m, 2H, Ar$_{ortho}$C**H**(CH$_3$)$_2$), 1.50 (s, 27H, OSi(OC(C**H**$_3$)$_3$)$_3$), 1.36 (s, 9H, W(C**H**$_3$)$_3$), 1.25 (d, 12H, Ar$_{ortho}$CH(C**H**$_3$)$_3$).

(^{t}BuO)$_3$SiOLi. ^{1}H NMR (d_6-benzene) δ (ppm): 1.54 (s, 27H, LiOSi(OC(C**H**$_3$)$_3$)$_3$).

2.5 (50 mg, 0.11 mmol) and (^{t}BuO)$_3$SiOLi (31 mg, 0.11 mmol) were mixed in d_6-benzene yielding a bright yellow solution, which rapidly turned to an orange gel. Drying of the solution and extraction with hexane yielded a pale yellow solution shown to contain W{N(2,6-^{i}Pr-C$_6$H$_3$)}Me$_3$OSi(O^{t}Bu)$_3$. Remaining orange glassy solid could not be dissolved in common organic solvents, precluding characterisation.

2.2 (50 mg, 0.13 mmol) and (^{t}BuO)$_3$SiOLi (35.2 mg, 0.13 mmol) were charged in a Schlenk flask and stirred in benzene at 0 °C. The reaction was allowed to warm to room temperature over the course of an hour, yielding a bright yellow solution of W{N(2,6-Me-C$_6$H$_3$)}Me$_3$OSi(O^{t}Bu)$_3$.

^{1}H NMR (d_6-benzene) δ (ppm): 6.96 (d, 2H, Ar**H**$_{meta}$), 6.82 (t, 1H, Ar**H**$_{para}$), 2.48 (s, 6H, Ar$_{ortho}$C**H**$_3$), 1.50 (s, 27H, OSi(OC(C**H**$_3$)$_3$)$_3$), 1.29 (s, 9H, W(C**H**$_3$)$_3$).

2.1 (75 mg, 0.21 mmol) and (^{t}BuO)$_3$SiOLi (68.4 mg, 0.25 mmol) were reacted in benzene at 0 °C with stirring. After warming to room temperature the solution was dried and the product extracted with hexane. A colourless solid (10 mg) was obtained by cooling of the solution to −33 °C.

^{1}H NMR (d_6-benzene) δ (ppm): 7.24 (m, 2H, Ar**H**$_{ortho}$), 7.16 (m, 2H, Ar**H**$_{meta}$), 6.91 (m, 1H, Ar**H**$_{para}$), 1.49 (s, 27H, OSi(OC(C**H**$_3$)$_3$)$_3$), 1.22 (s, 9H, W(C**H**$_3$)$_3$, $^2J_{W–H}$ = 7.6 Hz).

2.6 (100 mg, 0.26 mmol) and (^{t}BuO)$_3$SiOLi (68.4 mg, 0.25 mmol) were contacted in pentane for 1 hour yielding a bright yellow solution. The product was filtered away from LiCl and cooled to −33 °C. Colourless crystals (5 mg) were obtained and shown to be highly dissordered by a single crystal X-ray diffraction study.

^{1}H NMR (d_6-benzene) δ (ppm): 7.21 (m, 2H, Ar**H**$_{ortho}$), 6.76 (m, 2H, Ar**H**$_{meta}$), 3.30 (s, 3H, Ar$_{para}$OC**H**$_3$), 1.51 (s, 27H, OSi(OC(C**H**$_3$)$_3$)$_3$), 1.23 (s, 9H, W(C**H**$_3$)$_3$, $^2J_{W–H}$ = 7.5 Hz).

2.3 (100 mg, 0.26 mmol) and (^{t}BuO)$_3$SiOLi (74 mg, 0.27 mmol) were reacted in pentane for 1 hour. The resulting yellow solution was filtered and dried, to yield a yellow solid (80% isolated yield).

^{1}H NMR (d_6-benzene) δ (ppm): 7.05 (s, 2H, Ar**H**$_{ortho}$), 6.61 (s, 1H, Ar**H**$_{para}$), 2.09 (s, 6H, Ar$_{meta}$C**H**$_3$), 1.51 (s, 27H, OSi(OC(C**H**$_3$)$_3$)$_3$), 1.27 (s, 9H, W(C**H**$_3$)$_3$, $^2J_{W–H}$ = 7.60 Hz).

In all of the above spectra silane resonances (0.2-0.3 ppm) were observed, from which the products could not be separated.

6.2.21. Reaction of 2.5 with (^{t}BuO)$_3$SiOH

2.5 (10 mg, 0.02 mmol) and (^{t}BuO)$_3$SiOH (6 mg, 0.02 mmol) were charged in a J. Young valve NMR spectroscopy tube and dissolved in d_6-benzene. The tube was sonicated periodically at 23 °C, and the emergence of new isopropyl methine resonances of roughly equal intensity were observed in the ^{1}H NMR spectrum.

^{1}H NMR (d_6-benzene) δ (ppm): 4.47, 4.17 and 3.91 (m, 2H, Ar$_{ortho}$C**H**(CH$_3$)$_2$).

The resonance at 3.91 matches that observed for W{N(2,6-^{i}Pr-C$_6$H$_3$)}Me$_3$OSi(O^{t}Bu)$_3$. After three days the largest signal still corresponded to **2.5** (3.53 ppm), hence the reaction was heated to 100 °C. After 2 hours this had led to an increase in intensity of the resonance at 4.17 ppm, however after heating overnight, a glassy orange solid had formed, which could not be redissolved.

6.2.22. Reaction with neopentyl lithium

2.5 (10 mg, 0.02 mmol) and NpLi (1.8 mg, 0.02 mmol) were charged into a J. Young valve NMR spectroscopy tube and dissolved in d_6-benzene. Effervescence was observed and the yellow solution became orange. Two species were formed in a 60:40 ratio, with the major product identified as W{N(2,6-^{i}Pr-C$_6$H$_3$)}(CH^{t}Bu)(CH$_2$^{t}Bu)$_2$. The other set of resonances are attributed to W{N(2,6-^{i}Pr-C$_6$H$_3$)}(CH^{t}Bu)(CH$_2$^{t}Bu)Me.

W{N(2,6-^{i}Pr-C$_6$H$_3$)}(CH^{t}Bu)(CH$_2$^{t}Bu)Me. ^{1}H NMR (d_6-benzene) δ (ppm): 6.67 (s, 1H, WC**H**C**(**CH$_3$)$_3$, $^2J_{W–H}$ = 15.0 Hz), 3.85 (m, 2H, Ar$_{ortho}$C**H**(CH$_3$)$_2$), 1.30 (s, 3H, WC**H**$_3$), 1.28 (d, 12H, Ar$_{ortho}$CH)C**H**$_3$)$_2$), 1.15 (s, 9H, WCH$_2$C(C**H**$_3$)$_3$), 1.14 (s, 9H, WCHC(C**H**$_3$)$_3$). Ar**H**$_{meta}$, Ar**H**$_{para}$ and WC**H**$_2$C(CH$_3$)$_3$ resonances could not be observed. Neopentane (0.91 ppm) and a small amount of methane (0.16 ppm) were also observed. Resonances for W{N(2,6-^{i}Pr-C$_6$H$_3$)}(CH^{t}Bu)(CH$_2$^{t}Bu)$_2$ matched those described in section 6.2.6.

^{13}C{^{1}H} NMR (d_6-benzene) δ (ppm): 56.1 (W**C**H$_3$), 33.0 (WCH$_2$C(**C**H$_3$)$_2$), 32.8 (WCHC(**C**H$_3$)$_3$), 28.7 (Ar$_{ortho}$**C**H(CH$_3$)$_2$), 23.8 (Ar$_{ortho}$CH(**C**H$_3$)$_2$). Aromatic and neopentyl α-carbon resonances were too weak to be observed. Resonances corresponding to W{N(2,6-^{i}Pr-C$_6$H$_3$)}(CH^{t}Bu)(CH$_2$^{t}Bu)$_2$ matched those described in the literature.[3]

Reaction of **2.5** (50 mg, 0.11 mmol) and NpLi (8.9 mg, 0.11 mmol) in benzene yielded an orange solution with effervescence observed. Filtration and drying of the solid yielded a brown oil. ^{1}H NMR spectroscopy showed multiple products with resonances corresponding to W{N(2,6-^{i}Pr-C_6H_3)}(CH^{t}Bu)($CH_2{}^t$Bu)$_2$ and W{N(2,6-^{i}Pr-C_6H_3)}(CH^{t}Bu)($CH_2{}^t$Bu)Me observed. The major product was postulated to be the methylidene complex W{N(2,6-^{i}Pr-C_6H_3)}(CH_2)($CH_2{}^t$Bu)Me. Recrystallisation from pentane at −33 °C was unsuccessful, and analysis of the mixture showed it had converted to a 50:50 mixture of W{N(2,6-^{i}Pr-C_6H_3)}(CH^{t}Bu)($CH_2{}^t$Bu)$_2$ and W{N(2,6-^{i}Pr-C_6H_3)}(CH^{t}Bu)($CH_2{}^t$Bu)Me.

W{N(2,6-^{i}Pr-C_6H_3)}(CH_2)($CH_2{}^t$Bu)Me. ^{1}H NMR (d_6-benzene) δ (ppm): 7.12 (s, 1H, WC**H**$_{syn}$H$_{anti}$), 7.07 (d, 2H, Ar**H**$_{meta}$), 6.96 (t, 1H, Ar**H**$_{para}$), 6.57 (s, 1H, WCH$_{syn}$**H**$_{anti}$, $^2J_{W–H}$ = 15.72), 3.78 (m, 2H, Ar$_{ortho}$C**H**$(CH_3)_2$), 1.70 (s, 2H, WC**H**$_2$C$(CH_3)_3$), 1.52 (s, 3H, WC**H**$_3$, $^2J_{W–H}$ = 5.88 Hz), 1.27 (d, 12H, Ar$_{ortho}$CH(C**H**$_3)_2$), 1.10 (s, 9H, WCH$_2$C(C**H**$_3)_3$). Resonances for W{N(2,6-^{i}Pr-C_6H_3)}(CH^{t}Bu)($CH_2{}^t$Bu)$_2$ and W{N(2,6-^{i}Pr-C_6H_3)}(CH^{t}Bu)($CH_2{}^t$Bu)Me matched those described previously. Neopentane (0.91 ppm) and methane (0.16 ppm) were also observed.

6.3. Experimental details for Chapter Three

6.3.1. Thermal vacuum treatment of AMO-LDHs

Dehydroxylations were conducted using a quartz tube sealed at one end and connected to a vacuum/nitrogen manifold at the other inside a Carbolite HST 12/200 tube furnace. Mg_3Al-SO_4 AMO-LDH (~1 g) was loaded into a crucible and placed inside the tube. The sample was placed under dynamic vacuum (10^{-3} mbar) and the Carbolite 3216P1 temperature controller set to heat to the desired temperature at a ramp rate of 5 °C min^{-1}. Once at temperature it was held for 6 hours before cooling, after which the samples were stored in a nitrogen filled glovebox. The temperatures chosen were 23, 100, 150, 200, 250, 275, 300, 350, 400 and 450 °C. Mg_3Al-CO_3 was dehydroxylated at 200 °C for comparison.

6.3.2. Thermogravimetric analysis (TGA)

Thermogravimetric analyses were performed by Mrs. Kanittika Ruengkajorn using a Mettler Toledo TGA/DSC 1 system. Samples (~10 mg) were quickly loaded from sealed vials into pre-tared alumina crucibles and placed under a flow of dry N_2. The crucibles were heated from 25–600 °C at a rate of 5 °C min^{-1} under a flow of dry N_2. Differential thermogravimetric analysis (DTG) is obtained from the 1st derivative of TGA data.

6.3.3. Specific surface area analysis

Specific surface areas (Brunauer-Emmett-Teller (BET) method) and pore volumes (Barrett-Joyner-Halenda (BJH) method) were analysed with the help of Dr. Alexander Kilpatrick, using a Micromeritics 3Flex Surface Characterisation Analyser. Samples (~100 mg) were loaded in the glovebox into BET tubes and then sealed with a checkseal. The adsorption and desorption of N_2 at 77 K was then measured. Prior to each measurement samples were degassed at 30 °C for 3 h.

6.3.4. Powder X-ray diffraction (XRD) analysis in capillary mode

Powder XRD samples were loaded in a glovebox into capillary tubes which were then flame sealed. Samples were run utilising a Siemens D5000 high-resolution X-ray powder diffractometer after mounting on a goniometer. The capillaries were spun during collection utilising a mask of 20 mm, 1/8° divergency, 1/8° antiscatter, a fixed slit of 1/4° at a step of 0.02° between 3 and 70°.

6.3.5. Scanning electron microscopy (SEM) imaging

SEM images were acquired by Mr. Phakpoom Angpanitcharoen at the Harwell Science and Innovation Campus on a JEOL JSM 6610 scanning electron microscope. Samples were mounted on adhesive carbon tape attached to metal stubs, and sputter coated with a 10 nm layer of platinum using a Quorum Q150T Sputter Coater prior to imaging.

6.3.6. Surface hydroxyl titrations with $Mg(CH_2Ph)_2(THF)_2$

In order to quantify the effect the dehydroxylation temperature has on the surface hydroxyl concentration, titrations were undertaken using $Mg(CH_2Ph)_2(THF)_2$.[7] Reactions were run in duplicate for the AMO-LDH samples treated between 200 and 450 °C in J. Young valve NMR spectroscopy tubes. AMO-LDH (5 mg) and $Mg(CH_2Ph)_2(THF)_2$ (~10 mg) were mixed in d_6-benzene (500 μL) containing $Si(SiMe_3)_4$ as an internal standard (c = 6.23 mmol dm^{-3}). Production of toluene resulting from protonation of the benzyl by the surface hydroxyls was monitored by ^{1}H NMR spectroscopy and the toluene methyl resonance integrated against that of $Si(SiMe_3)_4$.

6.3.7. Modelling the LDH surface structure

The structure of $LiAl_2(OD)_6Cl$[44] was plotted using CRYSTALMAKER software suite. Pictorial depictions of the dehydroxylated Mg_3Al-SO_4 AMO-LDHs were made by removing

surface OH groups based on the number expected per unit cell for the dehydroxylated samples. From these models, the average hydroxyl proximity could be measured. Random alteration of the colours of the layers to a 3:1 ratio was done using CorelDraw.

6.3.8. Synthesis of Mg_3Al-SO_4 AMO-LDH-MAO

This synthesis was based on a literature procedure.[45] Mg_3Al-SO_4 AMO-LDHs (thermally treated under vacuum at 150, 250, 350 and 450 °C for 6 hours) (100 mg) and MAO (35 mg) (MAO:LDH weight ratio = 0.26, 2:1 molar ratio based on starting AMO-LDH composition, $Mg_{0.75}Al_{0.25}(OH)_2(SO_4)_{0.125}$) were slurried in toluene (30 mL). The mixture was heated to 80 °C for 2 hours with intermittent swirling. Filtration and drying afforded Mg_3Al-SO_4 AMO-LDH-MAO in near quantitative isolated yield as off-white solids in all cases.

6.3.9. Immobilisation of $(^n BuCp)_2ZrCl_2$ onto Mg_3Al-SO_4 AMO-LDH-MAO

This synthesis was based on a literature procedure.[45] Mg_3Al-SO_4 AMO-LDH-MAO (100 mg) was slurried in toluene (20 mL) and a stock solution of $(^n BuCp)_2ZrCl_2$ (0.9 mg, 2 μmol) (MAO/Zr = 200) in toluene (10 mL) was added. The mixture was heated at 80 °C for 2 hours with regular swirling, after which the solution was clear and colourless. Filtering and drying furnished pale orange solids in near quantitative isolated yield in all cases.

6.3.10. Gel permeation chromatography (GPC)

Polyethylene samples for GPC analysis were characterised by Norner AS, Norway. Molecular weight (M_w), molecular number (M_n) and polydispersities (M_w/M_n) were an average of two data sets.

6.4. Experimental details for Chapter Four

Synthesis of $W\{N(2,6\text{-}F\text{-}C_6H_3)\}(^{13}CH_3)_3Cl$ (2.7*). Following the same procedure detailed for the synthesis of **2.7**; **1.7** (50 mg, 0.10 mmol) was reacted with $Al(^{13}CH_3)_3$ (1.1 eq.) in d_6-benzene in a J. Young valve NMR spectroscopy tube. Removal of the solvent and recrystallisation from hexane yielded **2.7*** (10 mg) as a yellow solid in 27% yield. The solution NMR spectroscopic data matched that of **2.7.**

6.4.1. General procedure for the immobilisation of complexes on sMAO

A W:Al ratio of 1:150 was used unless otherwise stated. sMAO (100 mg, 39.7% wt Al, 1.47 mmol) and $W(NR)Cl_4(THF)$, $W\{N(2,6\text{-}^i Pr\text{-}C_6H_3)\}Cl_4$, **2.7***, **3.6** or $W(O)Cl_4$ were mixed in 50 mL of toluene, and swirled at regular intervals at room temperature for 1 h. A colour

change from a white solid and coloured solution to a pale solid with a colourless solution was observed indicating that all of the tungsten complex had been immobilised. The solid was left to settle, the supernatant was filtered off and the solid dried in vacuo in near quantitative yield.

sMAO. White solid.

^{13}C-{^{1}H} CPMAS SSNMR δ (ppm): 177 (Ph**C**O_2), 129 (**Ph**CO_2), −7 (strong, Al**Me**).

FTIR (KBr mull) (cm^{-1}): 2947 (broad, aromatic C–H), 1599 (weak), 1540 (aromatic C–C), 1446 (aromatic C–C), 1266, 1219 (strong), 1093 (weak), 1030 (weak), 830 (broad, Al–O).

sMAO-1.1. Pale straw solid.

FTIR (KBr mull) (cm^{-1}): 2948 (broad, aromatic C–H), 1536 (weak), 1451 (weak), 1214, 803 (broad shoulder, strong), 687 (broad, strong, Al–O).

sMAO-1.2. Pale yellow solid.

FTIR (KBr mull) (cm^{-1}): 2953 (broad, aromatic C–H), 1540 (weak), 1446 (weak), 1220, 1094 (weak), 1020 (weak), 798 (broad shoulder, strong), 687 (broad, strong, Al–O).

sMAO-1.3. Pale yellow solid.

FTIR (KBr mull) (cm^{-1}): 2953 (broad, aromatic C–H), 1536 (weak), 1447 (weak), 1225, 814 (broad shoulder, strong), 693 (broad, strong, Al–O).

sMAO-1.4. Pale yellow solid.

FTIR (KBr mull) (cm^{-1}): 2958 (broad, aromatic C–H), 1536 (weak), 1451 (weak), 1388 (weak), 1261, 1220, 1094, 1020, 804 (broad shoulder, strong), 693 (broad, strong, Al–O).

sMAO-1.5. Yellow solid.

^{13}C{^{1}H} CPMAS SSNMR δ (ppm): 172 (Ph**C**O_2), 127 (**Ph**CO_2), 123 (**Ar**), 68 (**THF**), 45 (broad, W**C**H_3), 23.8 (Ar_{ortho}**C**$(CH_3)_2$), 19.2 (Ar_{ortho}C(**C**$H_3)_2$), 18 (THF), −7 (strong, Al**Me**).

FTIR (KBr mull) (cm^{-1}): 2958 (broad, aromatic C–H), 1535 (weak), 1441 (weak), 1267 (weak), 1220, 1094, 1024, 809 (broad shoulder, strong), 682 (broad, strong, Al–O).

sMAO-1.6. Pale yellow solid.

^{13}C{^{1}H} CPMAS SSNMR δ (ppm): 134-112 (**Ph**CO_2), −7 (strong, Al**Me**), due to weak signal to noise ratio, resonances for the tungsten imido complex could not be observed.

FTIR (KBr mull) (cm^{-1}): 2947 (broad, aromatic C–H), 1599 (weak), 1536, 1440, 1261 (weak), 1220, 1024 (weak), 824 (broad shoulder, strong), 676 (broad, strong, Al–O).

sMAO-1.7. Yellow solid.

$^{13}C\{^{1}H\}$ CPMAS SSNMR δ (ppm): 177 (Ph**C**O_2), 129 (**Ph**CO_2), 123 (**Ar**F), 105 (**Ar**), 100 (**Ar**), 67 (broad, **THF**), 18 (**THF**), −7 (strong, Al**Me**).

$^{19}F\{^{1}H\}$ HPDEC NMR δ (ppm): −123.

sMAO-1.8. Pale brown solid.

$^{13}C\{^{1}H\}$ CPMAS SSNMR δ (ppm): 177 (Ph**C**O_2), 129 (**Ph**CO_2), 73 (**THF**), 54 (W**C**H_3), 25 (**THF**), −8 (strong, Al**Me**).

$^{19}F\{^{1}H\}$ HPDEC SSNMR δ (ppm): −142 (broad, Al-F interaction), −69 (C**F**$_3$ supported complex).

FTIR (KBr mull) (cm^{-1}): 2958 (broad, aromatic C–H), 1536 (weak), 1447 (weak), 1383 (weak), 1267, 1220, 1094 (weak), 1020 (weak), 798 (broad shoulder, strong), 693 (broad, strong, Al–O).

sMAO-W{N(2,6-^{i}Pr-C_6H_3)}Cl_4. Pale yellow solid.

FTIR (KBr mull) (cm^{-1}): 2948 (broad, aromatic C–H), 1599, 1536, 1447, 1224, 1024 (weak), 813 (broad shoulder, strong), 672 (broad, strong, Al–O).

sMAO-2.7*. Yellow solid.

$^{13}C\{^{1}H\}$ CPMAS SSNMR δ (ppm): 177 (Ph**C**O_2), 155 (**Ar**F), 129 (**Ph**CO_2), 125 (**Ar**), 105 (**Ar**), 85 (**Ar**), 56, 45 (W(**C**$H_3)_3$), −7 (strong, Al**Me**).

$^{19}F\{^{1}H\}$ HPDEC SSNMR δ (ppm): −123.

sMAO-3.6. Pale yellow solid.

sMAO-W(O)Cl_4. Pale orange solid.

The ^{27}Al DPMAS or Hahn echo SSNMR spectra in all cases display multiple broad resonances between 500 and −500 ppm.

An NMR scale reaction of sMAO (20 mg, 0.29 mmol) and **1.3** (1 mg, 1.94 μmol) in d_6-benzene (0.5 mL), showed the complete disappearance of resonances attributed to **1.3** with only toluene present from sMAO synthesis and a small amount of methane observed in the ^{1}H NMR spectrum.

6.4.2. General procedure for testing the ethylene oligomerisation activity of the solid catalysts

Supported catalyst (5 mg, 0.47 μmol of W) was added to a J. Young valve NMR spectroscopy tube. Deuterated solvent (500 μL) containing either mesitylene (20.1 μmol), pyridine (9.93 μmol) or $Si(SiMe_3)_4$ (3.11 μmol) was added *via* microliter syringe. For supported complexes where the support was not either composed of MAO or the surface had not been contacted with MAO prior to supporting, MAO (2 mg) was added. The contents were freeze-pump-thaw degassed three times and 1 bar of ethylene introduced. The reaction was heated in an oil bath at a specified temperature and ^{1}H NMR spectra were taken periodically. TONs were calculated by integration of product peaks relative to the internal standard; 1-butene (1.90 ppm), *trans*-2-butene (1.50 ppm), *cis*-2-butene (1.57 ppm), propylene (1.54 ppm).

6.4.3. Scale-up oligomerisations

Scale-up oligomerisations were performed by Norner AS (Norway), utilising a 200 mL batch reactor. The temperature (75 °C) and stirring speed (320 rpm) were kept constant for all runs. Hexane or toluene were employed as the solvent and the ethylene partial pressure was varied between 1 and 19 bar. Product analysis was performed by GCMS. In an independent run, 1 drop of TEA was added to the catalyst slurry prior to ethylene adition. The polymer by-product was analysed by FTIR and shown to be UHMWPE.

6.4.4. Differential scanning calorimetry (DSC)

Differential scanning calorimetry experiments were performed by Mrs. Kanittika Ruengkajorn on a Mettler Toledo TGA/DSC 1 System in a temperature range of 25–250 °C at a rate of 5 °Cmin^{-1}.

6.4.5. Reactivity towards 1-hexene and 1-octene

sMAO-**1.7** (5 mg, 0.47 μmol of W) was added to a J. Young valve NMR spectroscopy tube and d_6-benzene (500 μL) and 1-hexene or 1-octene (40 μmol) added *via* microliter syringe. The tube was heated at 75 °C and ^{1}H NMR spectra recorded periodically. Isomerisation of the olefin was observed in both cases to yield the *cis*- and *trans*-2-alkenes.

6.4.6. Immobilisation of 1.5 on $LDH(X)_{150}$ ($X = SO_4^{2-}$, CO_3^{2-} or NO_3^-)

1.5 (5 mg, 9 μmol_W) and $LDH(X)_{150}$ ($X = SO_4^{2-}$, CO_3^{2-} or NO_3^-) were charged into a Schlenk flask and swirled intermittently in toluene (30 mL) for 1 hour at 23 °C. The solution

completely decolourised and a coloured solid was formed, filtration and drying yielded powdered solids in near quantitative yield in all cases.

LDH$(CO_3)_{150}$. FTIR (KBr mull) (cm^{-1}): 3500 (O–H, broad), 1548, 1368 cm^{-1} (CO_3, broad, strong).

MgAlNO_3. FTIR (KBr mull) (cm^{-1}): 3600 (O–H, broad), 1358 (NO_3, broad, strong).

MgAlSO_4. FTIR (KBr mull) (cm^{-1}): 3587 (O–H, broad), 1165 (SO_4, broad, strong).

LDH$(SO_4)_{150}$-1.5. Off white powder.
^{13}C{^{1}H} CPMAS SSNMR δ (ppm): 160 (**C**O_3, **Ar**), 35-16 (multiple ^{i}**Pr** resonances).
^{27}Al DPMAS SSNMR δ (ppm): 77 (weak, broad, tetrahedral Al), 8.5 (strong, octahedral Al).
FTIR (KBr mull) (cm^{-1}): 3560 (O–H, broad, strong), 2962 (aromatic C–H), 1604 (broad), 1265, 1156 (SO_4, strong), 1088 (strong), 802 (C–H oop).

LDH$(CO_3)_{150}$-1.5. Beige powder.
FTIR (KBr mull) (cm^{-1}): 3590 (O–H, broad, strong), 1550 (strong), 1372 (CO_3, strong), 1233.

LDH$(NO_3)_{150}$-1.5. Bright yellow powder.
^{13}C{^{1}H} CPMAS SSNMR δ (ppm): 160 (**C**O_3, **Ar**), 125 (**Ar**), 43-13 (multiple ^{i}**Pr** resonances).
^{27}Al DPMAS SSNMR δ (ppm): 70 (very weak, broad, tetrahedral Al), 9 (strong, octahedral Al).
FTIR (KBr mull) (cm^{-1}): 3603 (O–H, broad, strong), 2965 (aromatic C–H), 1355 (NO_3, strong), 1262, 1098, 1014, 798 (C–H oop).

6.4.7. Loading study of 1.5 on LDH$(CO_3)_{150}$

1.5 was mixed with LDH$(CO_3)_{150}$ (100 mg) in loadings of 5, 10, 15 and 20 wt% in a Schlenk flask. Toluene (30 mL) was added and the resulting slurries swirled for 1 hour at 23 °C. For loadings of 5 and 10 wt%, complete immobilisation was observed by complete decolourisation of the initial green solution. For loadings of 15 and 20 wt%, a green colouration to the solution persisted after 2 hours of regular swirling at 23 °C. Heating the mixtures to 60 °C resulted in complete decolourisation, however analysis of the supernatant by ^{1}H NMR spectroscopy showed the prescence of 2,6-diisopropylaniline, which was not observed for loadings of 5 or 10%.

2,6-diisopropylaniline. **^{1}H NMR** (d_6-benzene) δ (ppm): 7.05 (d, 2H, Ar**H**$_{meta}$), 6.89 (t, 1H, Ar**H**$_{para}$), 3.21 (s, 2H, ArN**H**$_2$), 2.65 (dq, 2H, ArC**H**$(CH_3)_2$), 1.15 (d, 12H, ArCH(C**H**$_3)_2$).

6.4.8. Decomposition study of 1.5 with HCl

1.5 (10 mg, 0.03 mmol) was dissolved in d_6-benzene to yield a green solution. HCl (2 M in ether, 9 μL, 0.02 mmol) was aded *via* microlitre syringe and the contents mixed. No change in either the colour of the solution or the ^{1}H NMR spectroscopic resonances for **1.5** were observed, even after heating at 60 °C for 18 hours.

6.4.9. Impregnation of alkyl aluminium reagents on LDH(SO$_4$)$_{150}$ and subsequent reaction with 1.5

LDH(SO$_4$)$_{150}$ (200 mg, 2.14 mmol) was slurried in toluene (20 mL) and a toluene solution (20 mL) of an alkyl aluminium reagent (MAO, TMA, DMAC or DEAC, 1.07 mmol) was added. The mixture was heated to 80 °C for 2 hours with regular swirling. Filtration and drying *in vacuo* yielded off white powders in all cases. The aluminium impregnated solids (100 mg) were then contacted with **1.5** (5 mg, 9 μmol) in toluene (30 mL) at 23 °C for 1 hour. When LDH(SO$_4$)$_{150}$-TMA or LDH(SO$_4$)$_{150}$-DMAC were employed, a change in colour of the solution from green to yellow was observed, shown to be formation of **2.5** by ^{1}H NMR spectroscopy. However, no grafting of the molecular complex was observed, even after heating at 80 °C for 1 hour. For LDH(SO$_4$)$_{150}$-MAO grafting was observed by complete decolouration of the solution and colouring of the solid, which was isolated in near quantitative yield after work-up.

LDH(SO$_4$)$_{150}$-MAO-1.5. Pale yellow solid.

^{13}C{^{1}H} CPMAS SSNMR δ (ppm): 165 (**C**O$_3$, **Ar**), 150-117 (**Ar**), 80-10 (W–**Me**, Al–**Me** and ^{i}**Pr**).

^{27}Al DPMAS SSNMR δ (ppm): 78 (weak, broad, tetrahedral Al), 8 (intense, octahedral Al).

6.4.10. Immobilisation by incipient wetness

1.5 (10 mg, 0.02 mmol) and either MAO, DMAC or TMA (0.04 mmol, Al/W = 2) were mixed in toluene (10 mL), yielding yellow solutions of **2.5** in all cases. The solution was added to a slurry of LDH(SO$_4$)$_{150}$ in toluene (10 mL). Comple decolourisation of the solution was observed in all cases after swirling for 1 hour at 23 °C. The solids were isolated as pale yellow powders in near quantitative yield after work-up. In subsequent reactions with

ethylene, decomposition liberating 2,6-diisopropylaniline was observed by ^{1}H NMR spectroscopy.

LDH(SO$_4$)$_{150}$-(1.5+MAO). Pale yellow solid.

^{13}C{^{1}H} CPMAS SSNMR δ (ppm): 160 (**C**O$_3$, **Ar**), 45-10 (W–**Me**, ^{i}**Pr**).

^{27}Al DPMAS SSNMR δ (ppm): 77 (weak, broad, tetrahedral Al), 8 (intense, octahedral Al).

6.4.11. Immobilisation of 2.5 on LDH(SO$_4$)$_{150}$

2.5 (10 mg, 0.02 mmol) and LDH(SO$_4$)$_{150}$ (200 mg) were mixed together as a slurry in toluene (30 mL). Intermitant swirling for 2 hours at 23 °C resulted in complete decolouration of the orange solution to yield a pale yellow solid after work-up, in near quantitative isolated yield. In a subsequent reaction with ethylene, decomposition liberating 2,6-diisopropylaniline was observed by ^{1}H NMR spectroscopy.

LDH(SO$_4$)-2.5. Pale yellow solid.

^{13}C{^{1}H} CPMAS SSNMR δ (ppm): 160 (**C**O$_3$, **Ar**), 34 (broad, W–**Me**), 22 (^{i}**Pr**), 16 (^{i}**Pr**).

^{27}Al DPMAS SSNMR δ (ppm): 77 (weak, broad, tetrahedral Al), 9 (intense, octahedral Al).

6.4.12. Loading study of 2.7 on LDH(SO$_4$)$_{300/450}$

LDH(SO$_4$)$_{300}$ or LDH(SO$_4$)$_{450}$ (10 mg) and **2.7** (1 eq. based on mol$_{OH}$ g^{-1} of the LDH, 5.17 and 3.95 mg respectively) were added to J. Young valve NMR tubes. d_6-Benzene (500 μL) containing Si(SiMe$_3$)$_4$ (3.11 μmol) was added and the tubes periodically agitated. ^{1}H NMR spectra were taken after 1 and 16 hours reaction time.

6.4.13. Immobilisation of W{N(2,6-^{i}Pr-C$_6$H$_3$)}(CH^{t}Bu)(CH$_2$^{t}Bu)$_2$ on LDH(CO$_3$)$_{150}$

W{N(2,6-^{i}Pr-C$_6$H$_3$)}(CH^{t}Bu)(CH$_2$^{t}Bu)$_2$ (5 mg, 9 μmol) and LDH(CO$_3$)$_{150}$ were contacted in toluene (30 mL) and swirled at regular intervals for 1 hour at 23 °C. Complete decolouration of the solution was observed, and a pale brown solid obtained in near quantitative isolated yield after filtration of the solvent and drying of the solid.

W{N(2,6-^{i}Pr-C$_6$H$_3$)}(CH^{t}Bu)(CH$_2$^{t}Bu)$_2$. FTIR (KBr mull) (cm^{-1}): 2963 (aromatic C–H), 1262, 1099, 1019, 800 (C–H oop).

LDH(CO$_3$)$_{150}$-W{N(2,6-^{i}Pr-C$_6$H$_3$)}(CH^{t}Bu)(CH$_2$^{t}Bu)$_2$. FTIR (KBr mull) (cm^{-1}): 3569 (OH, broad, strong), 2961 (aromatic C–H), 1545 (LDH, strong), 1358 (CO$_3$, strong), 1259, 1097, 1020, 797 (C–H oop).

6.4.14. Immobilisation of $W(O)Cl_4$ on $LDH(CO_3)_{150}$

$W(O)Cl_4$ (5 mg, 0.01 mmol) and $LDH(CO_3)_{150}$ were mixed in toluene (30 mL) and swirled intermittently for 1 hour at 23 °C. A colourless solution was obtained, which was filtered away, and the solid dried *in vacuo* to yield an off-white solid.

6.4.15. X-ray absorption spectroscopy (XAS)

W L1-edge XAS experiments were conducted on the B18 beamline at the Diamond Light Source synchrotron, Didcot, UK. Freshly prepared samples of $W(O)Cl_4$, **1.5**, $LDH(CO_3)_{150}$-$W(O)Cl_4$, $LDH(CO_3)_{150}$-$W\{N(2,6\text{-}^{i}Pr\text{-}C_6H_3)\}(CH^{t}Bu)(CH_2{}^{t}Bu)_2$ and $LDH(CO_3)_{150}$-**1.5** were pressed into pellets in an argon glovebox, as pure samples for the LDH immobilised species, or a mixture with boron nitride for the homogeneous complexes. The pellets were mounted on Kapton tape inside a specially designed gas tight cell. A Si (111) two-crystal monochromator with an energy resolution of 1.8 eV at the W L1-edge was used. 12 scans were acquired and averaged to increase the signal to noise ratio. Data processing were performed using IFEFFIT[46] with the Demeter package[47] (Athena and Artemis) with the help of Dr. Peter Wells and Dr. Emma Gibson from the UK Catalysis Hub.

6.4.16. Immobilisation of 1.5 on $SiO_{2\text{-}(150)}$

1.5 (10 mg, 0.03 mmol) was mixed with silica (200 mg) which had previoulsy been heated to 150 °C for 6 hours under vacuum ($SiO_{2\text{-}(150)}$). Toluene (30 mL) was added, and the mixture swirled periodically for 1 hour at 23 °C. Removal of the supernatant by filtration and drying the solid *in vacuo* yielded $SiO_{2\text{-}(150)}$-**1.5** as a tan solid.

^{13}C-{^{1}H} CPMAS SSNMR δ (ppm): 3500 (broad, O–H), 118 (weak, **Ar**), 22 ($Ar_{ortho}\mathbf{C}(CH_3)_2$), 17 ($Ar_{ortho}C(\mathbf{C}H_3)_2$).

FTIR (KBr mull) (cm^{-1}): 2963 (weak, aromatic C–H), 1264, 1101 (Si–O), 801.

6.4.17. Reaction of Grubbs 2nd generation (G2) and Hoveyda-Grubbs 2nd generation (HG2) catalysts with $LDH(SO_4)_{250/350/450}$

G2 or **HG2** were mixed with $LDH(SO_4)_{250/350/450}$ (100 mg, 1:10 mol_{Ru}:mol_{OH}) in toluene (30 mL). No decolouration of the solution was observed after 1 hour at 23 °C or after heating at 80 °C with regular swirling. Analysis of the supernatant by ^{1}H NMR spectroscopy showed the respective pure precursor complex. The solids obtained after drying *in vacuo* were off-white in all cases, and were shown to be inactive towards 1-octene (40 μL) at 75 °C in d_6-benzene (500 μL).

6.4.18. Immobilisation of G2 or HG2 on sMAO and their subsequent reactivity towards olefins

G2 or **HG2** were mixed with sMAO (200 mg, Al/W = 150) in toluene (30 mL). Swirling periodically for 1 hour at 23 °C, resulted in complete decolouration of the solution in both cases. Filtration of the solutions and drying of the solids, yielded sMAO-**G2** and sMAO-**HG2,** as pale yellow and pale pink solids respectively.

sMAO-**G2** or sMAO-**HG2** (5 mg, 0.4 μmol_{Ru}) were charged in J. Young valve NMR spectroscopy tubes and d_6-benzene (500 μL) containing $Si(SiMe_3)_4$ (3 μmol) as an internal NMR standard was added. The contents were freeze-pump-thaw degassed three times and ethylene (1 bar) was added. After 1 hour at 23 °C, a small amount of 1-butene formation was observed by ^{1}H NMR spectroscopy. Heating the tube at 75 °C yielded no further reactivity.

sMAO-**G2** or sMAO-**HG2** (5 mg, 0.4 μmol_{Ru}) were charged in J. Young valve NMR spectroscopy tubes and d_6-benzene (500 μL) containing $Si(SiMe_3)_4$ (3 μmol) as an internal NMR standard and 1-octene (3 μL, 40 μmol), added. After 1 hour at 23 °C, a small quantity of 7-tetradecene formation could be observed, which only increased slightly with heating at 75 °C for 16 hours.

6.5. Experimental details for Chapter Five

6.5.1. Synthesis of Ir($^{t\mathrm{Bu}}$PCP)HCl and Ir($^{t\mathrm{Bu}}$PCP)H_4

Ir($^{t\mathrm{Bu}}$PCP)HCl and Ir($^{t\mathrm{Bu}}$PCP)H_4 were synthesised according to literature procedures.[9]

Ir($^{t\mathrm{Bu}}$PCP)HCl. ^{1}H NMR (d_6-benzene) δ (ppm): 7.03 (d, 2H, Ar**H**$_{meta}$), 6.96 (s, 2H, Ar**H**$_{para}$), 3.11 (t, 2H, $Ar_{ortho}C\mathbf{H}_2P(C(CH_3)_3)_2$), 3.01 (dt, 2H, $Ar_{ortho}C\mathbf{H}_2P(C(CH_3)_3)_2$), 1.26 (m, 36H, $Ar_{ortho}CH_2P(C(C\mathbf{H}_3)_3)_2$), −42.58 (t, 1H, Ir**H**, $^1J_{Ir–H}$ = 12.04 Hz).

^{31}P{^{1}H} NMR (d_6-benzene) δ (ppm): 67.0.

^{1}H NMR (d_2-DCM) δ (ppm): 6.94 (d, 2H, Ar**H**$_{meta}$), 6.69 (s, 2H, Ar**H**$_{para}$), 3.26 (t, 2H, $Ar_{ortho}C\mathbf{H}_2P(C(CH_3)_3)_2$), 3.23 (dt, 2H, $Ar_{ortho}C\mathbf{H}_2P(C(CH_3)_3)_2$), 1.26 (m, 36H, $Ar_{ortho}CH_2P(C(C\mathbf{H}_3)_3)_2$), −42.88 (t, 1H, Ir**H**, $^1J_{Ir–H}$ = 12.52 Hz).

^{31}P{^{1}H} NMR (d_2-DCM) δ (ppm): 67.0.

^{1}H NMR (d_5-chlorobenzene) δ (ppm): 7.00 (d, 2H, Ar**H**$_{meta}$), 6.85 (t, 2H, Ar**H**$_{para}$), 3.19 (dt, 2H, $Ar_{ortho}C\mathbf{H}_2P(C(CH_3)_3)_2$), 3.08 (dt, 2H, $Ar_{ortho}C\mathbf{H}_2P(C(CH_3)_3)_2$), 1.35 (m, 36H, $Ar_{ortho}CH_2P(C(C\mathbf{H}_3)_3)_2$), −43.5 (t, 1H, Ir**H**, $^1J_{Ir–H}$ = 12.52 Hz).

^{31}P{^{1}H} NMR (d_5-chlorobenzene) δ (ppm): 67.1.

FTIR (KBr mull) (cm^{-1}): 2962 (broad, aromatic C–H), 1471 (aromatic C–C), 1384 (strong), 1266, 1097, 1020, 804.

Ir($^{t\mathrm{Bu}}$PCP)H$_4$. ^{1}H NMR (d_8-toluene) δ (ppm): 7.03 (m, 3H, Ar**H**$_{meta}$), 7.03 (m, 2H, Ar**H**$_{para}$), 3.26 (t, 4H, Ar$_{ortho}$C**H**$_2$P(C(CH$_3$)$_3$)$_2$), 1.16 (t, 36H, Ar$_{ortho}$CH$_2$P(C(C**H**$_3$)$_3$)$_2$), −9.17 (t, 1H, Ir**H**, $^1J_{\mathrm{Ir–H}}$ = 9.80 Hz).

^{31}P{^{1}H} NMR (d_8-toluene) δ (ppm): 72.8.

FTIR (KBr mull) (cm^{-1}): 2946 (broad, aromatic C–H), 2075 (Ir–H), 1906 (Ir–H), 1471 (aromatic C–C), 1388 (strong), 1261, 1179 (weak), 1092 (weak), 1020, 831, 804.

6.5.2. Synthesis of sMAO-Ir($^{t\mathrm{Bu}}$PCP)HCl

Ir($^{t\mathrm{Bu}}$PCP)HCl (12.2 mg, 0.02 mmol) and sMAO (200 mg, Al/Ir = 150) were combined in a Schlenk flask prior to toluene addition (30 mL). The contents were swirled periodically for 1 hour at 23 °C to yield a colourless solution. Filtration and drying of the solid afforded sMAO-Ir($^{t\mathrm{Bu}}$PCP)HCl as a yellow powder in near quantitative isolated yield.

^{13}C{^{1}H} CPMAS SSNMR δ (ppm): 177 (Ph**C**O$_2$), 136 (**Ph**CO$_2$), 132 (**Ph**CO$_2$), 128 (**Ph**CO$_2$), 37 (Ar$_{ortho}$**C**H$_2$P(C(CH$_3$)$_2$)), 29 (Ar$_{ortho}$CH$_2$P(**C**(CH$_3$)$_2$)), 27 (Ar$_{ortho}$CH$_2$P(C(**C**H$_3$)$_2$)), −7 (Al**Me**).

^{31}P-{^{1}H} CPMAS SSNMR δ (ppm): 78.

The ^{27}Al DPMAS SSNMR spectra displayed multiple broad resonances between 500 and −500 ppm.

FTIR (KBr mull) (cm^{-1}): 2951 (aromatic C–H), 1532 (weak), 1446 (weak), 1384, 1261 (weak), 1220, 1097 (weak), 1025 (weak), 804 (broad shoulder, strong), 688 (broad, strong, Al–O).

6.5.3. Reaction of Ir($^{t\mathrm{Bu}}$PCP)HCl with TMA (Al/Ir = 1)

Ir($^{t\mathrm{Bu}}$PCP)HCl (10 mg, 0.02 mmol) was dissolved in d_6-benzene in a J. Young valve NMR spectroscopy tube. TMA (1.5 μL, 0.02 mmol) was added, and the tube sealed and shaken. A colour change from yellow to red/orange was observed. ^{1}H NMR spectroscopy showed the presence of 3 distinct compounds in a 48:37:15 intensity ratio, with methane (0.16 ppm) also observed. The second most abundant was shown to be the previously reported Ir($^{t\mathrm{Bu}}$PCP)(N$_2$).[48] Drying of the solution *in vacuo* and extraction from hexane gave an orange solution. Orange crystals suitable for single crystal X-ray diffraction were grown by slow

evaporation of this solution (15% isolated yield), and were shown to be {Ir($^{t\text{Bu}}$PCP)}(N_2) which has previously been reported.[49]

Ir($^{t\text{Bu}}$PCP)(N_2). ^{1}H NMR (d_6-benzene) δ (ppm): 7.15 (d, 2H, Ar**H**$_{meta}$), 7.02 (t, 1H, Ar**H**$_{para}$), 3.18 (t, 4H, Ar$_{ortho}$C**H**$_2$P(C(CH$_3$)$_3$)$_2$), 1.28 (t, 36H, Ar$_{ortho}$CH$_2$P(C(C**H**$_3$)$_3$)$_2$).

^{31}P{^{1}H} NMR (d_6-benzene) δ (ppm): 72.2.

Major compound. ^{1}H NMR (d_6-benzene) δ (ppm): 6.88 (t, 1H, Ar**H**$_{para}$), 6.82 (d, 2H, Ar**H**$_{meta}$), 2.85 (dt, 2H, Ar$_{ortho}$C**H**$_2$P(C(CH$_3$)$_3$)$_2$), 2.85 (dt, 2H, Ar$_{ortho}$C**H**$_2$P(C(CH$_3$)$_3$)$_2$), 1.13 (dt, 36H, Ar$_{ortho}$CH$_2$P(C(C**H**$_3$)$_3$)$_2$).

^{31}P{^{1}H} NMR (d_6-benzene) δ (ppm): 68.1.

Minor compound. ^{1}H NMR (d_6-benzene) δ (ppm): 7.26 (d, 2H, Ar**H**$_{meta}$), 7.20 (t, 1H, Ar**H**$_{para}$), 3.36 (dt, 2H, Ar$_{ortho}$C**H**$_2$P(C(CH$_3$)$_3$)$_2$), 2.99 (dt, 2H, Ar$_{ortho}$C**H**$_2$P(C(CH$_3$)$_3$)$_2$), 1.23 (t, 18H, Ar$_{ortho}$CH$_2$P(C(C**H**$_3$)$_3$)$_2$), 1.09 (t, 18H, Ar$_{ortho}$CH$_2$P(C(C**H**$_3$)$_3$)$_2$).

^{31}P{^{1}H} NMR (d_6-benzene) δ (ppm): 68.6.

6.5.4. Reaction of Ir($^{t\text{Bu}}$PCP)HCl with MAO (Al/Ir = 150)

Ir($^{t\text{Bu}}$PCP)HCl (2 mg, 3 μmol) and MAO (28 mg, 0.48 mmol, Al/Ir = 150) were charged into a J. Young valve NMR spectroscopy tube to which d_6-benzene was added. A colour change from orange to bright yellow was observed upon agitating the mixture.

^{1}H NMR (d_6-benzene) δ (ppm): 7.05 (d, 2H, Ar**H**$_{meta}$), 6.96 (t, 1H, Ar**H**$_{para}$), 1.80-0.78 (broad, multiple resonances attributed to ^{t}Bu groups of multiple species), 0.20 to −0.60 (broad, MAO).

^{31}P{^{1}H} NMR (d_6-benzene) δ (ppm): 72.5, 72.1.

6.5.5. Synthesis of [Ir($^{t\text{Bu}}$PCP)H(N_2)][BAr$^F{}_4$]

Ir($^{t\text{Bu}}$PCP)HCl (10 mg, 0.02 mmol) and NaBAr$^F{}_4$ (14.2 mg, 0.02 mmol) were dissolved in either d_5-chlorobenzene or d_2-DCM with a colour change from orange to red observed. Orange crystals of [Ir($^{t\text{Bu}}$PCP)H(N_2)][BAr$^F{}_4$], suitable for a single crystal X-ray diffraction study, were grown by slow evaporation of a solution of d_5-chlorobenzene.

^{1}H NMR (d_5-chlorobenzene) δ (ppm): 8.23 (s, 8H, BAr**H**$_{ortho}$), 7.61 (s, 4H, BAr**H**$_{para}$), 6.91 (broad s, 2H, Ar**H**$_{meta}$), 6.84 (broad s, 1H, Ar**H**$_{para}$), 3.11 (broad s, 4H, Ar$_{ortho}$C**H**$_2$P(C(CH$_3$)$_3$)$_2$), 0.94 (broad s, 36H, Ar$_{ortho}$CH$_2$P(C(C**H**$_3$)$_3$)$_2$), −41.46 (broad s, 1H, Ir**H**), −44.57 (v. broad s, 1H, Ir**H**). The two Ir–H resonances are in a 55:45 ratio respectively.

$^{13}C\{^1H\}$ NMR (d_5-chlorobenzene) δ (ppm): 163.2 ($BAr_{meta}\mathbf{C}F_3$), 162.7 ($BAr_{meta}\mathbf{C}F_3$), 162.2 ($BAr_{meta}\mathbf{C}F_3$), 161.69 ($BAr_{meta}\mathbf{C}F_3$), 153.6 (**Ar**H), 135.2 ($B\mathbf{Ar}_{ortho}H$), 129.7 (**Ar**H), 128.8 (**Ar**H), 123.6 ($B\mathbf{Ar}_{ipso}$), 123.1 (**Ar**H), 120.9 ($B\mathbf{Ar}_{meta}CF_3$), 117.7 ($B\mathbf{Ar}_{para}H$), 38.3 ($Ar_{ortho}CH_2P(\mathbf{C}(CH_3)_3)_2$), 34.8 ($Ar_{ortho}\mathbf{C}H_2P(C(CH_3)_3)_2$), 32.6 ($Ar_{ortho}\mathbf{C}H_2P(C(CH_3)_3)_2$), 29.8 ($Ar_{ortho}CH_2P(C(\mathbf{C}H_3)_3)_2$), 28.1 ($Ar_{ortho}CH_2P(C(\mathbf{C}H_3)_3)_2$).

$^{31}P\{^1H\}$ NMR (d_6-benzene) δ (ppm): 74.4, 71.0.

$^{11}B\{^1H\}$ NMR (d_5-chlorobenzene) δ (ppm): 5.9.

$^{19}F\{^1H\}$ NMR (d_5-chlorobenzene) δ (ppm): −61.9.

^1H NMR (d_2-DCM) δ (ppm): 7.72 (s, 8H, $BAr\mathbf{H}_{ortho}$), 7.56 (s, 4H, $BAr\mathbf{H}_{para}$), 7.07 (broad s, 2H, $Ar\mathbf{H}_{meta}$), 7.07 (broad s, 1H, $Ar\mathbf{H}_{para}$), 3.49 (broad s, 4H, $Ar_{ortho}C\mathbf{H}_2P(C(CH_3)_3)_2$), 1.34 (broad m, 36H, $Ar_{ortho}CH_2P(C(C\mathbf{H}_3)_3)_2$), −41.23 (broad s, 1H, Ir**H**), −43.57 (v. broad s, 1H, Ir**H**), −44.62 (v. broad s, 1H, Ir**H**). The three Ir–H resonances are in a 30:20:50 ratio respectively.

$^{31}P\{^1H\}$ NMR (d_2-DCM) δ (ppm): 74.5 (weak, broad), 73.1 (weak, broad).

6.5.6. General procedure for hydrogenation reactions

Hydrogenation reactions were performed in J. Young valve NMR spectroscopy tubes. For heterogeneous complexes, a catalyst loading of 5 mg was employed (0.46 μmol_{Ir}); for molecular complexes a loading of 2 mg (3.21 μmol) was utilised. After addition of the solid, d_6-benzene (500 μL) containing $Si(SiMe_3)_4$ (3 μmol) as an internal standard was added. The contents were freeze-pump-thaw degassed three times prior to ethylene (1 bar) addition. The contents were once again frozen and the headspace evacuated, prior to addition of hydrogen (1 bar). Reactions were run at 23 °C and analysed periodically by ^1H NMR spectroscopy, which showed the formation of ethane (0.80 ppm) in all cases.

6.5.7. General procedure for transfer hydrogenation reactions

Hydrogenation reactions were performed in J. Young valve NMR spectroscopy tubes. For sMAO-Ir($^{t\mathrm{Bu}}$PCP)HCl a catalyst loading of 5 mg was employed (0.46 μmol_{Ir}), for Ir($^{t\mathrm{Bu}}$PCP)H_4 a loading of 2 mg (3.21 μmol) was utilised. After addition of the solid, d_6-benzene (500 μL) containing $Si(SiMe_3)_4$ (3 μmol) as an internal standard was added, followed by *tert*-butylethylene (TBE) (TBE/Ir = 300). For reactions with cyclooctane (COA), COA (COA/Ir = 300) was added and the tube freeze-pump-thaw degassed three times, after which argon was added. For reactions with ethane, the tubes were freeze-pump-thaw degassed three times and ethane (1 bar) added. Reactions were heated at 100 °C, and analysed

periodically by ^{1}H NMR spectroscopy. Formation of cyclooctene (COE) and *tert*-butylethane (TBA) was observed for the COA reaction. No traces of ethylene could be observed for the reaction with ethane.

COA. ^{1}H NMR (d_6-benzene) δ (ppm): 1.51 (s, 16H, $C_8\mathbf{H}_{16}$).

TBE. ^{1}H NMR (d_6-benzene) δ (ppm): 5.81 (m, 1H, $(CH_3)_3CC\mathbf{H}=CH_2$), 4.90 (m, 1H, $(CH_3)_3CCH=C\mathbf{H}_2$), 0.97 (s, 1H, $(C\mathbf{H}_3)_3CCH=CH_2$).

COE. ^{1}H NMR (d_6-benzene) δ (ppm): 5.63 (m, 2H, $C\mathbf{H}=C\mathbf{H}C_6H_{12}$), 2.08 (m), 1.50 (m).

TBA. ^{1}H NMR (d_6-benzene) δ (ppm): 1.19 (q, 2H, $(CH_3)_3CC\mathbf{H}_2CH_3$), 0.85 (s, 9H, $(C\mathbf{H}_3)_3CCH_2CH_3$), 0.81 (t, 3H, $(CH_3)_3CCH_2C\mathbf{H}_3$).

6.5.8. Co-immobilisation of 1.7 and Ir($^{t\mathrm{Bu}}$PCP)HCl on sMAO

1.7 (2.6 mg, 4.9 μmol), Ir($^{t\mathrm{Bu}}$PCP)HCl (3.1 mg, 4.9 μmol) and sMAO (100 mg, Al:Ir:W = 300:1:1) were charged in a Schlenk flask prior to addition of toluene (30 mL). The mixture was swirled intermittently for 1 hour at 23 °C, resulting in complete decolouration of the solution. A yellow solid was obtained in near quantitative isolated yield after filtering away the solution and drying the solid *in vacuo*.

^{13}C{^{1}H} CPMAS SSNMR δ (ppm): 177 ($\mathrm{Ph}\mathbf{C}O_2$), 136 ($\mathbf{Ph}CO_2$), 130 ($\mathbf{Ph}CO_2$), 128 ($\mathbf{Ph}CO_2$), 37 ($\mathrm{Ar}_{ortho}\mathbf{C}H_2P(C(CH_3)_2)$), 34 ($\mathrm{Ar}_{ortho}CH_2P(\mathbf{C}(CH_3)_2)$), 30 ($\mathrm{Ar}_{ortho}CH_2P(C(\mathbf{C}H_3)_2)$), −8 (Al**Me**).

^{31}P-{^{1}H} CPMAS SSNMR δ (ppm): 69.

^{19}F{^{1}H} HPDEC SSNMR δ (ppm): −123.

The ^{27}Al Hahn echo SSNMR spectra displayed multiple broad resonances between 700 and −700 ppm.

6.5.9. Reaction of sMAO(1.7/Ir($^{t\mathrm{Bu}}$PCP)HCl) with ethane

sMAO-(**1.7**/Ir($^{t\mathrm{Bu}}$PCP)HCl) (5 mg, 0.23 μmol_W, 0.23 μmol_{Ir}) was charged in a J. Young valve NMR spectroscopy tube. d_6-Benzene (500 μL) containing $Si(SiMe_3)_4$ (3 μmol) as an internal standard was added, followed by *tert*-butylethylene (TBE) (8.9 μL, 69 μmol, TBE/Ir = 300). The tube was freeze-pump-thaw degassed three times and ethane (1 bar) added. The reaction was heated at 100 °C, and analysed periodically by ^{1}H NMR spectroscopy over the course of 3 days. Only resonances corresponding to ethane and TBE could be observed after 3 days.

6.6. References

1. C. Chen, M. Yang, Q. Wang, J.-C. Buffet, and D. O'Hare, *J. Mater. Chem. A*, 2014, **2**, 15102–15110.
2. V. C. Gibson, T. P. Kee, and A. Shaw, *Polyhedron*, 1988, **7**, 579–580.
3. R. R. Schrock, R. T. DePue, J. Feldman, K. B. Yap, D. C. Yang, W. M. Davis, L. Park, M. DiMare, M. Schofield, J. Anhaus, E. Walborsky, E. Evitt, C. Krüger, and P. Betz, *Organometallics*, 1990, **9**, 2262–2275.
4. K. P. Bryliakov, E. P. Talsi, and M. Bochmann, *Organometallics*, 2004, **23**, 149–152.
5. E. P. Schram and N. Sudha, *Inorg. Chim. Acta*, 1991, **183**, 213–216.
6. J. Jarupatrakorn, M. P. Coles, and T. D. Tilley, *Chem. Mater.*, 2005, **17**, 1818–1828.
7. P. J. Bailey, R. A. Coxall, C. M. Dick, S. Fabre, L. C. Henderson, C. Herber, S. T. Liddle, D. Loroño-González, A. Parkin, and S. Parsons, *Chem. Eur. J.*, 2003, **9**, 4820–4828.
8. R. R. Schrock and J. D. Fellmann, *J. Am. Chem. Soc.*, 1978, **100**, 3359–3370.
9. M. Rimoldi and A. Mezzetti, *Inorg. Chem.*, 2014, **53**, 11974–11984.
10. P. Canonne, R. Boulanger, and B. Chantegrel, *Tetrahedron*, 1987, **43**, 663–668.
11. R. R. Schrock, J. Sancho, and S. F. Pederson, *Inorg. Synth.*, 1989, **26**, 46–47.
12. S. C. Watson and J. F. Eastham, *J. Organomet. Chem.*, 1967, **9**, 165–168.
13. S. R. Bahr and P. Boudjouk, *J. Org. Chem.*, 1992, **57**, 5545–5547.
14. E. Kaji and E. Yoshioka, *Solid polymethylaluminoxane composition and process for manufacturing same*, 2010, WO2010055652.
15. A. F. R. Kilpatrick, J.-C. Buffet, P. Nørby, N. H. Rees, N. P. Funnell, S. Sripothongnak, and D. O'Hare, *Chem. Mater.*, 2016, **28**, 7444–7450.
16. J. Cosier and A. M. Glazer, *J. Appl. Crystallogr.*, 1986, **19**, 105–107.
17. CrysAlisPro, Oxford Diffraction/Agilent Technologies UK LTD, Yarnton, England.
18. Z. Otwinowski and W. Minor, in *Macromolecular Crystallography Part A*, ed. J. B. T.-M. in E. Charles W. Carter, Academic Press, 1997, vol. Volume 276, pp. 307–326.
19. R. H. Blessing, *Acta Crystallogr. Sect. A*, 1995, **51**, 33–38.
20. A. Altomare, G. Cascarano, C. Giacovazzo, and A. Guagliardi, *J. Appl. Crystallogr.*, 1993, **26**, 343–350.
21. L. Palatinus and G. Chapuis, *J. Appl. Crystallogr.*, 2007, **40**, 786–790.
22. L. J. Farrugia, *J. Appl. Crystallogr.*, 2012, **45**, 849–854.
23. L. J. Farrugia, *J. Appl. Crystallogr.*, 1999, **32**, 837–838.
24. A. L. Spek, *J. Appl. Crystallogr.*, 2003, **36**, 7–13.
25. A.L. Spek, *PLATON, a Multipurp. Crystallogr. tool, Utrecht, Netherlands*, 1998.
26. F. Neese, Orca - an ab initio, DFT and Semiempirical Electronic Structure Package, Version 2.8, Revision 2360,Institut für Physikalische und Theoretische Chemie, Universität Bonn, Bonn (Germany)).
27. A. D. Becke, *J. Chem. Phys.*, 1986, **84**, 4524–4529.
28. J. P. Perdew and W. Yue, *Phys. Rev. B*, 1986, **33**, 8800–8802.
29. J. P. Perdew, *Phys. Rev. B*, 1986, **33**, 8822–8824.
30. E. van Lenthe, E. J. Baerends, and J. G. Snijders, *J. Chem. Phys.*, 1993, **99**, 4597.
31. E. van Lenthe, E. J. Baerends, and J. G. Snijders, *J. Chem. Phys.*, 1994, **101**, 9783.
32. E. van Lenthe, J. G. Snijders, and E. J. Baerends, *J. Chem. Phys.*, 1996, **105**, 6505.
33. D. A. Pantazis, X.-Y. Chen, C. R. Landis, and F. Neese, *J. Chem. Theory Comput.*, 2008, **4**, 908–919.
34. D. A. Pantazis and F. Neese, *J. Chem. Theory Comput.*, 2009, **5**, 2229–2238.
35. A. Schäfer, C. Huber, and R. Ahlrichs, *J. Chem. Phys.*, 1994, **100**, 5829.
36. F. Weigend and R. Ahlrichs, *Phys. Chem. Chem. Phys.*, 2005, **7**, 3297.
37. F. Weigend, *Phys. Chem. Chem. Phys.*, 2006, **8**, 1057.
38. K. Eichkorn, F. Weigend, O. Treutler, and R. Ahlrichs, *Theor. Chem. Accounts Theory, Comput. Model. (Theoretica Chim. Acta)*, 1997, **97**, 119–124.
39. K. Eichkorn, O. Treutler, H. Öhm, M. Häser, and R. Ahlrichs, *Chem. Phys. Lett.*, 1995, **240**, 283–290.

40. K. Eichkorn, O. Treutler, H. Öhm, M. Häser, and R. Ahlrichs, *Chem. Phys. Lett.*, 1995, **242**, 652–660.
41. E. F. Pettersen, T. D. Goddard, C. C. Huang, G. S. Couch, D. M. Greenblatt, E. C. Meng, and T. E. Ferrin, *J. Comput. Chem.*, 2004, **25**, 1605–1612.
42. D. C. Bradley, S. R. Hodge, J. D. Runnacles, M. Hughes, J. Mason, and R. L. Richards, *J. Chem. Soc. Dalton Trans.*, 1992, 1663–1668.
43. C. M. R. Wright, Z. R. Turner, J.-C. J.-C. Buffet, and D. O'Hare, *Chem. Commun.*, 2016, **52**, 2850–2853.
44. A. V Besserguenev, A. M. Fogg, R. J. Francis, S. J. Price, D. O'Hare, V. P. Isupov, and B. P. Tolochko, *Chem. Mater.*, 1997, **9**, 241–247.
45. J.-C. Buffet, Z. R. Turner, R. T. Cooper, and D. O'Hare, *Polym. Chem.*, 2015, **6**, 2493–2503.
46. M. Newville, *J. Synchrotron Radiat.*, 2001, **8**, 322–324.
47. B. Ravel and M. Newville, *J. Synchrotron Radiat.*, 2005, **12**, 537–541.
48. R. Ghosh, M. Kanzelberger, T. J. Emge, G. S. Hall, and A. S. Goldman, *Organometallics*, 2006, **25**, 5668–5671.
49. D. W. Lee, W. C. Kaska, and C. M. Jensen, *Organometallics*, 1998, **17**, 1–3.

Appendices

"The proper method for inquiring after the properties of things is to deduce them from experiments." **Isaac Newton**

Appendix for Chapter Two

2.1. $W(NR)Cl_4(THF)$ complexes (1.1-1.8)

2.1.1. Single crystal X-ray diffraction data tables

Crystal data		
Compound **CCDC number** **Chemical formula**	$W(NPh)Cl_4(THF)$ (**1.1**) 1518771 $C_{10}H_{13}Cl_4NOW$	$W\{N(2,6\text{-}Me\text{-}C_6H_3)\}Cl_4(THF)$ (**1.2**) 1518770 $C_{12}H_{17}Cl_4NOW$
Mr	488.86	516.92
Crystal system, space group	Monoclinic, $P2_1/c$	Triclinic, $P\bar{1}$
Temperature (K)	150	150
***a, b, c* (Å)**	14.7317(3), 7.1889(1), 13.9923(3)	7.9869(2), 8.7291(2), 12.9648(4)
α, β, γ (°)	90, 102.120(1), 90	85.609(1), 89.995(1), 64.329(1)
***V* (Å^3)**	1448.82(5)	811.73(4)
Z	4	2
μ (mm^{-1})	8.69	7.76
Crystal size (mm)	0.30 × 0.20 × 0.20	0.20 × 0.15 × 0.10
Data collection		
Diffractometer	Nonius KappaCCD diffractometer	Nonius KappaCCD diffractometer
Absorption correction	Multi-scan *SADABS*	Multi-scan *SADABS*
T_{min}, T_{max}	0.67, 1	0.74, 1.00
No. of measured, independent and observed [*I* > 2*s*(*I*)] reflections	6016, 3314, 2812	6820, 3709, 2978
R_{int}	0.030	0.051
$(\sin\theta/\lambda)_{max}$ (Å^{-1})	0.650	0.649
Refinement		
$R[F^2 > 2s(F^2)]$, $wR(F^2)$, S	0.031, 0.074, 1.09	0.039, 0.087, 1.01
No. of reflections	3314	3709
No. of parameters	154	174
No. of restraints	0	0
H-atom treatment	Constrained	Constrained
$(\Delta/\sigma)_{max}$	0.001	0.001
$\Delta\rho_{max}$, $\Delta\rho_{min}$ (e Å^{-3})	2.24, −1.45	1.95, −1.95
Absolute structure	-	-
Absolute structure parameter	-	-
Computer programs: Collect (Nonius BV, 1997-2000), *HKL SCALEPACK* (Otwinowski & Minor 1997), *HKL DENZO* and *SCALEPACK* (Otwinowski & Minor 1997), Palatinus, L.; Chapuis, G. J. Appl. Cryst. 2007, 40, 786-790., *SHELXL2014* (Sheldrick, 2014), *ORTEP-3 for Windows* (Farrugia, 1997), *WinGX* publication routines (Farrugia, 1999).		

Crystal data		
Compound **CCDC number** **Chemical formula**	W{N(3,5-Me-C_6H_3)}Cl_4(THF) (**1.3**) 1518775 $C_{12}H_{17}Cl_4NOW$	W{N(2,4,6-Me-C_6H_2)}Cl_4(THF) (**1.4**) 1518769 $C_{13}H_{19}Cl_4NOW$
Mr	516.92	530.94
Crystal system, space group	Triclinic, $P\bar{1}$	Triclinic, $P\bar{1}$
Temperature (K)	150	150
***a, b, c* (Å)**	8.6354(1), 9.6261(2), 10.9204(2)	7.8367(1), 8.7690(2), 14.2277(3)
α, β, γ (°)	101.470(1), 95.240(1), 107.534(1)	78.940(1), 89.844(1), 63.883(1)
***V* (Å^3)**	837.11(3)	857.88(3)
Z	2	2
μ (mm^{-1})	7.53	7.35
Crystal size (mm)	0.20 × 0.15 × 0.10	0.40 × 0.20 × 0.02
Data collection		
Diffractometer	Nonius KappaCCD diffractometer	Nonius KappaCCD diffractometer
Absorption correction	Multi-scan *SADABS*	Multi-scan *DENZO/SCALEPACK* (Otwinowski & Minor, 1997)
T_{min}, T_{max}	0.69, 1	0.744, 1.000
No. of measured, independent and observed [*I* > 2*s*(*I*)] reflections	7196, 3819, 3471	7214, 3936, 3594
R_{int}	0.025	0.028
(sin θ/λ)$_{max}$ (Å^{-1})	0.650	0.651
Refinement		
$R[F^2 > 2s(F^2)]$, $wR(F^2)$, S	0.028, 0.065, 1.13	0.028, 0.068, 1.08
No. of reflections	3819	3936
No. of parameters	175	184
No. of restraints	5	0
H-atom treatment	Constrained	Constrained
$(\Delta/\sigma)_{max}$	0.001	0.001
$\Delta\rho_{max}$, $\Delta\rho_{min}$ (e Å^{-3})	1.62, −1.41	1.71, −1.71
Absolute structure	-	-
Absolute structure parameter	-	-
Computer programs: Collect (Nonius BV, 1997-2000), *HKL SCALEPACK* (Otwinowski & Minor 1997), *HKL DENZO* and *SCALEPACK* (Otwinowski & Minor 1997), Palatinus, L.; Chapuis, G. J. Appl. Cryst. 2007, 40, 786-790., *SHELXL2014* (Sheldrick, 2014), *ORTEP-3 for Windows* (Farrugia, 1997), *WinGX* publication routines (Farrugia, 1999).		

Crystal data		
Compound **CCDC number** **Chemical formula**	W{N(2,6-^{i}Pr-C_6H_3)}Cl_4(THF) (**1.5**) 1434397 $C_{16}H_{25}Cl_4NOW$	W{N(4-OMe-C_6H_4)}Cl_4(THF) (**1.6**) 1518774 $C_{11}H_{15}Cl_4NO_2W$
Mr	573.02	518.89
Crystal system, space group	Triclinic, $P\bar{1}$	Monoclinic, $P2_1/c$
Temperature (K)	150	150
***a, b, c* (Å)**	8.5941(1), 14.1186(2), 17.4478(3)	13.2115(2), 8.0822(1), 15.7475(2)
α, β, γ (°)	95.806 (1), 98.562 (1), 97.484 (1)	90, 109.109(1), 90
***V* (Å^3)**	2059.88(5)	1588.83(4)
Z	4	4
μ (mm^{-1})	6.13	7.94
Crystal size (mm)	0.56 × 0.48 × 0.14	0.20 × 0.12 × 0.10
Data collection		
Diffractometer	Nonius KappaCCD diffractometer	Nonius KappaCCD diffractometer
Absorption correction	Multi-scan *DENZO/SCALEPACK* (Otwinowski & Minor, 1997)	Multi-scan Multi-scan from symmetry-related measurements using *SORTAV* (Blessing 1995)
T_{min}, T_{max}	0.76, 1.00	0.735, 1.000
No. of measured, independent and observed [*I* > 2*s*(*I*)] reflections	17151, 9396, 7987	7374, 3921, 3396
R_{int}	0.029	0.027
(sin θ/λ)$_{max}$ (Å^{-1})	0.650	0.666
Refinement		
$R[F^2 > 2s(F^2)]$, $wR(F^2)$, S	0.029, 0.069, 1.10	0.029, 0.075, 1.10
No. of reflections	9396	3921
No. of parameters	433	173
No. of restraints	1	0
H-atom treatment	Constrained	Constrained
(Δ/σ)$_{max}$	0.002	0.001
Δρ_{max}, Δρ_{min} (e Å^{-3})	1.66, -1.52	1.74, −1.67
Absolute structure	-	-
Absolute structure parameter	-	-
Computer programs: Collect (Nonius BV, 1997-2000), *HKL SCALEPACK* (Otwinowski & Minor 1997), *HKL DENZO* and *SCALEPACK* (Otwinowski & Minor 1997), Palatinus, L.; Chapuis, G. J. Appl. Cryst. 2007, 40, 786-790., *SHELXL2014* (Sheldrick, 2014), *ORTEP-3 for Windows* (Farrugia, 1997), *WinGX* publication routines (Farrugia, 1999).		

Crystal data		
Compound **CCDC number** **Chemical formula**	W{N(2,6-F-C_6H_3)}Cl_4(THF) (**1.7**) 1518772 $C_{10}H_{11}Cl_4F_2NOW$	W{N(3,5-CF_3-C_6H_3)}Cl_4(THF) (**1.8**) 1518773 $C_{12}H_{11}Cl_4F_6NOW$
Mr	524.85	624.87
Crystal system, space group	Triclinic, $P\bar{1}$	Triclinic, $P\bar{1}$
Temperature (K)	150	150
***a, b, c* (Å)**	8.1651(2), 9.4012(3), 9.9731(3)	8.9918(1), 10.3714(1), 10.9720(1)
α, β, γ (°)	87.462(2), 86.122(2), 79.773(2)	63.427(1), 86.047(1), 89.359(1)
***V* (Å^3)**	751.26(4)	912.74(2)
Z	2	2
μ (mm^{-1})	8.41	6.97
Crystal size (mm)	0.21 × 0.16 × 0.10	0.20 × 0.15 × 0.10
Data collection		
Diffractometer	SuperNova, Dual, Cu at zero, Atlas diffractometer	Nonius KappaCCD diffractometer
Absorption correction	Multi-scan *CrysAlis PRO* 1.171.38.41 (Rigaku Oxford Diffraction, 2015) Empirical absorption correction using spherical harmonics, implemented in SCALE3 ABSPACK scaling algorithm.	Multi-scan Multi-scan from symmetry-related measurements using *SORTAV* (Blessing 1995)
T_{min}*, *T_{max}	0.555, 1.000	0.714, 1.000
No. of measured, independent and observed [*I > 2s(I)*] reflections	15868, 3447, 3325	7916, 4161, 3919
R_{int}	0.040	0.019
(sin θ/λ)$_{max}$ (Å^{-1})	0.649	0.650
Refinement		
R*[*F*^{2} > 2*s*(*F*^{2})], *wR*(*F*^{2}), *S	0.016, 0.039, 1.00	0.024, 0.058, 1.10
No. of reflections	3447	4161
No. of parameters	172	226
No. of restraints	0	0
H-atom treatment	Constrained	Constrained
(Δ/σ)$_{max}$	0.001	0.001
Δρ_{max}, Δρ_{min} (e Å^{-3})	0.61, −0.88	1.58, −1.24
Absolute structure	-	-
Absolute structure parameter	-	-
Computer programs: Collect (Nonius BV, 1997-2000), *HKL SCALEPACK* (Otwinowski & Minor 1997), *HKL DENZO* and *SCALEPACK* (Otwinowski & Minor 1997), Palatinus, L.; Chapuis, G. J. Appl. Cryst. 2007, 40, 786-790., *SHELXL2014* (Sheldrick, 2014),). *CrysAlis PRO* (Agilent (2014). Agilent Technologies Ltd, Yarnton, Oxfordshire, England.), *ORTEP-3 for Windows* (Farrugia, 1997), *WinGX* publication routines (Farrugia, 1999).		

2.1.2. NMR spectra

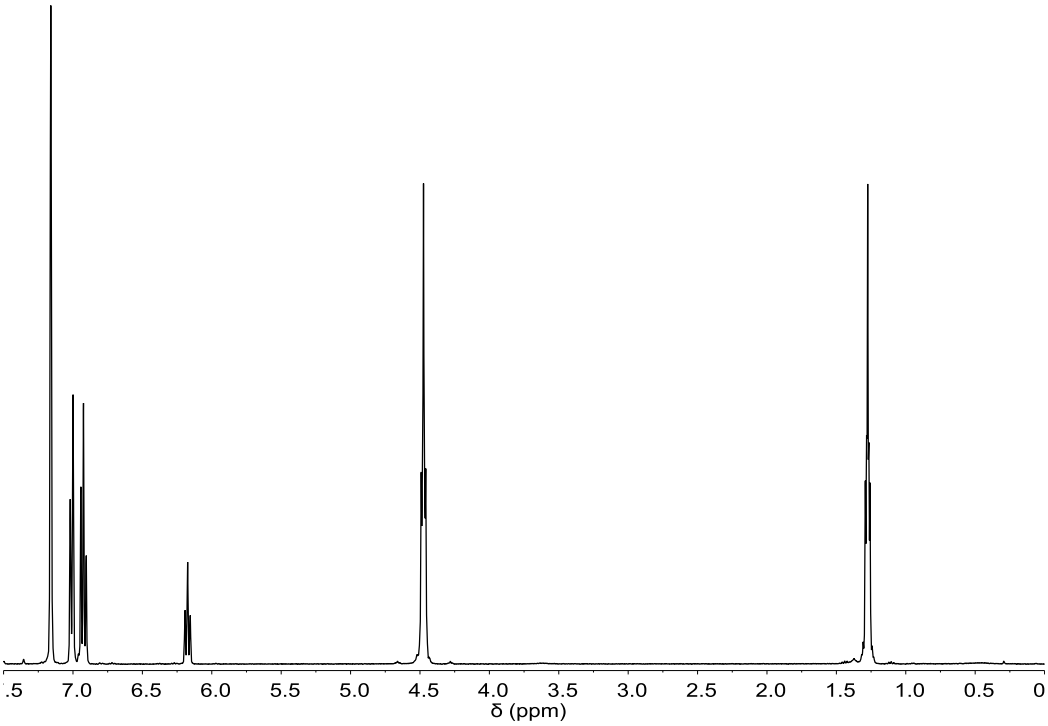


Figure A1. ^{1}H NMR spectrum (400 MHz, 23 °C) of **1.1** in d_6-benzene (7.16 ppm).

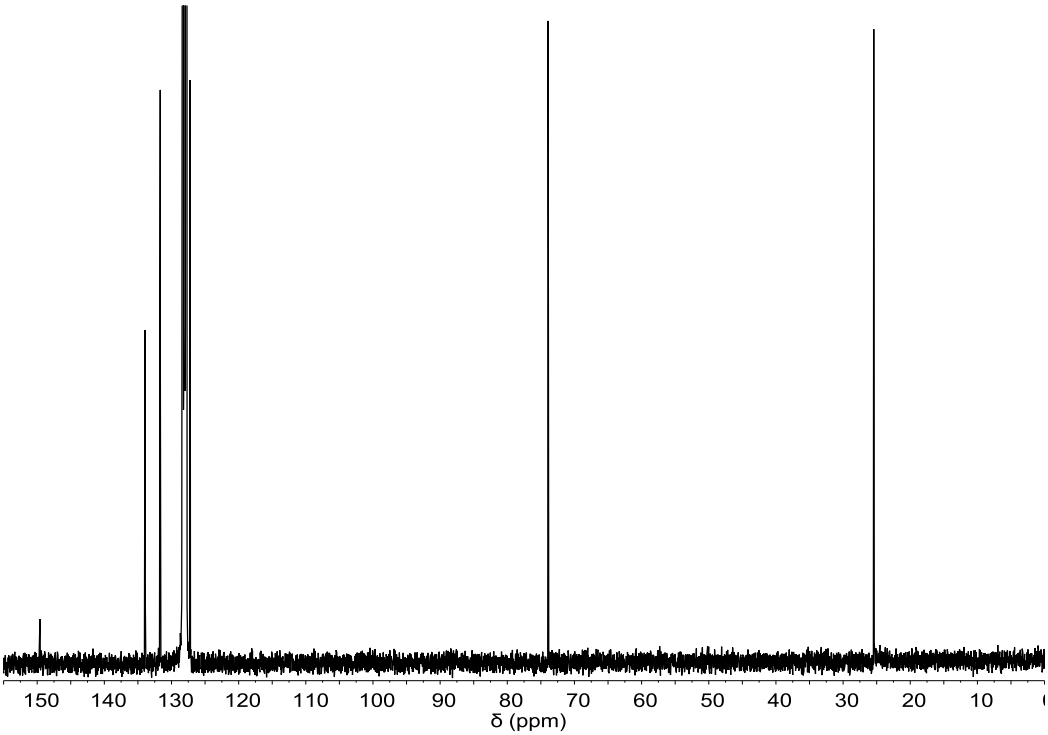


Figure A2. ^{13}C{^{1}H} NMR spectrum (400 MHz, 23 °C) of **1.1** in d_6-benzene (128.06 ppm).

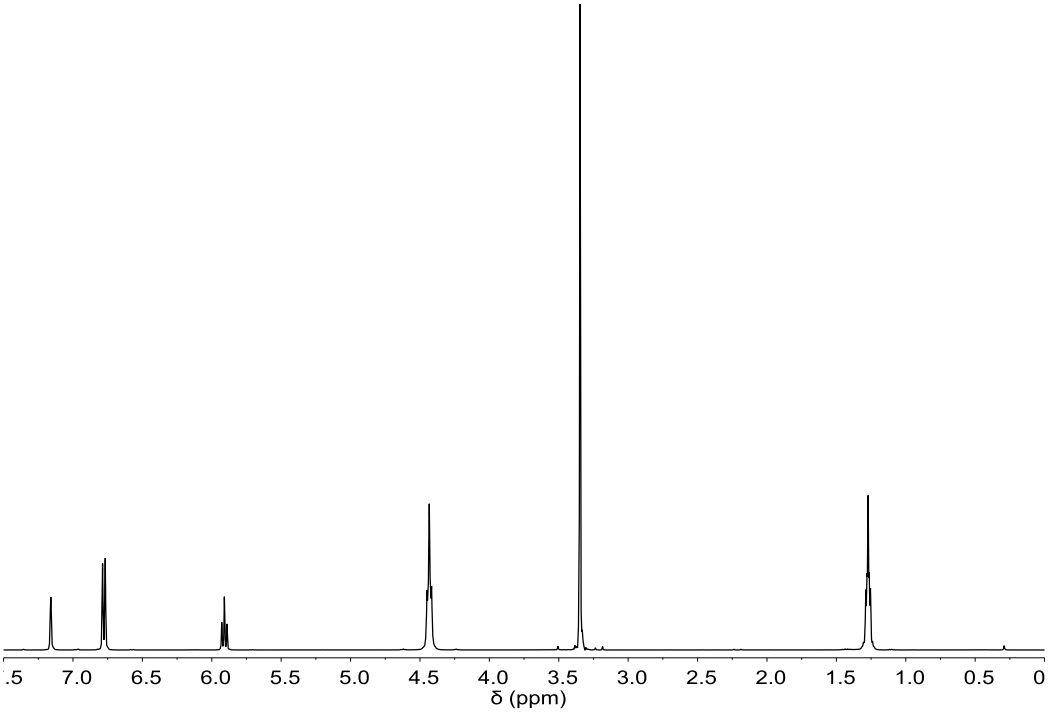


Figure A3. ^{1}H NMR spectrum (400 MHz, 23 °C) of **1.2** in d_6-benzene (7.16 ppm).

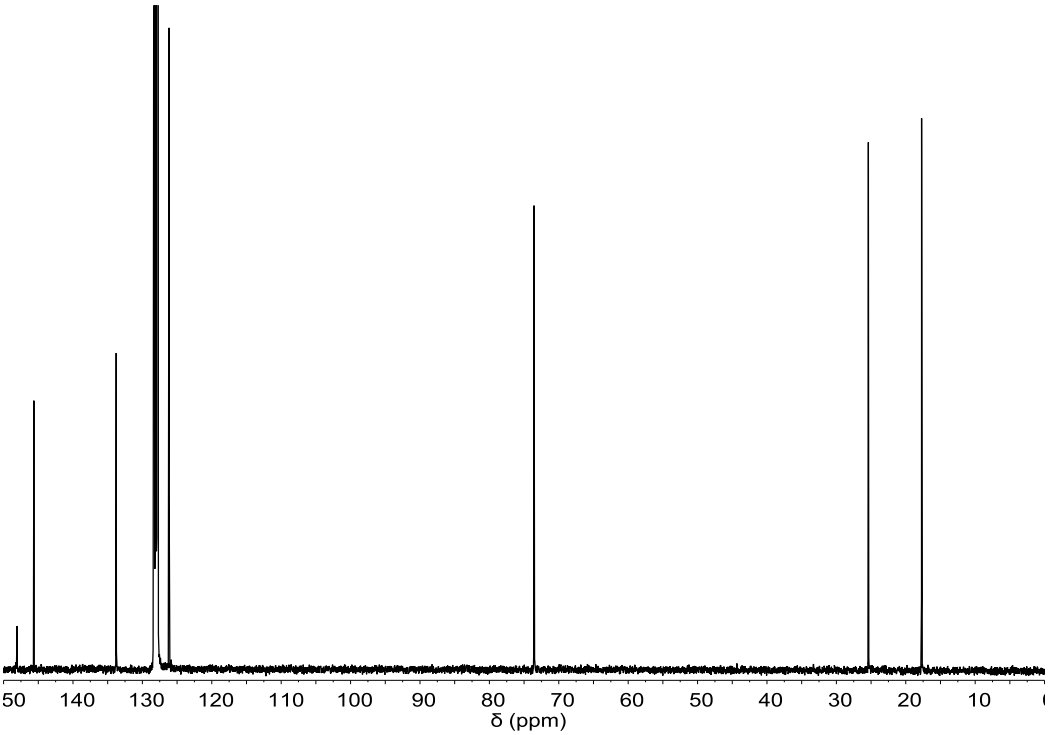


Figure A4. ^{13}C{^{1}H} NMR spectrum (400 MHz, 23 °C) of **1.2** in d_6-benzene (128.06 ppm).

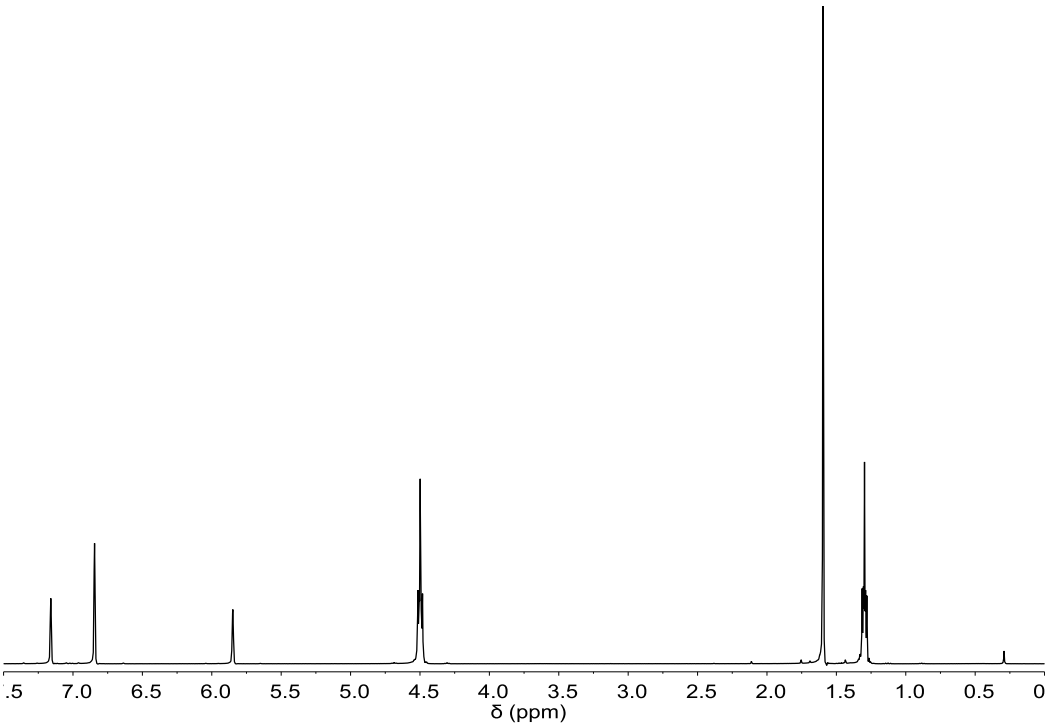


Figure A5. ^{1}H NMR spectrum (400 MHz, 23 °C) of **1.3** in d_6-benzene (7.16 ppm).

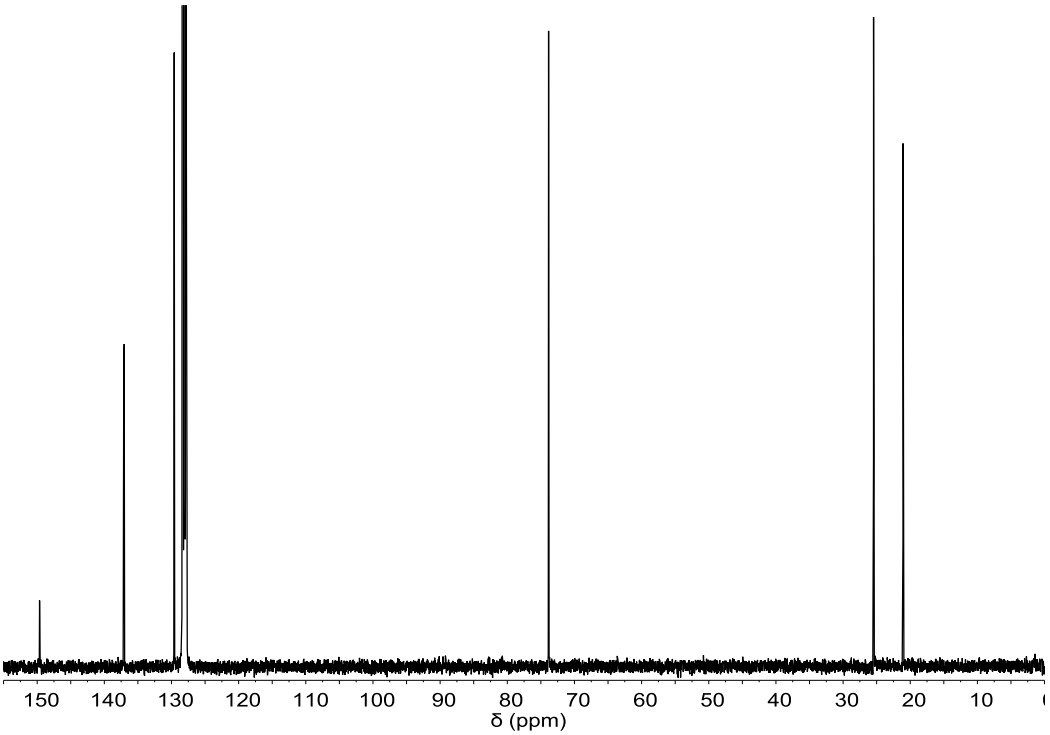


Figure A6. ^{13}C{^{1}H} NMR spectrum (400 MHz, 23 °C) of **1.3** in d_6-benzene (128.06 ppm).

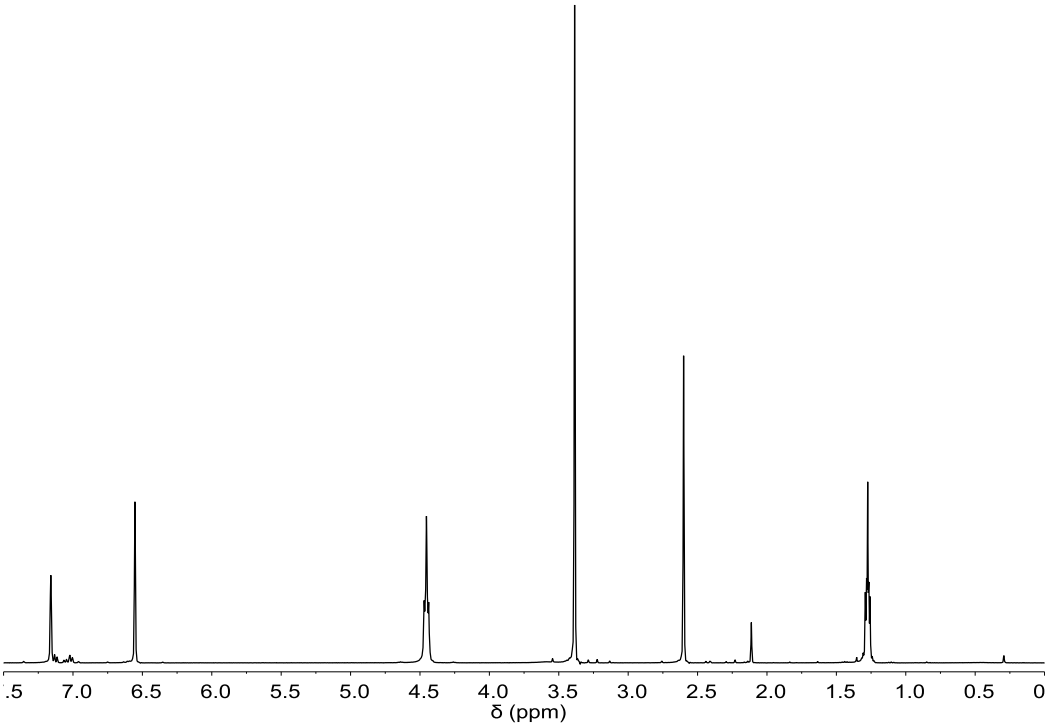


Figure A7. ^{1}H NMR spectrum (400 MHz, 23 °C) of **1.4** in d_6-benzene (7.16 ppm).

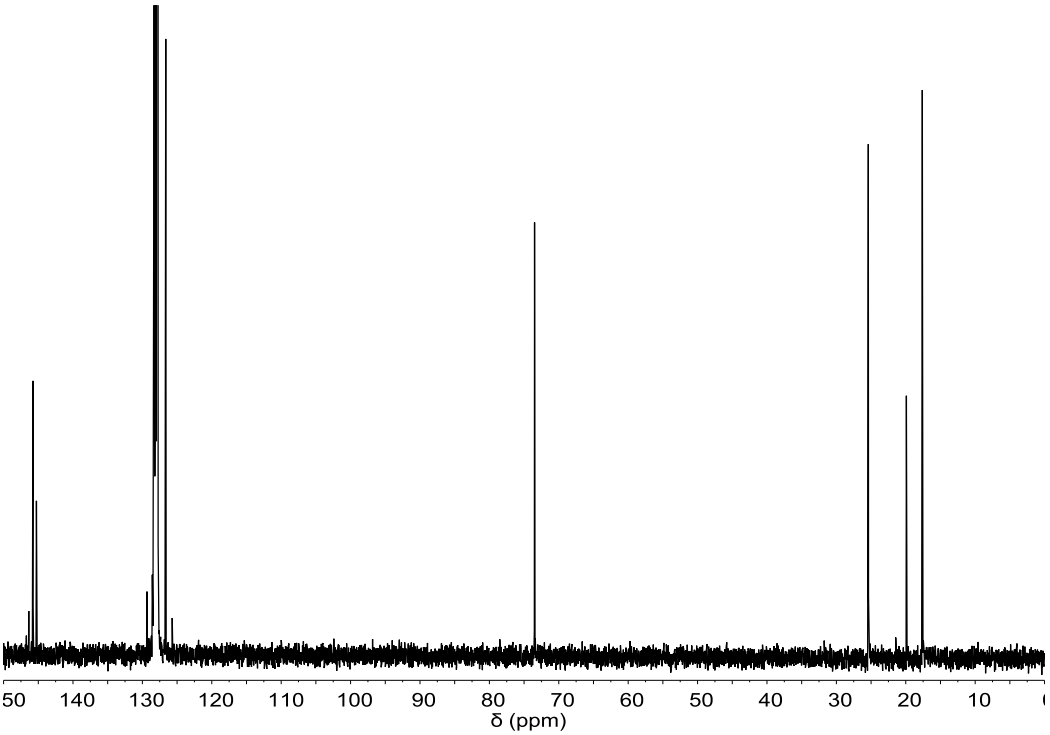


Figure A8. ^{13}C{^{1}H} NMR spectrum (400 MHz, 23 °C) of **1.4** in d_6-benzene (128.06 ppm).

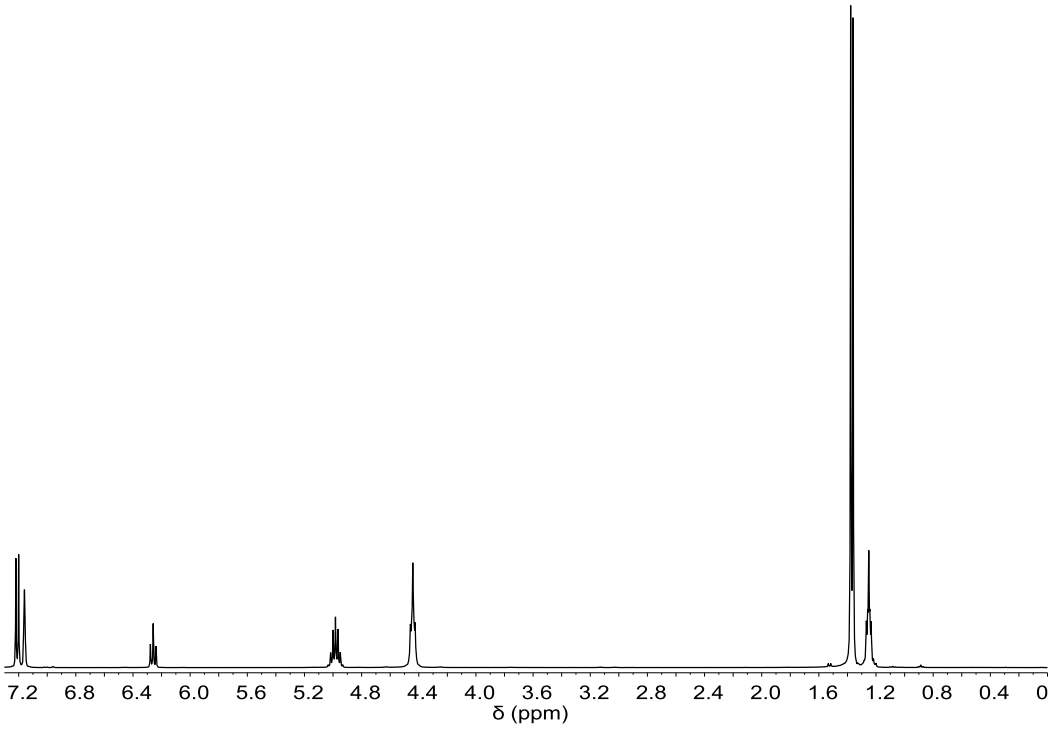


Figure A9. ^{1}H NMR spectrum (400 MHz, 23 °C) of **1.5** in d_6-benzene (7.16 ppm).

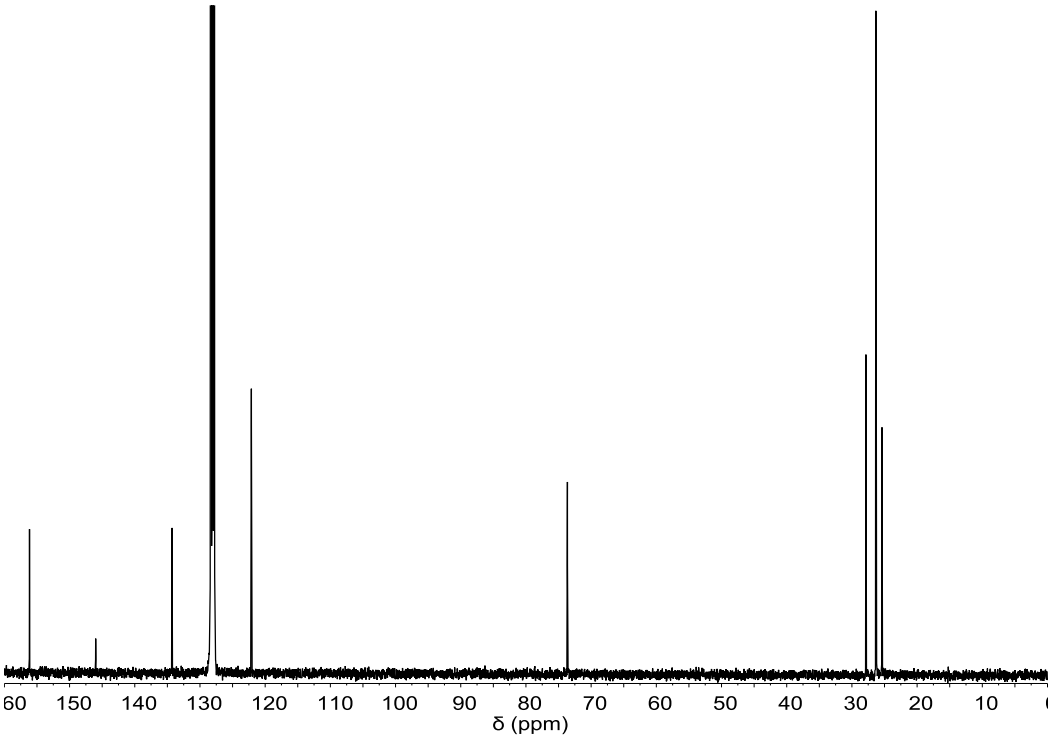


Figure A10. ^{13}C{^{1}H} NMR spectrum (400 MHz, 23 °C) of **1.5** in d_6-benzene (128.06 ppm).

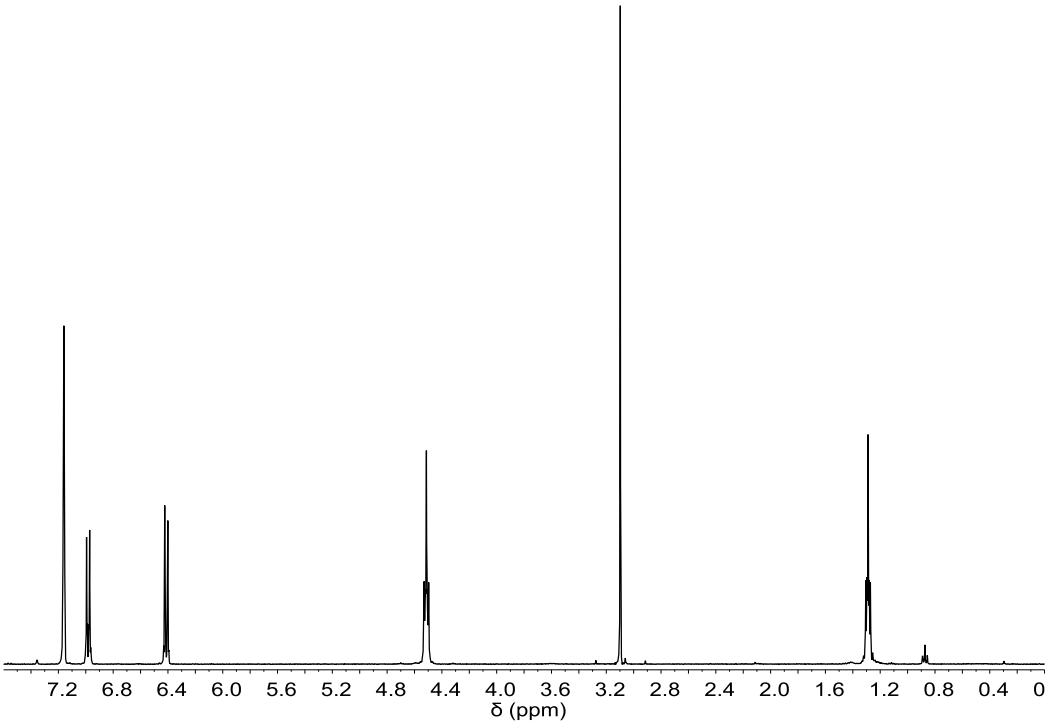


Figure A11. ^{1}H NMR spectrum (400 MHz, 23 °C) of **1.6** in d_6-benzene (7.16 ppm).

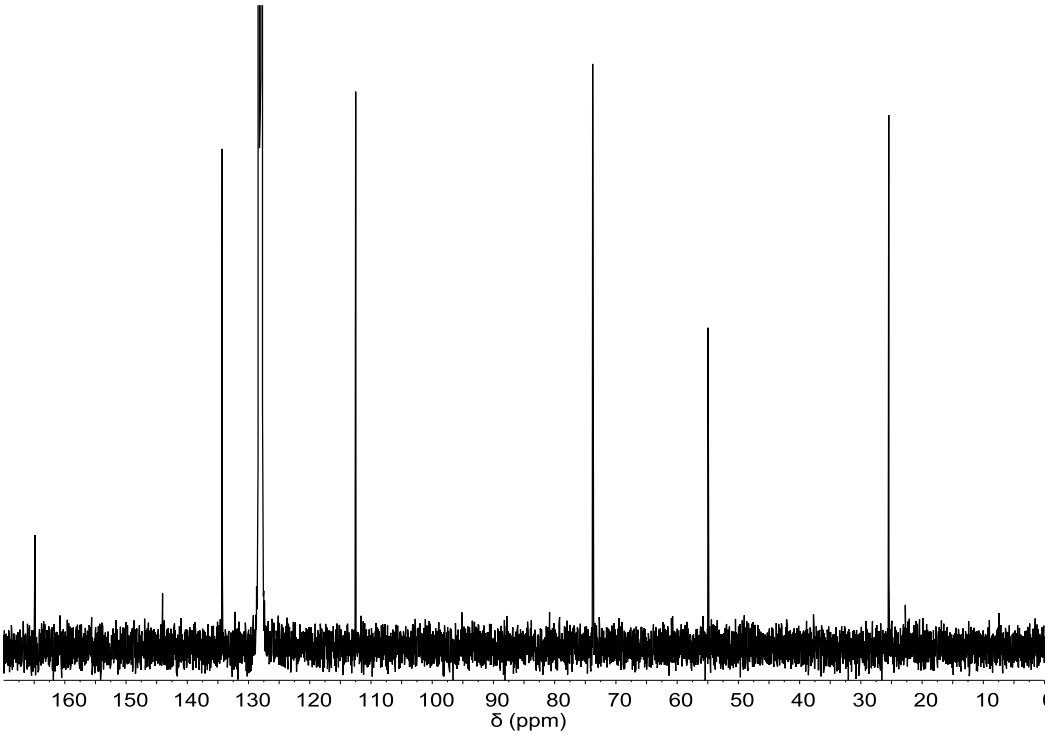


Figure A12. ^{13}C{^{1}H} NMR spectrum (400 MHz, 23 °C) of **1.6** in d_6-benzene (128.06 ppm).

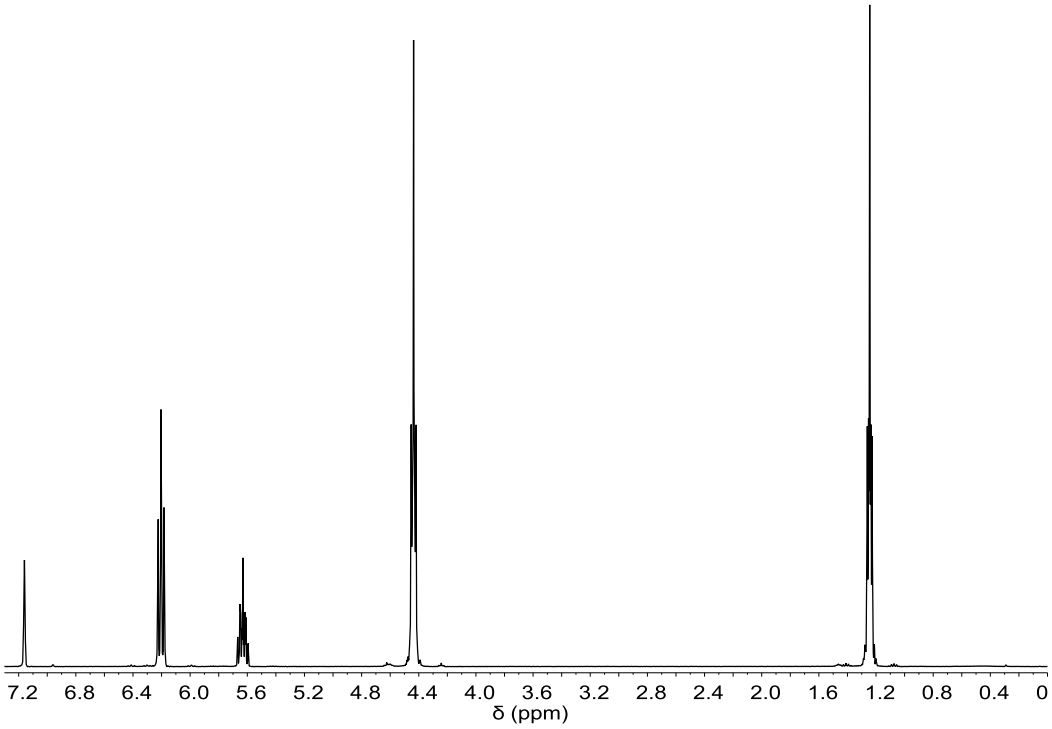


Figure A13. ^{1}H NMR spectrum (400 MHz, 23 °C) of **1.7** in d_6-benzene (7.16 ppm).

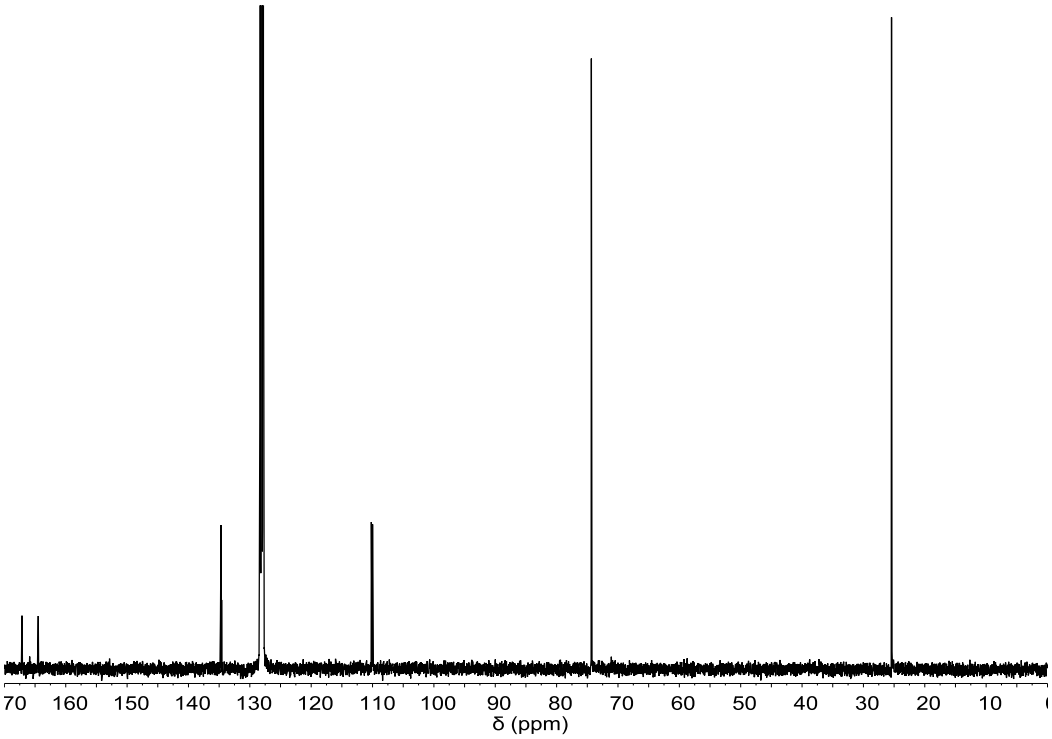


Figure A14. ^{13}C{^{1}H} NMR spectrum (400 MHz, 23 °C) of **1.7** in d_6-benzene (128.06 ppm).

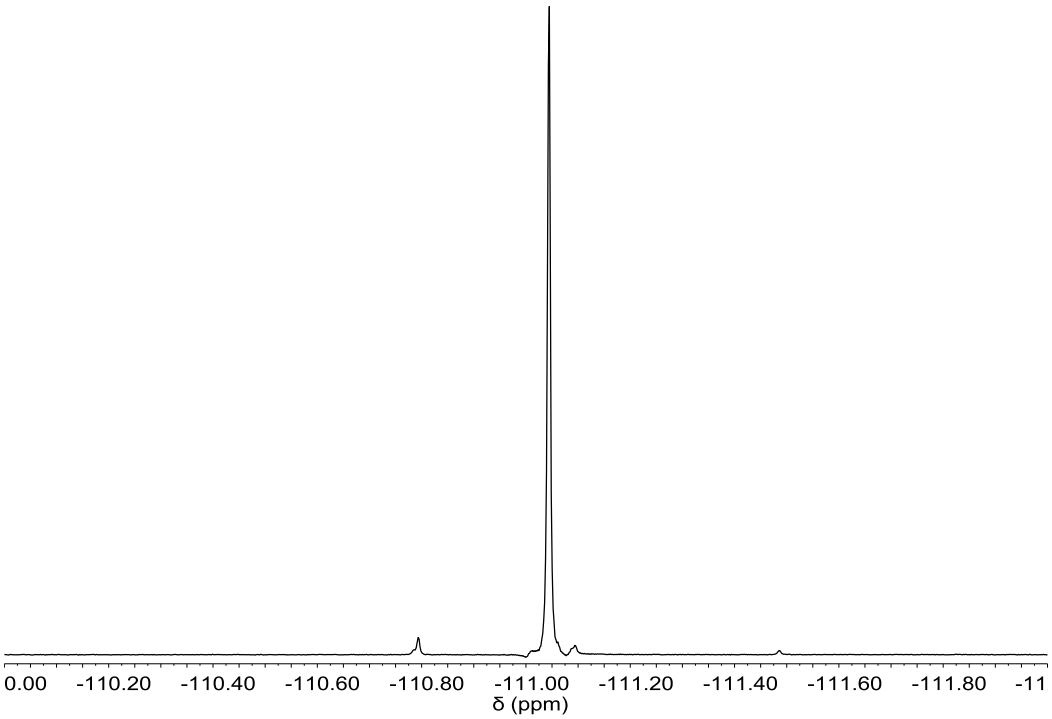


Figure A15. $^{19}F\{^{1}H\}$ NMR spectrum (400 MHz, 23 °C) of **1.7** in d_6-benzene.

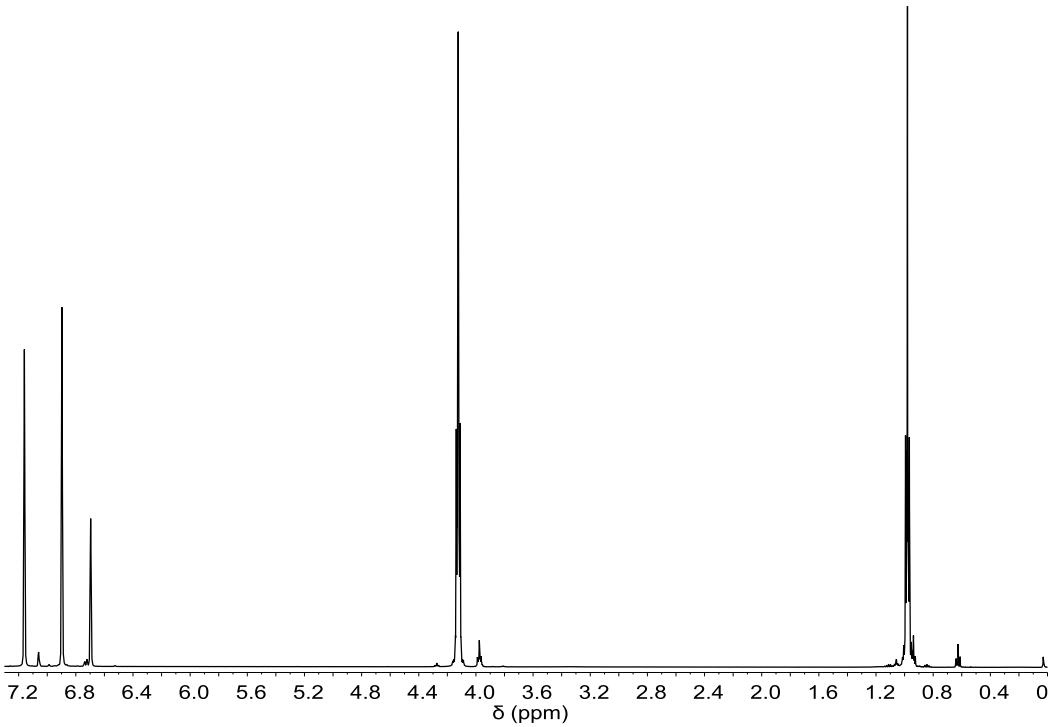


Figure A16. ^{1}H NMR spectrum (400 MHz, 23 °C) of **1.8** in d_6-benzene (7.16 ppm).

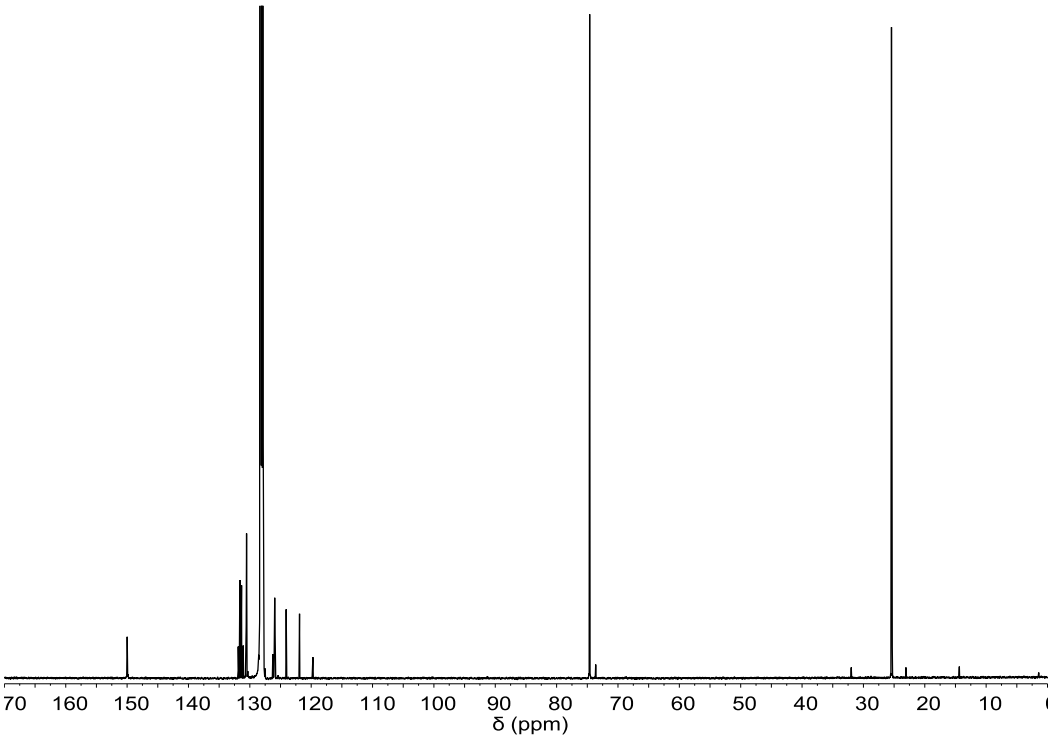


Figure A17. $^{13}C\{^{1}H\}$ NMR spectrum (400 MHz, 23 °C) of **1.8** in d_6-benzene (128.06 ppm).

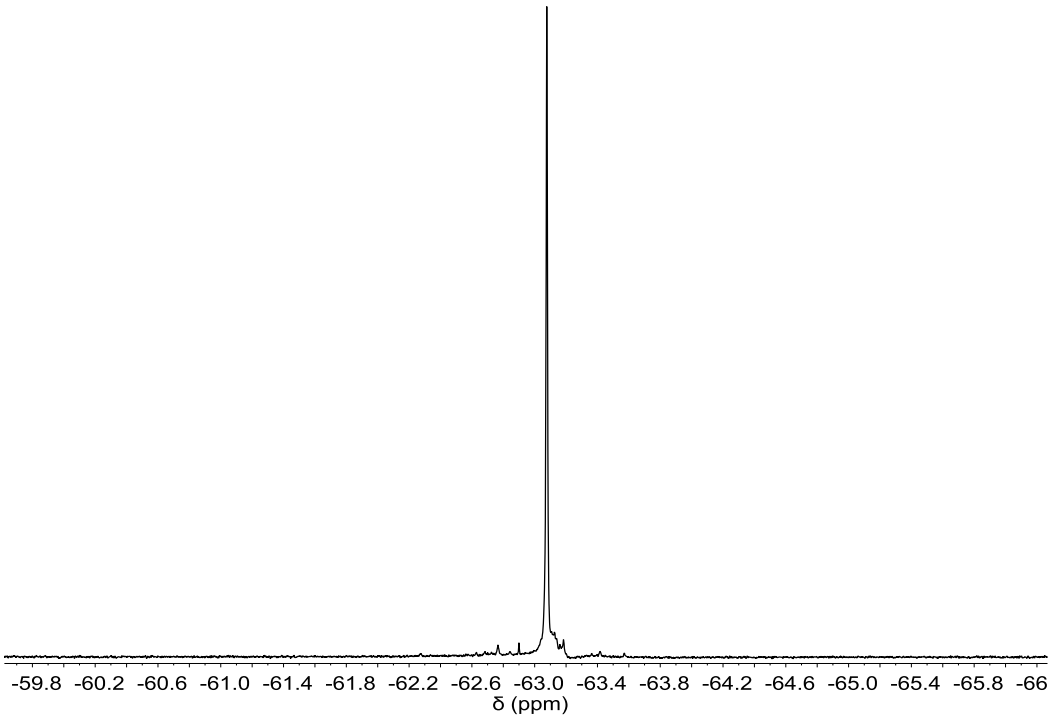


Figure A18. $^{19}F\{^{1}H\}$ NMR spectrum (400 MHz, 23 °C) of **1.8** in d_6-benzene.

2.1.3. FTIR spectra

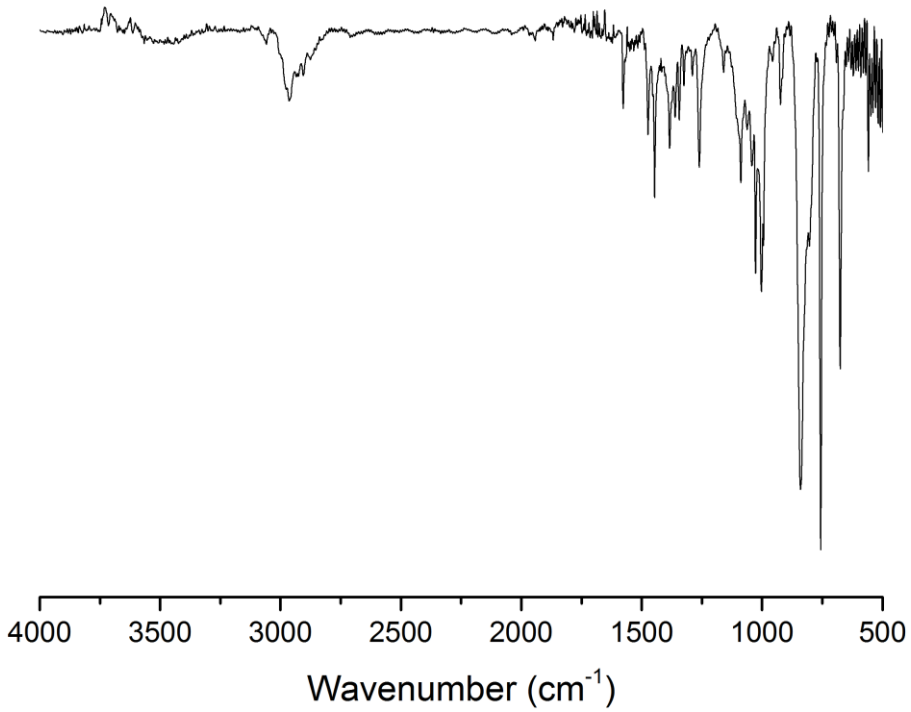


Figure A19. FTIR spectrum of **1.1**.

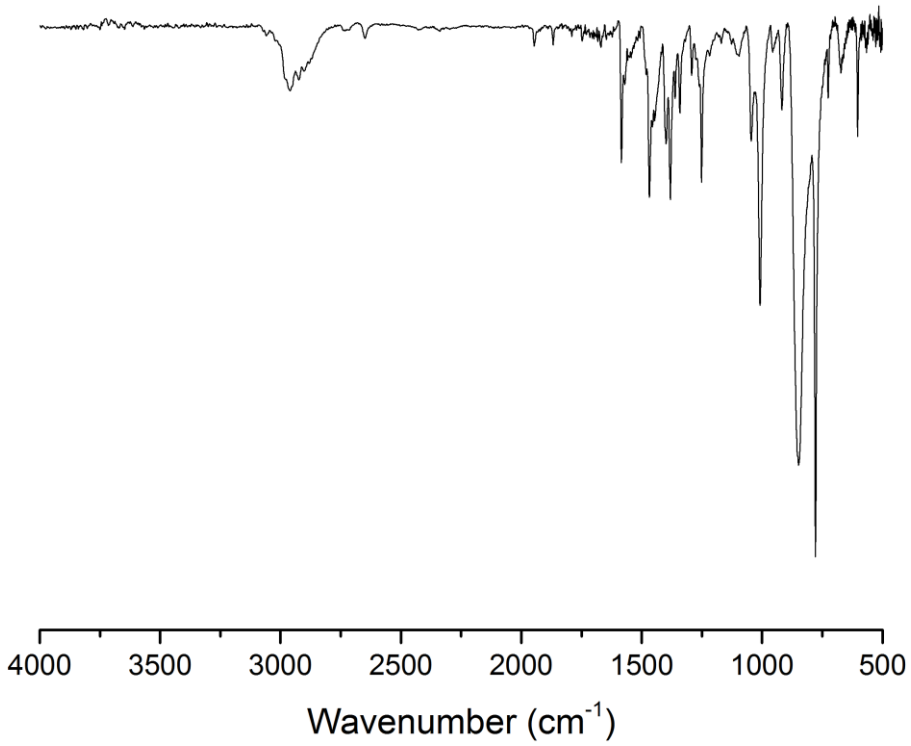


Figure A20. FTIR spectrum of **1.2**.

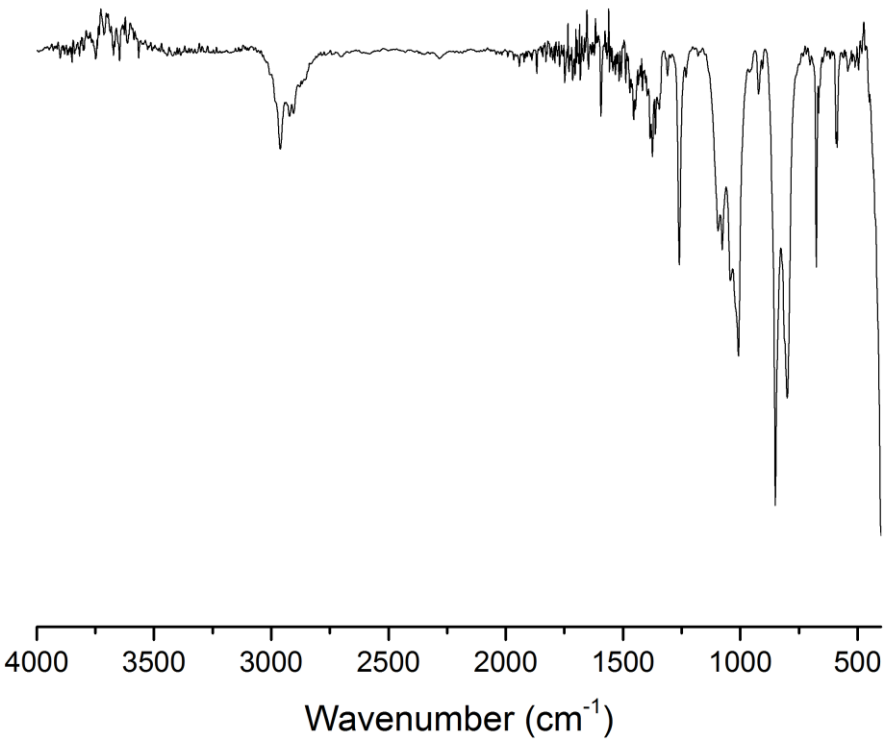


Figure A21. FTIR spectrum of **1.3**.

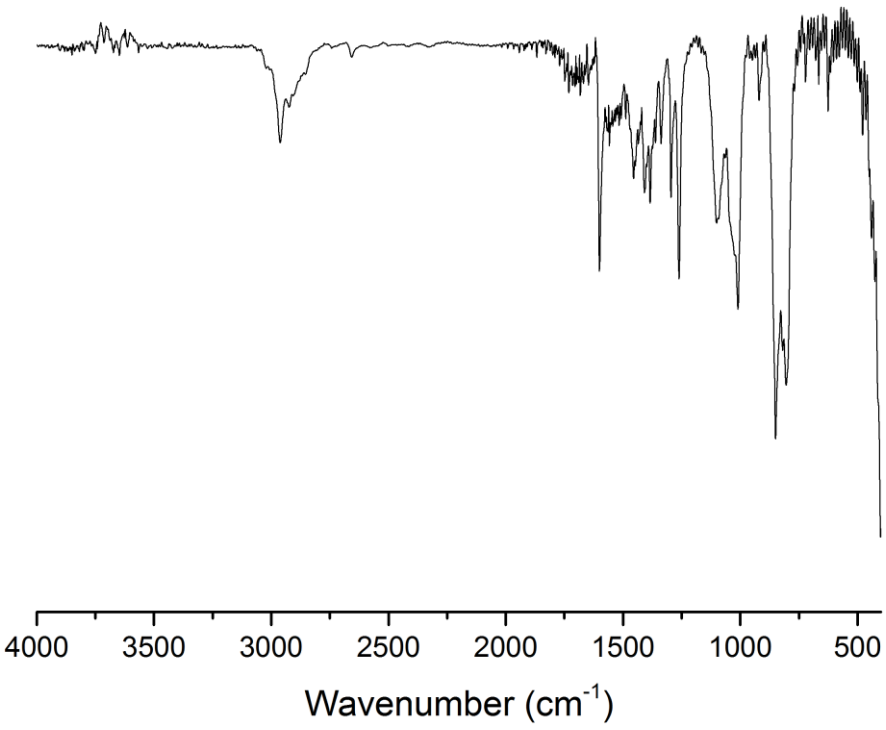


Figure A22. FTIR spectrum of **1.4**.

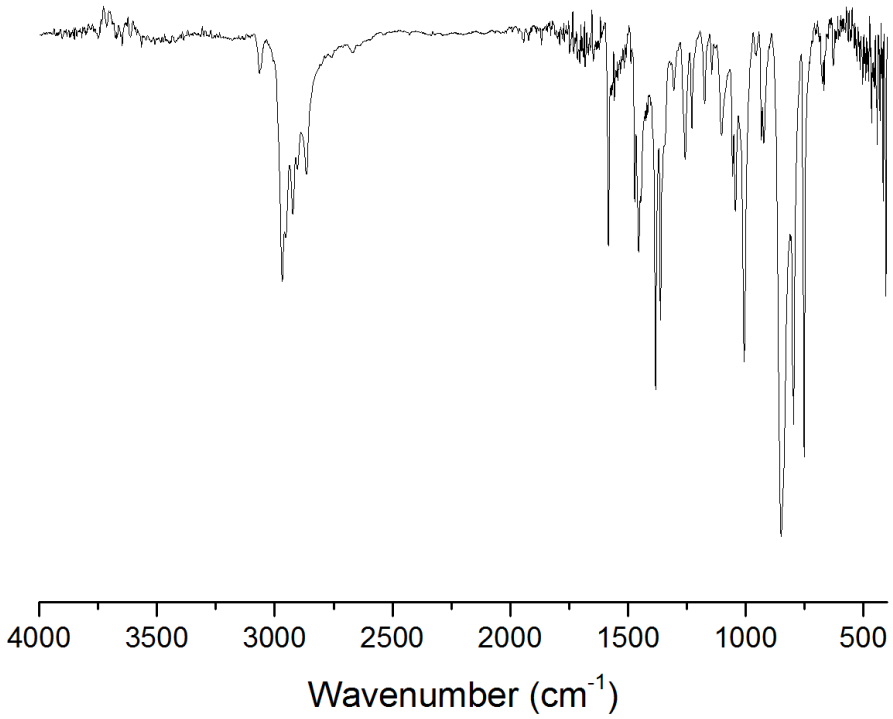


Figure A23. FTIR spectrum of **1.5**.

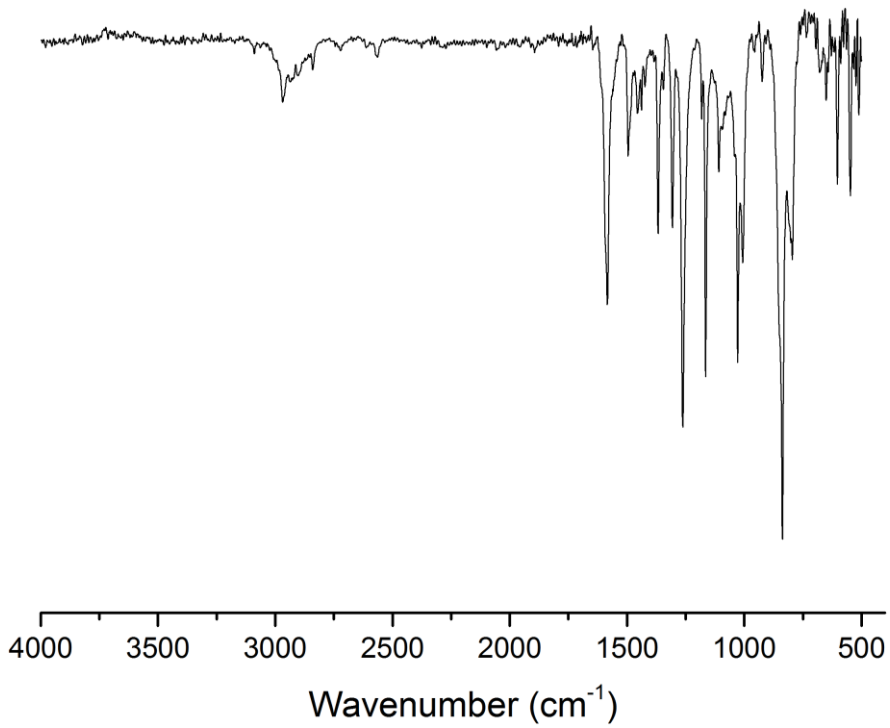


Figure A24. FTIR spectrum of **1.6**.

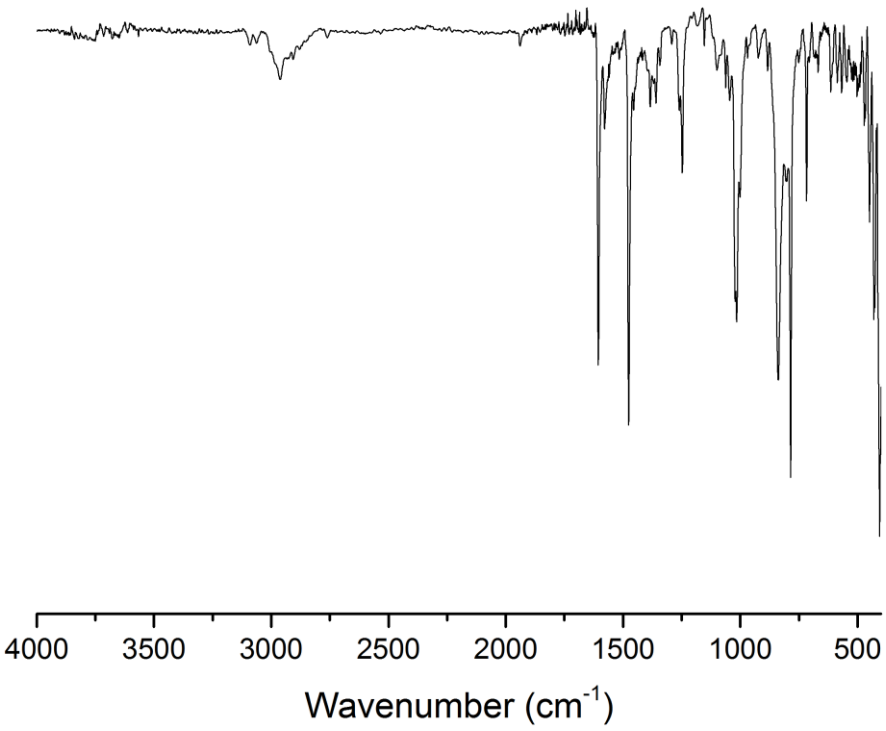


Figure A25. FTIR spectrum of **1.7**.

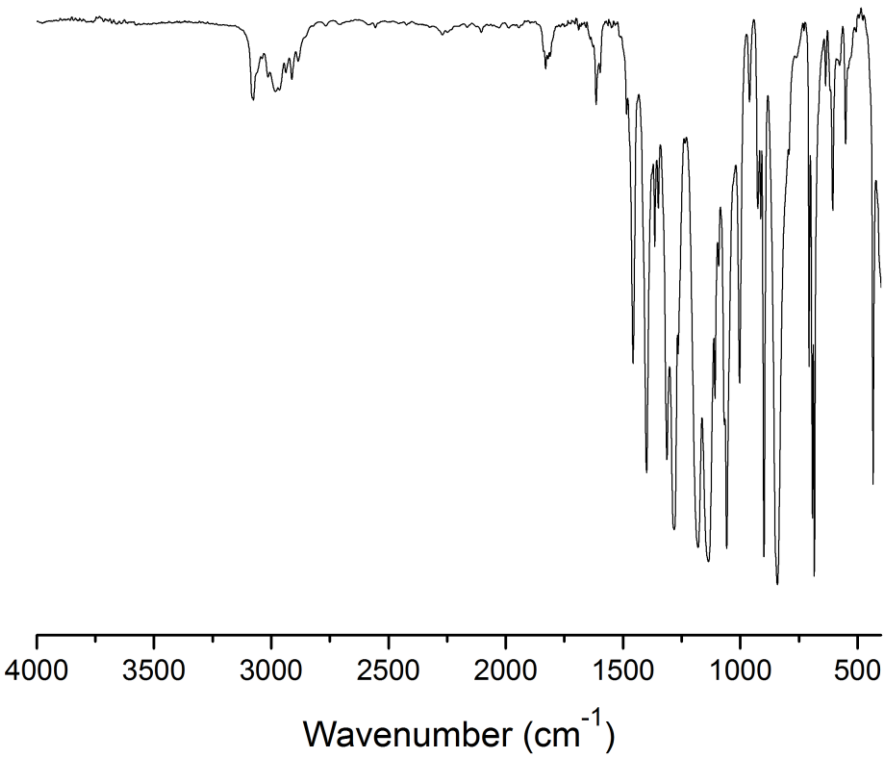


Figure A26. FTIR spectrum of **1.8**.

2.1.4. Solid angle calculations and spacefilled models

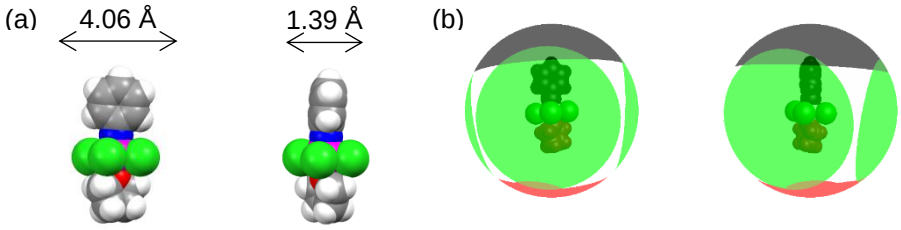


Figure A27. (a) Spacefilled molecular structure of W(NPh)Cl_4(THF) (**1.1**) showing the imido group from the front (left) and side on (right). (b) Solid-G calculations showing the steric protection afforded to the metal centre by the imido group (black), chlorides (green) and THF (red) from the front of the imido group (left) and side on (right).

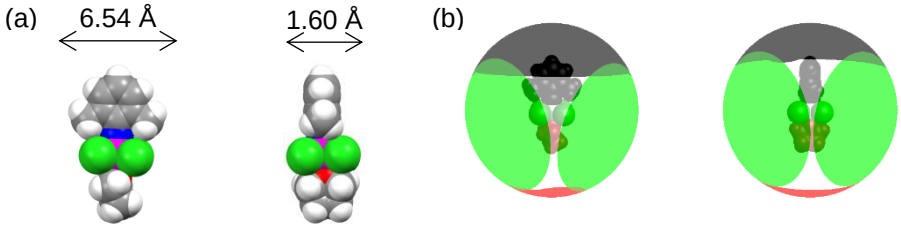


Figure A28. (a) Spacefilled molecular structure of W{N(2,6-Me-C_6H_3)}Cl_4(THF) (**1.2**) showing the imido group from the front (left) and side on (right). (b) Solid-G calculations showing the steric protection afforded to the metal centre by the imido group (black), chlorides (green) and THF (red) from the front of the imido group (left) and side on (right).

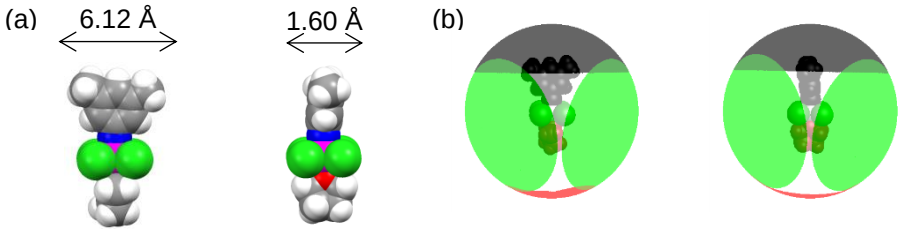


Figure A29. (a) Spacefilled molecular structure of W{N(3,5-Me-C_6H_3)}Cl_4(THF) (**1.3**) showing the imido group from the front (left) and side on (right). (b) Solid-G calculations showing the steric protection afforded to the metal centre by the imido group (black), chlorides (green) and THF (red) from the front of the imido group (left) and side on (right).

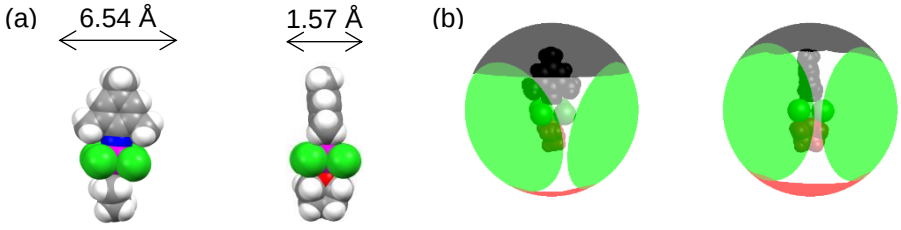


Figure A30. (a) Spacefilled molecular structure of W{N(2,4,6-Me-C_6H_2)}Cl_4(THF) (**1.4**) showing the imido group from the front (left) and side on (right). (b) Solid-G calculations showing the steric protection afforded to the metal centre by the imido group (black), chlorides (green) and THF (red) from the front of the imido group (left) and side on (right).

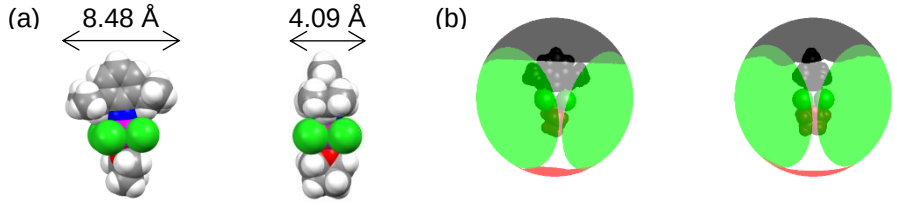


Figure A31. Spacefilled molecular structure of W{N(2,6-^{i}Pr-C_6H_3)}Cl_4(THF) (**1.5**) showing the imido group from the front (left) and side on (right). (b) Solid-G calculations showing the steric protection afforded to the metal centre by the 2,6-^{i}Pr imido group (black), chlorides (green) and THF (red) from the front of the imido group (left) and side on (right).

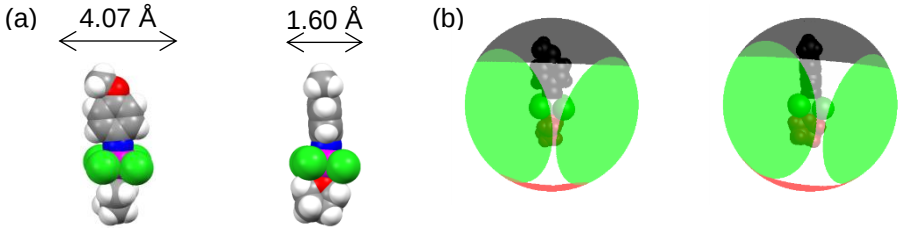


Figure A32. (a) Spacefilled molecular structure of W{N(4-OMe-C_6H_4)}Cl_4(THF) (**1.6**) showing the imido group from the front (left) and side on (right). (b) Solid-G calculations showing the steric protection afforded to the metal centre by the imido group (black), chlorides (green) and THF (red) from the front of the imido group (left) and side on (right).

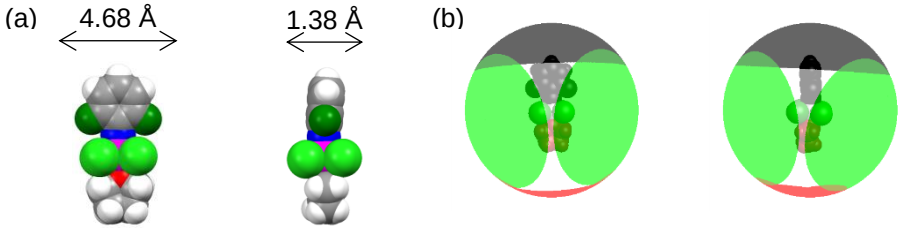


Figure A33. (a) Spacefilled molecular structure of W{N(2,6-F-C_6H_3)}Cl_4(THF) (**1.7**) showing the imido group from the front (left) and side on (right). (b) Solid-G calculations showing the steric protection afforded to the metal centre by the imido group (black), chlorides (green) and THF (red) from the front of the imido group (left) and side on (right).

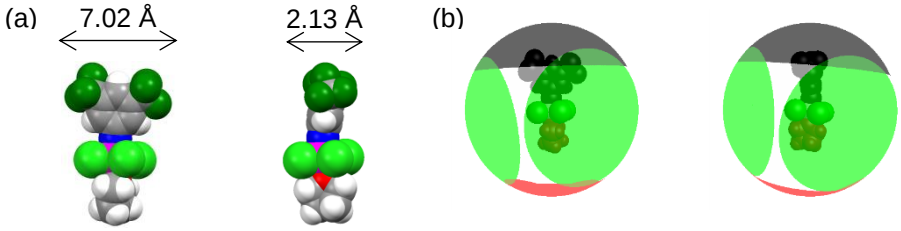


Figure A34. (a) Spacefilled molecular structure of W{N(3,5-CF_3-C_6H_3)}Cl_4(THF) (**1.8**) showing the imido group from the front (left) and side on (right). (b) Solid-G calculations showing the steric protection afforded to the metal centre by the imido group (black), chlorides (green) and THF (red) from the front of the imido group (left) and side on (right).

2.2. $W(NR)Me_3Cl$ complexes (2.1-2.8)

2.2.1. Single crystal X-ray diffraction data tables

Crystal data		
Compound **CCDC number** **Chemical formula**	$W(NPh)Me_3Cl$ (**2.1**) 1518777 $C_9H_{14}ClNW$	$W\{N(2,6\text{-}Me\text{-}C_6H_3)\}Me_3Cl$ (**2.2**) 1518776 $C_{11}H_{18}ClNW$
Mr	355.51	383.56
Crystal system, space group	Monoclinic, $P2_1/m$	Monoclinic, $P2_1/c$
Temperature (K)	150	150
***a, b, c* (Å)**	6.3636(2), 7.2907(2), 11.9698(3)	10.4810(2), 10.8951(3), 12.1474(3)
α, β, γ (°)	90, 93.495(2), 90	90, 110.473(1), 90
***V* (Å^3)**	554.31(3)	1299.51(5)
Z	2	4
μ (mm^{-1})	10.61	9.06
Crystal size (mm)	0.20 × 0.15 × 0.10	0.10 × 0.07 × 0.05
Data collection		
Diffractometer	Nonius KappaCCD diffractometer	Nonius KappaCCD diffractometer
Absorption correction	Multi-scan Multi-scan from symmetry-related measurements using *SORTAV* (Blessing 1995)	Multi-scan Multi-scan from symmetry-related measurements using *SORTAV* (Blessing 1995)
T_{min}, T_{max}	0.695, 1.000	0.708, 1.000
No. of measured, independent and observed [*I* > 2*s*(*I*)] reflections	2527, 1367, 1208	5749, 2964, 2473
R_{int}	0.045	0.027
$(\sin\theta/\lambda)_{max}$ (Å^{-1})	0.650	0.650
Refinement		
$R[F^2 > 2s(F^2)]$, $wR(F^2)$, S	0.038, 0.094, 1.03	0.032, 0.079, 1.06
No. of reflections	1367	2964
No. of parameters	77	132
No. of restraints	0	0
H-atom treatment	Constrained	Constrained
$(\Delta/\sigma)_{max}$	<0.001	0.001
$\Delta\rho_{max}$, $\Delta\rho_{min}$ (e Å^{-3})	1.90, −2.13	2.28, −1.69
Absolute structure	-	-
Absolute structure parameter	-	-
Computer programs: Collect (Nonius BV, 1997-2000), *HKL SCALEPACK* (Otwinowski & Minor 1997), *HKL DENZO* and *SCALEPACK* (Otwinowski & Minor 1997), Palatinus, L.; Chapuis, G. J. Appl. Cryst. 2007, 40, 786-790., *SHELXL2014* (Sheldrick, 2014), *ORTEP-3 for Windows* (Farrugia, 1997), *WinGX* publication routines (Farrugia, 1999).		

Crystal data		
Compound **CCDC number** **Chemical formula**	W{N(3,5-Me-C_6H_3)}Me_3Cl (**2.3**) 1543007 $C_{11}H_{18}ClNW$	W{N(2,6-^{i}Pr-C_6H_3)}Me_3Cl (**2.5**) 1434396 $C_{15}H_{26}ClNW$
Mr	383.56	439.67
Crystal system, space group	Orthorhombic, *Pnma*	Orthorhombic, *Pna*2_1
Temperature (K)	150	150
***a, b, c* (Å)**	21.1055(3), 7.2526(1), 17.4808(3)	13.1669(1), 12.7572(1), 20.0394(2)
α, β, γ (°)	90	90
***V* (Å^3)**	2675.78(7)	3366.07(5)
Z	8	8
μ (mm^{-1})	17.55	7.01
Crystal size (mm)	0.30 × 0.23 × 0.15	0.22 × 0.20 × 0.18
Data collection		
Diffractometer	SuperNova, Dual, Cu at zero, Atlas	Nonius KappaCCD diffractometer
Absorption correction	Multi-scan CrysAlis PRO 1.171.38.41 (Rigaku Oxford Diffraction, 2015) Empirical absorption correction using spherical harmonics, implemented in SCALE3 ABSPACK scaling algorithm.	Multi-scan *DENZO/SCALEPACK* (Otwinowski & Minor, 1997)
T_{min}, T_{max}	0.106, 1.000	0.75, 1.00
No. of measured, independent and observed [*I* > 2*s*(*I*)] reflections	8777, 2949, 2795	64889, 7358, 6627
R_{int}	0.054	-
(sin θ/λ)$_{max}$ (Å^{-1})	0.625	0.650
Refinement		
$R[F^2 > 2s(F^2)]$, $wR(F^2)$, S	0.043, 0.122, 1.10	0.030, 0.073, 0.96
No. of reflections	2949	7358
No. of parameters	158	340
No. of restraints	0	1
H-atom treatment	H-atom parameters constrained	H-atom parameters constrained
(Δ/σ)$_{max}$	0.001	0.001
Δρ_{max}, Δρ_{min} (e Å^{-3})	2.52, −1.75	1.93, -1.79
Absolute structure	-	Refined as an inversion twin.
Absolute structure parameter	-	0.495 (16)
Computer programs: Collect (Nonius BV, 1997-2000), *HKL SCALEPACK* (Otwinowski & Minor 1997), *HKL DENZO* and *SCALEPACK* (Otwinowski & Minor 1997), Palatinus, L.; Chapuis, G. J. Appl. Cryst. 2007, 40, 786-790., *SHELXL2014* (Sheldrick, 2014), *CrysAlis PRO* (Agilent (2014). Agilent Technologies Ltd, Yarnton, Oxfordshire, England.), *ORTEP-3 for Windows* (Farrugia, 1997), *WinGX* publication routines (Farrugia, 1999).		

Crystal data		
Compound **CCDC number** **Chemical formula**	W{N(4-OMe-C_6H_4)}Me_3Cl (**2.6**) 1518779 $C_{10}H_{16}ClNOW$	W{N(2,6-F-C_6H_3)}Me_3Cl (**2.7**) 1518778 $C_9H_{12}ClF_2NW$
Mr	385.54	391.50
Crystal system, space group	Monoclinic, $P2_1$	Triclinic, $P\bar{1}$
Temperature (K)	150	150
***a, b, c* (Å)**	6.0476(3), 7.3129(3), 14.2223(6)	7.3092(1), 7.5096(1), 11.8873(2)
α, β, γ (°)	90, 97.885(4), 90	90.124(1), 95.770(1), 118.542(1)
***V* (Å^3)**	623.04(5)	569.34(2)
Z	2	2
μ (mm^{-1})	18.92	10.37
Crystal size (mm)	0.06 × 0.05 × 0.04	0.15 × 0.12 × 0.10
Data collection		
Diffractometer	SuperNova, Dual, Cu at zero, Atlas diffractometer	Nonius KappaCCD diffractometer
Absorption correction	Multi-scan *CrysAlis PRO*, Agilent Technologies, Version 1.171.37.35 (release 13-08-2014 CrysAlis171 .NET) (compiled Aug 13 2014,18:06:01) Empirical absorption correction using spherical harmonics, implemented in SCALE3 ABSPACK scaling algorithm.	Multi-scan Multi-scan from symmetry-related measurements using *SORTAV* (Blessing 1995)
T_{min}, T_{max}	0.736, 1.000	0.728, 1.000
No. of measured, independent and observed [*I* > 2*s*(*I*)] reflections	3247, 3247, 3164	4939, 2615, 2426
R_{int}	-	0.036
$(\sin\theta/\lambda)_{max}$ (Å^{-1})	0.629	0.651
Refinement		
$R[F^2 > 2s(F^2)]$, $wR(F^2)$, S	0.039, 0.108, 1.10	0.031, 0.080, 1.04
No. of reflections	3247	2615
No. of parameters	119	130
No. of restraints	5	0
H-atom treatment	Constrained	Constrained
$(\Delta/\sigma)_{max}$	0.001	<0.001
$\Delta\rho_{max}$, $\Delta\rho_{min}$ (e Å^{-3})	1.39, −1.65	2.13, −3.00
Absolute structure	Classical Flack method preferred over Parsons because s.u. lower.	-
Absolute structure parameter	0.56(3)	-
Computer programs: Collect (Nonius BV, 1997-2000), *HKL SCALEPACK* (Otwinowski & Minor 1997), *HKL DENZO* and *SCALEPACK* (Otwinowski & Minor 1997), Palatinus, L.; Chapuis, G. J. Appl. Cryst. 2007, 40, 786-790., *SHELXL2014* (Sheldrick, 2014), *CrysAlis PRO* (Agilent (2014). Agilent Technologies Ltd, Yarnton, Oxfordshire, England.), *ORTEP-3 for Windows* (Farrugia, 1997), *WinGX* publication routines (Farrugia, 1999).		

2.2.2. NMR spectra

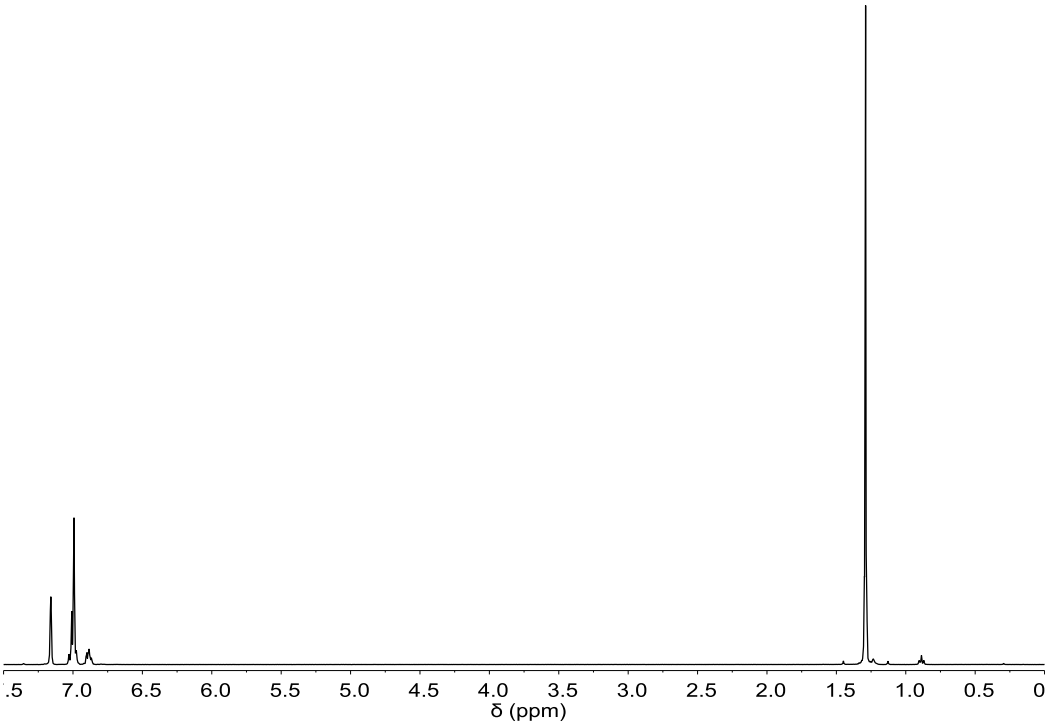


Figure A35. ^{1}H NMR spectrum (400 MHz, 23 °C) of **2.1** in d_6-benzene (7.16 ppm).

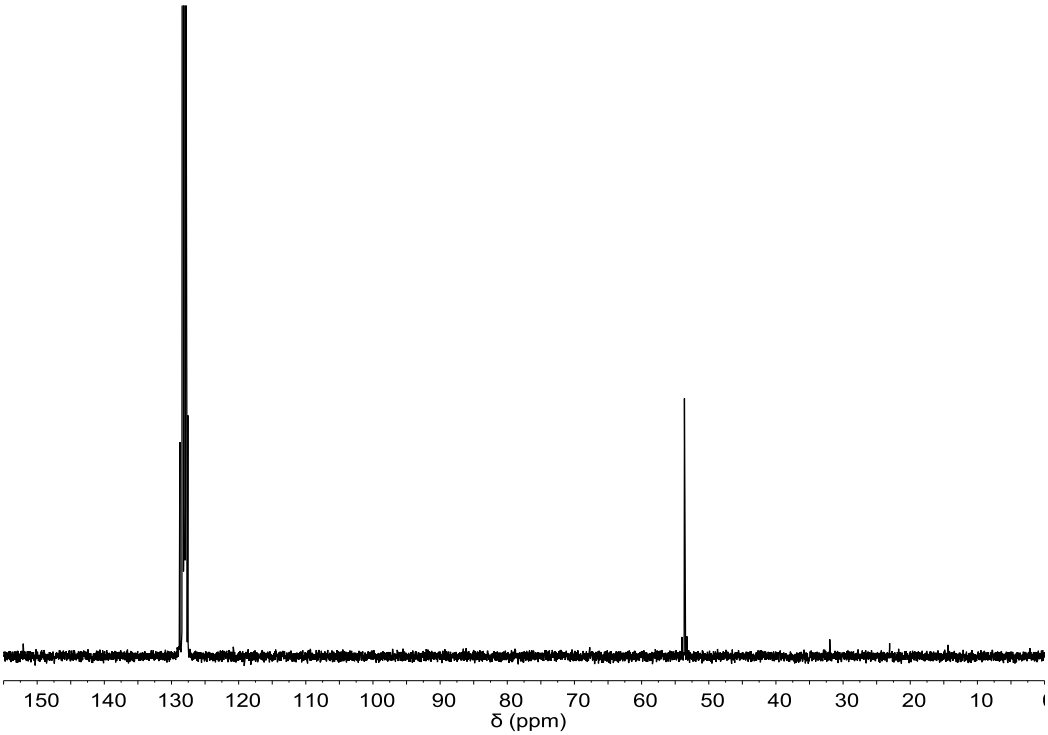


Figure A36. ^{13}C{^{1}H} NMR spectrum (400 MHz, 23 °C) of **2.1** in d_6-benzene (128.06 ppm).

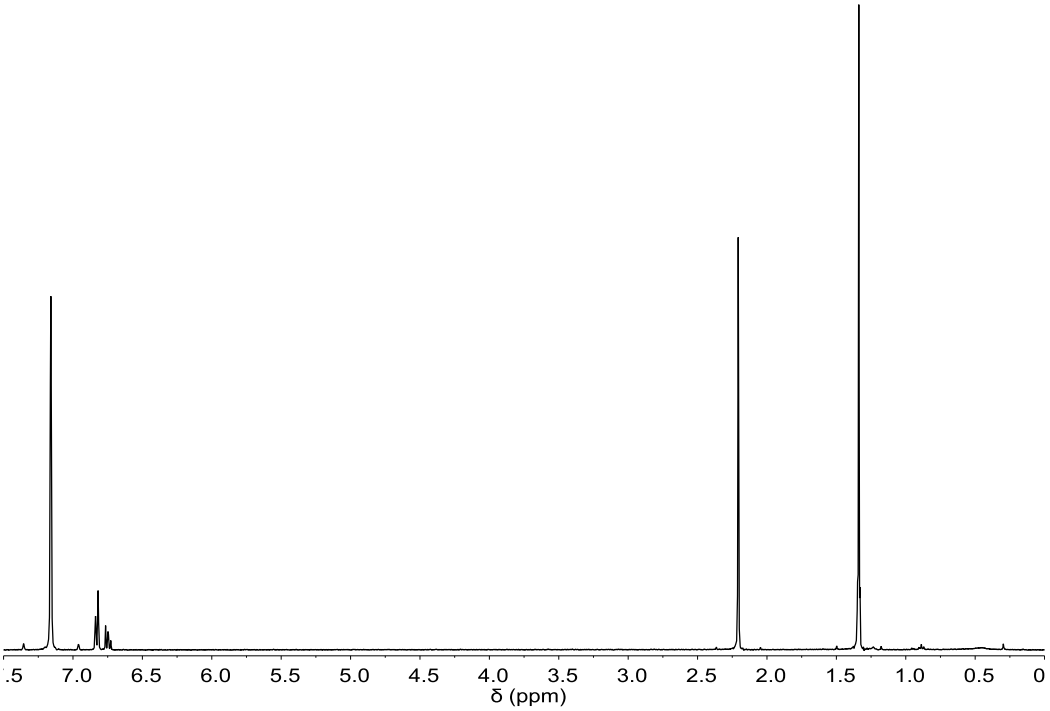


Figure A37. ^{1}H NMR spectrum (400 MHz, 23 °C) of **2.2** in d_6-benzene (7.16 ppm).

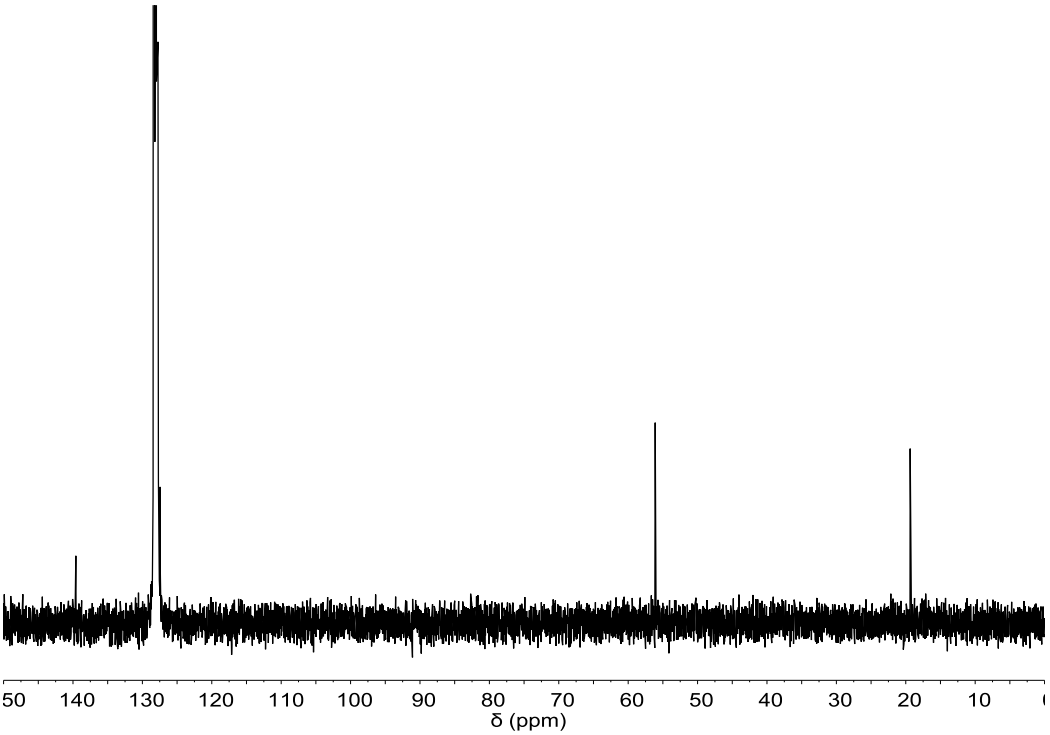


Figure A38. ^{13}C{^{1}H} NMR spectrum (400 MHz, 23 °C) of **2.2** in d_6-benzene (128.06 ppm).

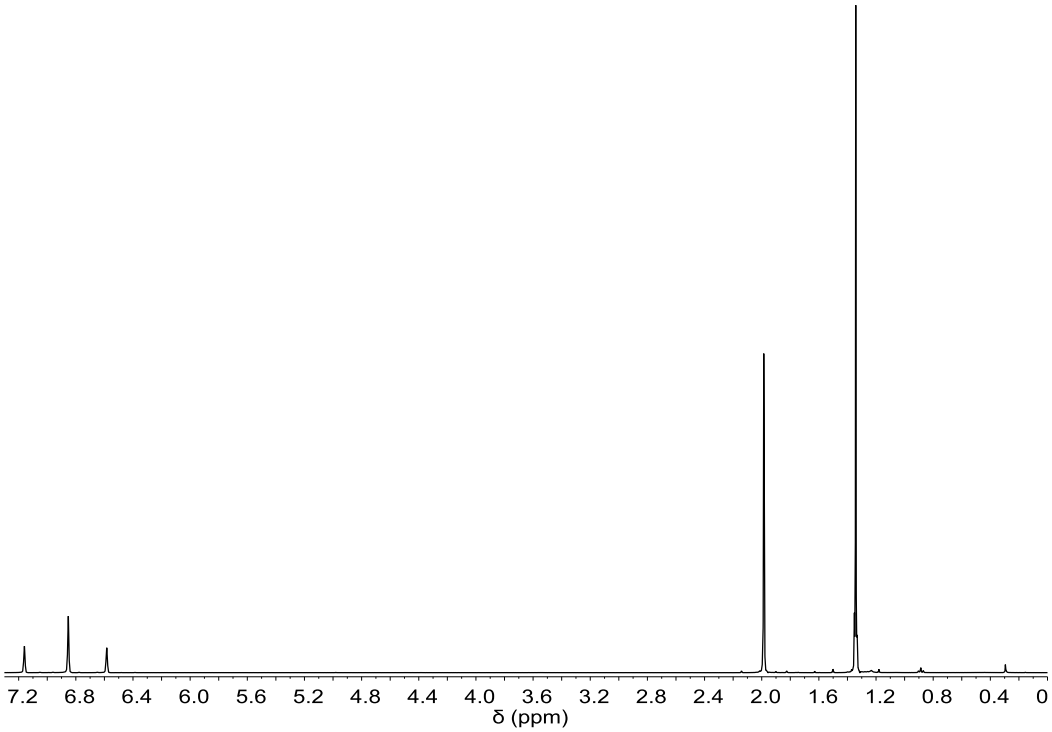


Figure A39. ^{1}H NMR spectrum (400 MHz, 23 °C) of **2.3** in d_6-benzene (7.16 ppm).

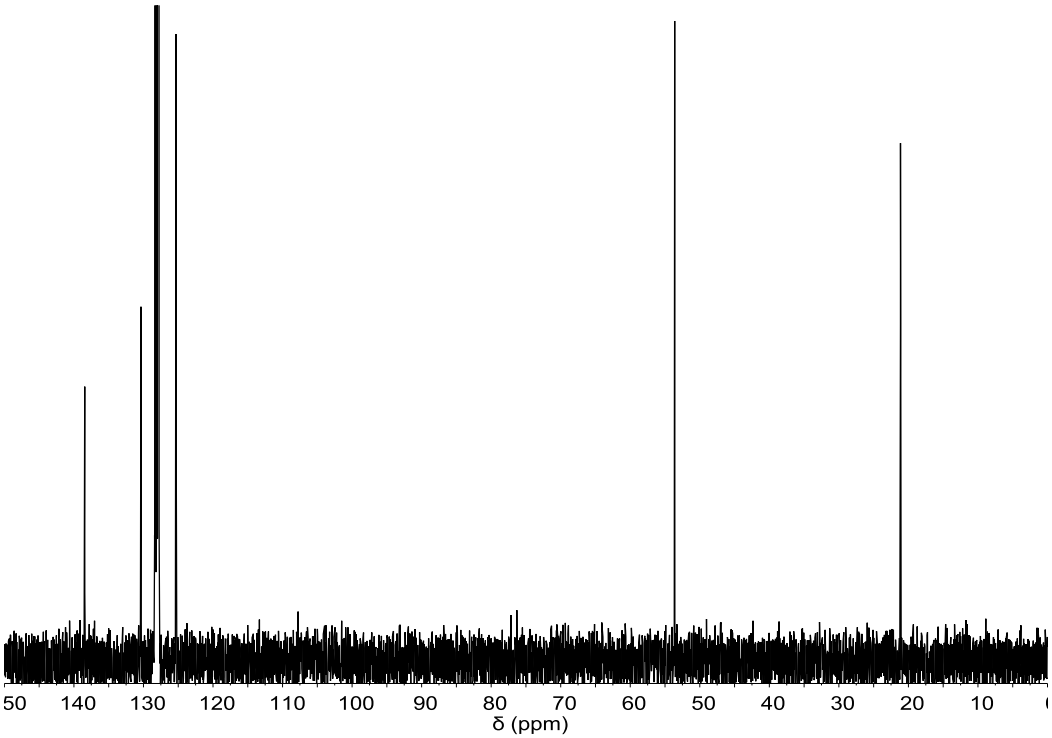


Figure A40. ^{13}C{^{1}H} NMR spectrum (400 MHz, 23 °C) of **2.3** in d_6-benzene (128.06 ppm).

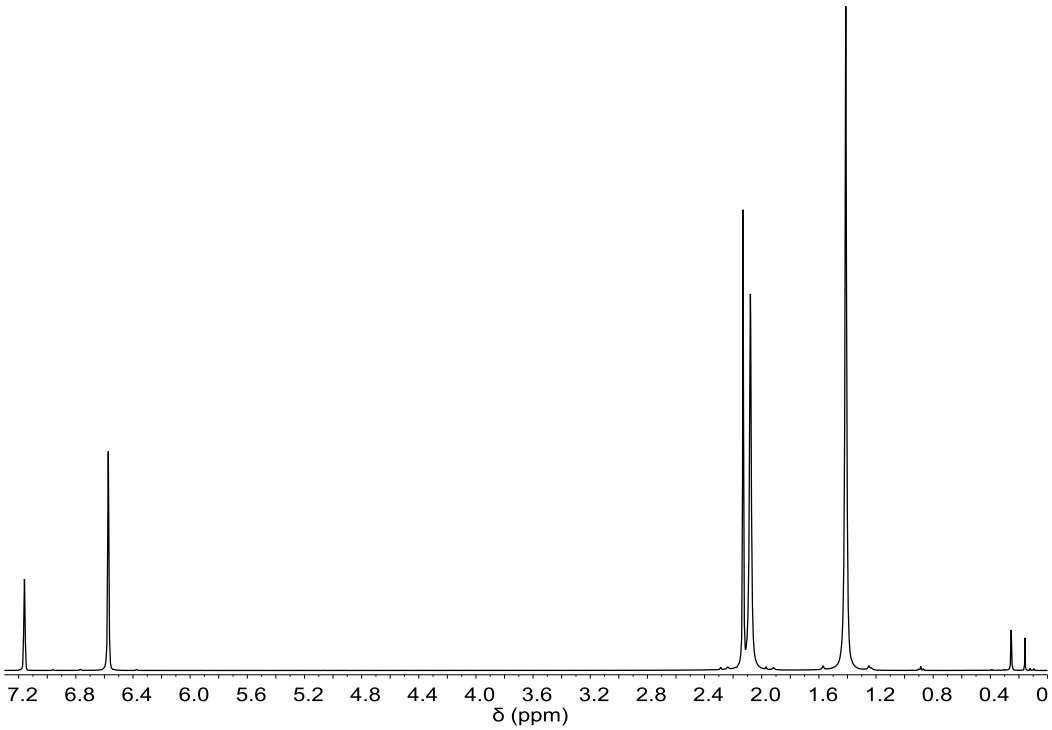


Figure A41. ^{1}H NMR spectrum (400 MHz, 23 °C) of **2.4** in d_6-benzene (7.16 ppm).

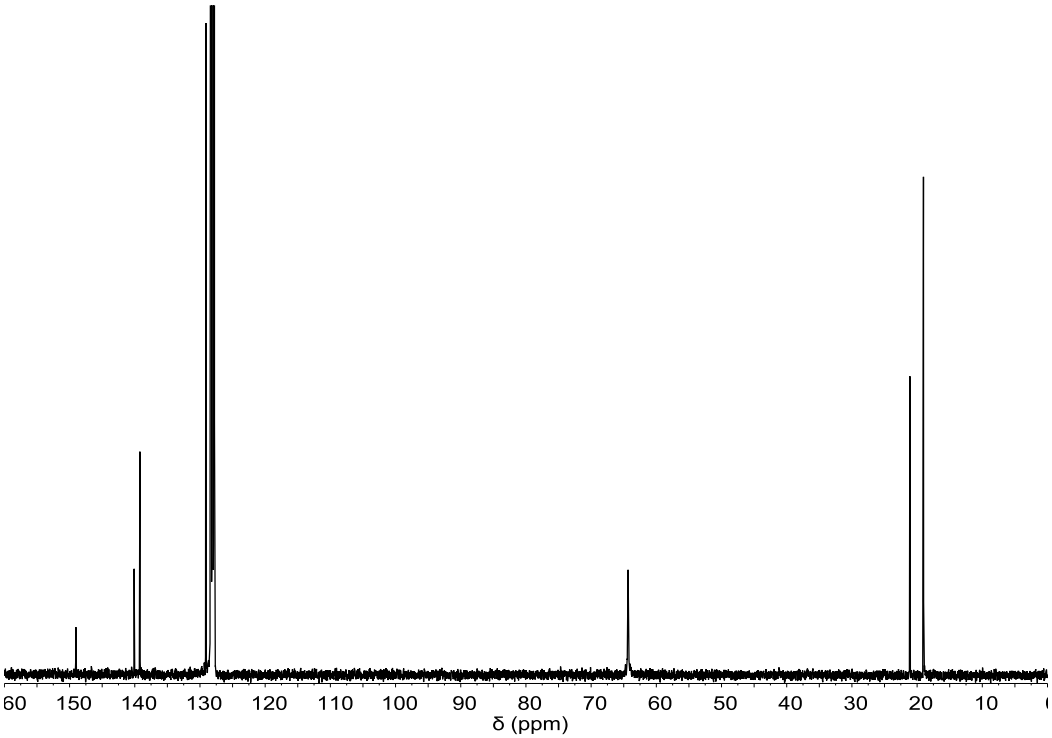


Figure A42. ^{13}C{^{1}H} NMR spectrum (400 MHz, 23 °C) of **2.4** in d_6-benzene (128.06 ppm).

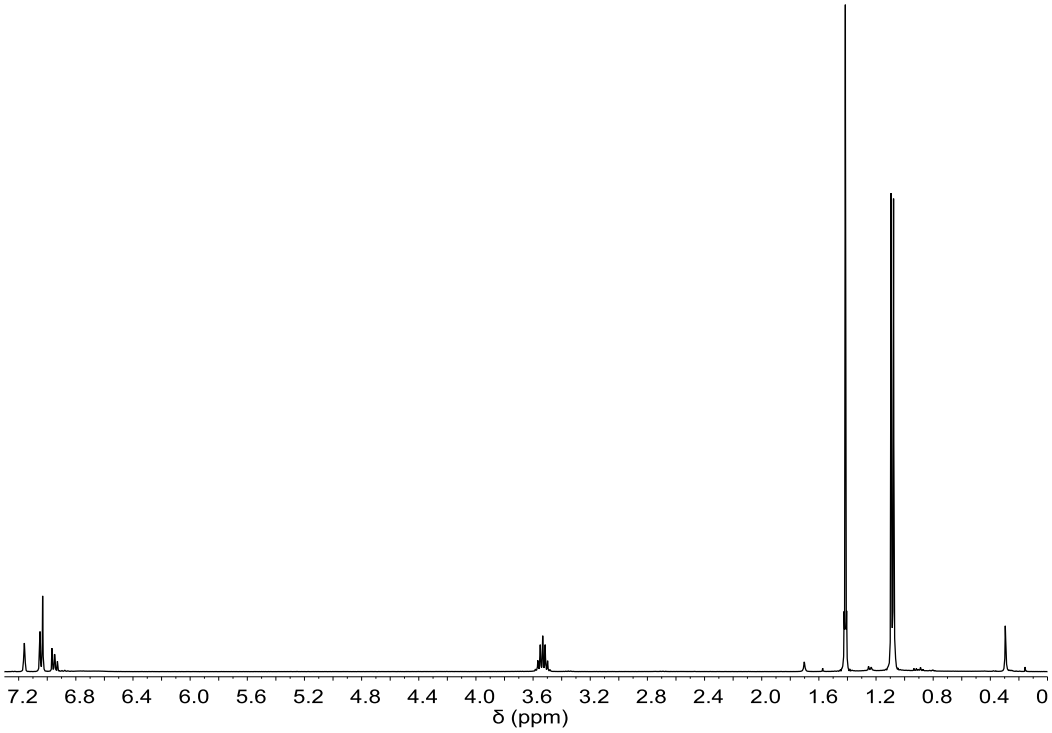


Figure A43. ^{1}H NMR spectrum (400 MHz, 23 °C) of **2.5** in d_6-benzene (7.16 ppm).

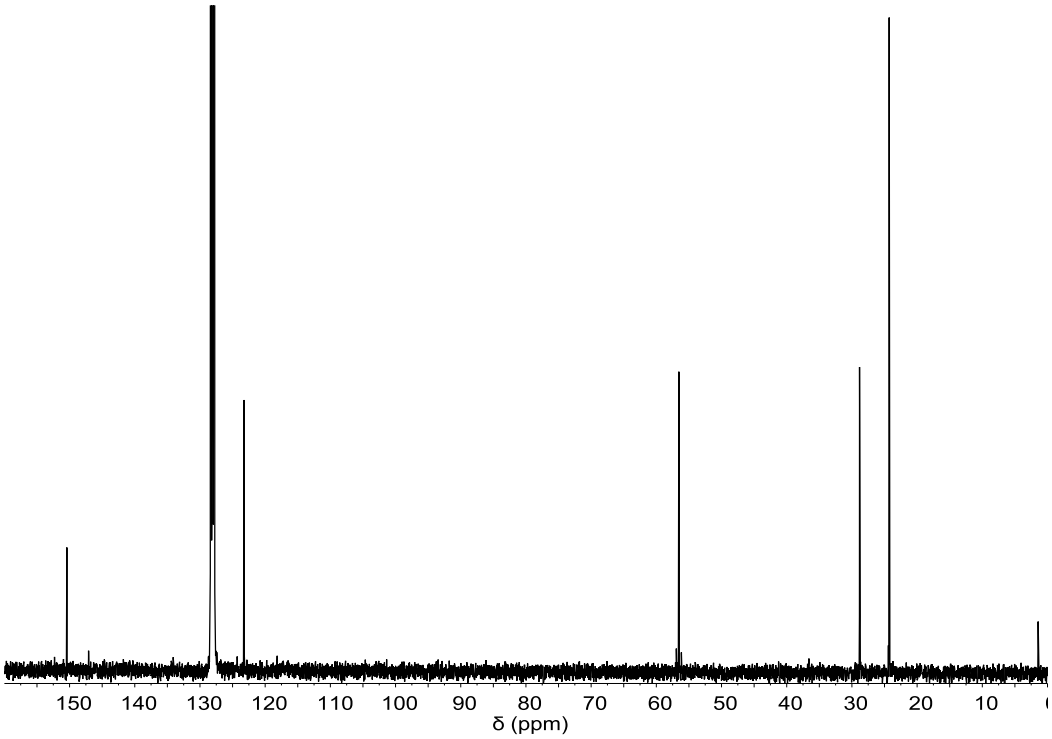


Figure A44. ^{13}C{^{1}H} NMR spectrum (400 MHz, 23 °C) of **2.5** in d_6-benzene (128.06 ppm).

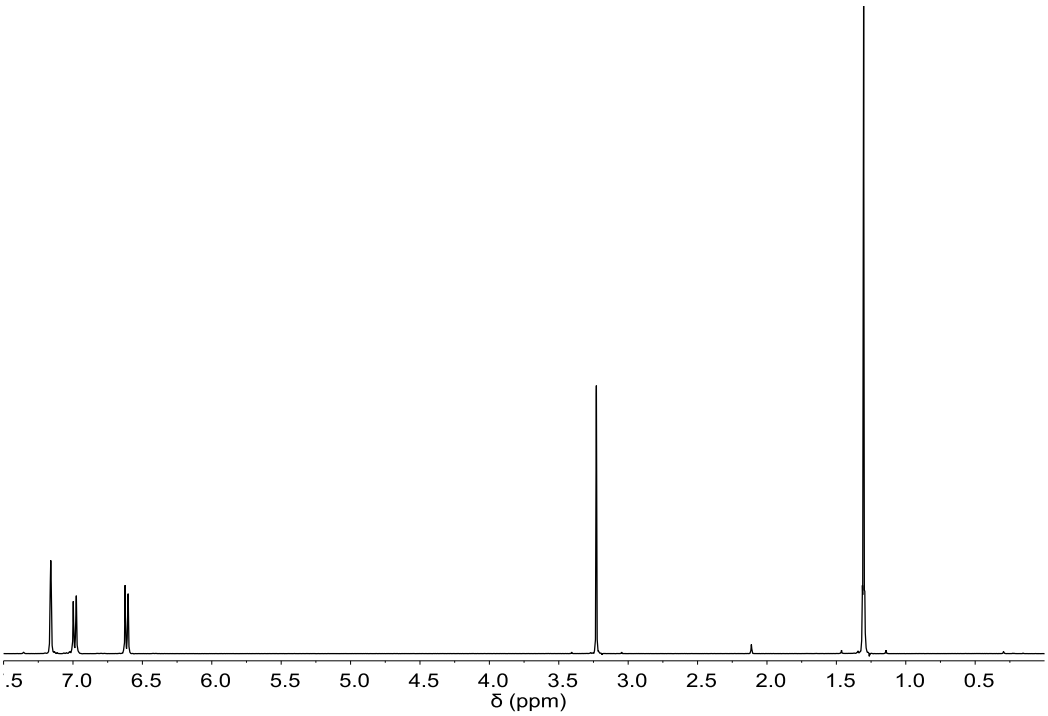


Figure A45. ^{1}H NMR spectrum (400 MHz, 23 °C) of **2.6** in d_6-benzene (7.16 ppm).

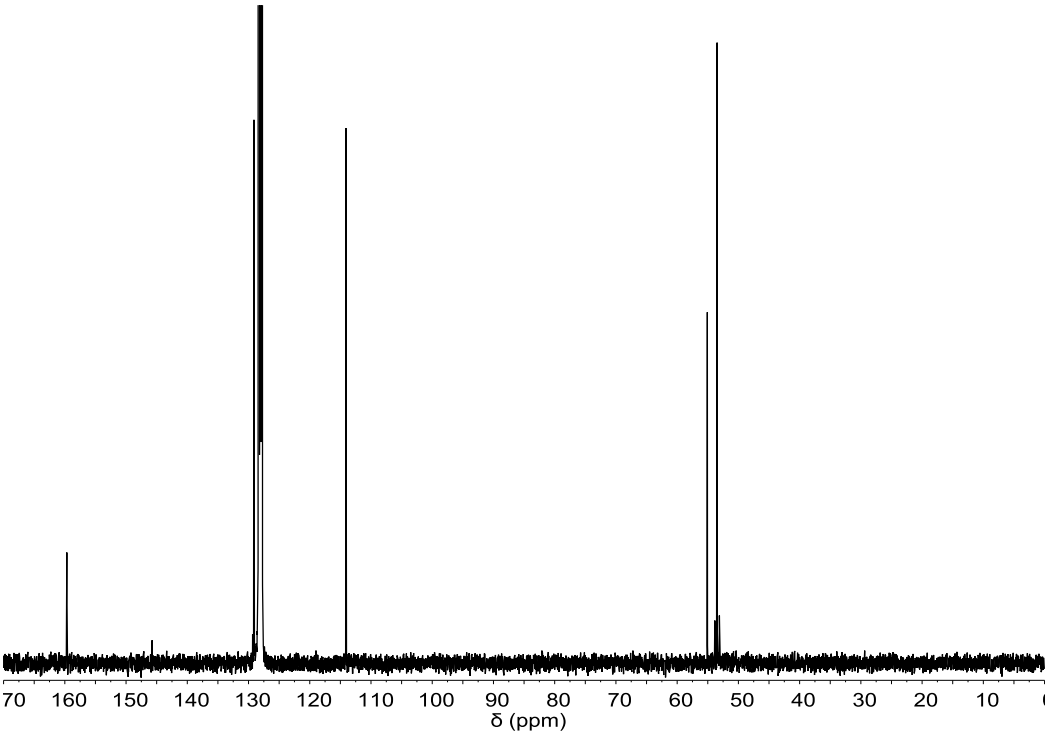


Figure A46. ^{13}C{^{1}H} NMR spectrum (400 MHz, 23 °C) of **2.6** in d_6-benzene (128.06 ppm).

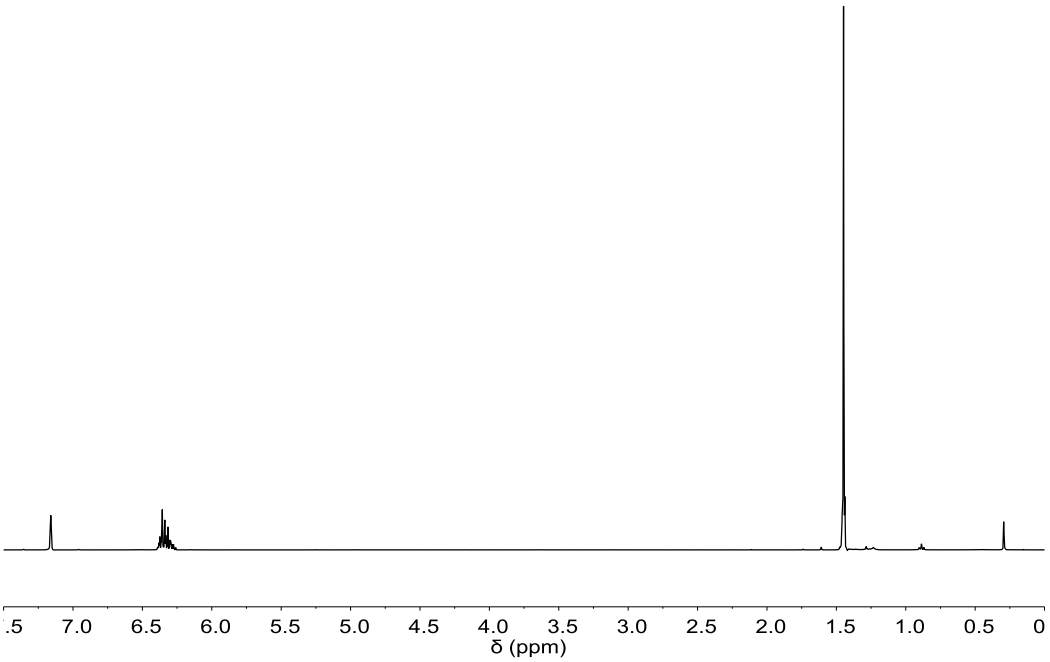


Figure A47. ^{1}H NMR spectrum (400 MHz, 23 °C) of **2.7** in d_6-benzene (7.16 ppm).

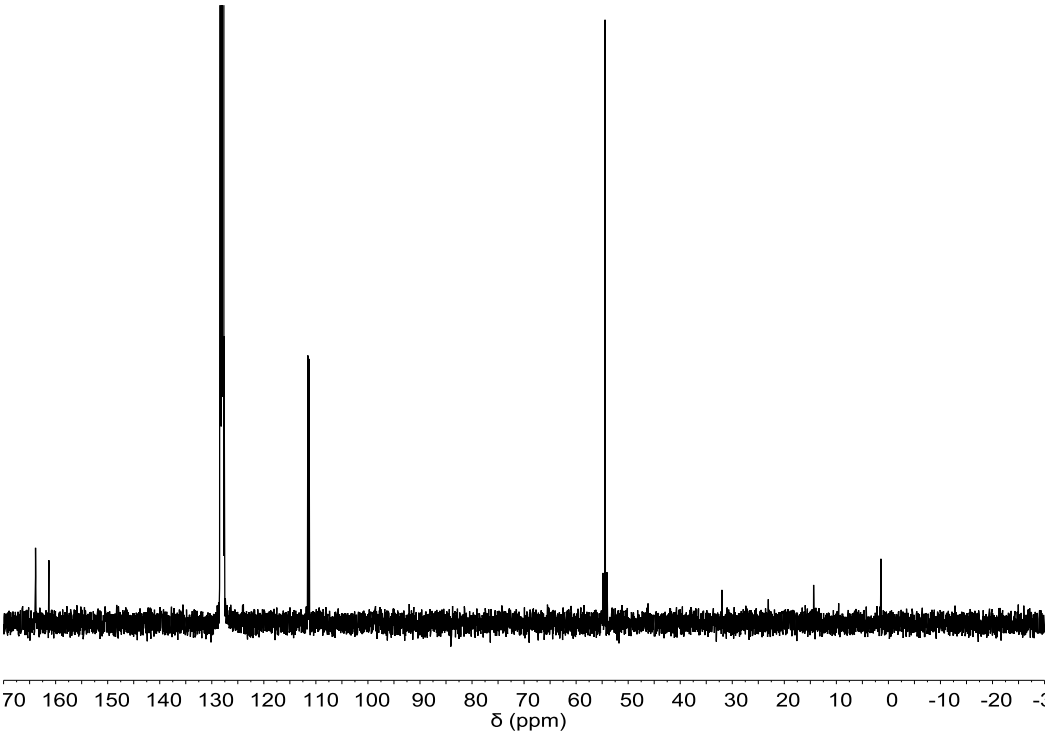


Figure A48. ^{13}C{^{1}H} NMR spectrum (400 MHz, 23 °C) of **2.7** in d_6-benzene (128.06 ppm).

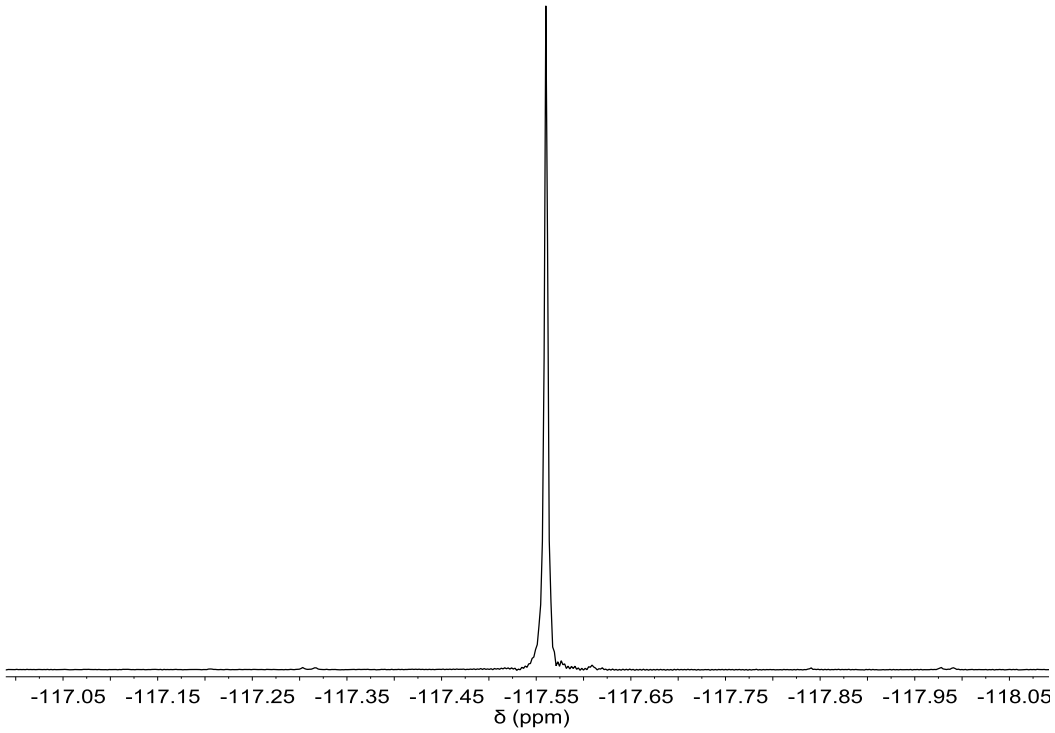


Figure A49. $^{19}F\{^{1}H\}$ NMR spectrum (400 MHz, 23 °C) of **2.7** in d_6-benzene.

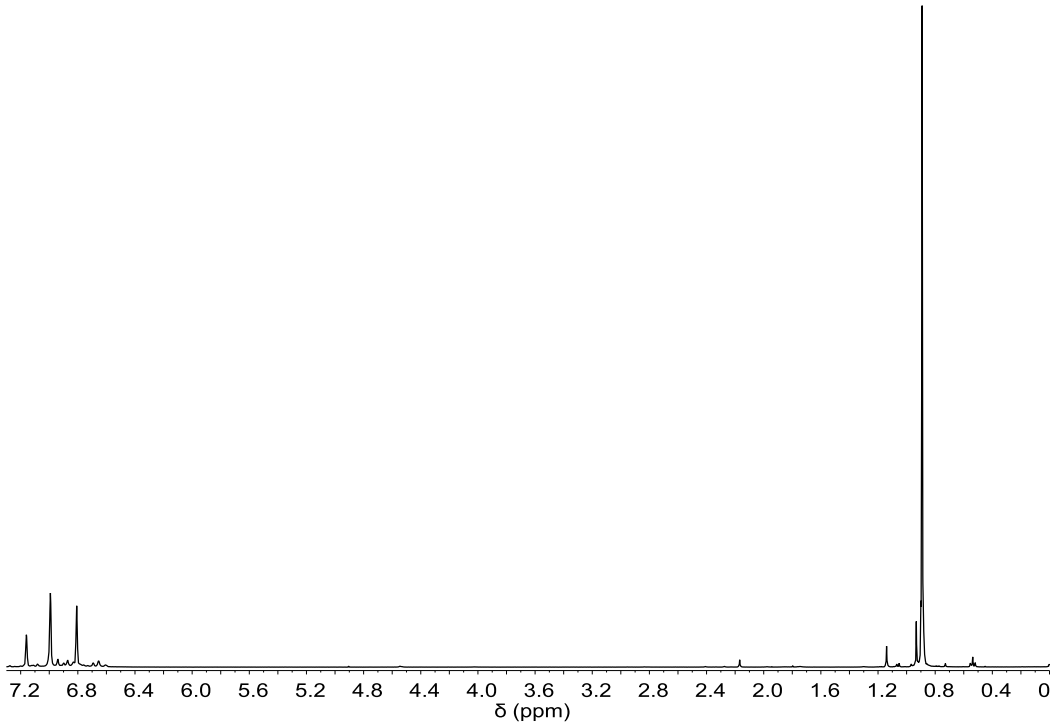


Figure A50. ^{1}H NMR spectrum (400 MHz, 23 °C) of **2.8** in d_6-benzene (7.16 ppm).

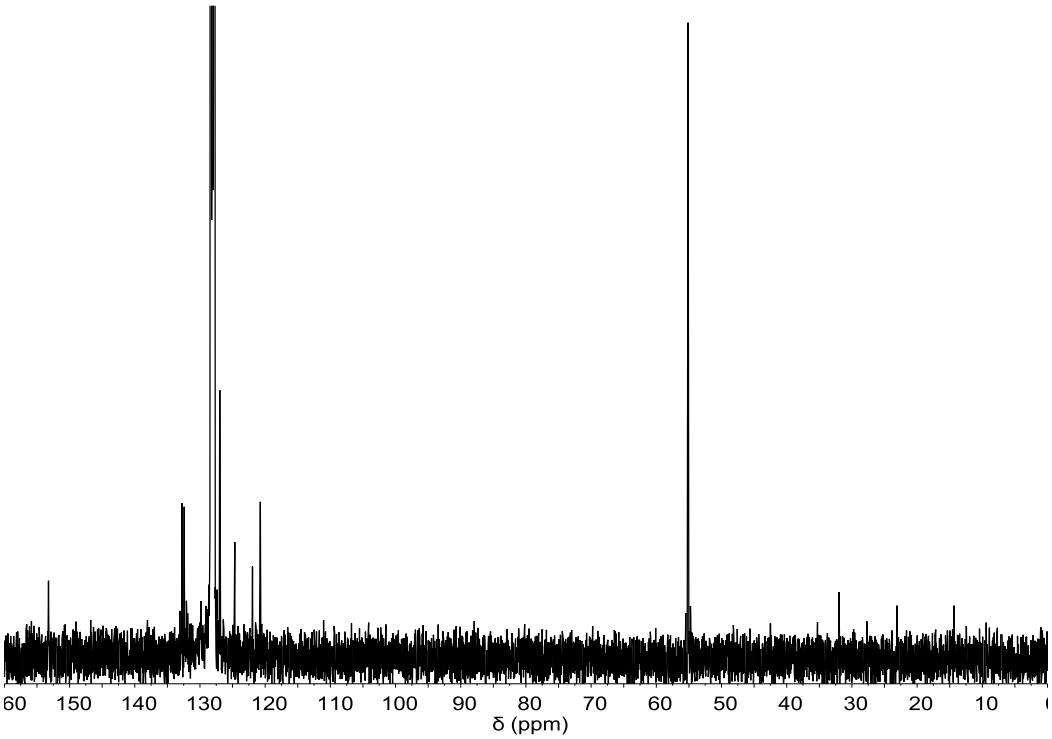


Figure A51. $^{13}C\{^{1}H\}$ NMR spectrum (400 MHz, 23 °C) of **2.8** in d_6-benzene (128.06 ppm).

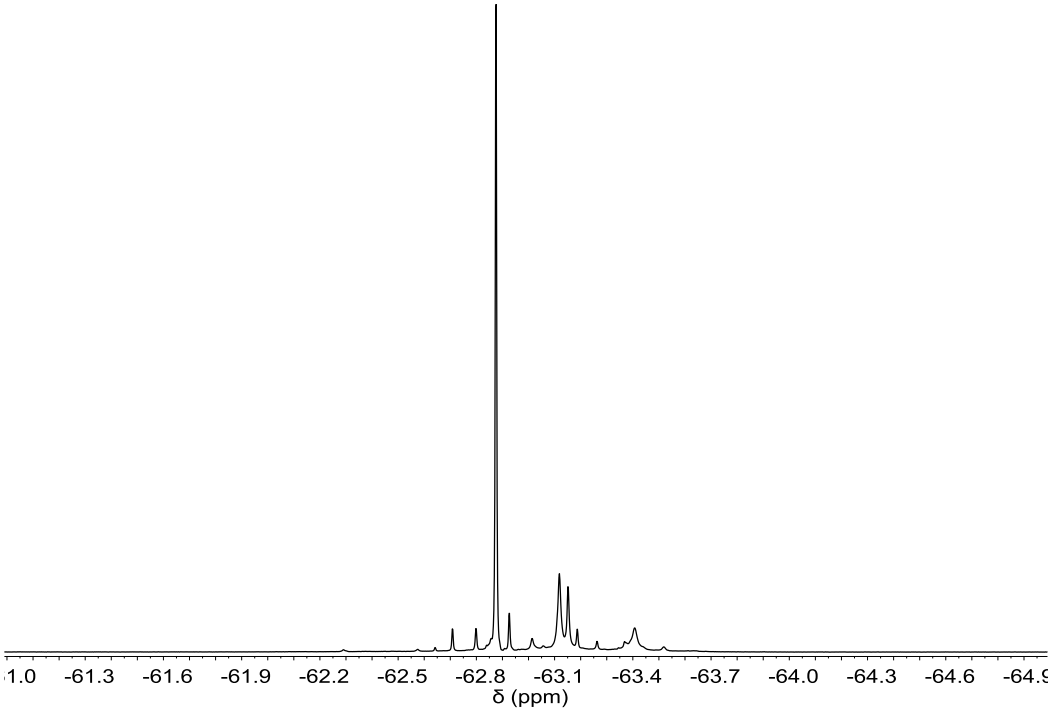


Figure A52. $^{19}F\{^{1}H\}$ NMR spectrum (400 MHz, 23 °C) of **2.8** in d_6-benzene.

2.2.3. FTIR spectra

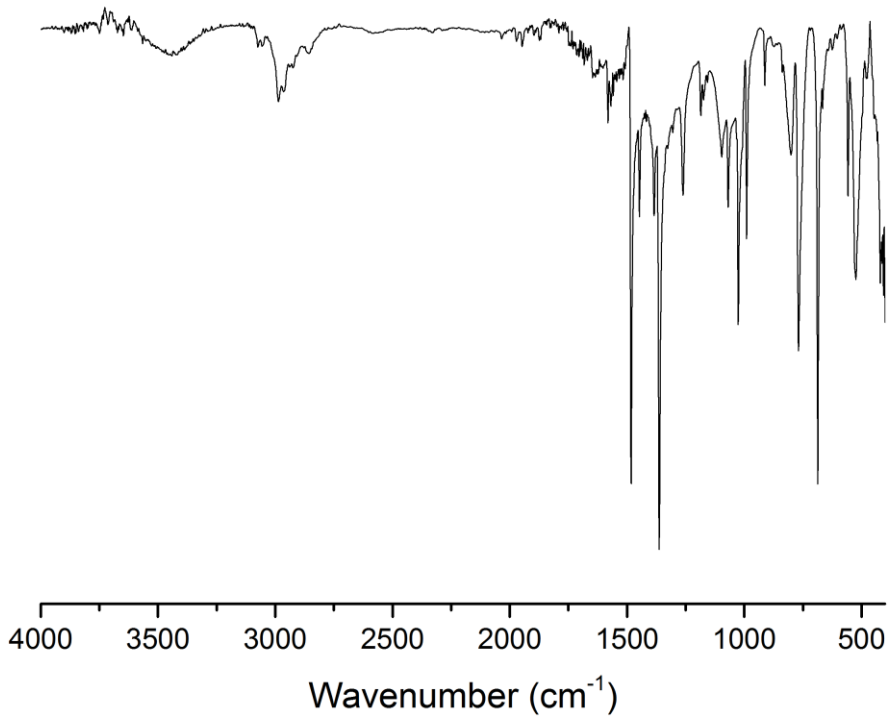


Figure A53. FTIR spectrum of **2.1**.

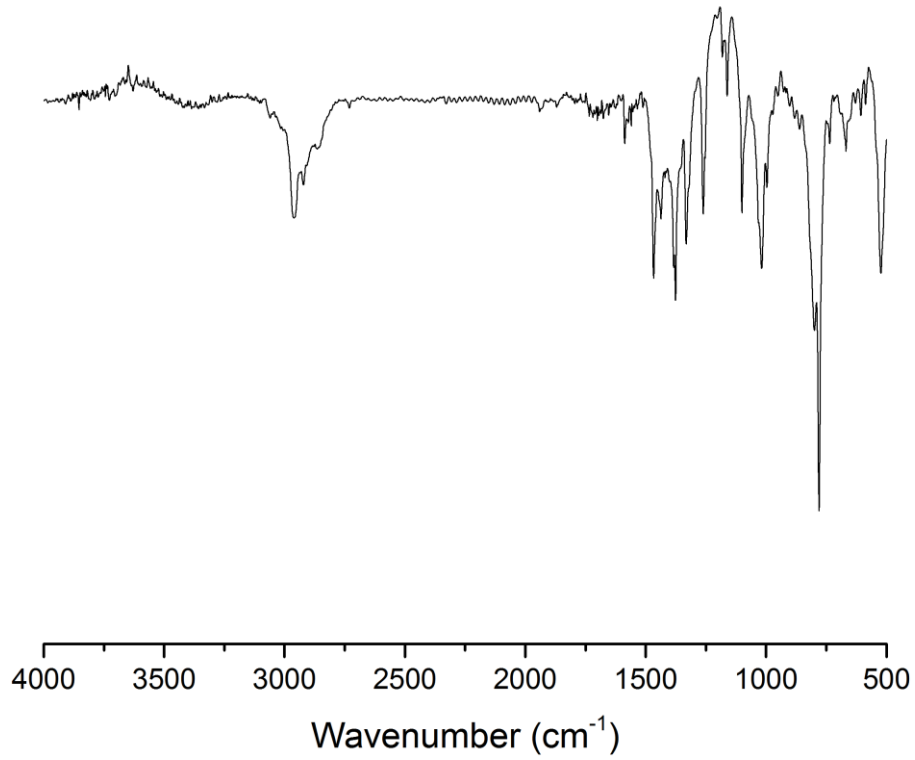


Figure A54. FTIR spectrum of **2.2**.

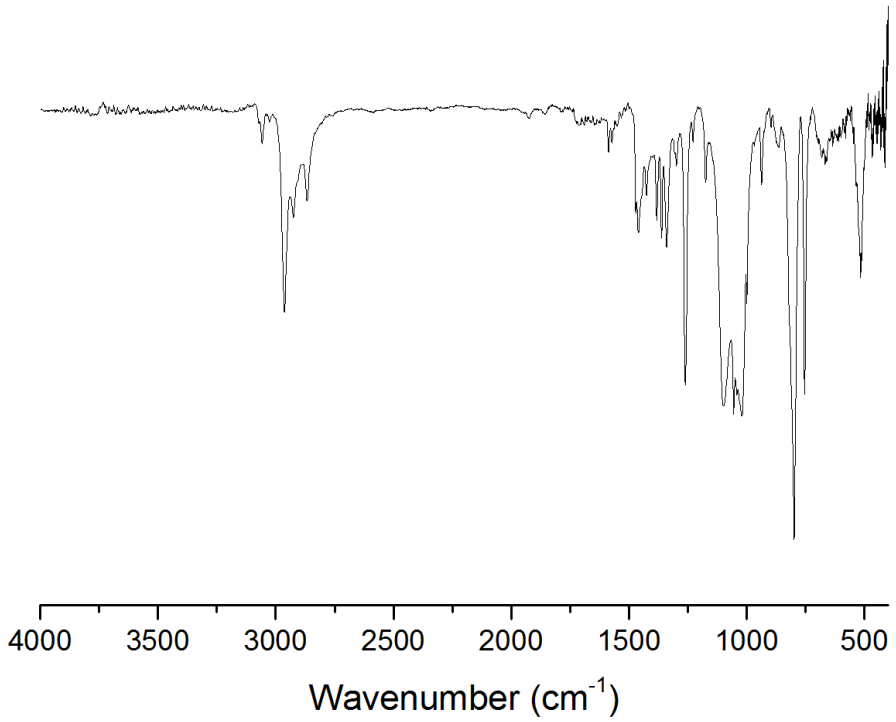


Figure A55. FTIR spectrum of **2.5**.

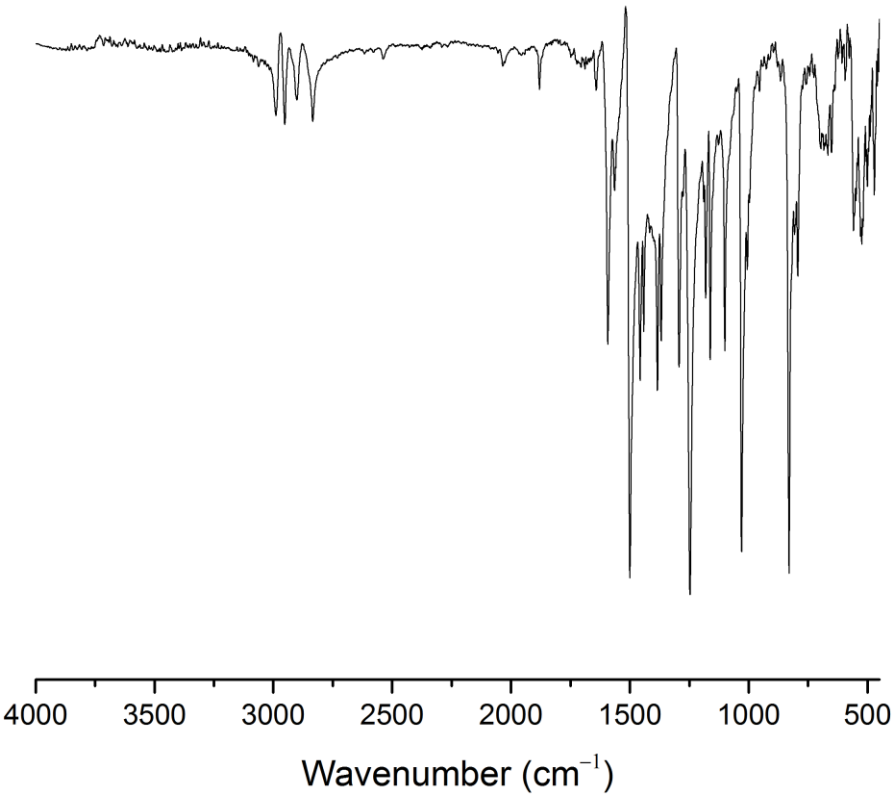


Figure A56. FTIR spectrum of **2.6**.

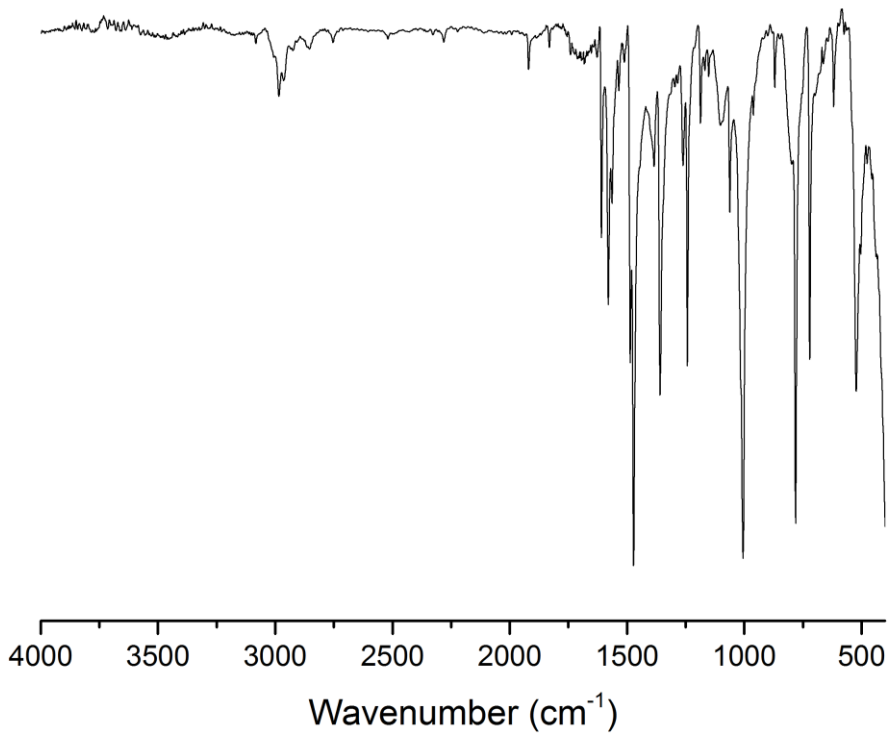


Figure A57. FTIR spectrum of **2.7**.

2.2.4. Solid angle calculations and spacefilled models

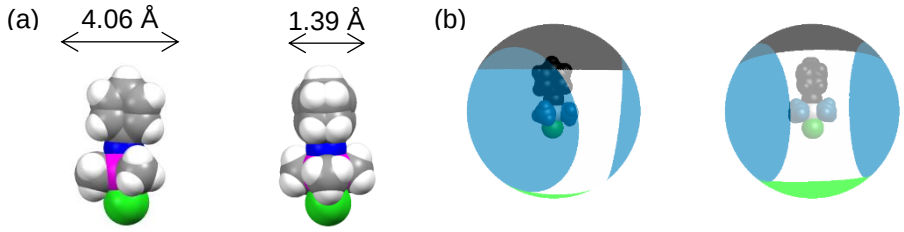


Figure A58. (a) Spacefilled molecular structure of W(NPh)Me_3Cl (**2.1**) showing the imido group from the front (left) and side on (right). (b) Solid-G calculations showing the steric protection afforded to the metal centre by the imido group (black), chlorides (green) and methyl groups (blue) from the front of the imido group (left) and side on (right).

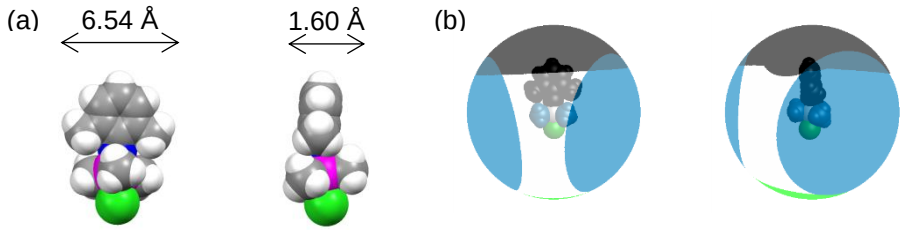


Figure A59. (a) Spacefilled molecular structure of W{N(2,6-Me-C_6H_3)}Me_3Cl (**2.2**) showing the imido group from the front (left) and side on (right). (b) Solid-G calculations showing the steric protection afforded to the metal centre by the imido group (black), chlorides (green) and methyl groups (blue) from the front of the imido group (left) and side on (right).

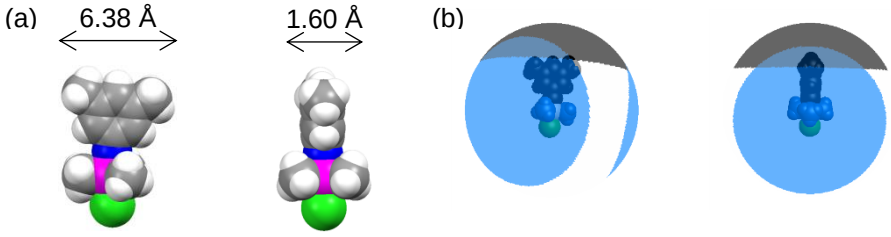


Figure A60. (a) Spacefilled molecular structure of W{N(3,5-Me-C_6H_3)}Me_3Cl (**2.3**) showing the imido group from the front (left) and side on (right). (b) Solid-G calculations showing the steric protection afforded to the metal centre by the imido group (black), chlorides (green) and methyl groups (blue) from the front of the imido group (left) and side on (right).

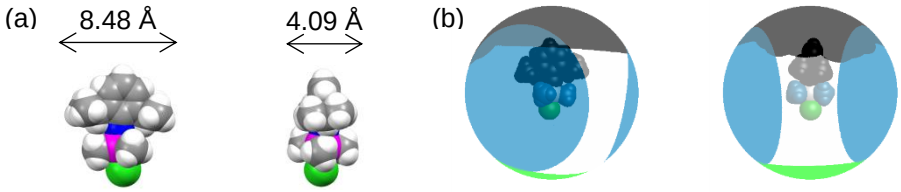


Figure A61. (a) Spacefilled molecular structure of W{N(2,6-^{i}Pr-C_6H_3)}Me_3Cl (**2.5**) showing the imido group from the front (left) and side on (right). (b) Solid-G calculations showing the steric protection afforded to the metal centre by the imido group (black), chlorides (green) and methyl groups (blue) from the front of the imido group (left) and side on (right).

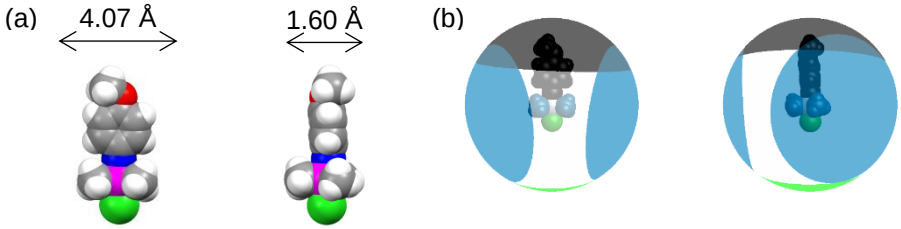


Figure A62. (a) Spacefilled molecular structure of W{N(4-OMe-C_6H_4)}Me_3Cl (**2.6**) showing the imido group from the front (left) and side on (right). (b) Solid-G calculations showing the steric protection afforded to the metal centre by the imido group (black), chlorides (green) and methyl groups (blue) from the front of the imido group (left) and side on (right).

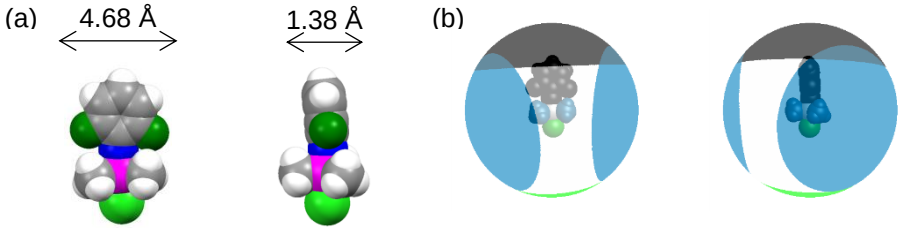


Figure A63. (a) Spacefilled molecular structure of W{N(2,6-F-C_6H_3)}Me_3Cl (**2.7**) showing the imido group from the front (left) and side on (right). (b) Solid-G calculations showing the steric protection afforded to the metal centre by the imido group (black), chlorides (green) and methyl groups (blue) from the front of the imido group (left) and side on (right).

2.3. Synthesis of $W(O)Me_3Cl$

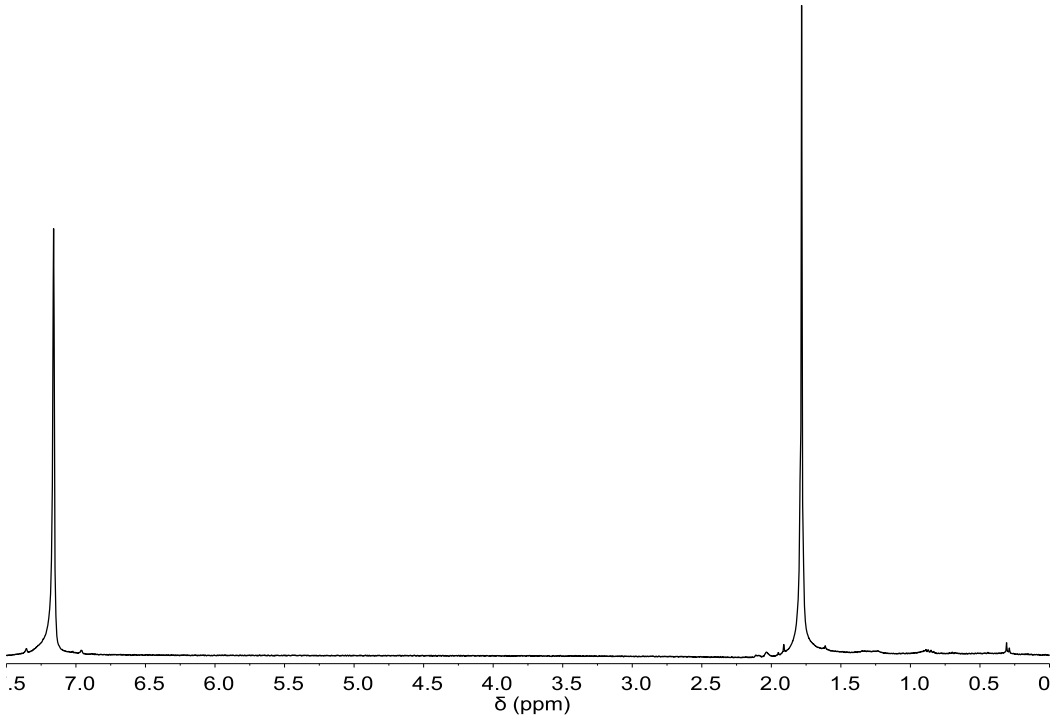


Figure A64. ^{1}H NMR spectrum (400 MHz, 23 °C) of the product formed from reaction of $W(O)Cl_4$ and TMA in d_6-benzene (7.16 ppm), showing a singlet W–C**H**$_3$ resonance at 1.83 ppm.

2.4. Oligomerisation reactions with 2.5

Table A1. Turnover number (TON) for the varying W:MAO ratios over time

Time (h)	**1:2 TON ($mol_{C_2H_4}mol_W^{-1}h^{-1}$)**	**1:5 TON ($mol_{C_2H_4}mol_W^{-1}h^{-1}$)**	**1:10 TON ($mol_{C_2H_4}mol_W^{-1}h^{-1}$)**	**1:20 TON ($mol_{C_2H_4}mol_W^{-1}h^{-1}$)**
0	0	0	0	0
2	0.79	1.96	1.33	0.59
4	1.27	-	-	-
17	11.09	13.55	10.18	7.33
23	15.64	-	-	-
36.5	-	20.28	16.86	12.48
38	24.11	-	-	-
56.5	-	24.37	19.31	14.58

Table A2. 1-butene selectivity for the varying W:MAO ratios.

Time (h)	1:2 1-Butene selectivity (%)	1:5 1-Butene selectivity (%)	1:10 1-Butene selectivity (%)	1:20 1-Butene selectivity (%)
2	100	100	100	100
4	100	-	-	-
17	100	70.9	65.4	36.4
23	96.7	64.9	59.9	33.6
36.5	-	55.6	56.8	29.8
38	96.4	-	-	-
44.5	94.7	-	-	-
56.5	-	45.9	45	27

Table A3. Percentage composition of olefinic products for the 1:5 W:MAO ratio.

Time (h)	Ethylene (%)	1-Butene (%)	2-Butenes (%)	Propylene (%)	Total (butenes+propylene) (%)
0	100	0	0	0	0
2	91.8	8.2	0	0	8.2
17	50.7	37.5	10.3	1.5	49.3
36.5	43.3	35.1	18.7	2.8	56.7
56.5	34.5	34.4	27	4.1	65.5

Table A4. GCMS integrations for the varying W:MAO ratios.

Products	1:5 Peak integration	1:10 Peak integration	1:20 Peak integration
Methane	131,394	123,398	75,712
Ethane	8,041	13,109	16,234
Ethylene	127,903	196,131	226,055
Propylene	166,061	25,453	10,536
Butane	8,431	10,755	9,375
trans-2-Butene	592,610	362,736	253,674
1-Butene	1,067,944	814,000	270,162
cis-2-Butene	660,460	461,662	266,087

Table A5. Percentage composition of products from GCMS traces for the varying W:MAO ratios.

Products	1:5 % makeup	1:10 % makeup	1:20 % makeup
Methane	4.75	6.15	6.71
Ethane	0.29	0.65	1.44
Ethylene	4.63	9.77	20.04
Propylene	6.01	1.27	0.93
Butane	0.31	0.54	0.83
trans-2-Butene	21.44	18.07	22.49
1-Butene	38.64	40.55	23.95
cis-2-Butene	23.90	23.00	23.59

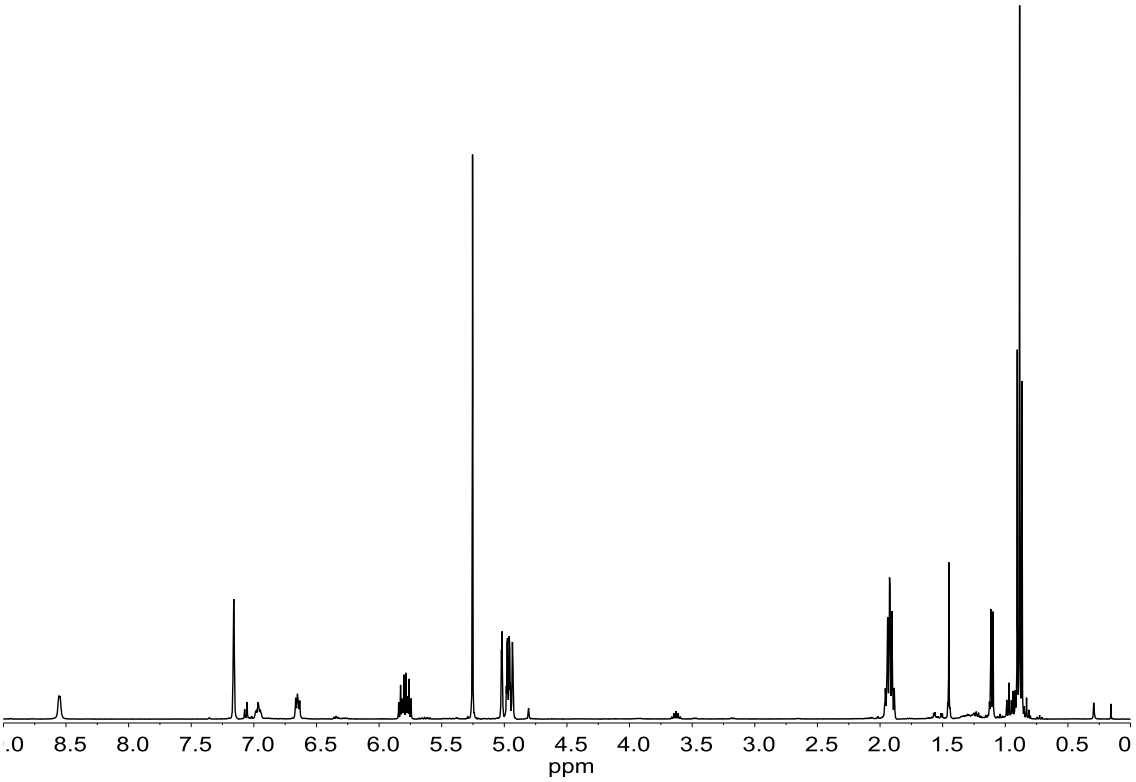


Figure A65. ^{1}H NMR spectrum (400 MHz, 23 °C) of the 1:2 W:MAO ratio after 38 h showing resonances for the complex **2.5** (7.1, 3.7, 1.4 and 1.1 ppm), 1-butene (5.6, 5.0, 1.9 and 0.9 ppm), ethylene (5.3 ppm), pyridine (8.6, 7.0 and 6.7 ppm) and d_6-benzene (7.16 ppm).

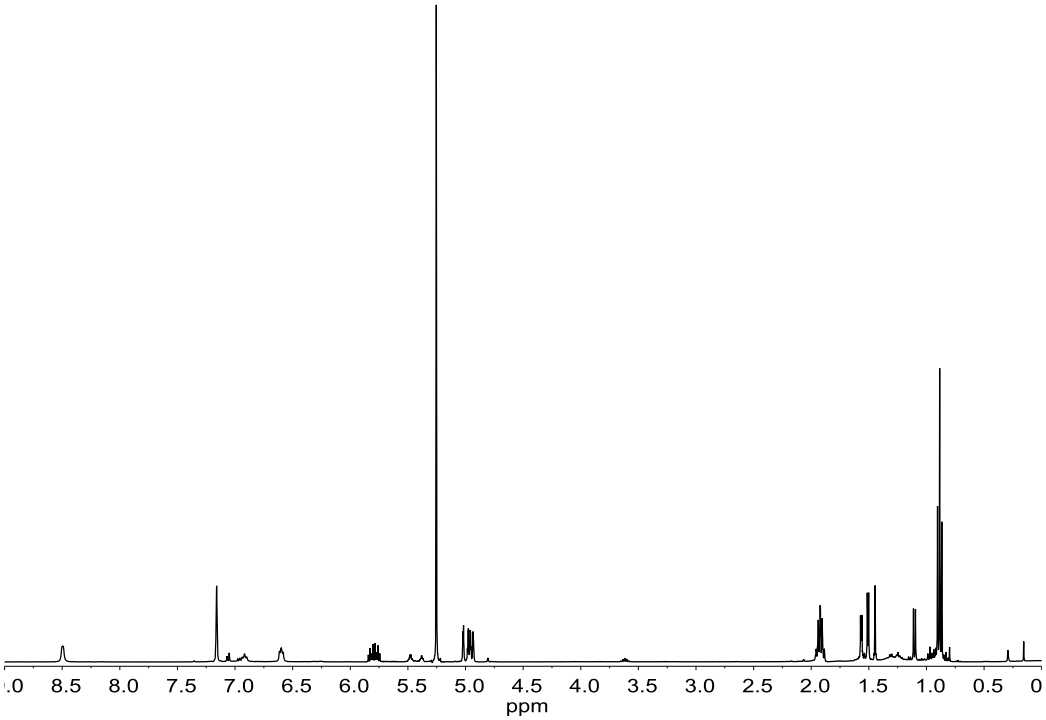


Figure A66. ^{1}H NMR (400 MHz, 23 °C) spectrum of the 1:5 after 36.5 h showing resonances for the complex **2.5** (7.1, 3.7, 1.4 and 1.1 ppm), 1-butene (5.6, 5.0, 1.9 and 0.9 ppm), 2-butenes, propylene, ethylene (5.3 ppm), pyridine (8.6, 7.0 and 6.7 ppm) and d_6-benzene (7.16 ppm).

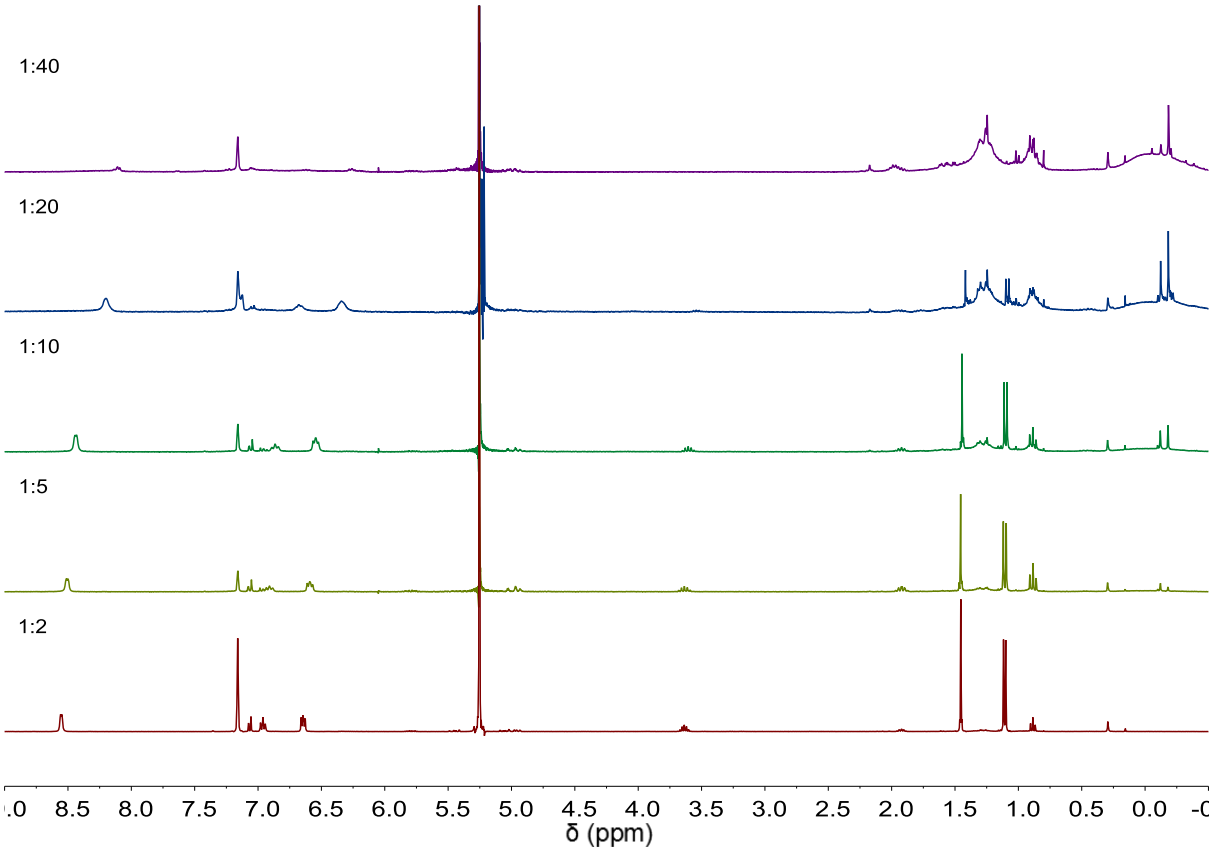


Figure A67. ^{1}H NMR spectra (400 MHz, 23 °C) for the homogeneous W:MAO ratios after 2 hours at 100 °C in d_6-benzene (7.16 ppm) showing decomposition of the complex at higher MAO loadings.

Table A6. 1-butene production for W:DMAC = 1:2 (DMAC = dimethylaluminiumchloride) at 100 °C and 1 bar ethylene in d_6-benzene. [W{N(2,6-^{i}Pr-C_6H_3)}$Me_3Cl]_0$ = 4.55 µmol.

Time/h	1-butene/µmol
1	0.7
17	8.6
23	16.6
46	30.5

2.5. Reaction of 2.5 with $AlCl_3$

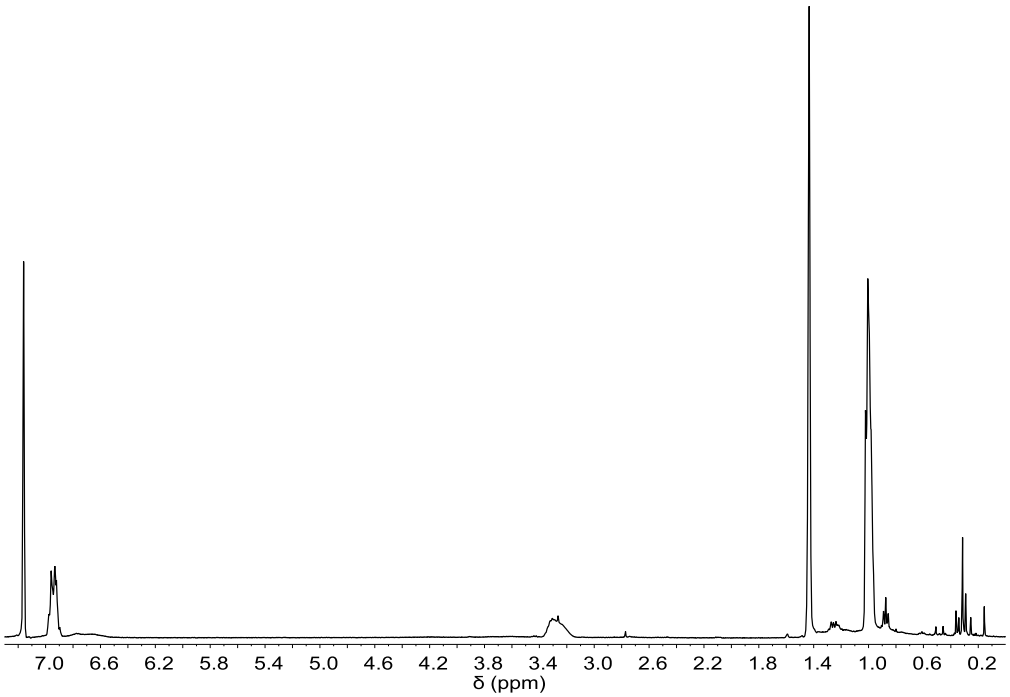


Figure A68. ^{1}H NMR spectrum (400 MHz, 23 °C) in d_6-benzene (7.16 ppm) of the reaction between **2.5** and $AlCl_3$, yielding W{N(2,6-^{i}Pr-C_6H_3)}Me_3(μ-Cl)$AlCl_3$ and [W{N(2,6-^{i}Pr-C_6H_3)}Me_3][$AlCl_4$].

2.6. Temperature study

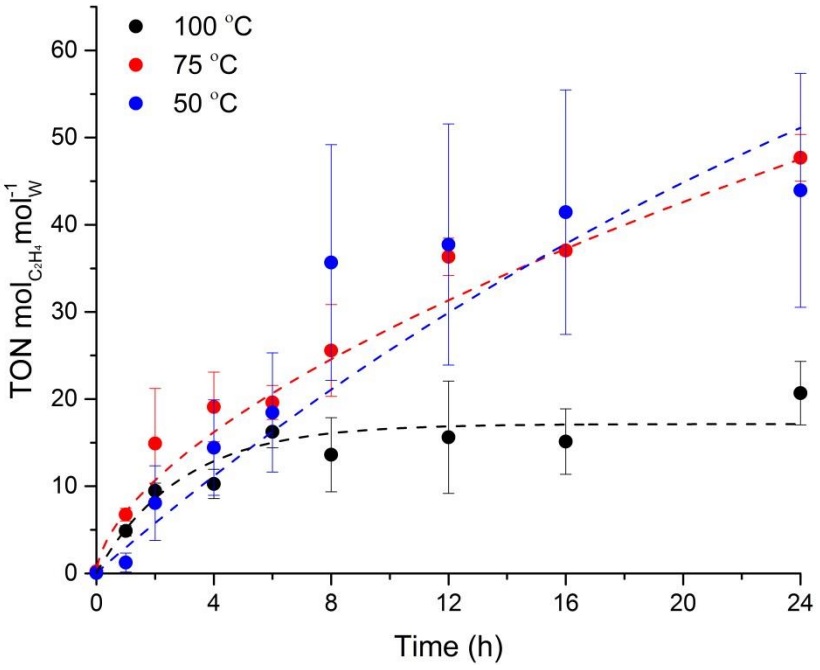


Figure A69. Temperature study for the ethylene oligomerisation reaction between **2.6** and MAO at 50, 75 and 100 °C. Error bars at 1 standard deviation, data points an average of values for each set of runs. Trend lines only a guide for eye.

2.7. Reaction of 2.5 with propylene

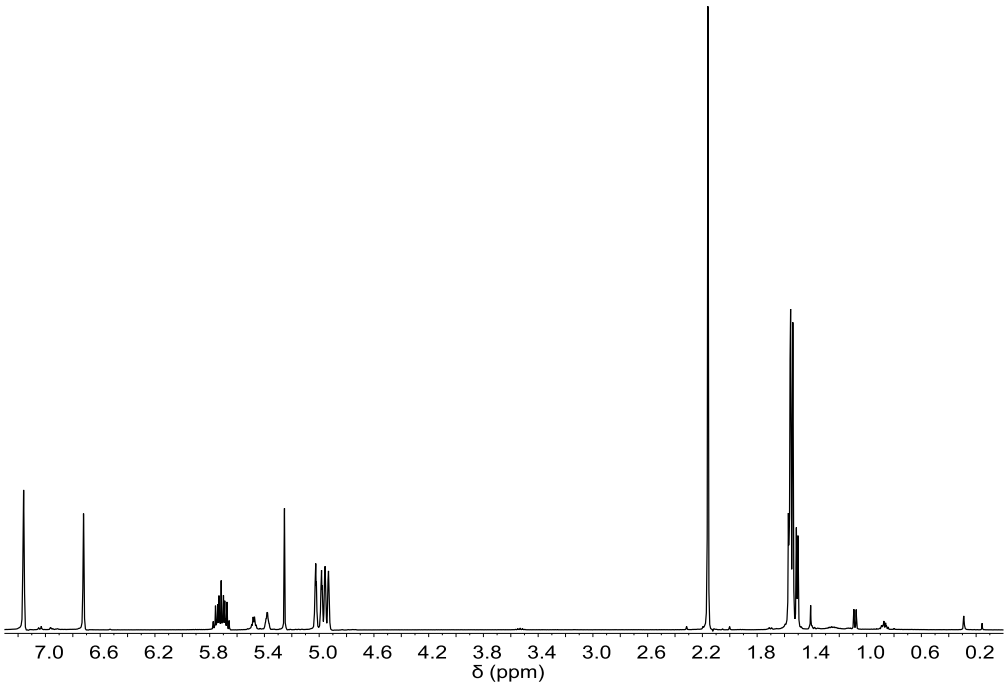


Figure A70. ^{1}H NMR spectrum (400 MHz, 23 °C) of the reaction between **2.5** (7.03, 6.96, 3.53, 1.41 and 1.09 ppm) and propylene (5.72, 4.98, and 1.55 ppm) at 100 °C in d_6-benzene (7.16 ppm) containing mesitylene (6.72 and 2.16 ppm), yielding ethylene (5.25 ppm), *trans*-2-butene (5.47 and 1.57 ppm) and *cis*-2-butene (5.38 and 1.50 ppm).

2.8. Reaction of 2.7 with 1-hexene and 1-octene

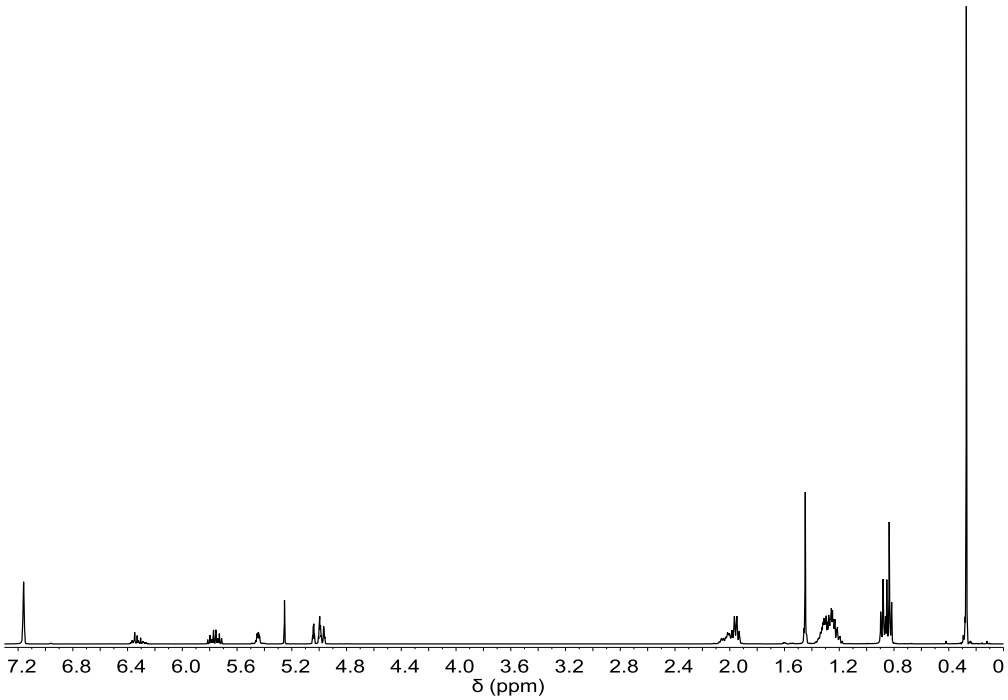


Figure A71. ^{1}H NMR spectrum (400 MHz, 23 °C) of the reaction between **2.7** (6.35, 6.30 and 1.45 ppm) and 1-hexene (5.77, 5.00, 1.96, 1.25 and 0.84 ppm) at 75 °C in d_6-benzene (7.16 ppm) containing $Si(SiMe_3)_4$ (0.27 ppm), yielding ethylene (5.25 ppm) and *trans*-5-undecene (5.45, 2.02, 1.31 and 0.88 ppm).

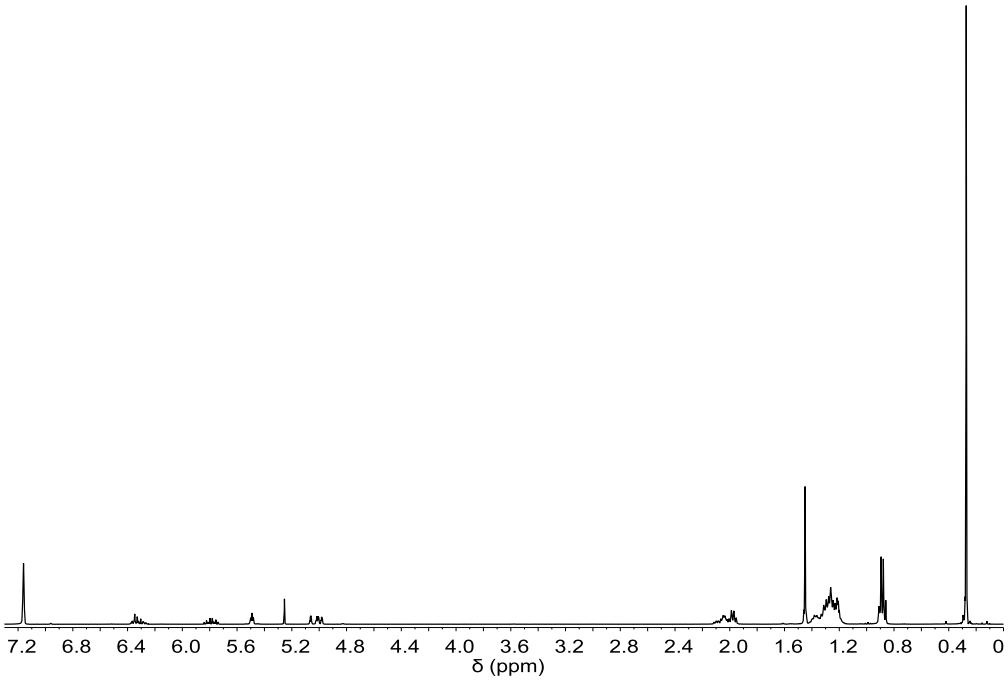


Figure A72. ^{1}H NMR spectrum (400 MHz, 23 °C) of the reaction between **2.7** (6.35, 6.30 and 1.45 ppm) and 1-octene (5.80, 5.01, 1.99, 1.30, 1.25 and 0.88 ppm) at 75 °C in d_6-benzene (7.16 ppm) containing $Si(SiMe_3)_4$ (0.27 ppm), yielding ethylene (5.25 ppm) and *trans*-6-tridecene (5.49, 2.09, 2.04, 1.38 and 0.89 ppm).

2.9. Reactions with $NaBAr^F_4$

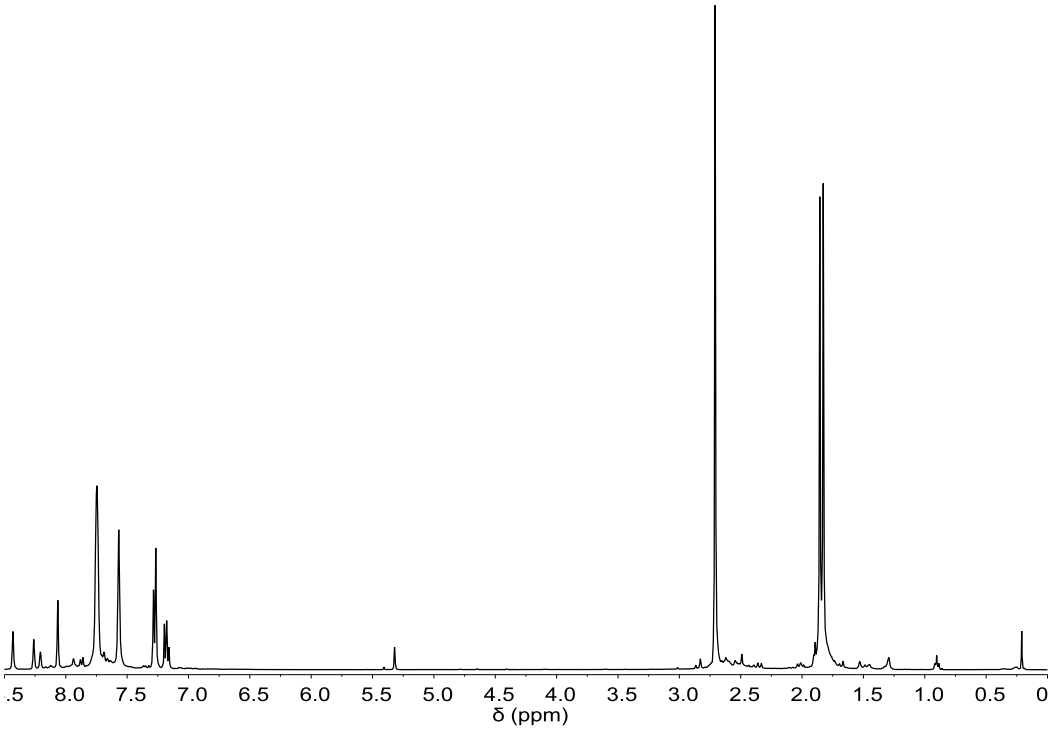


Figure A73. ^{1}H NMR spectrum (400 MHz, 23 °C) of the reaction between **2.2** and $NaBAr^F_4$ in d_2-DCM (5.32 ppm).

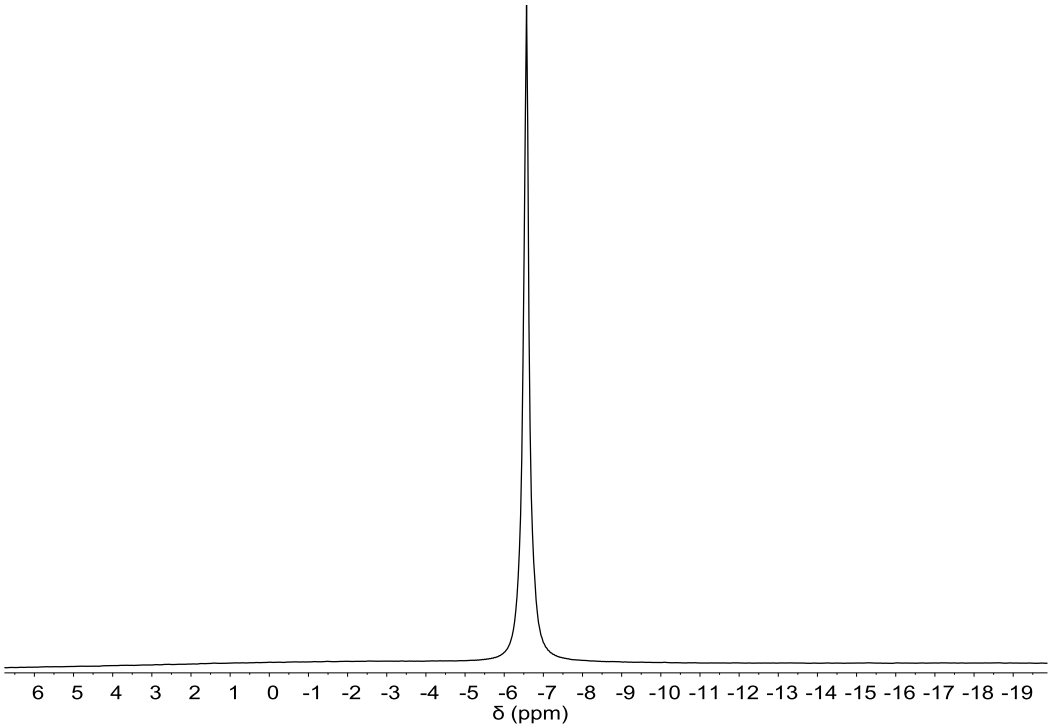


Figure A74. $^{11}B\{^1H\}$ NMR spectrum (400 MHz, 23 °C) of the reaction between **2.2** and $NaBAr^F_4$ in d_2-DCM.

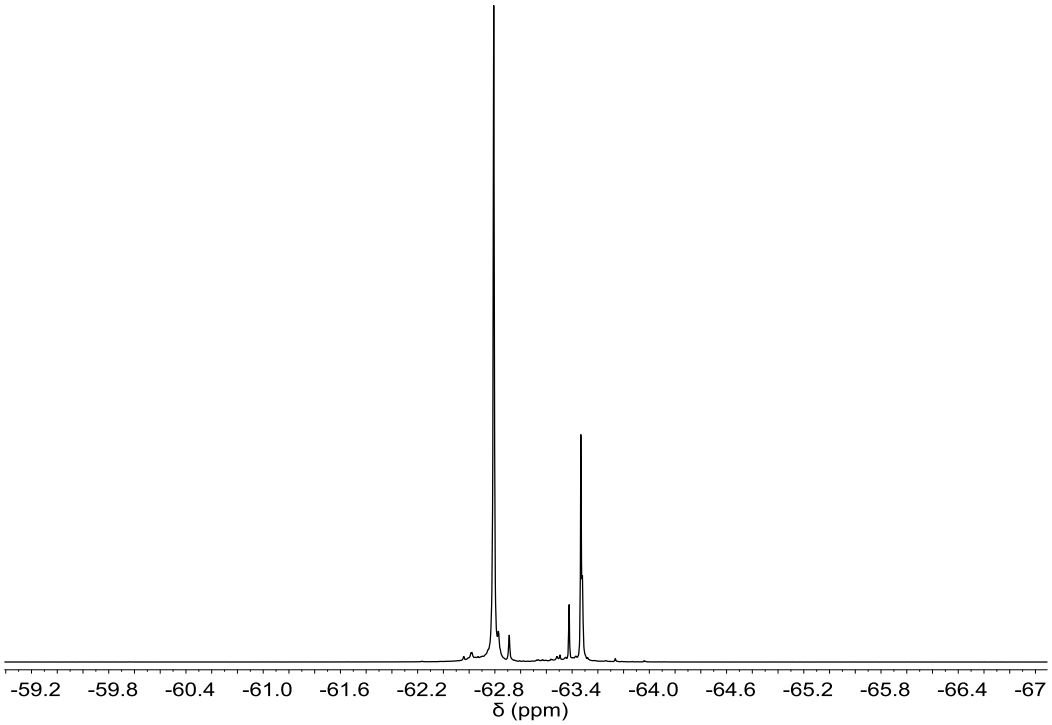


Figure A75. $^{19}F\{^{1}H\}$ NMR spectrum (400 MHz, 23 °C) of the reaction between **2.2** and $NaBAr^{F}_{4}$ in d_2-DCM.

2.10. Reactions with $AgPF_6$

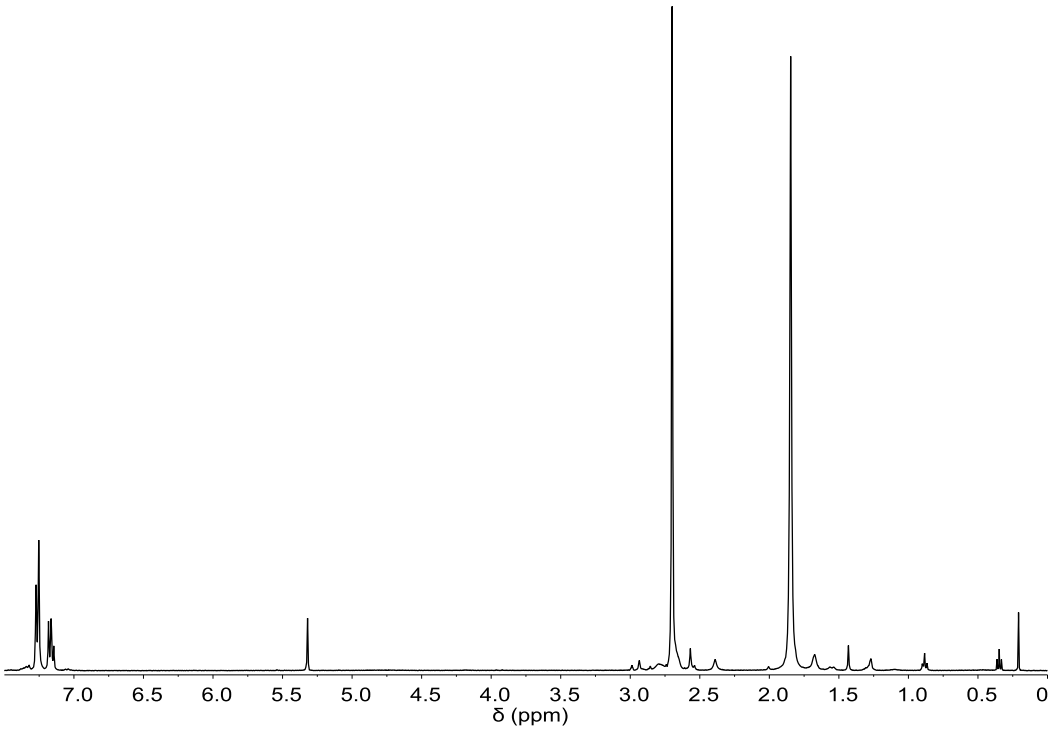


Figure A76. ^{1}H NMR spectrum (400 MHz, 23 °C) of the reaction between **2.2** and $AgPF_6$ in d_2-DCM (5.32 ppm).

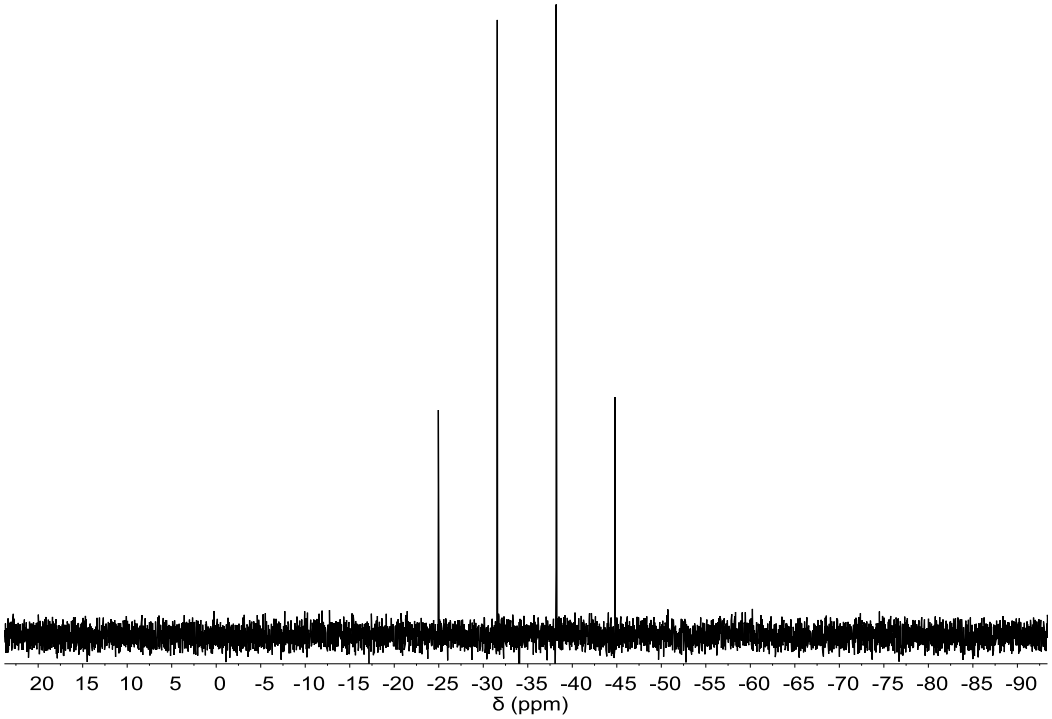


Figure A77. $^{31}P\{^{1}H\}$ NMR spectrum (400 MHz, 23 °C) of the reaction between **2.2** and $AgPF_6$ in d_2-DCM.

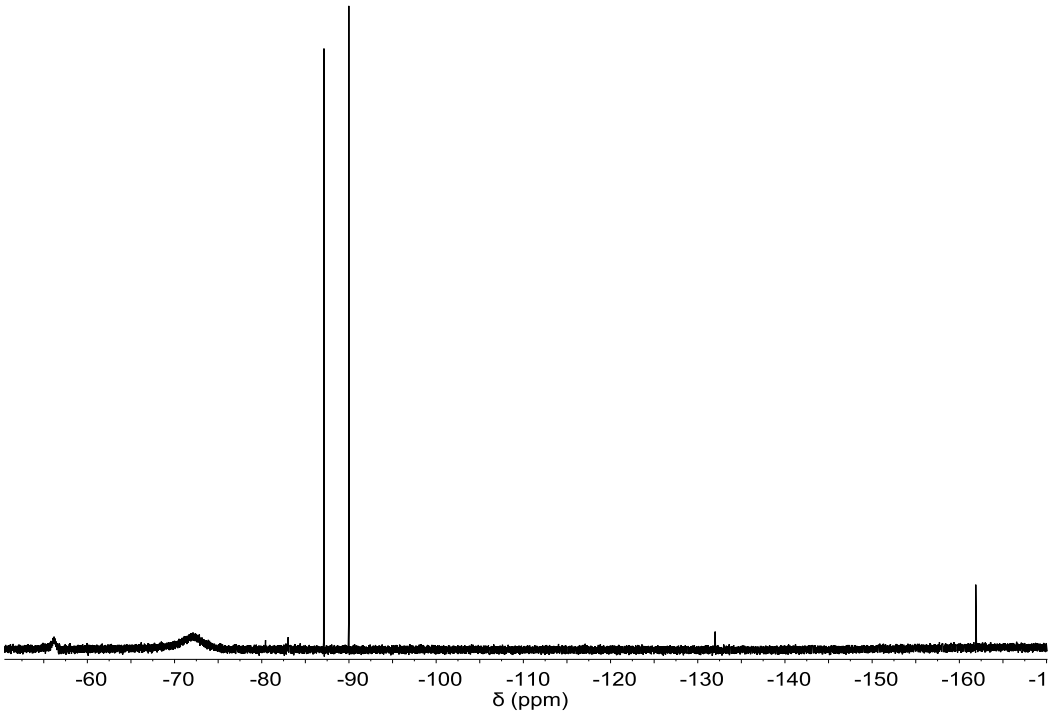


Figure A78. $^{19}F\{^{1}H\}$ NMR spectrum (400 MHz, 23 °C) of the reaction between **2.2** and $AgPF_6$ in d_2-DCM.

2.11. Synthesis of W{N(4-OMe-C_6H_4)}Me_3Cp (3.6)

2.11.1. Single crystal X-ray diffraction data table

Crystal data	
Compound **Chemical formula**	W{N(4-OMe-C_6H_4)}Me_3Cp (**3.6**) $C_{15}H_{21}NOW$
Mr	369.05
Crystal system, space group	Orthorhombic, *Pbca*
Temperature (K)	150
***a, b, c* (Å)**	9.8411 (1), 14.3208 (2), 20.9111 (3)
α, β, γ (°)	90
***V* (Å^3)**	2947.05 (7)
Z	9
μ (mm^{-1})	14.43
Crystal size (mm)	0.25 × 0.18 × 0.06
Data collection	
Diffractometer	SuperNova, Dual, Cu at zero, Atlas
Absorption correction	Multi-scan *CrysAlis PRO* 1.171.38.43b (Rigaku Oxford Diffraction, 2015) Empirical absorption correction using spherical harmonics, implemented in SCALE3 ABSPACK scaling algorithm.
T_{min}, T_{max}	0.174, 1.000
No. of measured, independent and observed [*I* > 2*s*(*I*)] reflections	3005, 3005, 2871
R_{int}	0.046
(sin θ/λ)$_{max}$ (Å^{-1})	0.625
Refinement	
R*[*F*^{2} > 2*s*(*F*^{2})], *wR*(*F*^{2}), *S	0.026, 0.068, 1.13
No. of reflections	3005
No. of parameters	167
No. of restraints	0
H-atom treatment	Constrained
(Δ/σ)$_{max}$	0.001
Δρ_{max}, Δρ_{min} (e Å^{-3})	1.35, −1.53
Absolute structure	-
Absolute structure parameter	-
Computer programs: Collect (Nonius BV, 1997-2000), *HKL SCALEPACK* (Otwinowski & Minor 1997), *HKL DENZO* and *SCALEPACK* (Otwinowski & Minor 1997), Palatinus, L.; Chapuis, G. J. Appl. Cryst. 2007, 40, 786-790., *SHELXL2014* (Sheldrick, 2014), *CrysAlis PRO* (Agilent (2014). Agilent Technologies Ltd, Yarnton, Oxfordshire, England.), *ORTEP-3 for Windows* (Farrugia, 1997), *WinGX* publication routines (Farrugia, 1999).	

2.11.2. NMR spectra

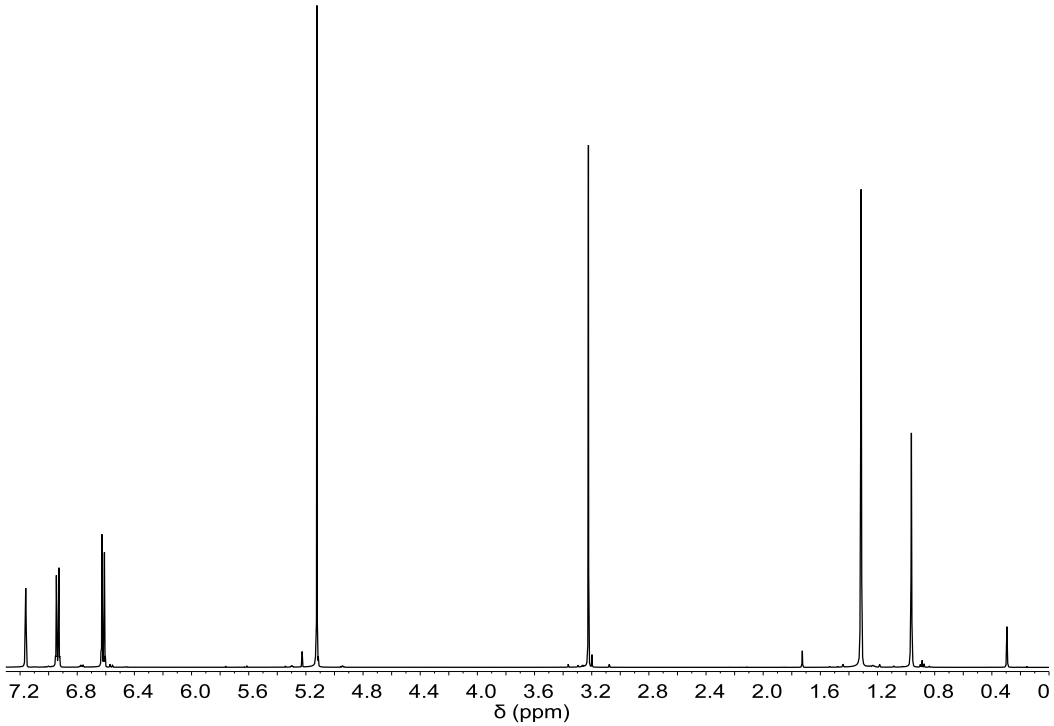


Figure A79. ^{1}H NMR spectrum (400 MHz, 23 °C) of **3.6** in d_6-benzene (7.16 ppm).

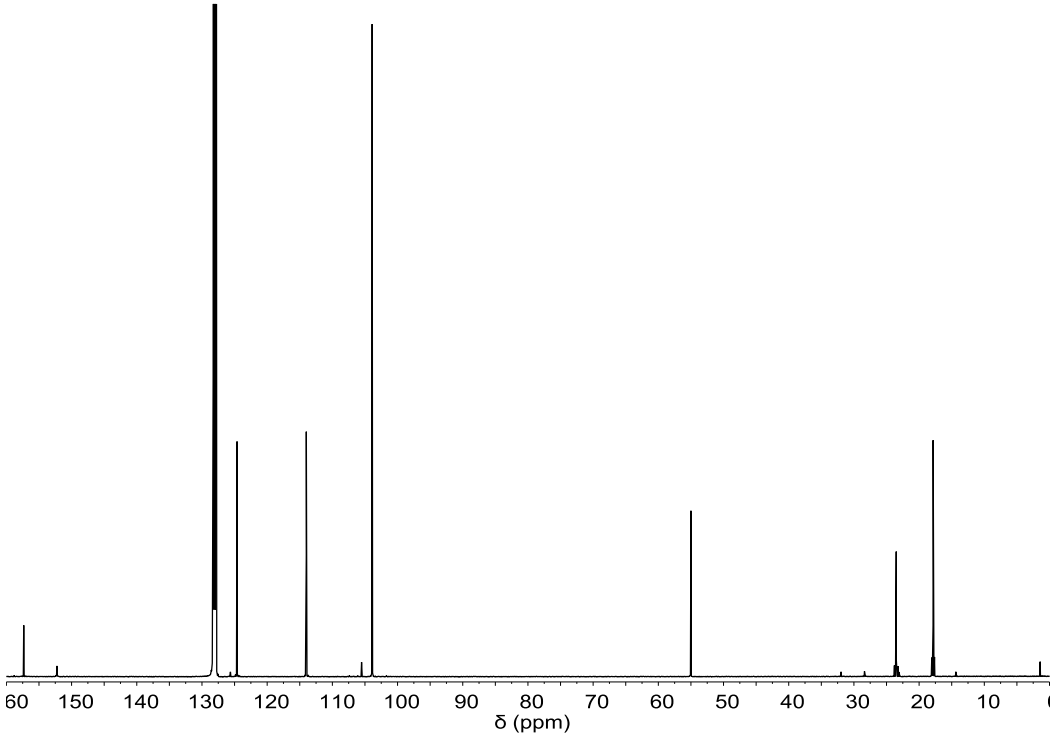


Figure A80. ^{13}C{^{1}H} NMR spectrum (400 MHz, 23 °C) of **3.6** in d_6-benzene (128.06 ppm).

Appendix for Chapter Three

3.1. Thermogravimetric Analysis

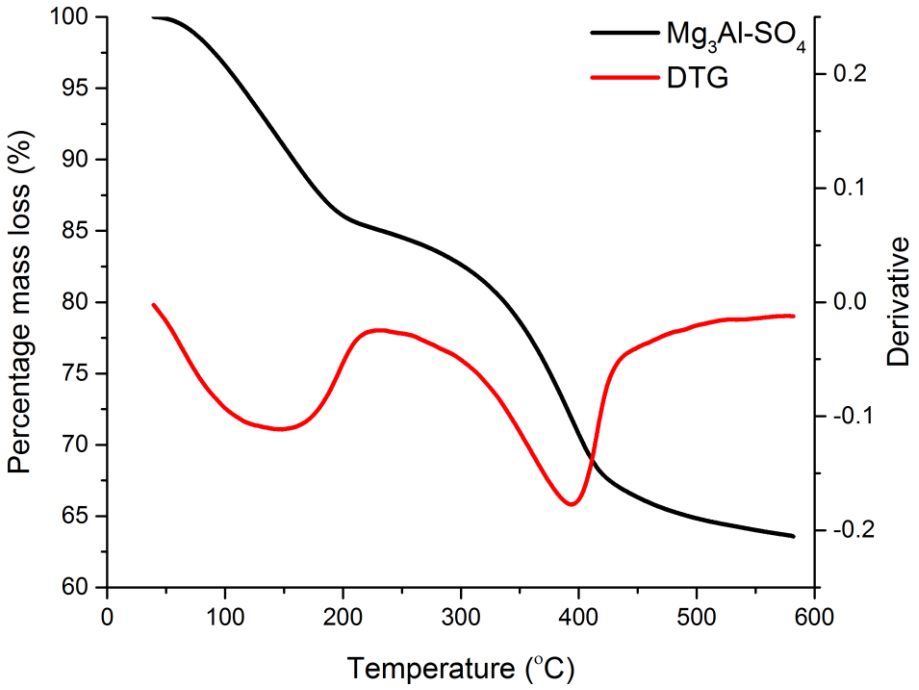


Figure A81. TGA and differential thermogravimetric (DTG) analysis of the $Mg_3Al\text{-}SO_4$ AMO-LDH starting material.

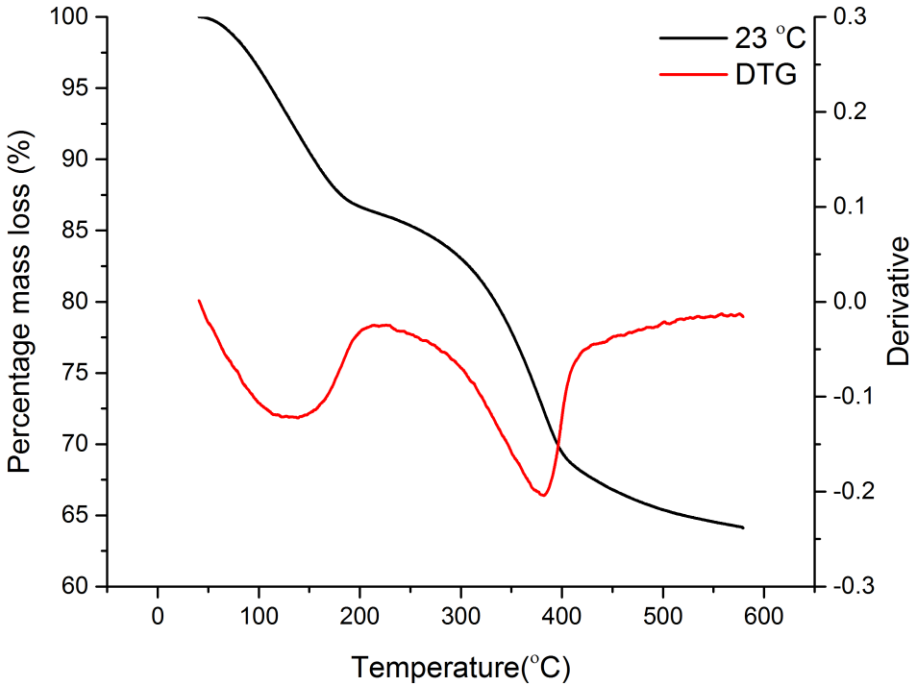


Figure A82. TGA and differential thermogravimetric (DTG) analysis of the $Mg_3Al\text{-}SO_4$ AMO-LDH thermally treated at 23 °C for 6 hours under vacuum.

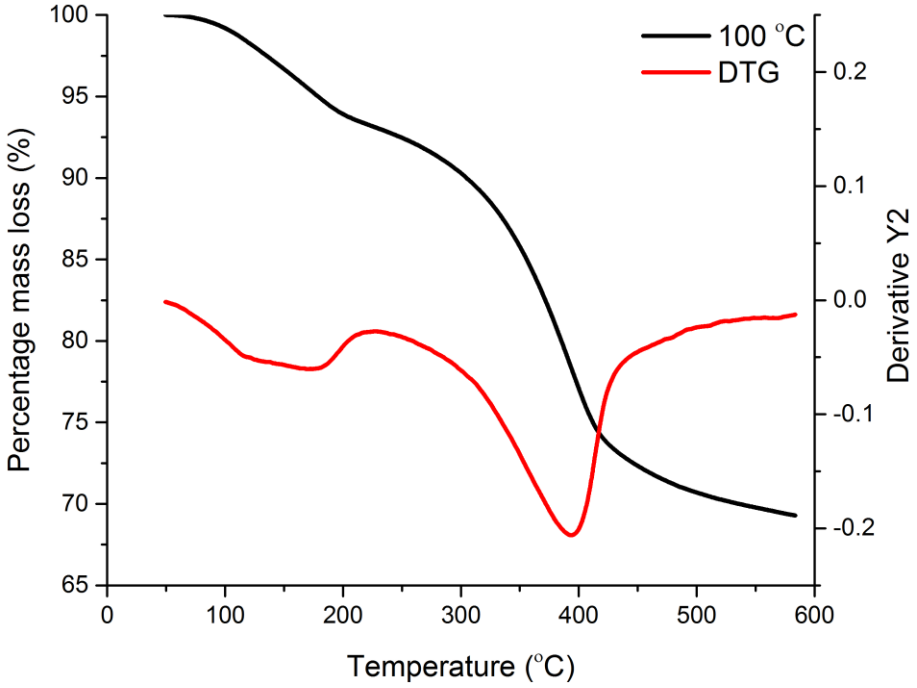


Figure A83. TGA and differential thermogravimetric (DTG) analysis of the Mg_3Al-SO_4 AMO-LDH thermally treated at 100 °C for 6 hours under vacuum.

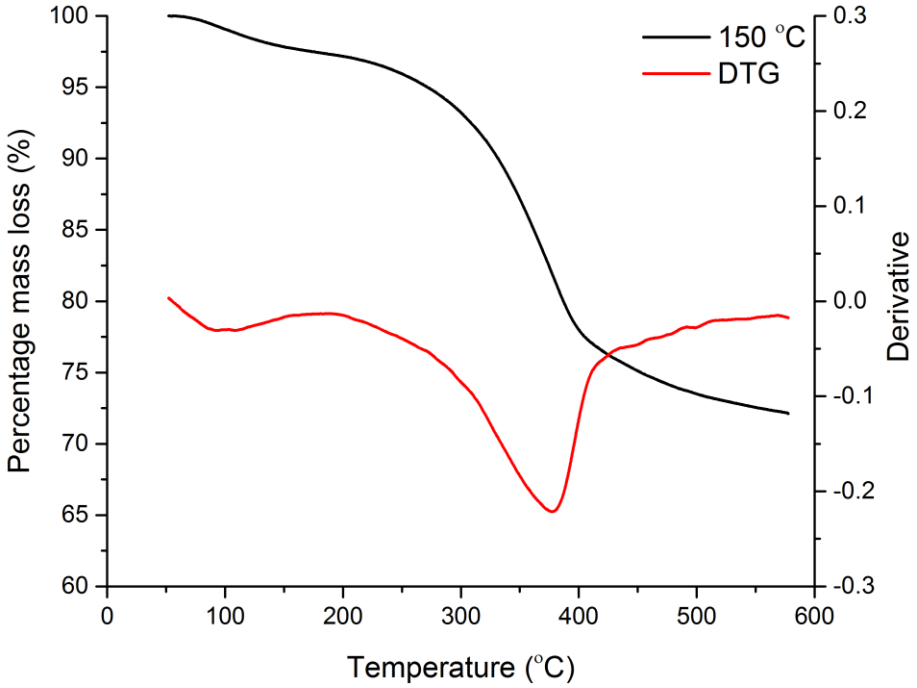


Figure A84. TGA and differential thermogravimetric (DTG) analysis of the Mg_3Al-SO_4 AMO-LDH thermally treated at 150 °C for 6 hours under vacuum.

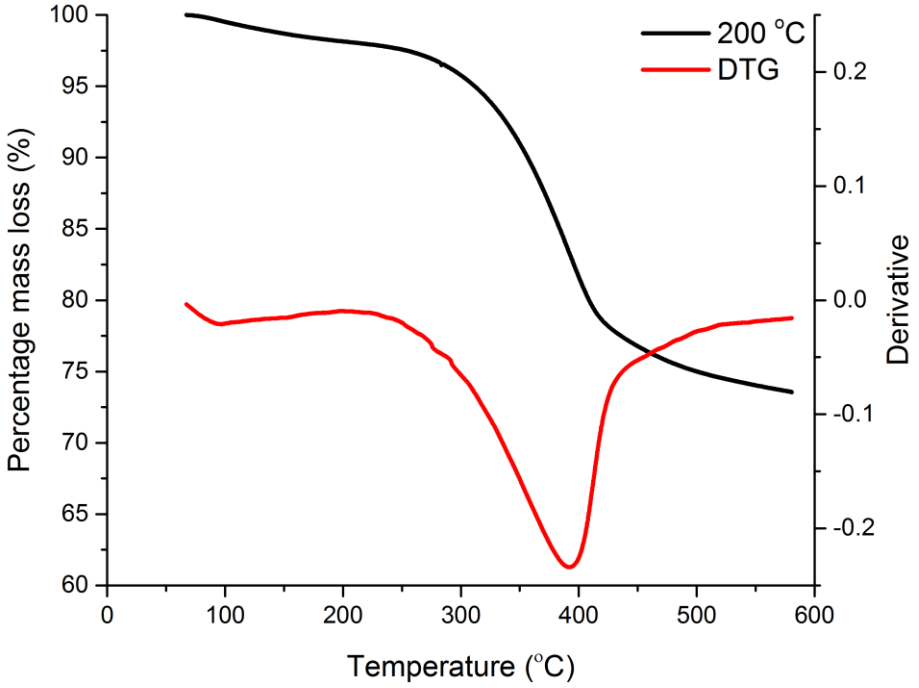


Figure A85. TGA and differential thermogravimetric (DTG) analysis of the Mg_3Al-SO_4 AMO-LDH thermally treated at 200 °C for 6 hours under vacuum.

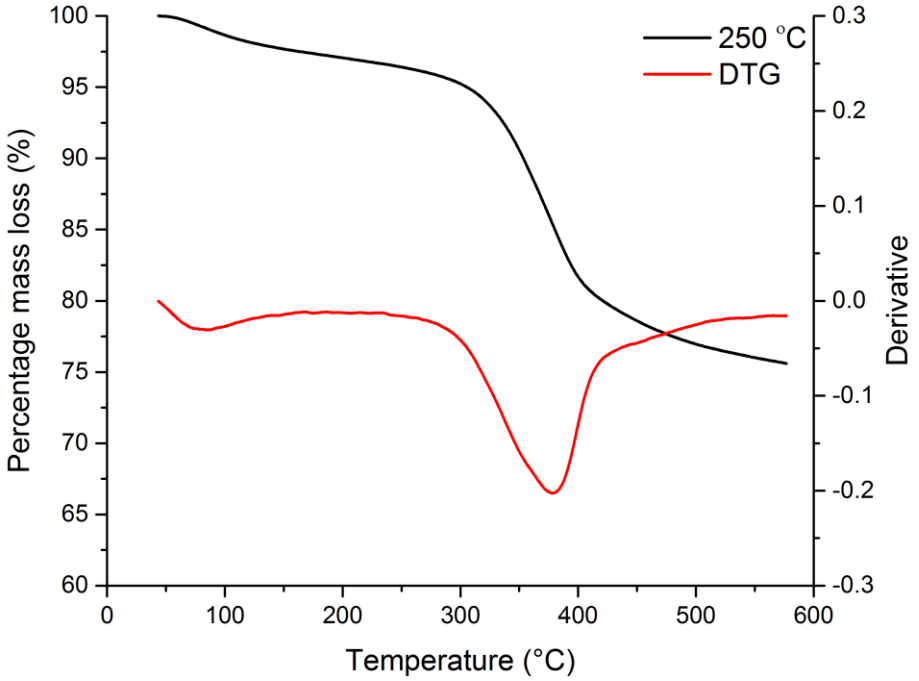


Figure A86. TGA and differential thermogravimetric (DTG) analysis of the Mg_3Al-SO_4 AMO-LDH thermally treated at 250 °C for 6 hours under vacuum.

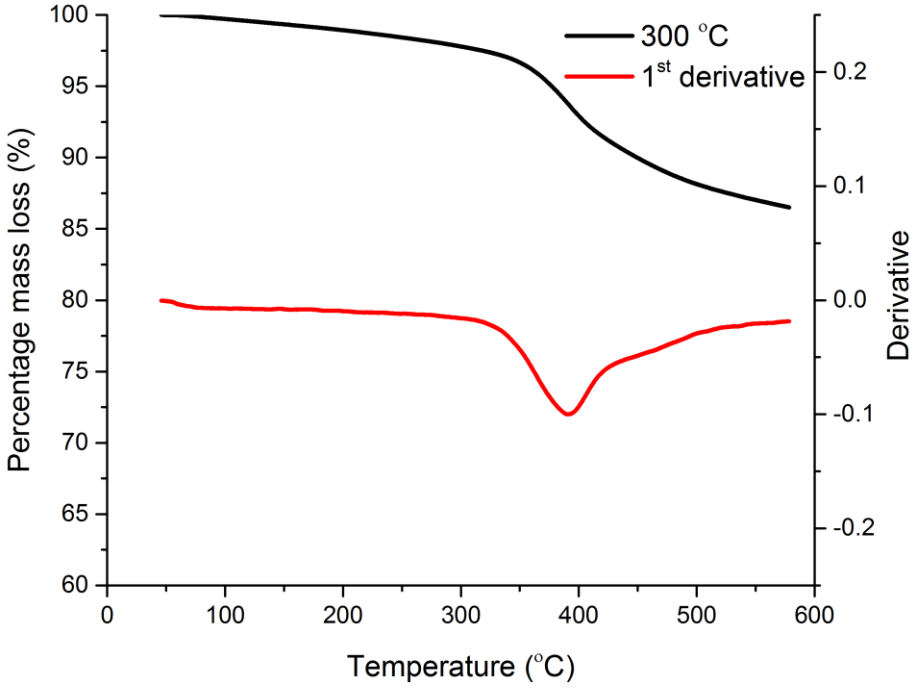


Figure A87. TGA and differential thermogravimetric (DTG) analysis of the Mg_3Al-SO_4 AMO-LDH thermally treated at 300 °C for 6 hours under vacuum.

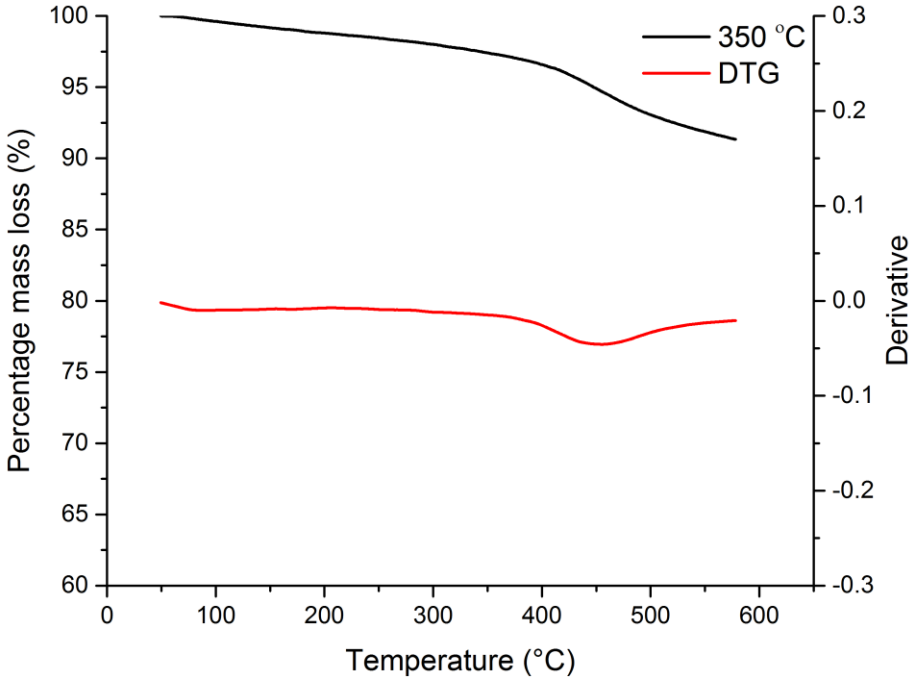


Figure A88. TGA and differential thermogravimetric (DTG) analysis of the Mg_3Al-SO_4 AMO-LDH thermally treated at 350 °C for 6 hours under vacuum.

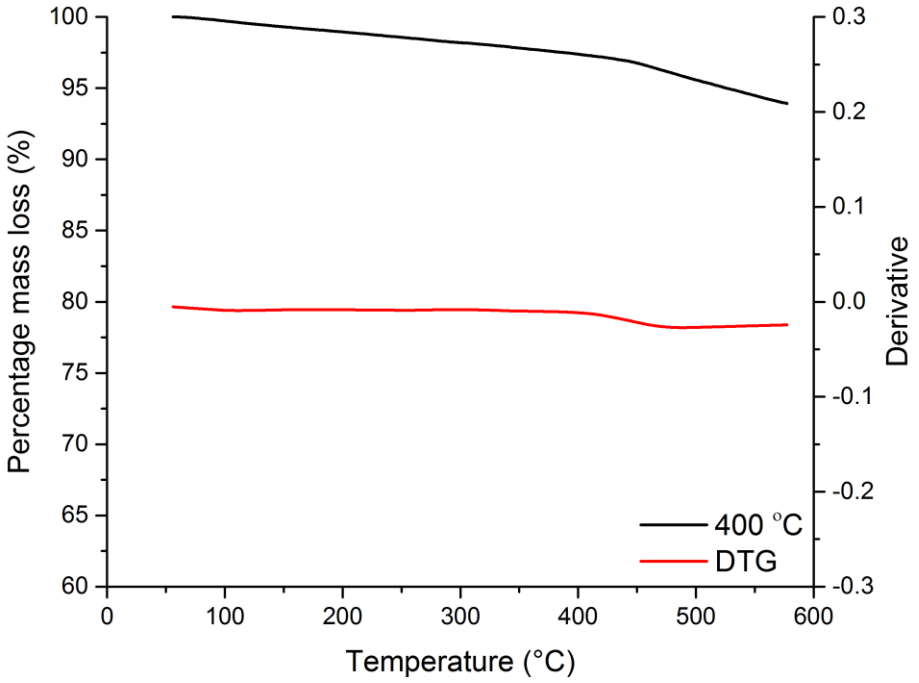


Figure A89. TGA and differential thermogravimetric (DTG) analysis of the Mg_3Al-SO_4 AMO-LDH thermally treated at 400 °C for 6 hours under vacuum.

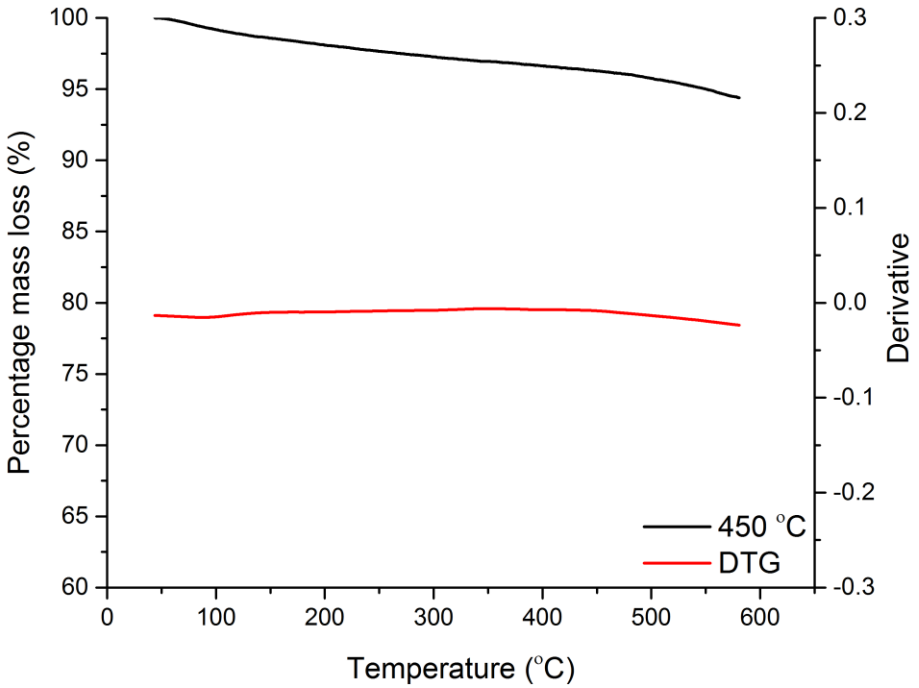


Figure A90. TGA and differential thermogravimetric (DTG) analysis of the Mg_3Al-SO_4 AMO-LDH thermally treated at 450 °C for 6 hours under vacuum.

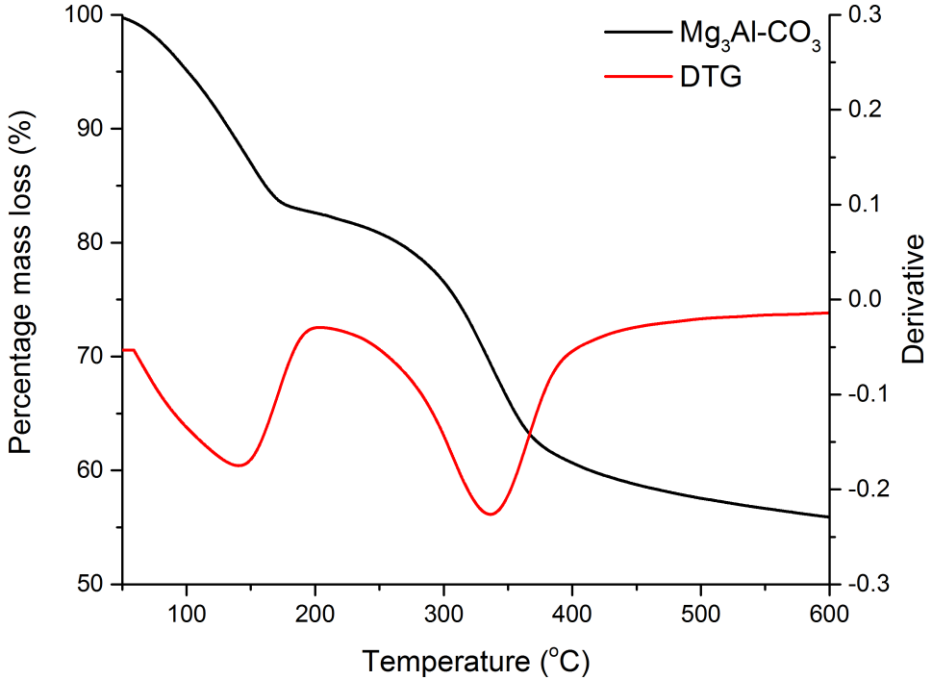


Figure A91. TGA and differential thermogravimetric (DTG) analysis of the $Mg_3Al\text{-}CO_3$ AMO-LDH starting material.

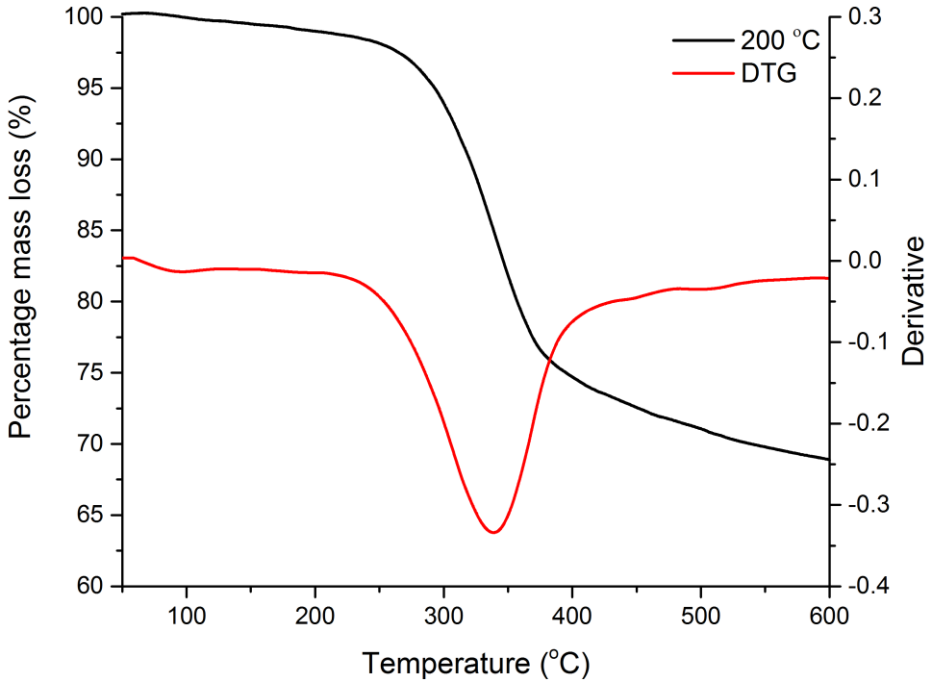


Figure A92. TGA and differential thermogravimetric (DTG) analysis of the $Mg_3Al\text{-}CO_3$ AMO-LDH thermally treated at 200 °C for 6 hours under vacuum.

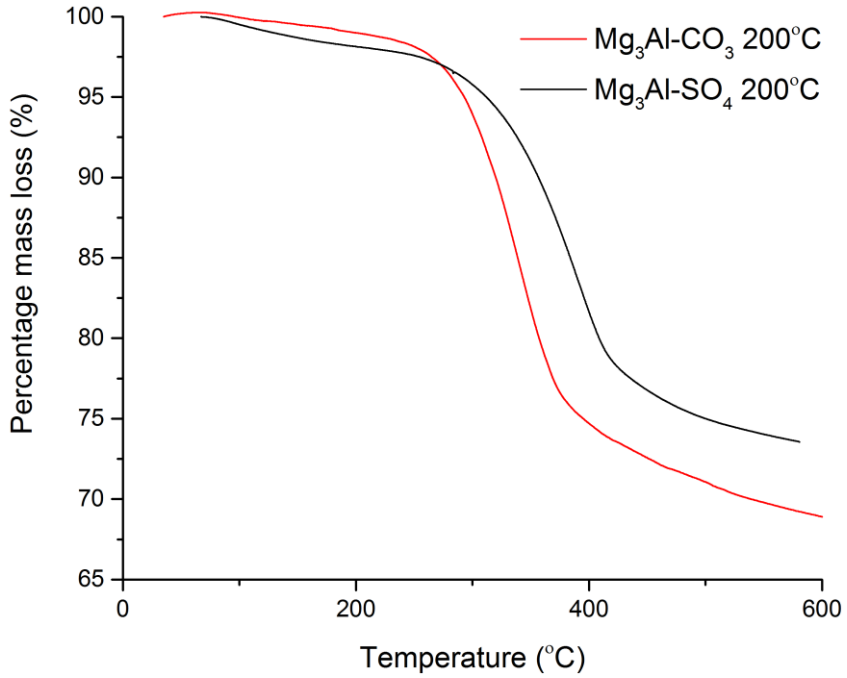


Figure A93. TGA curves for Mg_3Al-SO_4 and Mg_3Al-CO_3 AMO-LDHs thermally treated at 200 °C for 6 hours under vacuum.

Table A7. Temperatures corresponding to the minima in the DTG for the AMO-LDH samples.

AMO-LDH	Dehydroxylation temperature (°C)	Minima in the DTG (°C)	
Mg_3Al-SO_4	starting material	145	398
Mg_3Al-SO_4	23	138	382
Mg_3Al-SO_4	100	170	394
Mg_3Al-SO_4	150	-	377
Mg_3Al-SO_4	200	-	392
Mg_3Al-SO_4	250	-	378
Mg_3Al-SO_4	300	-	391
Mg_3Al-SO_4	350	-	455
Mg_3Al-SO_4	400	-	489
Mg_3Al-SO_4	450	-	-
Mg_3Al-CO_3	starting material	140	336
Mg_3Al-CO_3	200	-	339

3.2. PXRD data

Table A8. Shift in the Mg_3Al-SO_4 peaks in the PXRD after thermal treatment under vacuum.

Sample	*003* position, 2θ (°)	*006* position, 2θ (°)[a]	*009* position, 2θ (°)	*110* position, 2θ (°)
Mg_3Al-SO_4	10.4	21.2	34.8	60.6
100 °C	11.9	22.0	18.1	60.8
200 °C	12.7	-	-	60.6
300 °C	-	-	-	61.4

[a] Peak obscured by background signal from the capillary spinner. At 400 °C only peaks corresponding to MgO (2θ = 43 and 63°) are observed.

3.3. BET isotherms and BJH pore volume distributions

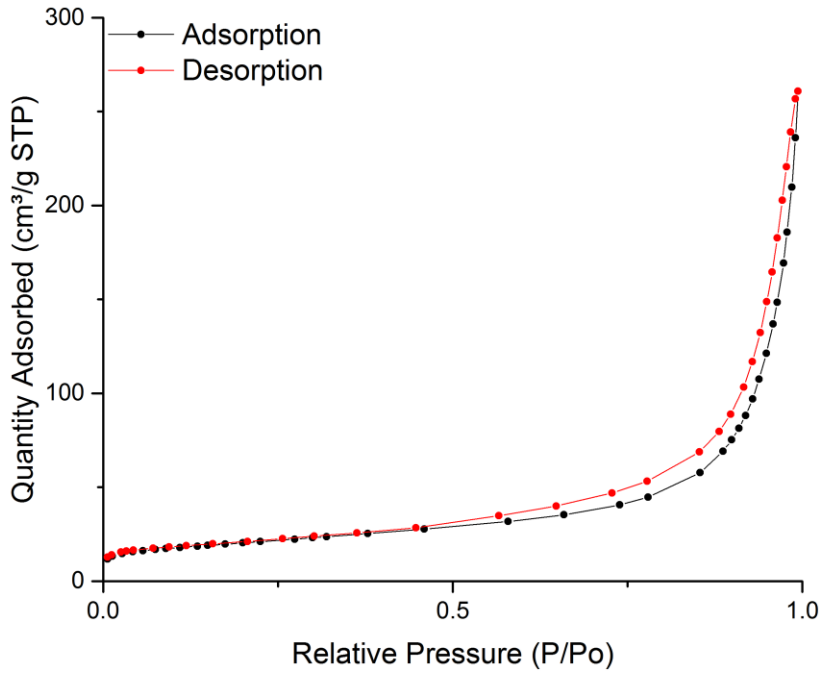


Figure A94. BET adsorption and desorption isotherms for Mg_3Al-SO_4 AMO-LDH thermally treated at 23 °C for 6 hours under vacuum.

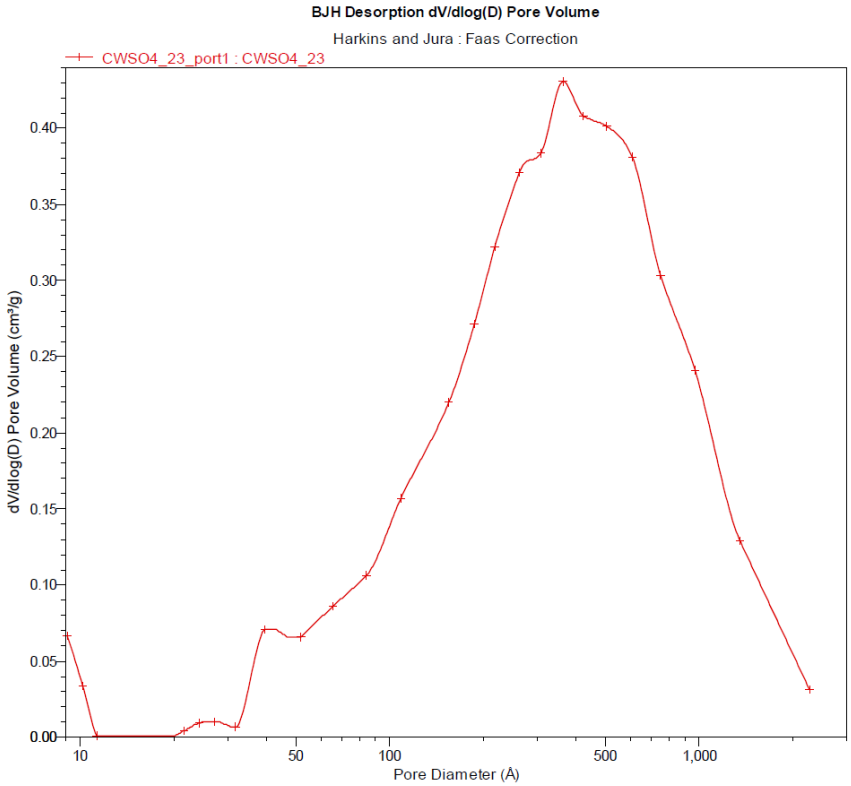


Figure A95. Pore volume distribution for Mg_3Al-SO_4 AMO-LDH thermally treated at 23 °C for 6 hours under vacuum.

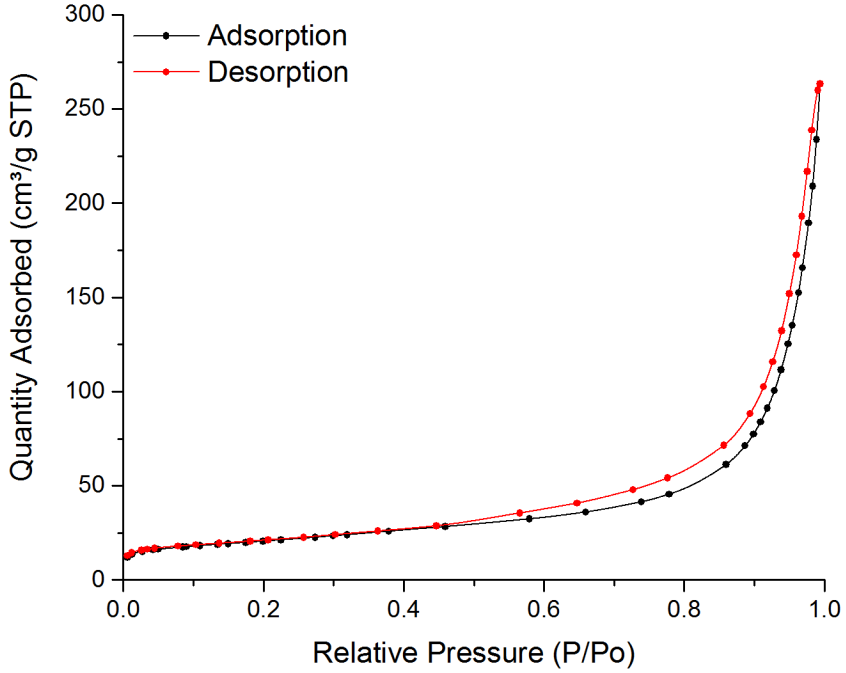


Figure A96. BET adsorption and desorption isotherms for Mg_3Al-SO_4 AMO-LDH thermally treated at 100 °C for 6 hours under vacuum.

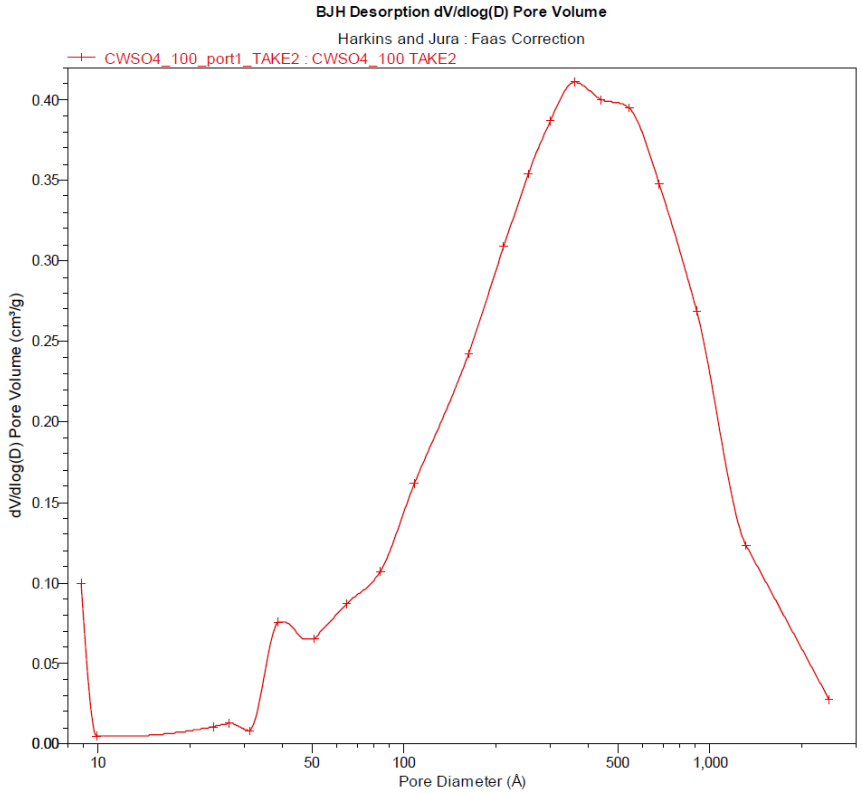


Figure A97. Pore volume distribution for Mg_3Al-SO_4 AMO-LDH thermally treated at 100 °C for 6 hours under vacuum.

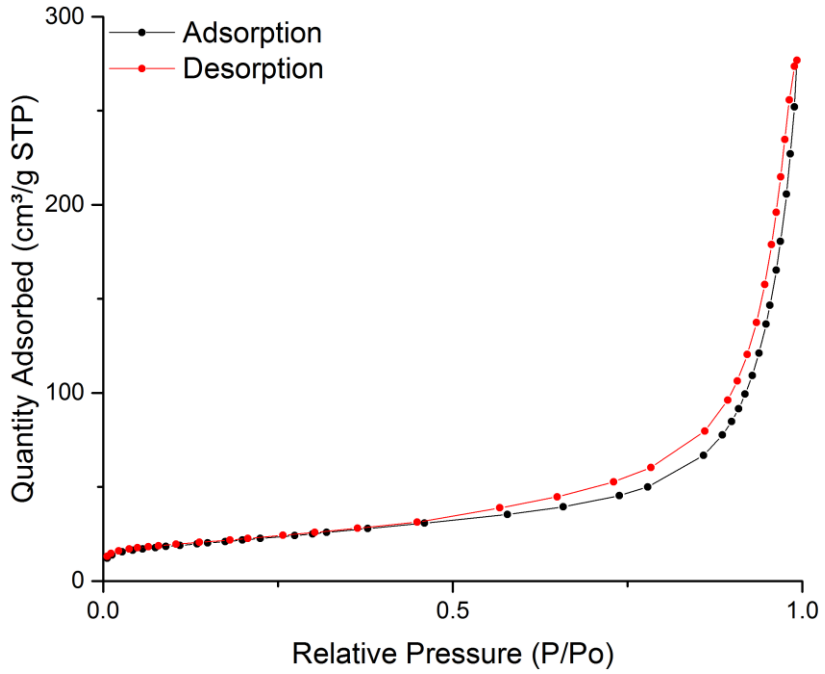


Figure A98. BET adsorption and desorption isotherms for Mg_3Al-SO_4 AMO-LDH thermally treated at 150 °C for 6 hours under vacuum.

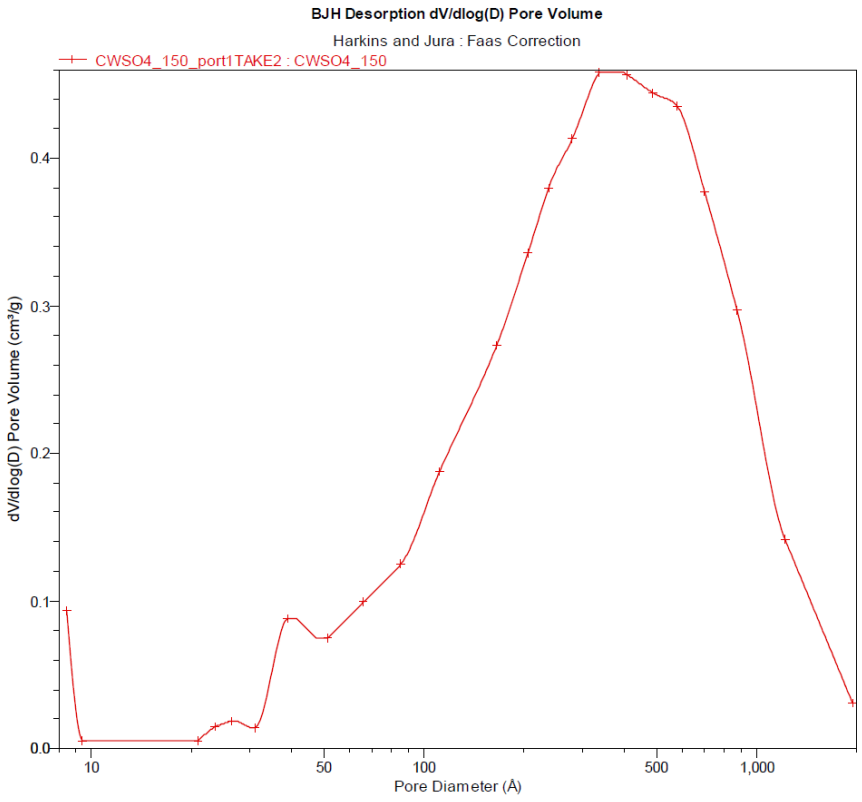


Figure A99. Pore volume distribution for Mg_3Al-SO_4 AMO-LDH thermally treated at 150 °C for 6 hours under vacuum.

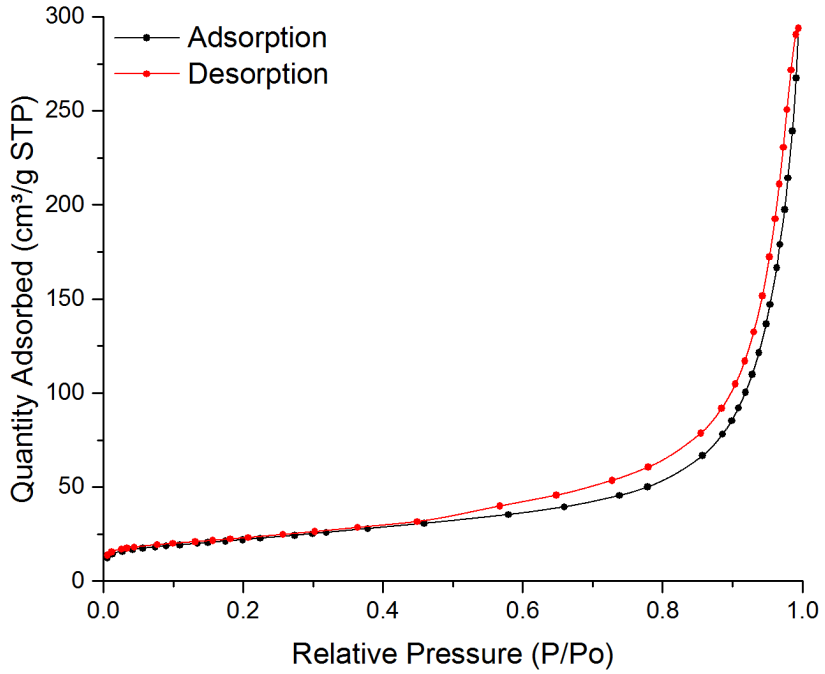


Figure A100. BET adsorption and desorption isotherms for Mg_3Al-SO_4 AMO-LDH thermally treated at 200 °C for 6 hours under vacuum.

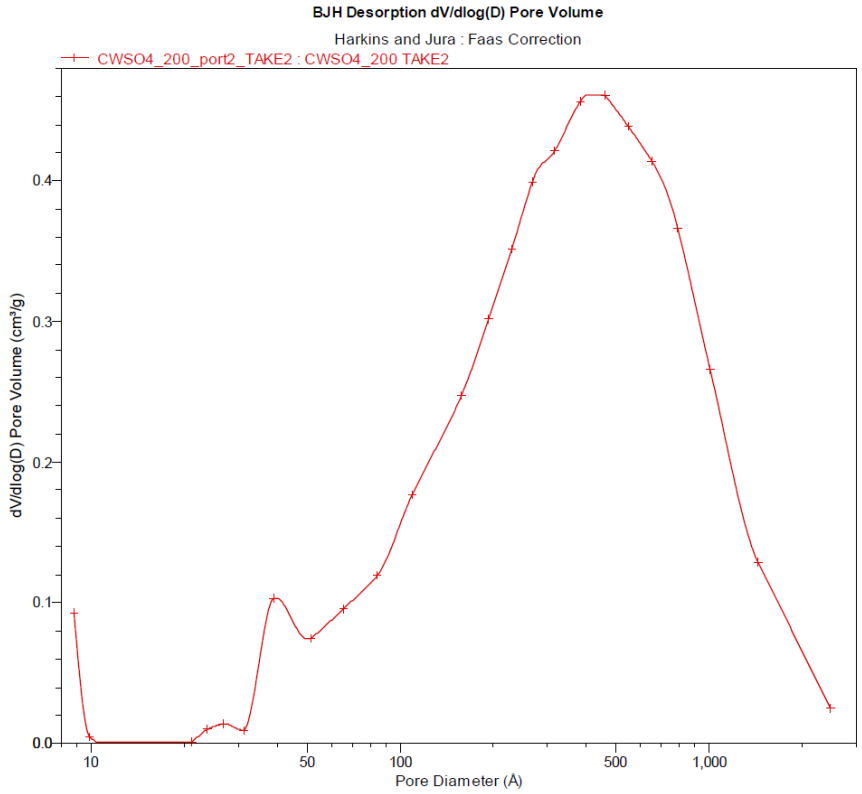


Figure A101. Pore volume distribution for Mg_3Al-SO_4 AMO-LDH thermally treated at 200 °C for 6 hours under vacuum.

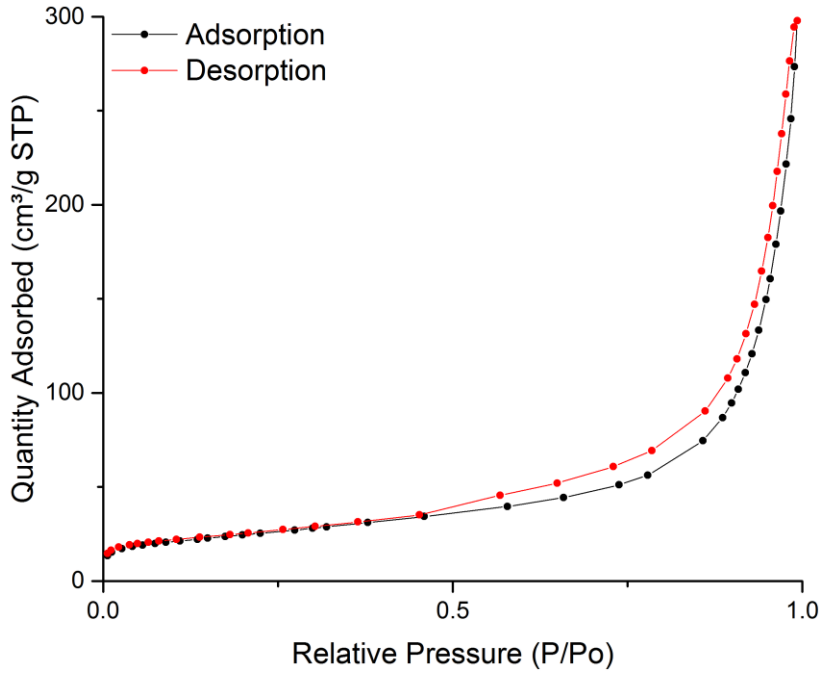


Figure A102. BET adsorption and desorption isotherms for Mg_3Al-SO_4 AMO-LDH thermally treated at 250 °C for 6 hours under vacuum.

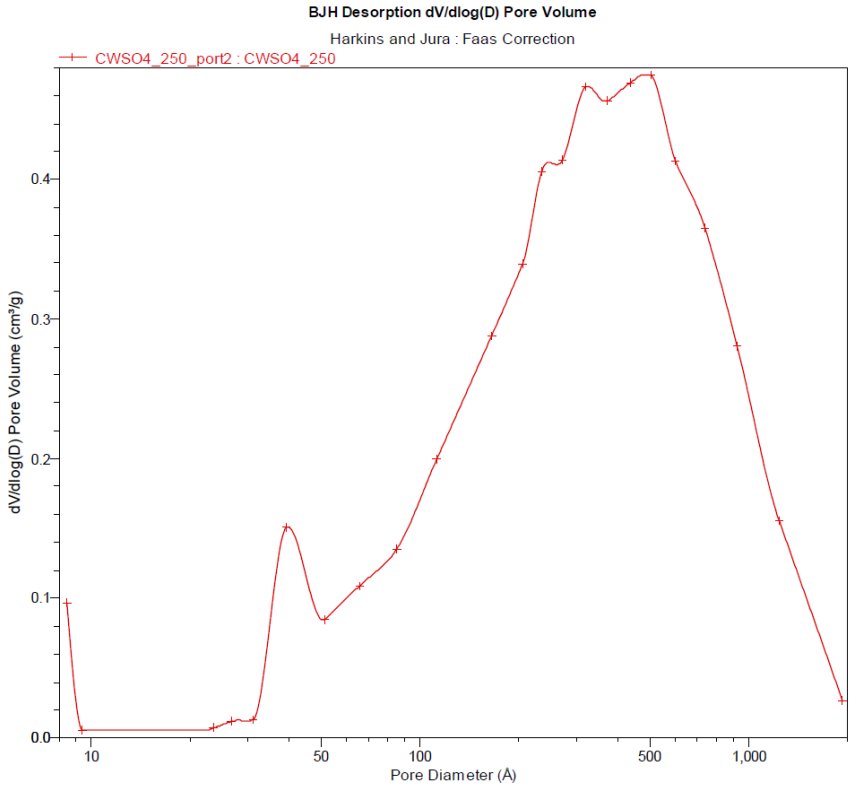


Figure A103. Pore volume distribution for Mg_3Al-SO_4 AMO-LDH thermally treated at 250 °C for 6 hours under vacuum.

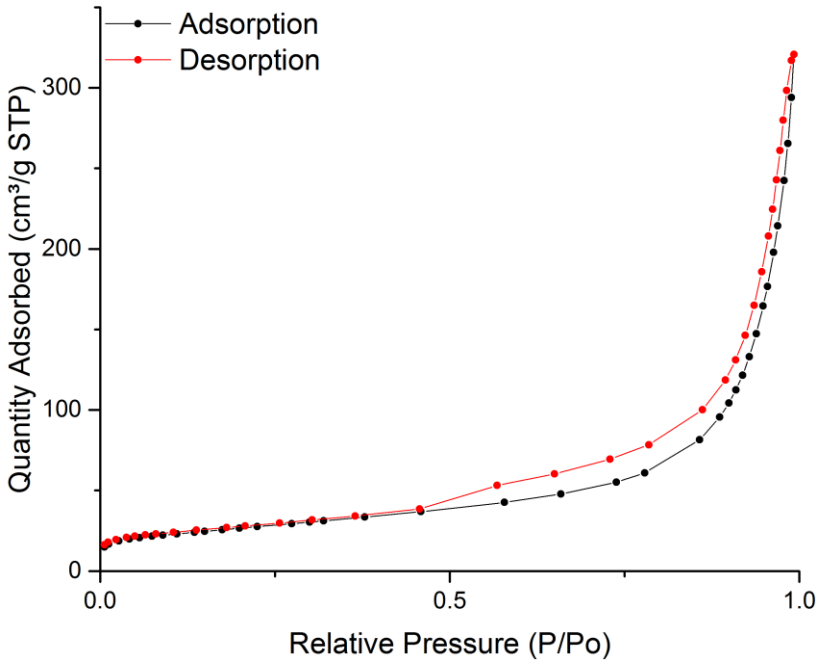


Figure A104. BET adsorption and desorption isotherms for Mg_3Al-SO_4 AMO-LDH thermally treated at 275 °C for 6 hours under vacuum.

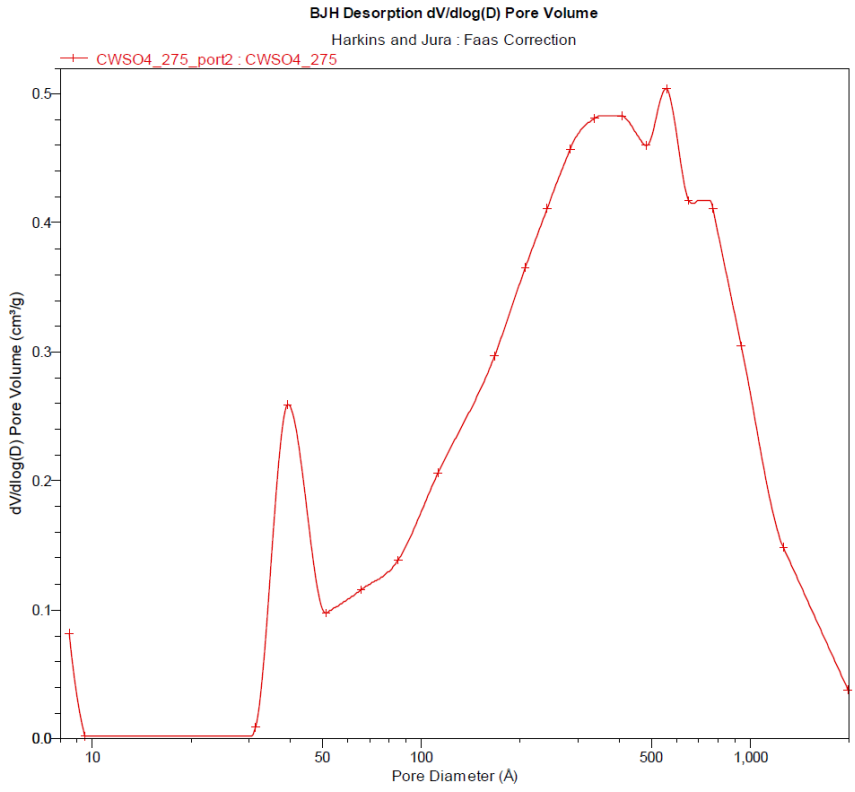


Figure A105. Pore volume distribution for Mg_3Al-SO_4 AMO-LDH thermally treated at 275 °C for 6 hours under vacuum.

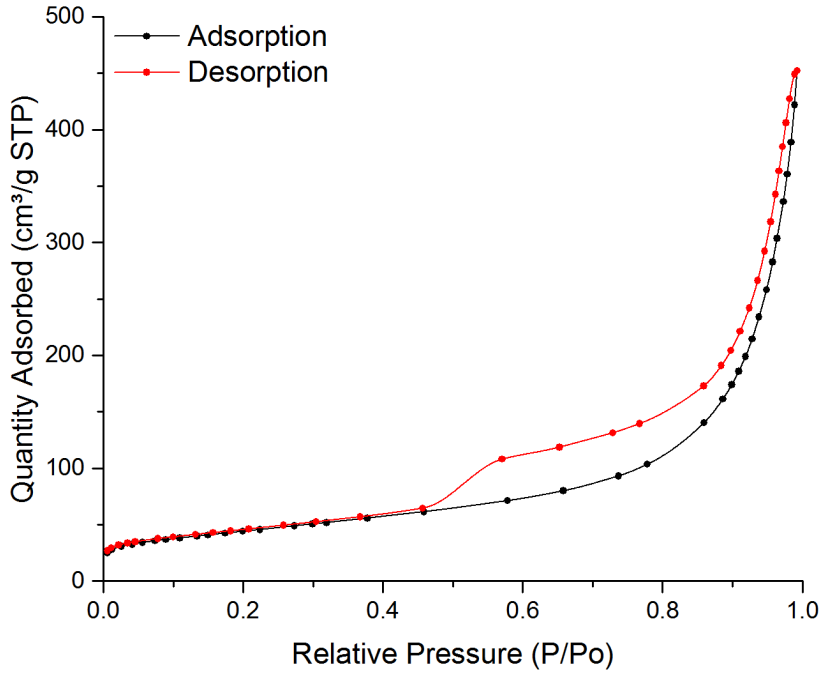


Figure A106. BET adsorption and desorption isotherms for Mg_3Al-SO_4 AMO-LDH thermally treated at 300 °C for 6 hours under vacuum.

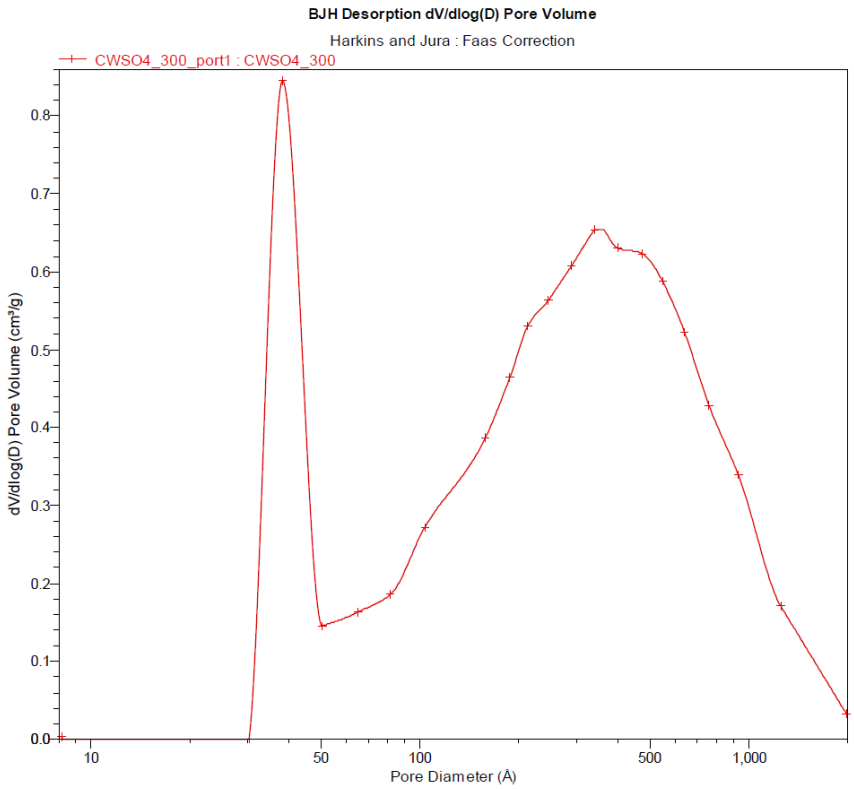


Figure A107. Pore volume distribution for Mg_3Al-SO_4 AMO-LDH thermally treated at 300 °C for 6 hours under vacuum.

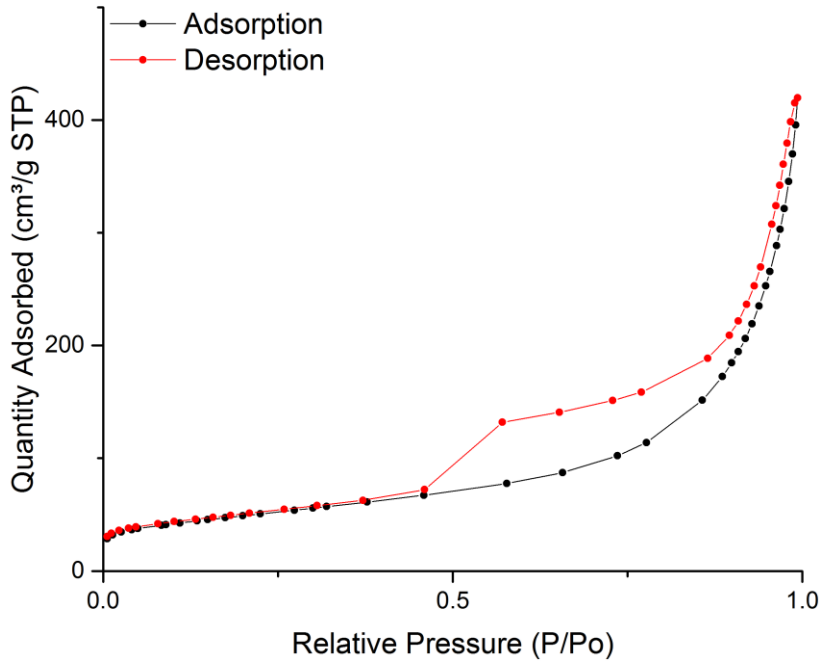


Figure A108. BET adsorption and desorption isotherms for Mg_3Al-SO_4 AMO-LDH thermally treated at 350 °C for 6 hours under vacuum.

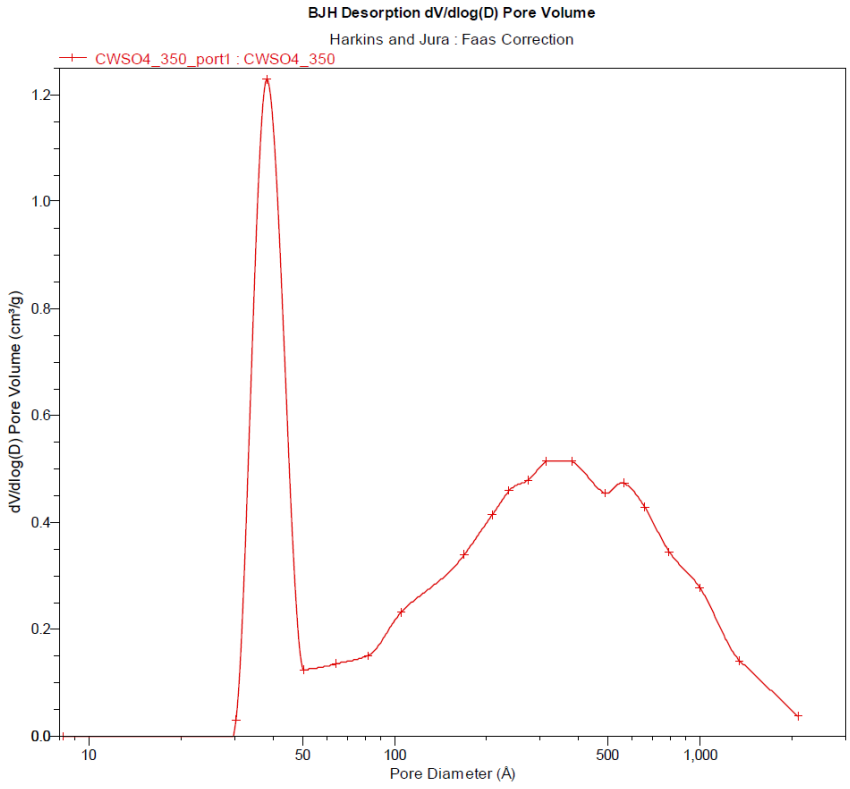


Figure A109. Pore volume distribution for Mg_3Al-SO_4 AMO-LDH thermally treated at 350 °C for 6 hours under vacuum.

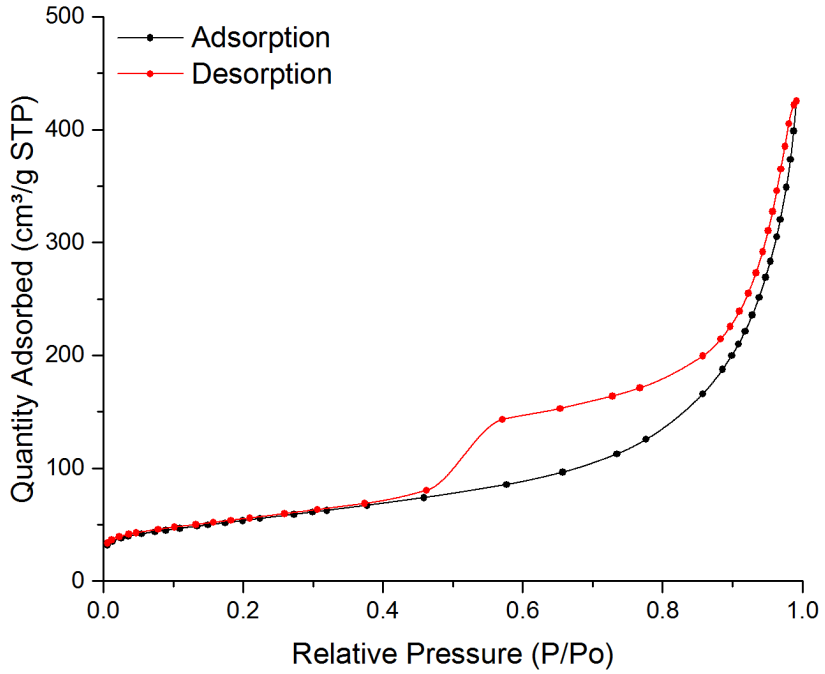


Figure A110. BET adsorption and desorption isotherms for Mg_3Al-SO_4 AMO-LDH thermally treated at 400 °C for 6 hours under vacuum.

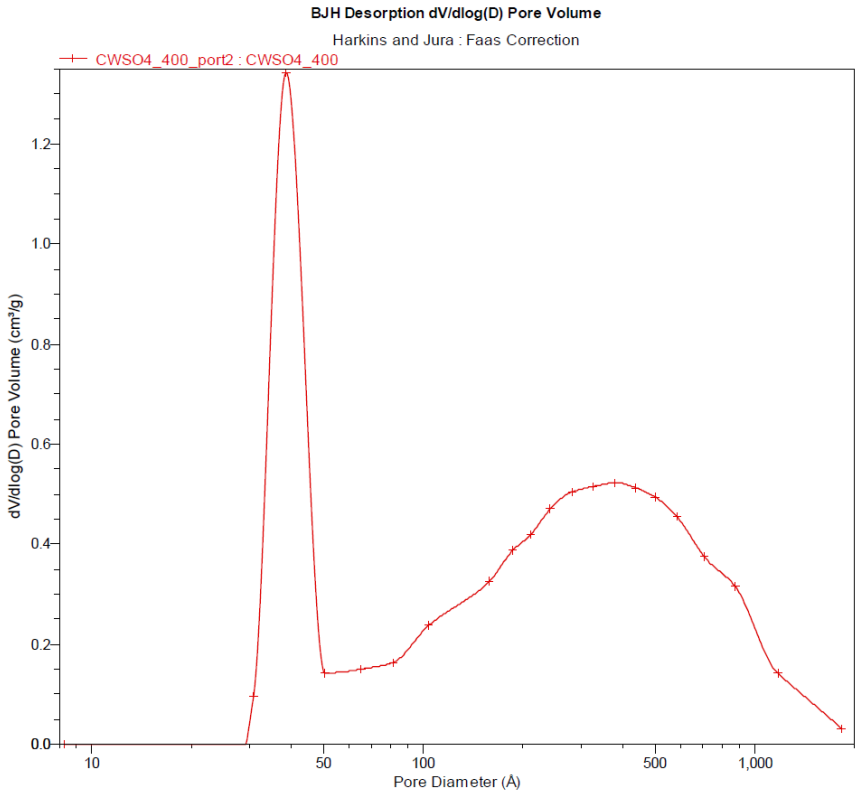


Figure A111. Pore volume distribution for Mg_3Al-SO_4 AMO-LDH thermally treated at 400 °C for 6 hours under vacuum.

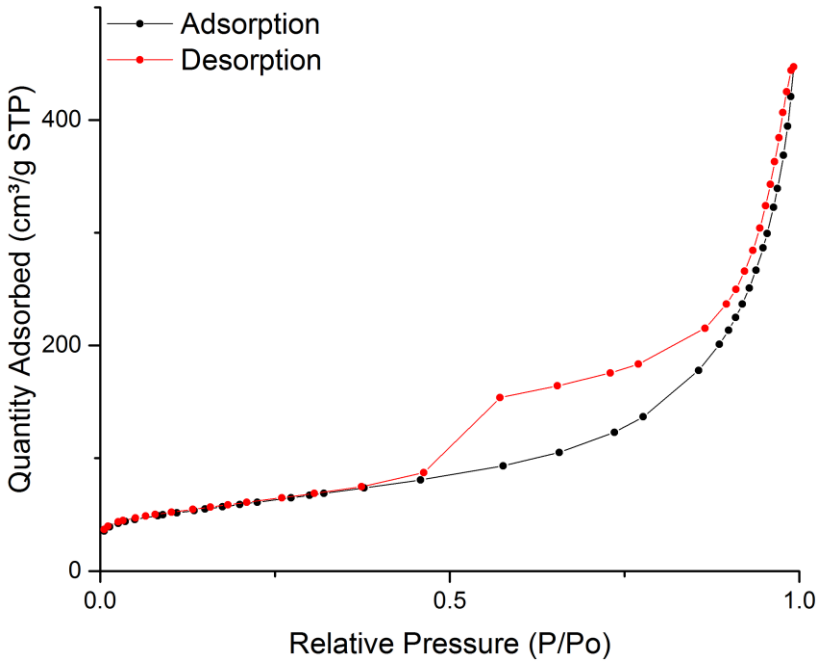


Figure A112. BET adsorption and desorption isotherms for Mg_3Al-SO_4 AMO-LDH thermally treated at 450 °C for 6 hours under vacuum.

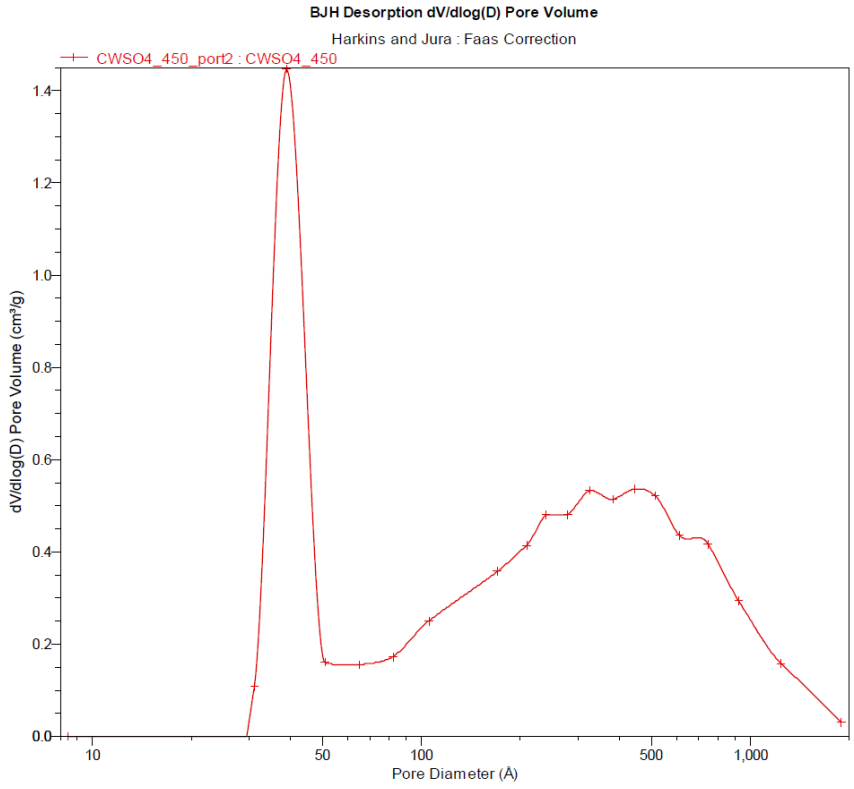


Figure A113. Pore volume distribution for Mg_3Al-SO_4 AMO-LDH thermally treated at 450 °C for 6 hours under vacuum.

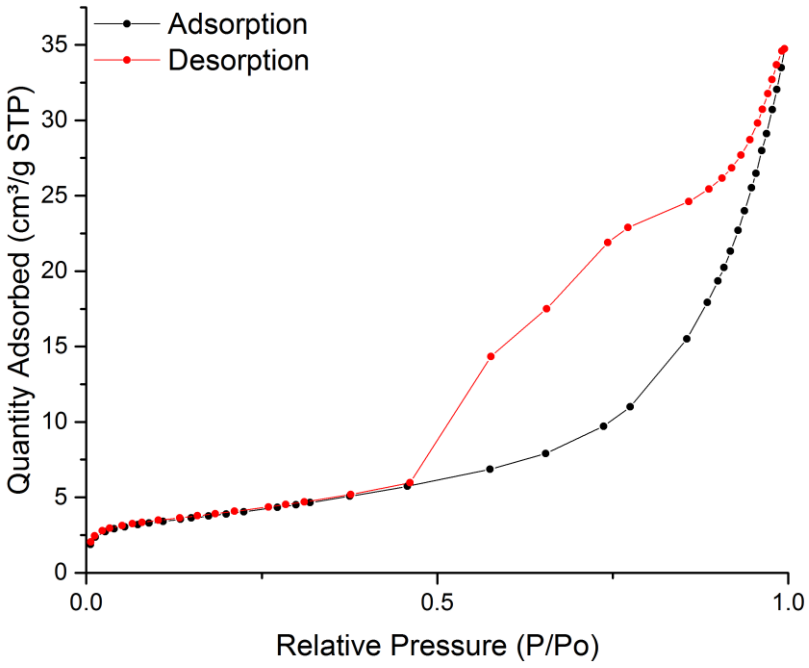


Figure A114. BET adsorption and desorption isotherms for Mg_3Al-CO_3 AMO-LDH thermally treated at 200 °C for 6 hours under vacuum.

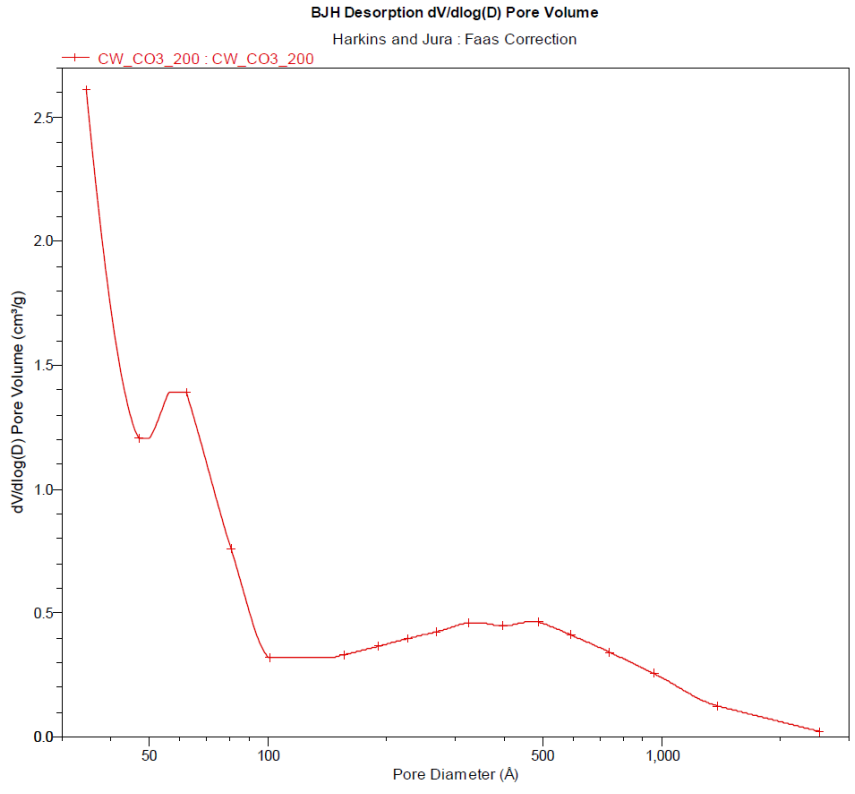


Figure A115. Pore volume distribution for Mg_3Al-CO_3 AMO-LDH thermally treated at 200 °C for 6 hours under vacuum.

Table A9. BET surface areas and pore volumes for the calcined Mg_3Al-SO_4 AMO-LDH samples.

Dehydroxylation temperature (°C)	**BET surface area (m^2g^{-1})**	**BJH total pore volume (cm^3g^{-1})**	**Mesopores 30-50 Å (%)**
23	72	0.40	4.4
100	73	0.41	4.8
150	77	0.43	5.3
200	78	0.45	4.8
250	88	0.46	6.5
275	95	0.49	8.0
300	158	0.69	16.0
350	175	0.65	24.8
400	191	0.65	26.8
450	211	0.70	27.3
Mg_3Al-CO_3 200 °C	313	1.21	-

3.4. SEM imaging

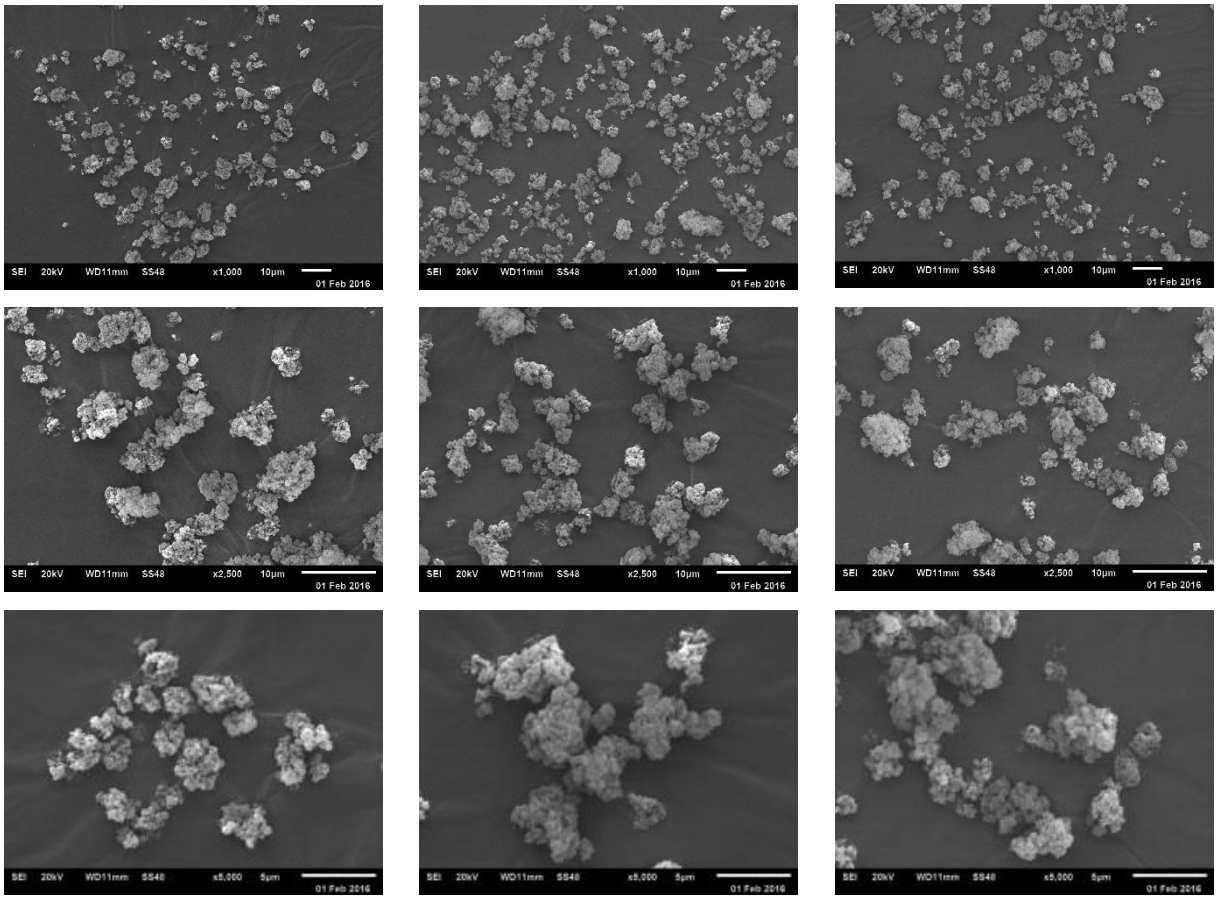


Figure A116. SEM images of Mg_3Al-SO_4 AMO-LDH and the samples thermally treated under vacuum at 200 and 400 °C for 6 hours.

3.5. Surface hydroxyl titrations

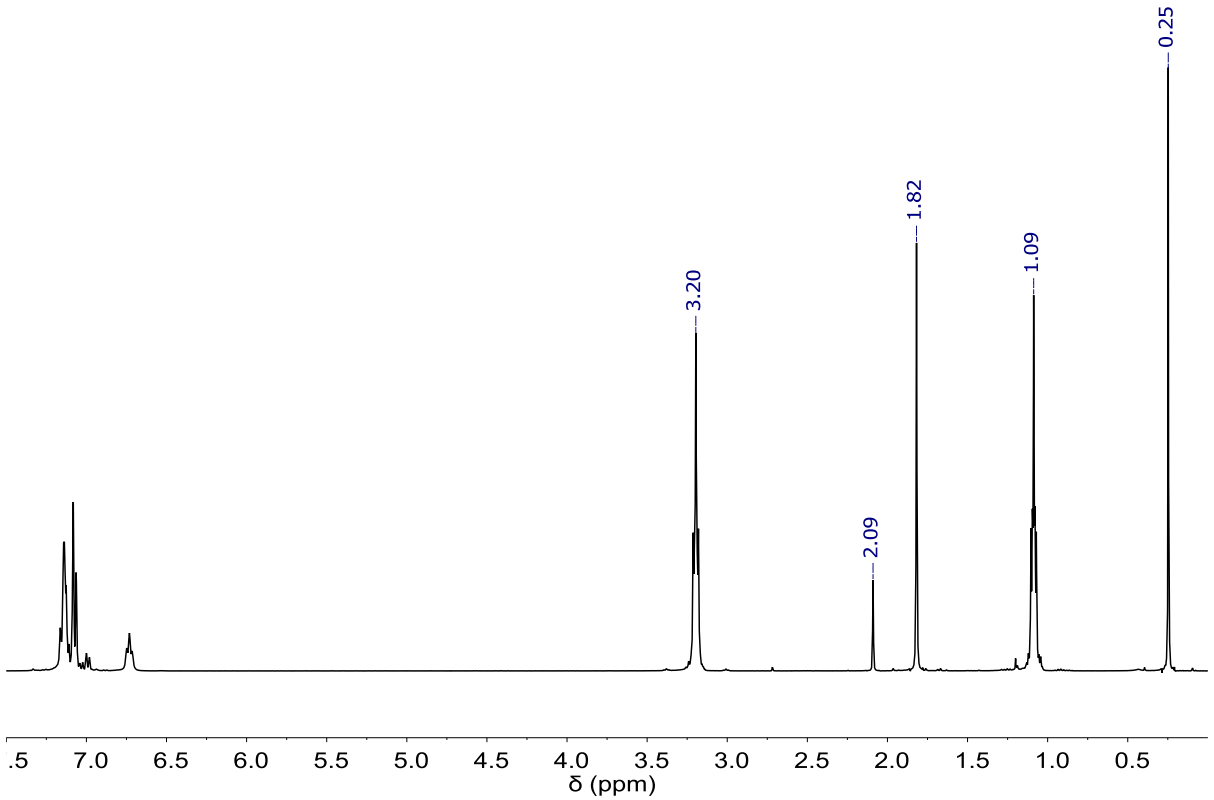


Figure A117. Example ^{1}H NMR spectroscopic titration (400 MHz, 23 °C) of Mg_3Al-SO_4 LDH thermally treated under vacuum at 200 °C for 6 hours in d_6-benzene (7.16 ppm). The toluene resonance at 2.09 ppm was integrated against the $Si(SiMe_3)_4$ standard (0.25 ppm). Resonances at 3.2, 1.82 and 1.09 correspond to $Mg(CH_2Ph)_2(THF)_2$.

Appendix for Chapter Four

4.1. Characterisation of sMAO immobilised complexes

4.1.1. Solid-state NMR (SSNMR) spectroscopy

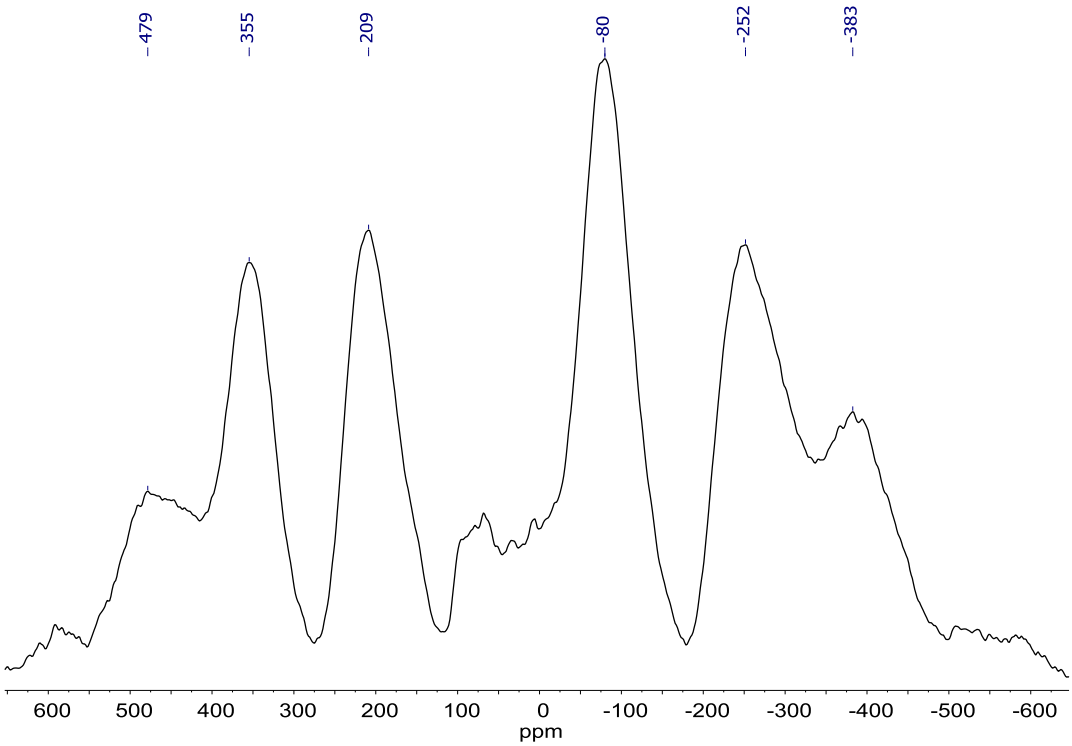


Figure A118. ^{27}Al DPMAS SSNMR spectrum (15 kHz, 400 MHz, 23 °C) of sMAO-**1.5**.

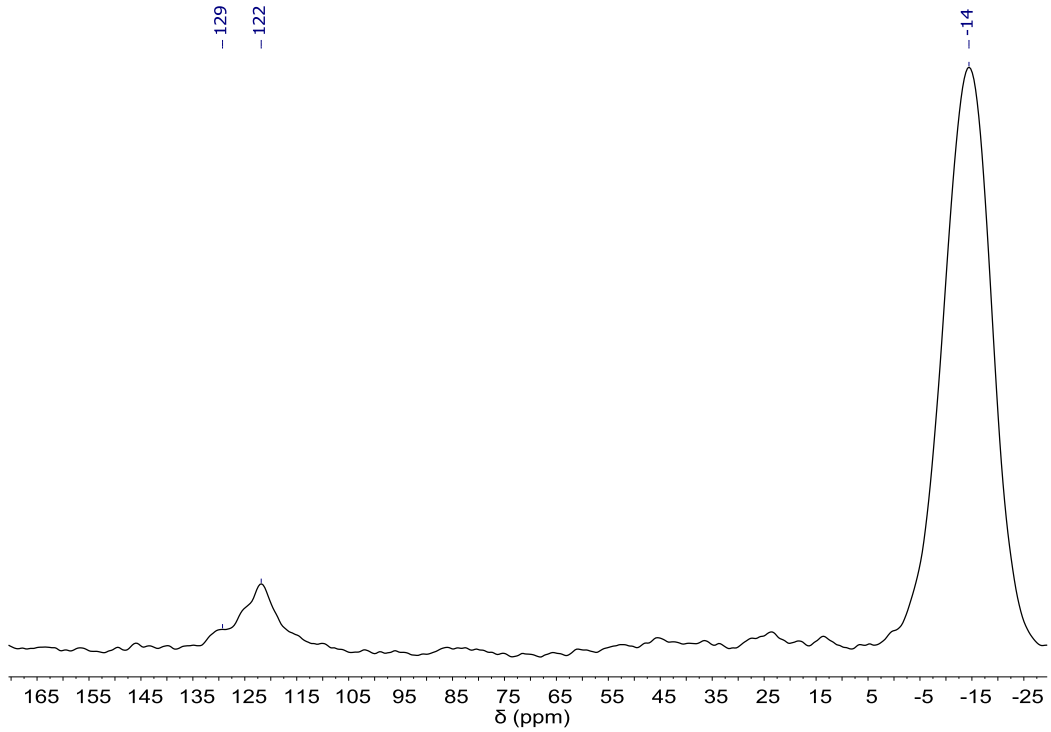


Figure A119. ^{13}C-{^{1}H} CPMAS SSNMR spectrum (10 kHz, 400 MHz, 23 °C) of sMAO-**1.6**.

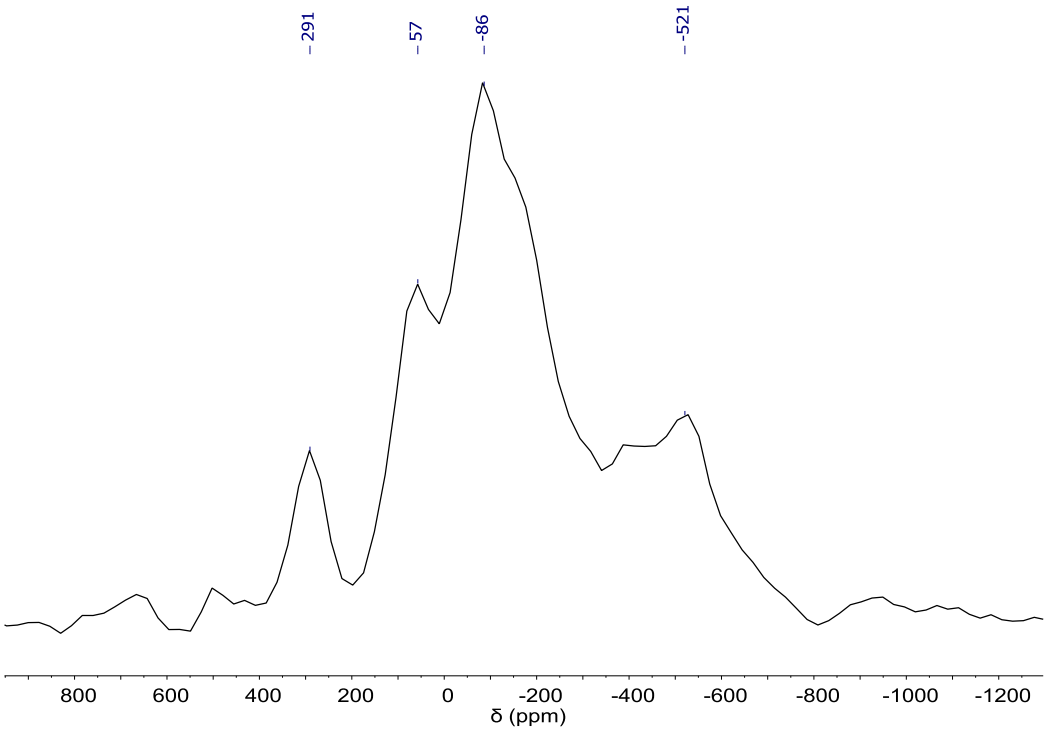


Figure A120. ^{27}Al Hahn echo SSNMR spectrum (24 kHz, 400 MHz, 23 °C) of sMAO-**1.6**.

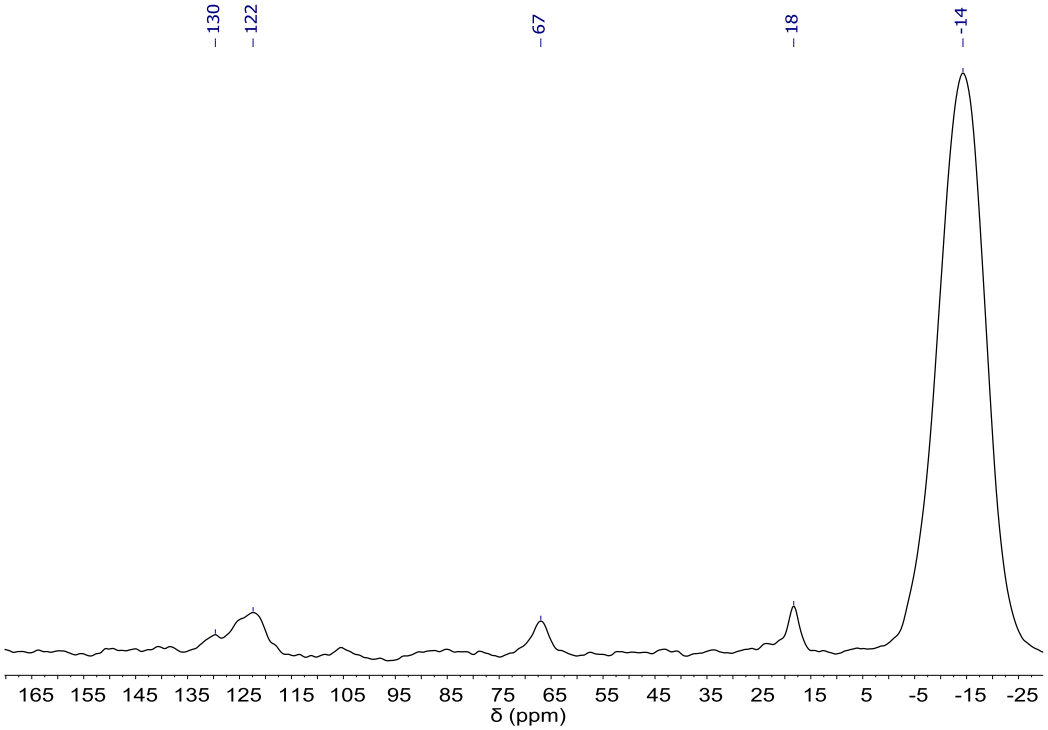


Figure A121. ^{13}C-{^{1}H} CPMAS {^{19}F} decoupled SSNMR spectrum (10 kHz, 400 MHz, 23 °C) of sMAO-**1.7**.

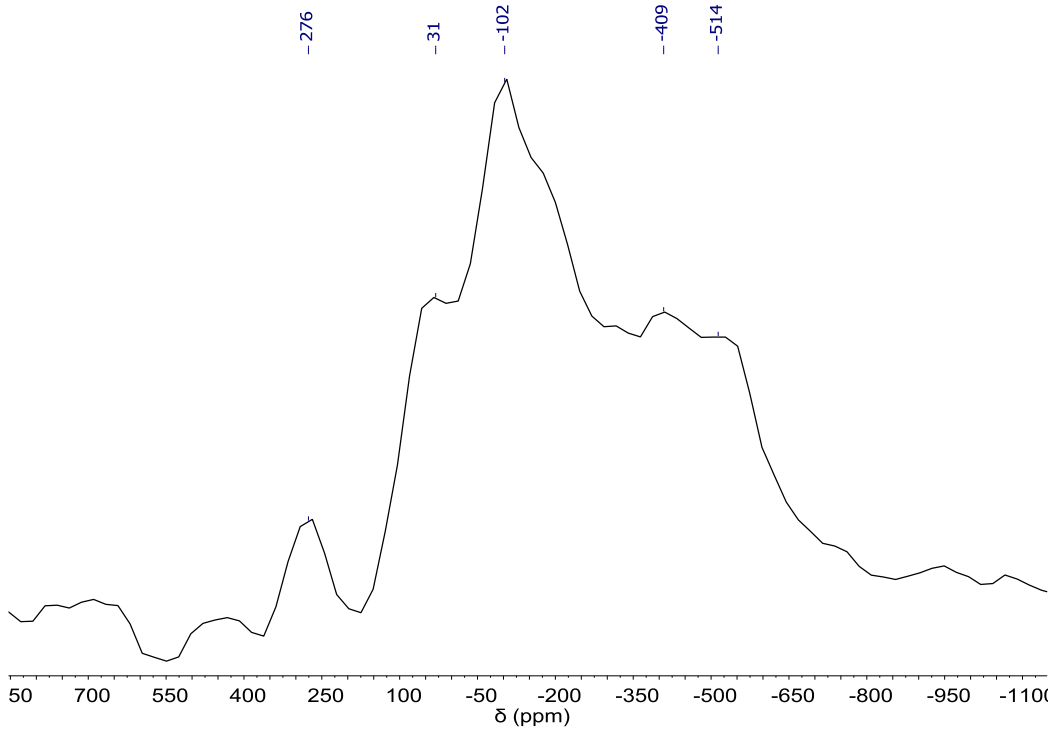


Figure A122. ^{27}Al Hahn echo SSNMR spectrum (24 kHz, 400 MHz, 23 °C) of sMAO-**1.7**.

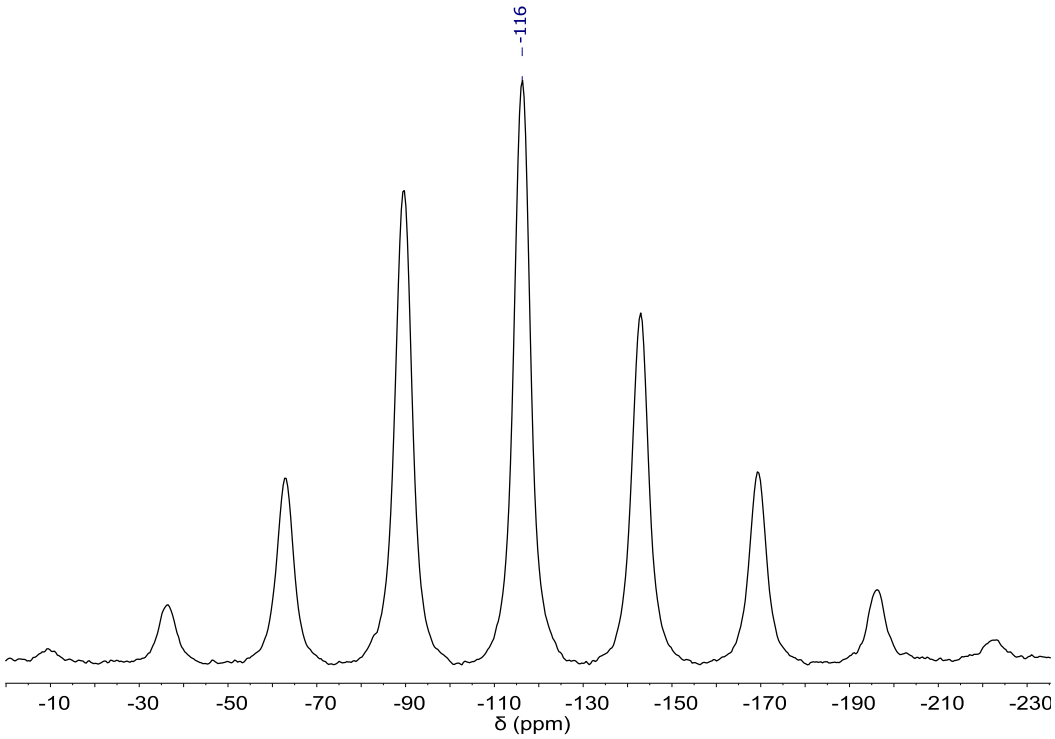


Figure A123. One pulse ^{19}F MAS SSNMR spectrum (10 kHz, 400 MHz, 23 °C) of **2.7**.

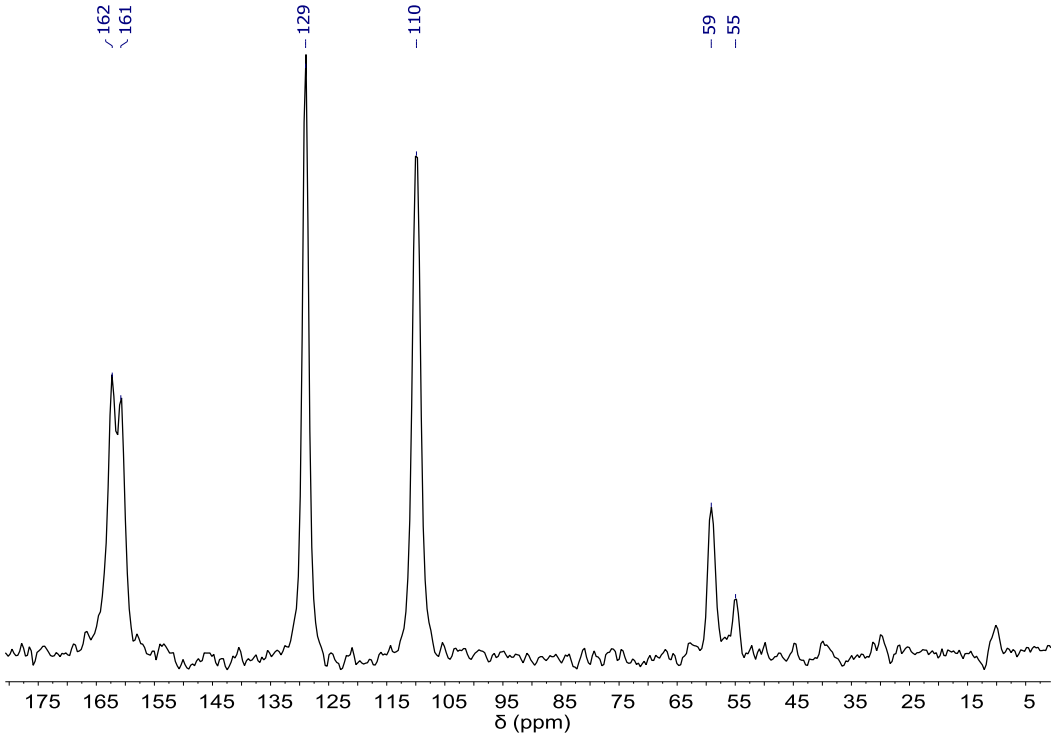


Figure A124. ^{13}C-{^{19}F} CPMAS {^{1}H} decoupled SSNMR spectrum (10 kHz, 400 MHz, 23 °C) of **2.7**.

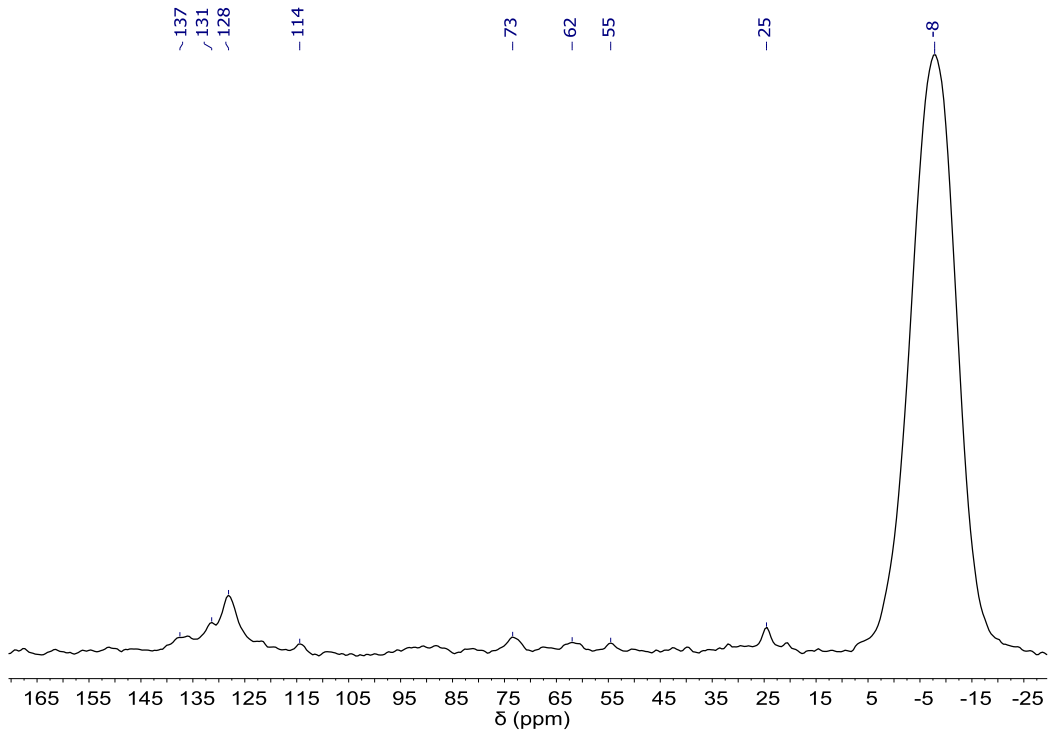


Figure A125. ^{13}C-{^{1}H} CPMAS SSNMR spectrum (10 kHz, 400 MHz, 23 °C) of sMAO-**1.8**.

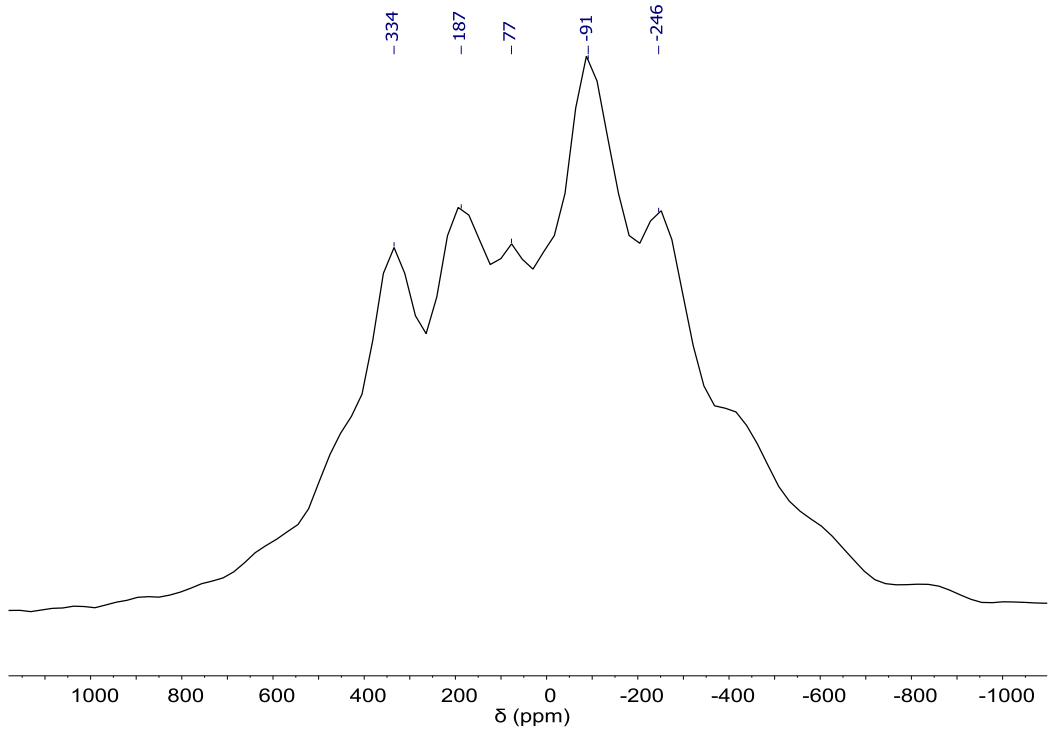


Figure A126. ^{27}Al Hahn echo SSNMR spectrum (15 kHz, 400 MHz, 23 °C) of sMAO-**1.8**.

4.1.2. FTIR spectroscopy

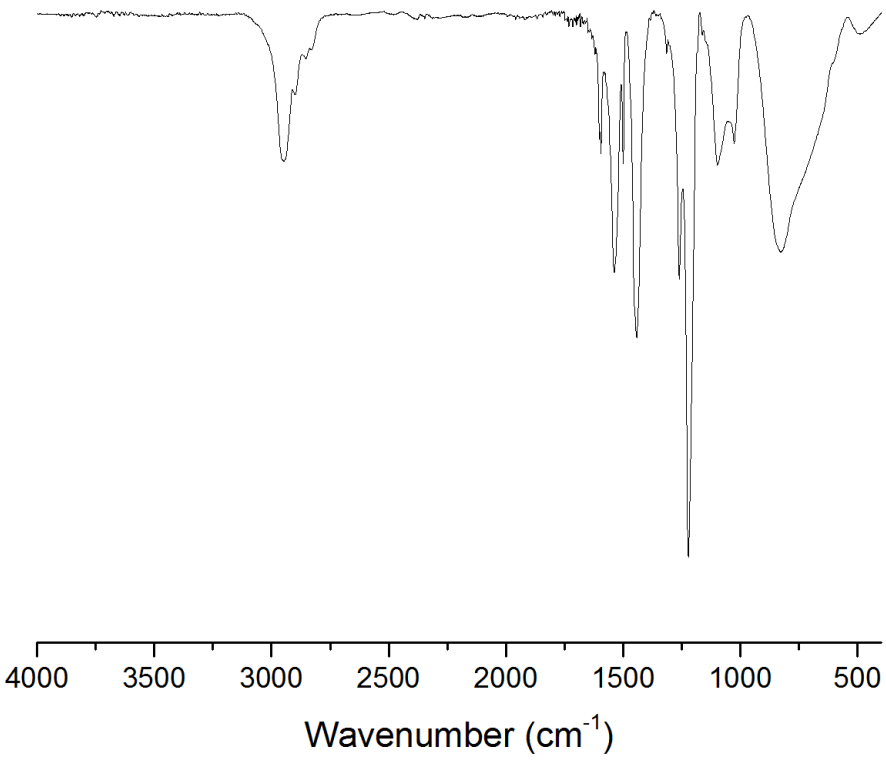


Figure A127. FTIR spectrum of sMAO.

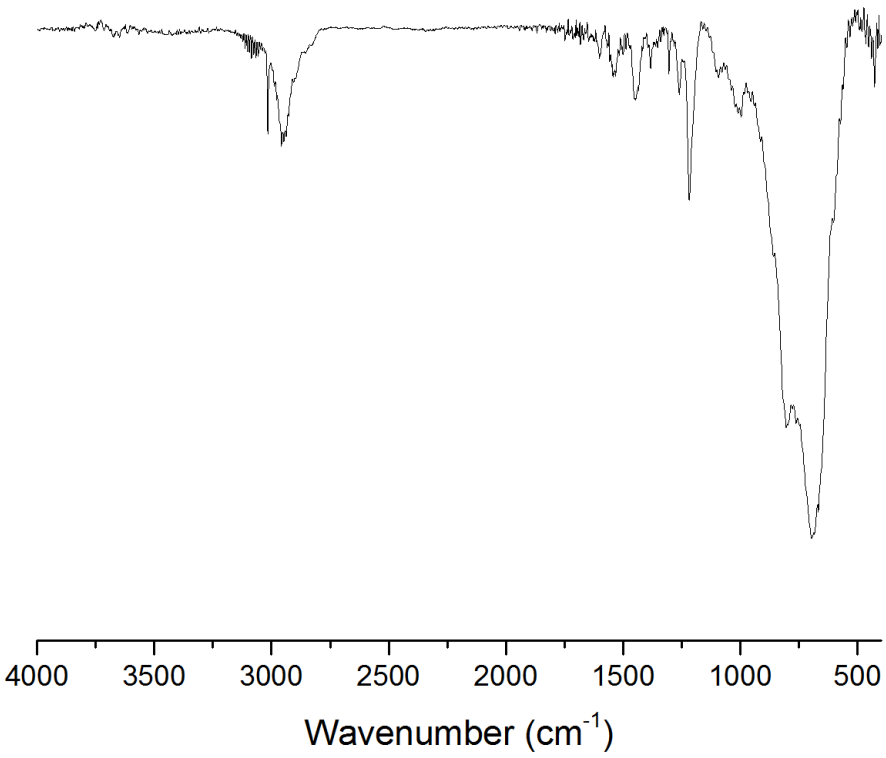


Figure A128. FTIR spectrum of sMAO-**1.1**.

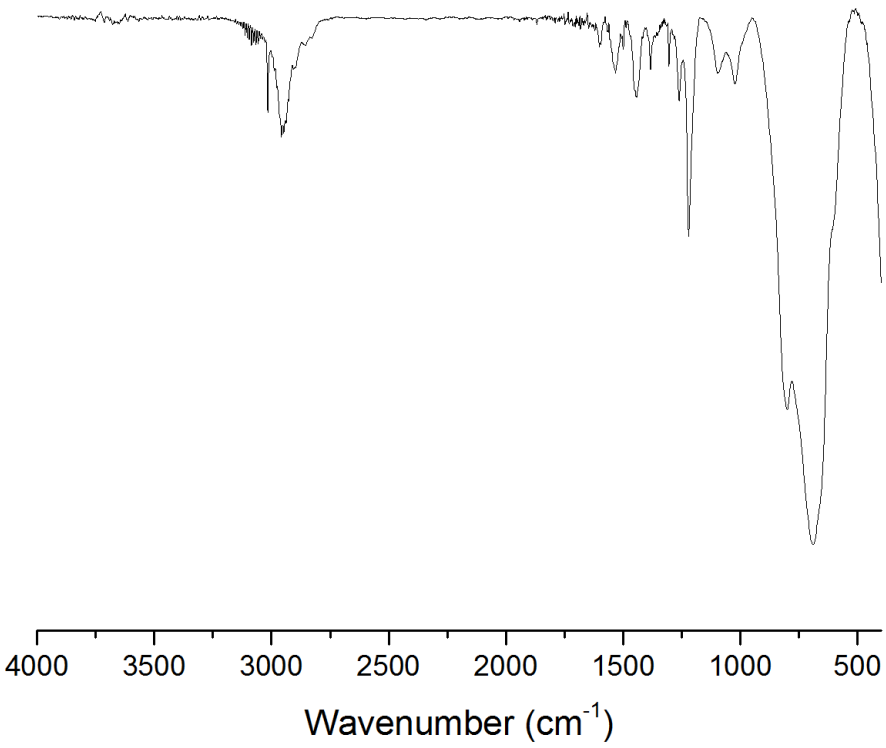


Figure A129. FTIR spectrum of sMAO-**1.2**.

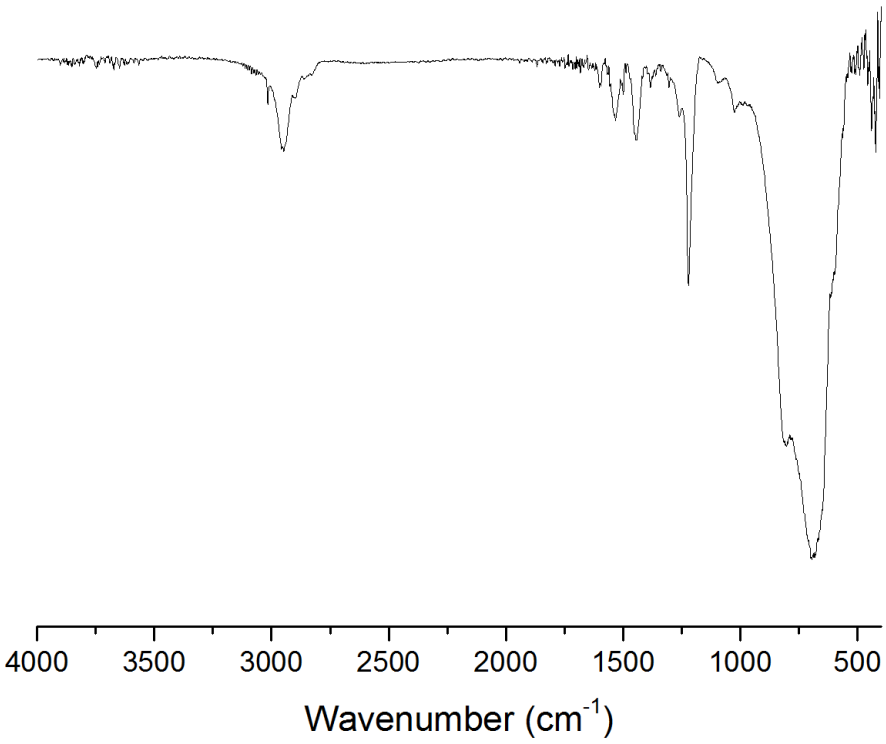


Figure A130. FTIR spectrum of sMAO-**1.3**.

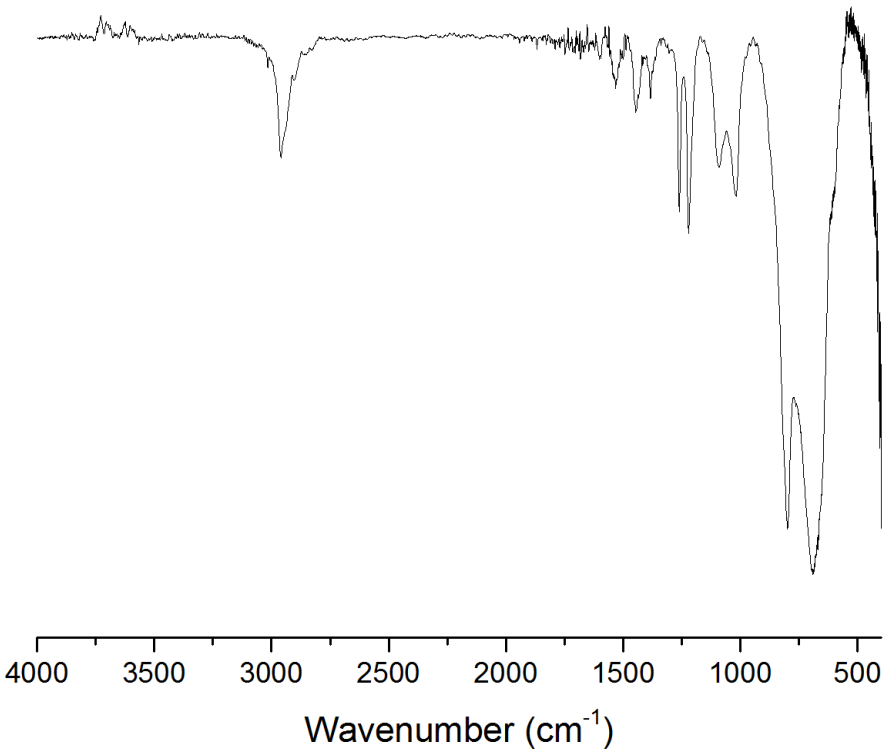


Figure A131. FTIR spectrum of sMAO-**1.4**.

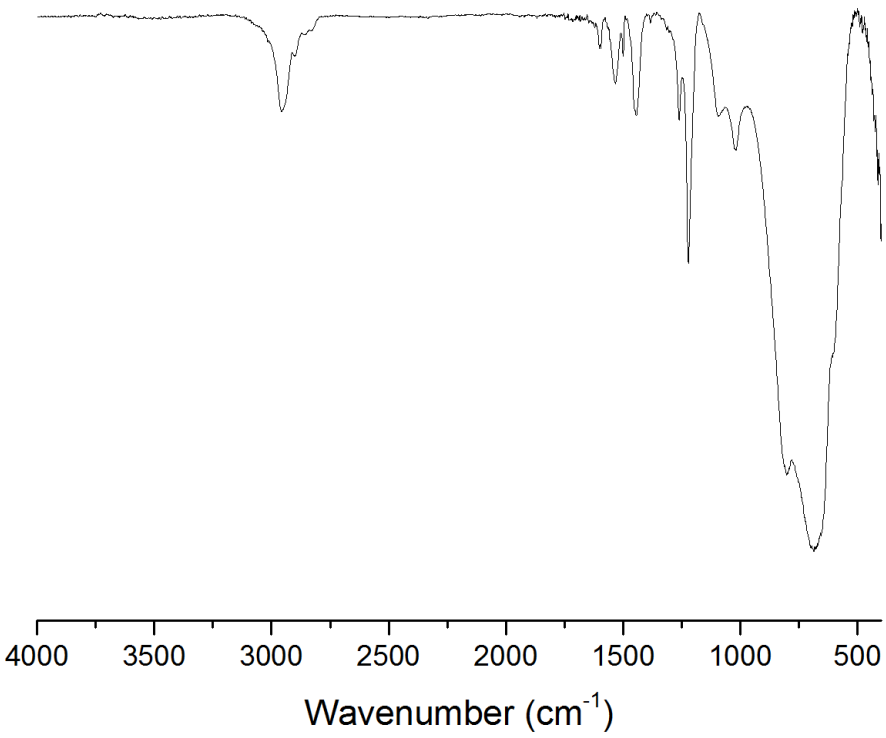


Figure A132. FTIR spectrum of sMAO-**1.5**.

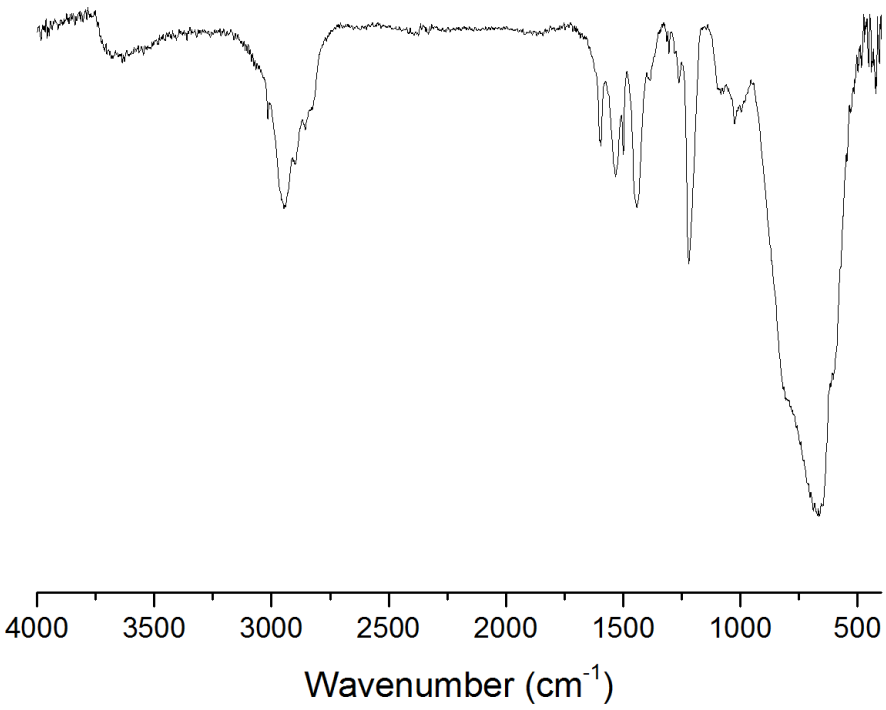


Figure A133. FTIR spectrum of sMAO-**1.6**.

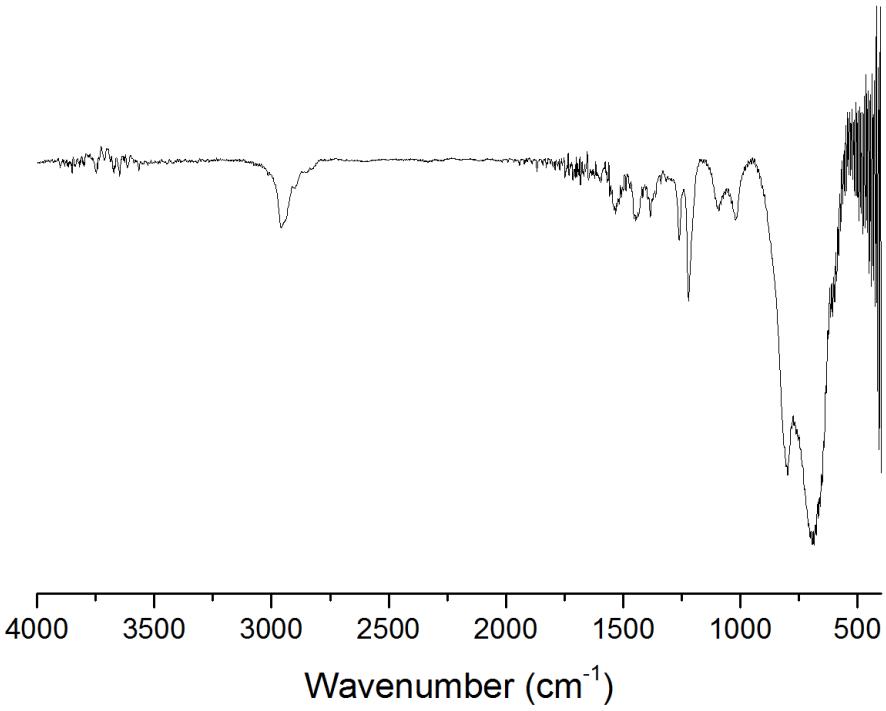


Figure A134. FTIR spectrum of sMAO-**1.7**.

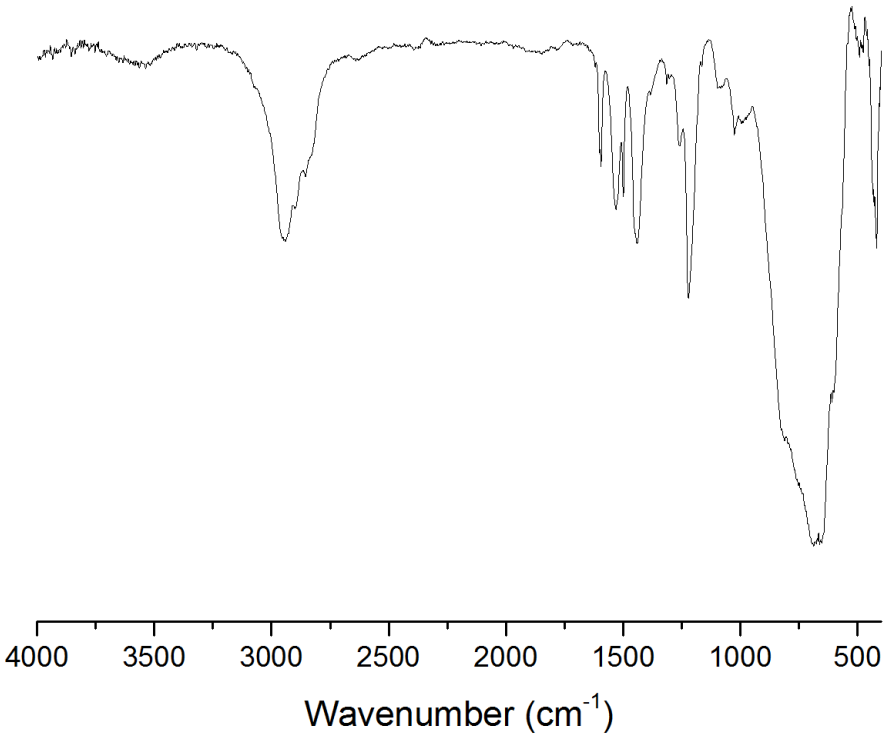


Figure A135. FTIR spectrum of sMAO-**1.8**.

4.2. Oligomerisation studies with sMAO supported complexes

4.2.1. Activity correlations with structural and spectroscopic parameters of W(NR)Cl_4(THF) complexes (1.1–1.8)

Table A10. Pearson correlation of structural parameters determined from the molecular structures and spectroscopic parameters from solution NMR spectroscopy for all W(NR)Cl_4(THF) complexes (**1.1**–**1.8**).

	W–N (Å)	**W–N–C_{ipso} (°)**	**δ C_{ipso} (ppm)**	**$G_{2.28}$(imido) (%)**	**pKa (RNH_3^+)**
TOF ($mol_{C_2H_4} mol^{-1}_W h^{-1}$)	−0.16	−0.31	0.52	−0.11	−0.58

TOF calculated after 8 hours.

Table A11. Pearson correlation of structural parameters determined from the molecular structures and spectroscopic parameters from solution NMR spectroscopy for the phenyl and alkyl substituted W(NR)Cl_4(THF) complexes (**1.1**–**1.5**).

	W–N (Å)	**W–N–C_{ipso} (°)**	**δ C_{ipso} (ppm)**	**$G_{2.28}$(imido) (%)**	**pKa (RNH_3^+)**
TOF ($mol_{C_2H_4} mol^{-1}_W h^{-1}$)	−0.33	−0.21	0.81	0.20	−0.34

TOF calculated after 8 hours.

Table A12. Pearson correlation of structural parameters determined from the molecular structures (**2.1**–**2.3** and **2.5**–**2.7**) and spectroscopic parameters from solution NMR spectroscopy for all the W(NR)Me_3Cl complexes (**2.1**–**2.8**).

	W–N (Å)	**W–Cl (Å)**	**W–N–C_{ipso} (°)**	**δ C_{ipso} (ppm)**	**δ W–Me (ppm)**	**$G_{2.28}$(imido) (%)**
TOF ($mol_{C_2H_4} mol^{-1}_W h^{-1}$)	0.31	−0.28	−0.24	0.06	0.55	0.31

TOF calculated after 8 hours.

4.2.2. Reactivity towards 1-hexene and 1-octene

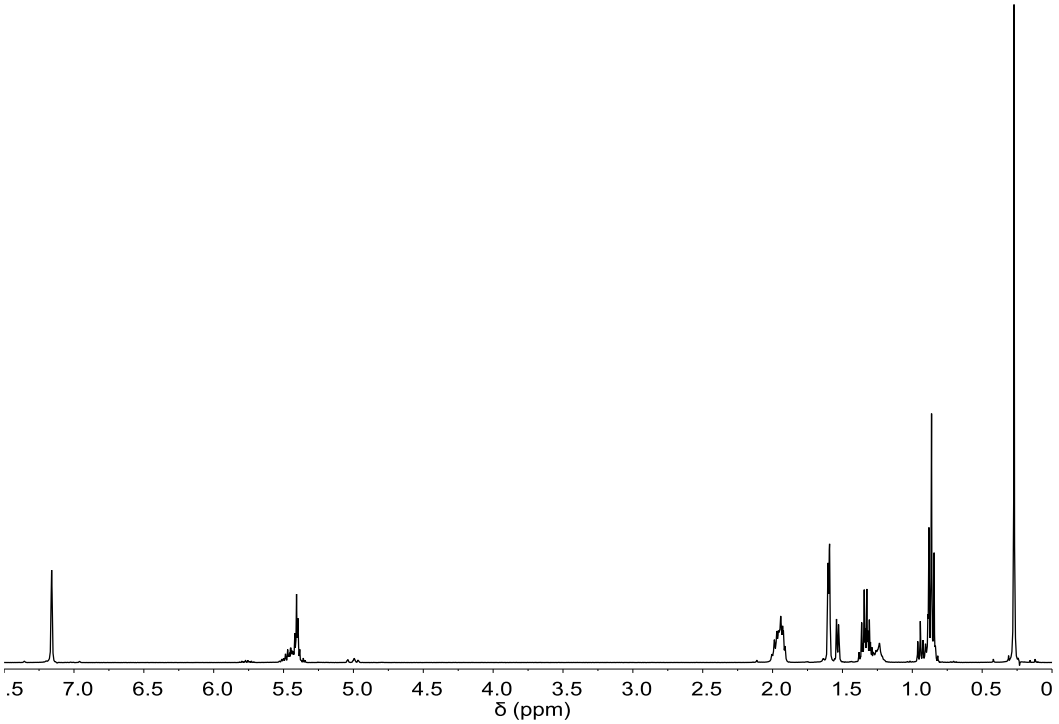


Figure A136. ^{1}H NMR spectrum (400 MHz, 23 °C) of the reaction between sMAO-**1.7** (Al/W = 150) and 1-hexene after 4 hours at 75 °C in d_6-benzene (7.16 ppm) containing $Si(SiMe_3)_4$ (0.27 ppm), showing almost complete isomerisation of the α-olefin to *cis*- and *trans*-2-hexene.

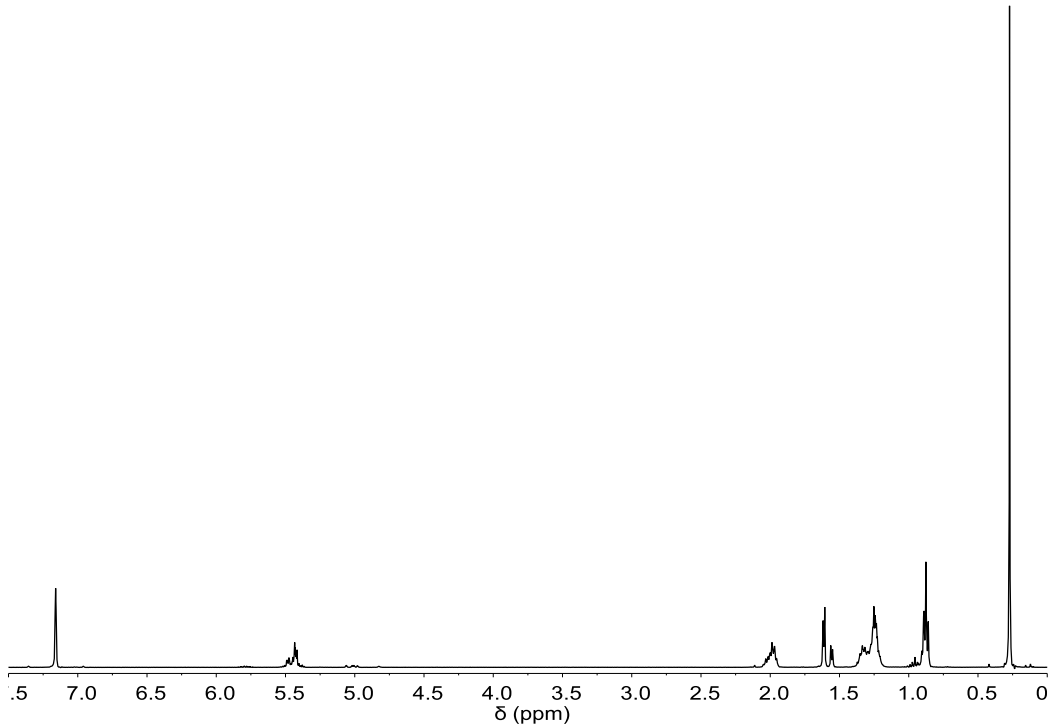


Figure A137. ^{1}H NMR spectrum (400 MHz, 23 °C) of the reaction between sMAO-**1.7** (Al/W = 150) and 1-octene after 4 hours at 75 °C in d_6-benzene (7.16 ppm) containing $Si(SiMe_3)_4$ (0.27 ppm), showing almost complete isomerisation of the α-olefin to *cis*- and *trans*-2-octene.

4.2.3. Temperature study of ethylene oligomerisation utilising sMAO-1.5

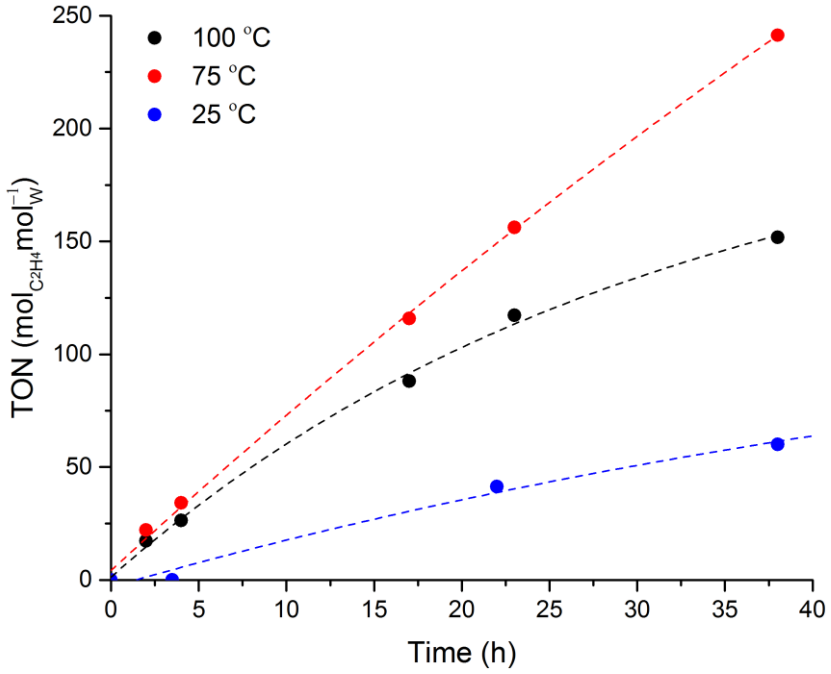


Figure A138. Variation in the temperature for the oligomerisation of ethylene (1 bar) with sMAO-**1.5** (25, 75 and 100 °C). $[W]_0$ = 0.41 µmol, Al/W = 150, 5 mg catalyst, d_6-benzene, pyridine internal standard.

4.2.4. Solvent study

Table A13. Dielectric constants and donor numbers for solvents used in this study.

Solvent	Dielectric Constant (ε)	Donor Number
Octane	Heptane = 1.9	Heptane = 0
Benzene	2.3	0.1
Toluene	2.4	0.1
THF	7.6	20
DCM	8.9	1
Pyridine	12.4	33.1
Chlorobenzene	5.62	3.3
Bromobenzene	5.4	3
Mesitylene	*p*-Xylene = 2.3	10

4.2.5. Loading study

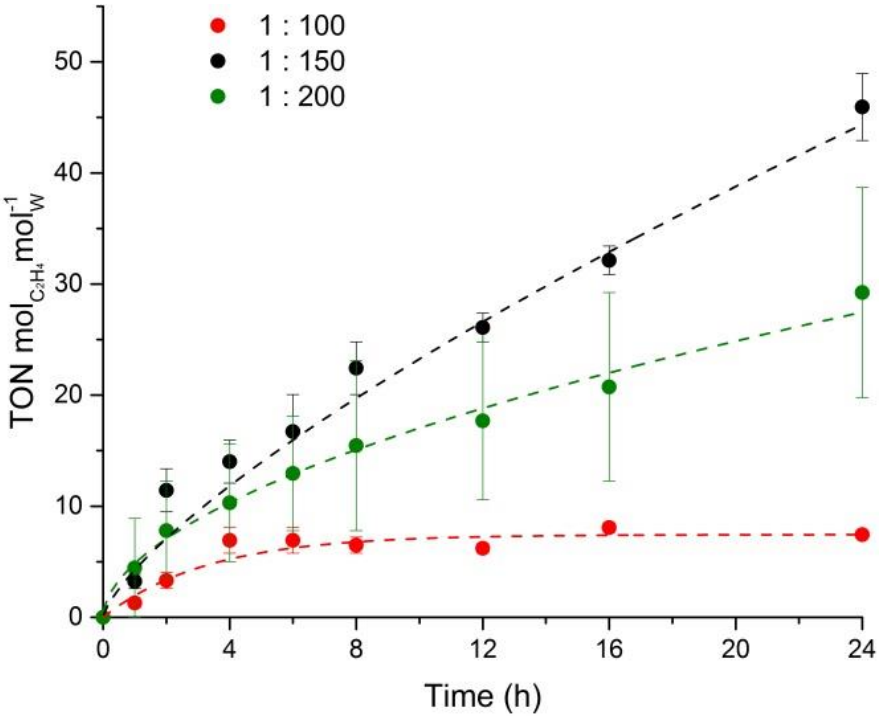


Figure A139. Effect of complex loading on the oligomerization activity of sMAO-**1.6**. Al/W = 100, 150 and 200.

4.2.6. Scale-up polymer analysis

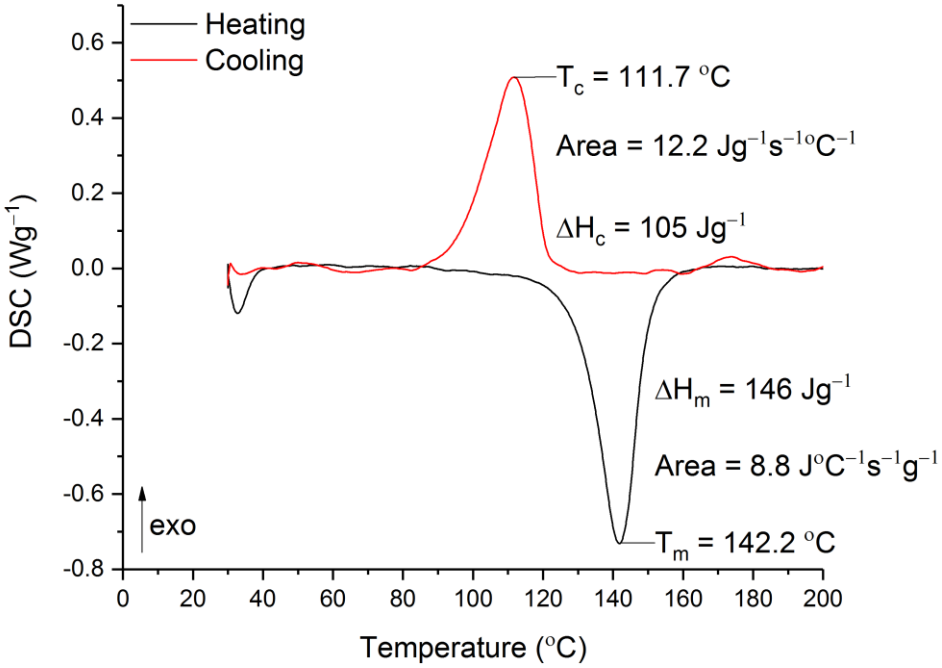


Figure A140. DSC analysis of polyethylene produced by sMAO-**1.5**. 100 mg cat., toluene, 75 °C, 19 bar ethylene, 24 h, 1 drop TEA added prior to ethylene addition.

4.3. Layered double hydroxide (LDH) supported complexes

4.3.1. Variation of the interlayer anion

4.3.1.1. SSNMR spectroscopy

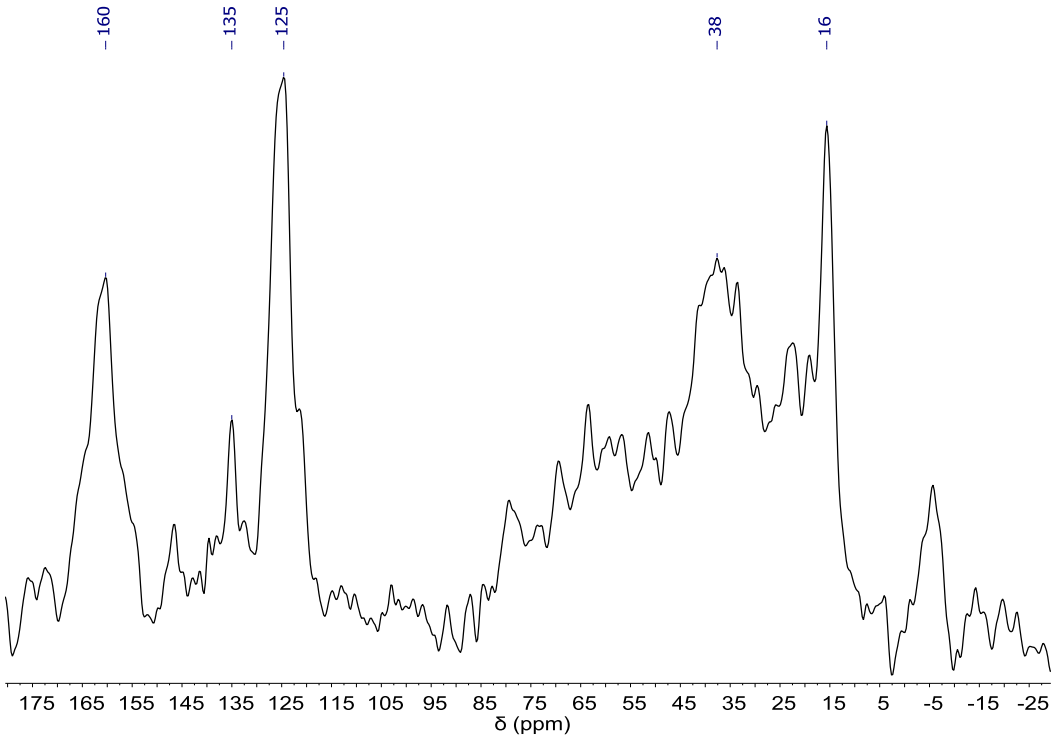


Figure A141. ^{13}C-{^{1}H} CPMAS SSNMR spectrum (10 kHz, 400 MHz, 23 °C) of LDH$(NO_3)_{150}$-**1.5**.

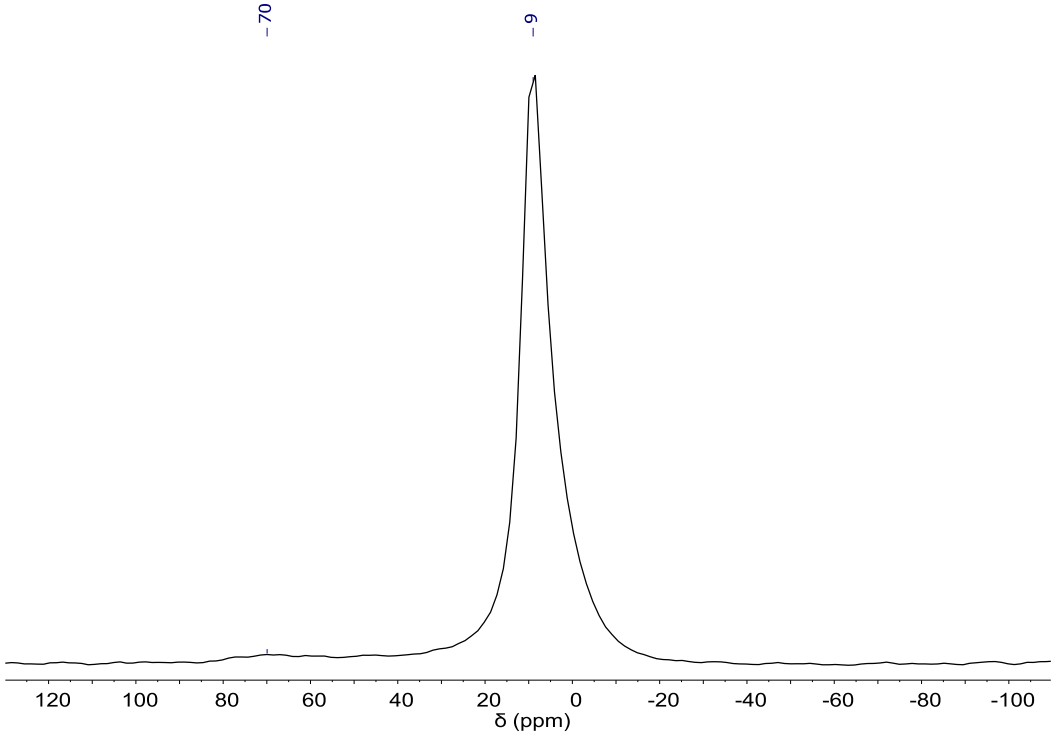


Figure A142. ^{27}Al DPMAS SSNMR spectrum (15 kHz, 400 MHz, 23 °C) of LDH$(NO_3)_{150}$-**1.5**.

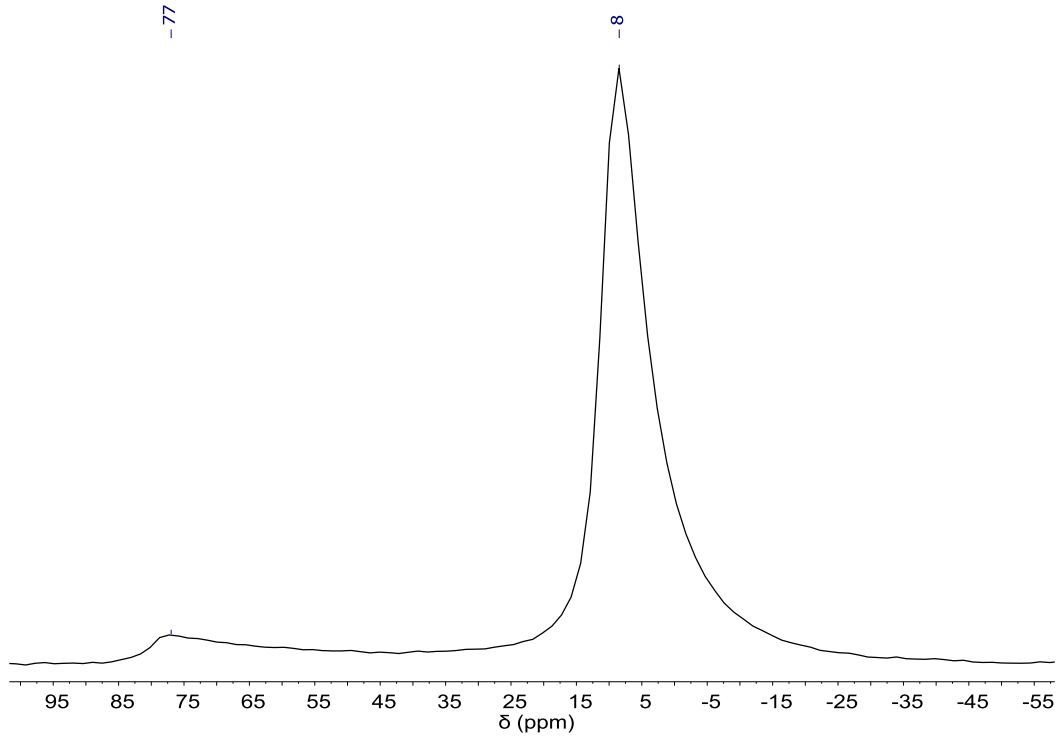


Figure A143. ^{27}Al DPMAS SSNMR spectrum (15 kHz, 400 MHz, 23 °C) of LDH$(SO_4)_{150}$-**1.5**.

4.3.1.2. FTIR spectroscopy

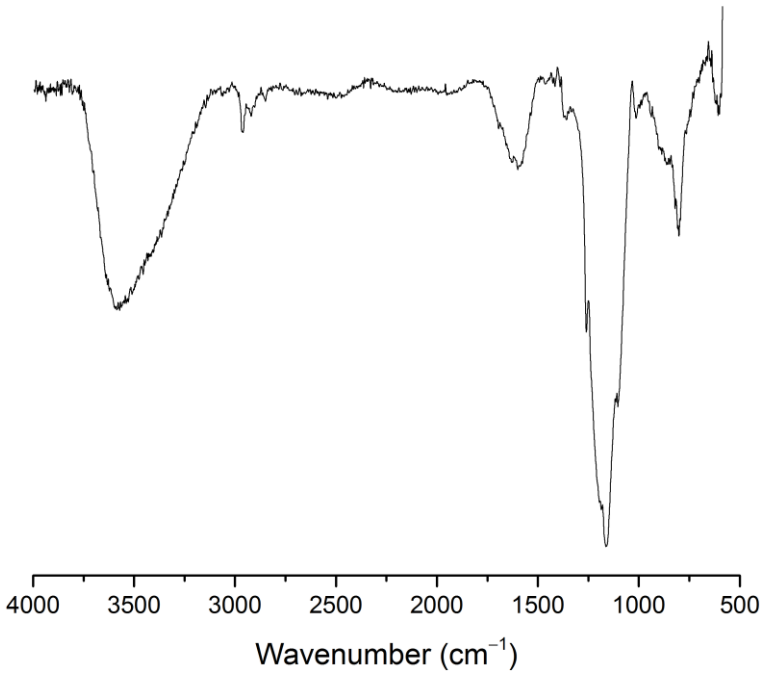


Figure A144. FTIR spectrum of LDH$(SO_4)_{150}$.

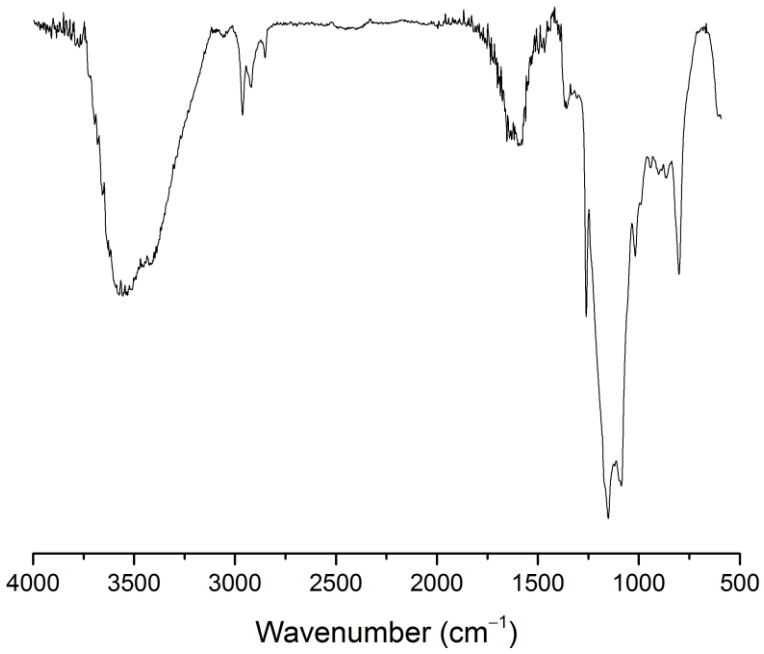


Figure A145. FTIR spectrum of LDH$(SO_4)_{150}$-**1.5**.

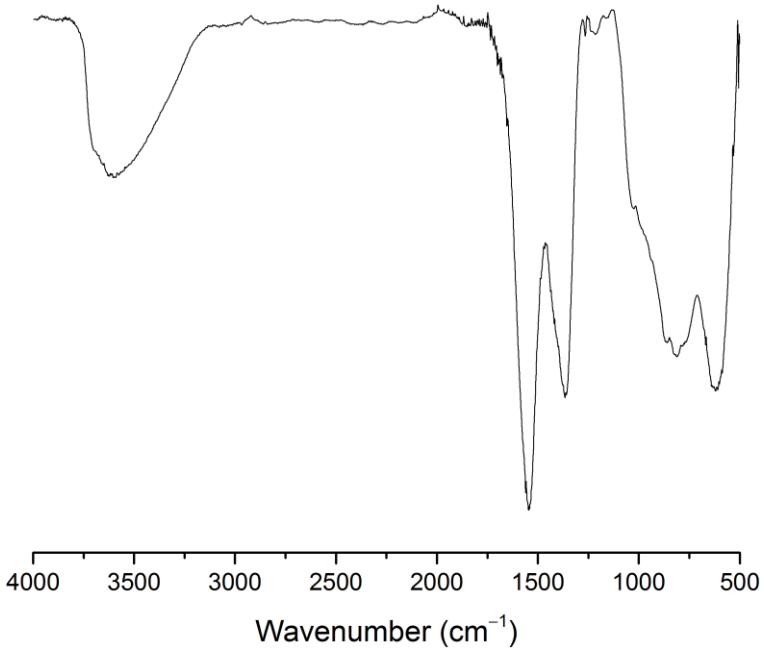


Figure A146. FTIR spectrum of LDH$(CO_3)_{150}$.

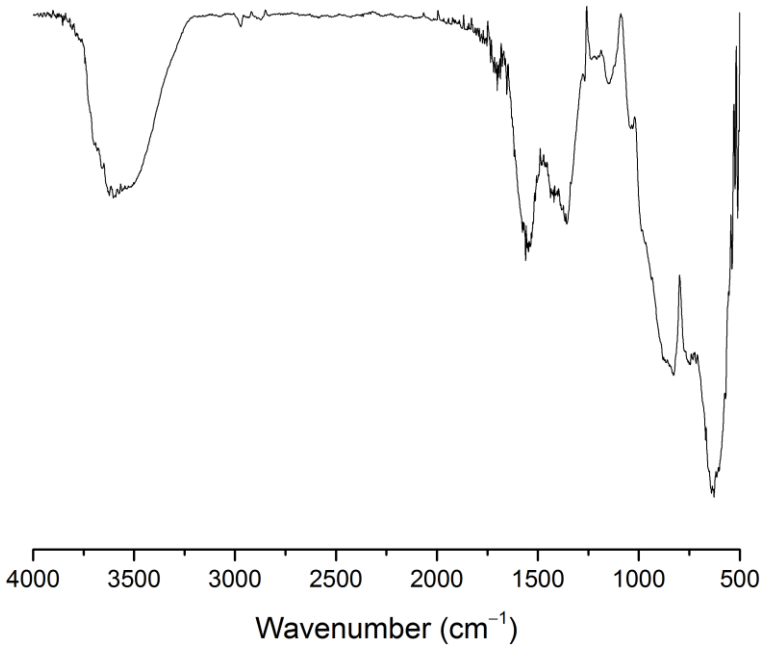


Figure A147. FTIR spectrum of LDH$(CO_3)_{150}$-**1.5**.

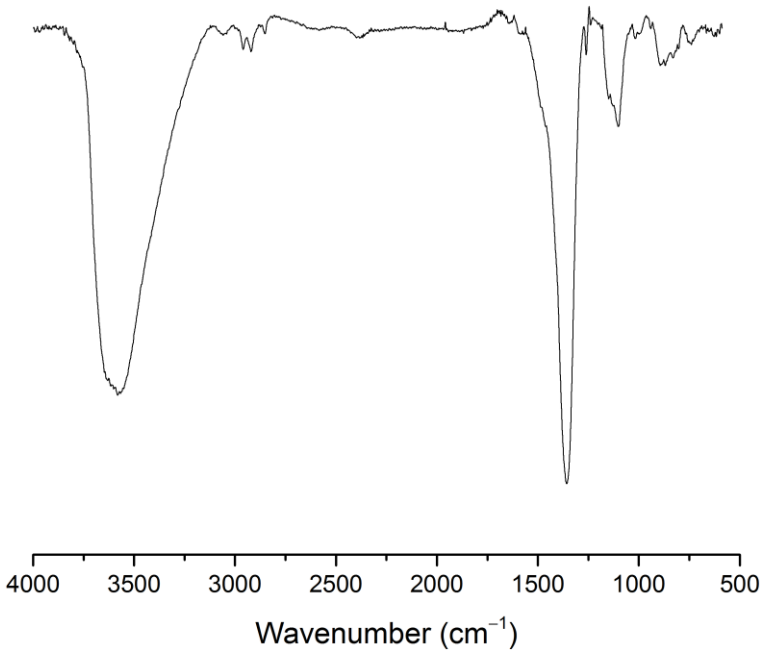


Figure A148. FTIR spectrum of LDH$(NO_3)_{150}$.

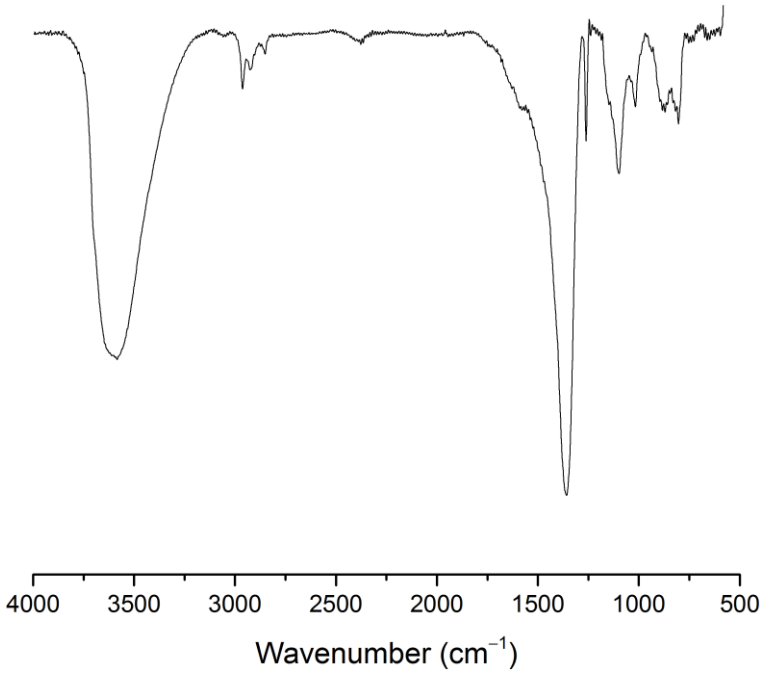


Figure A149. FTIR spectrum of LDH$(NO_3)_{150}$-**1.5**.

4.3.2. Impregnation with MAO

4.3.2.1. LDH$(SO_4)_{150}$-MAO-1.5

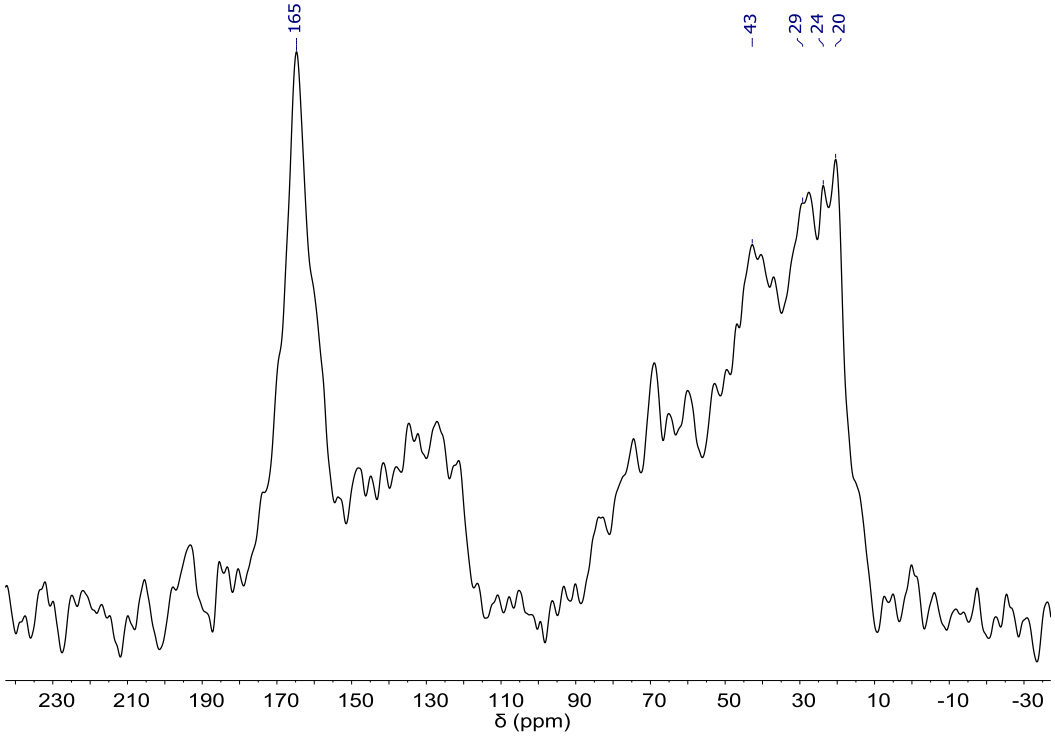


Figure A150. ^{13}C-{^{1}H} CPMAS SSNMR spectrum (10 kHz, 400 MHz, 23 °C) of LDH$(SO_4)_{150}$-MAO-**1.5**.

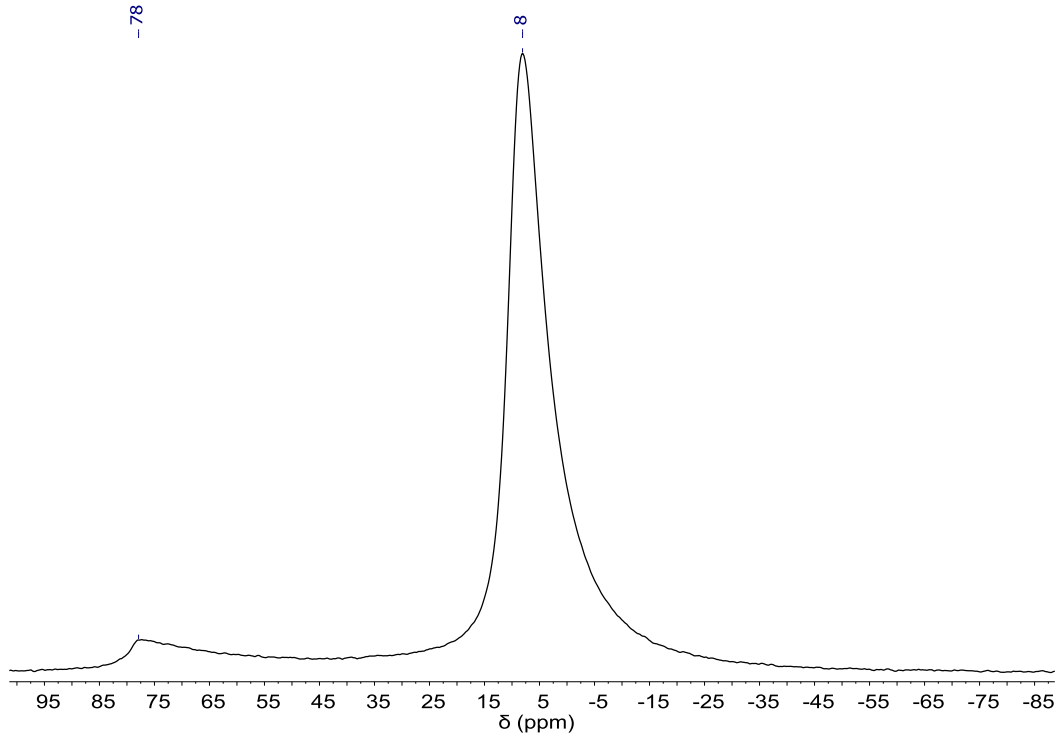


Figure A151. ^{27}Al DPMAS SSNMR spectrum (15 kHz, 400 MHz, 23 °C) of LDH$(SO_4)_{150}$-MAO-**1.5**.

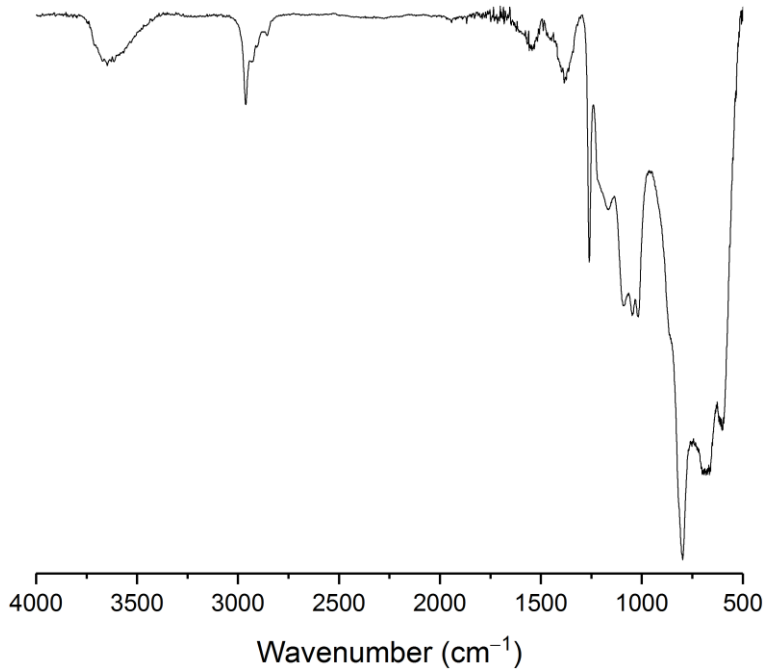


Figure A152. FTIR spectrum of LDH$(SO_4)_{150}$-MAO-**1.5**.

4.3.2.2. Immobilisation of a mixture of 1.5 and MAO on $LDH(SO_4)_{150}$ by incipient wetness

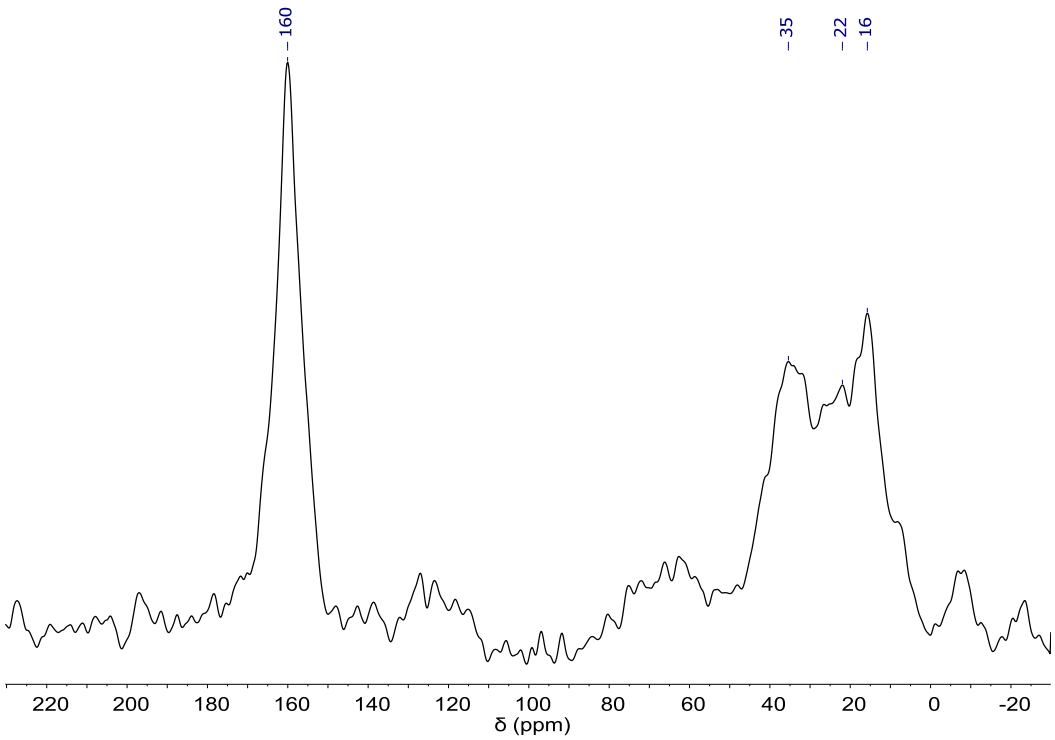


Figure A153. ^{13}C-{^{1}H} CPMAS SSNMR spectrum (10 kHz, 400 MHz, 23 °C) of $LDH(SO_4)_{150}$-(**1.5** + 2MAO**),** formed by incipient wetness.

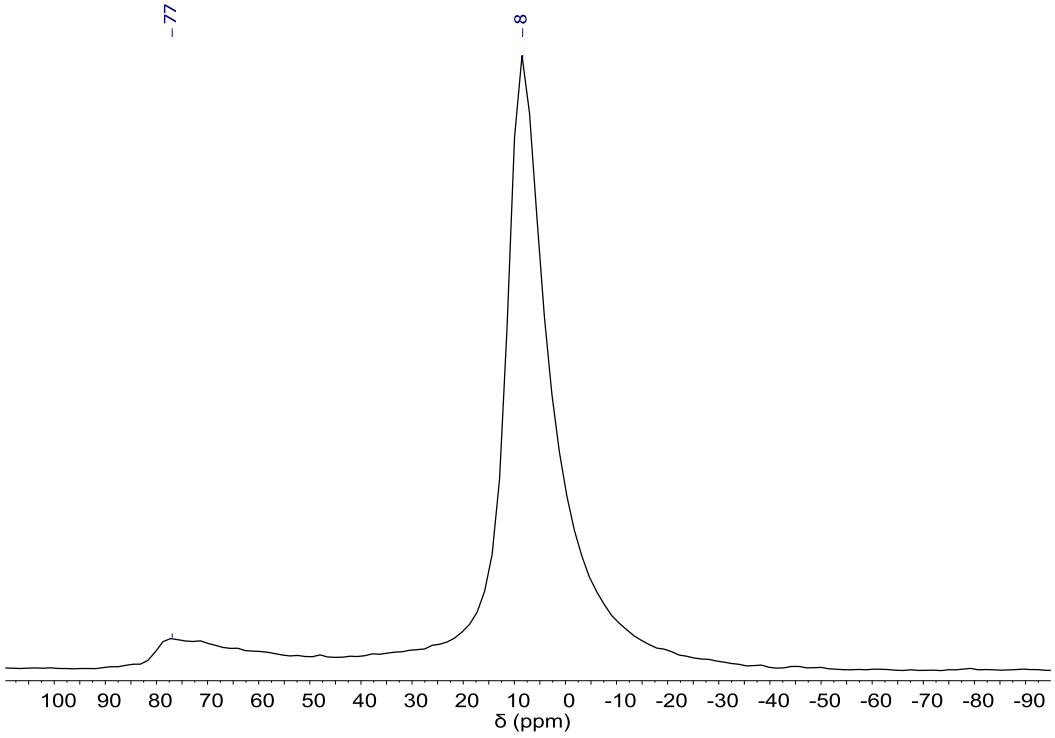


Figure A154. ^{27}Al DPMAS SSNMR spectrum (15 kHz, 400 MHz, 23 °C) of $LDH(SO_4)_{150}$-(**1.5** + 2MAO**),** formed by incipient wetness.

4.3.3. LDH$(SO_4)_{150}$-2.5

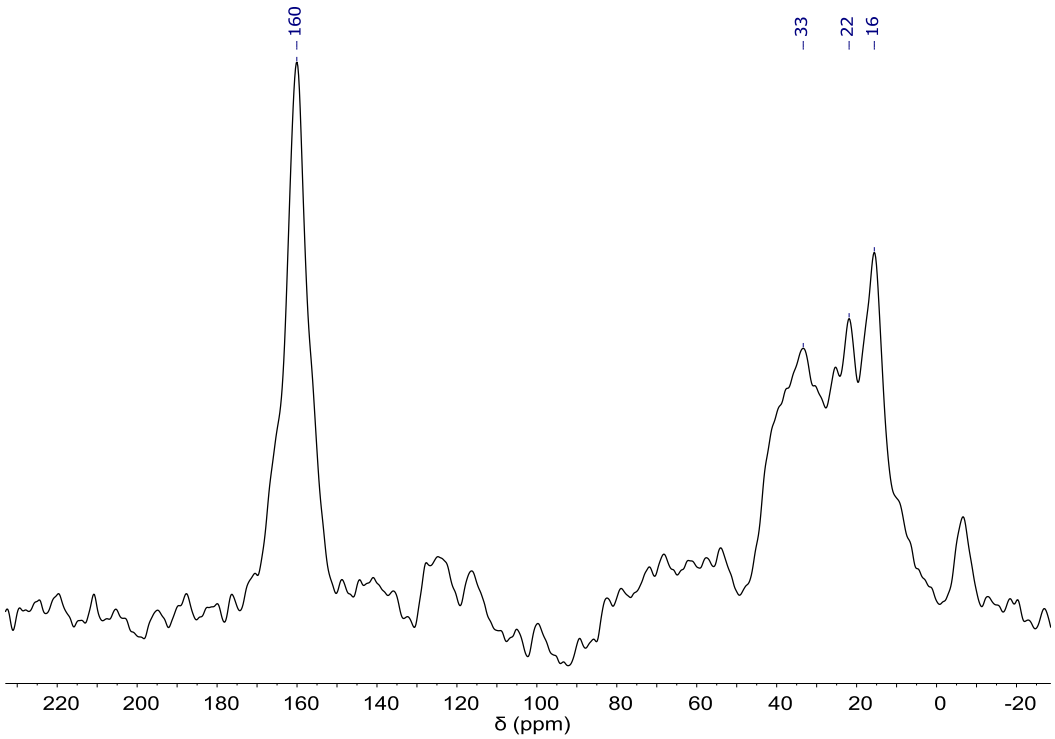


Figure A155. ^{13}C-{^{1}H} CPMAS SSNMR spectrum (10 kHz, 400 MHz, 23 °C) of LDH$(SO_4)_{150}$-**2.5**.

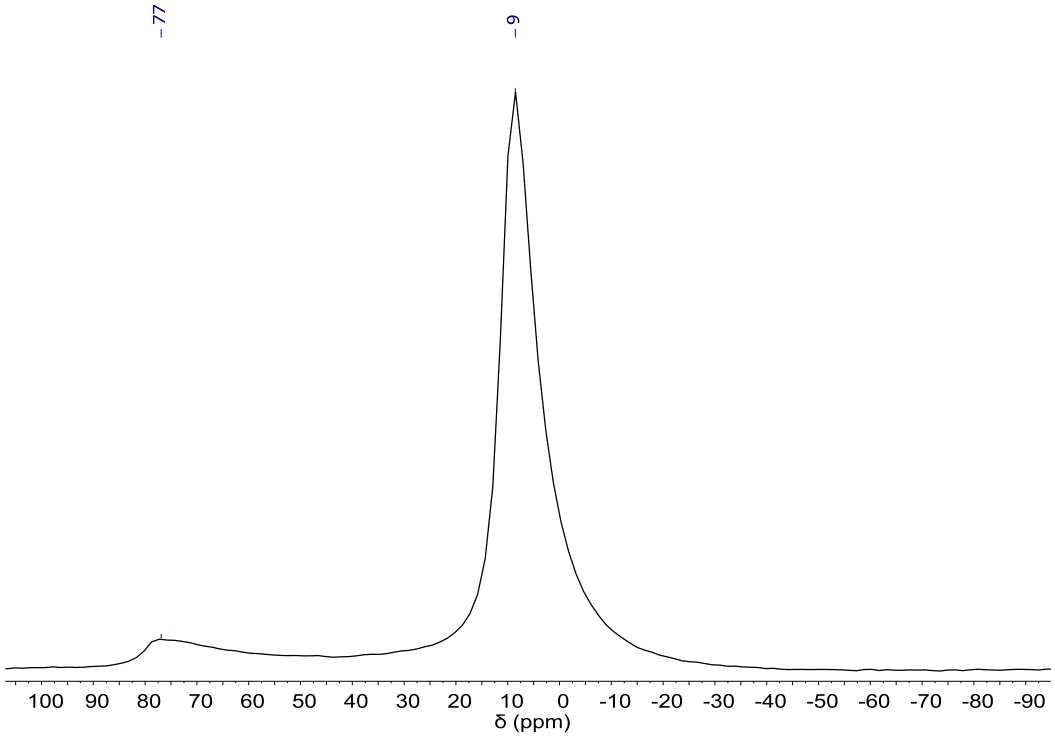


Figure A156. ^{27}Al DPMAS SSNMR spectrum (15 kHz, 400 MHz, 23 °C) of LDH$(SO_4)_{150}$-**2.5**.

4.3.4. Effect of dehydroxylating the AMO-LDH support

4.3.4.1. SSNMR spectroscopy

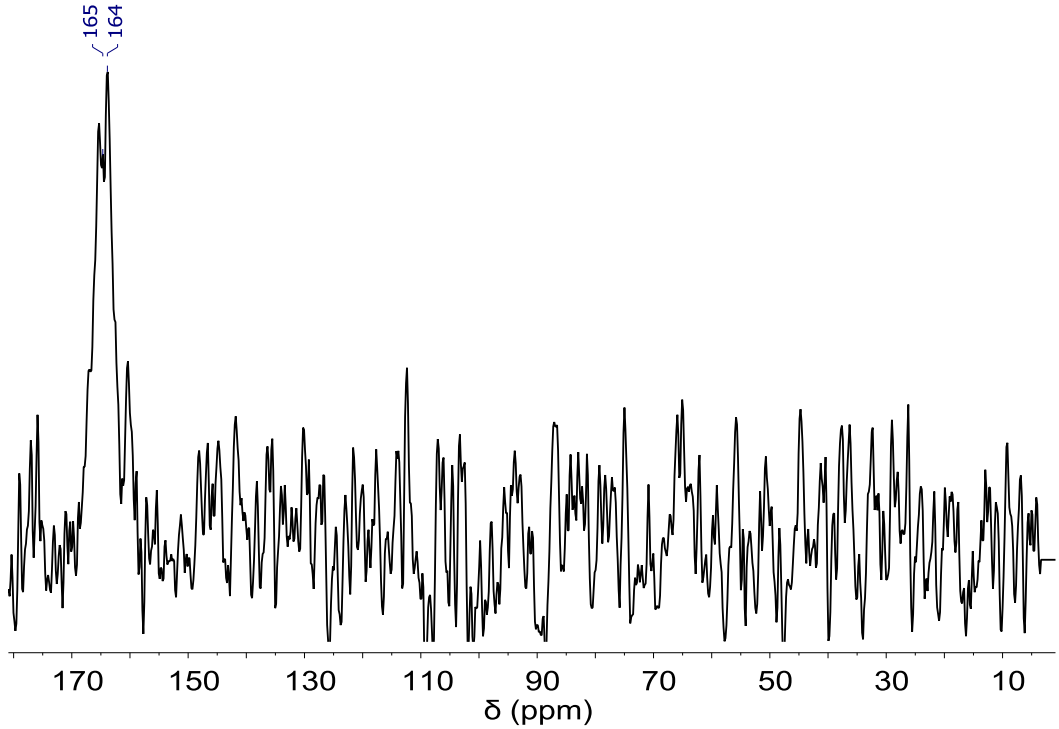


Figure A157. ^{13}C-{^{1}H} CPMAS {^{19}F} decoupled SSNMR spectrum (10 kHz, 400 MHz, 23 °C) of LDH$(SO_4)_{250}$-**2.7**.

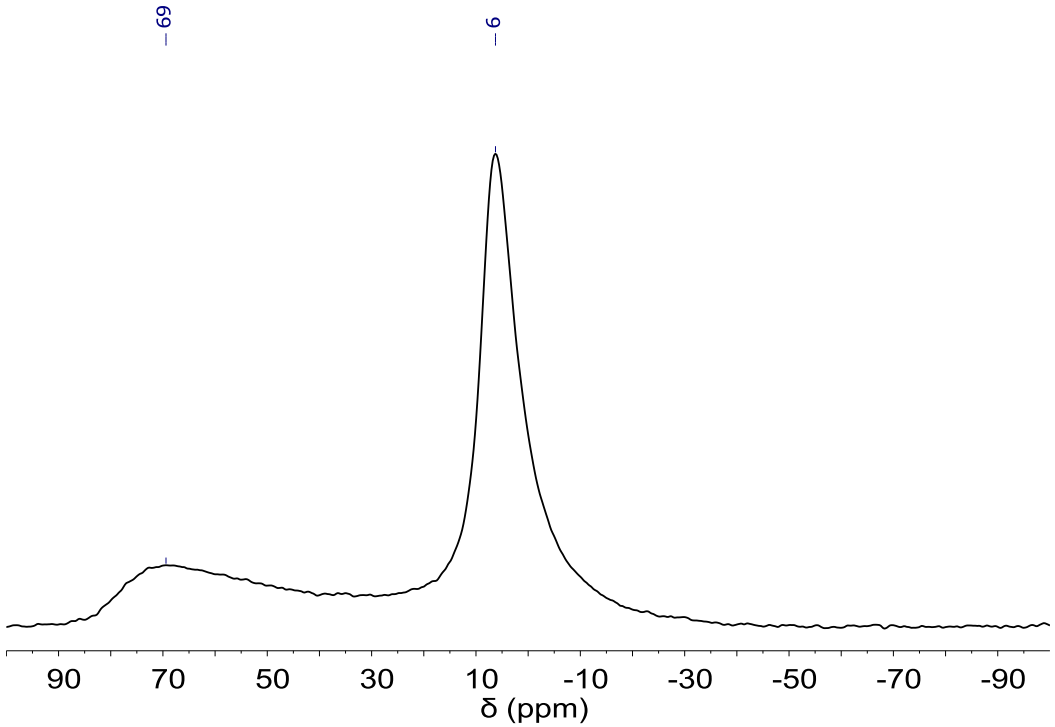


Figure A158. ^{27}Al DPMAS SSNMR spectrum (15 kHz, 400 MHz, 23 °C) of LDH$(SO_4)_{250}$-**2.7**.

4.3.4.2. FTIR spectroscopy

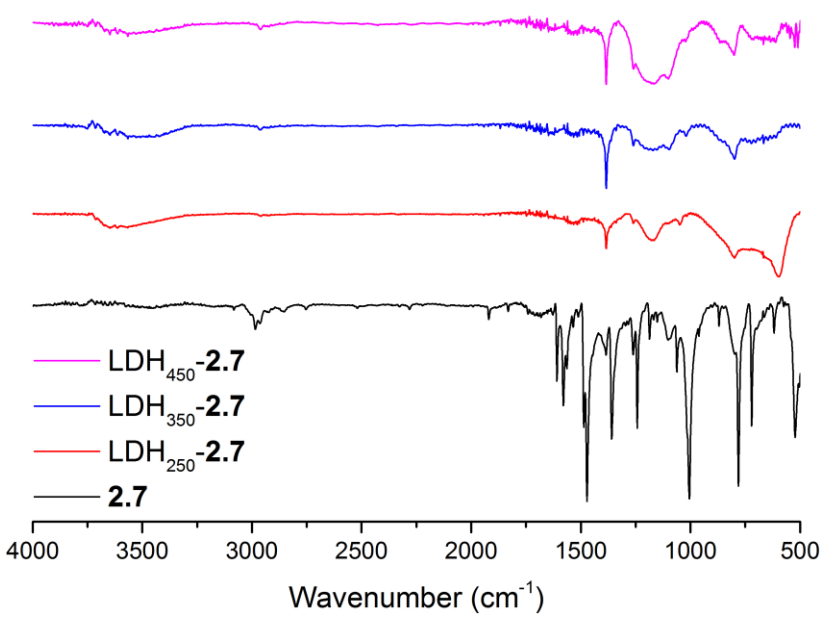


Figure A159. Comparison of the FTIR spectra of **2.7** with $LDH(SO_4)_{250/350/450}$-**2.7**.

4.3.5. XAS analysis

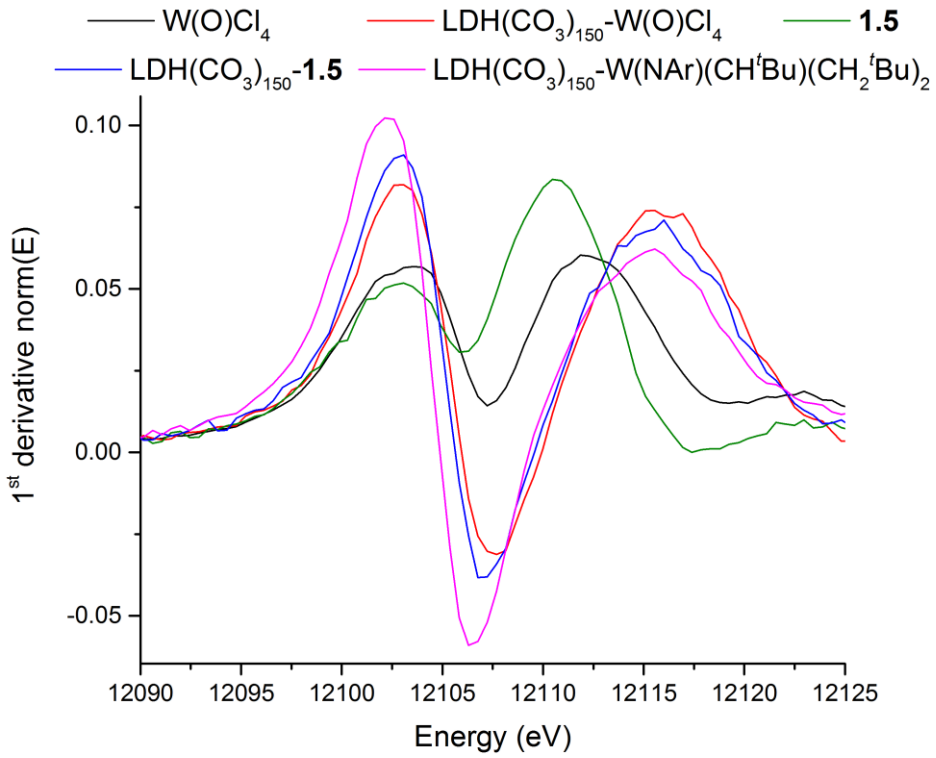


Figure A160. Comparison of the 1st derivative of the normalised W L1-edge spectra for $W(O)Cl_4$, $LDH(CO_3)_{150}$-$W(O)Cl_4$, **1.5**, $LDH(CO_3)_{150}$-**1.5** and $LDH(CO_3)_{150}$-$W(NAr)(CH^tBu)(CH_2{}^tBu)_2$ (Ar = 2,6-^{i}Pr-C_6H_3).

Appendix for Chapter Five

5.1. sMAO-Ir($^{t\text{Bu}}$PCP)HCl

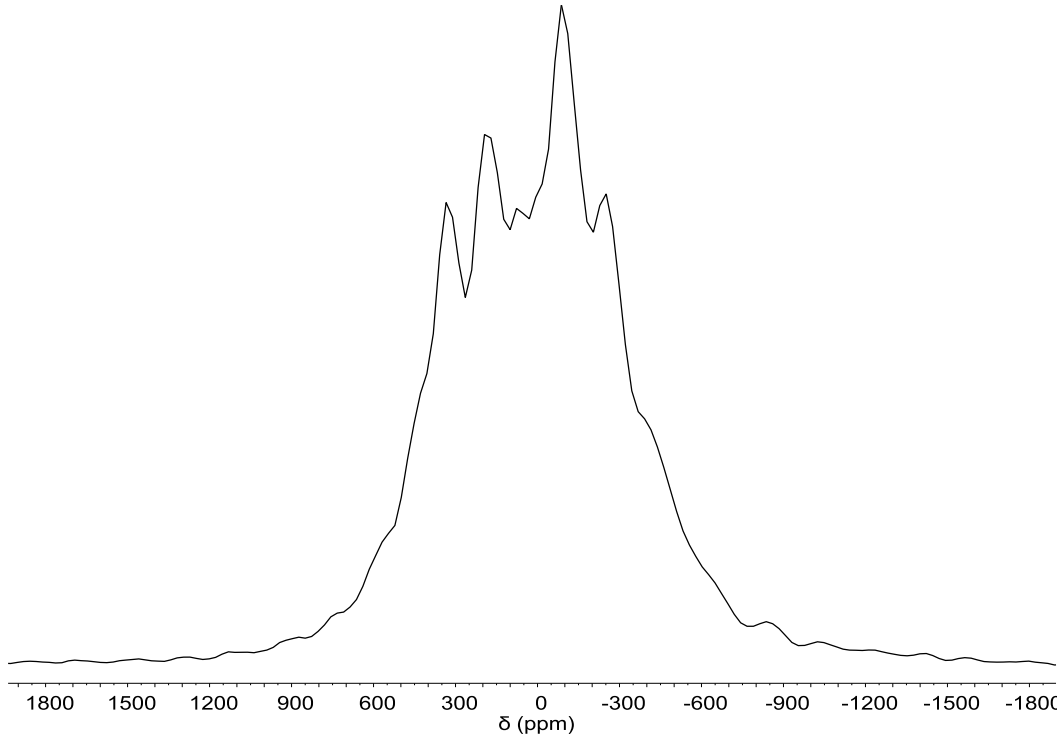


Figure A161. ^{27}Al DPMAS SSNMR spectrum (15 kHz, 400 MHz, 23 °C) of sMAO-Ir($^{t\text{Bu}}$PCP)HCl.

5.2. Reaction of Ir($^{t\mathrm{Bu}}$PCP)HCl with MAO (Al/Ir = 150)

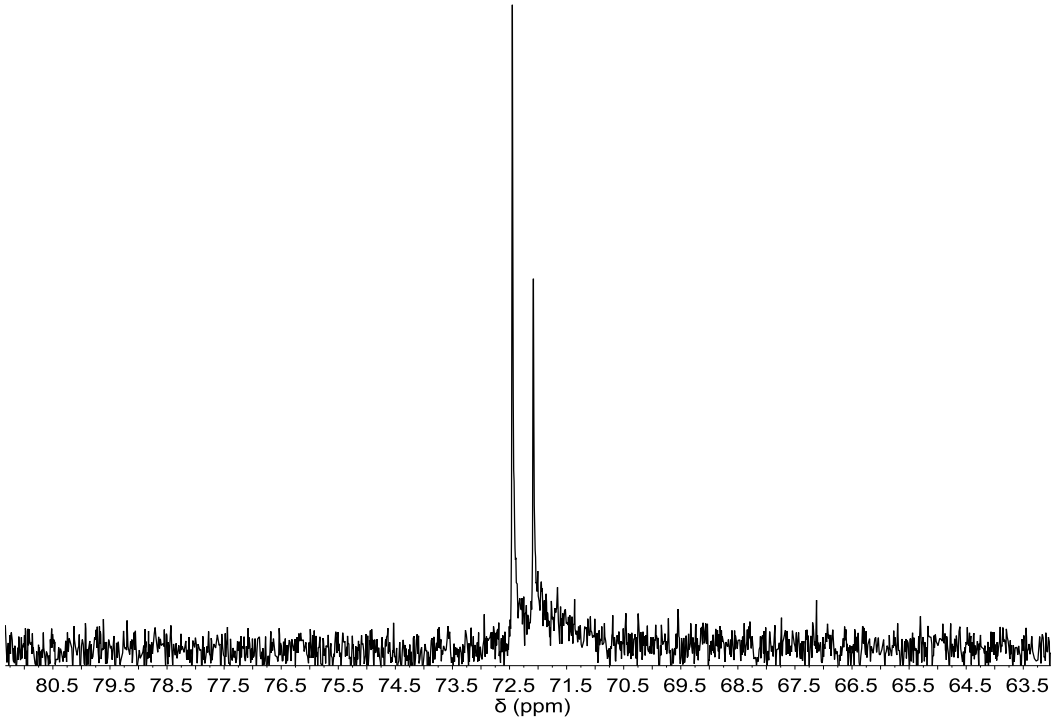


Figure A162. $^{31}P\{^{1}H\}$ NMR spectrum (400 MHz, 23 °C) of the reaction between Ir($^{t\mathrm{Bu}}$PCP)HCl and MAO (Al/Ir = 150) in d_6-benzene.

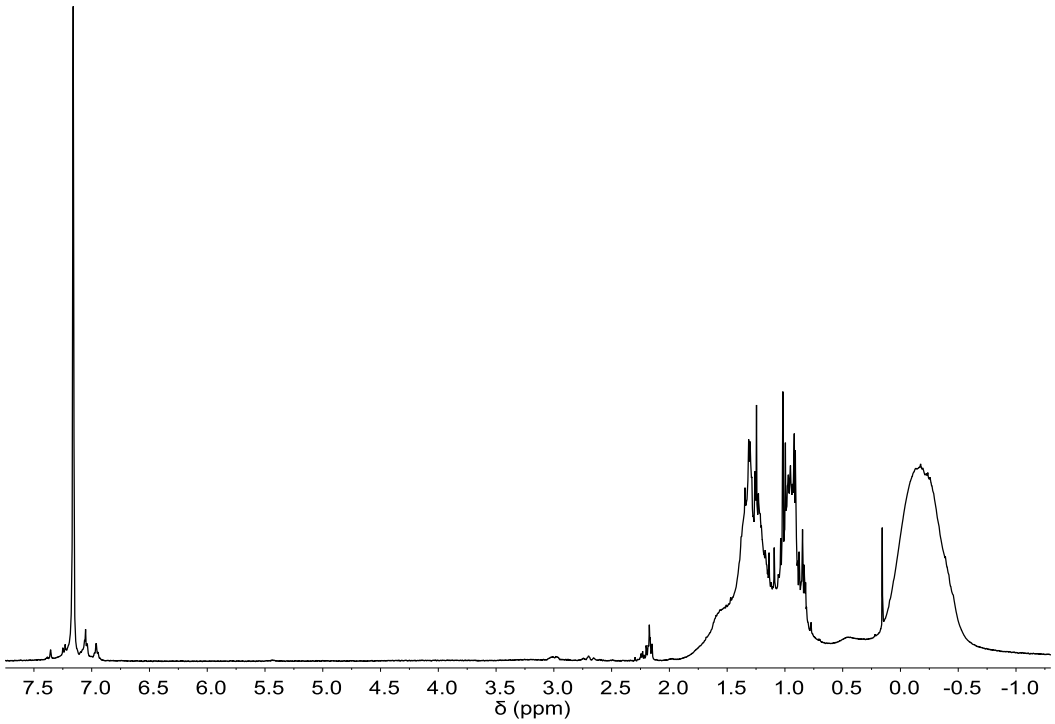


Figure A163. ^{1}H NMR spectrum (400 MHz, 23 °C) of the reaction between Ir($^{t\mathrm{Bu}}$PCP)HCl and MAO (Al/Ir = 150) in d_6-benzene (7.16 ppm).

5.3. Reaction of Ir($^{t\mathrm{Bu}}$PCP)HCl with TMA

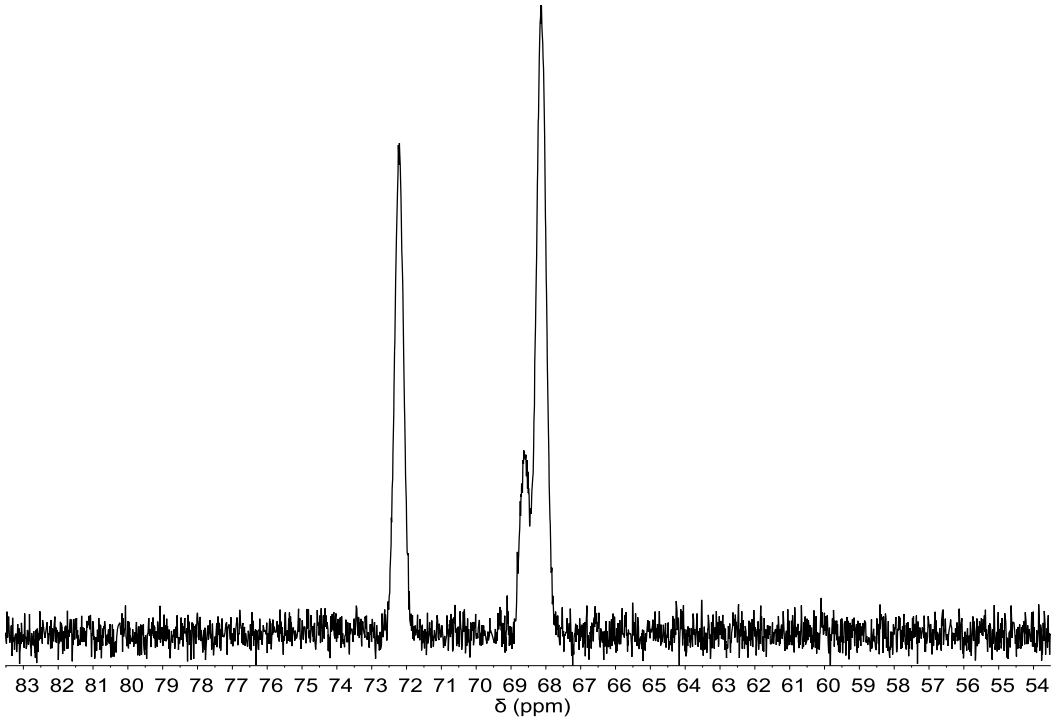


Figure A164. $^{31}P\{^{1}H\}$ NMR spectrum (400 MHz, 23 °C) of the reaction between Ir($^{t\mathrm{Bu}}$PCP)HCl and TMA in d_6-benzene.

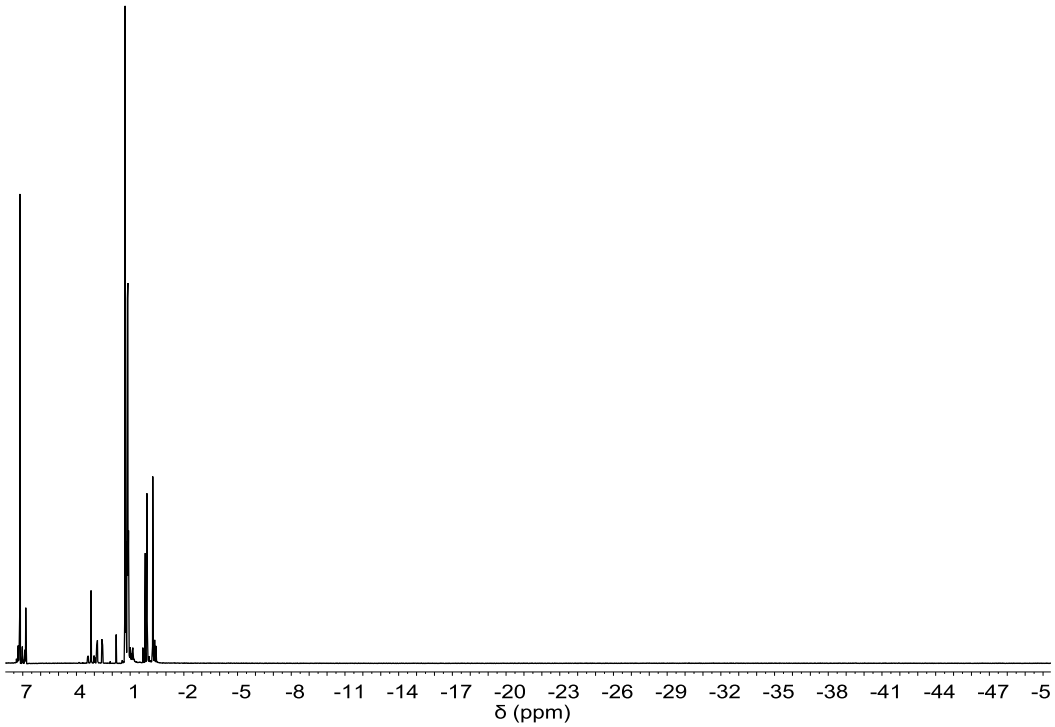


Figure A165. ^{1}H NMR spectrum (400 MHz, 23 °C) of the reaction between Ir($^{t\mathrm{Bu}}$PCP)HCl and TMA in d_6-benzene (7.16 ppm).

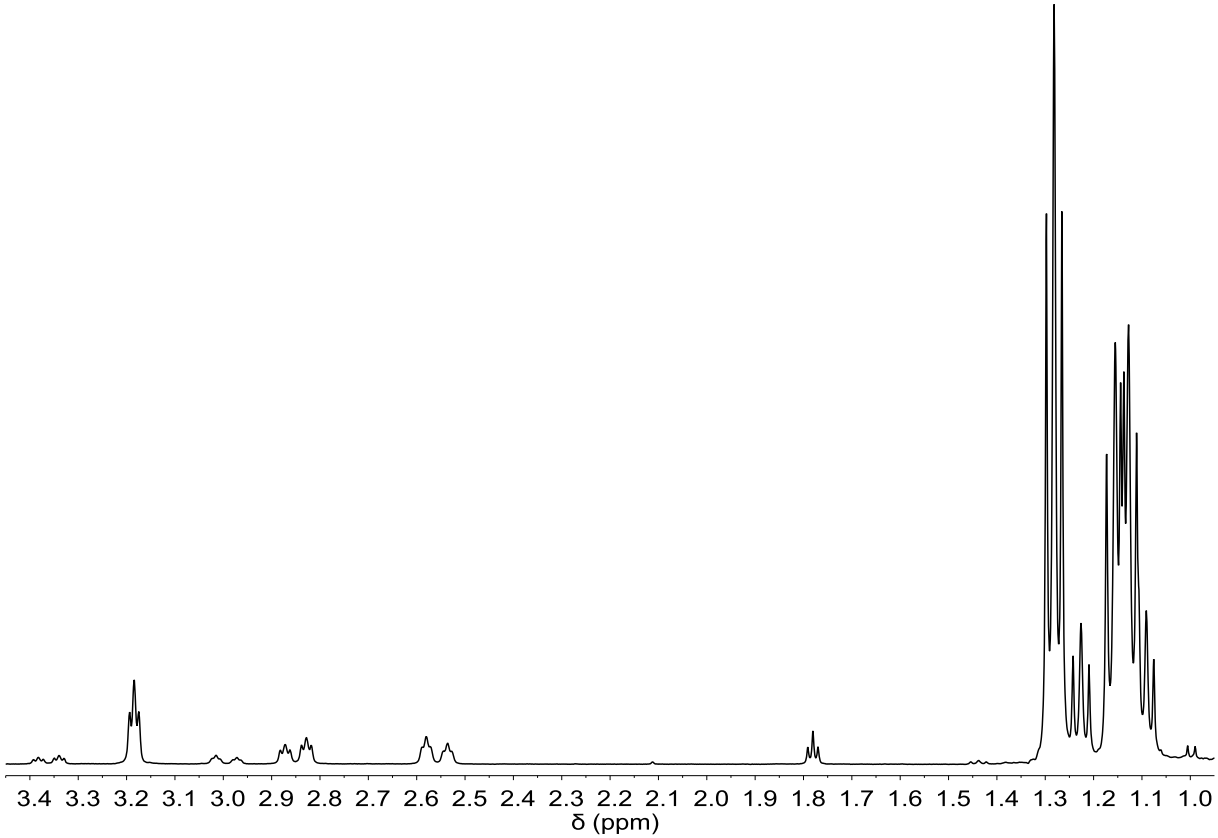


Figure A166. ^{1}H NMR spectrum (400 MHz, 23 °C) of the reaction between Ir($^{t\text{Bu}}$PCP)HCl and TMA in d_6-benzene (7.16 ppm) focussed on the region between 3.4 and 1 ppm.

5.4. Reaction of Ir($^{t\mathrm{Bu}}$PCP)HCl with NaBAr$^{\mathrm{F}}_4$

5.4.1. NMR spectroscopy

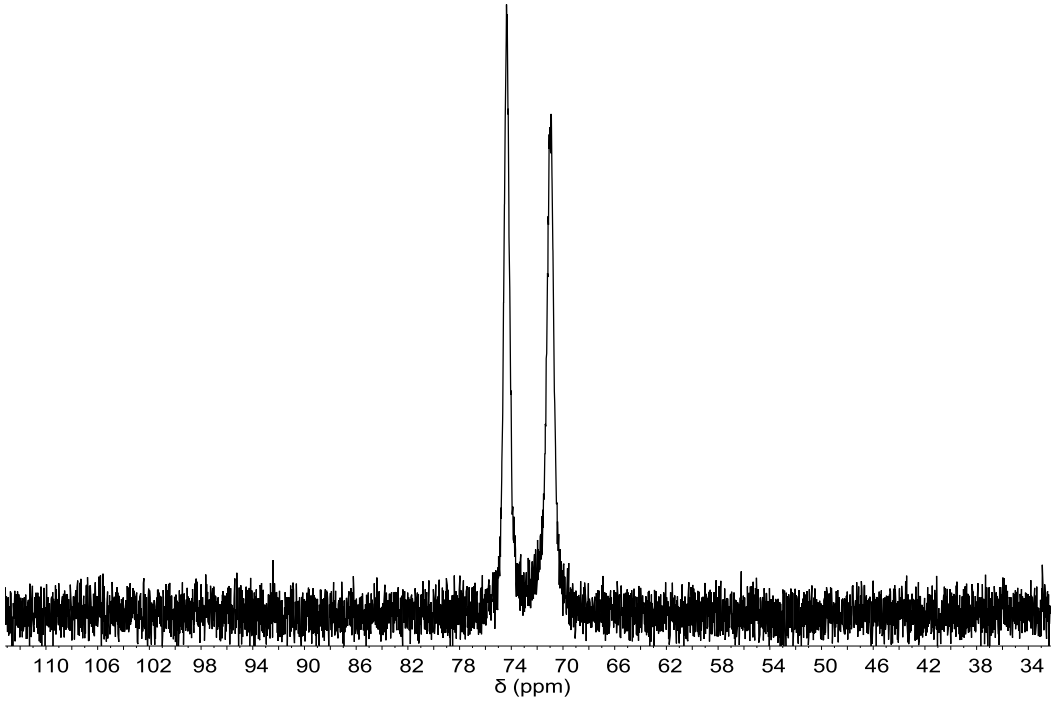


Figure A167. $^{31}P\{^{1}H\}$ NMR spectrum (400 MHz, 23 °C) of the reaction between Ir($^{t\mathrm{Bu}}$PCP)HCl and NaBAr$^{\mathrm{F}}_4$ in d_5-chlorobenzene.

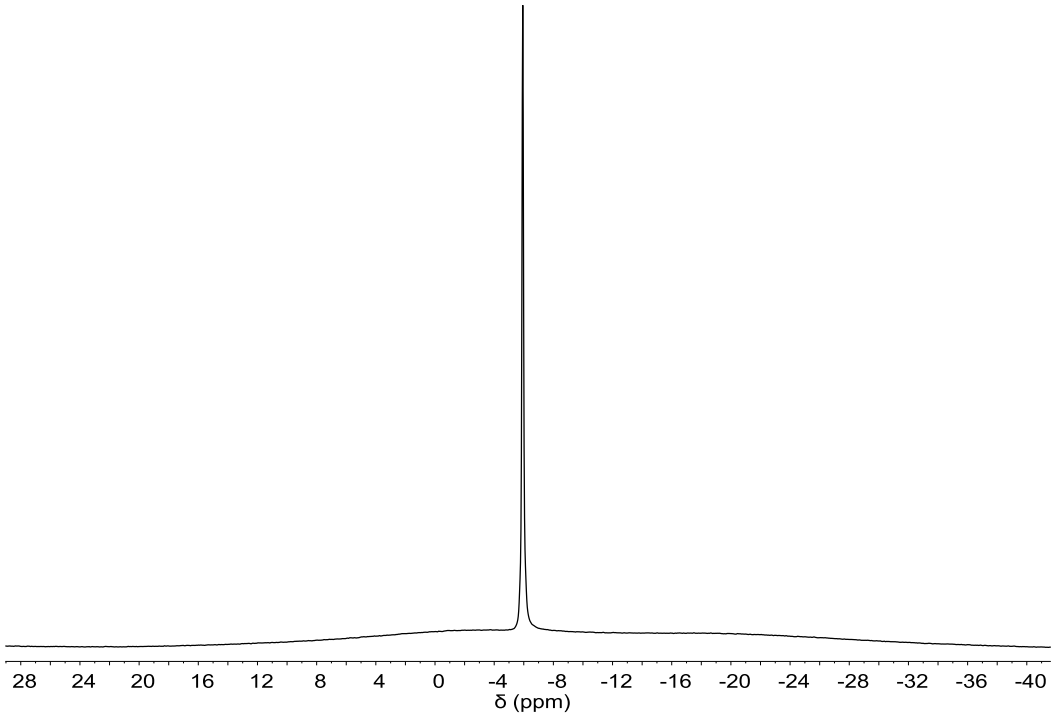


Figure A168. $^{11}B\{^{1}H\}$ NMR spectrum (400 MHz, 23 °C) of the reaction between Ir($^{t\mathrm{Bu}}$PCP)HCl and NaBAr$^{\mathrm{F}}_4$ in d_5-chlorobenzene.

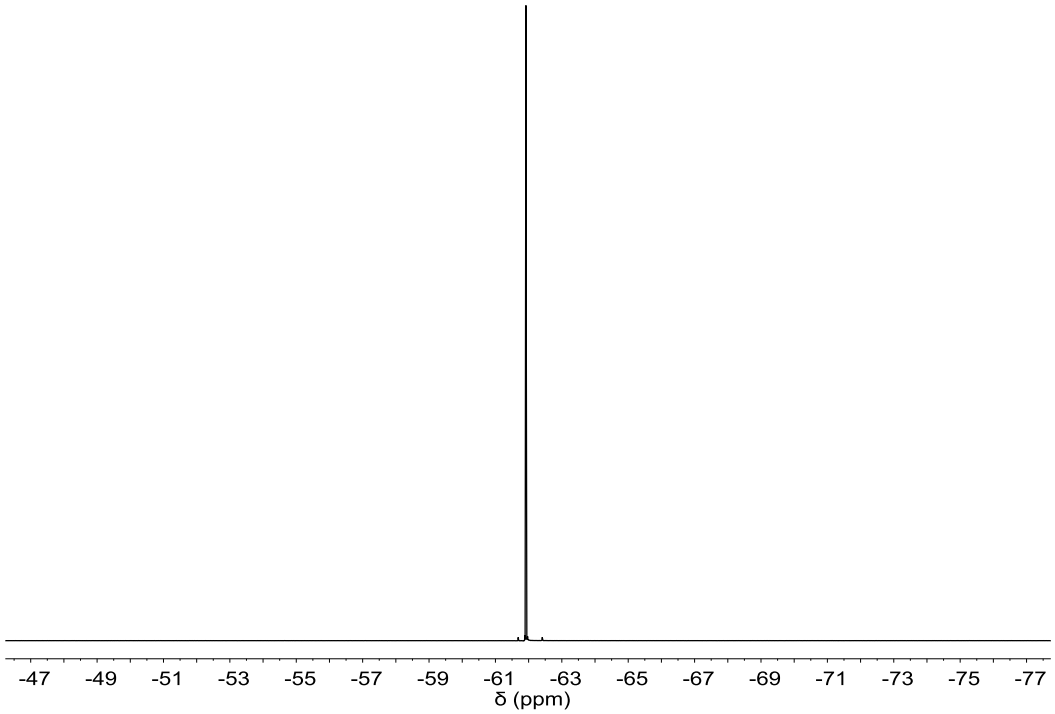


Figure A169. $^{19}F\{^{1}H\}$ NMR spectrum (400 MHz, 23 °C) of the reaction between Ir($^{t\text{Bu}}$PCP)HCl and $NaBAr^{F}_{4}$ in d_5-chlorobenzene.

5.4.2. Single crystal X-ray diffraction data table

Crystal data	
Compound **Chemical formula**	[Ir($^{t\text{Bu}}$PCP)H(N_2)][$BAr^F{}_4$] $C_{32}H_{12}BF_{24}\cdot C_{24}H_{43}IrN_2P_2$
Mr	1476.97
Crystal system, space group	Monoclinic, $P2_1/c$
Temperature (K)	150
***a, b, c* (Å)**	12.6668(3), 12.6032(2), 39.1512(8)
α, β, γ (°)	90, 96.177(2), 90
***V* (Å^3)**	6213.9 (2)
Z	4
μ (mm^{-1})	5.64
Crystal size (mm)	0.24 × 0.16 × 0.12
Data collection	
Diffractometer	SuperNova, Dual, Cu at zero, Atlas
Absorption correction	Multi-scan *CrysAlis PRO* 1.171.38.41 (Rigaku Oxford Diffraction, 2015) Empirical absorption correction using spherical harmonics, implemented in SCALE3 ABSPACK scaling algorithm.
T_{min}, T_{max}	0.718, 1.000
No. of measured, independent and observed [*I* > 2*s*(*I*)] reflections	65184, 12686, 11626
R_{int}	0.046
(sin θ/λ)$_{max}$ (Å^{-1})	0.625
Refinement	
R*[F^2 > 2*s*(F^2)], *wR*(F^2), *S	0.040, 0.097, 1.09
No. of reflections	12686
No. of parameters	881
No. of restraints	226
H-atom treatment	H-atom parameters constrained
(Δ/σ)$_{max}$	0.002
Δρ_{max}, Δρ_{min} (e Å^{-3})	1.20, −1.26
Absolute structure	-
Absolute structure parameter	-
Computer programs: Collect (Nonius BV, 1997-2000), *HKL SCALEPACK* (Otwinowski & Minor 1997), *HKL DENZO* and *SCALEPACK* (Otwinowski & Minor 1997), Palatinus, L.; Chapuis, G. J. Appl. Cryst. 2007, 40, 786-790., *SHELXL2014* (Sheldrick, 2014), *CrysAlis PRO* (Agilent (2014). Agilent Technologies Ltd, Yarnton, Oxfordshire, England.), *ORTEP-3 for Windows* (Farrugia, 1997), *WinGX* publication routines (Farrugia, 1999).	

5.5. Hydrogenation reactions

5.5.1. Reaction between Ir($^{t\mathrm{Bu}}$PCP)H_4 and ethylene



Figure A170. Addition of hydrogen (1 bar) to a mixture of ethylene and Ir($^{t\mathrm{Bu}}$PCP)H_4 in d_6-benzene.

5.5.2. Hydrogenation of ethylene with Ir($^{t\mathrm{Bu}}$PCP)HCl and TMA (Al/W = 1)

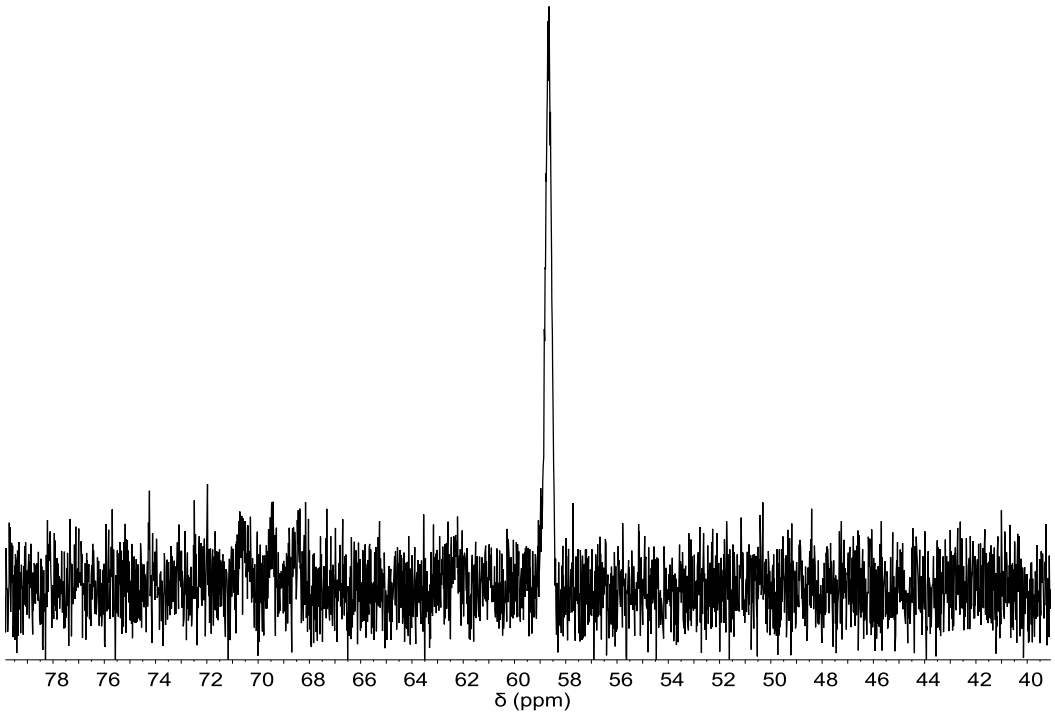


Figure A171. $^{31}P\{^{1}H\}$ NMR spectrum (400 MHz, 23 °C) straight after addition of H_2 (1 bar) to Ir($^{t\mathrm{Bu}}$PCP)HCl/TMA (Al/W = 1) and ethylene in d_6-benzene.

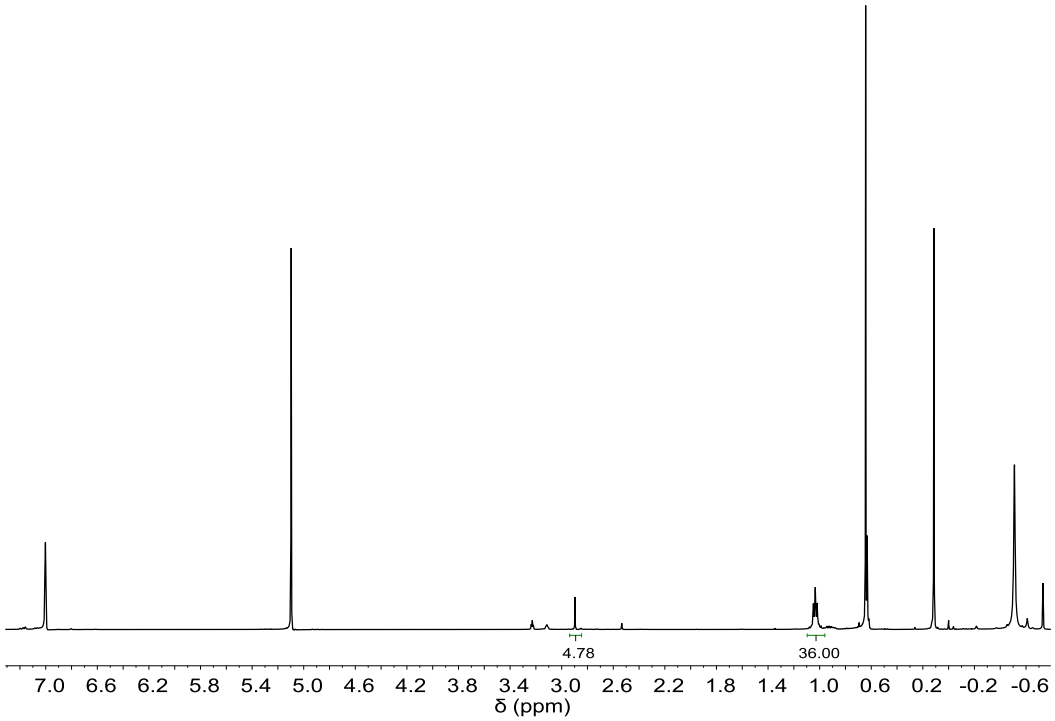


Figure A172. ^{1}H NMR spectrum (400 MHz, 23 °C) straight after addition of H_2 (1 bar) to Ir($^{t\text{Bu}}$PCP)HCl/TMA (Al/W = 1) and ethylene in d_6-benzene.

5.5.3. Reaction of Ir($^{t\text{Bu}}$PCP)HCl and MAO (Al/W = 150) with ethylene

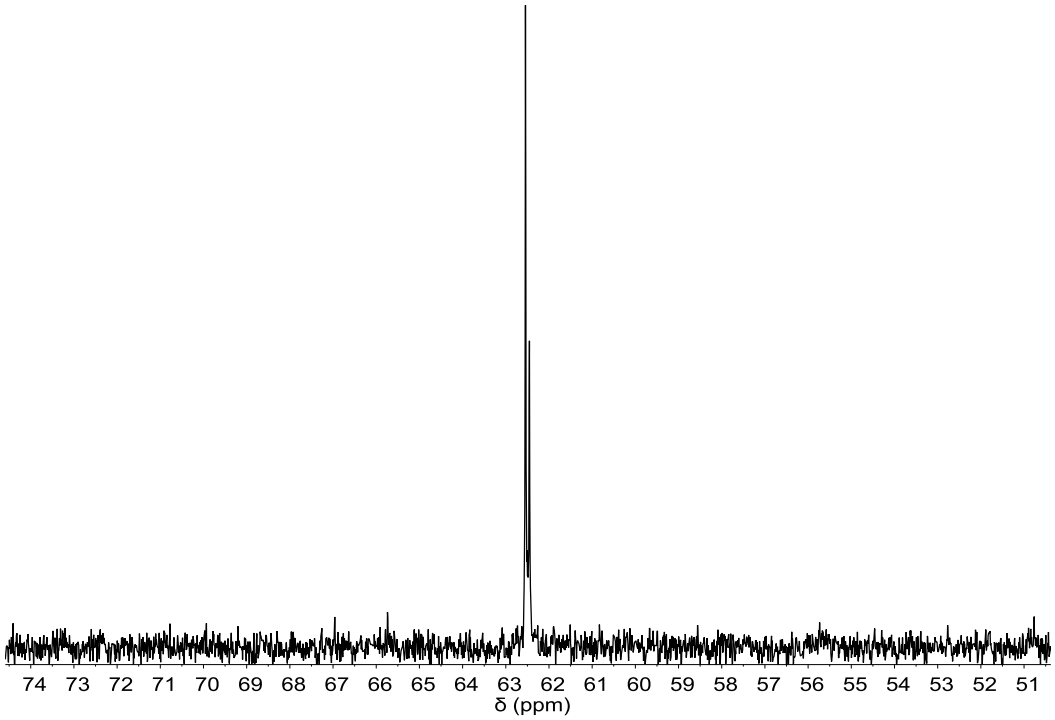


Figure A173. ^{31}P{^{1}H} NMR spectrum (400 MHz, 23 °C) after addition of ethylene (1 bar) to a mixture of Ir($^{t\text{Bu}}$PCP)HCl and MAO (Al/W = 150) in d_6-benzene.

5.5.4. Hydrogenation of ethylene with Ir($^{t\mathrm{Bu}}$PCP)HCl and MAO (Al/W = 150)

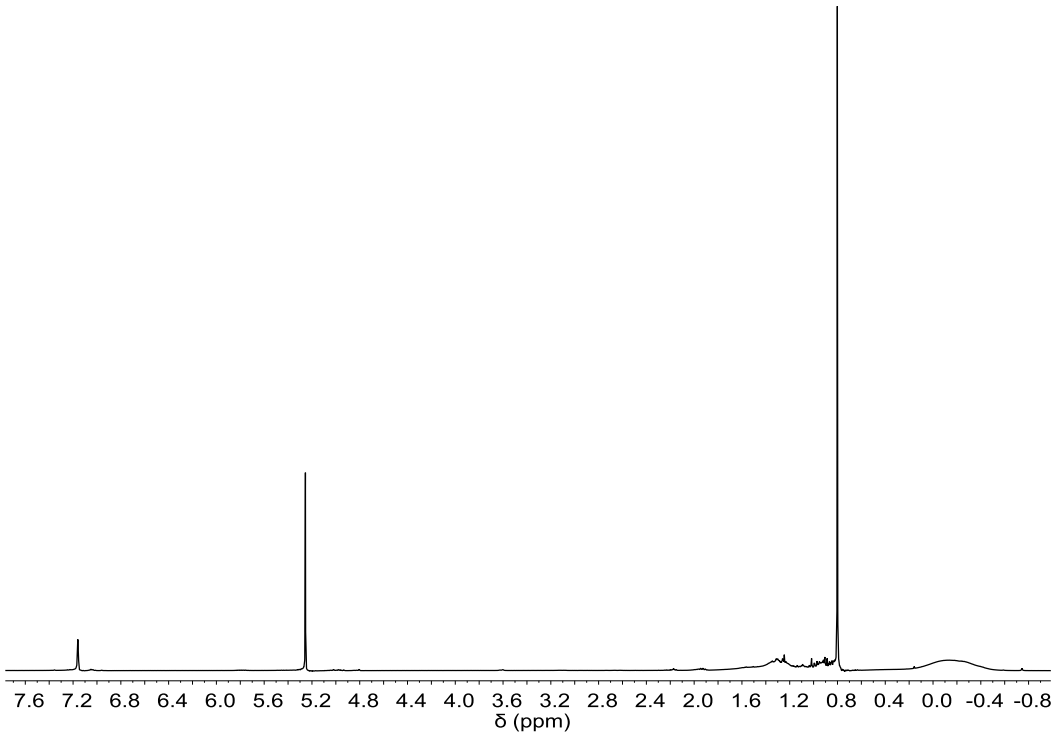


Figure A174. ^{1}H NMR spectrum (400 MHz, 23 °C) taken 15 minutes after addition of H_2 (1 bar) to a mixture of Ir($^{t\mathrm{Bu}}$PCP)HCl, MAO (Al/W = 150) and ethylene in d_6-benzene (7.16 ppm). 70% conversion of ethylene (5.25 ppm) to ethane (0.80 ppm).

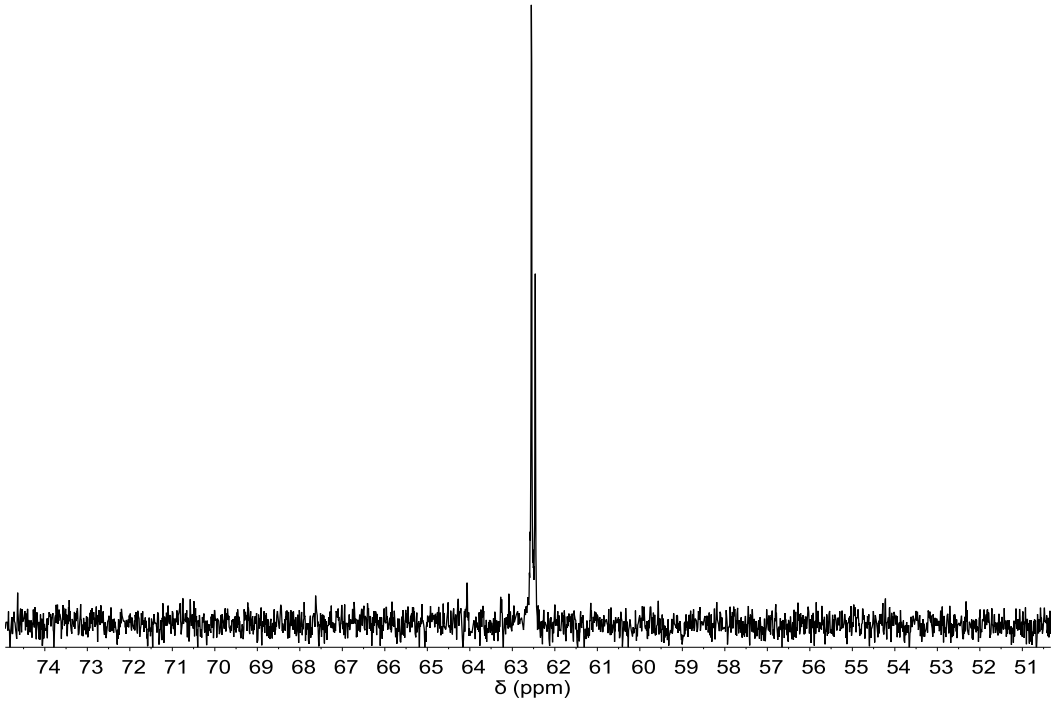


Figure A175. ^{31}P{^{1}H} NMR spectrum (400 MHz, 23 °C) after addition of H_2 (1 bar) to a mixture of Ir($^{t\mathrm{Bu}}$PCP)HCl, MAO (Al/W = 150) and ethylene in d_6-benzene.